LA-7082-PR
Progress Report
c. 4

UC-20
Issued: March 1978

LASL

Controlled Thermonuclear Research Program

January—December 1976

Compiled by

Keith S. Thomas

los alamos
scientific laboratory
of the University of California
LOS ALAMOS, NEW MEXICO 87545

An Affirmative Action/Equal Opportunity Employer

UNITED STATES
DEPARTMENT OF ENERGY
CONTRACT W-7405-ENG. 36

The four most recent reports in this series, unclassified, are LA-5250-PR, LA-5656-PR, LA-6044-PR, and LA-6582-PR.

Work supported by US Energy Research and Development Administration, Division of Magnetic Fusion.

Printed in the United States of America. Available from
National Technical Information Service
U.S. Department of Commerce
5285 Port Royal Road
Springfield, VA 22161

Microfiche	$ 3.00	126-150	7.25	251-275	10.75	376-400	13.00	501-525	15.25
001-025	4.00	151-175	8.00	276-300	11.00	401-425	13.25	526-550	15.50
026-050	4.50	176-200	9.00	301-325	11.75	426-450	14.00	551-575	16.25
051-075	5.25	201-225	9.25	326-350	12.00	451-475	14.50	576-600	16.50
076-100	6.00	226-250	9.50	351-375	12.50	476-500	15.00	601-up	--1
101-125	6.50								

1. Add $2.50 for each additional 100-page increment from 601 pages up.

ABSTRACT

This report presents the status of the Controlled Thermonuclear Research Program at the Los Alamos Scientific Laboratory for calendar year 1976.

CONTENTS

I. INTRODUCTION 1

II. SCYLLAC FEEDBACK SECTOR EXPERIMENTS 3
A. Introduction and Summary 3
B. Review of Scyllac Theory 5
C. Experimental Arrangement 7
D. Results with Feedback Stabilization in a Uniform Toroidal Discharge Tube 11
E. Results with a Helical Discharge Tube 15
F. Excluded Flux Measurements 19
G. Propagation of m = 1 Waves 20
H. Diffusion 23
I. Scyllac Magnetohydrodynamics 27
J. Scyllac Feedback System Development 32
K. Preparations for ℓ = 1,2 Equilibrium Experiments 34
L. Similarity Between Wall Stabilization and ℓ = 2 Feedback 38
References 39

III. STAGED THETA-PINCH PROGRAM 41
A. Introduction 41
B. Staged Theta Pinch 41
C. Resonant Heating Experiment 46
D. Summary 49
References 49

IV. TOROIDAL REVERSED-FIELD PINCH 50
A. Summary 50
B. Comparison of ZT-1 and ZT-S Stability Results 50
C. Field Diffusion and Ideal MHD Stability 53
D. Resistive MHD Stability 57
E. Temperature and Density Measurements on ZT-S 58
F. Plasma Impurities 60
G. Energy Balance Measurements on ZT-S 64
H. ZT-40 Toroidal, Reversed-Field Z-Pinch 64
References 66

V. SCYLLA IV-P LINEAR THETA-PINCH EXPERIMENTS 67
A. Introduction 67
B. Experimental Arrangement 67
C. Experimental Results Without End Plugs 69
D. Plasma End Loss Studies 76
E. Initial Experimental Results with Solid End Plugs 83
References 86

VI. GUN INJECTION EXPERIMENT 88
A. Introduction 88
B. Experimental Results 89
C. Summary and Plans for Further Investigation 92
References 93

VII. SCYLLA I-C, LASER-PLASMA INTERACTION STUDIES 94
A. Introduction 94
B. Interferometry 94
C. Plasma Spectroscopy 96
D. Calorimetry 97
E. Backscatter Spectroscopy 98
F. Summary 99
References 99

VIII. FIELD REVERSAL THETA PINCH 100
A. Introduction 100
B. Description 101
C. Engineering 102
D. Diagnostics 103
E. Experimental Program and Plasma Results 104
F. Conclusion 104
References 104

IX. IMPLOSION HEATING EXPERIMENT (IHX) 106
A. Introduction and Summary 106
B. Experimental Results 106
C. Diagnostic Improvements 107
References 109

X. EXPERIMENTAL PLASMA PHYSICS 110
A. Summary 110
B. Electromagnetic Wave Absorption, Plasma Heating and Energy Transport in the Q-Machine 110
C. Progress on an Experiment for Studying Nonlinear Interactions Between Plasma and Travelling Electromagnetic Waves 124
D. Q-Machine Hot Plate Development 125
References 125

XI. PLASMA DIAGNOSTICS 127
A. Introduction 127
B. Spatially Resolved Thomson Scattering 127
C. Heterodyne Interferometry 133
D. On-Line Beta Measurement for Scylla IV-P 137
E. Miscellaneous 139
References 140

XII. HIGH-BETA TOKAMAK 141
A. Introduction 141
B. High-Beta Tokamak Physics 141
C. Construction of the Proposed Machine 141
D. Comparison with Other Experiments 142
E. Problems at Long Confinement 143

XIII. THEORY 144
A. Introduction 144
B. Plasma Microtheory 144
C. Magnetohydrodynamics 152
D. Exploratory Concepts 163
References 164

XIV. COMPUTERS 165
A. Introduction 165
B. CTR User Service Center 165
C. Automated Data Processing and Computer Control 166
Reference 167

XV. ENGINEERING 168
A. ZT-40 168
B. Device and Component Development 176
References 181

XVI. MAGNETIC ENERGY TRANSFER AND STORAGE 182
A. Summary 182
B. HVDC Interrupter Tests 182
C. 300-kJ Test Facility 183
D. Superconducting Wire Development 184
E. 300-kJ, 10-kA Coil Development Program 185
F. SFTR Prototype METS System 188
G. Homopolar Development Program 191
H. Tokamak Ohmic Heating Program 192
I. Miscellaneous 194
References 195

XVII. MAGNETIC CONFINEMENT SYSTEMS STUDIES 196
A. Introduction 196
B. Systems Studies 196
C. Neutronic Studies 208
D. Insulator Research 211
E. Alloy Research 214
F. Applications of Laser Fusion-Feasibility and Systems Studies 215
References 216

XVIII. INTENSE NEUTRON SOURCE FACILITY 218
A. Introduction 218
B. Intense Neutron Source Facility 218
C. Beam-on-Target Facility 219
References 222

PUBLICATIONS 223

I. INTRODUCTION

F. L. Ribe, G. A. Sawyer, K. S. Thomas

During 1976, the Scyllac experiment was operated as an 8-m sector with derated plasma parameters to allow for greater feedback control of the plasma column motions. Experiments were conducted using discharge tubes both with and without helical distortions. In both cases, improvements in the feedback system and the addition of helical trimming windings extended plasma confinement from 10 s to 25 s. An improved theoretical and experimental understanding of the variations in plasma equilibrium with time was obtained indicating that the loss of plasma confinement was the result of loss of equilibrium. Design and fabrication was begun on an $\ell=1,2$ helical system which should greatly reduce the equilibrium problems.

The Staged Theta-Pinch experiment achieved its primary goal of producing large diameter, high-temperature theta-pinch plasmas using separate implosion and compression capacitor banks. In addition, the experiment operated at full design voltage much more reliably than could be expected of a "state of the art" device. Results from the Resonant Heating experiment motivated several important improvements in the hybrid computer code and provided a better understanding of the plasma behavior during the first microsecond.

In the Reversed Field Pinch program, experiments were carried out on ZT-S, a scaled-up version of ZT-I. Plasma confinement time was found to scale as the square of the plasma minor diameter. A new larger device, ZT-40, was proposed, reviewed, and given approval for construction. The basic objectives of the new experiment will be to extend the confinement time to a few hundred microseconds, operate in a regime of low impurities so that the radiation barrier is overcome, and explore the production and maintenance of stable configurations for both field programming and self-reversal modes of operation.

The Scylla IV-P experiment began operation in January. Plasma parameters and stability characteristics were determined. Plasma end loss was measured and a detailed study of plasma flow out the ends was conducted. Initial end-stoppering experiments using quartz end plugs were carried out. The results indicate that the insertion of the plugs eliminates particle loss from the ends of the theta pinch and increases the energy confinement time.

The Gun Injection experiment, which is studying the possibility of using a gun plasma to replace the implosion-generated plasma in a theta pinch, became operational. Studies of the plasma produced by the gun and of its penetration into a steady-state magnetic field produced by a solenoid were begun and preliminary results obtained.

Experiments on the interaction of a CO_2 laser beam with a dense, independently produced target plasma continued in the Scylla I-C experiment. Both classical (heating, refraction) and non-classical (stimulated backscatter) processes were studied. Experiments were concluded in October so that the experiment could be converted to another geometry.

A Field Reversal Theta-Pinch program was begun in July. This configuration has recently shown unexpectedly favorable stability characteristics which are of special interest to the mirror program. Two existing experiments, the Resonant Heating experiment and the Scylla I-C experiment, were converted to the field-reversal theta-pinch geometry to study this configuration in different plasma regimes.

The Implosion Heating experiment operated reliably throughout the year. Extensive measurements of density and magnetic field as a function of radius and time were obtained for a variety of experimental conditions. These measurements were found to agree remarkably well with numerical simulations performed at LASL and elsewhere.

The experimental plasma physics group continued their studies into the physics of the ac electrical resistivity and the thermal conductivity along magnetic field lines. The weak-field resistivity of a plasma, in which controlled levels of plasma wave turbulence are maintained,

was measured with a new dual mode microwave resonator technique. In another set of experiments, the actual growth in time of the parametric instabilities was observed. In addition, an experiment was begun to study the effect of a steady electron drift on plasma ac resistivity and has yielded the experimental observation of negative inverse bremsstrahlung absorption due to electron drift.

In the plasma diagnostics area, the spatially resolved Thomson scattering experiment obtained data on Scylla IV-P. High-frequency, gas-laser heterodyne interferometry was extended to longer wavelengths and development was begun on a new system which utilizes the high time resolution thus available for repeated spatial scanning of plasmas whose temporal changes occur on a microsecond time scale.

A proposal was prepared for the construction of a High Beta Tokamak. This experiment would use LASL high-voltage capacitor bank technology to produce a tokamak-like plasma with high beta values.

The theory group continued to make important contributions to the understanding of results from the experimental programs. The major success occurred in MHD theory where a much clearer understanding of the Scyllac experiment was achieved. Calculations were carried out to study equilibrium and impurity radiation in the ZT-40 experiment, to determine the effects of end plugs on a linear theta-pinch plasma and to study plasma compression by imploding liners. Work in the area of microtheory indicated that the lower hybrid drift instability may not be as dangerous as previously thought. The hybrid codes were improved and continued to have remarkable success in reproducing experimental results.

Use of the CTR PDP-10 computer and network link to the MFE Computer Center 7600 increased dramatically during the year. There were also significant advances in the use of both microcomputers and the PDP-10 for experiment control and data collection.

The primary activity of the engineering group was the design of the ZT-40 experiment. Other activities included the design and building of a quartz tube-forming machine, work on the end-fed coil, and tests on various electrical components.

Significant progress was made toward development of the superconducting magnetic energy transfer and storage system for use in future pulsed plasma devices. Two new programs were initiated in the last quarter of the year. The first was a development program to fabricate a large-energy, fast-discharge homopolar machine. The second program deals with the development of switches and superconducting coils for the pulsed ohmic heating associated with large-scale tokamak devices.

The work of the magnetic confinement systems studies group was primarily concerned with the continuing reassessment of pulsed, high-beta systems. Areas of general research included thermal-shock analyses, MHD effects in reactor-like, high-beta plasmas, transient neutral gas charge exchange, and more realistic plasma engineering modeling. The neutronics task was supportive of both RTPR blanket redesign and the more general needs of the national fusion community. The chemical, structural, and electrical effects in CTR-related insulators were addressed by the insulator research task, and the alloy reasearch task pursued the thermal-shock testing of various first-wall specimens.

Design and engineering work continued on the Intense Neutron Source Facility. Primary emphasis during the year was the final design and testing leading to the operation of a Beam-On-Target test stand which will utilize a proton beam on a hydrogen gas jet target.

II. SCYLLAC FEEDBACK SECTOR EXPERIMENTS

R. R. Bartsch, E. L. Cantrell, B. L. Freeman, K. B. Freese,
R. F. Gribble, F. C. Jahoda, K. J. Johnson, R. Kristal,
K. J. Kutac, G. Miller, W. E. Quinn, R. E. Siemon

A. INTRODUCTION AND SUMMARY

The purpose of the Scyllac experiments is to study and achieve plasma equilibrium and stability of a theta-pinch plasma in the toroidal geometry of a large aspect ratio, high-beta Stellarator. The fundamental idea is to bend a theta pinch into a toroidal configuration in such a way as to retain as nearly as possible the advantages of a linear theta pinch, while eliminating particle end loss and thermal conduction to the ends. In a torus the combination of plasma pressure and the gradient of the toroidal compression field produce an outward force on the plasma column. In Scyllac this toroidal force is compensated, and a high-beta toroidal equilibrium is achieved by superimposing on the main toroidal theta-pinch field a small ℓ=1 helical field along with an even smaller ℓ=0 and/or ℓ=2 field. Such a configuration is MHD unstable for long wavelength m=1 modes, which moves the plasma bodily off the equilibrium circle. Higher order m modes (m<2) are stabilized by finite-Larmor-radius effects. Stabilization of m=1 modes can be provided by either feedback or wall stabilization, and the physics is similar for both cases. The present confinement experiments use a conventional, unstaged, highly compressed theta-pinch plasma, and therefore feedback control is being used for plasma stabilization.

Scyllac equilibrium using ℓ=1,0 fields has been studied experimentally at Los Alamos in several configurations, the 5-m sector[1] (R=2.38 m), the 8-m sector[1] (R=4 m), the full torus[2] (R=4 m), and the feedback sector[3] (R=4 m). In each of these experiments it was possible to change the plasma motion from toroidally outward (roughly uniformly around the length of the machine), terminating in an outer wall hit, to inward, terminating in a inner wall hit, by adjusting either the initial filling pressure, or the current in driven trimming windings. The assumption was that for some intermediate adjustment, there existed a perfect, although unstable, m=1, k=0 equilibrium. However, with the help of experiments with feedback, understanding has progressed and the situation is perceived as being more complicated. The $F_{1,0}$ equilibrium force depends both on the applied magnetic fields and the diamagnetic response, or equivalently the δ's, of the plasma. Transient oscillations of the bumpy ℓ=0 and helical ℓ=1 plasma distortions, δ_0 and δ_1, develop in setting up the plasma equilibrium.[4] An oscillatory axial plasma motion (period ~ 10 μs in the feedback sector) results between regions of maxima and minima in the magnetic field with a corresponding oscillation of δ_0. Thus an oscillation of the equilibrium compensating force, $F_{1,0}$, occurs which makes it difficult to control the plasma during the transient phase and to achieve the desired equilibrium at later times. The δ_0 transient occurs because the plasma is produced in a discharge tube with uniform cross section beginning with a homogeneous gas fill. The plasma implodes to an approximately uniform column on the discharge tube axis with the subsequent development of the plasma distortions δ_0 and δ_1 which overshoot their equilibrium values and oscillate. The use of a helical discharge tube has eliminated the δ_1 helical oscillations and the use of a bumpy helical tube could eliminate the slower more troublesome δ_0 oscillations.

Experiments show a correlation between the δ_0 oscillation and an oscillation of the net force acting on the plasma as measured by the column acceleration. The measured magnetic flux excluded by the plasma column also shows the δ_0 oscillations. Both experiment and theory indicate that the δ_0 plasma distortion is nonsinusoidal with a peaking in the regions of magnetic field minima. A possibly quite significant observation is that both luminosity and excluded flux measurements indicate a decay of the δ_0 distortion

in time, owing to a decrease of plasma radius in the field minimum region.

Barnes and Brackbill have succeeded in finding ℓ=1,0 diffuse profile equilibria with a 3-D MHD code.[5] These equilibria require approximately 60% larger applied helical fields for β = 0.65 than predicted by the MHD sharp-boundary theory, from which the present ℓ=1,0 compression coil was designed. This implies that long-term force balance requires a higher plasma beta and/or additional equilibrium trimming fields. Force analysis of plasma trajectories in the derated sector experiment show a long-term equilibrium force imbalance in approximate agreement with the difference between diffuse-profile and sharp-boundary theories.

At the present time, new =2 equilibrium trimming circuits which provide a greater variety of field waveforms are being used to obtain a better long-term equilibrium. Since the calculations of Barnes and Brackbill show that ℓ=1,0 equilibrium does indeed exist, the equilibrium problem reduces to being able to survive the initial transient phase.

The plasma is unstable to the long wavelength m=1 mode. The growth rates and scaling of the m=1 instability have been measured in several experiments and are in agreement with small δ sharp-boundary MHD theory.[4] Feedback stabilization is being used to control the m=1 instability and provide corrections to the plasma equilibrium. The feedback system has been improved over the initial design and now has a delay-risetime response of 1.0 μs to (1-1/e) of peak current, with a maximum ℓ=2 feedback field of ~ 80 G at a radius of 1 cm. This results in a force which is 20% of the outward toroidal force. A new segmented photodiode position detector has been developed which provides a fast position signal having an accuracy of $\pm$ 1 mm.[6]

In the earlier feedback sector experiments, with a uniform toroidal tube and with an ℓ=2 prepulse applied during the preionization phase by the feedback system, closed-loop feedback stabilization controlled the plasma motions in both the horizontal and vertical planes and extended the plasma confinement from 10 to 25 μs. In the helical discharge tube the use of only closed-loop feedback stabilization controls the plasma motions in both the horizontal and vertical planes and extends the plasma confinement from 10 to 25 μs. Experimental observations indicate that the loss of plasma confinement at 25 μs results from equilibrium problems related to δ_0 and long-term force imbalance as discussed above, and perhaps to end effects. These phenomena cause the plasma column to move around with an amplitude that is outside the range of feedback control. Nevertheless, the data clearly show feedback control of the m=1 instability.

The propagation velocity of plasma motions in the end regions becomes a factor in the interpretation of results in these feedback stabilization experiments carried out in a sector rather than in a full torus. The propagation of m=1 waves, launched near the center of the sector, was observed at approximately the Alfvén speed in good agreement with the theoretical predictions of the small δ sharp-boundary model.[7] These experiments indicate that the plasma motions near the ends of the sector do propagate and appear in the center region as additional nonequilibrium forces.

In Scyllac a small change in the plasma beta, owing to losses of particles or energy either through the ends or radially, can cause a loss of toroidal equilibrium. A theoretical study of radial particle losses by resistive diffusion indicate that radial particle losses can have a significant effect in the feedback sector with its derated plasma temperatures of 100 to 140 eV. The effect of possible anomalous resistivity caused by the lower hybrid drift instability would be to produce a low-density halo surrounding the plasma column.

A magnetohydrodynamic model of the Scyllac plasma based on small δ dynamics and a sharp-boundary plasma has been developed[8] and used to reproduce the observed plasma trajectories and to predict the plasma confinement time with feedback stabilization. Given the known mechanisms for a decrease of plasma beta, the model predicts a confinement time of 30 μs without the use of auxiliary equilibrium trimming fields. Using nonlinear ℓ=0 MHD the equilibrium of a constant pressure theta-pinch plasma column has been calculated in the presence of a long wavelength

ℓ=0 field without the assumption of small plasma distortions. The calculated plasma equilibrium shape has a nonsinusoidal axial bumpiness with a local bulging in the minimum magnetic field region, which is in good agreement with the overloading of the groove regions with plasma observed in the experiments. The calculated equilibrium force, with the δ_0 oscillatory effects included, is very similar to the measured force obtained by computing the acceleration from the plasma trajectories.

A modification of the plasma position detectors to a 16-element quasi-quantized type,[6] which is sensitive only to the most intense portion of the plasma luminosity has improved the feedback system accuracy and capability. A new feedback signal processor-analyzer has been developed which analyzes the toroidal mode structure of the plasma column and drives each power module according to the weighted mode sum that represents the actual plasma position corresponding to the toroidal position of its ℓ=2 coil. An equilibrium trimming circuit has been developed to provide a current step with a waveform having a sinusoidal rise of 3.7 μs followed by a variable rise or fall of current with almost constant slope for 50 μs.

An ℓ=1,2 equilibrium configuration has been designed and fabricated for the feedback sector. This design uses a large helical plasma distortion, δ_1 ~ 3, in combination with a δ_2 elliptical plasma distortion, which is produced by a rotating quadrupole field, to achieve high-beta toroidal equilibrium. The ℓ=1,2 equilibrium configuration has advantages over the ℓ=1,0 system: it eliminates the δ_0 plasma distortion and its associated transient and anomalous effects; the equilibrium is independent of the ℓ=2 diamagnetic field of the plasma in contrast to the strong dependence on the ℓ=0 diamagnetic field in the ℓ=1,0 configuration; there is a weaker equilibrium dependence on plasma beta; and the parameters of the plasma will be uniform along the column. The larger δ_1 helical distortion is advantageous because it leads to plasma equilibria with smaller growth rates of the m=1 instability and also to a greater feedback stabilization force. The arc length of the ℓ=1,2 sector will be increased by 40%, from 8.4 to 11.7 m, over that of the present sector to help in the disentanglement of equilibrium problems from end effects.

B. REVIEW OF SCYLLAC THEORY

The simplest theoretical model that explains the important features of Scyllac is the sharp-boundary MHD model. In this model the theta-pinch equilibrium consists of a constant pressure plasma of radius a, confined by a longitudinal magnetic field B_o. The plasma pressure is $\beta B_o^2/2$ and the magnetic field inside the plasma is $B_o\sqrt{1-\beta}$. The Scyllac concept is to bend a theta pinch into a torus to eliminate end loss, with the radius large enough so that this basic configuration is only slightly perturbed.

1. Toroidal Force. Owing to the gradient in the magnetic field produced by toroidal curvature, a toroidal theta-pinch plasma experiences an outward force per unit length (divided by the mass per unit length) given by

$$F_R = \beta\, v_A^2/R \qquad (1)$$

where R is the radius of the torus and v_A the Alfven velocity, using the outside magnetic field and the constant plasma density. Because of the toroidal force, for plasma confinement in a torus additional magnetic fields must be applied to produce a compensating inward force.

2. Interference Force. Helical magnetic field perturbations $B = \nabla\chi$ with $\chi \sim \sin(\ell\theta - hz)$ in general produce a body force on the plasma. The force results from the interference of ℓ and $\ell+1$ helical fields. If the plasma shape is given by $r=a\,[1+\Sigma\delta_\rho\cos(\ell\theta - hz)]$, the body force is

$$F_{0,1} = hv_A^2 \frac{B_{\ell=0}}{B_o}\frac{B_{\ell=1}}{B_o} - \frac{ha}{2}\frac{B_{\ell=0}}{B_o}\delta_1 + \frac{B_{\ell=1}}{B_o}\delta_0 ,$$

$$F_{\ell,\ell+1} = \frac{2v_A^2}{a}\left(-\frac{B_\ell}{B_o}\,\frac{B_{\ell+1}}{B_o} + ha\,\frac{B_{\ell+1}}{B_o}\,\delta_\ell\right), \quad \ell \geq 1 \qquad (2)$$

where $B_{\ell=0}$ is the modulation of the vacuum magnetic field on axis and B is the ℓ-helical amplitude of the radial vacuum field at r=a. This force depends only on the shape of the plasma and is the force that would be experienced by a copper rod with the same shape as the plasma placed in the same magnetic field.

3. Scyllac Equilibrium. Helical magnetic fields applied to a theta-pinch plasma column cause helical deformations of the plasma shape. These are given by

$$\delta_0 = -\frac{B_{\ell=0}}{2\,B_o(1-\beta)}\ ,$$

$$\delta_\ell = \frac{B_\ell}{B_o\,ha(1-\beta/2)}\ , \quad \ell \geq 1\ . \qquad (3)$$

Substituting these values in Eq. (2) the equilibrium interference force is obtained,

$$F_{0,1} = \frac{1}{2}\,h^2 v_A^2\,a\,\beta(3-2\beta)\delta_0\delta_1\ , \quad \ell=0$$

$$F_{\ell,\ell+1} = h^2 v_A^2\,a\,\beta(2-\beta)\,\delta_1\delta_2\ , \quad \ell \geq 1. \qquad (4)$$

In Scyllac, toroidal equilibrium is achieved by using inward directed interference forces to balance the outward toroidal force.

4. m=1 Instability. A theta pinch with helical fields is MHD unstable for perturbations $\xi = \nabla\phi$ with $\phi \sim \cos(m\theta - hz)$. The m=1, k=0 instability is of greatest importance and can be understood in terms of a body force produced by ℓ and $\ell \pm 1$ helical magnetic fields. As the plasma shifts sideways an ℓ-helical magnetic field perturbation appears, in the plasma centered coordinate frame, to have additional $\ell+1$ and $\ell-1$ components. These produce a body force on the plasma that is destabilizing.

The least unstable configuration involves a large $\ell=1$ and smaller $\ell=0$ or $\ell=2$ to produce the toroidal equilibrium. The m=1 growth rate is given by

$$\gamma_1^2 = h^2 v_A^2\left[\delta_1^2\frac{2(ha)^2}{8}\,\frac{\beta(2-\beta)(4-3\beta)}{1-\beta} + \delta_0^2\,\frac{\beta(3-2\beta)(1-\beta)}{2-\beta} + \delta_2^2\,\frac{\beta(2-\beta)}{2} \pm \delta_0\delta_2\,\frac{\beta(4-3\beta)}{2} - \beta^2\left(\frac{a}{b}\right)^4\delta_1^2\right] - k^2 v_A^2(2-\beta)\ . \qquad (5)$$

The $\pm\,\delta_0\delta_2$ term (small because δ_0 and δ_2 are small) indicates that the growth rates are different for displacements in the plane of the torus (+) and out of it (-).

5. m ≥ 2 Instability. As in the case of m=1 a long wavelength m≥2 deformation of the plasma couples with an ℓ-helical magnetic field to produce $\ell \pm m$ helical fields. These produce a long wavelength m≥2 force that is destabilizing. For m=2 the growth rate is given by

$$\gamma_2^2 = h^2 v_A^2\left[\delta_1^2\,\frac{\beta^3}{2-\beta} + \beta(3-2\beta)\,\delta_0^2 + \beta(2-\beta)\,\delta_2^2\right] - k^2 v_A^2\,(2-\beta)\ . \qquad (6)$$

6. FLR Stabilization of m ≥ 2 Modes. Finite Larmor radius effects, outside of the scope of MHD, stabilizes m≥2 modes. The equation of motion for a long wavelength deformation of the plasma is modified by the addition of a shear viscous damping term due to finite Larmor radius as follows:

$$\ddot{\xi}_m - i\,\frac{m(m-1)}{2}\,\omega_c\left(\frac{r_L}{a}\right)^2\dot{\xi}_m = \gamma_m^2\,\xi_m \quad , \qquad (7)$$

where ω_c is the ion cyclotron frequency and r_L the ion Larmor radius using the magnetic field inside the plasma. This results in stability for large enough damping. The most stringent requirement for stability is for m=2. The stability criteria, neglecting the small δ_0^2 and δ_2^2 terms in the growth rate and assuming $T_e = \alpha\, T_i$, is

$$\frac{T_i(\text{keV})}{a(\text{cm})^2}\;\frac{(2-\beta)^3}{\beta^2(1-\beta)} \geq 0.4\;(1+\alpha)\;B_{\ell=1}\,(\text{kG})^2 \quad . \qquad (8)$$

7. Stabilization of m=1. Two methods of providing m=1 stability are being pursued, wall stabilization and feedback stabilization. Using wall stabilization, the problem is to produce a hot plasma in a theta pinch with a/b sufficiently large. Feedback stabilization consists of detecting long wavelength m=1 displacements and using a controlled ℓ=2 field (ℓ=2 is to be preferred over ℓ=0) to produce an $F_{1,2}$ force proportional to the plasma displacement to counteract the unstable force. For stability the delay time τ of the feedback system must be sufficiently small and in practice for successful feedback $\gamma_1\tau$ must be less than about 1/2.

C. EXPERIMENTAL ARRANGEMENT

1. Feedback Sector. The Scyllac feedback sector was specifically designed to minimize the m=1 growth rate and hence to accommodate technological limitations in the existing feedback system.[4] The time response and the output-current capability of the feedback amplifier system were insufficient to control the unstable motion with the full torus plasma parameters, Table II-I. In order to reduce the instability growth rate to a value compatible with the response time of the feedback system, the main compression field was reduced from ~ 40 kG to ~ 17 kG and the plasma parameters derated accordingly as shown in Table II-I. A 120° sector (8.4-m arc-length) of the full torus (R=4 m) was modified for the initial feedback experiments.

TABLE II-I

SCYLLAC PARAMETERS

Parameters	Full Torus Experiment	Derated Sector Experiment
B(kG)	40	17
$\tau/4(\mu s)$	3.7	3.5
a(cm)	1.0	1.0
$n \times 10^{16}(cm^{-3})$	2.7	2.0
T_e(eV)	500	120
T_i(eV)	800	120
β	0.8	0.65
$v_A(cm/\mu s)$	37.6	18.5
$\lambda_{1,0}$(cm)	41.9	62.8
δ_1	0.71	1.4
δ_0	0.16	0.2
$\gamma_1 \times 10^{-6}(s^{-1})$	0.70	0.3
$\gamma_1\tau_{FB}$	1.0	0.33

The ℓ=1,0 equilibrium field configuration for the sector was designed using MHD sharp-boundary theory and β = 0.65, consistent with the lower plasma temperature.[4] The equilibrium fields, $B_{\ell=1}/B$ = 0.4095 and $B_{\ell=0}/B$ = 0.147, were produced by machining the inner surface of the compression coil to coincide with a computed ℓ=1,0 flux surface. The theoretical value of the vertical field component, $B_v/B_o = B_{\ell=1}B_{\ell=0}/4\,B^2$, was also included in the flux surface calculations. Figure II-1 shows a section of the compression coil which has an average inner diameter of 24 cm. The ℓ=1,0 flux surface of the coil was machined by the profile-tracer method on a lathe, using a master profile produced by a three-dimensional milling machine from a computer-generated tape.

The magnetic fields generated by the shaped compression coil were probed to verify the design fields. The measurements showed that the coils produced the design value of $B_{\ell=0}$ and $B_{\ell=1}$ within the measurement error and that the ℓ=2 feedback coils do not perturb these fields. Figure II-2 shows the waveform of the main toroidal field.

The discharge tube for the sector consisted of four quartz tube sections, each with a uniform toroidal bore of 8.8 cm and an arc length of 2.5 m, and a special short section with polished regions for side-on holographic interferometry. The sections were butted with an outer ceramic

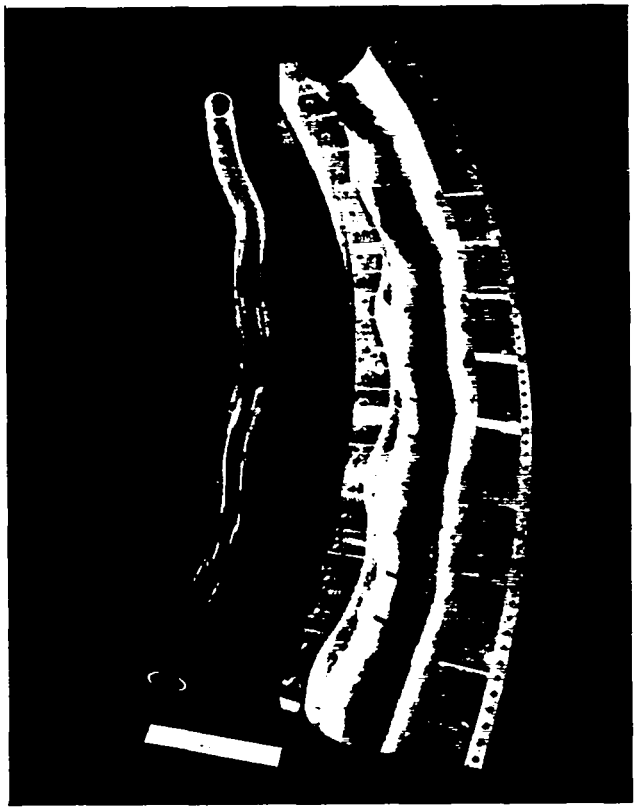

Figure II-1
Section of the ℓ=1,0 shaped compression coil and a length of the helical, toroidal discharge tube.

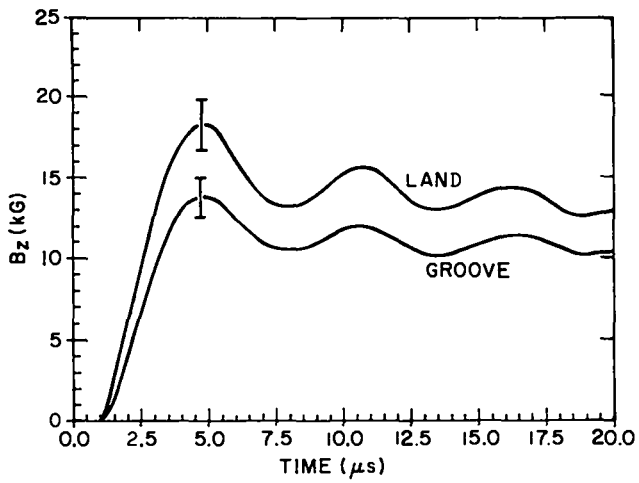

Figure II-2
Waveform of the toroidal magnetic field in regions of field maxima (Land) and minima (Groove).

ring and o-ring seals, and pumped from the ends which were electrically isolated from ground. No external path for axial z-currents was provided.

Figure II-3 shows a plan view of the sector with its various diagnostic viewing slots. The following measurements were used to study the high-beta toroidal plasma: (a) as many as six high-speed streak cameras are used to record the transverse motions of the plasma column at various locations around the torus; (b) the five feedback position detector pairs also provide plasma column trajectories in each of the sector coils; (c) a coupled-cavity He-Ne laser interferometer is used to measure the time-history of the plasma electron density along a chord of the plasma cross section; (d) two twenty-channel luminosity profile apparatuses provide self-luminous profiles of the plasma column. These luminosity profiles give the plasma radius, and in conjunction with the coupled-cavity inteferometer data, give absolute density profiles; (e) balanced magnetic loop and probe arrangements measure the magnetic flux excluded by the plasma column. Combined with the relative density profiles from the luminosity measurement, the excluded flux can be expressed in terms of the plasma beta; (f) Thomson scattering of laser light is used to determine the plasma electron temperature; (g) a side-on holographic interferometer gives space and time resolved absolute plasma electron density profiles; and (h) numerous magnetic-field probes and Rogowski loops are used to monitor the machine and feedback system.

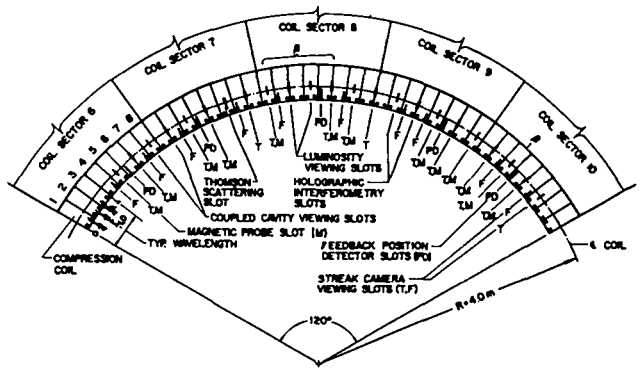

Figure II-3
Plan view of the Scyllac feedback sector showing the various diagnostic viewing slots and the collector plate current feeds.

2. Feedback Stabilization System. The feedback stabilization system, Fig. II-4, consists of four basic components: (a) plasma position detectors, silicon photodetectors, designed to detect plasma motion away from the equilibrium position; (b) intermediate amplifiers containing signal processing units, which produce an output voltage proportional to the sum of plasma position and velocity with separate gain controls; (c) power amplifier modules, each of which consists of five separate stages of amplification ending in the push-pull operation of two ML-8618 high-power triodes operating with outputs as high as 1 kA at a plate voltage of 35 kV; and (d) $\ell=2$ feedback coils located inside the main compression coil and driven by the power modules.

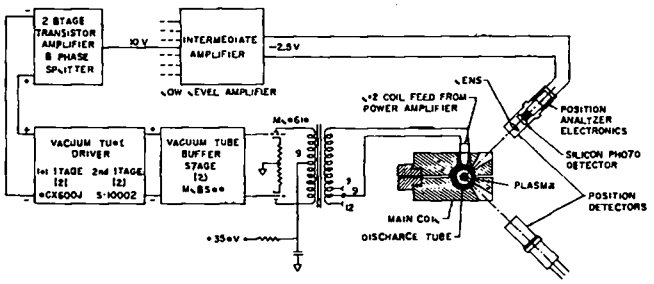

Figure II-4
Schematic diagram of the Scyllac feedback stabilization system.

Figure II-5 is a photograph of the derated sector with the feedback stabilization system installed. Five position detector stations are approximately equally spaced around the five-rack sector. Two orthogonal detectors at each station view the plasma at $\pm$ 45° to the horizontal plane of the torus at toroidal positions hz = $7\pi/8$ and hz = $9\pi/8$ in a wavelength so that the $\ell=1$ helical displacement of the plasma column should, in theory, be purely in and out along the position detector viewing direction and not be apparent to the position detectors. In practice, however, a remnant of the $\ell=1$ oscillation still appeared on the position detector signals. These detectors sense the position of the plasma column and feed the analogue processing circuits, which drive the feedback amplifiers. The outputs of the power modules are coupled through output transformers to the $\ell=2$ feedback coils.

Thirteen $\ell=2$ feedback coils, each an $\ell=1,0$ wavelength long (62.8 cm), Fig. II-6, are positioned over the quartz discharge tube inside the main compression coil. Two feedback power modules are used for each $\ell=1,0$ wavelength; one module drives one of the $\ell=2$ windings and provides the transverse force in one of the position detector directions while the second module energizes the other $\ell=2$ winding, which is rotated 45° relative to the first winding, and produces

Figure II-5
Photograph of the Scyllac feedback sector with the feedback apparatus installed.

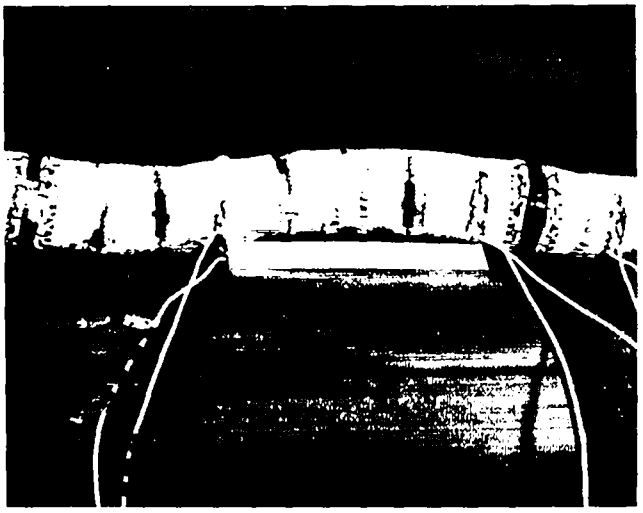

Figure II-6
$\ell=2$ feedback coils wound on Scyllac helical discharge tube with $\delta_{1,a}$ = 1.4 cm.

the force in the perpendicular direction. Each position detector controls several power modules. The electrical performance of the feedback system is monitored by the Sigma II computer by a data acquisition channel for each power module and 6 channels for each position detector and analogue processor.

The delay plus risetime, τ, of the feedback system has been measured to be 1.4 μs, to 90% of full output current. This is for a transformer turns ratio of 9:7 (27-μH module load) and standard operating conditions: 9-V filament voltage and 32.5-kV plate voltage. The delay time to 10% current output was measured to be 0.5 μs and the 90% risetime, 0.9 μs. In computing $\gamma\tau$ it is more reasonable to use a time somewhat shorter than the time to 90% of full output since the current has appreciable values before that time. Using the time for (1-1/e) = 0.63 of full output as an effective time we find τ_{eff} = 1 μs and $\gamma\tau$ = 0.3 to 0.4.

Auxiliary ℓ=0 windings were also used in the initial experiments to assist in trimming the ℓ=1,0 plasma equilibrium. Single-turn windings installed in groove and land regions were connected in series opposition in each ℓ=1,0 wavelength to provide an auxiliary force on the plasma column in the plane (horizontal) of the torus. Similar windings located midway between land and groove regions produced a force in the plane (vertical) perpendicular to that of the torus. These windings were energized by two small capacitor banks with independent triggering systems.

3. Feedback Sector with Helical Discharge Tube. Ideally the walls of the vacuum vessel in the Scyllac torus should coincide with a magnetic flux surface of the toroidal equilibrium field configurations to optimize the development of the plasma equilibrium distortions and the plasma to wall separation. In all the previous Scyllac experiments a quartz discharge tube with a uniform toroidal bore was used. In this arrangement, the theta-pinch plasma implodes to the axis of the discharge tube followed by the development of the δ_1 and δ_0 equilibrium plasma distortions. Transient effects involving δ_1 helical oscillations and δ_0 axial variations result and complicate the achievement of the toroidal plasma equilibrium. In a discharge tube which is shaped to a magnetic flux surface, the plasma should implode to the appropriate equilibrium distortions without transient oscillatory behavior.

A mechanical device for shaping a straight cylindrical quartz tube into a helical, toroidal tube has been constructed and used to fabricate helical discharge tubes, Fig. II-1 (helix radius = 1.4 cm), for the present ℓ=1,0 coil configuration. The device incorporates the original tube forming development at the Max-Planck Institute for Plasma Physics in Garching, and is also designed to have sufficient flexibility to form quartz tubes with diameters in the range of 5 to 20 cm into major toroidal radii in the range of 3 m to infinity with helical radii up to 7 cm.

The compression coil has the same ℓ=1,0 shaped inner surface used in the previous feedback sector experiments with the uniform toroidal discharge tube. There are 13 ℓ=1,0 wavelengths of the periodic ℓ=1 helical and ℓ=0 bumpy equilibrium fields.

The arrangement of the feedback stabilization system is essentially the same as in the previous feedback experiments with a uniform toroidal discharge tube. ℓ=2 feedback coils have been wound directly on the helical quartz discharge tubes, Fig. II-6. Each coil consists of two four-turn sinusoidal sections which are connected in series by external leads and have an installed series inductance of 16 μH including 1.2-m leads.

Additional single-turn ℓ=2 coils were also installed to provide fine adjustment of the toroidal plasma equilibrium. Two sets of coils separated by 45° and rotated 22.5° with respect to the feedback coils can be used to provide equilibrium correction forces in the horizontal and vertical directions. Each coil has an inductance of 3 μH. These coils are not strongly coupled to the ℓ=2 feedback coils which are oriented to provide forces at +/- 45° to the horizontal. Small, slow-rising capacitor energy storage circuits were used to drive these ℓ=2 trimming coils. Fast-rising current pulses were also available to null the slow fields at the time of the main implosion or for independent trimming. Six separate combinations of fast and slow

circuits were used to energize three sets of four adjacent wavelengths of the ℓ=1,0 field configuration in both the horizontal and vertical planes. Each circuit had an independently adjustable output of $B_{\ell=2}$ = 24 G/kA.

D. RESULTS WITH FEEDBACK STABILIZATION IN A UNIFORM TOROIDAL DISCHARGE TUBE

In initial experiments with the closed-loop feedback stabilization system applied to the Scyllac derated sector, the feedback system was successful in controlling plasma motions and the m=1 instability in the vertical plane, perpendicular to that of the torus.[4] In these initial experiments feedback was less successful in the horizontal plane because plasma m=1 motions in the plane of the torus were influenced by nonequilibrium forces of substantial magnitude which caused a loss of equilibrium. Experimental results and analyses of the plasma trajectories indicated that the loss of equilibrium resulted from transient effects in setting up the equilibrium plasma distortions, δ_0 and δ_1, in the uniform toroidal discharge tube. A transient force results from the oscillations of the δ_0 and δ_1 plasma distortions. The δ_0 oscillations, which are slower ($\tau \sim 10\ \mu s$) and involve a "sloshing" of plasma between land and groove regions, make it difficult to achieve toroidal equilibrium. The application of an ℓ=2 programmed field pulse during the initial plasma preionization phase resulted in a substantial improvement in setting the initial plasma column into an equilibrium position on the minor toroidal axis following the implosion phase of the main discharge. Subsequent application of the closed-loop feedback system resulted in improved plasma confinement to 25 μs with the feedback stabilization system successfully controlling the plasma motions in the vertical plane and extending the plasma confinement in the horizontal plane of the torus.

1. Plasma Trajectory Analysis and Equilibrium Transients. The streak photographs of Fig. II-7 show simultaneous plasma trajectories in land and groove regions in the horizontal plane of the torus without and with auxiliary fields and feedback. Upward in the streak photographs is outward away from the major axis of the torus. In

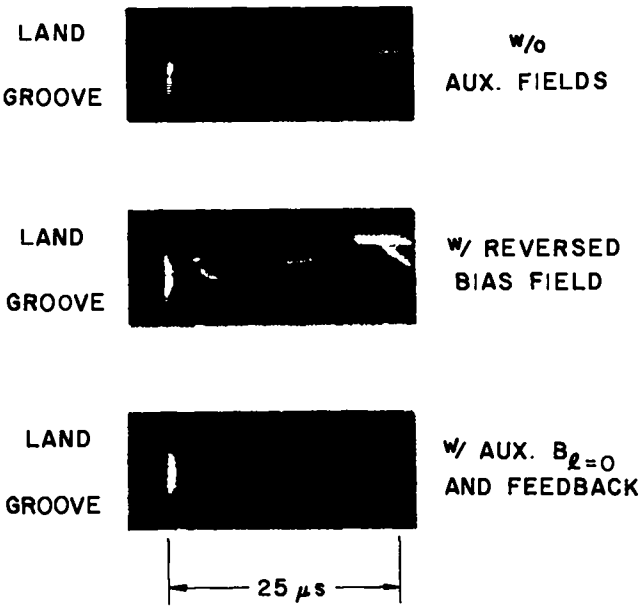

Figure II-7
Streak photographs showing plasma motion in toroidal (horizontal) plane: upper streak in each photograph is taken in region of maximum magnetic field and lower streak in region of minimum field.

each streak photograph the plasma motion is characterized by the following: (a) initial δ_1 helical oscillations which damp out; (b) a stably confined period of apparent equilibrium; (c) the helical plasma distortion δ_1, which is directly proportional to the separation of the plasma trajectories in land and groove regions; (d) a fatter plasma column in the groove region relative to the land indicating the bumpy plasma distortion δ_0; and (e) an outward m=1 motion terminating the plasma confinement. These streak photographs show that the application of auxiliary fields prolongs the onset of the outward m=1 motion.

During the initial stable period, the application of either a programmed ℓ=0 or ℓ=2 field drives the plasma column inward in the toroidal plane to the discharge tube wall. However, once the onset of the outward motion occurs, a force comparable to an appreciable fraction of the F_R toroidal force is required to overcome it. The magnitude of the force causing the outward m=1 motion indicates a loss of equilibrium in the toroidal plane, rather than just the m=1 instability. Hence the inability of the feedback system to control the outward motion. Experimental results and analyses of the plasma

trajectories indicate that the loss of equilibrium may result from the transients in setting up the equilibrium plasma distortions, δ_0 and δ_1. In particular, the time variation of the bumpy distortion δ_0 owing to variation between land and groove regions appears to be a major factor.

The trajectory of the centroid of the plasma column is obtained from the simultaneous land and groove streak photographs and is used to determine the net body force on the plasma column. The data are smoothed by fitting to a high-degree polynomial to facilitate taking the second derivative of the trajectory which gives the acceleration of the column. The net force, F_{NET}, acting on the plasma column required to produce a typical observed trajectory, upper plot of Fig. II-8 includes the destabilizing force, F_γ, which is a function of the displacement of the centroid, ξ, and the m=1 growth rate, γ, $F_\gamma \propto \gamma^2 \xi$. The force, F_X, producing the loss of equilibrium in the derated sector experiments is $F_X = F_{NET} - F_\gamma$. The lower plot of Fig. II-8 shows the time dependence of F_X obtained by correcting the net force for the position dependent F_γ. The

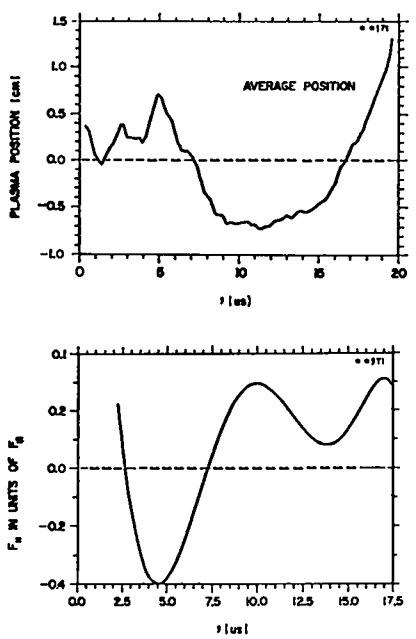

Figure II-8
Centroid position of plasma column in horizontal plane (upper plot) and the net force, F_X (lower plot), derived from the above trajectory.

force approaches an asymptotic value of 20% of the toroidal force, F_R. For successful feedback stabilization, it is required that the plasma column be located near the equilibrium position at a time when it has reasonably small momentum. Both the rapid variations as well as the magnitudes of the force and plasma excursions indicate that feedback control is marginal in the horizontal plane.

This analysis of the observed plasma trajectories, which yields the net force acting on the plasma column, indicates that transients which develop in setting up the equilibrium plasma distortions make it difficult to achieve equilibrium at late times. The effect of the reverse bias field Fig. II-7 is to produce a nearly uniform inward directed force. This permits the column to survive the initial outward force, however an increase in the reverse bias field to compensate the late time force imbalance causes the plasma to strike the inner wall owing to the inward directed transient. Similar results were obtained with programmed auxiliary fields (ℓ=0 or ℓ=2). If the auxiliary fields were applied at early times, the combined effects of these fields and the inward transient caused the plasma to strike the inner wall of the discharge tube. On the other hand, the rapid reversal of the transient force, Fig. II-8, required that a programmed field actuated after the inward transient has a risetime less than was available with the existing system. Thus, the presence of the inward transient prevents the application of programmed fields or increased reverse bias which would bring the column into equilibrium at later times.

A set of experiments were undertaken with the objective of cancelling or suppressing the inward directed transient force so that an increased reverse bias field and/or programmed field could be applied to correct the imbalance at later times. The ℓ=0 auxiliary windings were driven in the programmed mode using a small capacitor bank with switching times arranged so that the field was crowbarred on the peak of the second half cycle. When combined with the ℓ=1 equilibrium field, this ℓ=0 field provided an initial outward force followed by an inward force. In addition to the programmed ℓ=0 field, the reverse bias was

increased to a range of values which would normally drive the plasma to the inner wall at early times. Figure II-9 compares streak photographs of the plasma with and without the programmed field. Both had reverse bias; however, there was a larger reverse bias field in discharge 9467 which also had the programmed ℓ=0 field.

The streak photographs were analyzed to give the net force on the plasma column. Figures II-10 and -11 show the result of the analysis. The

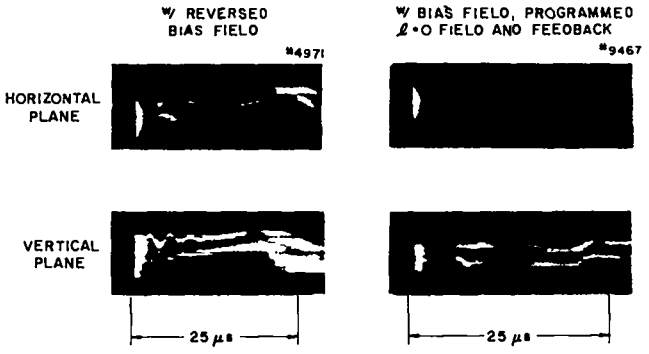

Figure II-9
Streak photographs showing plasma motions without and with ℓ=0 programmed field and feedback.

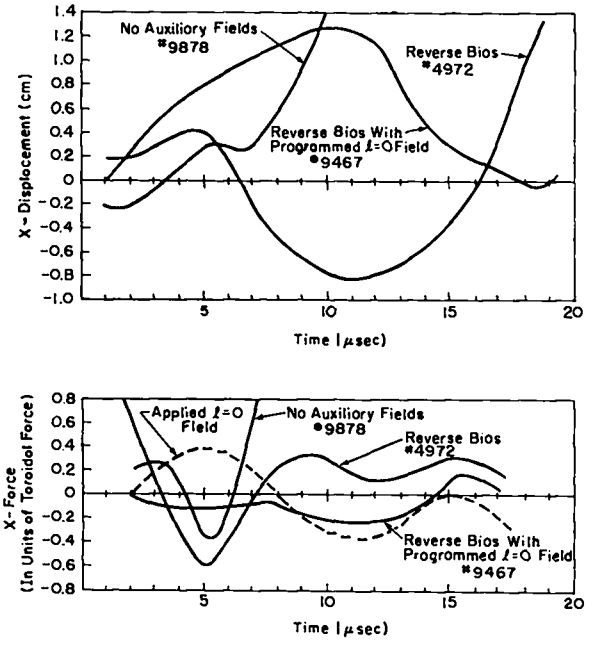

Figure II-10
Plasma trajectories in horizontal plane (upper plot) and corresponding calculated net force on the plasma column (lower plot) for the indicated auxiliary fields.

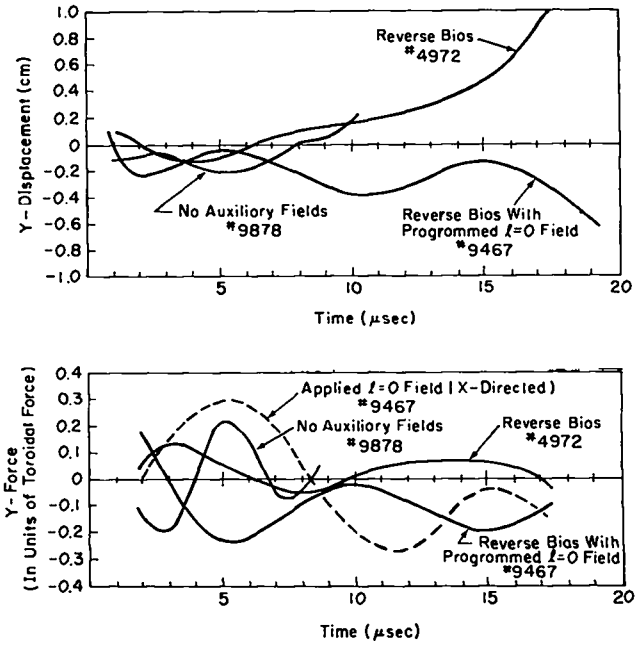

Figure II-11
Plasma trajectories in vertical plane (upper plot) and corresponding calculated net force on the plasma column (lower plot) for the indicated auxiliary fields.

trajectories for the three cases are quite different. In discharge 9878 with neither reverse bias nor programmed fields, the plasma moves rapidly outward striking the wall in ~ 10 - 12 μs. The column in discharge 4972 with reverse bias only swings inward initially but succumbs to outward forces and strikes the outer wall at ~ 20 - 22 μs. The shot with the programmed field, 9467, moves outward until ~ 10 - 12 μs and then moves back to the axis. The force analysis in Fig. II-10 (lower) shows the suppression of the inward transient by the programmed ℓ=0 force.

Analysis similar to that done for the horizontal behavior was performed for the motion in the vertical plane. With the exception of m=1 unstable motion, the plasma column has generally been well behaved in the vertical plane. The force analysis of the vertical motion, Fig. II-11 (lower), reveals that there is suprisingly strong coupling of the horizontally phased applied ℓ=0 field to the vertical plasma motion. In fact unless the feedback system was operating, the plasma would move in the vertical plane, striking the wall in ~ 12 μs. The reasons for the cross-coupling between the horizontally phased ℓ=0 field

and the vertical force are not clear. Possible explanations include imperfections in the phasing of the ℓ=0 windings (due to viewing ports, etc.) and "phase shifting" of the ℓ=1 equilibrium distortion during the δ_1 oscillations.

The results of these experiments and analyses of the transient force behavior suggest that suppression of these forces is possible using programmed auxiliary fields.

2. Feedback Stabilization Experiments with an ℓ=2.

"Preconditioned" Plasma. A study of the effect of an applied ℓ=2 field on the plasma in the Scyllac Feedback Sector Experiment during the preionization and implosion phases was motivated by proposed experiments which would use capacitor driven ℓ=2 fields to "trim" the plasma equilibrium and might necessarily be applied during these times of the discharge. The ℓ=2 field was generated by operating the feedback power amplifiers in a programmed mode to provide pulses of variable time width and amplitude. The presence of the ℓ=2 field during the implosion phase did not improve the plasma behavior.

The results obtained when the ℓ=2 field was applied during the initial plasma preionization phase were quite different from previous observations made on the preionization itself and in subsequent plasma column motion after implosion. Characteristically, a ringing theta preionization field will cause plasma ionization during the first zero crossing of the field. With the ℓ=2 prepulse, ionization did not begin until the second zero crossing and continued to increase through the third and fourth zero crossings. With the onset of the implosion and subsequent plasma formation, the compressed column formed more in the central portion of the discharge tube, Fig. II-12 (# 9933), without the characteristic outward shift (Fig. II-12, # 9878), and the terminating motion was of a different nature than that observed without the ℓ=2 programmed pulse. An interesting aspect of this behavior is that the spatial phase of the ℓ=2 field relative to the ℓ=1 helical equilibrium field was unimportant. This lead to early speculation that the net effect of the presence of the ℓ=2 field at preionization time was to cause the ionization to take place

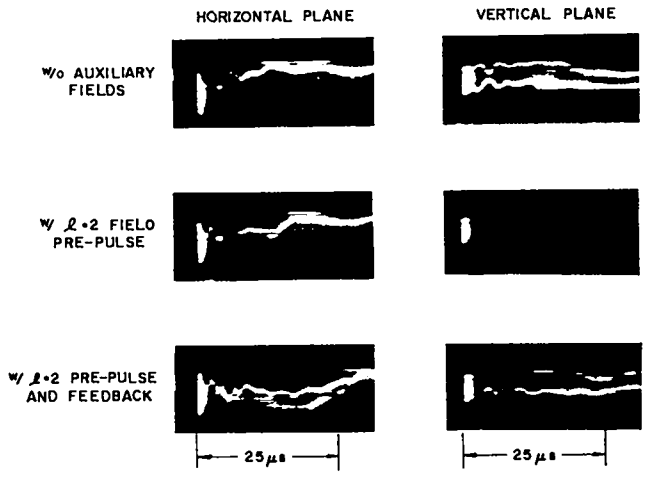

Figure II-12
Streak photographs of plasma motions showing the effects of a prepulse of an ℓ=2 field without and with feedback stabilization.

from the center of the tube toward the wall which would tend to exclude trapped magnetic fields. In order to test this hypothesis, a Z-pinch preionization method was employed. The net result was that the enhanced plasma behavior was not reproduced, although the preionization was lower than with the theta preionization, and, in fact, the behavior was poorer than normal. Thus, the improved compressed plasma column behavior is probably not due to the exclusion of fields in the preionized plasma and will require further study before it is well understood.

The plasma behavior resulting from the application of the ℓ=2 programmed field with the theta preionization more nearly satisfied requirements for feedback stabilization. Hence, a series of experiments were undertaken in which the feedback amplifiers were first turned on in the programmed mode for ~ 7 μs during preionization, turned off for about 20 μs, and then turned back on under the control of the position detectors, i.e., closed-loop feedback operation. The closed-loop condition was initiated after the implosion and initial δ_1 helical oscillations. This resulted in much improved plasma confinement over previous attempts with definite indications that the feedback system was following and controlling the plasma behavior. Confinement was terminated at ~ 25 μs.

The streak photographs showing "normal" sector behavior, Fig. II-12 (# 9878), are to be contrasted with streaks displaying plasma behavior with feedback system operating in a programmed-closed loop configuration, Fig. II-12 (# 403). Figure II-13 shows the plasma motions, heavy lines, observed by the plasma position detectors and the feedback output current for discharge #403. The lower plots are the average of the plasma trajectories recorded by the five position detector stations. These data, Figs. II-12 and -13, show successful feedback control of the plasma motions and extend the confinement time of the plasma in the Scyllac Feedback Sector without the addition of auxiliary bias or ℓ=0 fields.

However, force analysis of the plasma trajectories continued to indicate that transients from the equilibrium dynamics still play a dominant role in determining the plasma trajectory. The excursions in the forces are more than twice the maximum force available from the feedback power amplifier system. While the plasma confinement times are increased, the feedback stabilization system cannot overcome and control these large equilibrium force imbalances.

E. RESULTS WITH A HELICAL DISCHARGE TUBE

The plasma equilibrium and stability have been studied in a helical discharge tube with ℓ=2 trimming fields and closed-loop feedback stabilization. The helically shaped toroidal quartz tube, which has a helical radius of 1.4 cm, was fabricated for the existing ℓ=1,0 equilibrium configuration (cf. section C3). The experiments were performed with deuterium filling pressures in the range of 10 to 20 mTorr. The discharge cleaning of the helical tube required more plasma discharges than in previous tubes. Initial experiments with a 40-kV bank voltage, B ≃ 17 kG, gave plasma temperatures of 90 to 110 eV. Experiments at 45 kV gave plasma temperatures of 110 to 140 eV. Subsequent operation at 40 kV yielded temperatures in the 120 to 150 eV range.

1. Transient Plasma Oscillations. The use of the helical discharge tube eliminated the δ_1 helical oscillations observed previously in uniform toroidal tubes. Figure II-14 compares a set of dual streak photographs showing the plasma motions at half wavelength separations near the center of the sector in the previous experiments with the uniform toroidal tube, Fig. II-14A, and in the helical toroidal tube, Fig. II-14B. The

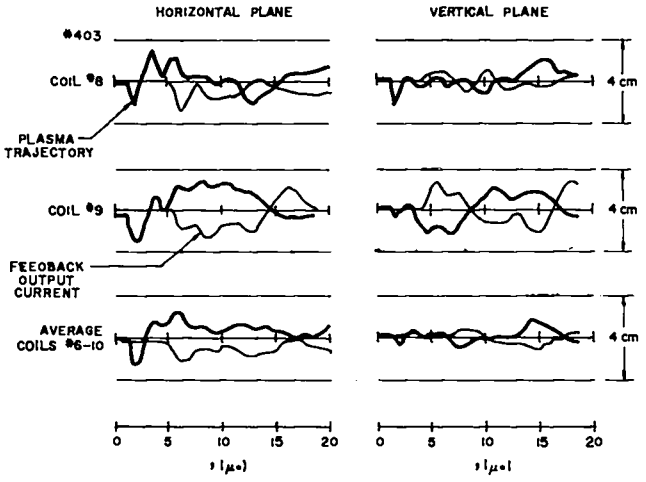

Figure II-13
Plasma position plots and feedback output currents observed at the indicated positions around the sector on the same discharge as the lower streak photographs of Fig. II-12.

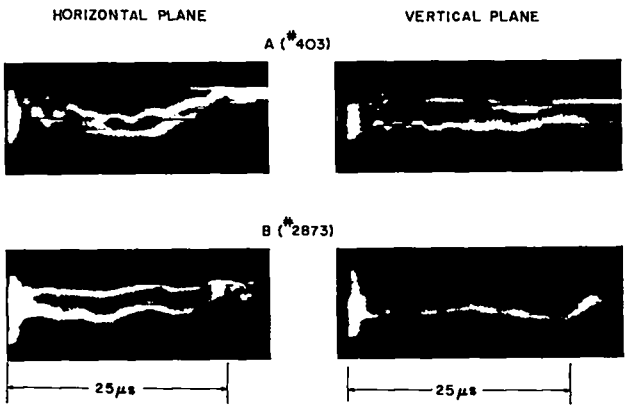

Figure II-14
Dual streak photographs comparing plasma motions in the uniform toroidal tube (A) and the helical discharge tube (B). Horizontal plane: each dual streak shows plasma column in regions of maximum magnetic field, hz=0 (upper streak), and minimum field, hz=π (lower streak), separated by one-half on ℓ=1,0 wavelength. Vertical plane: dual streaks taken one-half wavelength apart, hz=π/2 and 3π/2, at positions of intermediate magnetic field.

helical oscillations, Fig. II-14A, develop because the plasma implodes to the axis of the uniform discharge tube rather than to the equilibrium helical magnetic axis as in Fig. II-14B with the helical tube. The helical tube also improves the plasma to wall separation by the resulting concentricity of the plasma column and the tube wall as well as by the elimination of the δ_1 helical oscillations.

The slower δ_0 axial oscillations, $\omega_o \simeq hv_A \sqrt{\beta(1-\beta)}$, remain and appear in the streak photographs of Fig. II-14B as a time variation of the plasma diameter. Miller has reproduced the observed plasma trajectories in an MHD sharp-boundary dynamical model and confirmed the existence of the δ_0 oscillations, (cf. section G).[8] The sharp-boundary equilibrium force produced by the $\ell=1$ and $\ell=0$ fields varies with the transient δ_0 plasma oscillations making the achievement of the proper plasma equilibrium difficult. The δ_0 oscillations result from the development of a bumpy plasma column in a discharge tube with a uniform cross section. These oscillations could probably be eliminatd by the use of a "bumpy" discharge tube, i.e., a shaped discharge tube whose walls follow a magnetic flux surface of the $\ell=1,0$ configuration.

2. Results with $\ell=2$ Equilibrium Trimming Fields. The application of $\ell=2$ trimming fields to produce correcting forces in both the horizontal and vertical planes resulted in cross-coupling which made it difficult to achieve a good plasma equilibrium. Six separate small capacitor banks were used to drive three sets of $\ell=2$ coils in each the horizontal and vertical planes. Each set consisted of four $\ell=2$ windings in adjacent wavelengths of the horizontal plane connected in a series-parallel arrangement and driven by a slow-rising sinusoidal current ($\tau/4$ ~ 50-90 μs) with the option of a fast "notch" pulse to null the $\ell=2$ field during the plasma implosion. A considerable effort was expended in attempting to adjust the trimming fields to provide the best equilibrium and plasma confinement. Figure II-15 shows plasma trajectories on one of the better discharges with both horizontal and vertical $\ell=2$ trimming fields.

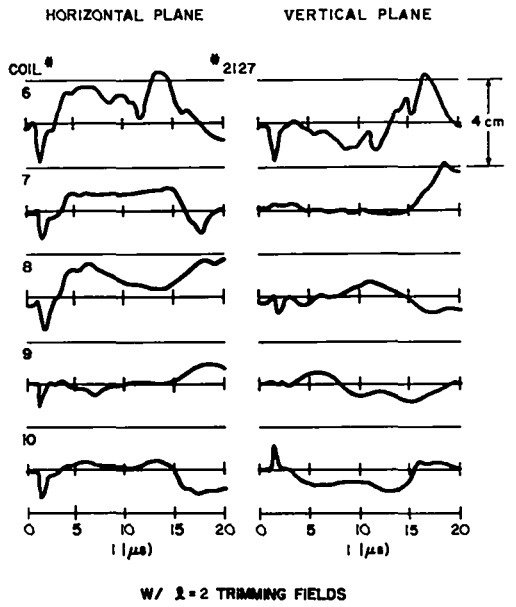

Figure II-15
Plasma trajectories on one of the better discharges with $\ell=2$ trimming fields producing correction forces in horizontal and vertical plasma.

The slow sinusoidal $\ell=2$ equilibrium trimming fields are not sufficient to completely overcome the effects of the δ_0 transient oscillations. The $\ell=2$ field magnitude required for equilibrium near the end of the transient phase is too large at earlier times when δ_0 oscillates to a maximum and results in an inner wall collision of the plasma column. This phenomenon is partially compensated by the application of a fast sinusoidal $\ell=2$ pulse phased such that the resulting force pushes outward as δ_0 approaches a maximum.

The observed cross-coupling of the forces produced by the equilibrium trimming fields between the horizontal and vertical planes is not understood. Errors in the discharge tube position within the compression coil can result in such cross-coupling which leads to plasma column motion partially in a direction orthogonal to an applied $\ell=2$ force. If the discharge tube is displaced from the helical axis of the $\ell=1,0$ field configuration, the equilibrium position of the plasma column will not be at the center of the $\ell=2$ field generated by coils wound directly on the tube. Analysis shows that a horizontally displaced $\ell=2$ field leads to $\ell=1$ components which are phased to

vertical displacement of the $\ell=2$ fields with respect to the $\ell=1,0$ fields, leads to an $\ell=1$ component which beats against the $\ell=0$ field to provide an orthogonal force for either vertical or horizontal $\ell=2$ fields. However checks of the discharge tube and $\ell=2$ coil positions show them to be approximately centered in the compression coil.

3. Feedback Stabilization Results with the Helical Discharge Tube. Closed-loop feedback stabilization was applied to the sector with both the horizontal and vertical $\ell=2$ trimming windings energized. The magnitude of the $\ell=2$ trimming fields were in the range of 10 to 50 G. Figure II-14B is a dual streak photograph showing the plasma motion in the horizontal plane of the torus at positions of maximum (upper, land region) and minimum (lower, groove region) magnetic field separated by a half wavelength of the $\ell=1,0$ field. Figure II-16 shows the plasma column trajectories, in both the horizontal and vertical planes, observed by the plasma position detectors at five locations approximately equally spaced around the sector. The data of Figs. II-14B and -16 were taken on the same discharge and at a deuterium filling pressure of 16 mTorr. These data suggest that the feedback stabilization is controlling the plasma motion for 20 to 25 μs. The plasma confinement is terminated by a disturbance that develops in the end coil section (# 6), upper trajectories. It appears that this disturbance propagates into coil section # 7 and results in a motion in the vertical plane. There is concern that such end effects in the toroidal sector limit the plasma confinement time. A "shorting-out" of the electron sheath may be occurring in the sector and inducing a rotational wobble as in the linear theta-pinch experiments. Such a development in a toroidal sector would very likely terminate the plasma confinement in approximately an Alfven time, which is ~ 20 μs in the feedback sector.

The plasma equilibrium improved with the number of discharges in that the magnitude of the $\ell=2$ trimming fields required for toroidal equilibrium decreased. The phenomenon was attributed to continued discharge tube cleaning and a resulting higher plasma beta. Figure II-17 shows plasma column trajectories obtained from the plasma position detectors on a discharge without auxiliary equilibrium trimming fields and in the

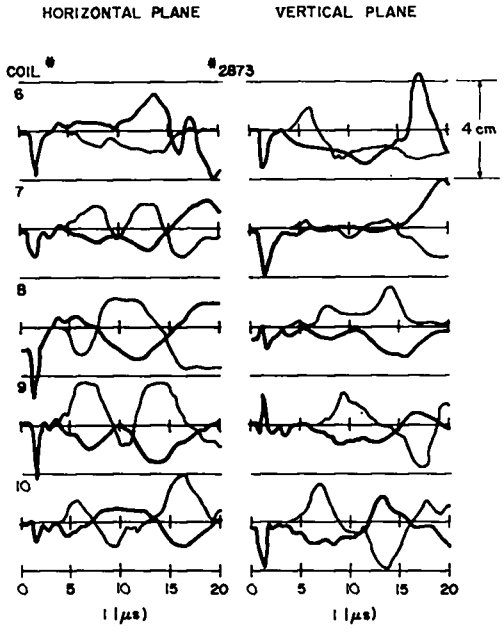

Figure II-16
Plasma trajectories (heavy lines) and feedback output current (light lines) with $\ell=2$ equilibrium trimming fields and closed-loop feedback stabilization.

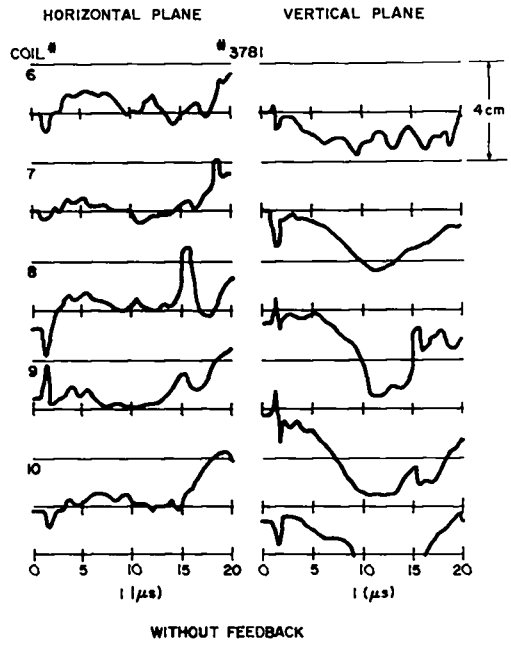

Figure II-17
Plasma trajectories without auxiliary fields and with feedback stabilization after approximately 2000 plasma discharges in the helical tube.

absence of feedback stabilization. The deuterium filling pressure was 16 mTorr. The plasma column remains approximately centered on the toroidal axis in the horizontal plane for 15 μs. A downward plasma motion develops in the vertical plane which eventually terminates the plasma confinement. This motion appears to be the m=1 instability and is likely initiated by a small displacement of the column from its equilibrium position.

Figure II-18 shows plasma column trajectories with feedback stabilization applied to discharges of the type shown in Fig. II-17 without additional equilibrium trimming fields. In this case the closed-loop feedback system is controlling the m=1 instability observed in Fig. II-17 and confining the plasma for times of up to 25 μs. In Fig. II-18, the plasma column in the end regions, coil sections 6 and 10, begins to move outward near the end of the trajectories. This may be an end effect manifesting itself in terms of a decrease in the plasma beta or an onset of the rotational plasma wobble discussed above.

A comparison of Figs. II-17 and -18 shows that the feedback stabilization system extends the plasma confinement time from 10 μs to times greater than 20 μs without other auxiliary fields.

4. Force Analysis of Plasma Trajectories. Force analyses of the plasma trajectories with feedback stabilization and without additional equilibrium trimming fields as typified by Fig. II-18 give the net force on the plasma column. The net force determined from the central plasma trajectories of Fig. II-18 is shown in Fig. II-19. The net force in the horizontal plane oscillates undamped about the equilibrium values.

These force analyses of discharges in the helical discharge tube, with feedback stabilization and without additional equilibrium trimming fields, show that the net force on the plasma column in the horizontal plane is oscillating about the equilibrium value without an average force imbalance in contrast to some of the earlier results in the uniform toroidal discharge tube, Fig. II-10. The oscillations are believed to derive from the δ_0 plasma oscillations or end effects in the sector. A significant result in these experiments is that plasma equilibrium is achieved with the $\ell=1,0$ equilibrium fields

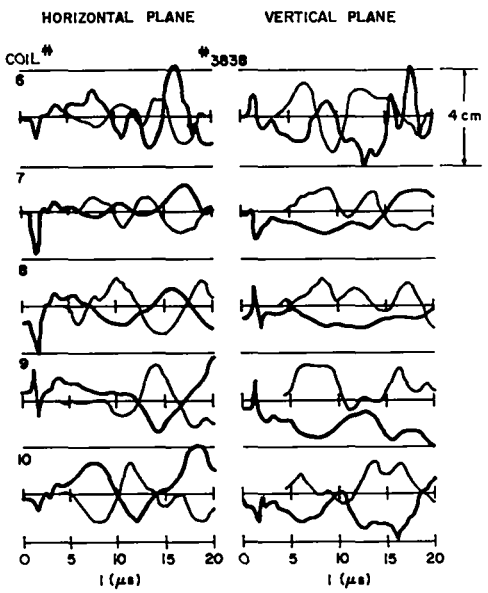

Figure II-18
Plasma trajectories (heavy lines) and feedback output current (light lines) with closed-loop feedback stabilization and without other auxiliary fields.

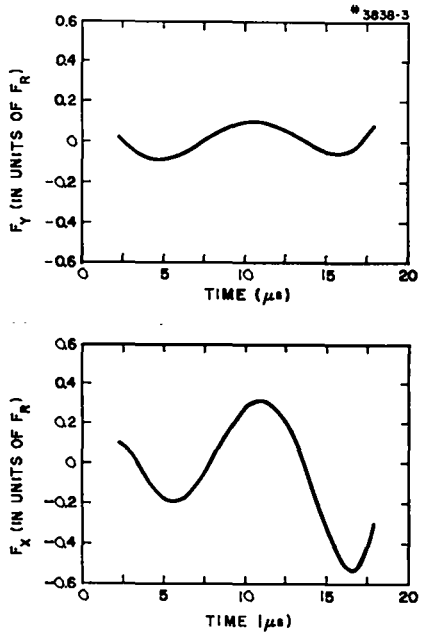

Figure II-19
Average plasma trajectories (upper plot) on two separate discharges in horizontal plane of central region of sector and corresponding calculated net forces (lower plot) on the plasma column on the discharge of Fig. II-19 (solid line).

designed on the basis of MHD sharp-boundary theory. Of course the plasma beta may be higher than the 0.65 design value, which would reduce the equilibrium fields required for equilibrium.

The increase of the equilibrium $F_{1,0}$ force noted above (section 3) and attributed to discharge tube cleaning continued beyond the plasma behavior characterized by Figs. II-18 and -19. After a few hundred additional discharges, the plasma was terminated by an inward rather than an outward motion of the column. This was compensated by applying an ℓ=2 trimming field pulse which resulted in an outward force on the plasma column.

F. EXCLUDED FLUX MEASUREMENTS

The excluded flux in adjacent land and groove regions have been simultaneously measured for shots with filling pressure in the range 5-40 mTorr. The data are shown in Fig. II-20. Setting up the optimum equilibrium at these different pressures using trimming windings is difficult and was not done so there was generally an early wall hit. However previous experience indicates that wall hits do not have a large effect on excluded flux, and this is borne out by the general similarity of this data to previous excluded flux measurements without wall hits.[9,10] A significant feature of the data shown in Fig. II-20 is that at high filling pressures, a sinusoidal δ_0 oscillation is apparent. This is direct experimental evidence for the existence under some conditions of such an oscillation. An oscillation of δ_0, if it occurs, would cause the $F_{1,0}$ toroidal equilibrium force to be strongly time dependent.

For comparison with the data the excluded flux has been calculated using the nonlinear dynamic model [see section G.2] and the results shown in Fig. II-21. In this model the excluded flux is simply

$$\phi_{ex} = \pi a^2 B - \phi_{in} \ , \qquad (9)$$

where a is the plasma radius and B the magnetic field at that z position, and ϕ_{in} is the constant included flux,

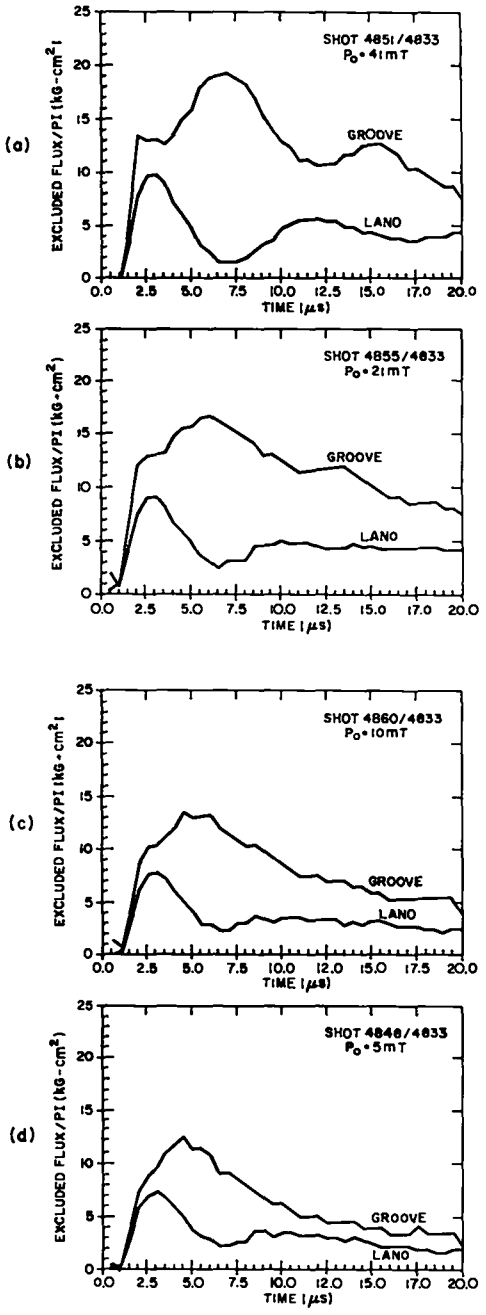

Figure II-20
Plots of the magnetic flux excluded by the plasma column measured simultaneously in adjacent land and groove region at various initial deuterium filling pressures: (a) P_o = 41 mTorr; (b) 21 mTorr; (c) 10 mTorr; and (d) 5 mTorr.

$$\phi_{in} = \pi a^2 B_o \sqrt{1-\beta} \ . \qquad (10)$$

Thus for B constant, the oscillations in included flux are simply those of the plasma radius.

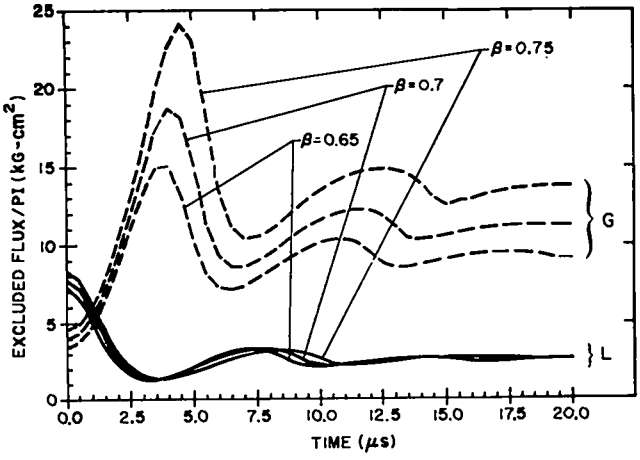

Figure II-21
Excluded flux calculated using the nonlinear dynamic model for the indicated plasma betas in land (L) and groove (G) regions.

The parameter values used were B_o = 13 kG, $B_{\ell=0}/B_o$ = 0.147, h = 0.1 cm^{-1}, v_A = 15 cm/μs, a = 1 cm, τ = 2.5 μs and β as indicated in Fig. II-21. The parameters v_A, τ, a, and β are not known well and one can imagine adjusting these to achieve a fit to the measured excluded flux, however, this has not been done.

G. PROPAGATION OF m=1 WAVES

The propagation of an m=1 displacement of the plasma column along the minor toroidal axis of the Scyllac sector is of interest because of possible limitations of the plasma confinement time in the sector due to end effects. It is known from numerous experimental observations that the ends of the sector behave quite differently than the central sections. The end behavior is characterized by large accelerations and displacements with generally early wall hits. This is probably the result of the abrupt transition from the toroidal field geometry which results in a lack of equilibrium in the end regions. The confinement in the central region is likely to be limited by the propagation time of these displacements to the central region of the sector. The propagation velocity of this wave thus becomes an important factor for interpreting the results of the Scyllac feedback stabilization experiments carried out in a toroidal sector rather than a full torus.

In order to experimentally measure the propagation of m=1 waves, a disturbance was launched in the central region of the sector by locally accelerating the column in the vertical direction. This was done by driving a single wavelength of the ℓ=2 equilibrium trimming coils. The "Jones"[11] circuits (cf. Sec. J 5) used to deliver the current waveform shown in Fig. II-22. Different wavelengths were activated, and the resulting displacements were observed with the feedback position detector stations located at different points along the sector. The vertical direction for the launched m=1 wave was chosen to eliminate the additional complication due to imperfect

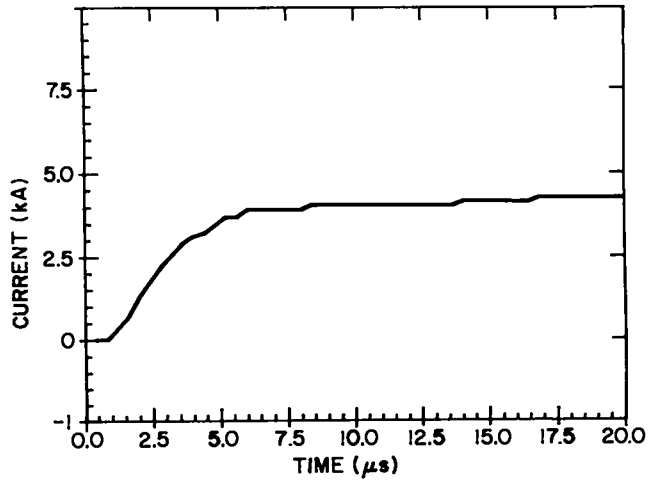

Figure II-22
Waveform of the "Jones" circuit output current used to drive the ℓ=2 equilibrium trimming coils in the m=1 wave propagation experiments.

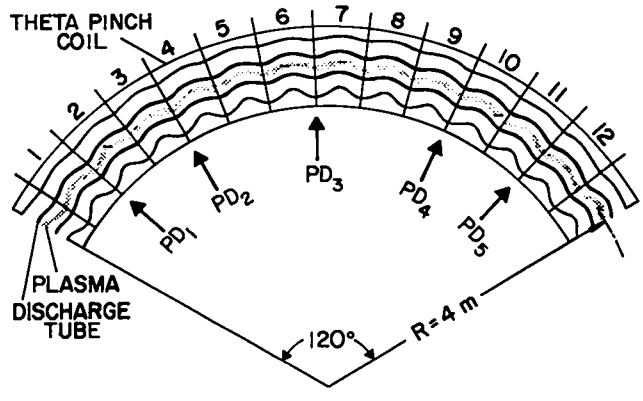

Figure II-23
Schematic of the feedback sector showing the location of the plasma position detectors and the nomenclature of the trimming coil wavelengths.

horizontal equilibrium. Figure II-23 shows the relative location of the position detector stations and the nomenclature of the trimming coil wavelengths.

Position detector signals are routinely recorded on biomations and the data transferred after every shot to the disk of the SIGMA 2. This information was then transferred via magnetic tape to the PDP-10 which was used for the analysis.

To reduce the influence of shot-to-shot variations in the experiment, the data were collected in two sets with each set composed of several shots. One of the sets included shots without the localized vertical acceleration and the other set of shots had the single $\ell=2$ wavelength activated. The trajectories contained within each set were then averaged. Figure II-24 shows the comparison of the two sets of data as observed at the five position detector stations for waves launched in the "J" wavelength (cf. Fig. II-23). The error bars on these figures are the maximum deviations within the set from the mean and represent the range of the data.

The small δ sharp boundary model provides a theoretical framework for the wave propagation experiments. The equation of motion for m=1 displacements is the following:

$$\frac{\partial^2 \xi}{2t^2} + (2-\beta)\, v_A^2 \frac{\partial^2 \xi}{\partial z^2} - \gamma_0^2 \xi = f(t)\, \delta(z), \quad (11)$$

where f(t) is the force which is applied at z=0 and γ_0 is the m=1, k=0 instability growth rate. The force was the $F_{1,2}$ interference force produced by driving a current in a one wavelength $\ell=2$ winding. In terms of the applied $\ell=2$ field,

$$f(t) = \frac{4\pi v_A^2}{ha} \frac{\beta}{2-\beta} \frac{B_{\ell=1}}{B_o} \frac{B_{\ell=2}(t)}{B_o} . \quad (12)$$

The $\ell=2$ field was produced by a four-wire winding with radius r_w = 5.8 cm and the magnitude of the $\ell=2$ field in Gauss is given by

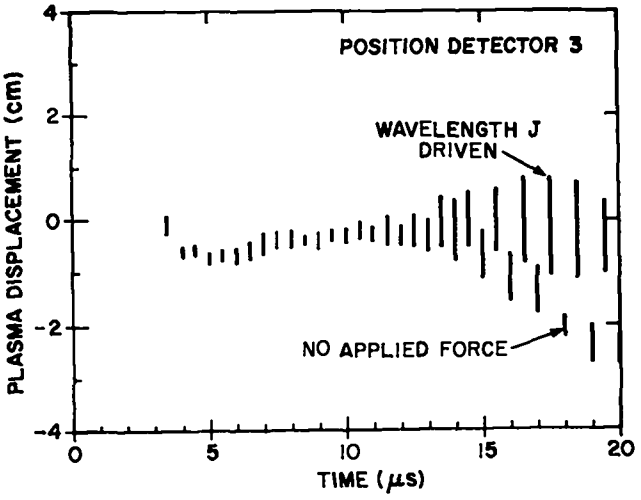

Figure II-24
Comparison of two sets of data as observed at the position detector station No. 3 for waves launched in the J (No. 10) wavelength.

$$B_{\ell=2}(G) = 0.8\, a(cm)\, I(A)/r_w(cm)^2 ,$$

where I is the current in amperes.

The solution of Eq. (11) is as follows:[12]

$$\xi(z,t) = \int_{-\infty}^{t} G(z,t-t')\, f(t')\, dt' , \quad (13)$$

where

$$G(z,t) = \theta(t) \int_0^{\infty} \frac{dk}{2\pi} \cos kz\, S(t) ,$$

$$S(t) = \frac{\sinh \gamma t}{\gamma} , \quad k < k_c$$

$$S(t) = \frac{\sin \omega t}{\omega} , \quad k > k_c$$

$$\gamma = \sqrt{\gamma_0^2 - k^2 v_A^2 (2-\beta)} ,$$

$$\omega = k^2 v_A^2 (2-\beta) - \gamma_0^2 ,$$

$$k_c = \gamma_0 / v_A \sqrt{2-\beta} .$$

The theory of Grossmann and Tataronis[13] applies to m=1 oscillations of a uniform plasma column (without the k=0 instability term) and shows the existence of damping when the plasma pressure profile is diffuse. For an oscillation with wave number k there is an imaginary part of the frequency which leads to damping ~ exp(- ηkt) with

$$\eta = \frac{\pi}{4} \frac{v_A}{\sqrt{2-\beta}} \left(\frac{a_2}{a_1}\right)^2 \left(\frac{a_2}{a_1} - 1\right) . \qquad (14)$$

In this model the plasma pressure is assumed to be constant out to a radius a_1 and then to drop linearly to zero at a radius a_2. The observed damping of the ℓ=1 oscillations (k=0.1 cm^{-1}, τ = 2.5 μs) determines η to be = 4 cm/μs, which from Eq. (3) gives a_2/a_1 = 1.2. The dispersion relation in the Grossmann-Tataronis theory is quite complicated but if the unstable term is added in a simple way it implies that there is no damping of the unstable part of the spectrum.

Another, less physical, method of introducing damping is to add a term $-\mu\partial^3 \xi / {}^2z\partial t$ to the left-hand side of Eq. (11). This allows the effect of damping on the entire spectrum to be calculated in a straightforward way. The damping of the stable part of the spectrum in this case is ~ exp $(-\mu k^2 t/2)$ and while the unstable growth rates are reduced the critical wave number k_c remains exactly the same. The coefficient μ is determined phenomenologically from the observed damping of the ℓ=1 oscillations and has the value μ = 80 $cm^2/\mu s$. In Fig. II-25 are shown the differences between the measured plasma trajectories with and without the applied force. The errors bars include the rms deviation of the data and an estimate of absolute position detector accuracy. Also plotted are the displacements calculated from Eq. (12) assuming the following parameter values: $B_{\ell=1}/B_o$ = 0.0946, h = 0.1 cm^{-1}, B_o = 13 kG, a = 1 cm, γ_o = 0.3 μs^{-1}, v_A = 20 cm/μs, and β = 0.7. There is no damping since the damping would produce a hardly perceptible effect in Fig. II-25. The effect of damping is shown in Fig. II-26 which has the same parameter values as Fig. II-25 except

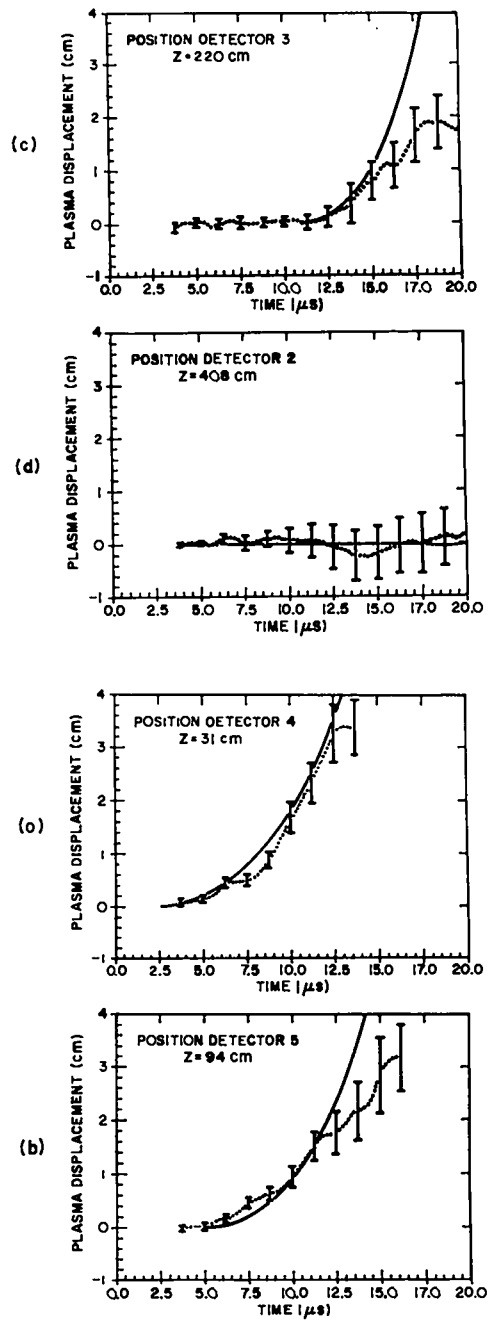

Figure II-25
Plots of the differences between the measured plasma trajectories with and without the applied force and the calculated displacements (solid lines) at various distances, z, from the location of the applied force: (a) z = 31 cm; (b) z = 94 cm; (c) 220 cm; and (d) z = 408 cm.

that γ_o is zero and the damping factors η or μ are as shown. The damping actually reduces the arrival time of the disturbance which in the unstable case leads to a greater displacement with damping than without. In general, the application of a constant force to the end of the plasma

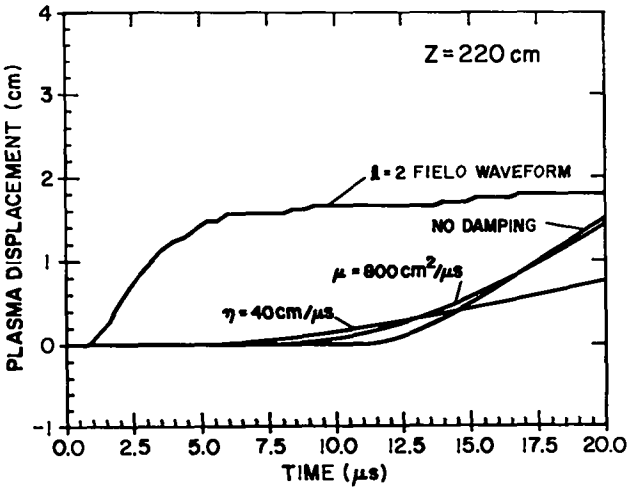

Figure II-26
Effect of damping on the wave propagation is shown for the indicated values of η and μ with the same parameter values as Fig. II-25 except $\gamma_0 = 0$.

column produces at some location z, a pulse of acceleration which in the damped case is smaller, but arrives earlier.

The question of what effect propagation of nonequilibrium forces from the ends has on feedback stabilization is complicated because of the nonlinear nature of the feedback system. The simplest point of view is to assume that the forces involved are much larger than the maximum feedback force so that feedback has a negligible effect and the situation is as already described.

The conclusion from this study is that forces applied to the sector plasma at the ends do indeed propagate and would appear in the center region as additional nonequilibrium forces. The measured propagation time over the 4-m distance from the ends to the center of the ℓ=1,0 sector is 17 μs ± 2 μs.

H. DIFFUSION

In Scyllac, a relatively small change in beta causes a loss of MHD equilibrium. Beta (~ nT) can decrease in time owing to losses of particles (n) or energy (T), either through the ends or radially. Radial particle losses by resistive diffusion are considered in this section. The conclusion is that radial particle diffusion is a significant effect for the derated experiments. For T_e = 100 eV and a plasma radius of 1 cm, the time required for a 10% decrease in beta is 11 μs.

For the early stages of diffusion of an equilibrium theta pinch the temperature can be assumed constant in time and it will be assumed constant in space as well. With constant temperature it can be shown that the following equation describes the diffusion process,

$$\frac{\partial B}{\partial t} + \frac{\partial B}{\partial r}\frac{1}{(B_o^2-B^2)r}\int_o^r r\frac{\partial B^2}{\partial t}\,dr$$

$$= \frac{B_o^2-B^2}{B_o^2+B^2}\,\frac{1}{r}\frac{\partial}{\partial r}\,r\eta\frac{\partial B}{\partial r}\ . \qquad (15)$$

The equilibrium condition,

$$nT + \frac{B^2}{2} = \frac{B_o^2}{2} \qquad (16)$$

holds at all times (neglecting small acceleration terms) and this relates n to B. A completely equivalent equation can be written for n instead of B. Equation (15) is actually simpler than it first appears since the integral term is small and as a first approximation can be neglected.

In Eq. (15) the resistivity has the units (length)^2/time. The conversion for Gaussian cgs or MKS units is a follows:

$$\eta(cm^2/\mu s) = \eta_{cgs}\ (sec)\ 7.16 \times 10^{13}\ ,$$

$$\eta(cm^2/\mu s) = \eta_{MKS}\ (ohm\text{-}m)\ 7960\ .$$

From Eq. (15) it is seen that if B is measured in units of B_0, r in units of a characteristic length a, and t in units of a^2/η, Eq. (15) assumes a universal form depending only on the shape of B (or n or β) as a function of r. In Fig. II-27 are shown numerical solutions of Eq. (15) for B profiles of the rigid rotor type corresponding to various central beta values β_0. The rigid rotor profile[14,15] is given by

$$B = B_0 \tanh\left[\frac{r^2}{a^2} + \tanh^{-1}\left(1-\beta_0\right)^{1/2}\right]. \qquad (17)$$

In Fig. II-28, are shown the times for 10% and 25% loss of β on axis for rigid rotor and Gaussian (density) profiles versus β_0. It is clear from these results that the basic resistive time a^2/η gives the time scale for high-beta diffusion. Since the usually discussed low-beta diffusion time $(a^2/\eta)(p^2/p)$ vanishes in the high-

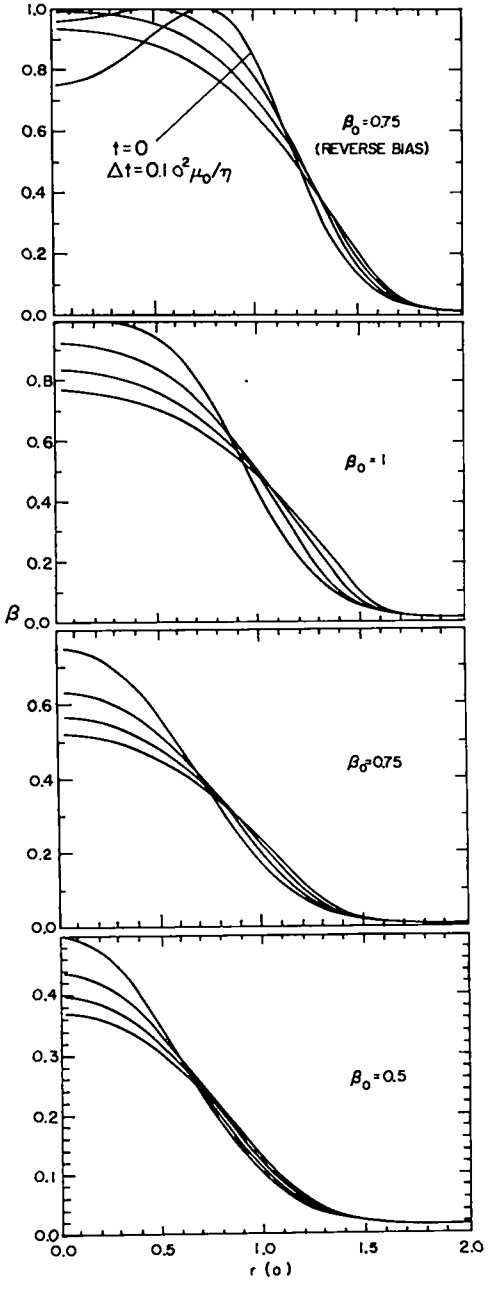

Figure II-27
Graphs of calculated plasma beta profiles of the rigid-rotor type corresponding to the indicated central beta values β_0.

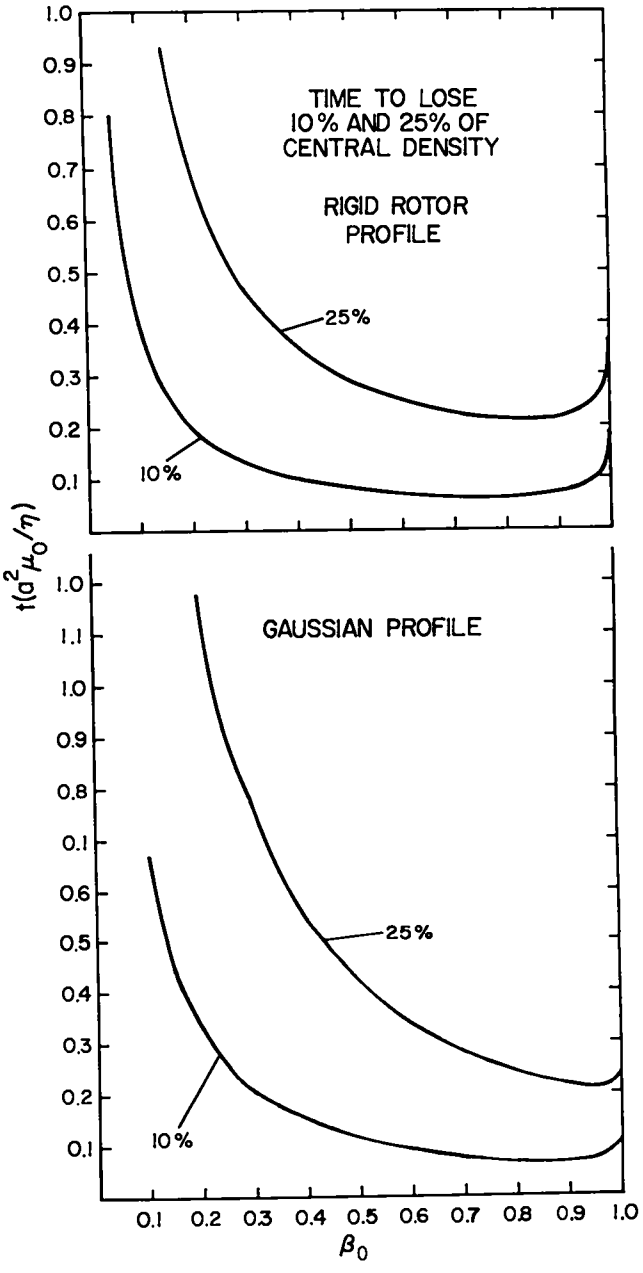

Figure II-28
Plots of calculated times for 10% and 25% loss of plasma β on axis for rigid rotor and Gaussian density profiles vs β_0.

beta limit (B→0) it is important to clarify this point.

1. Classical Resistivity. The formulas for the resistivity will be given in Gaussian cgs units. Classical resistivity is due to a drag on the drifting, current carrying electrons due to electron-ion Coulomb collisions. The resistivity is given by[16,17]

$$\eta = \frac{4\,(2\pi\, m_e)^{1/2}\, e^2\, \ell n\, \Lambda}{3\, T_e^{3/2}}$$

$$\eta = 2.5 \times 10^{-4}\, \frac{\ell n\, \Lambda/10}{(T_e/1\ \text{keV})^{3/2}}\ \text{cm}^2/\mu\text{s} \quad , \qquad (18)$$

with

$$\ell n\, \Lambda = \ell n \left[\left(\frac{3}{\pi}\right)^{1/2} \frac{m^{1/2}\, T_e}{e h\, n^{1/2}} \right] \text{for } T_e > 40 \text{ eV} \quad ,$$

$$\ell n\, \Lambda = 13.8 + \log(T_e/1\ \text{keV}) - 0.5 \log(n_e/10^{16}\ \text{cm}^{-3}) \quad .$$

For the derated Scyllac sector experiment, assuming T_e = 120 eV the resistivity is 0.007 $\text{cm}^2/\mu\text{s}$ and the classical resistive diffusion time for a = 1 cm is 140 μs.

2. Anomalous Resistivity.

Of the many possible microstabilities that might be responsible for an anomalous resistivity in a theta pinch, the general consensus at the present time seems to be that the lower hybrid drift instability is the most important. This is an unstable electrostatic oscillation of the plasma driven by the diamagnetic drift of the ions. The diamagnetic drift velocity is the fluid velocity in a coordinate frame where the electric field is zero,

$$v_{Di} = \frac{1}{enB} \frac{\partial (nT_i)}{\partial r} \quad .$$

The resistivity depends on the level of fluctuating fields ultimately produced by the instability, that is, the saturation level. The calculation of Davidson and Gladd[18] assumes the maximum conceivable fluctuation level and results in a very large resistivity, so large as to be inconsistent with theta-pinch experiments. For example for the conditions of the present derated sector experiment, which happen to be very similar to those of the Culham diffusion experiment[19] the resistivity calculated using the Davidson-Gladd formula is greater than 0.2 $\text{cm}^2/\mu\text{s}$ over the range 0.2 cm $\lesssim r \lesssim$ 2 cm, which leads to a diffusion time for a = 1 cm of less than 5 μs.

A model for the saturation process based on the electrostatic trapping of ions in the potential well of the unstable wave[20,21] gives more reasonable diffusion times and is favored by numerical simulation results.[22] The resistivity for saturation due to ion trapping is given by

$$\eta_{anom} = \frac{\pi 15/2}{2^{19/2}} \left(\frac{v_{Di}}{v_i}\right)^8 \left(\frac{\omega_{ce}}{\omega_{pe}}\right)^2 \frac{1}{(\omega_{ce}\omega_{ci})^{1/2}} \quad ,$$

$$\eta_{anom} = 1.35 \times 10^{-15}\, \frac{(T_i/1\ \text{keV})^4}{(B/10\ \text{kG})^7 (N/10^{16}\ \text{cm}^{-3})} \left(\frac{1}{n}\frac{\partial n}{\partial r(\text{cm})}\right)^8 \frac{\text{cm}^2}{\mu\text{s}} \quad . \qquad (19)$$

However, there is an uncertainty in the ion trapping saturation condition of a numerical factor of about π. Unfortunately, in the resistivity, this numerical factor enters as $\pi^4 \simeq 100$. The more pessimistic case has been assumed and the resistivity would be 100 times less in the optimistic case.

In Fig. II-29 are shown β profiles versus time for the conditions of the present derated sector experiment and the Scyllac full torus

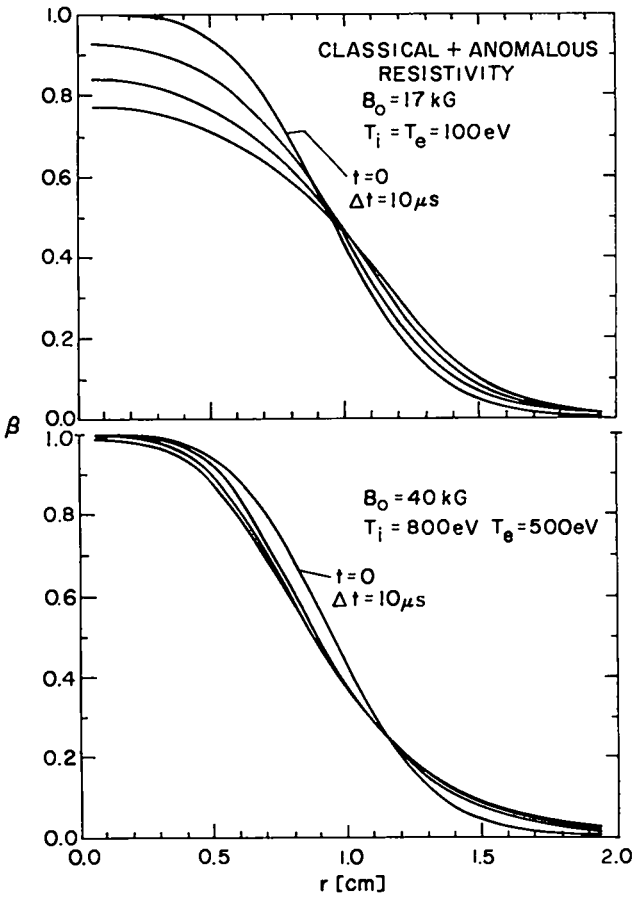

Figure II-29
Graphs of calculated plasma β profiles vs times for the parameters of the derated feedback sector experiment (upper plot) and the Scyllac full torus experiment (lower plot).

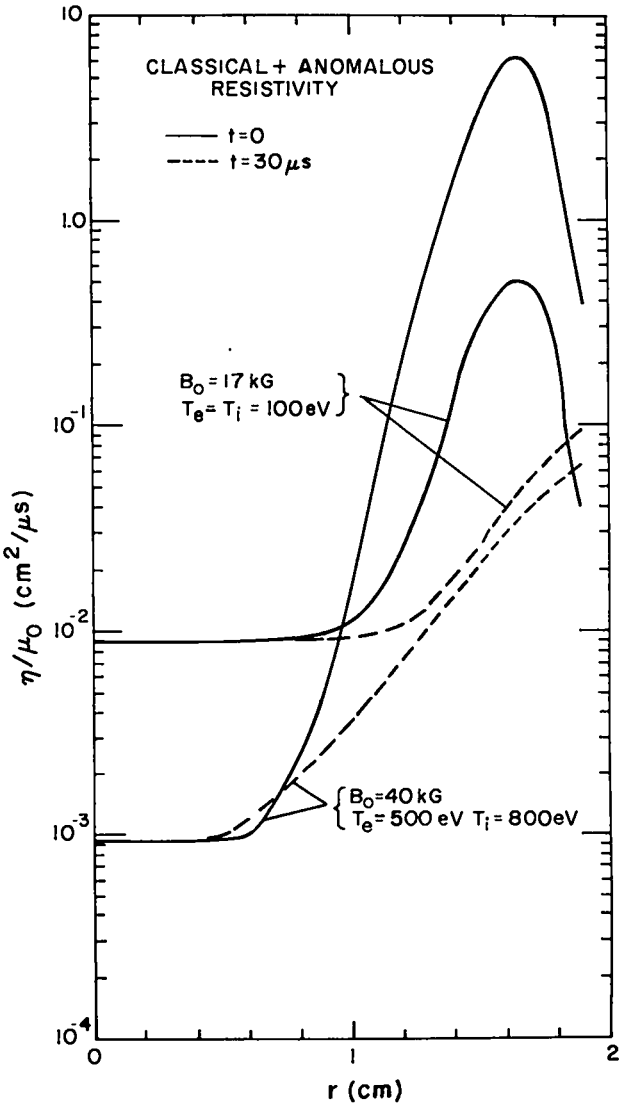

Figure II-30
Plots of the calculated sum of anomalous and classical resistivity for the parameters of the feedback sector and full torus experiments. The large anomalous resistivity occurs only outside the main plasma column where a density of ~ 1% of the central column was assumed.

experiment. The central β is 1 since this was the case for both experiments at hz = π (groove). Diffusion of the central plasma calculated using the sum of anomalous and classical resistivity is about the same as for classical resistivity alone. This is somewhat surprising since in Fig. II-30 it is shown that the actual anomalous resistivity can be orders of magnitude greater than classical. However, the large anomalous resistivity occurs only in the outer plasma region and in fact the only reason it remains finite is that a minimum density (~ 1% of the central density) was assumed outside the main column. The anomalous resistivity has a tendency to decrease with time since plasma moves to the outer region and thereby decreases $\frac{1}{n}\frac{\partial n}{\partial r}$. This seems to be the main effect of the anomalous resistivity given by Eq. (19), namely, to cause formation of a low-density halo surrounding the main plasma column.

3. Resistive Tearing Modes. Since in some of the feedback sector experiments a reverse magnetic bias field has been used, an estimate of the growth rate of the resistive tearing mode is of interest. The growth rate is approximately given by[23]

$$\gamma \sim \left(\frac{v_A}{a}\right)^{2/5} \left(\frac{n}{a^2}\right)^{3/5} \left(\frac{1}{ka}\right)^{2/5} \qquad (20)$$

with

$$\left(\frac{a}{v_A}\frac{n}{a^2}\right)^{1/4} < ka < 1 \quad ,$$

where v_A is the Alfven velocity, and k is the wave number of the mode in the z direction. Using parameter values for the sector feedback experiment, a/v_A = 0.1 μs, a^2/η = 140 μs, the growth rate is 0.13 μs/$(ka)^{2/5}$. The minimum permissible k for a = 1 cm is 0.16 cm^{-1}, thus $\gamma_{max} \sim 0.3\ \mu s^{-1}$. This growth rate is approximately equal to that of the m=1, k=0 instability, so if this mode actually occurs it would have an important effect.

4. Effect of Diffusion on Excluded Flux. Using the solutions of Eq. (15) shown in Fig. II-27, it is possible to calculate the excluded flux as a function of time. This is done to see if resistive diffusion can account for the decrease of excluded flux observed experimentally in the groove region. Suprisingly the flux through an area larger than and including the plasma is found to be an approximate constant of the motion.

Excluded flux through a loop of radius R is given by

$$\phi_{ex} = \int_0^R (B_0 - B)\, 2\pi r\, dr \quad ,$$

where B(r,t) is the magnetic field solution of Eq. (11). In Fig. II-31 this quantity, normalized to the value at t=0 is plotted as a function of time. The radius R is 2 cm and the initial central beta is 0.7. The pressure profiles as a function of time are as shown in Fig. II-27. Figure II-31 shows that the decrease in excluded flux is quite small, only 6% after one characteristic diffusion time. Thus resistive diffusion cannot explain the large decreases in excluded flux observed in the groove region.

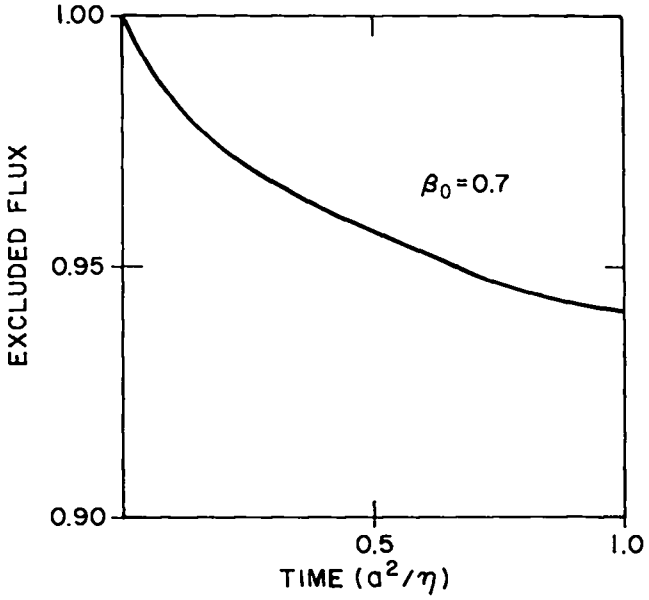

Figure II-31
Calculated magnetic flux excluded by the plasma column as a function of time.

I. SCYLLAC MAGNETOHYDRODYNAMICS

1. Calculations Using the Small δ Dynamic Model. In the approximation that the plasma shape is nearly cylindrical (small δ's) and that the plasma pressure is nearly constant (sharp-boundary), a fairly simple set of differential equations completely describing the motion exist.[8] A computer code using this model, which also incorporates a time varying β, has been written. The changes in β are attributed to: 1) a decrease of the main B_z magnetic field; 2) a decrease in temperature; and 3) particle diffusion, using a separate characteristic time for each of these processes. The decrease in the main field actually increases β, while the other processes decrease it. The plasma radius was also allowed to vary, in response to the change in magnetic field and temperature, but for ha small, as is the case, changes in radius have practically no effect.

The object of these calculations was first to attempt to reproduce the characteristic in-out trajectories observed in the experiment and second to estimate the longest confinement time with feedback to be reasonably expected given the known mechanisms for a decrease of β. The results are inconclusive on the first point and on the second,

30 μs seems to be about the confinement time limit without the use of auxiliary equilibrium trimming fields.

The model assumed very simple initial conditions with the plasma a stationary column in the center of the discharge tube at the initial time. This corresponds to idealizing the implosion-compression as being instantaneous while in fact it takes several microseconds. The effect of m=0, k=0 transients that would be excited is also neglected. The data seem to indicate that the implosion compression reduces the outward m=1, k=0 motion that the model predicts during this initial period.

In Fig. II-32 are shown calculated m=1, k=0 trajectories and accelerations for the conditions of the uniform discharge tube experiments without auxiliary fields. The parameters used in the calculations were as follows: B_o = 17 kG, $B_{\ell=0}/B_o$ = 0.147, $B_{\ell=1}/B_o$ = 0.0946, $n_e = 2 \times 10^{16}$ cm^{-3}, a = 1 cm, h = 0.1 cm^{-1}, R = 400 cm, and γ_{ad} = 5/3. The ℓ_1 and ℓ_0 oscillations were assumed to have exponential damping with characteristic times τ_1 = 3 μs and τ_o = 5.6 μs, with the first time fairly well determined by the data, but the second unfortunately not. The 1/e time for decrease of the main field was taken as 190 μs and that for the temperature 100 μs, determined by a crude fit to Thomson scattering data having only a few points at later times and these with a large spread. The diffusion time was assumed to be 60 μs corresponding to classical diffusion with Z_{eff} = 1 and T_e = 70 eV, somewhat lower than the measured temperatures of 100-120 eV so as to overestimate the diffusion if it is purely classical. The remaining parameter β was adjusted to give the longest confinement time. Three β values near the optimum are shown in Fig. II-32.

The values of β necessary for long confinement times using this model are greater than the β limit given by pressure balance without curvature effects, $\beta_{max} = (1-B_{\ell=0}/B_o)^2 = 0.73$. However for small changes in near 1, of most importance is the change in δ_0, since δ_0 and not β directly affects the body force on the plasma. In the nonlinear theory, δ_0 becomes very large as $\beta \to \beta_{max}$ just as it does in the linear approximation as $\beta \to 1$. Thus it is reasonable in a linear model to allow any β up to 1. This is taken up in more detail in subsequent sections that discuss the nonlinear MHD theory for the ℓ=0 case.

In Fig. II-33 are shown graphs of calculated plasma trajectories with feedback but otherwise

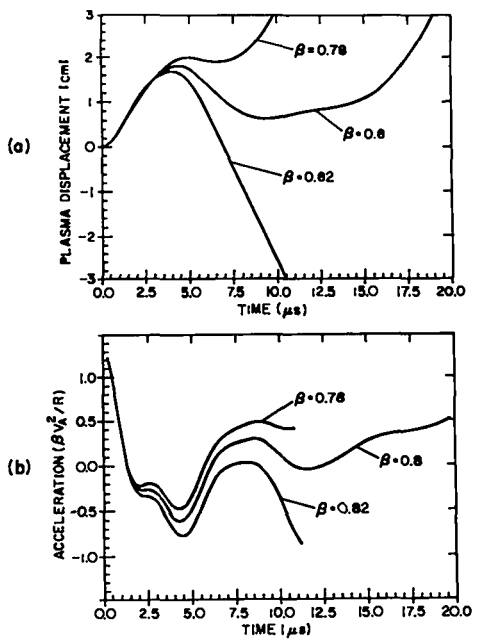

Figure II-32
Calculated plasma trajectories and accelerations for the conditions of the uniform discharge tube experiments without auxiliary fields.

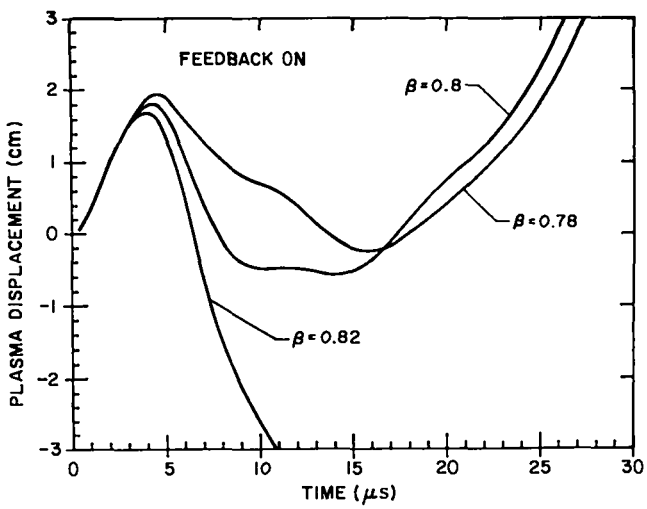

Figure II-33
Graphs of calculated plasma trajectories with feedback stabilization for the conditions of the uniform discharge tube experiments.

under the same conditions as in Fig. II-32. The delay time and the maximum feedback field give $\gamma\tau = 0.3$ and $\xi_{max} = 1.5$ cm, approximately the experimental values. The position and velocity gains were roughly optimum, $\alpha = 1.5$, $\tau_1 = 2.3\ \tau$.

The feedback system was turned on at 4 μs and no additional programmed fields were used. The turn-on time has an important effect. Obviously too late a time does not allow for much improvement using feedback and surprisingly, too early a time also is not optimum. For example turning on the feedback system at t=0 leads to tracking of the ℓ=0 force transient and an actual shortening of the confinement time.

As usual, with complicated numerical calculations having many poorly determined parameters, it is mainly a guess whether or not the calculation corresponds to reality. There is an in-out behavior of the calculated trajectories for $\beta = 0.8$ in Fig. II-32 in quite good agreement except for an overall outward shift with observed trajectories. However, it is believed that too delicate a balance of large unstable forces is required in the model for it to be precisely the in-out effect observed in the experiment. The real physics probably involves a suppression of the initial outward force transient, smaller unstable forces, a more precipitous loss of equilibrium involving a decrease of δ_0 in addition to that caused by decrease of β, as suggested by excluded flux measurements, and propagating end effects.

2. Nonlinear ℓ=0 Magnetohydrodynamics.

a. Equilibrium. The equilibrium of a constant pressure theta-pinch plasma column in the presence of a long wavelength ℓ=0 field can be calculated quite easily without assuming the plasma deformation is small. The pressure balance condition is

$$P = \frac{\beta B_o^2}{2} = \frac{B_{out}^2}{2} - \frac{B_{in}^2}{2} , \qquad (21)$$

where B_{out} is the external bumpy field, $B_{out} = B_o + B_{\ell=0} \cos hz$, and B_{in}, the magnetic field inside the plasma, is determined by flux conservation,

$$B_{in}\, r^2 = B_0(1-\beta_0)^{1/2}\, a^2 . \qquad (22)$$

Here it is necessary to distinguish β_0, the plasma beta before application of $B_{\ell=0}$, from β, the final equilibrium beta. Finally there is the adiabatic law, since it is necessary to allow for an overall expansion of the plasma,

$$\frac{\beta B_o^2}{2} V^\gamma = \frac{\beta_0\, B_o^2}{2} V_o^\gamma , \qquad (23)$$

where

$$V = \int \pi r^2 dz ,$$

and

$$V_0 = \pi a^2 L .$$

If we imagine applying an ℓ=0 field to a straight plasma column with radius a, in a field B_0, with initial pressure $_0B_0^2/2$, Eqs. (21) and (22) determine the plasma shape,

$$r = \left[\frac{1 - \beta_i}{\left(\frac{B_{out}}{B_o}\right)^2 - \beta}\right]^{1/4} a . \qquad (24)$$

The final beta value is obtained using Eq. (23)

$$\beta_0 = \beta \left[\int \frac{r}{a}^2 \frac{dz}{L}\right]^\gamma , \qquad (25)$$

which must be solved in conjunction with Eq. (24). This can be done by calculating Eqs. (24) and (25) for a sequence of decreasing β's starting very near the maximum permissible value $\beta = \frac{B_{out}}{B_o}^2_{min}$. The radius as a function of z starts out with a large bulge occurring where $(B_{out}/B_0)^2 \simeq \beta$ and a large total volume. As β decreases Eq. (25) is eventually satisfied for some $\beta < \beta_0$.

In Fig. II-34 are shown examples of the plasma equilibrium shape for $B_{\ell=0}/B_0 = 0.147$, $h = 0.1\ cm^{-1}$, $a = 1$ cm, $\gamma = 5/3$, and the β values as indicated. The β_0 values were 0.6, 0.7, 0.8, and 0.9. A local bulging out of plasma in the minimum magnetic field region (groove) results when β is near its limiting value. This is probably undesirable because it enhances the unfavorable curvature in this region. It is possible to speculate that this may be related to the decrease in excluded flux observed in the groove but not the land regions.

b. Dynamics. In the case of incompressible flow, a simple dynamic theory of plasma motion in a long wavelength bumpy field can be constructed without using the small δ assumption. The z- component of Euler's equation is

$$\ell \frac{\partial v_z}{\partial t} = - \frac{\partial P}{\partial z} - \frac{1}{2}\left(\frac{\partial B_{out}^2}{\partial z} - \frac{\partial B_{in}^2}{\partial z}\right) , \qquad (26)$$

where

$$B_{in}^2 = B_0^2(1-\beta)\ (a/R)^4$$

from flux conservation. The shape of the plasma is given by $r = R(z,t)$. To relate R to v_z the incompressibility condition $\nabla \cdot v = 0$ is used,

$$\frac{1}{r}\frac{\partial}{\partial r}(r\, v_r) + \frac{\partial v_z}{\partial z} = 0 \quad .$$

This is integrated over r from r = 0 to r = R to obtain

$$R\, v_r = - \frac{R^2}{2}\frac{\partial v_z}{\partial z} \quad ,$$

which together with $\frac{\partial R}{\partial t} = v_r - \frac{\partial R}{\partial z} v_z$ gives the result

$$\frac{\partial R}{\partial t} = - \frac{R}{2}\frac{\partial v_z}{\partial z} - \frac{\partial R}{\partial z} v_z \quad . \qquad (27)$$

Equations (26) and (27) can be solved numerically and the results are given in Fig. II-35 for $B_{\ell=0}/B_0 = 0.147$, $\beta = 0.7$, $v_A = 18$ cm/μs, $h = 0.1\ cm^{-1}$ and $a = 1$ cm. An additional

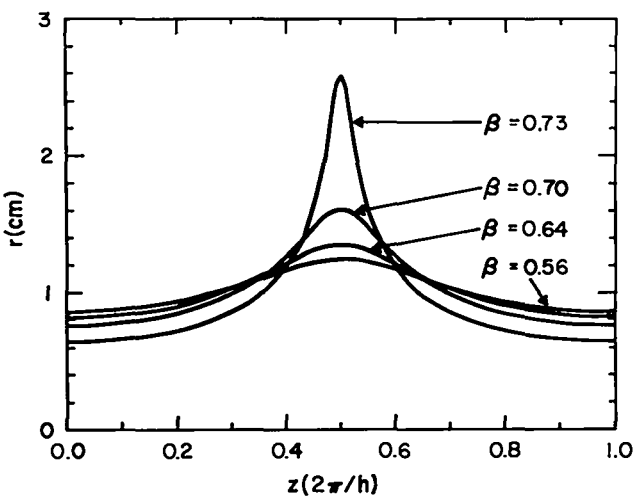

Figure II-34
Plots of the calculated plasma equilibrium shape for various values of the plasma beta with the feedback sector values of $B_{\ell=0}/B_0 = 0.147$ and $h = 0.1\ cm^{-1}$.

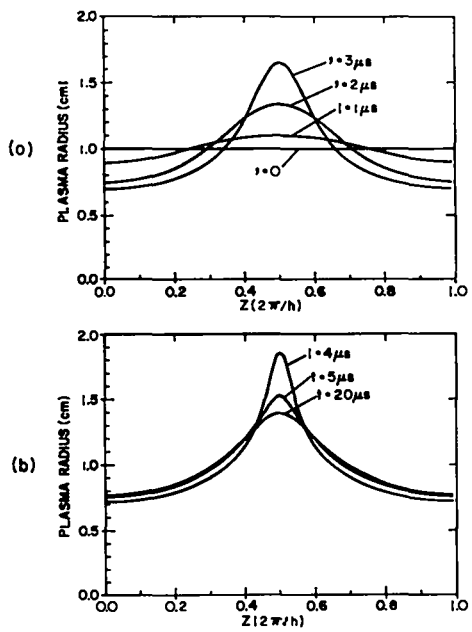

Figure II-35
Graphs of the calculated, δ_0 plasma shape as it approaches equilibrium for the feedback sector parameters.

term $-\rho v_z/\tau$ with $\tau = 2.5$ μs has been added to the right-hand side of Eq. (26) to provide damping. With damping the solution R(z,t) of Eqs. (26) and (28) becomes constant as $t \to \infty$ and agrees with the equilibrium solution discussed in the previous section if in the equilibrium solution β_0 is identified with the present quantity β and $\gamma \to \infty$.

The nonlinear ℓ=0 theory accounts for the apparent overloading of the groove regions with plasma observed in the experiment. In Fig. II-36 are shown measured values of line density at two times for an initial filling pressure of 19 mTorr. The measured line density at 5 μs is about twice the value predicted by small δ equilibrium theory and to explain the line density in the groove using small δ theory would require $\delta_0 = 1$, which implies a total squeezing off of the land region.

The plasma shape R(z,t) can be Fourier analyzed to obtain an equivalent $\delta_0(t)$, the quantity that enters into the $F_{1,0}$ interference force. This is plotted in Fig. II-37 (actually $-\delta_0$ is plotted), which shows a behavior quite similar to that obtained from the linear model

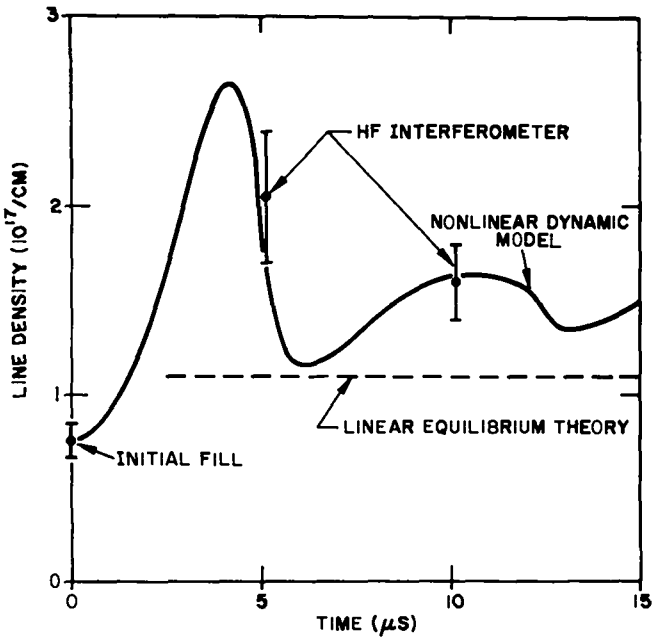

Figure II-36
Measured values of the plasma line density in a groove region at two times for an initial filling pressure of 19 mTorr compared with theory.

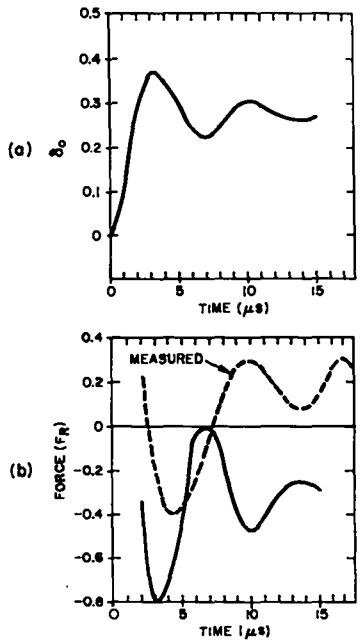

Figure II-37
(a) Plot of $\delta_0(t)$ obtained from a Fourier analysis of the plasma shape R(z,t). (b) Plot of the variation in $F_{1,0}$ owing to the δ_0 oscillation (dashed lines) compared with the measured force derived from the plasma trajectories (solid line).

where δ_0 undergoes a simple damped sinusoidal oscillation. The $F_{1,0}$ force is given by

$$F_{1,0} = \pi B_o^2 \, ha^2 \, L \, \frac{B_{\ell=0}}{B_o} \, \frac{B_{\ell=1}}{B_o} \left[1 - \frac{ha}{2} \frac{\delta_1}{B_{\ell=1}/B_o} + \frac{\delta_0}{B_{\ell=0}/B_o} \right] . \qquad (28)$$

So that for $\delta_1 = B_{\ell=1}/[ha\ B_o(1-\beta/2)]$,

$$F_{1,0} - \frac{1-\beta}{2-\beta} + \frac{\delta_0}{B_{\ell=0}/B_o} . \qquad (29)$$

The variation in $F_{1,0}$ due to the δ_0 oscillation is plotted in Fig. II-37(b). This is remarkably similar in shape to the measured force obtained by computing the acceleration of the plasma trajectories.

J. SCYLLAC FEEDBACK SYSTEM DEVELOPMENT

1. Feedback Power Modules. The modified Scyllac Feedback System has been in full operation on the sector experiment for the past year. Due to the addition of a fourth vacuum tube stage in the power amplifier, the system reliability has been greatly improved. There have been no transistor and few vacuum tube failures during 1976. The major problem that has existed from the development period is the arcing of the power amplifier output tube due to the intense, local surface heating of the anode that occurs with operation in the unique feedback system application. This difficulty is reduced by *in situ* exercising of the amplifiers and by operating at less than maximum levels of plate voltage and current. During the year the system was operated at high filament power for 84 hours during which there were about 1200 Scyllac feedback shots and 84 module failures. About 30% of these failures resulted from loss of cathode emission of the amplifier output tube; the rest were mainly component faults owing to external arcs in the confined module space where voltages to 120 kV were produced. A recent addition of silicon carbide varistors between the output tube anodes has reduced the external arc probability by about a factor of three without affecting output current risetime.

2. New Feedback Position Detectors. A significant improvement in the feedback system accuracy and capability was the change in plasma position detectors to the 16-element quasi-quantized type that is sensitive only to the position of the most intense portion of the plasma luminosity. The previous plasma position detector suffered from variation in sensitivity and loss of accuracy owing to variations in the plasma background light. Figure II-38 shows the comparison of the detector output as compared with that from the 20-channel luminosity device for two different levels of plasma light. A beam splitter was used so that both devices viewed the same plasma light. Differences between the two methods are due to the fact that the luminosity radius is the center of a computer Gaussian fit to the luminosity data that is not always symmetrical. A third generation of 16-element position detectors

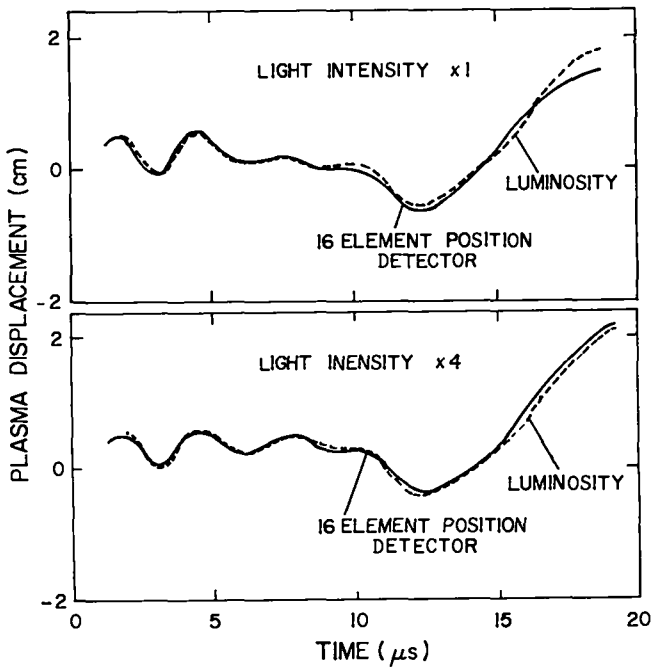

Figure II-38
Comparison of the output from the feedback position detectors with that from the 20-channel luminosity device for two different levels of plasma light.

is being fabricated that incorporates an automatic gain control to improve sensitivity. The present system requires constant operation monitoring of the detector to ensure that the plasma light level variation falls within a window whose upper and lower bounds are about a factor of 1.5 above and below the optimum level. In addition, the new system will provide a signal approximately proportional to the plasma radius for diagnostics of the plasma column.

3. New Feedback Signal Processor-Analyzer. The last major alteration to the feedback system is replacement of the intermediate amplifier that processes the detector signals and distributes them to the power amplifier modules. At present the system consists of 10 independent (five for each coordinate) units connecting the 10 detectors to a like number of groups of modules, a gross approximation to the actual z-dependence of plasma position. Each intermediate amplifier has a switch for programmed closure of the feedback

loop, a differentiation for introducing damping, and means for remote control of gain and damping. The new system consists of a single chassis with provisions for up to 22 detector signal inputs to compute up to 9 axial modes for each coordinate. Each module will be driven by a summing amplifier that reconstructs from the mode signals the weighted mode sum that represents the actual plasma position corresponding to the z position of the driven $\ell=2$ coil. There are independent controls for gain and damping for each mode. Since with the $\ell=1,2$ equilibrium configuration the position detectors will view horizontal and vertical motion whereas the $\ell=2$ force coordinates are 45° to the vertical, the independent module amplifier will also perform a coordinate rotation. A feedback loop closing switch is provided in the mode analyzing amplifiers, also included in the system is a built-in test signal generator to simulate detection signals for testing the mode analyzers and module drivers. Signal delay time should be about the same as for the present system, the amplifiers are faster but the signal paths are longer.

4. Other Development Items. There were several areas of development related to feedback carried out by feedback personnel during the year. An energy conserving pulsed feedback system using fast switching silicon controlled rectifiers was investigated. Such a system using presently available components would be appreciably more expensive than that of the present vacuum tube type but would offer the considerable advantages of greater feedback force, greater reliability and essentially zero power consumption. Evaluation of the power amplifier modules for possible use as driving sources for I_z currents, traveling wave mirrors, etc., was carried sufficiently to indicate that with some modification a module could provide 500 A at 25 kV over the frequency range from 0.3 to 1.5 MHz. Construction was begun on a 100-MHz, 1-MW pulsed, 4-kW CW power oscillator for preionization and/or plasma tube cleaning.

5. Equilibrium Trimming Circuit. A system was designed and fabricated to drive Scyllac $\ell=2$ equilibrium trimming windings. This system employs a "Jones" circuit[11] to provide a current step of up to 7 kA to 4 series $\ell=2$ windings with a wave shape having a quarter-cycle sine wave rise-time of 7 μs followed by a variable rise or fall of current of almost constant slope (± 10%) for 50 μs. To obtain a wide range of amplitudes, one vacuum gap and two ignitrons are used. For accurate control and reproducibility of the wave shape, separately controlled vacuum tube voltage regulators with constant current charging are used: one 50 kV at 5 mA and one 12 kV at 100 mA per circuit. The simplified circuit is shown in Fig. II-39 where S1 is an ignitron triggered by a master firing set; S2 is an ignitron fired by S3; S3 is a GE vacuum gap triggered by a Scyllac 8-kV pulser; C1 is 180 μF at 10 kV; C2 is 1.8 μF at 60 kV; L1 is 25 μH; and L2 is the $\ell=2$ trimming coil load of about 16 μH. Figure II-39 shows some possible wave shapes where S3 is fired 160 μs after S1 and V(C2) is varied from 20 to 40 kV. Fifteen units were constructed.

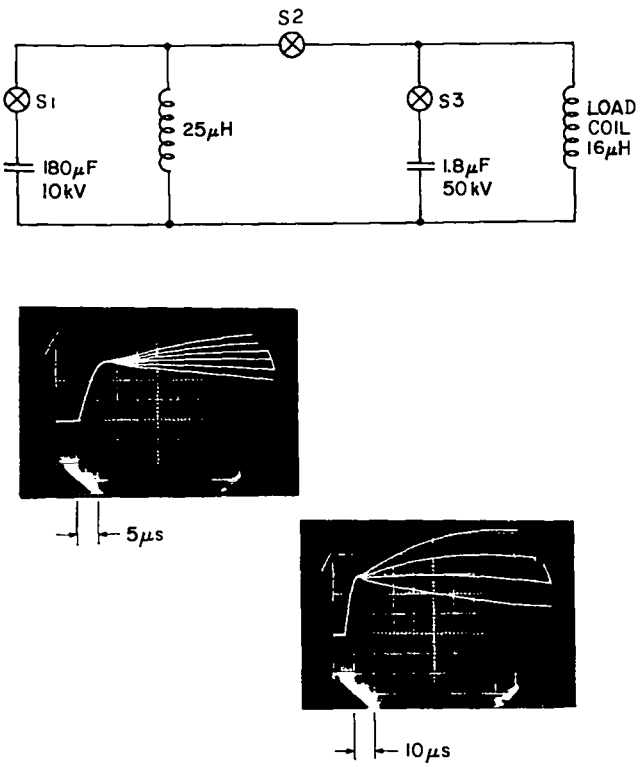

Figure II-39
Schematic diagram of "Jones" circuit connected to $\ell=2$ trimming coils and waveforms of the current produced in the trimming coils.

K. PREPARATIONS FOR ℓ=1,2 EQUILIBRIUM EXPERIMENTS

An ℓ=1,2 equilibrium configuration has been designed and fabricated for the Scyllac Feedback Sector. This design uses a large helical plasma distortion, $\delta_1 \sim 3$, in combination with a δ_2 plasma distortion, which is produced by a rotating quadrupole field (ℓ=2), to achieve high-beta toroidal equilibrium. This equilibrium configuration has the following advantages: (1) It eliminates the bumpy δ_0 plasma distortion and its transient effects, which have contributed to equilibrium difficulties in the ℓ=1,0 experiments. In addition δ_0 produces a nonsinusoidal asymmetry in the relative plasma cross sections which appears to produce undesirable effects including the δ_0 transient oscillations and an anomally in the magnetic flux excluded by the plasma column; (2) The equilibrium is independent of the δ_2 plasma distortion and has a weaker dependence on the plasma beta; and; (3) The parameters of the plasma column such as plasma beta and density will be uniform along the column.

In addition, the larger δ_1 has significant advantages in the stabilization of the m=1 instability. In feedback stabilization, the larger δ_1 reduces the growth rate of the m=1 instability and thereby relaxes both the delay-risetime requirement and the magnitude of the feedback field. The required feedback field is further reduced since it also depends inversely on δ_1. The utilization of the larger helical plasma distortions δ_1 requires the use of a helically shaped discharge tube in order to set up the toroidal plasma equilibrium and maintain an appropriate region between the plasma column and the tube wall. The present quartz forming device (cf. section C.3) with minor modifications has the capability for producing a tube with a larger helical radius.

1. Design of the ℓ=1,2 Equilibrium Configuration. The design of an ℓ=1,2 equilibrium field configuration was based on MHD sharp-boundary theory. Theoretical work by Barnes and Brackbill at LASL and by Betancourt and Garabedian at NYU on diffuse-profile equilibria for Scyllac indicate that the sharp-boundary description gives equilibrium fields which are low by 60% in the case of the ℓ=1,0 configuration and 20% for the ℓ=1,2 system. However, at the time this design was carried out there were unresolved questions in the diffuse profile theory concerning the ℓ=1,2 configuration. Therefore, since the diffuse-profile correction for the ℓ=1,2 system was small and equilibrium trimming fields were planned, the design proceeded on the basis of sharp-boundary theory.

In the sharp-boundary theory of an ℓ=1,2 equilibrium configuration, the ℓ=2 field produces an elliptical plasma distortion,

$$\delta_2 = B_{\ell=2}/ha(1-\beta/2)B, \tag{30}$$

and the ℓ=1 field a helical distortion,

$$\delta_1 = B_{\ell=1}/ha(1-\beta/2)B, \tag{31}$$

which results in a z-independent equilibrating force,

$$F_{1,2} = \beta(1-\beta/2)\, B^2h^2a^3\, \delta_1\delta_2/4 \ . \tag{32}$$

Equating this $F_{1,2}$ force to the outward toroidal force, $F_R = \beta B^2a^2/4R$, gives the equilibrium condition

$$\delta_1\delta_2 = 1/(1-\beta/2)\, h^2aR \ . \tag{33}$$

The growth rate of the m=1 instability is given by

$$\gamma^2 = h^2v_A^2[g_1(\beta)h^2a^2\delta_1^2 + g_2(\beta)\delta_2^2], \tag{34}$$

where

$$g_1(\beta) = \beta(4-3\beta)(2-\beta)/8(1-\beta)$$

and

$$g_2(\beta) = (1-\beta/2) \ .$$

The equilibrium parameters for the $\ell=1,2$ configuration were determined as follows. A δ_1 plasma distortion of approximately three is assumed and the growth rate of the m=1 instability is minimized with respect to h, the $\ell=1,2$ wave number, and the δ_2 plasma distortion. The minimization procedure gives

$$h = \left(\frac{g_2}{2g_1}\right)^{1/6} \frac{1}{(1-\beta/2)^{1/3}\,(\delta_1 a)^{2/3}\,R^{1/3}} \qquad (35)$$

and

$$\delta_2 = \frac{1}{(1-\beta/2)\,h^2\,R\,\delta_1 a} \quad . \qquad (36)$$

From a practical viewpoint, it is desirable for the wavelength of the $\ell=1,2$ configuration to be an integral number of the arc length of the existing compression coil sections. These considerations result in the following discrete $\ell=1,2$ wavelengths of interest: $\lambda_{1,2}$ = 83.776 cm, h = 0.0750 cm^{-1}; $\lambda_{1,2}$ = 104.720 cm, h = 0.060 cm^{-1}; and $\lambda_{1,2}$ = 125.664 cm, h = 0.050 cm^{-1}. Since the wavelength choice as well as the wave number h are being limited, Eq. (6) is solved for $\delta_1 a$,

$$\delta_1 a = \left(\frac{g_2}{2g_1}\right)^{1/4} \frac{1}{(1-\beta/2)^{1/2}\,h^{3/2}\,R^{1/2}} \quad . \qquad (37)$$

Figure II-40 graphs the growth rate of the m=1 instability as a function of the helical plasma distortion, δ_1, for various values of h computed from Eqs. (34), (37), and (38). An Alfven speed of 20 cm/μs and a plasma beta of 0.6 are assumed. Considering the discrete values of h above and the desired δ_1 value of approximately three, the m=1 growth rate is a minimum for h = 0.06 cm^{-1}, Fig. II-42. These considerations combined with the projected plasma parameters, particularly the plasma beta, and the planned use of $\ell=2$ equilibrium trimming fields resulted in the selection of the following equilibrium design

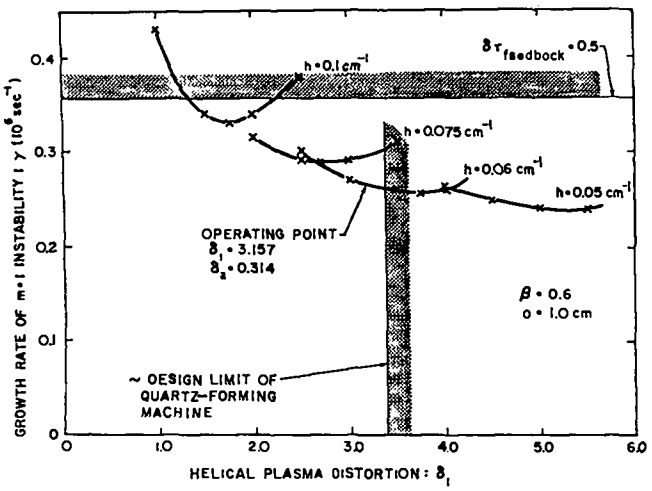

Figure II-40
Graphs of the growth rates of the m=1 instability as a function of the helical plasma distortion δ_1 for various values of the $\ell=1,2$ wavenumber h.

parameters: h = 0.06 cm^{-1}; β = 0.6; $\delta_1 a$ = 3.157 cm; $\delta_2 a$ = 0.314 cm; $B_{\ell=1}/B$ = 0.1326; and $B_{\ell=2}/B$ = 0.0132.

One of the objectives in this design is to be able to achieve plasma equilibria over a wide range of plasma beta values through the use of $\ell=2$ trimming fields. Computing $\delta_1 a$ from Eq. (31) with $B_{\ell=1}/B$ fixed above, δ_2 from the equilibrium condition, Eq. (33), and the $B_{\ell=2}$ equilibrium field from Eq. (30), Table II-II gives the expected working range of the parameters for this $\ell=1,2$ design with a possible limitation on achieving the higher plasma beta values. The feedback field required for stabilizing the m=1 mode is calculated from $B^{FB}_{\ell=2} = (\gamma/v_A)^2\,\xi\,B/\beta h\delta_1$, where ξ is the displacement from equilibrium and B is the magnitude of the main toroidal field. For the Table II-II computations, ξ=1 cm and B=15 kG.

2. Compression Coil with $\ell=1,2$ Flux Surface. The inner surface of the compression coil is machined to coincide with an $\ell=1,2$ magnetic flux surface to generate the $\ell=1$ and $\ell=2$ equilibrium fields.

An approximate analytic solution for the coil flux surface has been determined following the procedure used by Weitzner for an $\ell=1,0$ system.[24] In the case of the $\ell=1,2$ system it is necessary to retain both $\ell=1$ and $\ell=2$ fields to zeroth order in an expansion solution of $B \cdot \nabla\psi = 0$, since the amplitude of the $\ell=2$ field required for toroidal

TABLE II-II

PARAMETERS FOR THE SELECTED $\ell=1,2$ CONFIGURATION

β	0.4	0.5	0.6	0.7	0.8
$\delta_1 a$ (cm)	2.762	2.947	3.157	3.400	3.683
δ_2	0.314	0.314	0.314	0.314	0.314
$B_{\ell=2}/B_o$	0.01508	0.01414	0.01320	0.01225	0.01131
γ (MHz)	0.245	0.273	0.299	0.328	0.368
$B_{\ell=2}$(G)	34.1	31.5	29.6	28.3	28.8

equilibrium near the minor axis is on the same order as the $\ell=1$ field at the position of the compression coil surface. For a magnetic field system consisting of $\ell=1$, $\ell=2$, vertical and $\ell=3/m=2$ fields in addition to the main field, B_o, the fields and flux function as determined from the expansion solution to $B \cdot \nabla\phi = 0$ are given by ($h \ll 1$),

$$\bar{B} = B_o \bar{1}_z + \nabla\phi \qquad (38)$$

$$\phi = -\frac{1}{ha}\frac{B_{\ell=1}}{B_o}\frac{B_{\ell=2}}{B_o} r \sin\theta + \frac{B_{\ell=1}}{B_o} r \sin(\theta-hz)$$

$$+ \frac{B_{\ell=2}}{B_o}\frac{r^2}{2a}\sin(2\theta-hz)$$

$$- \frac{2r^3}{3r_w^2\, ha}\frac{B_{\ell=1}}{B_o}\frac{B_{\ell=2}}{B_o}\sin(3\theta-2hz) \quad ,$$

and

$$\psi = \frac{r^2}{2} - \frac{r}{h} - \frac{1}{ha}\frac{B_{\ell=1}}{B_o}\frac{B_{\ell=2}}{B_o}\cos(2\theta-hz)$$

$$+ \frac{B_{\ell=1}}{B_o}\cos(\theta-hz) = \frac{r}{ha}\frac{B_{\ell=2}}{B_o}\cos(2\theta-hz)$$

$$- \frac{1}{ha}\frac{B_{\ell=1}}{B_o}\frac{B_{\ell=2}}{B_o}\frac{r^2}{r_w^2}\cos(3\theta-2ha) \quad ,$$

where r_w is the average radius of the inside of the compression coil.

The amplitude of the vertical field given above, $(1/ha)\, B_{\ell=1}/B_o\, B_{\ell=2}/B_o$, for a system with $\delta_1 = 3.157$, $\delta_2 = 0.314$, $\beta = 0.6$, $\lambda = 104.72$ cm, and $a = 1.0$ cm is calculated to be 0.029. This is to be compared with the value determined by utilizing the flux surface program of 0.03. The vertical field amplitude is determined by the beating of the $\ell=1$ and $\ell=2$ fields. The $\ell=3/m=2$ component is added to beat against the $\ell=2$ field to counteract the vertical field beating against the $\ell=2$ field. The amplitude of the $\ell=3/m=2$ field is -2 times the amplitude of the vertical field at the mean coil radius. At the location of the plasma, $r \sim 1.0$ cm, the amplitude of the required $\ell=3/m=2$ component is a factor of $\sim (a/b)^2$ smaller than the vertical field. The amplitude of the $\ell=3/m=2$ component will therefore be $\sim 0.0006\, B_o$ at $r = a$ and should be negligible.

The flux function given above checks approximately with an analytic expression for a rotating displaced ellipse with dimensions given in Fig. II-41.

A new computer code utilizing the above equations for the magnetic fields and many of the techniques of the original $\ell=1,0$ code has been written to compute the magnetic flux surfaces of the $\ell=1,2$ configuration. The flow diagram for the code is given in Fig. II-42. The flux surface

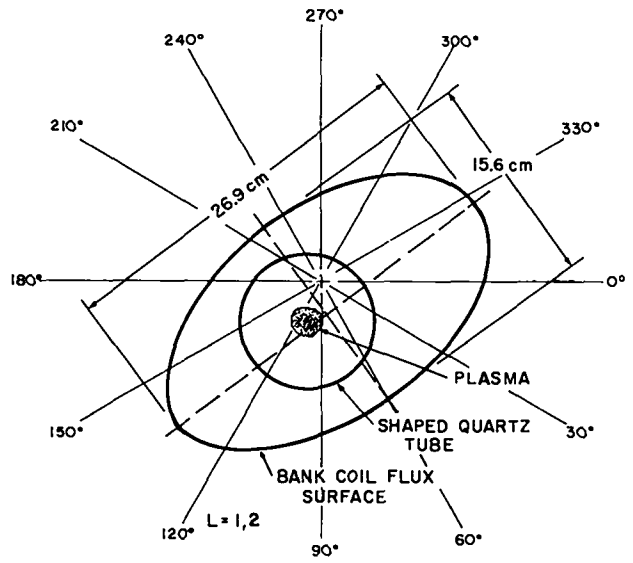

FIGURE A

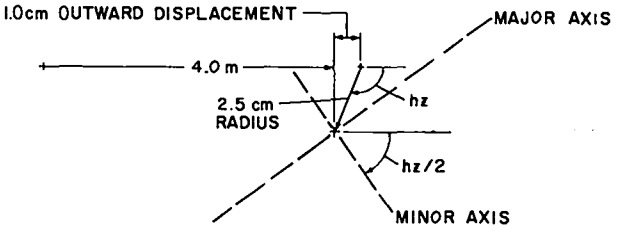

FIGURE B

Figure II-41
(A) $\ell=1,2$ elliptical flux surface profile at $z = 0.3\ \lambda$ ($hz=0.6\ \pi$). (B) Location of origin and orientation of axes of the $\ell+1,2$ rotating elliptical flux surface.

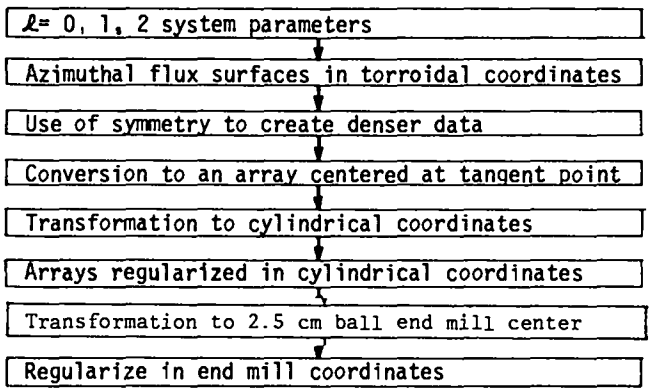

Figure II-42
Flow diagram of computer code to generate tape mill instructions for fabricating Scyllac coil mandrels.

output data from the 7600 was transformed to produce the tape drives for controlling a three-dimensional milling machine. The mill produced mandrels of the coil flux surface which were used with a hydraulic profile-tracer arrangement on a lathe to machine the inner surface of the single-turn compression coils. Figure II-43 is a photograph of a section of the new coil. A typical coil cross section is shown in Fig. II-44 with the helical quartz tube, tube support, and $\ell=2$ windings.

The primary field components of the new $\ell=1,2$ coils have been measured with single wavelength $\ell=1$, $\ell=2$, and vertical-field probe coils wound on a section of a toroidal discharge tube. The measured values agree with the design values to within the measurement error.

3. Status of the $\ell=1,2$ Feedback Sector. The plans for the modification of the $\ell=1,0$ feedback sector to the $\ell=1,2$ configuration have been worked out in detail. During the changeover the arc length of the feedback sector will be increased by 40% from 8.4 to 11.7 m through the addition of two energy storage racks. The modifications will begin as soon as the present $\ell=1,0$ experiments are completed.

The fabrication of the $\ell=1,2$ compression coils have been completed. The quartz-forming

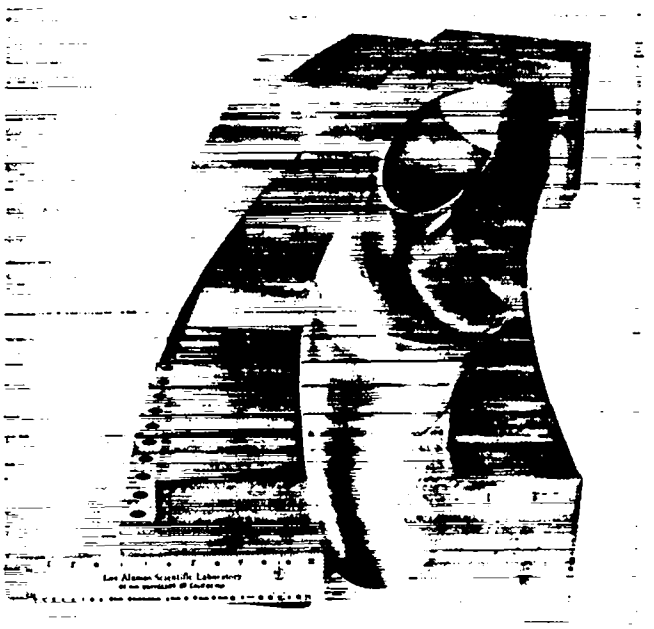

Figure II-43
Photograph of the $\ell=1,2$ flux surface machined in the Scyllac compression coils.

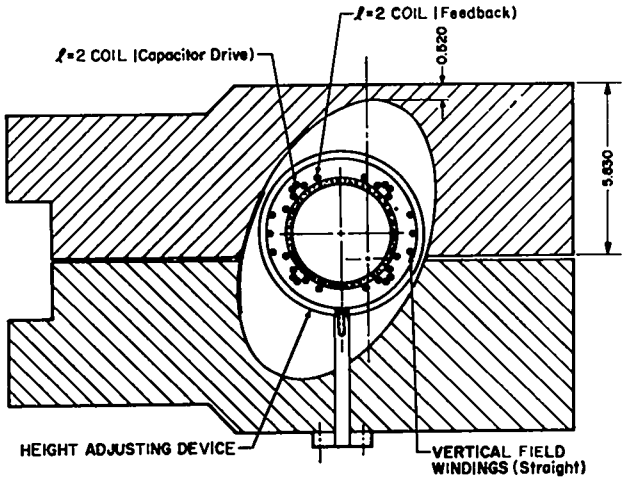

Figure II-44
Compression coil cross-section showing the inner bore shaped to an ℓ=1,2 flux surface. The helical quartz discharge tube and its support, ℓ=2 feedback and trimming windings, and vertical field windings are also shown.

device has been modified and helical quartz discharge tubes fabricated with a helix radius of 3 cm for the ℓ=1,2 configuration. The ℓ=1,2 sector is being assembled off the Scyllac sector in order to fit the discharge tubes into the sector and wind the ℓ=2 feedback and equilibrium trimming windings directly on the discharge tube.

L. SIMILARITY BETWEEN WALL STABILIZATION AND ℓ=2 FEEDBACK

It has been postulated that wall stabilization is similar to ℓ=2 feedback. The following gives a relatively quick demonstration of the ℓ=2 nature of wall stabilization. Consider a straight ℓ=1 system with a plasma centered in a coil. The fields of this system are given by (hr << 1)

$$\bar{B} = B_o \left[\bar{I}_z + \nabla\phi\right]$$

$$\phi = \frac{B_{\ell=1}}{B_o}\left[hr\left(1 + \frac{(hr)^2}{8}\right) - \frac{(ha)^2\ \beta/2}{(1-\beta/2)\ hr}\right]\frac{\sin(\theta-hz)}{h} .$$

If the plasma column is displaced transversely by x_o, the column sees the compression field as a combination of ℓ=1,0 and two fields

$$r\sin\theta = r'\sin\theta' + x_o \ ;\ r\cos\theta = r'\cos\theta'$$

$$\phi(r',\theta') = \frac{B_{\ell=1}}{B_o}\left[hr'\frac{\sin(\theta'-hz)}{h} - \frac{h\,x_o\sin hz}{h} + \frac{h\,x_o}{8}(hr')^2\frac{\sin(2\theta'-hz)}{h} + \ldots . + \text{reaction terms in displaced system}\right].$$

The ℓ=0 and ℓ=2 fields seen by the displaced column can be shown to lead to the m=1 instability. The reaction term for the ℓ=1 field is unchanged in amplitude (since the ℓ=1 field in the displaced system has the original amplitude). The fields of the displaced, helical plasma column are given by the following potential including the ℓ=1 reaction term

$$\phi = \frac{B_{\ell=1}}{B_o}\left[hr\left(1 + \frac{(hr)^2}{8}\right)\frac{\sin(\theta-hz)}{h} - \frac{(ha)^2\ (\beta/2)\ \sin(\theta'-hz)}{(1-\beta/2)\ hr'} + \ell=0 \text{ and } \ell=2 \text{ reaction terms due to displacement}\right].$$

The $I_n(hr)$ fields have been reexpressed in terms of the r,θ (undisplaced) coordinate system. Fields derived from the above expression do not completely match the boundary condition at the compression coil surface (B·n = 0). Transforming the ℓ=1 reaction term to the r,θ coordinates

$$\phi = \frac{B_{\ell=1}}{B_o}\left[hr\left(1+\frac{(hr)^2}{8}\right)\frac{\sin(\theta-hz)}{h}\right.$$

$$-\frac{(ha)^2\,\beta/2}{(1-\beta/2)\,hr}\,\frac{\sin(\theta-hz)}{h}-\frac{h\,x_o}{(hr)^2}\,\frac{\sin(2\theta-hz)}{h}$$

$$\frac{(ha)^2\,\beta/2}{(1-\beta/2}+\ell=0 \text{ and } \ell=2 \text{ reaction terms}$$

$$\left.\text{due to displacement}\right].$$

The first two terms are the original $\ell=1$ field which satisfies $B\cdot n = 0$ at the compression coil surface. The third term is an $\ell=2$ term which must satisfy $B\cdot n = 0$ at the coil surface by the addition of a second-order reaction term of the form

$$\Delta\phi = \frac{B_{\ell=2}}{B_o}\,\frac{r^2}{2a}\sin(2\theta-hz)\ .$$

For a nearly circular compression coil surface, the normal is approximately a unit vector in the radial direction. $B\cdot n = 0$ means that the radial reaction field ($\ell=2$ component) must be matched by the radial component δ_r $(\Delta\phi)$ at r=b. Therefore

$$\frac{B_{\ell=2}}{B_o} = -\frac{a}{b}\,\frac{2hx_o}{hb^3}\,\frac{(ha)^2\,\beta/2}{1-\beta/2}\,\frac{B_{\ell=1}}{B_o}$$

$$= -2\left(\frac{a}{b}\right)^4 hx_o\,\frac{\beta}{2}\,\delta_1\ .$$

The $F_{1,2}$ force on the plasma column due to the $\ell=2$ reaction field from the wall is given by

$$F_{1,2} = \beta(1-\beta/2)\,B_o^2\,\frac{h^2a^3\delta_1\delta_2}{4} = \beta\,B_o^2\,\frac{ha^2\delta_1}{4}$$

$$\frac{B_{\ell=2}}{B_o} = -\beta^2\left(\frac{a}{b}\right)^4 (ha)^2\,\frac{\delta_1^2}{4}\,B_o^2\,x_o\ .$$

The equation of motion therefore includes terms of the form

$$\frac{d^2x_o}{dt^2} = x_o\left[-\frac{\beta^2h^2B_o^2}{4\pi\rho}\left(\frac{a}{b}\right)^4\delta_1^2+\ldots.\right].$$

This is the standard wall stabilization term as given by sharp-boundary theory. The $\ell=2$ surface current in the nearly cylindrical surface is given by

$$\left(\frac{K_s}{B_o}\right)_{\ell=2} = 2\,\frac{B_{\ell=1}}{B_o}\,hx_o\left(\frac{a}{b}\right)^2\,\frac{\beta/2}{1-\beta/2}\cos(2\theta-hz)$$

$$\left[\frac{2i_z}{hb}-i_\theta\right].$$

Currents of this form and the corresponding form for a "Y" displacement should not be disturbed by flux conservers, etc., if wall stabilization is to be effective.

REFERENCES

1. W. R. Ellis, F. C. Jahoda, R. Kristal, W. E. Quinn, G. A. Sawyer, and R. E. Siemon, "Plasma Equilibrium and Stability in the Scyllac Toroidal Sector Experiments," Nuclear Fusion 14, 841 (1974).

2. E. L. Cantrell, W. R. Ellis, H. W. Harris, F. C. Jahoda, R. Kristal, M. D. Machalek, J. R. McConnell, W. E. Quinn, F. L. Ribe, G. A. Sawyer, F. T. Seibel, and R. E. Siemon, "Plasma Experiments in the Scyllac Toroidal Theta Pinch," Plasma Physics and Controlled Nuclear Fusion Research, (IAEA, Vienna, 1175), Vol. III, p. 13.

3. E. L. Cantrell, W. R. Ellis, B. L. Freeman, R. F. Gribble, W. D. Gutscher, K. J. Johnson, K. F. Kutac, G. Miller, W. E. Quinn, "Scyllac Feedback Stabilization Experiments," Proc. Third Topical Cong. on Pulsed, High Beta Plasma, Culham, England, Sept. 9-12, 1975.

4. G. A. Sawyer, compiler, "LASL Controlled Thermonuclear Research Program, January-December 1975," Los Alamos Scientific Laboratory report, LA-6582-PR, December, 1976.

5. D. C. Barnes, J. U. Brackbill, R. Y. Dagazian, J. P. Friedberg, W. Schneider, O. Betancourt, and P. Garabedian, Proc. 6th IAEA Conference, Berchtesgadens, West Germany, October 6-13, 1976.

6. R. Gribble and G. Miller, Rev. Sci. Instrum. 48, 778 (1977).

7. E. L. Cantrell, G. Miller, W. E. Quinn, and W. Riesenfeld, Nucl. Fusion (to be published 1977).

8. G. Miller, "Long Wavelength m=1 Magnetohydrodynamics of a Theta Pinch," Phys. Fluids 20, 928 (1977).

9. F. L. Ribe, compiler, "LASL Controlled Thermonuclear Research Program, January-December 1974," Los Alamos Scientific Laboratory report, LA-6044-PR, August 1975.

10. CTR-3 Quarterly Progress Reports; January-March 1975, p. 28 and April-June 1975, p. 14. Los Alamos Scientific Laboratory internal documents.

11. E. S. Weibel and I. R. Jones, Rev. of Sci. Instr. 32, 972 (1961).

12. W. Riesenfeld, private communication.

13. W. Grossmann and J. Tataronis, Z. Physik, 261 (1973).

14. R. L. Morse, "Equilibria of Collisionless Plasma," Los Alamos Scientific Laboratory report, LA-3844-MS (1969).

15. R. L. Morse and J. P. Friedberg, "Rigid Drift Model of High-Temperature Plasma Containment," Phys. Fluids 13, 531 (1970).

16. S. I. Braginskii, "Transport Processes in a Plasma," in Reviews of Plasma Physics, Vol. 1, M. A. Leontovich, Ed., Consultants Bureau Enterprises, New York (1965).

17. L. Spitzer, Jr., Physics of Fully Ionized Gases, (Interscience, New York, 1962).

18. R. C. Davidson and N. T. Gladd, "Anomalous Transport Properties Associated with the Lower Hybrid-Drift Instability," Phys. Fluids 18, 1327 (1975).

19. H.A.B. Bodin and A. A. Newton, "Study of the Diffusion of High-β Plasma in a Theta Pinch," Phys. Fluids 12, 2175 (1969).

20. W. M. Manheimer, "Strong Turbulence Theory of Nonlinear Stabilization and Harmonic Generation," Phys. Fluids 14, 579 (1971).

21. R. L. Dewar, "Saturation of Kinetic Plasma Instabilities by Particle Trapping," Phys. Fluids 16, 431 (1973).

22. D. Winske and D. W. Hewett, "Flute Instabilities in Two-Dimensional Simulations of Strongly Inhomogeneous Theta-Pinch Plasma," Phys. Rev. Lett. 35, 937 (1975).

23. H. P. Furth, J. Kileen, and M. N. Rosenbluth, "Finite-Resitivity Instabilities of a Sheet Pinch," Phys. Fluids 6, 459 (1963).

24. H. Weitzner (private communication).

III. STAGED THETA-PINCH PROGRAM

K. S. Thomas, W. H. Borkenhagen, C. J. Buchenauer, D. L. Call,
J. N. Downing, C. F. Hammer, A. R. Jacobson, R. K. Linford,
E. M. Little, D. A. Platts, and E. G. Sherwood

A. INTRODUCTION

Previous theta pinches have performed initial implosion heating of the ions and subsequent adiabatic compression with a single capacitor bank power supply. Projected theta-pinch feasibility experiments and fusion reactors, however, will require separation of the two functions to achieve greater implosion heating and less adiabatic compression. The Staged Theta-Pinch program is designed to study the technological and physics problems associated with separating the two functions.

The principal experiment in the program is the 4.5-m-long linear Staged Theta Pinch (STP). The experiment uses a low-energy, high-voltage capacitor bank (PFN I) to produce the plasma and a lower voltage, higher energy capacitor bank to provide a variable amount of adiabatic compression. A second low-energy, high-voltage capacitor bank (PFN II) is available to shape the implosion magnetic field and to assist in containing the plasma before it contacts the wall of the discharge chamber. The STP experiment produces high-temperature plasmas with a much larger ratio of plasma radius to discharge tube radius than theta pinches which utilize a single capacitor bank for both implosion heating and adiabatic compression. By adjusting the relative timing between the three capacitor banks, the effect of magnetic field amplitude and time history on the properties of the STP plasma have been investigated.

Initial plasma studies have concentrated on optimizing the plasma temperature and radius while minimizing the plasma outside the main plasma column. Plasma behavior has been studied for initial D_2 fills of 5 mTorr to 15 mTorr and PFN-I voltages from 65 kV to the full design voltage of 125 kV. Plasmas have been produced with a ratio of plasma radius to discharge tube radius of 0.45 to 0.55 and ion temperatures of up to 1300 eV.

The other experiment in the program was the 0.9-m-long Resonant Heating Experiment (RHX). During 1976, the experiment was used primarily to study the effect of preionization levels on plasma sweep-up during the initial implosion and to make a detailed comparison of the experimental plasma density profiles with the predictions of a numerical code developed by Sgro and Nielson.[1] The experiment was terminated in July 1976.

B. STAGED THETA PINCH

1. Description. The layout of the STP experiment in the old Scylla-IV experimental area is shown in Fig. III-1 and two photographs of the experiment are shown in Figs. III-2 and III-3.

The Staging bank, which is the Scylla-IV main bank, is located on a platform above the high-voltage implosion circuit. The start switches for the staging bank have been moved down to the collector plate in order to isolate the load cables from the high-voltage circuit. This necessitated the replacement of the start switch in the Scylla-IV capacitor gaps with a shorting column. The crowbar system was left intact. The high-voltage gaps are connected directly into the collector plates to minimize source inductance. The 22-cm-i.d. main coil is fed from two sides to

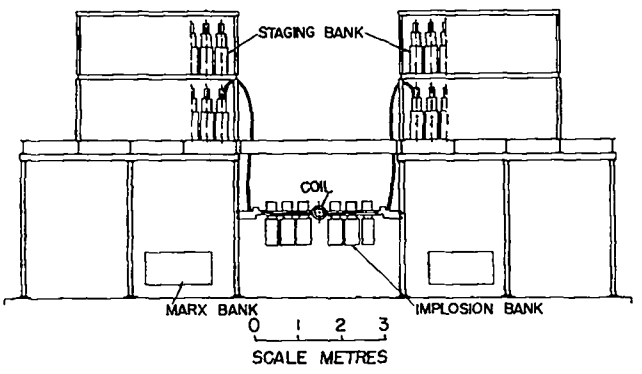

Fig. III-1.
Layout of the Staged Theta-Pinch experiment.

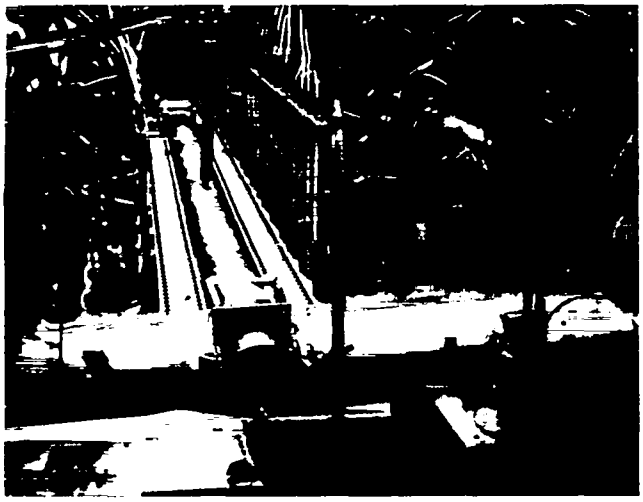

Fig. III-2.
Photograph of Staged Theta-Pinch experiment showing top of collector plates and compression coil.

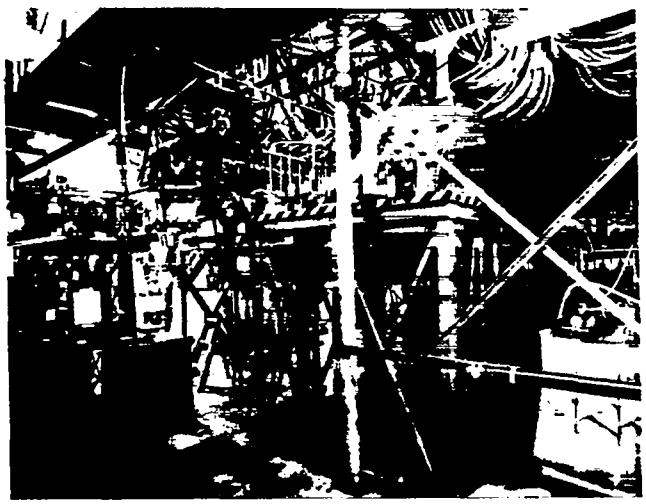

Fig. III-3.
Photograph of Staged Theta-Pinch experiment showing side view of the experiment.

increase the magnetic field risetimes. Because the components are the same on both sides of the machine, the two sides of the experiment operate at different voltage polarities.

A circuit diagram of one-half of the experiment is shown in Fig. III-4. Table III-I gives the electrical parameters of the various capacitor banks when they are operated alone with no plasma in the discharge tube.

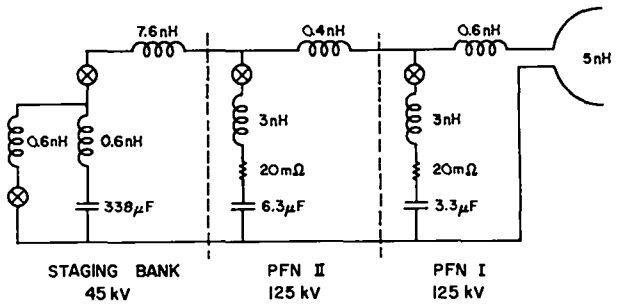

Fig. III-4.
Circuit diagram of one-half of the Staged Theta Pinch experiment.

TABLE III-I
ELECTRICAL PARAMETERS

	PFN I	PFN II	Staging
Capacitance	6.6 μF	12.6 μF	675.2 μF
Voltage	125 kV	125 kV	45 kV
Energy	52 kJ	98 kJ	684 kJ
Risetime (τ/4)	0.26 μs	0.35 μs	3.7 μs
Peak Magnetic field	5 kG	6 kG	14.5 kG

2. Engineering. In September 1976, the Staged Theta Pinch first operated reliably at its full design voltage of 125 kV on the implosion banks (PFN I and II). Also, under these conditions, magnetic field waveforms were produced which generated large-diameter, high-temperature plasma columns with only a low level of plasma outside the main column. To achieve these results three improvements in the experiment were necessary.

a. Resistance was added to the PFN circuits. This was necessary in order to reduce late time modulations of the magnetic field which caused magnetic flux to move into and out of the discharge tube, creating "secondary" plasma. The resistors used were liquid resistors which mounted on top of the capacitors under the PFN gaps. Initially the value of the resistors was 0.2 Ω. In November 1976, the value of the resistors in the PFN-II circuit was raised to 0.5 Ω. This further reduced the late time magnetic field oscillations.

b. The new Staging spark gaps described in the 1975 Annual Report[2] were installed. This eliminated corona problems which had limited the voltage at which the experiment could be operated. The gaps installed were cast out of fiber glass and

epoxy. A gap made of fiber glass-filled polypropylene was developed and these gaps will be used in the future as spares are needed.

c. Submaster trigger gaps made from modified PFN gaps were installed on the PFN I and II banks. Also it was found that to operate at 125 kV it was necessary to trigger the negative PFN banks with positive triggers and the positive PFN banks with negative triggers. The different polarity submasters are triggered by a common master by inverting the master trigger pulse between the master and one of the submasters.

3. Experimental Program.

a. Operating Conditions. In early 1976, two plasma studies were conducted. The implosion phase was studied over a range of about a factor of two in initial magnetic field rise and from 5-15 mTorr initial D_2 fill. Also, magnetoacoustic heating of the plasma column was studied by generating a plasma column with the Staging bank and then modulating the magnetic field at the plasma's natural oscillation frequency with the PFN I bank.

After the resistance was added to the PFN circuits, a series of data runs were conducted with PFN voltages from 70 to 125 kV. Initial D_2 fills of 5-15 mTorr were used and the magnetic field waveform was varied to study the effects of various waveforms on plasma behavior.

b. Diagnostics. The principal diagnostics used to measure plasma behavior were two interferometers[3,4] and an excluded flux apparatus.[5] Various magnetic probes, both external and internal to the discharge tube were used. Also, streak pictures of the plasma column were made end-on and side-on.

Plasma density profiles were measured with a holographic interferometer[3] which made interferograms at two times during each plasma discharge. A diagram of the apparatus is shown in Fig. III-5. To determine the absolute density at one radial position, a new quadrature interferometer[4] was developed. A diagram of the interferometer is shown in Fig. III-6. The interferometer differs from an ordinary Mach-Zehnder in that the reference beam is changed from plane to circular polarization. Both components of the circularly polarized beam

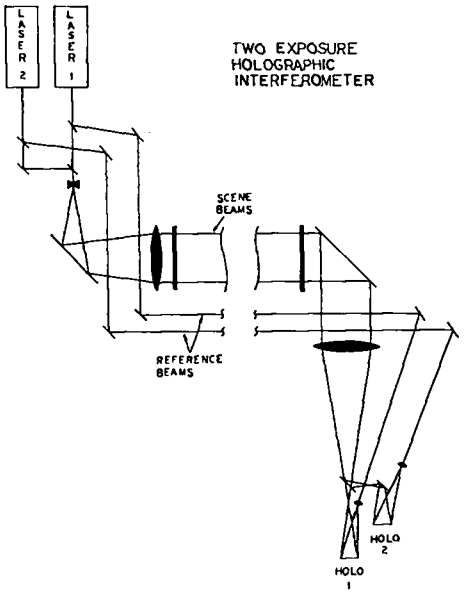

Fig. III-5.
Diagram of the holographic interferometer.

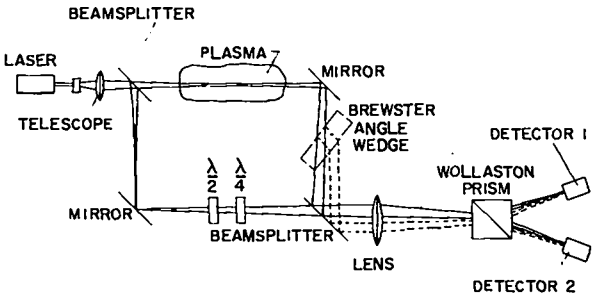

Fig. III-6.
Diagram of the quadrature interferometer. Dashed lines indicate displacement of beams during calibration procedure.

interfere with the scene beam. Thus, with proper separation of the beams, the device becomes two interferometers which are always 90° out of phase with each other. This eliminates many of the problems associated with ordinary Mach-Zehnder interferometers. A full description of the apparatus is being published.[4]

c. Plasma Results.

(1) Plasma Studies of Staged Plasma Columns. For the studies reported here, the preionization level at the time of the main discharge was ~ 60% for radial positions less than 9 cm. From this position outward it decreased monotonically to a value of 20-30% at the discharge wall. Also for all cases the plasma β on axis at the peak of the

main compression field was equal to 1 within experimental error.

In all cases some plasma remained outside the main plasma column. The minimum value for this plasma was 0.5-1 x 10^{14} cm^{-3}. When the plasma outside the main column was held to this level, plasma columns were produced with radii of 4.5-5.0 cm. Because the plasma column had a diffuse profile, the plasma radius was chosen as the 1/e point in the density profile. This approximates the radius of a sharp boundary plasma with the same peak density and line density (particles/unit length of plasma column). In addition, this radius is the one which would be used in determining if the plasma could be wall stabilized in a helical geometry.[6] The sum of the electron and ion temperatures ($T_e + T_i$) was determined from pressure balance at the peak of the compression field and ranged from 400 eV to 1500 eV. If it is assumed that electron temperature is determined by the transfer of energy from the ions to the electrons and subsequent loss by thermal conduction out the ends of the experiment,[7] then the electron temperature should be 100-150 eV. This implies a range of ion temperatures of 300-1350 eV. A typical example is shown in Fig. III-7, which shows the plasma density profile

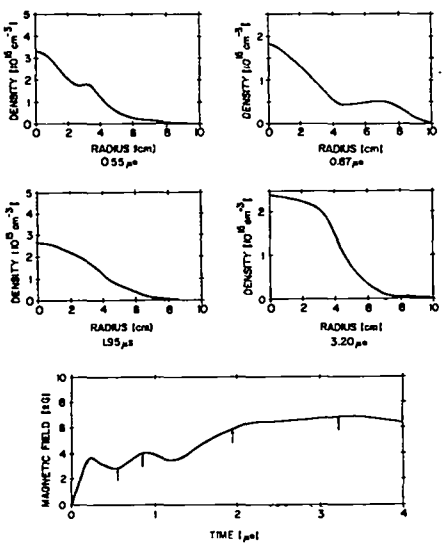

Fig. III-7.
Density vs radius for the four times indicated on the magnetic field waveform shown. PFN voltage - 100 kV, Staging voltage - 20 kV, fill - 10 mTorr D_2.

at four times during the plasma discharge along with the magnetic field waveform.

In optimizing plasma temperature and radius in combination with a low level of plasma outside the main column, two factors were found to be important.

(a) The most important parameter in the production of plasma outside the main plasma column was the amount of magnetic flux which left the discharge tube after the initial implosion. This is illustrated in Fig. III-8, which shows the magnetic field, a holographic interferogram, and the reduced data from the interferogram for two cases. Figure III-8(a) is for a "step-function" waveform[8] where no flux leaves the discharge tube. In Fig. III-8(b) the dip in the magnetic field caused flux to move outward. This flux carried low-density plasma into the wall and caused the creation of additional plasma.

(b) The magnetic field waveform which produced the optimum results involved a certain amount of "field programming."[8] After the initial field rise the external field dipped, but because of the change in plasma area, no magnetic flux left the discharge tube. Numerical code results[1,9] show that the plasma ions have a complicated spatial and velocity distribution. It is probable that the highest energy ions are moving outward at the time of the magnetic field dip so less work is done by them on the magnetic field than would be the case if the field did not dip. Thus more energy is left in the plasma after the implosion and reexpansion phase than would

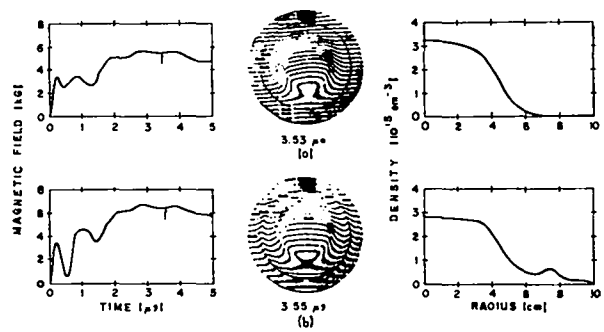

Fig. III-8.
Magnetic field waveform, holographic interferogram, and density vs radius for (a) "step-function" waveform and (b) "field programming" waveform. PFN voltage - 70 kV, Staging voltage - 15 kV, fill - 10 mTorr D_2.

occur for a "step function" magnetic field waveform. This theoretical prediction is supported by the experimental results. As measured by the excluded flux apparatus, the more the plasma reexpanded after the initial implosion, the larger the plasma radius and temperature. Of course if the field dip was too large, magnetic flux was drawn out of the discharge tube and "secondary" plasma was formed. These points are illustrated in Fig. III-9, which shows the plasma column density vs radius for the three magnetic field waveforms shown. The experimental conditions were those for which the Sgro-Nielson code predicted resonance between the electric circuit and the plasma column. In all cases $\beta \approx 1$ so the plasma density on axis was inversely proportional to the plasma temperature. As seen from the center example, a certain amount of "field programming" increased the plasma temperature and radius without producing a large amount of "secondary" plasma. In the lower example, the plasma temperature and radius were even larger but "secondary" plasma was produced by the plasma drawn into the discharge tube wall as flux was removed from the discharge tube.

(2) Implosion Studies. Implosion studies were conducted under a range of experimental conditions. Unlike the studies on Scylla I-B and IHX, which concentrated on studying the implosion dynamics, the purpose of these experiments was to determine the amount of plasma outside the main column after the initial implosion. One set of experiments was run at 65 kV on the PFN banks and for initial D_2 fills of 5 and 10 mTorr. For these cases PFN I and PFN II were sequenced so that the external magnetic field rose to 2.9 kG in 200 ns and then was constant for 700 ns, after which time it decreased to zero. In other studies PFN I and PFN II were fired simultaneously. Charge voltage was 100 kV and initial fill levels were 5, 10, and 15 mTorr D_2. This produced an initial magnetic field rise which was equal to that expected if PFN I was operated alone at 125 kV. In these cases, the magnetic field rose to 6 kG in 180 ns. The waveform was almost flattopped as a result of the varying inductance of the circuit resulting from the plasma implosion and reexpansion.

Results of these studies are shown in Figs. III-10 and III-11 where plasma density is plotted vs radius for six representative times. Figure III-10 shows the results for 65-kV PFN voltage and 10-mTorr initial fill. Figure III-11 presents the results for 100-kV PFN voltage and 10-mTorr fill.

The two experimental cases differ in the following ways: (1) Peak density on the discharge tube axis is higher for the 100-kV case. (2) For the 100-kV case a well-defined reexpansion of the plasma column is observed. This does not occur at 65 kV. (3) The radial distribution of the low density plasma outside the main column is

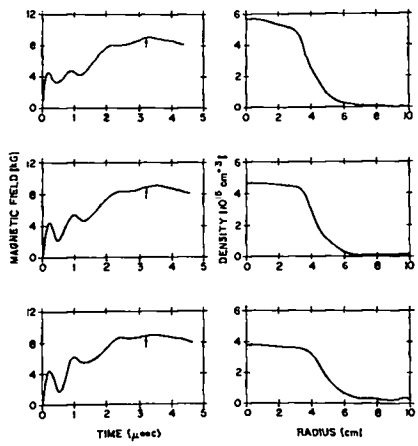

Fig. III-9.
Plasma density vs radius at peak magnetic field for the three magnetic field waveforms shown. PFN I voltage - 125 kV, PFN II voltage - 100 kV, Staging voltage - 25 kV, fill - 15 mTorr D_2.

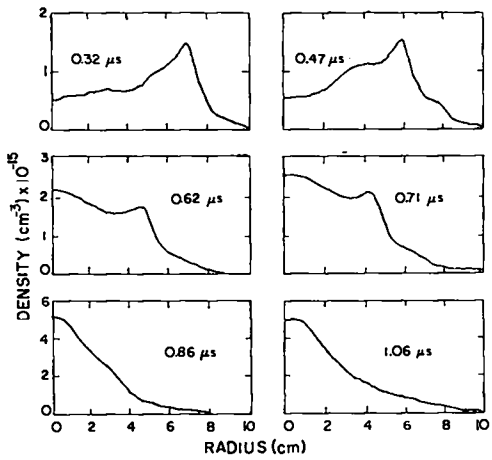

Fig. III-10.
Plasma density vs radius at six times for PFN voltage of 65 kV.

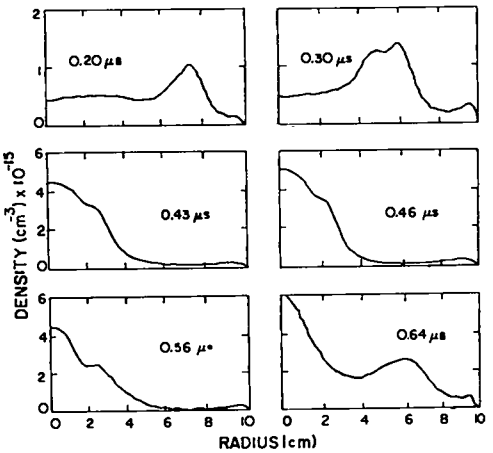

Fig. III-11.
Plasma density vs radius at six times for PFN voltage of 100 kV.

different. In the lower voltage case the density decreases monotonically to the discharge tube wall while for the 100-kV case a minimum occurs approximately halfway between the main column and the wall. Minimum plasma densities are about the same (∿ 10% of initial fill) in both cases.

(3) Magnetoacoustic Heating Studies. The magnetoacoustic heating studies conducted in April 1976 showed that externally driven magnetoacoustic plasma oscillations can be an effective method of providing auxiliary heating for theta-pinch plasmas. The magnetic field waveform with and without resonant modulation is shown in Fig. III-12(a). Figure III-12(b) shows the effect of the external modulation on plasma radius. At later times the area of the plasma column has increased by approximately 50% due to the field modulation. A more complete description of these studies has been published.[10]

C. RESONANT HEATING EXPERIMENT

1. Description. During 1976, the RHX operated in two configurations. For the first three months it was arranged as a 0.9-m version of the implosion circuits on the STP. The only difference was that the RHX had a secondary 0.4 μF preionization bank which was fired a short time before the initial implosion. In April the machine was changed to the resonant heating configuration. This involved replacing one of the PFN-I 0.2-μF capacitors on each side of the

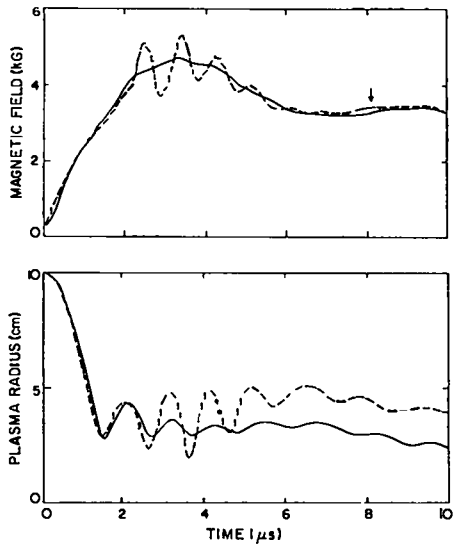

Fig. III-12.
(a) Magnetic field without (solid curve) and with (dashed curve) resonant modulation. The arrow indicates when $T_e + T_i$ is inferred from pressure balance. (b) Effective $\beta = 1$ radius, as derived from excluded flux data, without (solid curve) and with (dashed curve) resonant field modulation. The timing is the same in III-12(a).

experiment with a 0.4-μF capacitor. These capacitors then became part of the PFN-II circuit. The two PFN-I capacitors nearest the coil on each side of the machine were replaced with shorts, turning these PFN gaps into crowbar gaps.

2. Engineering. Three engineering changes were incorporated into the RHX to enable the experiment to perform its experimental program.

a. When the secondary preionization bank was installed it was found that the bank prefired when the primary preionization bank was fired. The problem was solved by installing low-inductance liquid resistors across the collector plates to dampen out the high-frequency electrical transients. These resistors did not appreciably affect the main magnetic field waveform.

b. Cable shorting trigger systems were developed for both the pulse-charged master trigger gaps and the dc-charged preionization banks. These systems are much simpler than the previously used Scyllac buffer systems, and they operate with much less jitter.

c. When the PFN gaps were converted for use as crowbar gaps it was found that the trigger system energy was insufficient to trigger them properly. Numerous modifications were made to the

trigger system to increase the energy. The understanding developed during the implementation of these changes led to greatly improved performance of the crowbar system. These design changes were incorporated and extended during the modification of the experiment to the Field Reversal Theta Pinch (see Sec. VIII of this report).

3. Experimental Program.

a. Operating Conditions. The objectives of the preionization study were twofold. First, to determine the effect of the secondary preionization on plasma sweep-up during the initial implosion. Secondly, to provide data for a detailed comparison of the experimental results with a numerical code.[1] In order to reduce the variables in the experiment the following conditions were held fixed. Capacitor bank voltages were 70 kV on the preionization banks and 65 kV on the PFN banks. Initial D_2 fill was 10 mTorr. The only parameters changed were the timing of the firing of the banks. Data were taken both with and without the secondary preionization bank.

The data were compared with the output of a numerical code which contained the hybrid simulation code[1] developed by Sgro and Nielson and a circuits code[11] developed by Nielson for an earlier hybrid code. Several modifications were made in the code to improve its correlation with the experiment. The three modifications which made the most significant improvement were: (1) making the initial density profile in the code agree with the experimentally measured preionized profile just prior to the implosion, (2) including the effects of axial electron thermal conduction to the ends, and (3) including an appropriate time-varying resistance for the spark gaps in the circuit code.

Before these improvements were made, the code predicted that, when the RHX was modified to the resonant heating mode, it would produce marginal but interesting experimental verification of the resonant heating concept.[11] The "improved" code however, predicted that the RHX was not adequate. Because of electron thermal conduction, the RHX is not long enough to prevent serious field diffusion by the time of plasma reexpansion. In addition, a properly designed crowbar system in conjunction with a Marshall coil would be required to overcome the bad effects of the "turn-on" resistance of real crowbar gaps. Both of these effects resulted in the code predicting that the plasma would hit the wall after the initial implosion.

In spite of this pessimistic prediction, the RHX was modified in April to the resonant heating mode in hopes that the experimental results would at least provide an important check on the validity of the code. The next two months were spent improving the behavior of the crowbar system. During this process the magnetic field behavior approached that predicted by the code on the occasional shot when the crowbar worked well, but the lack of repeatability prevented careful plasma diagnosis.

The crowbar problem was finally solved just when the RHX was scheduled to be converted to the Field Reversal Theta Pinch (FRTP). The hurriedly obtained data then showed a new problem of unrepeatable plasma inventory and behavior. Because of this unexplained problem as well as the pessimistic code predictions, further delay of the conversion did not appear wise. The conversion to the FRTP began in mid-July.

After the experiment had been disassembled it was discovered that a sticking valve on the D_2 gas fill system was probably the reason for the nonreproducible results. No conclusions could be drawn from the data obtained so no results are given below.

b. Diagnostics. Plasma diagnostics included magnetic probes, both internal and external to the discharge tube, and two interferometers. A double-pass holographic interferometer[3] gave the plasma density profile at one time during the plasma discharge. A HeNe laser interferometer[12] in a double-pass geometry gave plasma density vs time at one radial position. For the plasma studies reported below, data were taken at 1-cm increments in radial position.

c. Plasma Results. The highly repeatable temporal and spatial behavior of the plasma density when the RHX was operated in the STP implosion mode is shown in Fig. III-13. The circles are HeNe interferometer data that have

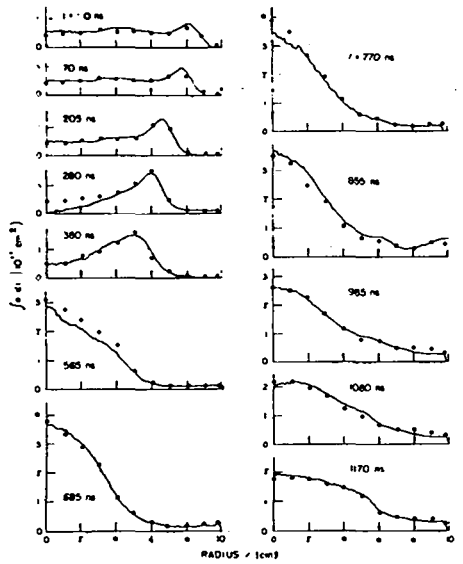

Fig. III-13.
A sequence of density profiles showing the temporal evolution of the plasma. The circles are He-Ne data and the lines are computer reduced holographic interferometer data. $\int ndl$ can be interpreted as density by dividing it by the nominal plasma length of 90 cm.

been averaged over at least three shots. The lines are computerized reductions of holograms and each profile represents a single shot. The time labeling each profile is measured from the initiation of the implosion field. This particular series of data was obtained with the secondary preionization turned on.

The following is a brief summary of the results obtained from analyzing data like that in Fig. III-13 with the output of the computer code.

(1) Application of the secondary preionization bank about 200 ns before the main implosion increased plasma sweep-up by about a factor of two. It also began to push the plasma off the wall (see the T = -15 ns profile in Fig. III-13) and probably increased the plasma temperature near the wall. The use of secondary preionization also changed the characteristics of the implosion so that the use of classical resistivity in the code gave a better agreement between experiment and theory than the Chodura model[13] which most accurately predicts results in the STP and IHX.[2]

(2) Comparison with the numerical code indicates that ionization of neutrals is not as rapid in the experiment as the code predicts. This is probably due to either a depletion of the high-energy tail of the Maxwellian electron velocity distribution or to greater thermal conduction effects in the experiment than is included in the code.

(3) The sign of the flux trapped in the plasma during the initial preionization strongly affected the implosion even though a variation from 20-80 G in the magnitude of the trapped field made little difference. Positive trapped flux resulted in a smaller but a longer time-duration density peak on axis. This indicated that the ions were either less energetic, or the magnetic field in the plasma core was larger, or both. Negative trapped flux resulted in lower preionization in the center and is observed as the only meaningful discrepancy between the HeNe and holographic interferometer data shown in Fig. III-13. Only shots with positive trapped flux were used to obtain the averaged HeNe data, but the holograms obtained at t = 280 ns, 565 ns, and 770 ns were apparently obtained when the trapped flux was negative.

(4) Essentially no neutrals are ionized during the implosion as shown by the temporal behavior of the electron inventory in Fig. III-14. The inventory begins to rise when the small quantity of plasma is pulled out toward the wall by the escaping flux. Note the increased density outside the main column at t = 565 ns in Fig. III-13 and the corresponding rise in

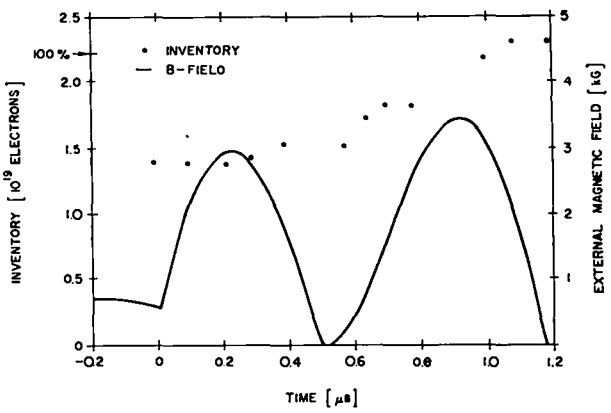

Fig. III-14.
A comparison of the temporal behavior of the external B field and the total plasma inventory as determined from the holographic interferometer data shown in Fig. III-13.

inventory between 600 and 700 ns. The next sharp rise in inventory occurs at about 850 ns and is localized for r > 8 cm as seen in Fig. III-13. This time corresponds to the arrival near the wall of the fastest ions as seen in the phase space plots generated by the computer code. The code indicates that these ions are successfully turned around by the second magnetic field peak (see Fig. III-14) but they (or the associated electrons) apparently ionize the neutrals left behind (r > 8 cm) by the initial implosion.

D. SUMMARY

During 1976, the Staged Theta-Pinch Experiment achieved its primary goal of producing large-diameter, high-temperature theta-pinch plasmas using separate implosion and compression capacitor banks. In the process it was found that some "free expansion" heating of the plasma column could be achieved without producing extra plasma outside the main plasma column. In addition, the experiment operated at its full design voltage of 125 kV much more reliably than could be expected of a "state of the art" device.

The data obtained from the RHX in the STP implosion mode motivated several important improvements in the hybrid code and provided a better understanding of the plasma behavior during the first microsecond. The results indicate that the use of secondary preionization would probably reduce, but not eliminate, the formation of secondary plasma in the STP when large modulation is allowed as shown at the bottom of Fig. III-9. The results of the improved code also show that a longer theta pinch with an improved crowbar system would be required to adequately test the resonant heating concept.

REFERENCES

1. A. G. Sgro and C. W. Nielson, Phys. Fluids 19, 126 (1976).
2. G. A. Sawyer, compiler, "LASL Controlled Thermonuclear Research Program, January-December 1975, "Los Alamos Scientific Laboratory report LA-6582-PR (December 1976).
3. R. E. Siemon and F. C. Jahoda in "Developments in Holography," (Society of Photo-Optical Instrumentation Engineers Seminar Proceedings, Boston, 1971) Vol. 25, p. 199.
4. C. J. Buchenauer and A. R. Jacobson, submitted for publication in Rev. Sci. Instrum.
5. G. A. Sawyer, V. A. Finlayson, F. C. Jahoda, and K. S. Thomas Phys. Fluids 10, 1564 (1967).
6. G. Berge and J. P. Freidberg, Phys. Fluids 18, 1362 (1975).
7. R. L. Morse, Phys. Fluids 16, 545 (1973).
8. J. P. Freidberg, R. L. Morse, and F. L. Ribe, "Staged Theta Pinches with Implosion Heating," Symp. Tech. of Controlled Thermonuclear Fusion Experiments and Engineering Aspects of Fusion Reactors, Austin, Texas, Nov. 20-22, 1972.
9. S. Hamasaki and N. A. Krall, Nucl. Fusion 16. 599 (1976).
10. A. R. Jacobson, C. J. Buchenauer, J. N. Downing, and K. S. Thomas, Phys. Rev. Lett. 37, 897 (1976).
11. LA-6044-PR, LASL Controlled Thermonuclear Research Program (1975).
12. J. E. Hammel and D. J. Rode, Bull. Am. Phys. Soc. 9, 793 (1967).
13. R. Chodura, Nucl. Fusion 15, 55 (1975).

IV. TOROIDAL REVERSED-FIELD PINCH

D. A. Baker, L. C. Burkhardt, J. N. DiMarco, A. Haberstich
R. B. Howell, H. J. Karr, M. D. Machalek, S. Ortolani, A. E. Schofield

A. SUMMARY

The reversed-field pinch (RFP) with its MHD stable, high beta configuration offers the possibility of leading to relatively small fusion reactors. The current LASL RFP program has as its basic objectives determination of favorable operating parameters and scaling properties of heating, diffusion, and lifetime of the pinch.

This past year experiments were carried out on ZT-S, the scaled-up version of ZT-I. The two experiments differed primarily in the fact that the minor diameter of the discharge tube was increased from 10.3 cm on ZT-I to 15.4 cm on ZT-S. The magnetic cores, the control system and field energy supplies of the ZT-I experiment were retained for ZT-S. A 15.4-cm bore was the largest vacuum tube that the old magnetic cores could accommodate. The primary object of the new experiment was to determine the scaling of the confinement of the pinch with increased minor diameter of the discharge vessel. Because the confinement time of the experiments is limited by field diffusion, one expects confinement time to scale as the field diffusion time, i.e., as d^2/D where d is the minor diameter of the plasma region and D is the field diffusion coefficient.

The confinement time has been found to increase from the 10-15 μs in ZT-I to 25-30 μs in the larger bore ZT-S device. Thus the confinement time scales approximately as the square of the minor diameter. The field diffusion, as expected, was observed to proceed at a slower rate. The time taken for the toroidal current to become uniform over the cross section increased about a factor of two and decay of the programmed reversed field was reduced by a larger factor.

Electron temperatures as measured by Thomson scattering are low, 12-15 eV, and are probably limited by the line radiation from impurities. The impurity level measured in ZT-S was found to be mainly oxygen in amounts of 0.3 to 0.5%. Mass spectrometer measurements indicated that after a discharge the dominant impurity present was H_2O (not D_2O), which is evidently escaping from the walls of the discharge tube. No high mass species corresponding to hydrocarbons from O-ring seals were observed.

Ideal MHD analysis of the magnetic probe data showed that, by suitable field programming, the desired stable configurations can be produced. These favorable plasma-field profiles degrade due to finite resistivity. A resistive tearing-mode, stability analysis of the profiles indicates that there can be unstable resistive modes at wave numbers which are either stable or weakly unstable according to ideal MHD theory. The resistive mode analysis does not reveal any unstable modes at radii outside the zero point in the toroidal field. The nonideal MHD calculations indicate that growth rates of the resistive modes are slowed considerably by viscosity.

The encouraging scaling results have led to a proposal to build a next generation reversed-field Z-pinch experiment called ZT-40. During this year the larger device was proposed, reviewed, and given approval for construction. The basic objectives of the new, larger (40-cm bore) experiment will be (1) to extend the confinement time to a few hundred microseconds, (2) operate in a regime of low impurities so that the radiation barrier is overcome, and (3) explore the production and maintenance of the stable configurations for both field programming and self-reversal modes of operation. The experiment is to have sufficient flexibility to allow operation with field risetimes ranging from a few microseconds to a millisecond, and for average total current densities up to ~ 3 kA/cm^2.

The present goal is to have the ZT-40 experiment operating without power crowbars in calendar year 1979. The power crowbars for sustaining the fields will be added at a later date, in 1980.

B. COMPARISON OF ZT-I AND ZT-S STABILITY RESULTS

One conclusion derived from the ZT-I results is that pinch stable time is limited by the diffusion of the magnetic field. All other parameters being equal, ZT-S should have an

increased stable time proportional to the square of the scaling factor S, assuming a simple isotropic model for diffusion. S = 1.5 is the ratio of the minor bore of the ZT-S discharge tube to that of the ZT-I tube. To obtain comparison data, the gas filling pressure of 35 mtorr and the rates of change of I_ϕ and ϕ_ϕ (toroidal flux) were approximately the same. The magnitude of I_ϕ scaled as S is 40 kA for ZT-I and 60 kA for ZT-S. The streak photographs, ϕ_ϕ, B_ϕ, and B_ϕ Fourier cosine-sine probe traces shown in Figs. IV-1 and IV-2 show that the stable time is increased by a factor of approximately two. The Fourier probes have an initial signal due to the 1/R effect of the toroidal magnetic field, the larger signal

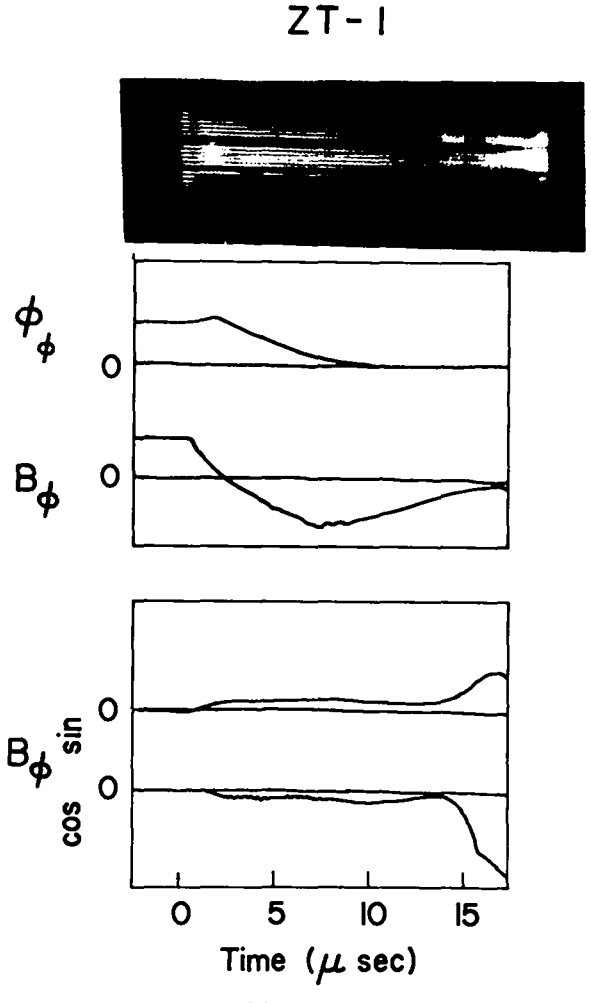

Fig. IV-1.
Data obtained from ZT-I. Shown vs time are streak photograph, toroidal flux ϕ_ϕ, toroidal magnetic field at the wall B_ϕ, and fourier probe signals of the plasma displacement.

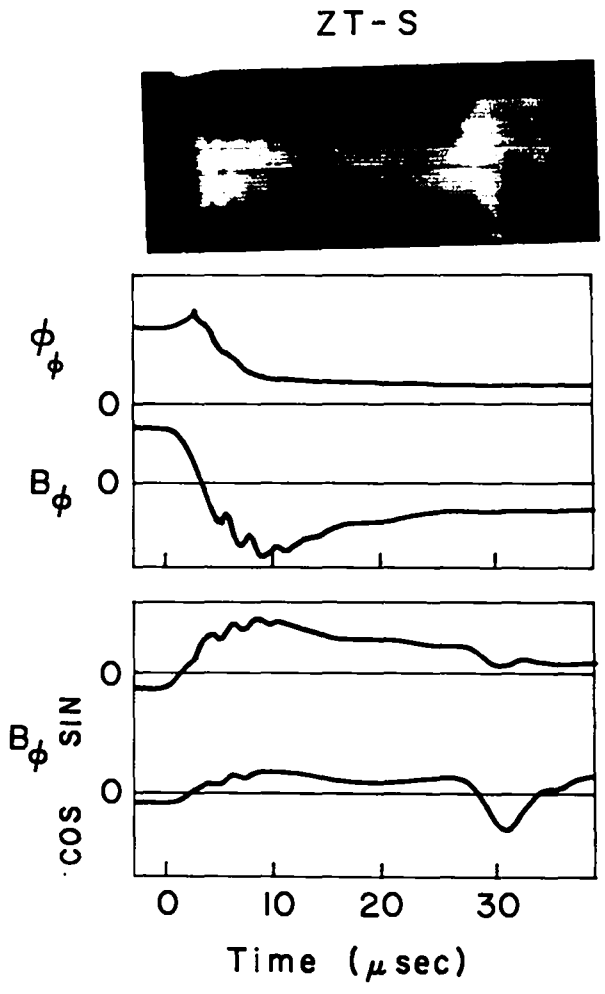

Fig. IV-2.
Data obtained from ZT-S. Shown vs time are streak photograph, toroidal flux ϕ_ϕ, toroidal magnetic field at the wall B_ϕ, and fourier probe signals of the plasma displacement.

obtained for ZT-S in Fig. IV-2 being due to an increase in gain. ZT-I shows an unstable perturbation developing at ~ 13 μs while the equivalent time for ZT-S is ~ 28 μs. This increase in stable time then generally confirms classical S^2 scaling.

A further illustration of the reduced time scale for diffusion is shown in Figs. IV-3, IV-4, and IV-5. Again, in these experiments the rates of change of I_ϕ and ϕ_ϕ were approximately constant for both cases. The magnitude of I_ϕ was 32 kA for ZT-I and 72 kA for ZT-S, and the bias field was adjusted to give approximately the same compression ratio, as measured on streak photographs. Figure IV-3 shows the poloidal magnetic field profile obtained from ZT-I. From the slope it can

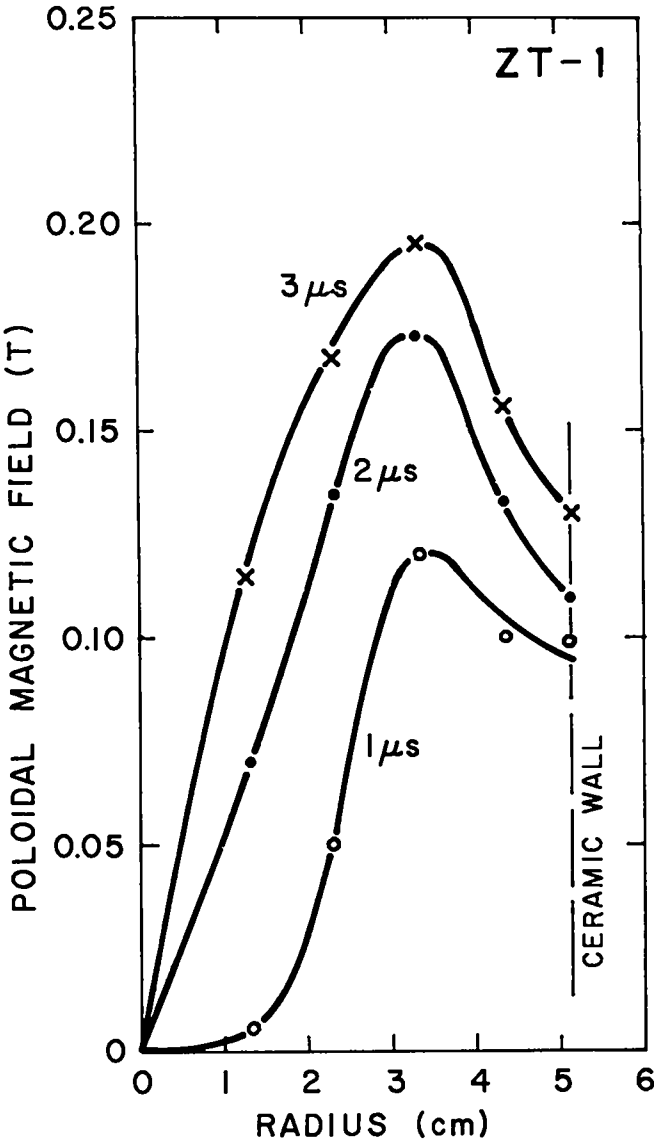

Fig. IV-3.
Profiles of the radial dependence of the poloidal magnetic field for selected times in the ZT-I experiment.

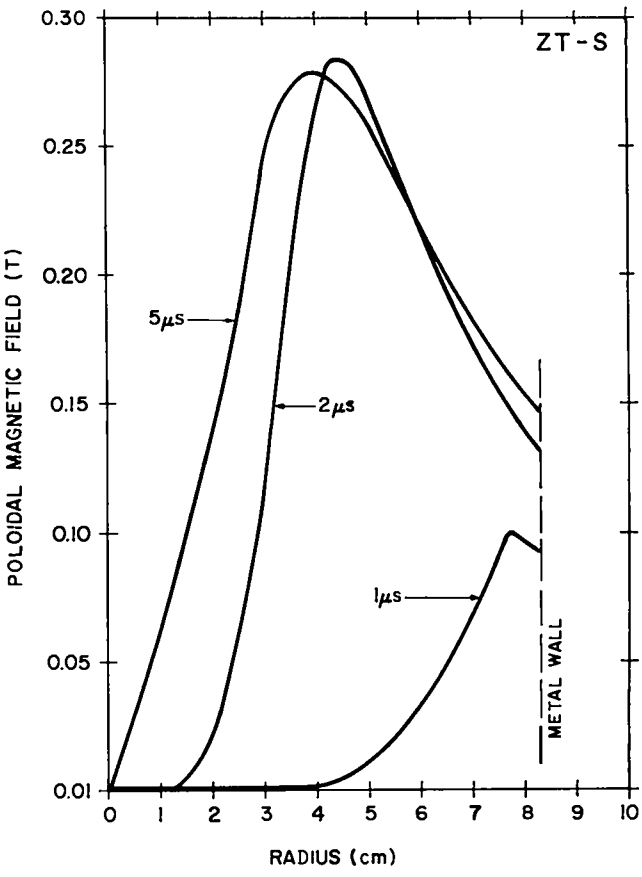

Fig. IV-4.
Profiles of the radial dependence of the poloidal magnetic field for selected times in the ZT-S experiment.

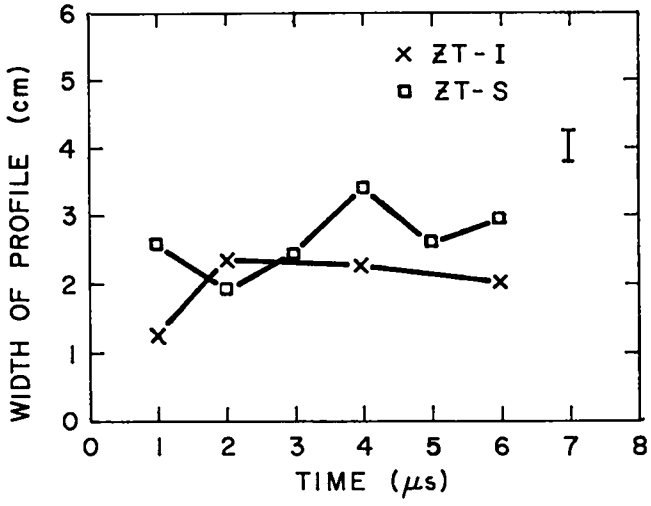

Fig. IV-5.
Comparison of the sheath width measured in ZT-I and ZT-S vs time.

be seen that at 2 μs in ZT-I, the toroidal current density has penetrated to the axis and is uniform out to the pinch radius of 2.5 cm. Figure IV-4 shows that in ZT-S at least 5 μs are required to produce an approximately equivalent profile but, even then, the toroidal current density is not yet uniform out to the pinch radius. The maximum current density occurs at - 2.5 cm, still well away from the axis. Another indication of current diffusion can be seen in Fig. IV-5, which measures the 10% to 90% width of the rising portion of the poloidal magnetic field profile. This technique is used to obtain a measure of the width of the current sheet rather than attempt to take

derivatives of the magnetic field profile. Figure IV-5 shows that during the implosion time (~ 3 μs) the approximate width of the current density profile is the same for ZT-I and ZT-S. Afterwards the profile for ZT-S is slightly wider.

For the same initial conditions in both experiments, the sheath width and the diffusion time of the toroidal current were greater in ZT-S. However, for ZT-S the plasma electron temperature is higher (~ 12 eV compared to ~ 7 eV for comparable conditions in ZT-I). The diffusion time of the reversed field should then be expected to be even longer than calculated from geometrical scaling. In comparing the B_ϕ traces shown in Figs. IV-1 and IV-2 it is noted that the reversed field has indeed taken longer to decay to zero than predicted from S^2 scaling.

The above work used spark gaps as crowbar switches. Some additional work was done with metal-to-metal crowbar switches,[1] which were located right in the feed plates that drive the toroidal current. The metal-to-metal switches themselves have an inductance of ~ 1 nH and the inductance between these switches and the pinch is quite small. In contrast, the spark gap crowbar switches are located at the capacitor bank. The spark gaps themselves have a higher inductance than the metal-to-metal switches, and the spark gaps are isolated from the pinch by a larger inductance and resistance, which influence the pinch current decay. A comparison of the current vs time for the two crowbars is shown in Fig. IV-6. Also shown are streaks obtained with the two types of crowbars. The metal-to-metal crowbar is very effective in reducing the electric field at the surface of the discharge tube, which at 7 μs is 117 V/m, compared to 670 V/m for the spark gap switches. The most noticeable effect observed with metal-to-metal switches [Fig. IV-6(b)] is the reduction of light outside the main pinch and an increase in the number of bounces that can be discerned. The stable time for this mode is ~ 32 μs and the toroidal current 1/e decay time is ~ 40 μs.

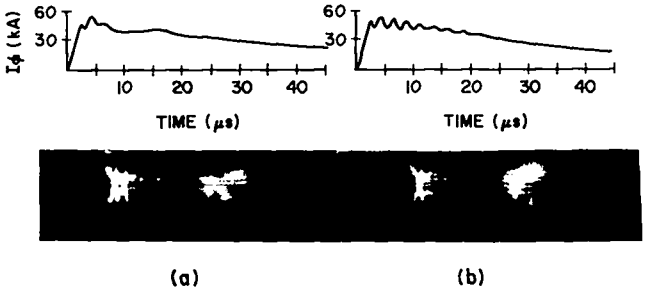

Fig. IV-6.
Comparison of the toroidal current for (a) spark gap crowbar and (b) metal-to-metal crowbar on ZT-S. The pinch behavior is shown in the streak photograph below the current.

C. FIELD DIFFUSION AND IDEAL MHD STABILITY

The ZT-S results presented here have been obtained with peak toroidal currents of 60 kA and filling pressures of 18 or 34 mtorr of 90% D_2 + 10% He. The preionization voltage was 5 kV at 18 mtorr and 4 or 5 kV at 34 mtorr. The 4- and 5-kV cases at the higher filling pressure are referred to as low and high PI conditions, respectively. The risetime of the toroidal current to maximum amplitude was of the order of 6 μs, and that of the reversed toroidal magnetic field was approximately 8 μs.

Plasma radii defined as the radii containing 80% and 50% of the plasma kinetic energy are shown in Fig. IV-7 as functions of time for the high PI condition. The corresponding result at 18 mtorr indicates an 80% radius of 0.045 m and a 50% radius of 0.035 m. The 18-mtorr radii remain essentially constant for the 22-μs duration of the data analysis.

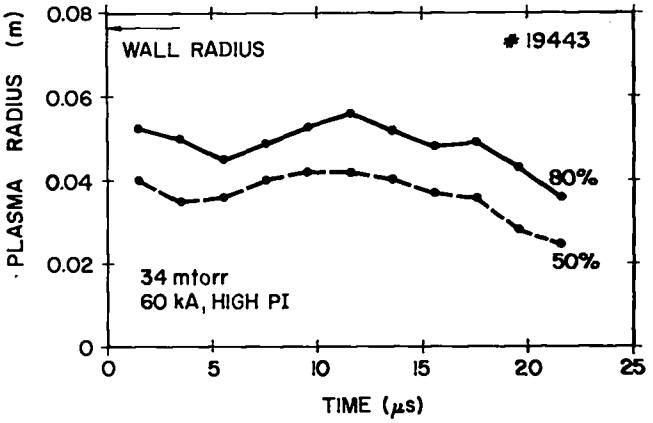

Fig. IV-7.
Plasma radii containing 50% and 80% of the transverse plasma kinetic energy as functions of time.

An estimate of the diffusion time of the poloidal field in the two cases is obtained by comparing the value of the toroidal current density on axis with that of the highest current density in the discharge. The current penetration time is found to be of the order of 10 μs at 34 mtorr and 12 μs at 18 mtorr. The longer time could be due to the higher electron temperature observed at 18 mtorr.

In Fig. IV-8 are plotted the growth times of the fastest m = 1 modes. These ideal MHD modes are calculated on the basis of experimental magnetic field profiles measured by means of internal magnetic probes. Each data analysis is based on an average of five or six shots.

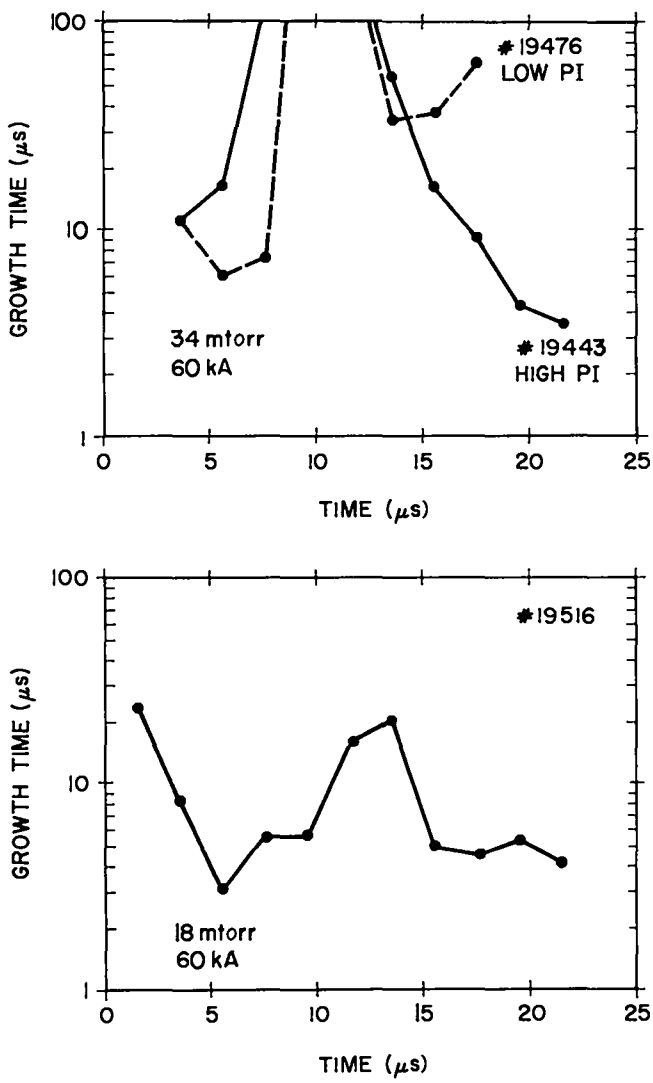

Fig. IV-8.
Growth times of ideal m = 1 modes as functions of time for three discharge conditions indicated in the figure.

The ideal MHD stability results are similar to those predicted in ZT-I at somewhat larger toroidal current densities, in the sense that the discharges show favorable stability shortly after the implosion. This phase is followed by a gradual deterioration of the stable field configuration until a gross instability is observed on streak photographs as well as on the sine-cosine probe signals. The observed stable configuration time is approximately 20 μs at 34 mtorr, high PI, 25 μs at 34 mtorr, low PI, and 25 μs at 18 mtorr. Streaks at 34 mtorr, low PI, show a slow upward drift of the discharge. This upward drift occurred in each of the discharges used in the stability analysis, and resulted in a gradual shift of the measured magnetic field profiles. The assumption of cylindrical symmetry was therefore violated at late times thus requiring the 34 mtorr, low PI analysis to be terminated at 17.5 μs.

Figure IV-9 shows the poloidal betas as functions of time for the three discharge conditions. The beta values are seen to be generally rising in time, thus making it increasingly difficult to control the MHD stability of the pinches. Plots of the plasma energy content as functions of time show that most of this increase is due to a drooping of the toroidal current rather than an increase in plasma internal energy. The toroidal current decays by 20% during the time interval shown, resulting in a 40% increase in beta. The dips in the poloidal beta at 8 to 12 μs coincide with the appearance of a "halo" on the streak photographs. This suggests that some of the plasma kinetic energy is released to the wall at these times. The affected region appears to be near the outer edge of the pinch. The electron temperature near the center of the discharge is not noticeably affected by these dips.

The gradual deterioration of the MHD stable time during the late phase of the pinches is due, as in ZT-I, to the evolution of the magnetic field configuration, which is believed to be caused by diffusion. An estimate of the parallel resistivity $\eta_{\parallel}$ responsible for this diffusion is obtained

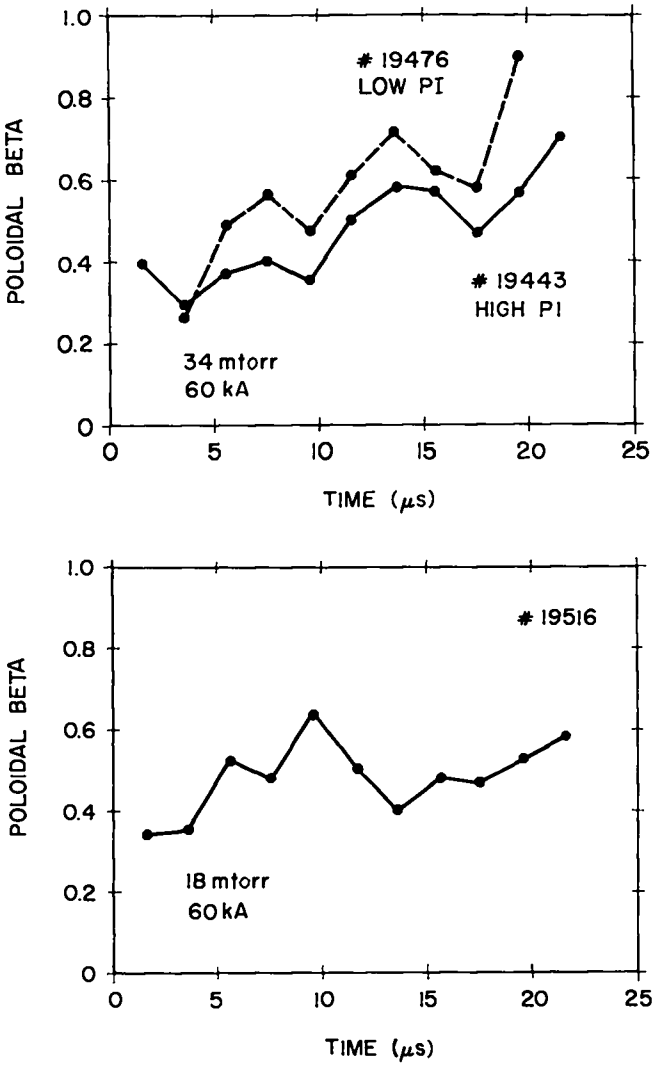

Fig. IV-9.
Poloidal betas as functions of time for the three discharge conditions of Fig. IV-8.

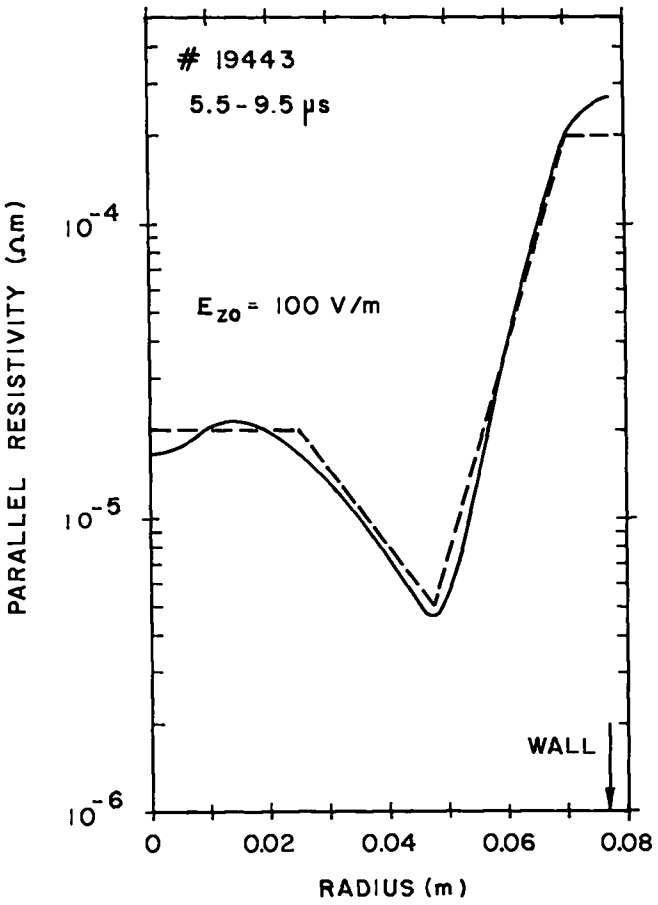

Fig. IV-10.
Parallel resistivity as function of radius during the post implosion interval of 5.5 to 9.5 μs, with 34 mtorr, high PI. Solid curve: as calculated with the generalized Ohm's law. Dashed curve: value used in the MHD simulation.

by solving the generalized Ohm's law in the linear cylindrical discharge approximation

$$\eta_{\parallel} = \frac{E_z B_z + E_\theta B_\theta}{j_z B_z + j_\theta B_\theta} \quad ,$$

where E, B, and j are the electric field, the magnetic field, and the current density, respectively. The electric fields are obtained from the time derivatives of the magnetic fields and the value of the axial electric field is inferred from the voltage applied to the experiment. Figure IV-10 shows the parallel resistivity profile obtained in this fashion during the time interval of 5.5 to 9.5 μs of the 34-mtorr high-PI discharge condition.

The expression for the perpendicular component of the resistivity,

$$\eta_{\perp} = \frac{E_z B_\theta - E_\theta B_z}{j_z B_\theta - j_\theta B_z} + u_r \frac{B^2}{j_z B_\theta - j_\theta B_z} \quad ;$$

contains the radial plasma velocity u_r, which is not directly available experimentally. If, however, a certain ratio of the perpendicular to the parallel resistivities is assumed, then the generalized Ohm's law can be solved for u_r.

Figure IV-11(a) shows the time dependence of the calculated plasma velocity at a given radial position of 0.04 m for the cases $\eta_\perp = 0$ and $\eta_\perp = 5\ \eta_\parallel$. The variations in plasma velocity correlate well with the oscillations in the decaying axial current plotted in Fig. IV-11(b). In fact, the oscillations of the axial current are felt throughout the radius of the discharge.

The calculated plasma velocity profiles have been used to initiate postimplosion MHD simulations under the assumption of dynamic rather than static equilibrium. Figure IV-12 shows the result of such a simulation performed by means of a one-dimensional two-fluid code. The solid curves represent measured magnetic fields at 34 mtorr,

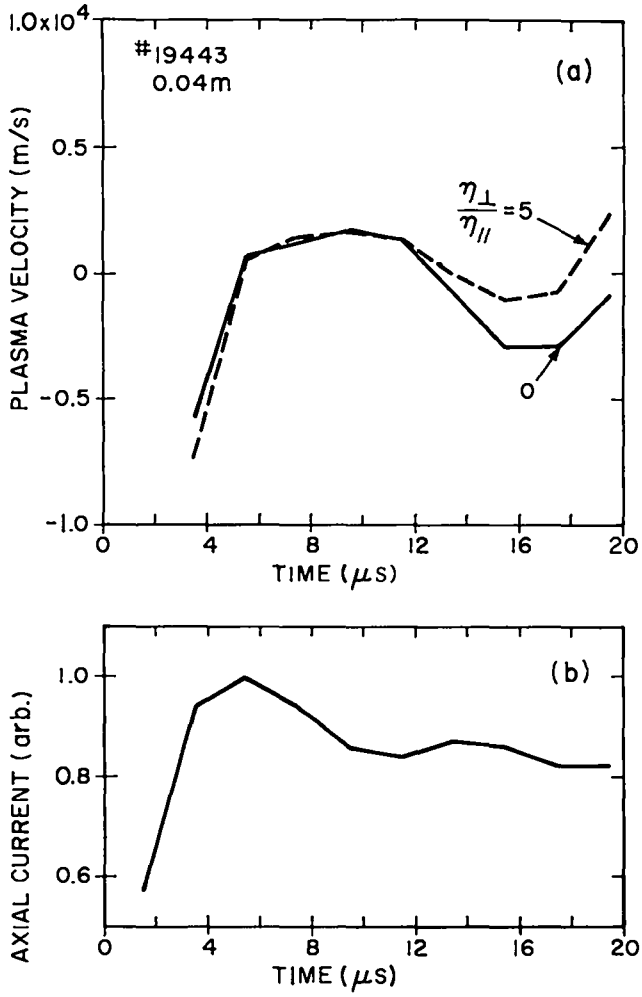

Fig. IV-11.
Comparison of radial plasma velocity (a) and toroidal current (b) as functions of time. The plasma velocity is calculated for two ratios of the perpendicular to parallel resistivities.

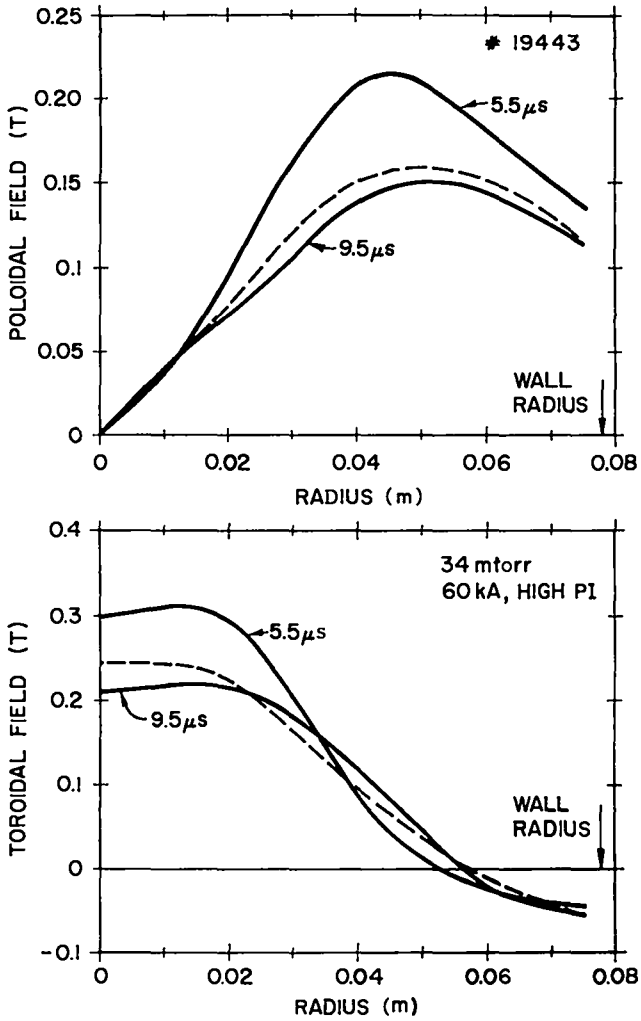

Fig. IV-12.
Measured poloidal and toroidal magnetic fields as functions of radius, at 5.5 and 9.5 μs, in the discharge. The dashed lines, at 9.5 μs, indicate the result of the MHD simulation.

high PI. The experimental profiles at 5.5 μs are used as initial conditions and the simulation is carried out for 4 μs, using the value of parallel resistivity indicated by the dashed line in Fig. IV-10. The result represented by the dashed lines in Fig. IV-12 is then compared with the measurement at 9.5 μs. The best fit, in this particular case, is achieved with a ratio $\eta_\perp/\eta_\parallel$ of 5. The good agreement between calculation and measurement confirms that the observed evolution of the magnetic field configuration can be interpreted in terms of plasma motion and diffusion.

Figure IV-13 shows classical electron temperature profiles corresponding to the $\eta_{\parallel}$ profile of Fig. IV-10 and to a perpendicular resistivity equal to five times $\eta_{\parallel}$. The predicted temperature is seen to be higher at the edge of the plasma than at the center of the discharge. This behavior is also present in the measured electron temperature represented by the data points in the figure. These temperatures were obtained by Thomson scattering on discharges having a slightly smaller radius than those used during the profile measurements. Comparison of predicted and measured temperatures shows that under this mode of operation, the postimplosion resistivity of ZT-S is close to classical.

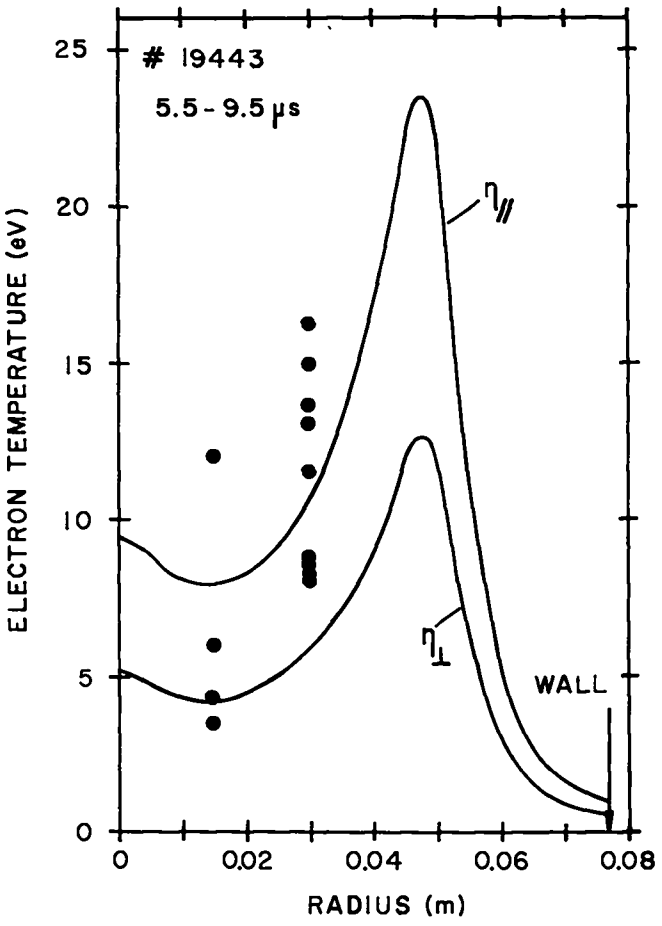

Fig. IV-13.
Classical electron temperatures as functions of radius corresponding to the parallel resistivity $\eta_{\parallel}$ of Fig. IV-10 and to a perpendicular resistivity $\eta_{\perp}$ equal to 5 times $\eta_{\parallel}$. Data points are temperatures measured by Thomson scattering.

D. RESISTIVE MHD STABILITY

The stability of three ZT-S configurations to resistive MHD modes has been investigated by means of two codes written by Dibiase.[2] The first code assumes compressibility, resistivity, viscosity, and thermal conductivity. The other, incompressible code includes resistivity only. The codes have been modified to read experimental distributions of the magnetic fields. As in the ideal MHD case, the calculations have been restricted to m = 1 modes. The configurations that have been examined are the 60-kA, 34-mtorr, high PI case at 5.5 and 7.5 μs, and the 60-kA, 18-mtorr case at 5.5 μs.

Results for the two 34 mtorr cases are shown in Fig. IV-14. The shaded areas are regions in k-space (k is the wave number along the major circumference of the torus) which are predicted to be stable according to ideal MHD stability theory. The regions immediately to the left of the ordinates may contain unstable modes localized near the axis of the experiment, depending on the reliability of the data near the magnetic axis. The region located to the left of the two shaded areas, in Fig. IV-14(b), contains slowly growing, localized Suydam modes. These ideal localized modes are somewhat faster growing at 5.5 μs. Their growth rates are indicated by the dashed curve in Fig. IV-14(a).

The results of the resistive mode analysis are represented by the solid and dotted curves in the figure. The solid curves are obtained with resistivity and viscosity, and the dotted curves with resistivity only. The value of the magnetic Reynold's number in the first case was set at 100. The resistivity was chosen to be uniform, so that the results pertain to resistive tearing modes. To assign a time scale to the calculated growth times, a resistive diffusion time of 10 μs has been postulated.

The results reported in the figure indicate the presence of resistive instabilities at wave numbers which are either stable or only weakly unstable according to ideal MHD theory. The growth rates of these resistive modes are relatively slow, if one includes viscosity in the analysis. The resistive mode analysis does not reveal any positive-k modes. The same general

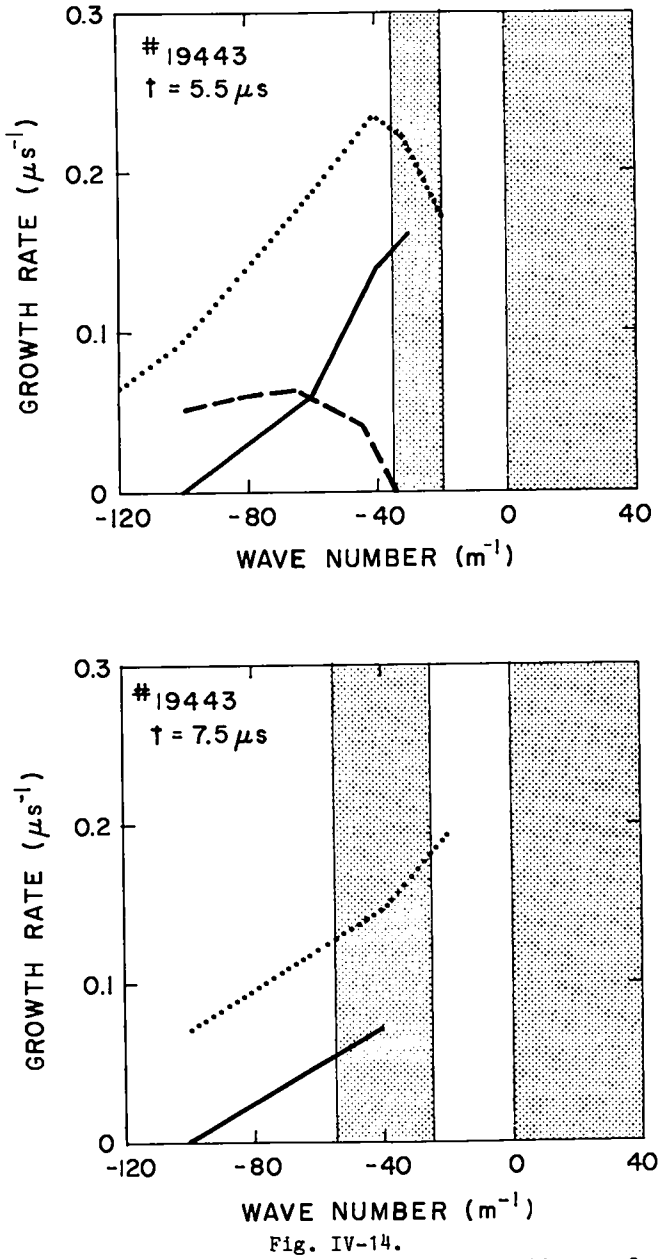

Fig. IV-14.
Growth rates of m = 1 modes as functions of longitudinal wave number k, (a) at 5.5 μs, (b) at 7.5 μs, with 34 mtorr, high PI. Dashed line: ideal MHD, dotted lines: resistive modes, solid lines: resistive modes with viscosity. The shaded areas are fully stable according to ideal MHD.

behavior occurs for the 18-mtorr configuration. However, the ideal modes have somewhat faster growth rates, and the resistive modes have less impact on the overall stability than in the first two cases.

E. TEMPERATURE AND DENSITY MEASUREMENTS ON ZT-S

1. Electron Temperature

a. Thomson Scattering. The electron temperature in ZT-S has been measured by Thomson scattering as a function of time at two radial positions, under the discharge conditions described in Sec. C.

Figure IV-15 shows the electron temperature at 1.5-cm radius of the 18-mtorr discharge. The error bars are statistical error bars representing the standard deviations of two or more shots. A temperature of more than 10 eV is seen to be maintained for 25 μs, the stable configuration time of the discharge. The maximum electron temperature is of the order of 15 eV. Figure IV-15 also shows the time dependence of the electron density on an arbitrary scale. Instrumental scattering prevents an absolute measurement of the density at this time. The

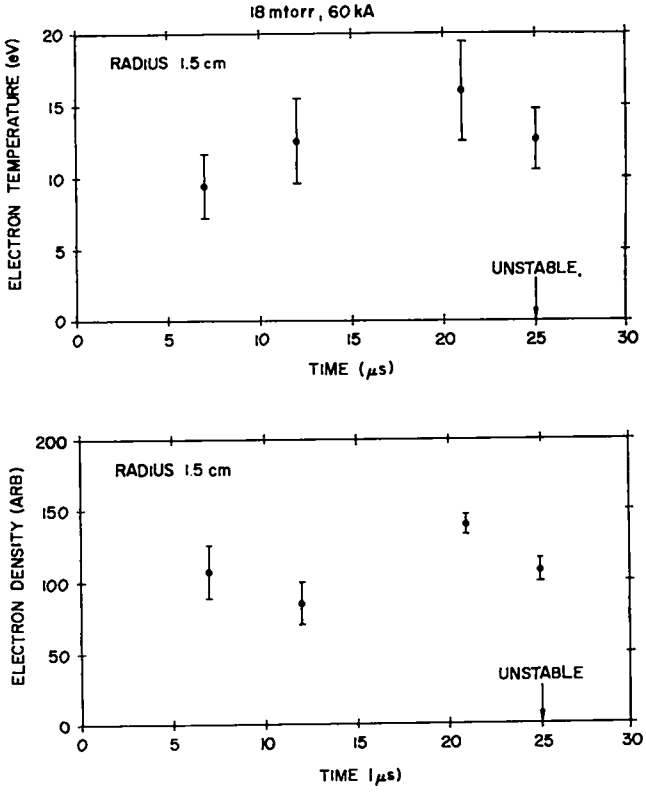

Fig. IV-15.
Thomson scattering measurements of the electron temperature (upper graph) and relative electron density (lower graph) as functions of time at 1.5-cm radius. Arrows indicate the onset of an instability on streak photographs. Filling pressure, 18 mtorr.

slight dip in density at 12 μs might be related to the appearance of the "halo" on the streak photographs. The temperature, however, does not seem to be affected.

Electron temperatures for the 34 mtorr, high PI case are shown in Fig. IV-16 at 1.5- and 3-cm radii. Reasonably high temperatures are, again, maintained for the entire 20-μs duration of the grossly stable discharges. The electron temperature is seen to be peaked initially at the edge of the plasma and to become uniform towards the end of the stable configuration time. The maximum temperature is of the order of 12 eV and the subsequently uniform temperature is 7 or 8 eV. As mentioned earlier, the temperature measured at the edge of the discharge between 7 and 11 μs is in good agreement with the classical temperature derived from the diffusion of the magnetic field.

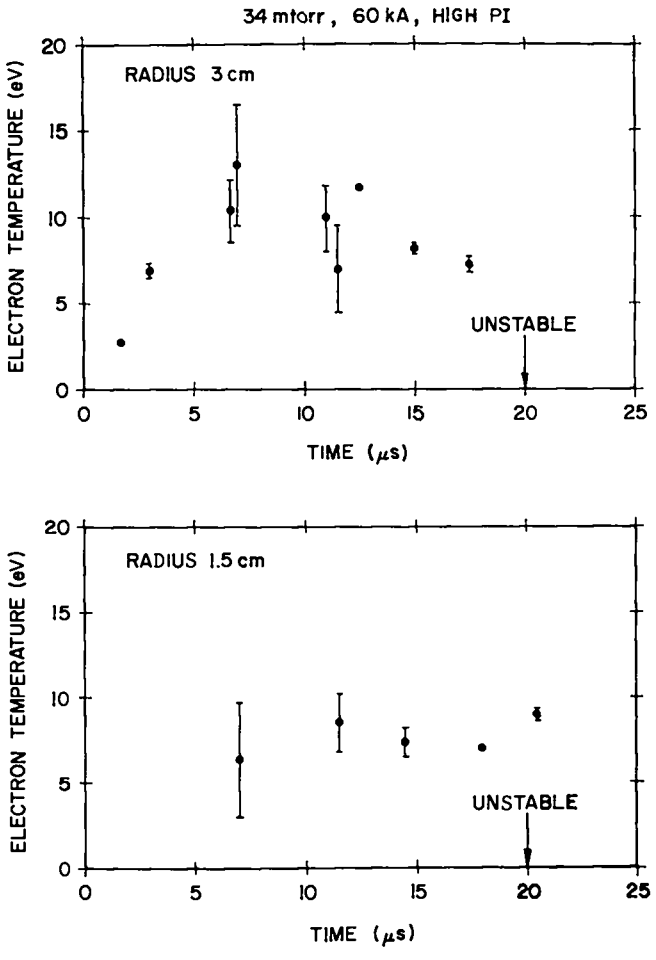

Fig. IV-16.
Thomson scattering measurements of the electron temperatures at 3-cm radius (upper graph) and 1.5-cm radius (lower graph). Filling pressure, 34 mtorr.

Figure IV-17 shows a plot of the electron temperature at 1-cm radius in ZT-I for a discharge current of 36 kA with an 11-mtorr filling pressure of 80% D_2 + 20% He. The toroidal current density was somewhat higher than the current density in ZT-S, whereas the filling density was lower than that of the 18-mtorr discharges in ZT-S. Comparison of the ZT-I with the 18-mtorr ZT-S results shows an electron temperature increase in ZT-S by a factor of 2.5.

b. X-Ray Measurements. The production of higher energy x rays in ZT-S is of interest primarily because any x-ray background can impair the measurement of electron temperatures by the differential x-ray method being used for measurements of T_e at low plasma density operation. On the basis of the data so far, as an x-ray source, ZT-S does not differ grossly from ZT-I.

The emanations appear to occur in the 50- to 500-keV range, with the softer x rays coming earlier, the harder coming later in the discharge. Greater reproducibility is observed at pressure > 10 mtorr. Signals tend to be extinguished by a small ceramic probe on the axis of the machine. Signals also are suppressed by as little as 0.7% N_2 impurity gas added to the D_2. At least a few tens of gauss B_z are needed for the machine to produce x rays but yields continue with fields as high as a few kilogauss. A local dc magnetic field on the order of ten gauss, perpendicular to

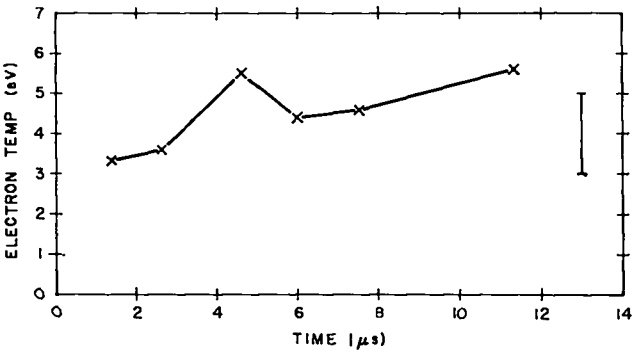

Fig. IV-17.
Thomson scattering measurement of electron temperature at 1-cm radius in ZT-1. Filling pressure, 11 mtorr.

the B_z field, substantially reduces and alters x-ray generation.

The time histories of x-ray yields for two pressures, 19 and 35 mtorr, are shown in Fig. IV-18. Traces were taken with a detector sensitive to lower energy radiation, with a preionization bank voltage of 5 kV, and a forward B_z of 0.1 T.

2. Ion Temperature. Ion temperatures were measured on ZT-S using the Doppler broadening of the HeII 0.4686-μm line. The variation of T_i versus time is shown in Fig. IV-19 for two shots at a filling pressure of 18 mtorr. Also measurements of T_i for the same conditions but at 34-mtorr filling pressure yielded about 11.0 eV.

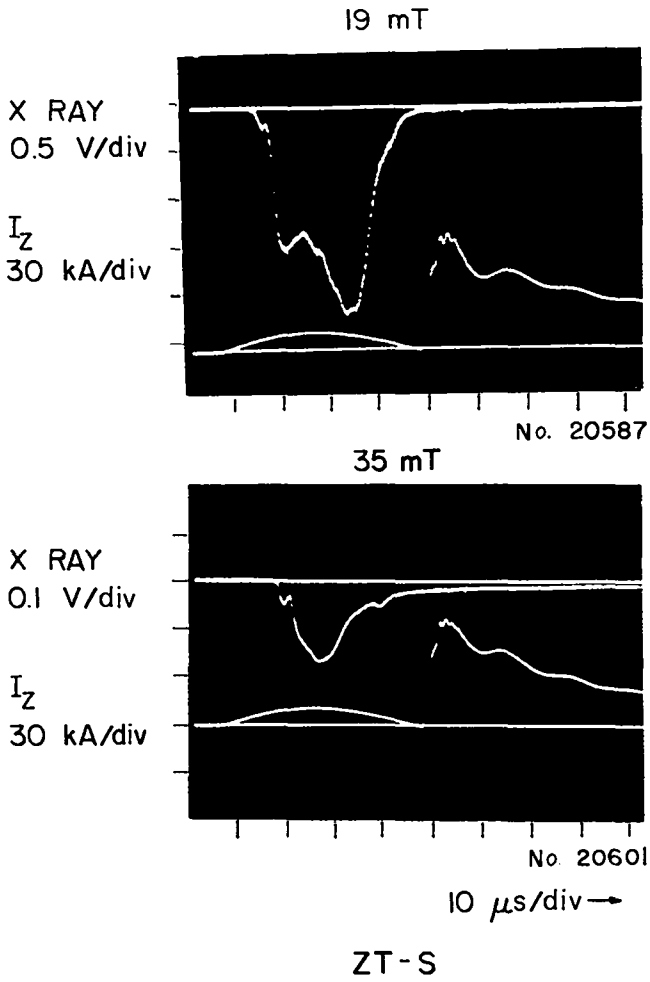

Fig. IV-18.
The time history of x-ray production in ZT-S for two pressures of D_2 with a NaI type detector whose shielding allows detection into the lower (~ 60 keV) energy range of x rays.

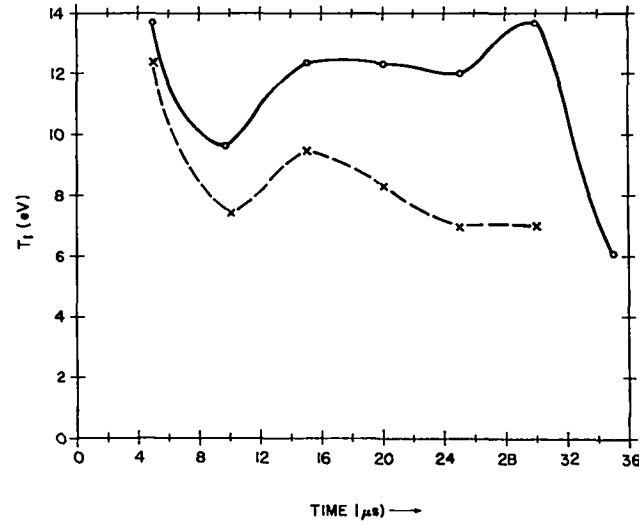

Fig. IV-19.
Ion temperature vs time for I_ϕ = 60 kA, B_ϕ = 0.059 T and P_o = 18 mtorr.

These are averages radially since the observed emission comes from a chord of the plasma. The Stark corrections were made using the recently obtained density measurements discussed in the next section.

3. Electron Density. Radial density measurements were made using the coupled cavity Ashby Jephcott interferometer at 3.39 μ. Measurements were made for 17 chords across the minor diameter of the torus and the density profile then obtained by an Abel inversion. A typical profile is shown in Fig. IV-20 in the postimplosion phase of the discharge. Assuming a reasonable density gradient on the outside, this profile represents ~ 60% ionization. The general indication of hollow profiles agrees with other diagnostics, although the return to zero on axis is probably an artifact of the Abel inversion technique.

F. PLASMA IMPURITIES

1. Residual Gas Analysis Before and After Discharge. Mass scans of the residual impurity gas in ZT-S were made with a Veeco GA-4 Vacuum Gas Analyzer over the range from 10 to 300 mass units. Although ~ 25 ion species were observed within the range (logarithmic scale) of the analyzer, approximately 95% of the total existed in 8 ion types as listed in Table IV-I. Due to the different sensitivities of the analyzer for different gases, the relative peak heights are

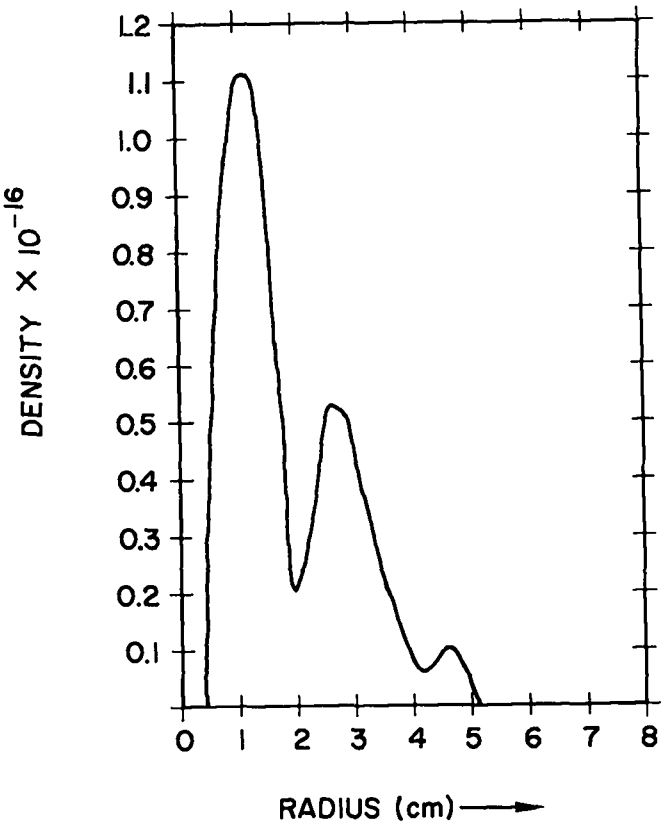

Fig. IV-20.
Density profile at 10 μs after Z current of 60 kA is applied; B_z bias field is 0.06 T and the filling pressure is 14 mtorr.

only a rough indication of the partial pressures of the impurities.

TABLE IV-I

MASS IMPURITY ANALYSIS FOR ZT-S AFTER DISCHARGE
(Corrected for Impurities in Detector and Auxiliary Vacuum Line)

Ion Mass (Mass Units)	Possible Ion Identity	Peak Amplitude (Relative Units)	% of Total
12	C	2.1	1.7%
14	N, CH_2, CD	6.1	4.9%
16	O, CD_2, NH_2	6.8	5.5%
17	OH, NH_3	2.6	2.1%
18	H_2O, ND_2, CD_3, CH_4	82.9	67.0%
19	DHO	4.8	3.9%
28	N_2, CO	9.8	7.9%
32	O_2	2.2	1.8%

Mass 18, probably water vapor, is the major impurity. Notably absent in the mass scan were high mass peaks above ~ 40 mass units. The presence of heavy hydrocarbon molecules from O-rings in the system was anticipated but was not observed.

The same gases were detected before and after the discharge with some minor shifting of relative amplitudes--e.g., O_2 was reduced from 5.3% to 1.8% by the discharge and apparently combined with hydrogen during the discharge period. The amplitudes of the impurity peaks were increased by a factor of $\gtrsim 4$ by the discharge. These impurities were probably released by discharge bombardment during the initial stages of pinch formation. This was also observed in the spectroscopic impurity measurements described in the next section.

The major impurity peaks are shown in the oscilloscope trace (linear scale) of Fig. IV-21 obtained in conjunction with the mass analyzer. C, N, O, OH, H_2O, N_2, O_2 form the lines observed with H_2O having the largest amplitude.

2. Spectroscopic Determination of Impurity Level During Discharge. Measurements were made of the impurity content of ZT-S by adding known small amounts of impurity gases to the discharge and observing the increase in intensity of spectral lines. The line observed for oxygen was the OIII line at 0.3265 μm.

At 34 mtorr there was found to be 0.35% oxygen present for a toroidal current of 60 kA and a bias field of 0.06 T. When the filling pressure was 18 mtorr a percentage of oxygen > 0.5% was found to be present. These measurements were made with the magnetic field probes inserted into the discharge. With the probes removed, contrary to expectations, a higher oxygen impurity of 1% was found. In each of these cases the amount of oxygen contributed by outgassing was only about 0.15% at 18 mtorr and 0.08% at 34 mtorr. The balance of the impurity observed was removed from the walls during the initial stage of the pinch discharge. As was shown in the previous section, the major contributor to outgassing from the walls was found to be H_2O.

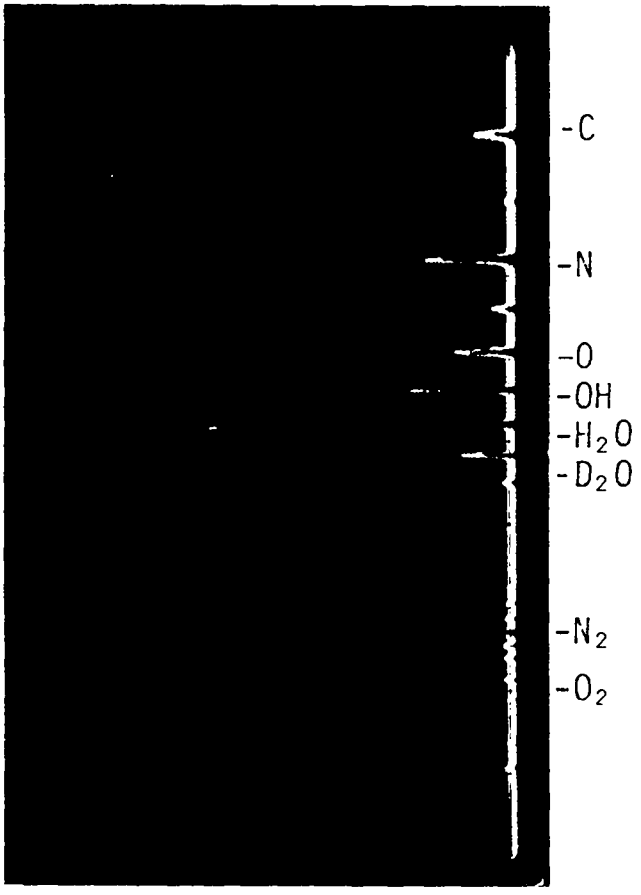

Fig. IV-21.
Mass analyzer oscilloscope trace of residual gas after discharge of 60 kA with 18 mtorr D_2 filling pressure. The H_2O peak exceeds the scope deflection limit and is saturated. The O_2 peak is larger before the discharge and is evidently dissociated and combined into OH, H_2O, and D_2 by the discharge.

This effect of having more impurities with the probe out than in was investigated. It was found that about 3 cm into the discharge the transition in impurity concentration took place.

3. Calculations of Impurity Tolerance Limitations for ZT-S and ZT-40. A potentially important effect in the ZT experiments is the energy loss by radiation from impurities. Impurity ionization and line radiation losses can act as a barrier to obtaining plasma temperatures above a few tens of electron volts. Measurements of the impurity content in the ZT-I and ZT-S plasmas have been made and calculations have been carried out of the power loss and the resulting effects on T_e and T_i.

Radiation power loss was obtained with the POWRAD computer code using the theoretical equations of McWhirter.[3] A factor of 5 was inserted into the line excitation rates to bring the results in line with the more recent measurements and calculations.[4] Results for the radiated power are shown in Fig. IV-22 for typical ZT-S filling density and fractional impurity (FI) level for assumed electron temperatures ranging from 10 eV to 50 eV. (The ordinate is proportional to n_e x FI and the abscissa is inversely proportional to n_e.) When the radiated power level exceeds or equals the input power, the plasma temperature falls or is fixed at that level. The results of Fig. IV-22 show the first radiation barrier, which is transcended only when T_e exceeds ~ 30 to 50 eV.

If it is assumed that the ZT-S electron temperature is ~ 10 eV, in approximate agreement with the Thomson scattering measurements, and the

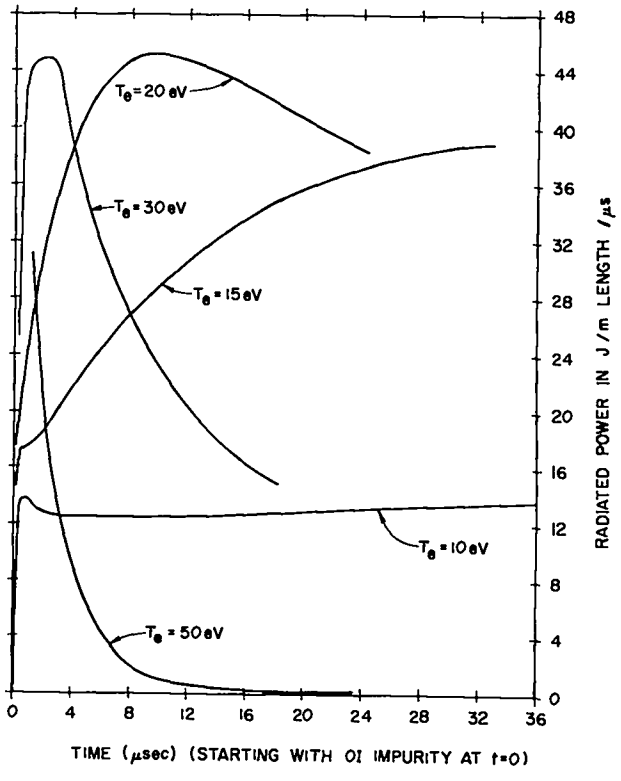

Fig. IV-22.
Radiated power in megawatts per meter length computed with the POWRAD code for an initial plasma density n_{eo} = 1.3 x 10^{15} cm^{-3}, compression = 4, fractional impurity = 0.004 O_2 for the indicated plasma electron temperatures.

plasma parameters are those described for Fig. IV-22, the energy loss rate is in good agreement with the energy loss measurements determined from probe data and pressure balance shown in Fig. IV-23.

The theoretical effect of the impurity radiation on T_e and T_i was determined initially using the IMPRAD 2 computer code which calculates the time dependent plasma temperature resulting from the opposing effects of ohmic heating and impurity radiation losses. Classical Spitzer resistivity with effective Z modification is assumed in the ohmic heating calculation and the impurity losses are calculated as in the POWRAD code mentioned above. Ion-electron energy equilibration is also assumed to be classical.[5] This code has now been revised to update the ionization, recombination, and excitation coefficients from the 10-yr-old McWhirter values. The new code uses tabular values from the Appleton Laboratory Tables and Graphs by H. P. Summers. The functional dependence given by the McWhirter equations is retained.

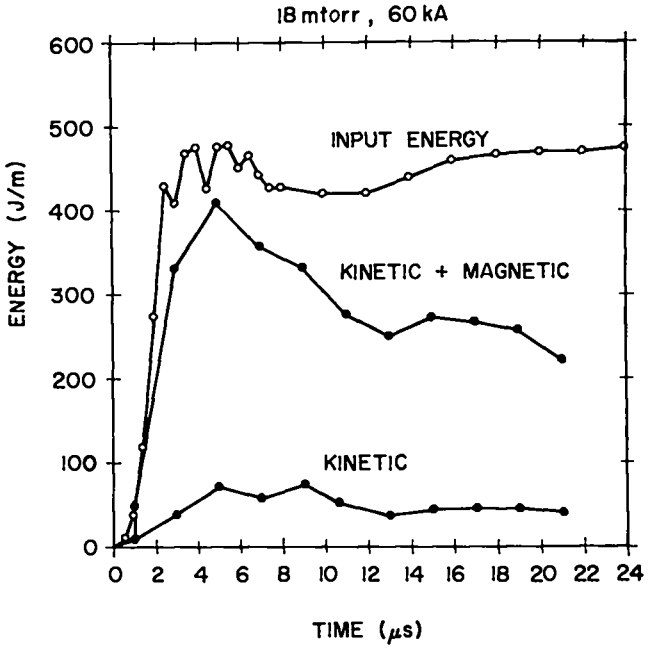

Fig. IV-23.
Energy balance for I_ϕ = 50 kA, filling pressure = 18 mtorr.

There are several factors which determine the value of T_e and T_i in these calculations. Factors favoring high T_e and T_i in general are:

a. Lower plasma density--to reduce the radiation excitation and afford fewer particles to divide up the ohmic heating energy.
b. High Current density--to increase the ohmic heating rate.
c. High initial T_{eo} or T_{io}--from shock heating, for example.
d. Low impurity levels--to reduce radiation.
e. Anomalous heating, beam injection, rf heating etc. (These are not included in the analysis here but may be of use in the future.)

In Tokamak systems the radiation barrier is overcome because of the relatively low plasma density. In θ pinches, high initial T_i assists in passing over the barrier. In the ZT systems, the best compromise among these parameters must be found with compression ratios less than ~ 2.5 to satisfy stability requirements.

Figure IV-24 shows the theoretical limiting values of current density and plasma density for selected fractional impurity levels obtained from the revised computer code. To avoid having T_e and T_i fixed in time, rather than rising as ohmic heating continues, it is necessary to have values of current density and plasma density above each parametric curve for the indicated fractional impurity level shown in the figure. These results are demonstrated for particular cases of plasma density, current density, and fractional impurity levels in Figs. IV-25 and IV-26 which show the time-dependent behavior of T_i and T_e. Figure IV-26 shows the effect of an assumed initial ion temperature of 100 eV (e.g., shock heating) on the time-dependent T_i and T_e. For this case, appreciably higher values of initial impurity can be tolerated.

The amounts of impurity that can be tolerated for the operating conditions of ZT-S and the expected conditions for ZT-40 are small but not less than those obtained in other experimental devices.[6-10]

Experimental measurements of the radiation loss from the ZT-S experiment are currently being made. These results will be compared with losses observed from energy balance experimental

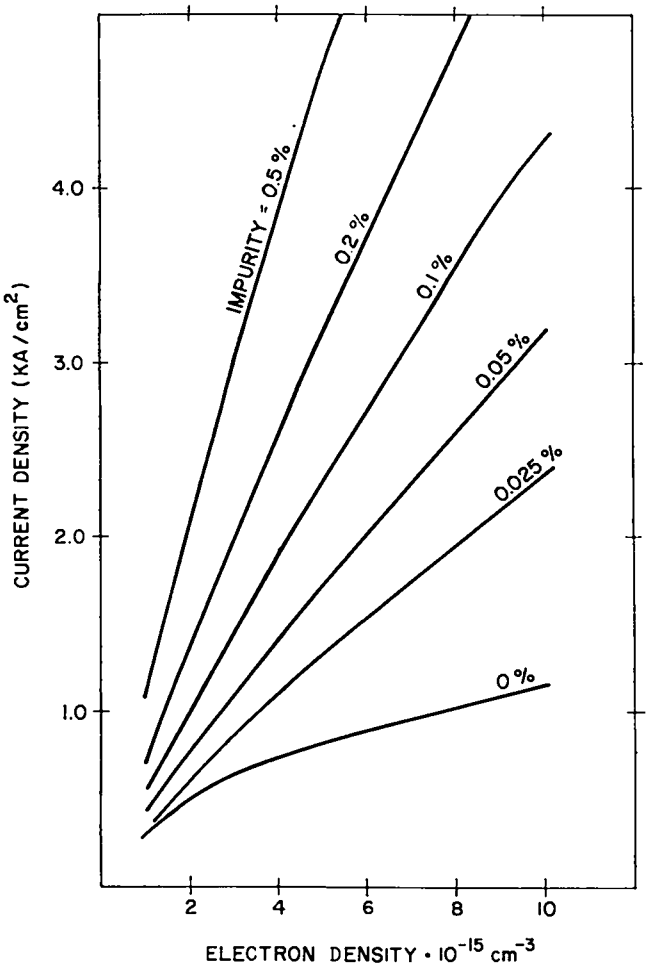

Fig. IV-24.
Plot of computed threshold electron and current densities (for selected fractional impurity levels) for which ohmic heating - radiation loss. For j and n_e above each parametric curve, T_e and T_i will increase with time.

measurements and the theoretical predictions described above.

G. ENERGY BALANCE MEASUREMENTS ON ZT-S

The energy input inside the ceramic wall was compared to the energy contained in the plasma and magnetic field as determined from magnetic probe data and pressure balance. These calculations were made for two different pressures, 18 and 34 mtorr and peak I_ϕ of 50 kA. The 18-mtorr case is shown in Fig. IV-23 and shows a large energy loss rate of about 12 J/m/μs. The ratio of plasma to magnetic field energy gives a total $\beta \approx 18\%$. The 34-mtorr case is shown in Fig. IV-27 and it shows an energy loss rate of - 25J/m/μs during the

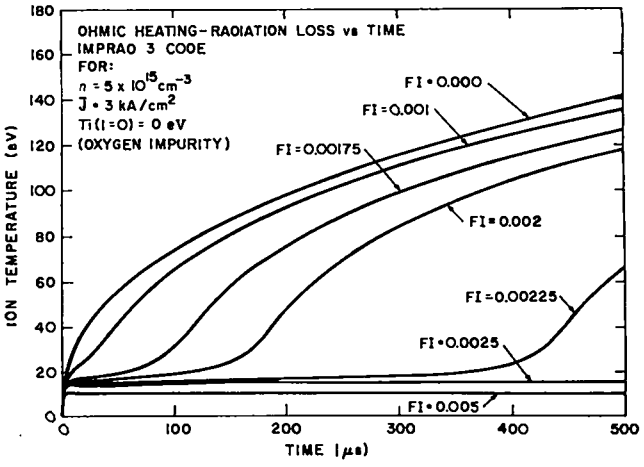

Fig. IV-25.
Plot of theoretical values of T_e and T_i vs time determined by classical ohmic heating opposed by impurity radiation loss.

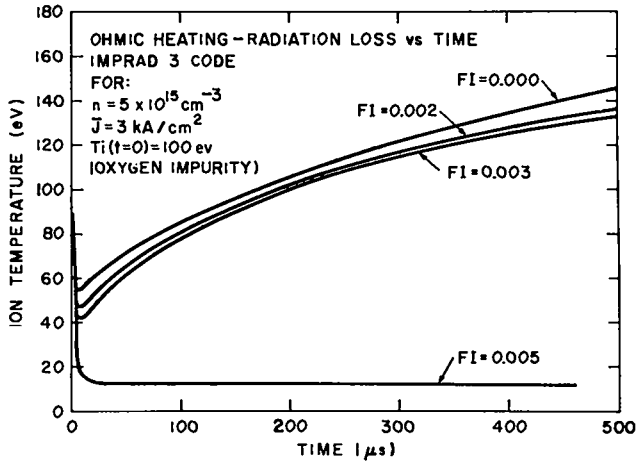

Fig. IV-26.
Plot of theoretical values of T_e and T_i vs time determined by classical ohmic heating opposed by impurity radiation loss with an assumed initial ion temperature of 100 eV.

first 10 μs. The total β for the high PI case is 23%. The input energy shown in Fig. IV-27 is for the high PI case.

H. ZT-40 TOROIDAL, REVERSED-FIELD Z-PINCH

1. General Objectives. The next generation experiment in the LASL toroidal Z-pinch program, ZT-40 (originally called ZT-P), was given final go ahead approval by DMFE in December 1976. ZT-40 is a logical step up from the present reversed-field ZT-S device, and a primary objective of ZT-40 will be to demonstrate confinement time scaling (up to

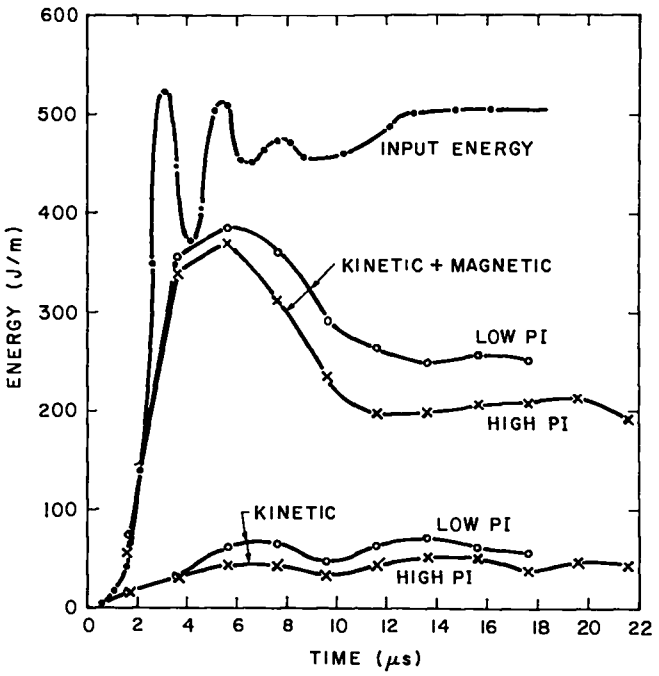

Fig. IV-27.
Energy balance inside for I_ϕ = 50 kA, filling pressure = 34 mtorr.

150-200 μs) from the results of ZT-I and ZT-S. A second objective will be to operate in a regime clean enough to overcome the impurity radiation barrier at T_e - 15 eV and raise the temperature to $T_i = T_e$ - 100 - 200 eV. A third objective of ZT-40 will be to determine the ranges of the current and electron densities which allow the production of MHD stable configurations. This last objective relates to the projected size of potential fusion reactors based on this approach.

A wide range of sizes and configurations was considered for the ZT-40 device; the present design (with R = 114 cm and r = 20 cm) appears to be a proper size commensurate with considerations of scaling studies, manpower resources, available plant facility, and funding allotments. It is projected that the first plasma experiments on ZT-40 will begin in the calendar year 1979.

2. Design. The basic design of ZT-40 is a 40-cm bore torus with plasma aspect ratio of 5.7. The torus is fed at 12 points and has 12 magnetic iron cores equally spaced about the torus. A sketch of the device is shown in Fig. IV-28. A fewer number of feeds would allow greater machine access, but would mean a large developmental program in high-voltage technology to attain high reliability. The machine risetime is lengthened by shorting a fraction of the toroidal feed points and by series-paralleling the poloidal field windings. Very slow operation can be attained by energizing the field only with the power crowbar bank.

The initial experiments on ZT-40 will probably utilize a ceramic discharge tube. Further experiments with quartz and metal tubes are planned if further studies indicate their use will lead to cleaner discharges. The discharge tube is located inside a 2-cm-thick aluminum shell which serves as the primary conductor of a transformer with the plasma secondary and also as the conducting wall for stabilization of the plasma.

The vacuum system is designed as a four-point pumping system on the torus. Figure IV-29 shows a top view layout of the torus and the four pumping stations. The four stations will each have three small pumping apertures into the torus. Single, large apertures must be avoided to prevent large field perturbations inside the torus.

3. Machine Parameters. The basic machine parameters for ZT-40 are given in Table IV-II. A more complete description of the engineering details of ZT-40 is given in Sec. XV.

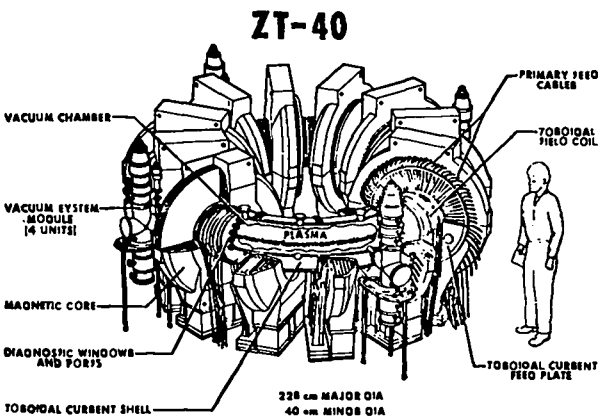

Fig. IV-28.
Schematic of the ZT-40 device.

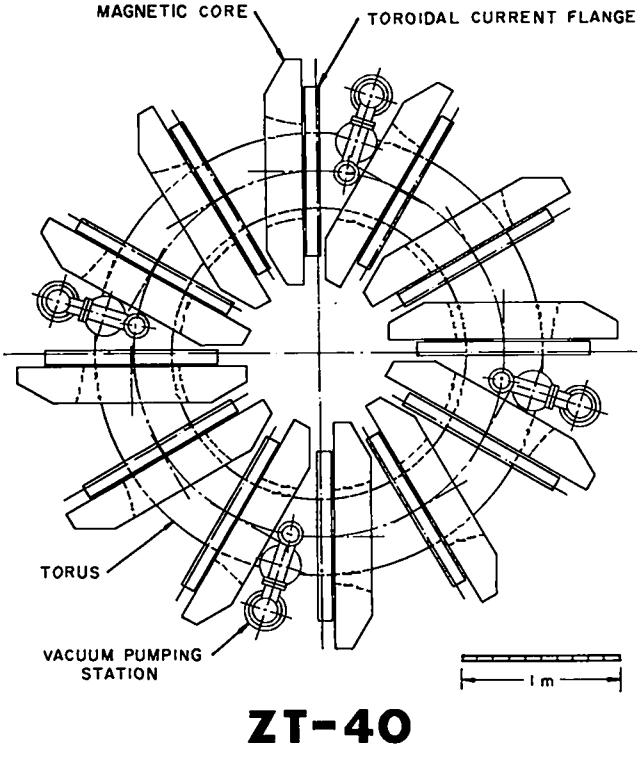

Fig. IV-29.
Sketch of the ZT-40 torus showing magnetic cores, toroidal current feeds and vacuum pumping stations.

TABLE IV-II

ZT-40 PHYSICS DESIGN PARAMETERS

Major radius	$R = 114$ cm
Minor vacuum chamber radius	$a = 20$ cm
Gas fill (D_2)	$p = 5$-30 mtorr
Electron density	$n_e = 10^{14}$-10^{16} cm^{-3}
Confinement time (assuming a^2 scaling)	$\tau_c = 150$-200 μs
Electron, ion temperature	$T_e \sim T_i = 100$-200 eV
Toroidal current	$I_\phi < 150$-600 kA
Mean toroidal current density	$J_\phi \lesssim 2$ kA/cm^2
Initial (toroidal) field	$B_\phi = 0.2 - 0.6$ T
Reversed-toroidal field	$B_{\phi R} = \leq -0.5$ T
Poloidal field	$B_\theta = \leq 0.6$ T
Range of plasma current risetime	$\tau = 2.5$ μs to ~1 ms
Base pressure	$p_o = 10^{-8}$ torr

REFERENCES

1. R. S. Dike and R. W. Kewish, Jr., "The Development of a High-Explosive Driver Crowbar Switch," Proc. 5th Sym on Engineering Problems of Fusion Research, Princeton, New Jersey (November 1973), IEEE, New York, p. 658.

2. J. A. Dibiase, "Numerical Studies of Resistive Instabilities in Diffuse Pinches," Ph.D. Thesis, University of California, Davis, Lawrence Livermore Laboratory Report UCRL-51591, May 1974.

3. R. W. P. McWhirter, Plasma Diagnostic Techniques, Huddleston and Leonard, Eds. (Academic Press, 1965) pp. 214-227.

4. "Atomic Data for Fusion," newsletter, Department of Magnetic Fusion Energy, Vol. 1, No. 3, (May-June 1975) Sec. B.3, "Experimental and Theoretical Collisions," p. 9.

5. C. L. Longmire, Elementary Plasma Physics, (Interscience Publishers, 1963) p. 205.

6. E. Meservey, N. Britz, D. Dimok, and E. Hinnov, PPPL report Matt 1175, December 1975.

7. R. Clausing, L. Emerson, L. Heatherly, R. Colehin, and J. Twitchell, J. Vac. Sci. Tech 13, 449 (1976).

8. R. R. Parker (Alcator Tokamak), private communication.

9. F. C. Jahoda (Scylla IV), private communication.

10. W. Engelhardt, W. Köppendörfer, M. Munich, and J. Simmer, Fourth European Conference on Controlled Fusion and plasma Physics, Rome, (1970) p. 50.

V. SCYLLA IV-P LINEAR THETA-PINCH EXPERIMENTS

K. F. McKenna, R. J. Commisso, C. A. Ekdahl, K. B. Freese,
R. Jones, R. W. Kewish, R. Kristal, W. E. Quinn, and R. E. Siemon

A. INTRODUCTION

The linear theta pinch is an attractive alternate approach to a high-beta fusion reactor. The advantages of this device are its ease of plasma heating, high plasma beta and density, demonstrated plasma equilibrium and neutral stability properties, and simple geometric configuration. However, in linear systems, particle loss through the ends and heat loss by electron and ion thermal conduction along the field lines present a fundamental limitation on the plasma confinement time which leads to reactor systems of uneconomical length. In addition, the plasma behavior and scaling in laboratory size devices has not been clearly identified. Accordingly, in order to obtain relevant reactor designs of economical length, plasma loss from the ends of the theta pinch must be significantly reduced and the appropriate scaling laws established.

The Scylla IV-P 5-m linear theta pinch was constructed to facilitate detailed studies of linear theta-pinch physics. The present primary objective of the Scylla IV-P experiment is the investigation of particle and energy end-loss physics and end-stoppering techniques.

Scylla IV-P became operational, with plasma, in January 1976. Since that time the following has been accomplished: (1) a large array of diagnostics have been installed and the hardware and software required for interfacing the diagnostics with the Scylla IV-P computer have been developed. A Thomson scattering apparatus and a side-on HF interferometer have been installed and are currently being tested; (2) the plasma parameters ($T_i \simeq 1$-2 keV, $n_e \simeq 15 \times 10^{16}$ cm^{-3}) and stability characteristics at 10-mTorr D_2 fill pressure and 45-kV primary bank voltage have been determined; these measurements establish a reference basis for subsequent experiments; (3) plasma end loss was examined with an end-on interferometer which responds to the electron density integrated over the length of the observable plasma column, and with internal magnetic field and pressure-sensitive probes which respond to local conditions within the axially flowing plasma near the coil ends. The local measurements indicate that the plasma flowing from the ends of the theta pinch remains remarkably columnated (as opposed to rapid radial expansion) while the internal magnetic fields are significantly altered from their vacuum configuration implying that the field lines are "frozen" into the outflowing plasma; (4) initial end-stoppering experiments using quartz end plugs have been carried out. The results indicate that the insertion of the plugs eliminates particle end loss from the ends of the theta pinch and increases the energy confinement time. The plasma stability characteristics were greatly enhanced in the presence of the plugs.

The planned near-term experiments on Scylla IV-P include the following: (1) a continued examination of the theta-pinch end-loss physics with particular emphasis on the identification of inward propagating area wave phenomena, electron and ion thermal conduction effects, and particle and energy end-loss scaling; (2) the detailed investigation of the plasma-plug interaction using solid end plugs of various materials in end-stoppering experiments. Cryogenic frozen gas and high-pressure puff gas injection end-plugging schemes will also be studied; (3) electromagnetic end-stoppering techniques such as the application of multiple mirror fields and possibly moving mirrors, will be investigated; and (4) the study of plasma injection into the ends of the theta pinch from coaxial plasma guns is planned. Analytical and computer models of the end-loss and end-stoppering processes are currently being developed, to complement the experimental program.

B. EXPERIMENTAL ARRANGEMENT

An elevation plan view of the Scylla IV-P theta pinch is shown in Fig. V-1. Rather than stacking the energy storage capacitor-spark gap units in conventional Scyllac-type racks, a three-level platform structure is used where the capacitor units are arranged in clusters composed

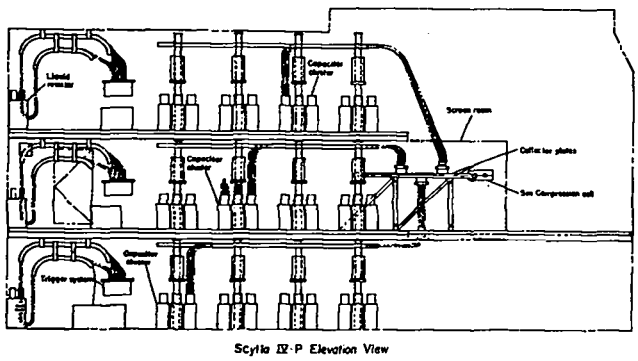

Figure V-1.
Elevation plan view of the Scylla IV-P device.

of nine capacitor units and one crowbar trigger unit. This arrangement facilitates trouble shooting and bank maintenance. The collector plates and 5-m long compression coil are situated on the middle platform level which also accommodates the majority of the plasma diagnostic systems. A photograph of the device is shown in Fig. V-2. Operation of Scylla IV-P is completely computer controlled. The computer also provides for "on-line" data reduction.

1. Compression Coil and Discharge Tube. The 5-m long, 11.2-cm diam. single turn compression coil is fed by five collector plate (parallel plate transmission line) assemblies, each assembly being 1-m wide and 3-m long. The energy from the capacitor bank is fed to the collector plates through coaxial cables connected to close packed cable cartridges located on both the top and bottom surfaces of the collector plates. The quartz discharge tube has an 8.8-cm inside diameter and extends 4.5 cm beyond the coil ends. Each end of the discharge tube is contained within a 20-cm-diameter, 50-cm-long quartz end bubble. This configuration minimizes plasma-wall interactions at the discharge tube ends and provides access for optical and internal plasma diagnostics.

Figure V-2.
Photograph of the "front end" of the Scylla IV-P device showing the 5-m compression coil and its current feeds.

2. Primary Capacitor Bank. The primary bank consists of 600, 1.85-μF, 60-kV capacitors with a total energy storage capacity of 2 MJ. Each capacitor is connected to the collector plate by its spark gap switch through six RG-17/14 coaxial cables. The bank operating range extends from 40 to 60 kV and produces a magnetic field of 1.1 kG/kV with a quarter cycle time of 3.3 μs. A Scyllac-type crowbar system extends the magnetic field in time with an L/R decay of $\sim$ 110 μs. The experimental results discussed below were obtained at a primary bank voltage of 45 kV which generates a peak magnetic field of 50 kG and an initial vacuum azimuthal electric field of $\sim$ 0.6 kV/cm at the inside wall of the discharge tube.

3. Preionization (PI) Bank. The optimum preionization bank configuration was determined from an experimental study of the preionized plasma parameters obtained with various PI bank conditions. A PI bank consisting of five 0.7-μF, 75-kV capacitors charged to 55 kV was determined to be optimum. A single capacitor is connected at the rear of each of the five collector plate assemblies by its spark gap through 6 RG-17/14 coaxial cables. The PI bank oscillates at $\sim$ 500 kH_z and produces a peak field of $\sim$ 2 kG.

4. Diagnostics and Data Acquisition. The diagnostics on the Scylla IV-P device have been arranged to permit investigation of the plasma parameters not only at the center of the plasma column but also at various positions along the coil axis and within the end bubbles located at the coil ends. A schematic of the Scylla IV-P diagnostic configuration is shown in Fig. V-3. The central plasma column has been studied using stereo viewing streak cameras, a 20-channel

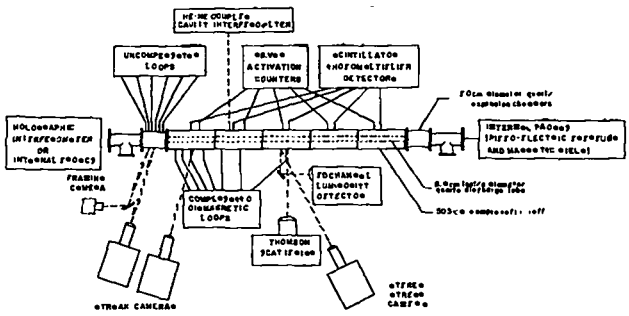

Figure V-3.
Schematic of the Scylla IV-P diagnostic configuration.

luminosity detector, silver and scintillator neutron detectors, and a diamagnetic loop-probe system. A Thomson scattering apparatus and an HF side-on interferometer are being positioned within the central 1-m coil section. Axial variations of the plasma parameters are studied with streak cameras, neutron detectors and diamagnetic loop-probe systems; In future experiments the Thomson scattering apparatus and an additional 20-channel luminosity detector will also be used to investigate axial plasma variations. The behavior of the plasma flowing out of the theta-pinch ends and into the end bubble regions is studied externally with framing and streak cameras and with total magnetic flux loops, and internally with pressure-sensitive piezoelectric probes and magnetic field probes. The axially averaged plasma electron density distribution is obtained with a holographic ruby laser interferometer which views the plasma column end-on. A He-Ne coupled cavity interferometer has been used to study the preionized plasma and is currently being modified so that coupled cavity density measurements can also be made during the primary bank discharge. In addition to the diagnostics shown in Fig. V-3, monochrometers which will permit spectroscopic plasma studies are being installed. A side-on ruby laser interferometer, to be used in the investigation of the plasma end-plug interaction, has been designed and will be implemented in the near future.

The Scylla IV-P computer monitored data acquisition system consists of 24 biomation channels and 48 Standard Engineering Corporation (SEC) units. All the data collected by these units are analyzed "on-line" by the Scylla IV-P Prime 300 computer. All the bank monitors, primary master gap, primary submasters, crowbar masters, and PI master, are monitored with the biomations and displayed on a hard copier along with the corresponding time delays and the primary bank waveform, quarter period and maximum field. The total magnetic flux loops, on one end bubble, are also monitored on biomations. The SEC units generally record the output from the diamagnetic loop-probes, the luminosity apparatus and the prompt neutron detectors. Other diagnostics are either monitored on oscilloscopes or are temporarily placed on the SEC units. The Thomson scattering apparatus is self-contained, having its own data acquisition and reduction system.

C. EXPERIMENTAL RESULTS WITHOUT END PLUGS

In order to determine the plasma parameters, stability behavior, and end-loss characteristics, which establish reference conditions for end-stoppering studies, experiments were conducted with the theta-pinch ends unobstructed. An initial static fill pressure of 10-mTorr D_2 and a primary bank voltage of 45 kV were used in these experiments. Before proceeding to the full primary bank plasma studies, the properties of the preionized plasma were investigated.

1. Preionization Studies. Ideally, the preionized plasma should be highly ionized, radially and axially uniform, and impurity free. Experiments were carried out to determine the preionization bank configuration which most closely produced these optimum conditions. In these studies the time-resolved plasma electron inventory was determined with a side-on 3.39-μ coupled cavity interferometer, the plasma radial uniformity was checked with an end-on ruby laser interferometer, and the relative impurity level was monitored using a monochrometer-photomultiplier combination tuned to the OII spectral line at 3973.3 Å.

A summary of the results of the preionization study is given in Table V-I where the PI bank configurations, energies, and applied capacitor voltages are listed along with the maximum ionization expressed as a percentage of full

TABLE V-I

PREIONIZATION EXPERIMENT SUMMARY

Number of 0.7 μF Capacitors	Capacitor Voltage (kV)	PI Bank Energy (kJ)	Maximum Ionization (%)	Ionization Decay e-folding time (μs)
10	50	8.8	136 ± 26	17
10	40	5.6	101 ± 8	22
5	60	6.3	95 ± 12	19
5	50	4.4	77 ± 8	27

ionization of the 10-mTorr fill gas, and the e-folding decay time from peak ionization .

Although a small degree of compression and radial variation of the preionized plasma at early times was indicated from examination of the end-on ruby laser interferograms, the plasma was observed to be highly uniform at times greater than a few microseconds after the time of gas breakdown (8 to 10 μs after initiation of the PI discharge). Thus, the measured ionization percentages greater than 100% (Table V-I) obtained at the higher PI bank energies cannot be attributed to errors in reduction of the side-on coupled cavity data due to plasma compression and radial nonuniformities. The excess electron inventory most probably results from wall impurity ionization. The spectroscopic data also indicated an increase in impurity radiation level with increased PI bank energy, the most significant increase occurring when the PI bank energy was increased from 6.3 to 8.8 kJ resulting in a factor of three jump in the relative impurity intensity level. A measure of the axial uniformity of the preionized plasma was obtained from the axially arrayed diamagnetic loop-probe data. These data indicated a more uniform axial distribution of the plasma when the five capacitor PI bank configuration was used.

As a consequence of these experimental results, a configuration consisting of five capacitors charged to 55 kV was chosen as an optimum compromise between ionization fraction, plasma uniformity and reproducibility, and impurity minimization. This PI bank system was used in all the experiments discussed below. In these experiments the primary bank discharge was applied - 20 μs after initiation of the preionization discharge.

2. Primary Discharge Plasma Stability Characteristics. Side-on stereo streak photographs of the primary discharge plasma were taken at an axial position 17 cm from the coil midplane. Figure V-4 presents typical streak pictures taken at two different camera sweep rates. The uppermost streak in each photograph shows the plasma column viewed from the top of the theta-pinch coil and an upward motion in this streak represents plasma movement toward the coil feed slot. The upper streak in each photograph shows the column viewed from the front of the coil and an upward

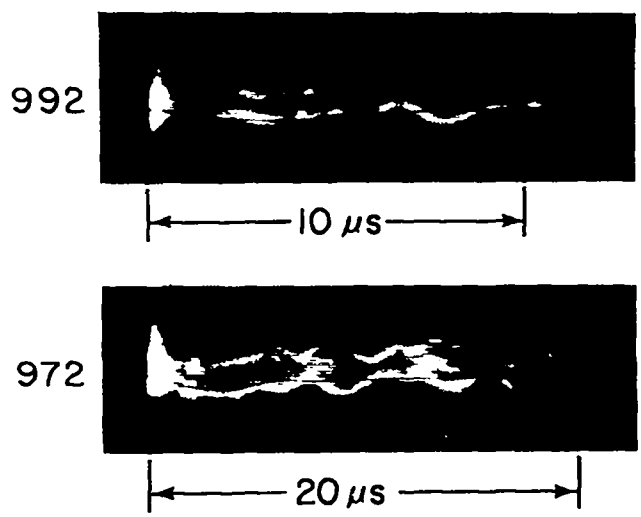

Figure V-4.
Stereoscopic streak photographs of the Scylla IV-P plasma column obtained at two different camera sweep rates at an axial position 17 cm from the coil midplane. The bottom streak in each photograph shows the plasma as viewed from the top of the theta-pinch coil and the upper streak shows the column viewed from the coil front.

motion in this case represents a plasma movement downward in the gravitational sense.

From examination of many stereo streak photographs the plasma stability time history can be described as follows: (1) a damped m=2 oscillation of the column is observed immediately after the termination of the implosion phase; (2) the plasma "wobble" or m=1 rotation begins ~ 4-5 μs after discharge initiation and never totally damps out; and (3) the plasma exhibits a slight m=2 distortion at times t $\geq$ 10 μs. The initial m=2 oscillation can be clearly identified as a rotating elliptical plasma cross section from the streak photographs of Fig. V-4a. The average frequency of the rotation is 0.81 $\pm$ 0.15 MH_z and the instability damps out after 3-4 μs.

The onset time of the m=1 wobble is 4.7 $\pm$ 0.6 μs. This instability is characterized by a frequency of 0.42 $\pm$ 0.05 MHz and a growth rate of 0.9 $\pm$ 0.1 MHz. The wobble generally attains a peak amplitude of ~ 2 cm, after which it begins to damp out. Figure V-5 shows a time projection of the wobble trajectory, reduced from the accompanying streak photograph, where "in" on the in-out axis indicates motion toward the coil feed shot and "up" on the up-down axis has the usual gravitational meaning. The plasma column rotates in the counter/clockwise direction, which is the direction expected for ion rotation due to end-shorting of the radial electric field in the plasma sheath. A limited number of stereo streak photographs were taken at an axial position 16 cm from the end of the coil. These data, in conjunction with simultaneous streaks taken near the coil midplane, indicate that the amplitude of the wobble increases toward the center of the coil and that there is little phase shift between the two axial positions, implying that the oscillation has a nodal point near the end of the coil.

The presence of an m=2 distortion of the plasma column at t $\geq$ 10 μs is also indicated from the end-on holographic interferograms (discussed below). However, since the interferometric technique measures an axially integrated density profile, whether or not the observed effect results from a local m=2 distortion or a distortion existing along the entire column length cannot be resolved by this diagnostic. An indication of the local behavior of the m=2 instability was obtained from the side-on, 20-channel, luminosity detector located 17 cm from the coil midplane. Figure V-6 shows an end-on interferogram, displaying the m=2 distortion at t

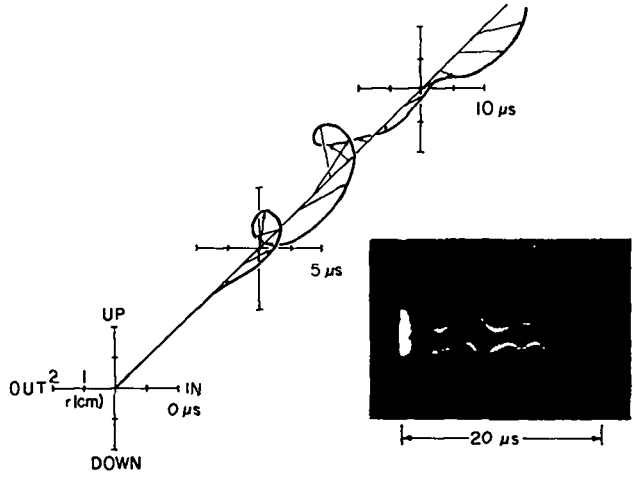

Figure V-5.
Time trajectory of the plasma column, reduced from the accompanying streak photograph.

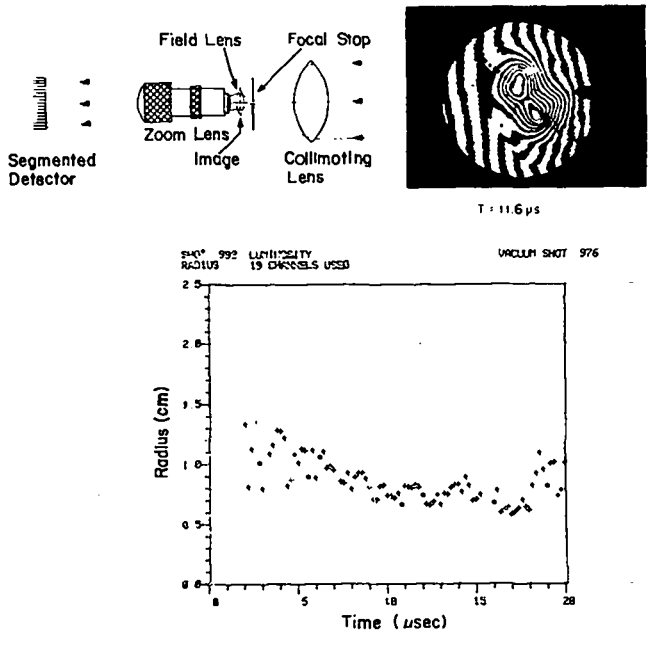

Figure V-6.
End-on interferogram, displaying m=2 distortion at t = 1.6 μs, and the time history of the local plasma column radius measured with the side-on luminosity detector shown schematically.

= 11.6 μs, and a time history of the local plasma column radius measured with the luminosity detector. Both data were obtained on the same discharge. The luminosity data shows an increase in plasma radius between 10.8 and 11.8 μs, consistent with the m=2 distortion indicated on the interferogram. Such a correlation does not absolutely identify the local character of the distortion but certainly does imply the existence of local m=2 behavior of the plasma. In order to clearly identify the nature of the local distortion, a second luminosity apparatus has been constructed and will be installed at 90 to the original apparatus. This scheme will provide a quantitative analog to the stereo streak camera technique and provide a local two-dimensional plasma profile.

3. Axially Averaged Plasma Density Measurement. The spatial and temporal evaluation of the axially averaged plasma electron density distribution was determined with an end-on, 30-ns pulsed, holographic ruby laser interferometer. Figure V-7 presents a time sequence of plasma column interferograms. Each interferogram was obtained on a separate discharge and the entire 8.8-cm diameter of the discharge tube was illuminated by the interferometer laser light. The fringe pattern on each interferogram was digitized and reduced with software developed for the CTR-PDP-10 computer. The results of this data reduction scheme, which does not require that the interferogram have a symmetric profile, give the axially averaged peak density, total integrated electron inventory, and a three-dimensional isometric plot of the axially averaged electron density distribution.

The time history of the axially averaged peak density, n_A, which does not necessarily occur on the discharge tube axis, is presented in Fig. V-8. A peak density of approximately 1.6 x 10^{16} cm^{-3} is obtained at peak compression. The peak density drops sharply with the decrease in the main field and subsequently decays gradually to a value of about 0.6 x 10^{16} cm^{-3} prior to the column breakup. The three-dimensional density plots corresponding to the interferogram sequence of Fig. V-7 are shown in Fig. V-9. The double density peaks observed on these plots for t > 11.6 μs are suggestive of the m=2 distortion discussed previously.

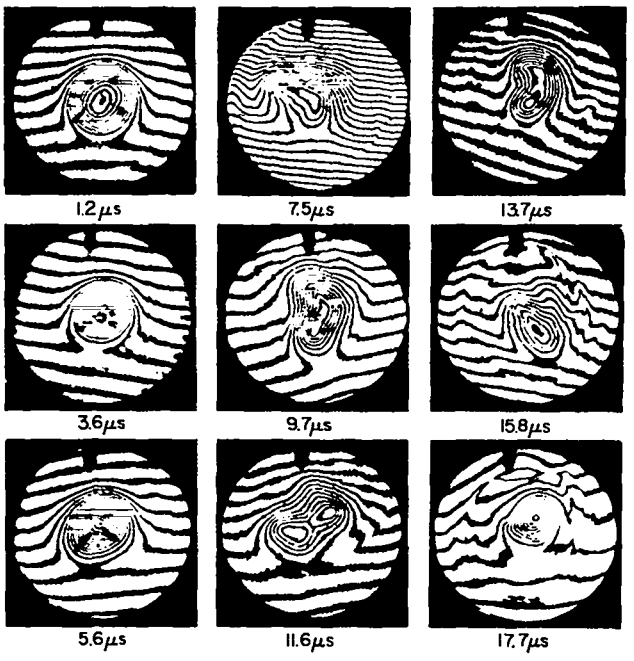

Figure V-7.
Time sequence of plasma column end-on interferograms.

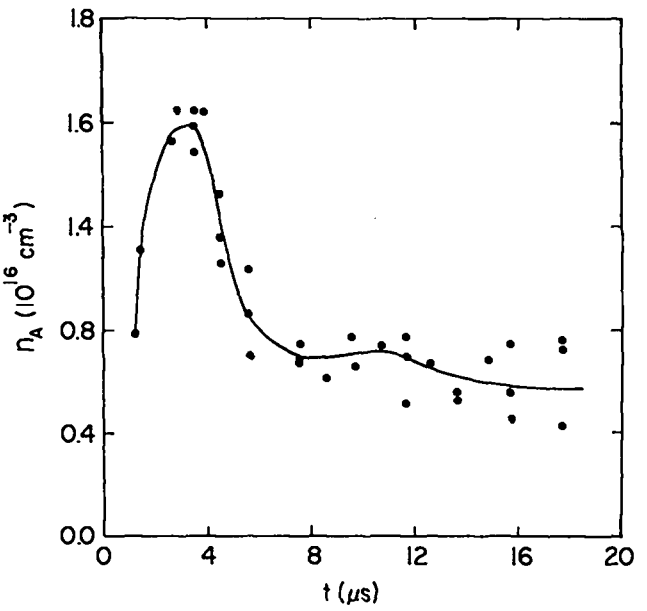

Figure V-8.
Time history of the plasma column peak density.

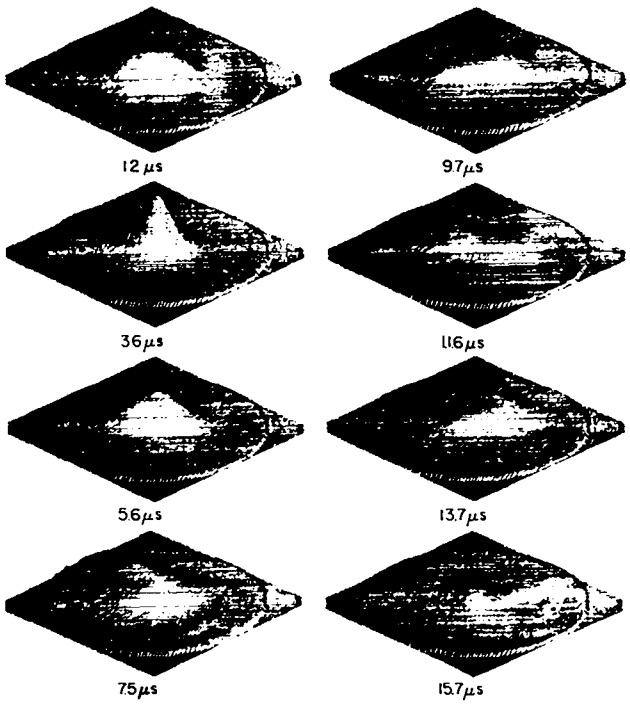

Figure V-9.
Three-dimensional plots of the plasma column density distribution.

4. Plasma Excluded Flux Measurements. The effective radius, r_{eff}, at which magnetic flux is excluded from the plasma and the axial evolution of r_{eff} have been determined from diamagnetic loop-probe measurements. Seven loop-probe systems are arranged along the discharge tube axis. With z=0 defining one end of the 500-cm-long theta-pinch coil, the loop-probes are located at z = 17, 34, 51, 83, 117, 151, and 250 cm.

Figure V-10 presents the excluded flux radius, r_{eff} versus time measured at each of the seven axial positions, z, noted above, and represents typical data. The excluded flux radius varies smoothly in time at axial positions z > 83 cm. However, near the coil end significant perturbations in the time evolution of r_{eff} are observed. Considering the data obtained at the axial station nearest the coil end (z=17 cm), three distinct "spikes" can be identified with the start of first spike at t = 4.9 ± 0.4 μs after discharge initiation; the second and third spikes begin at t = 8.0 ± 0.4 μs and t = 10.6 ± 0.3 μs, respectively. The first spike represents an increase of 80 ± 20% in the magnitude of r_{eff}

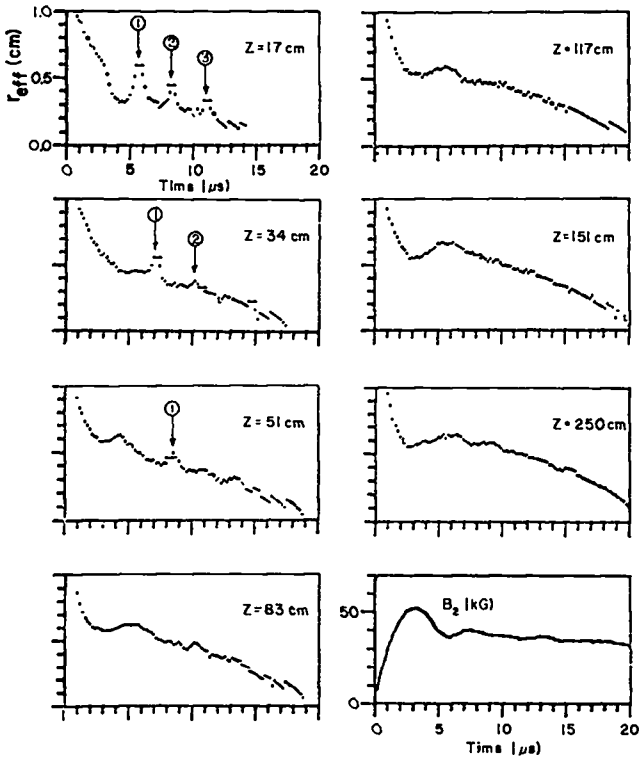

Figure V-10.
Typical time history of the plasma effective radius obtained simultaneously by seven diamagnetic loop-probe systems arrayed along the discharge tube axis, and the main magnetic field waveform. Z=0 defines the coil end.

measured immediately prior to the spike initiation; the second and third spikes are generally smaller in magnitude than the first. The inward propagation of the first spike can usually be identified on the excluded flux data taken at the z = 17-, 34-, and 51-cm positions, while the second and third spikes are found to decay beyond recognition at z > 34 cm. The inward velocity of the first spike, measured from the time of arrival at each loop-probe location, is ~ 1 x 10^7 cm/sec, about a factor of 4 lower than any characteristic plasma velocity. Although the origin of these plasma perturbations is presently unknown, it is of interest to note that the onset time of the first spike at z=17 cm approximately coincides with the observed onset time of the wobble instability as determined from the streak camera photographs.

The excluded flux radius measured at z = 250 cm is used in the plasma beta determination. From Fig. V-10, r_{eff} at z=250 cm is seen to attain a

value of about 0.6 cm for 2 μs < t < 10 μs. At times greater than 10 μs, the excluded flux radius decays to the relatively low value of ~ 0.1 cm at t=20 μs.

5. Plasma Radius and Beta Measurements. The plasma column radius at an axial position 17 cm from the theta-pinch coil midplane is measured using a 20-channel side-on viewing luminosity apparatus. The plasma radius data are combined with the excluded flux data to yield the plasma beta, assuming a Gaussian profile for the plasma radial density distribution. Figure V-11 presents the 1/e plasma radius and peak beta as a function of time along with the plasma position, excluded flux, and main field waveform. These data are generated "on-line" and Fig. V-11 is representative of a typical plasma discharge. Although the radius and beta data points display a large degree of scatter, estimates of average values can be made. The 1/e plasma radius attains an average maximum value of about 1.2 cm at peak field and then decays linearly to ~ 0.6 cm at t=20 μs. The average beta remains relatively constant at β ~ 0.7 for t > 11 s, subsequently decaying to zero at t ≃ 19-20 μs. The onset time of the plasma wobble (m=1) and subsequent plasma oscillations observed on the streak photographs are also identifiable on the plasma position data.

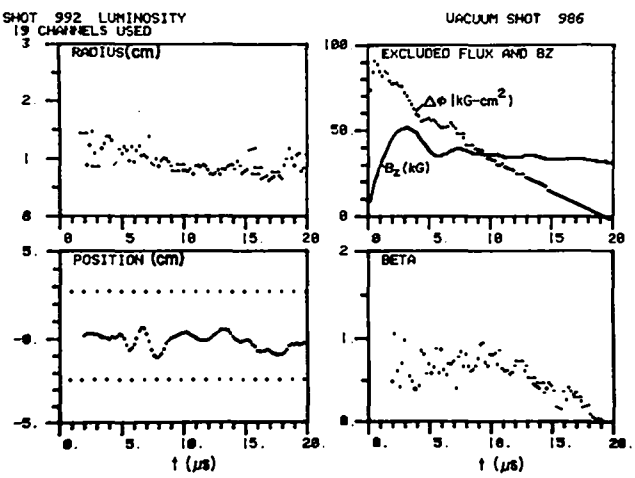

Figure V-11.
Plasma 1/e radius, centroid position, excluded flux and main field, and beta determined from the side-on luminosity apparatus and diamagnetic loop-probe located 17 cm from the coil midplane. Data for a typical plasma discharge.

6. Plasma Ion Temperature Measurements with Neutron Diagnostics. In the Scylla IV-P experiment, prompt measurements of the neutron emission rate are normalized to total yield measurements to provide an estimate of the ion temperature,[1] T_i. The normalization for these measurements is provided by time-integrated neutron yields determined with silver-foil activation counters constructed in the standard Los Alamos Scientific Laboratory geometry.[2] Five counters are used, and these are axially spaced 1 m apart with the first counter placed 0.5 m from the coil end. The counters have been calibrated in situ with a Pu-Be neutron source placed on the discharge tube axis. Observed yields are in excess of 10^8 neutrons/meter at the center of the theta pinch.

The prompt detectors, consisting of lead-shielded scintillator-photomultiplier combinations, are positioned at the same axial locations as the silver counters. Yields derived from prompt measurements have shown reasonable agreement with silver counter yields at the same locations. Extracting an ion temperature from the prompt detector signals requires a knowledge of the plasma radial density distribution and an inversion of the expression for the volume emission rate as a function of Maxwellian temperature T_i. The data analysis software currently in use calculates the ion temperature, T_i, at each axial position as a function of time based on the simple approximation of a Gaussian radial density profile with constant e-folding radius, a, and central density, n_A. An example of this "on-line" data reduction to T_i with a = 1.0 cm and n_A = 1.6 x 10^{16} cm^{-3} is shown in Fig. V-12.

An alternative procedure is to rely upon the reproducibility of the discharge and use the radius and peak density obtained from end-on interferograms. Plotted in Fig. V-13a are temperatures calculated from the interferometric data and the reaction rates measured at the times of the interferogram exposures. These precedures indicate a peak T_i ≃ 1.5 keV at about 3-4 μs and a decay to T_i ≃ 1.0 keV at about 15 μs, which agrees well with the results obtained assuming a constant density and radius. The fact that this method is relatively insensitive to small errors in n_A and a

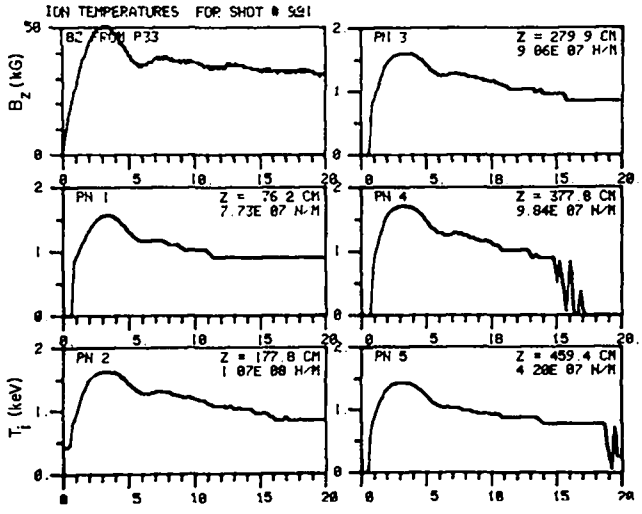

Figure V-12.
Time history of main magnetic field and ion temperatures obtained from on-line computer analysis of prompt neutron detector array data. Each plot shows the axial position, Z, of the detector, where Z=0 defines the coil end, and the total yield measured by silver counters.

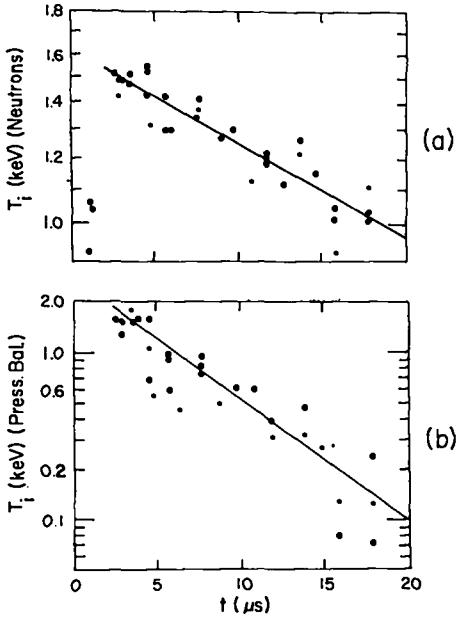

Figure V-13.
Ion temperature time history based on; a) prompt neutron detector data using plasma radius and central density obtained from end-on interferograms, b) pressure balance using beta determined from interferograms and excluded flux data.

results since T_i is approximately inversely proportional to $\sqrt{a\ n_A}$.

An independent estimate of the ion temperature is based on pressure balance in the plasma column. The peak plasma beta, β_A (not necessarily on the discharge tube axis), is calculated from a direct measurement of the plasma effective radius, r_{eff}, and the plasma radius, a, determined from the end-on interferometric data. Measurement of the magnetic field outside of the plasma column, B, is used with β_A to compute the peak plasma energy density, $\beta_A B^2/8\pi$, which by pressure balance is the peak thermal energy, $n_A k(T_e+T_i)$. Interferometric data for the central density n_A is used with Morse's model[3] for thermal electron conduction to the theta-pinch ends to determine the energy partitioning between electrons and ions, and thus extract an ion temperature. The time history of the ion temperature calculated by this method is shown in Fig. V-13b.

A comparison of the pressure-balance temperature with that determined from the neutron diagnostics indicates very good agreement at early times near peak magnetic field, but a large discrepancy exists between these results at later times. Several possible causes for this discrepancy are being investigated. It is possible that the proximity of the prompt detectors to the paraffin neutron moderators of the silver counters results in a high background gamma fluence from neutron-gamma interactions in the moderator material during the discharge. This possibility is amenable to experimental solution. It is also possible that the electron and ion energies are not partitioned according to Morse's model at late times. However, even if all the energy resided with the ions, there would still be a large discrepancy in the two results. It is also possible that the discrepancy results from uncertainty in using the end-on interferometric data to estimate plasma density and radius at the center of the pinch. As noted earlier, the neutron temperature is very nearly inversely proportional to $\sqrt{n_A}$ and $\sqrt{a}$. However, the pressure balance temperature is approximately inversely proportional to n_A and a^2, especially at late times when β_A is small. Thus the pressure balance temperature is four times more sensitive to errors in the radius than the neutron temperature, and twice as sensitive to errors in central

density. Either a partial stagnation of plasma at the ends of the coil, or ionization of impurities in the end regions can lead to an axial and radial electron distribution which tends to overestimate the central density and radius at the pinch center at late times.

D. PLASMA END LOSS STUDIES

With primary experimental efforts directed toward the generation, containment and stabilization of high-energy plasma in non linear configurations, the fundamental limitation on plasma containment in linear devices, namely plasma end loss, has received little experimental investigation. However, with the renewed interest in linear theta pinches as possible reactor systems, the problem of end effects must again be recognized as the major and limiting factor encountered in linear theta-pinch devices. The detailed processes governing the end-loss event have not been determined either experimentally[4,5] or theoretically.[6] Further, the applicability of continuum MHD or collisionless particle theories to the description and analysis of the plasma end-loss process and the appropriate end-loss scaling laws have not been clearly established. A principle objective of the Scylla IV-P experiment is to carry out more detailed studies of the end-loss phenomena than have previously been attempted, thus leading to a better understanding of the end-loss physics and providing a base on which analytical models can be developed.

1. Interferometric Studies of Particle End Loss. The particle end-loss time in linear theta pinches has classically been obtained using end-on interferometric techniques. An area integration over the interferogram fringe shift profile yields the total number of electrons within the path of the interferometer laser beam at the time during the discharge that the interferogram was taken. If the plasma expands radially after flowing out the ends of the device thus leaving the field of view of the interferometer, as is generally assumed, then the measured decay rate of the electron inventory determines the particle loss rate from the confines of the theta-pinch coil. However, end effects such as wall ablation at the ends of the discharge tube and the behavior of the plasma in the end regions can significantly confuse the interpretation of the interferograms assumed to be representative of only the confined plasma within the coil region. An attempt to identify the plasma behavior in the end regions has been carried out on the Scylla IV-P theta pinch and will be discussed below.

The total electron inventory obtained from the interferograms, Fig. V-7, is plotted as a function of time, after primary bank initiation, in Fig. V-14. The crosshatching has been introduced as a visual aid. The data were obtained during the early stages of the Scylla IV-P operation with plasma and therefore were not taken under optimum conditions of discharge tube cleanliness. A more precise interferometric determination of the electron inventory time history, with the theta pinch in a completely "clean" discharge condition, is presently in progress. The data of Fig. V-14 do represent the basic phenomenology of the Scylla IV-P particle end-loss process. The general characteristics of the inventory time history of Fig. V-14 are identical to those observed on the 5-m linear Scyllac device.[5] Specifically, the total particle

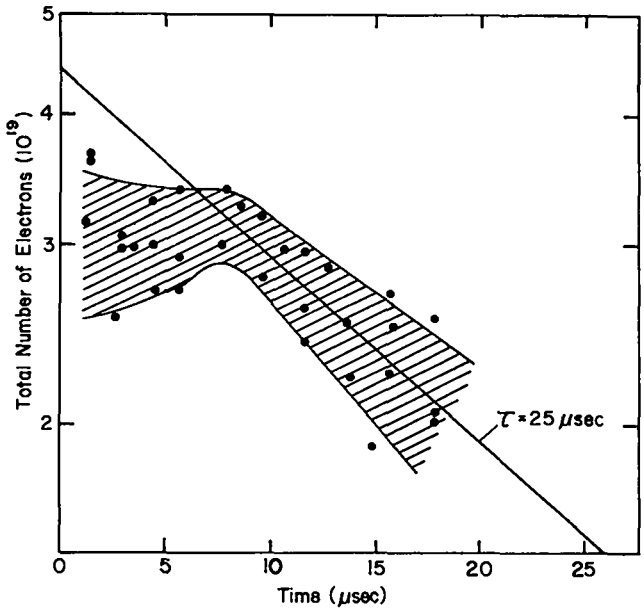

Figure V-14.
Time history of electron inventory determined from end-on interferograms. The straight line is a least square fit to data taken at times subsequent to 6 μs.

inventory is seen to remain relatively constant for an initial period of approximately 6- to 8-μs duration before an exponential decay is observed. The cause of this initial inventory plateau has not been previously understood. For the data subsequent to 6 μs, a least squares fit yields an inventory e-folding time of ~ 25 μs. This is greater than expected from simple scaling with previous experiments and can probably be attributed to the large data scatter and the initially unfavorable conditions of the discharge tube.

2. Framing and Streak Camera Studies in the End-Bubble Region. Studies of the gas flow from the plasma column into the vacuum vessels at the theta-pinch ends have been carried out using both short time exposure photography and a streak camera. A Beckman-Whitley framing camera, operating with a 10-ns exposure time, records the plasma self-luminosity and the luminosity produced from the plasma-wall contact at various times during the plasma flow event. A TRW streak camera, viewing the same end bubble as the framing camera, records the spatial and temporal development of the end region light for a period of approximately 10 μs after initiation of the main discharge. The field of view of both cameras encompassed the entire 45-cm length of the 20-cm i.d. end vacuum vessel.

Figure V-15 presents a typical streak photograph and several framing camera photographs of the plasma flow into the end-bubble region. Considering the streak photograph, two plasma light fronts are observed to enter the end region approximately 0.5 μs after discharge initiation. An initial "fast" front propagates through the entire length of the end bubble attaining a final velocity of about 0.9 x 10^7 cm/s; the initial velocity (of ~ 0.8 μs duration) is about 1.7 x 10^7 cm/sec. This fast luminous phenomena is also identified on the framing camera photographs at t = 1.1 and 1.6 μs and appears as a diffuse parabolic light front. The grainy light structure appearing on the early time framing camera photograph (t=1.1 μs) is not plasma light but "bleed-thru" on the image converter tube resulting from the intense radiation generated by the plasma wall contact at late stages of the end flow

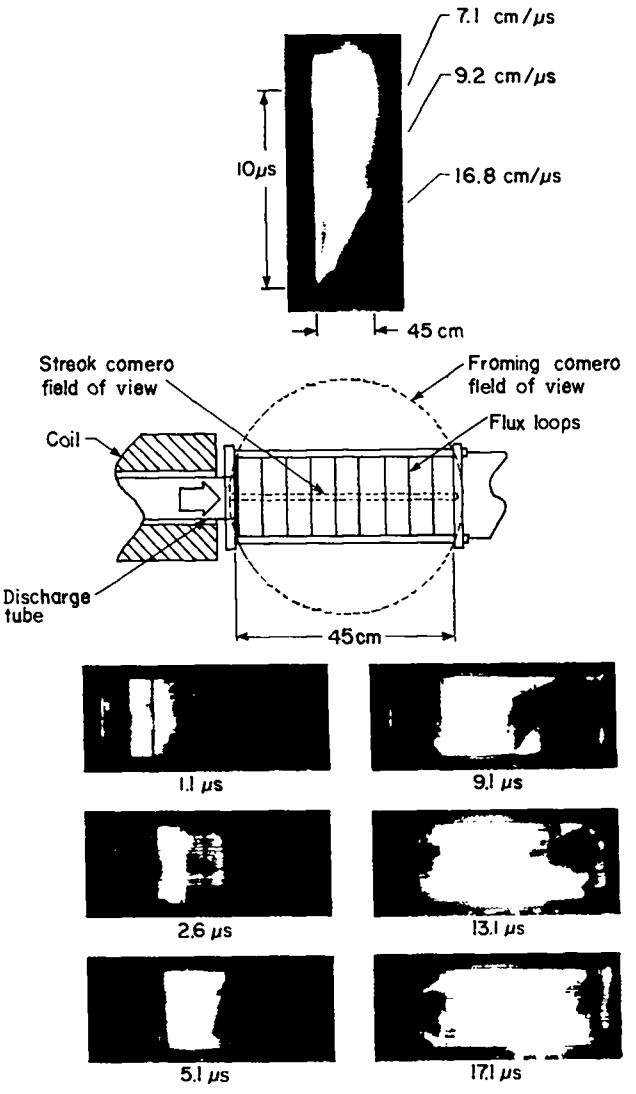

Figure V-15.
Streak and framing camera photographs of the plasma flow in the end bubble region.

process. The initial fast front is believed to be the result of an axially outward propagating "shock" initialized during the plasma implosion phase; the diverging magnetic field lines at the theta-pinch ends generate a radial magnetic field component, B_r, which can interact with j_θ in the imploding current sheath resulting in a $j_\theta B_r$ force which accelerates particles into the end-bubble region.

The second "slow" front appearing on the streak photograph propagates into the vacuum vessel with an initial velocity of about 0.7 x 10^7 cm/sec. This front rapidly decelerates and stagnates at about 3 μs at a position

approximately 20 cm from the theta-pinch coil end. From the framing camera photographs, this second front can be identified as a luminous ring resulting from the plasma-wall interaction. The temporal evolution of the end-bubble wall light can be observed on the framing camera photographs. The narrow band of light formed ~ 10 cm from the coil end shortly after discharge initiation propagates axially and continually broadens, nearly filling the entire vacuum vessel for t > 13 μs.

It should be noted that in dynamic plasma events, such as the end flow process, the observed light does not necessarily identify the mass distribution.[7] In addition, no conclusions concerning the magnetic field distribution can be made from observation of the plasma light. Experiments designed to determine the transient plasma mass and magnetic field distributions in the end regions are discussed below.

3. Total Magnetic Flux Measurements in the End-Bubble Region. The effect of plasma flow in the end-bubble region on the magnetic flux structure was determined using individual wire loops which encircle an end vacuum vessel. Nine loops were positioned 5 cm apart with the first loop 5 cm from the coil end (Fig. V-15). The axial distribution of magnetic flux, ϕ_v, in the absence of plasma flow was measured on discharges without gas (vacuum shots). The perturbed flux distribution, ϕ_p, resulting from the plasma-field interaction within the end-bubble region was measured on plasma discharges with an initial 10-mTorr gas fill pressure.

Figure V-16 presents typical data for ϕ_p/ϕ_v, the ratio of total measured magnetic flux with plasma flow to that obtained under vacuum conditions, versus axial position z within the end bubble where z=0 defines the theta-pinch coil end and -z values indicate positions external to the coil. Values of $\phi_p/\phi_v < 1$ indicate exclusion of the magnetic fields by the plasma. For $\phi_p = \phi_v$, the axial distribution of magnetic flux is identical for both plasma and vacuum discharges. It should be noted that the condition $\phi_p = \phi_v$ does not imply that the internal magnetic field structure is the same for both vacuum and plasma discharges but is rather a measure of the total

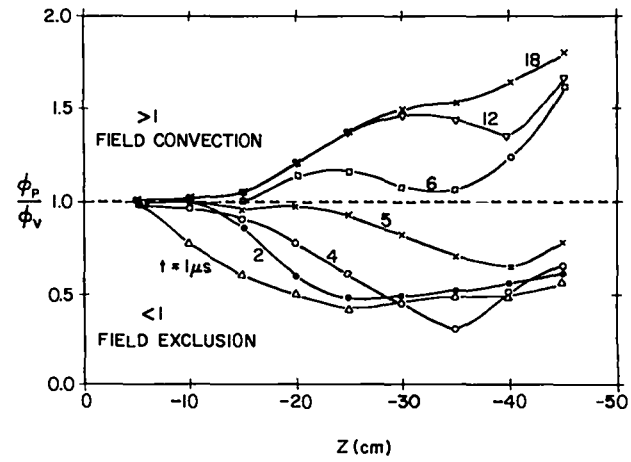

Figure V-16.
Evolution of ϕ_p/ϕ_v, the ratio of total flux in the end-bubble region with plasma to that measured under vacuum condition, vs axial position. Z=0 defines the coil end.

magnetic flux contained within the area defined by the loop. Values of $\phi_p/\phi_v > 1$ are obtained when, at a given axial location, the plasma-field interaction results in an increase in total magnetic flux over the value measured in the vacuum case. This condition can exist in the flow of a highly conductive plasma, where the magnetic fields inside the plasma are "frozen in" and are convected axially with the flowing plasma.

From inspection of Fig. V-16 it can be seen that during the initial stages of the plasma end flow event significant magnetic field exclusion occurs in the end-bubble region. At early times, t = 1.0 μs, partial exclusion of magnetic flux is observed at all axial positions $|z| > 5$ cm. Referring to Fig. V-15, a luminous band of light is observed at $|z| \sim 5$ cm on the framing camera photograph obtained at t = 1.1 μs. This luminous band results from the interaction of plasma with the end of the theta-pinch discharge tube which extends ~ 45 cm from the coil end. It thus appears that the plasma-wall interaction produces a ring of plasma of sufficient conductivity to partially prevent, at t = 1.0 μs, the penetration of magnetic flux into the end vacuum chamber. At t = 2.0 μs, Fig. V-16, partial flux exclusion is obtained only at axial positions $|z| > 15$ cm. Again referring to the framing camera photographs, Fig. V-15, an intense luminous band, resulting from the plasma wall interaction, is observed at

$|z|$ = 15 to 20 cm and t = 2.6 μs. The conductivity of this luminous band of plasma could again result in the exclusion of plasma at greater axial positions (larger $|z|$). Accordingly, as the region of intense plasma-wall interaction advances along the end vacuum vessel the quantity of magnetic flux excluded from the end vessel decreases. The plasma-wall interaction region stagnates at $|z| \sim 20$ cm and t ~ 3 μs. However, the magnitude of excluded flux continuously decreases after this time with ϕ_p/ϕ_v exceeding unity for t > 5.5 μs which indicates convection of the magnetic fields "frozen" into the axial flowing plasma. For t > 5.5 μs, ϕ_p/ϕ_v remains greater than unity at axial positions between 15 and 40 cm. The experimental observation time is presently limited to 20 μs. The observed values of ϕ_p/ϕ_v at $|z|$ = 40 and 45 cm are irreproducible from discharge to discharge, probably a result of the plasma interaction with the metal vacuum tee located 50 cm from the coil end, Fig. V-15.

4. Plasma End Flow Pressure Measurements.

In order to sense local plasma momentum flux, diagnostics must be placed in direct contact with the plasma. Piezoelectric pressure probes, which are optimum for this measurement, have been successfully employed in the investigation of pulsed plasma discharges.[4,7,8] In the Scylla IV-P experiment a small diameter pressure sensor was used to determine the plasma momentum flux at locations within the plasma near the coil ends.

A schematic of the piezoelectric pressure probe is shown in Fig. V-17a. The probe consists of a thin piezoelectric crystal sandwiched between two 0.2-cm-diam quartz acoustical delay lines 52- and 15-cm long. The longer quartz rod delays the arrival of the plasma pressure signal at the high electrical impedance (~ 6MΩ) piezoelectric crystal by ~ 91 μs, thus allowing the plasma discharge noise transients to decay to an acceptable level before the pressure signal is recorded. The acoustically matched 15-cm-long quartz backing rod at the rear face of the piezoelectric crystal delays the arrival of the reflected (from the end of the 15-cm-long rod) pressure pulse approximately 54 μs and thus defines the probe experimental observation time. The crystal-delay line assembly is mounted within a copper tube which is

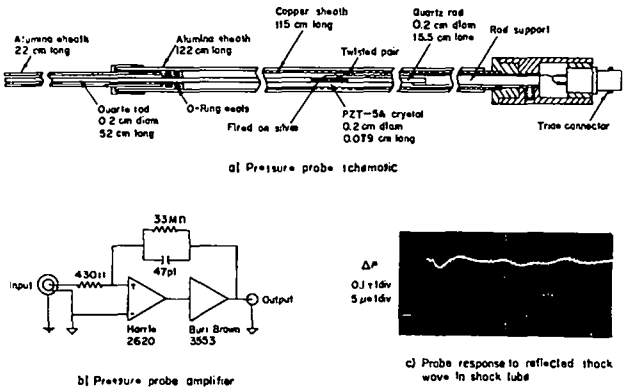

Figure V-17.
Pressure probe system and calibration waveform; a) pressure probe schematic, b) probe amplifier schematic, c) probe signature generated by a reflected shock wave in the end wall of a shock tube.

enclosed within a protective alumina sheath. The signal from the piezoelectric crystal is carried to a triax fitting at the probe end by a twisted wire pair. The probe output signal is then fed into an active capacitor unit which effectively eliminates the crystal signal amplitude reduction resulting from the capacitance of the crystal, twisted wire pair and signal cables. A line driver unit, shown schematically in Fig. V-17b, is used to drive the ~ 45 m of 50-ohm cable between the active capacitor unit and the recording oscilloscope.

The pressure probe system, including the probe unit itself and all associated electronic components and cabling, was calibrated and its response studied by using the constant pressure increment generated by a reflected shock wave in a simple gas dynamic shock tube. The pressure probe system calibration factor is $V/\Delta p = 0.11 \pm 0.006$ volts/megadyne/cm^2. The system response to the reflected shock pressure jump is shown in Fig. V-17c. The probe risetime is approximately 1.5 μs, which is more than an order of magnitude shorter than the time scale of the measured plasma pressure signal, but too long to resolve the detailed structure of fast transient phenomena. The probe RC decay time is determined by the parallel RC circuit in the amplifier unit and is about 1600 μs.

The pressure probe was inserted axially into the end-bubble region through a plate at the end of the theta-pinch vacuum tee. Data were recorded at axial positions z = -1, -6, -11, -16, and -26 cm, where z = 0 defines the end of the theta-pinch coil and -z values again indicate positions external to the coil. Radial measurements are made by rotating the probe about an axis located 91 cm from the coil end and R=0 defines the discharge tube center line. Figure V-18 shows the probe response under various discharge conditions. In the vacuum shot data record of Fig. V-18a, the oscilloscope trace was triggered at main bank time. The arrow labeled t_o indicates the acoustic delay time in the delay line between the plasma and the piezoelectric crystal, again this is the time required for a pressure pulse to be sensed by the crystal. All electrical noise transients have decayed by time t_o. Figure V-18b shows a vacuum shot pressure probe signature where the oscilloscope trace is delayed 75 μs from the time of the main bank discharge initiation and the sweep rate is 5 μs/cm, which are the recording conditions under which the plasma pressure data are collected. From examination of these data trace, it can be seen that extraneous effects that are not a result of local plasma pressure, such as magnetic loading of the piezoelectric crystal and discharge noise, are not present on the pressure probe electrical response. An additional perturbation to the pressure probe response can result from plasma impact on the probe protective alumina sheath; since the quartz delay line does contact the 0.4-cm-o.d. alumina sheath at a limited number of places, pressure impact loading of the sheath can be transmitted to the piezoelectric crystal. Figure V-18c shows the pressure probe response to a plasma discharge when direct contact between the plasma and the probe pressure sensing tip is broken by a 2-cm-long, 0.6-cm-o.d. alumina cap friction fitted over the probe tip. The small sinewave-like signal results from pressure impact loading of the protective alumina sheath and is easily subtracted from the recorded plasma pressure data. A typical pressure probe data record taken with 45-kV main bank voltage and 10-mTorr fill pressure at z = - 11 cm and R=0 cm is shown in Fig. V-18d. The "foot" seen on the data trace preceding the first large pressure spike results from impact loading of the probe sheath and should be neglected.

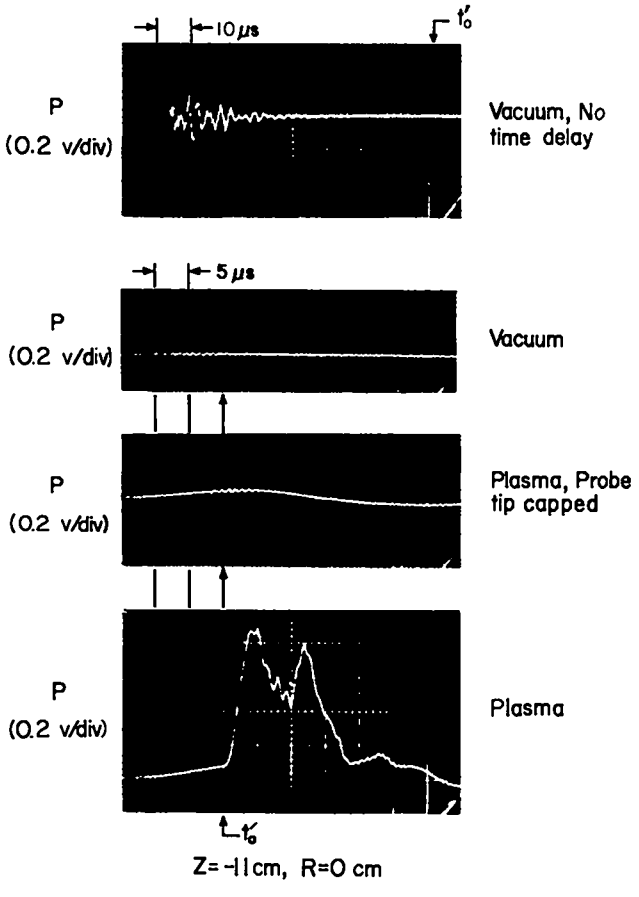

Figure V-18.
Pressure probe response within the end-bubble region under various discharge conditions.

Radial surveys of the end flow plasma pressure distribution, recorded at z = - 6 cm, are shown in Fig. V-19. The pressure profile measured at any given axial and radial position is characterized by either a single-pressure pulse of 10 μs or less duration as illustrated in Fig. V-19a or a double-pressure pulse with a total duration of > 20 μs as shown in Fig. V-19b. The amplitude and duration of the first pulse is approximately the same in both cases. The irreproducibility of the second pressure pulse is believed to result from the off-axis displacement of the plasma column due to the onset of the wobble instability. Accordingly, the m=1 displacement not only affects the plasma column

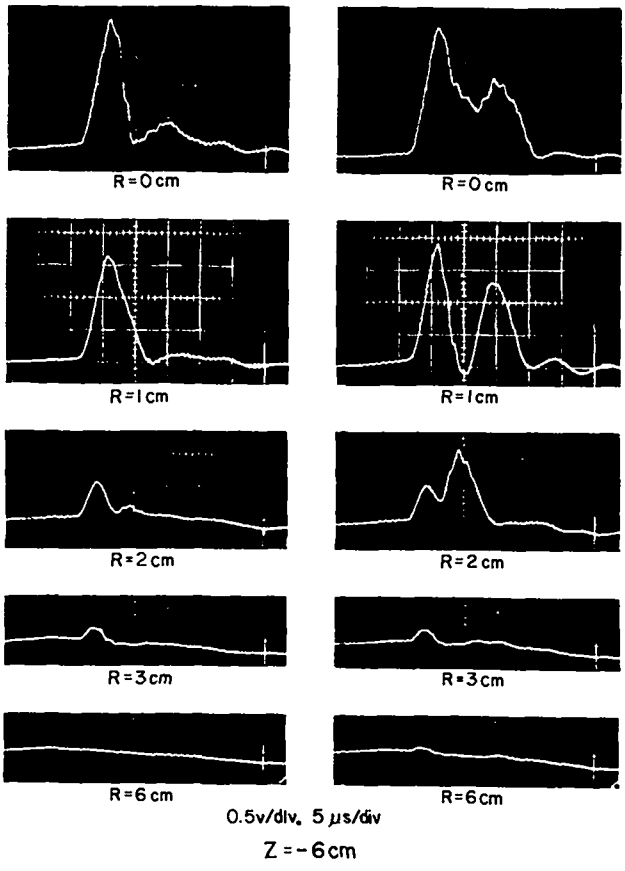

Figure V-19.
Radial pressure surveys at an axial position 6 cm from the theta-pinch coil ends; a) typical single pressure pulse data records, b) typical double pulse data records.

position within the confines of the theta pinch but also the distribution of axially flowing plasma in the end regions external to the coil.

The pressure measured by the probe is approximately equal to $n[k(T_e+T_i) + m_i v^2]$ where n is the local particle density, m_i is the ion mass, and v is the particle axial flow velocity. Assuming that the sum of the particle thermal and kinetic energies remains reasonably constant during the axial flow process, then the measured pressure is directly proportional to the local particle density and the pressure profiles can be interpreted as representing density profiles. Considering the pressure records of Fig. V-19, the significant decrease in measured pressure at radial positions > 2 cm indicates that the plasma flowing into the end vacuum chamber does not immediately expand to the wall, as is usually assumed, but rather remains highly columnated.

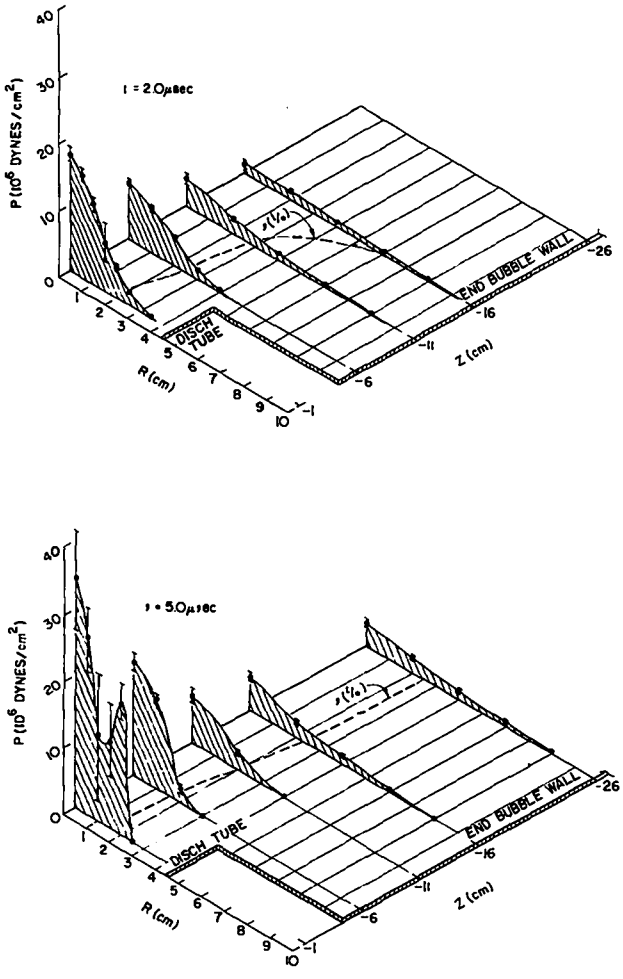

Figure V-20.
Plasma end flow pressure profiles at a) t = 2.0 μs and b) t = 5 μs.

This behavior is illustrated in Fig. V-20 where the pressure profiles are plotted for the entire flow field between z = - 1 and z = - 26 cm at two different times. Again, owing to the risetime limitation of the pressure probe, the detailed structure of highly transient behavior cannot be resolved and the profiles of Fig. V-20 therefore represent the large-scale phenomenology of the end flow event. Figure V-20 presents the pressure data obtained during the early stages of the flow into the end-bubble region. The broad radial pressure profile recorded at z = - 16 cm is associated with the axial driven "shock" initiated during the implosion phase and observed on the streak and framing photographs of Fig. V-15 and therefore does not represent mass flow from the main plasma column. At axial positions closer to the coil end, the plasma flowing from the plasma

column does not exhibit a rapid radial expansion. At later times, Fig. V-20, when the end flow is fully developed and the initial shock front has traversed the entire length of the end-bubble region, a highly columnated plasma flow is observed. The maximum 1/e plasma radius at z = - 26 cm, estimated from the pressure profiles of Fig. V-20, is about a factor of two smaller than the discharge tube radius and the 1/e radius at z = - 6 cm is only about 50% greater than the plasma column radius measured at the coil midplane. These measurements clearly indicate that the outflowing plasma does not expand immediately to the vacuum vessel wall after leaving the confines of the theta-pinch coil. In fact, little radial expansion is observed within the limits of the measured flow field.

As previously discussed, the time history of the plasma electron inventory determined from end-on interferograms (Fig. V-14) displayed an initial period of relatively constant inventory before an exponential decay was observed. This initial plateau effect can now be understood from the results of the end-flow plasma pressure measurements. The interferometer responds to all the electrons within the laser beam path. Since the plasma flowing from the theta-pinch ends remains columnated and therefore within the interferometer field of view, no decrease in electron inventory will be observed. The axially flowing plasma is believed to expand radially in the vicinity of the flux excluding metal vacuum tees which support the end-bubble chambers (Fig. V-15). Accordingly, the interferometrically observed electron inventory remains constant until plasma flowing from the main column interacts with the metal vacuum tees and expands out of the interferometer field of view.

The non-Gaussian nature of the pressure profile measured at z = - 1 cm, Fig. V-20, for times t > 4.0 μs is not understood. Such behavior could result from the off-axis plasma column motion initiated by the m=1 wobble instability. An alternative explanation is presented in the analytical results of Wessons MHD end-flow theory.[9] Wessons model predicts that the speed at which particles axially flow from the plasma column is proportional to $C_s(1-\beta)^{1/2}$ where C_s is the sound speed and β is the local value of the plasma beta. Accordingly, particles would be expected to be lost at a faster rate at off-axis radial positions where the local β is smaller than on axis. This "onion skin" effect has been observed in collisional plasma end-loss experiments.[10]

5. Internal Magnetic Field Probing in the End-Flow Region. The evolution of the magnetic field distribution in the end-bubble region was determined using the magnetic field probe array shown in Fig. V-21. The array consists of five 6.5-mm-o.d. alumina-jacketed probes radially spaced at 2.5-cm intervals. Each probe consists of two pickup coils, one of which is oriented to be sensitive to B_z and has an area (NA) of about 0.5 cm^2, and the other sensitive to the orthogonal component (B_θ or B_r) and has an NA of about 0.75 cm^2. The inductive risetime of each probe is less than 10 ns.

Figure V-22 presents the results of a preliminary analysis of the magnetic field probe data where the B_z field time histories have been averaged over several plasma discharges. The coordinate system is the same as that used to display the pressure probe data. The solid lines represent results obtained with plasma and the dashed lines represent vacuum field data. Near the coil end, z = - 6 cm, R=0, field exclusion is

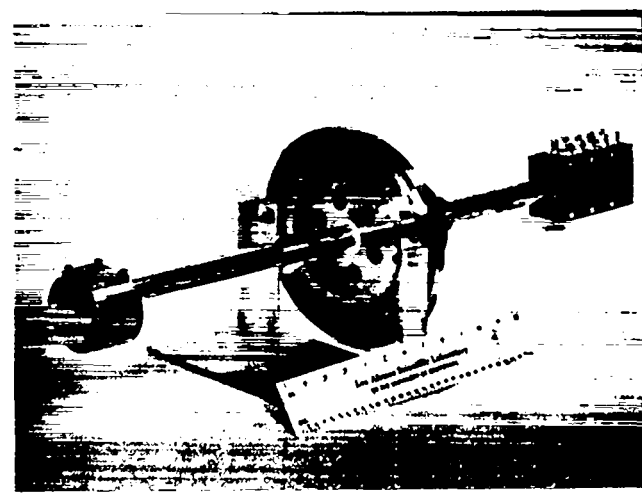

Figure V-21.

Internal magnetic field probe array.

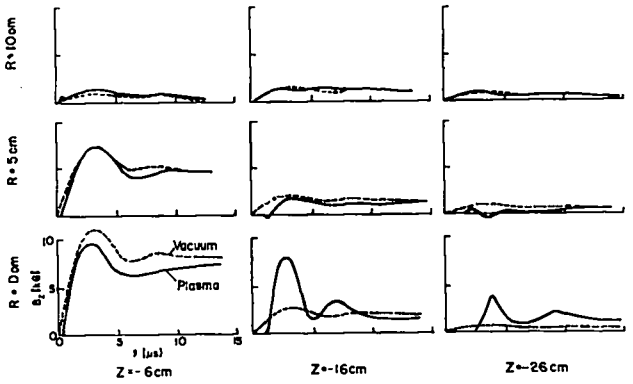

Figure V-22.
B_Z magnetic field time histories within the end bubble region.

observed but the characteristic structure of the magnetic field is not significantly altered, although a definite delay in the field arrival time is observable in the plasma case. Further down stream at z = - 16 and -26 cm, R=0, the measured magnetic field with plasma greatly exceeds the vacuum field value. This behavior not only indicates that the field structure is changed in the presence of plasma but also that magnetic field is "frozen" into the plasma and is convected axially with the gas flow.

The characteristics of the interaction between the axially flowing plasma and the magnetic field, neglecting the effect of magnetic forces on the motion, can be described by the vector magnetic diffusion equation given by,

$$\frac{\partial \bar{B}}{\partial t} = \eta \nabla^2 \bar{B} + \bar{\nabla} \times (\bar{V} \times \bar{B}) \ ,$$

where η is the magnetic diffusivity and V is the plasma velocity. Considering the limiting condition in the above equation where the plasma is stationary, $\bar{V} \longrightarrow 0$, the evaluation of the magnetic field can be seen to result from diffusion into the conducting plasma which is characterized by the magnetic diffusivity, $\eta = c^2/4\pi\sigma$, where σ is the plasma conductivity. Conversely, in the flow of a perfectly conducting fluid, $\sigma \longrightarrow \infty$, no relative motion between the magnetic field and the plasma exists. In this event, magnetic fields outside the plasma will not penetrate the gas and magnetic fields inside the plasma are "frozen" in and convected with the flow. The relative importance of the convective process compared to the diffusive process is indicated by the magnitude of the magnetic Reynolds number which can be expressed as

$$R_m = \frac{LV}{\eta} \ ,$$

where L is the characteristic system dimension and V is the axial plasma flow velocity. When $R_m >> 1$, the magnetic fields external to the plasma will not diffuse into the gas but any trapped field will flow downstream with the plasma. For $R_m < 1$, the magnetic field structure will be unaffected by the plasma motion. Considering the plasma end flow from Scylla IV-P and taking as characteristic flow parameters V ~ 10^7 cm/sec, L ~ 1 cm and T_e ~ 100 eV, the magnetic Reynolds number is approximately 10^3. Accordingly, the significant field convection observed experimentally is predicted analytically. Although this effect can be derived analytically, it has not previously been recognized in the treatment of the theta-pinch end-loss problem.

E. INITIAL EXPERIMENTAL RESULTS WITH SOLID END PLUGS

The loss of energy and particles from the ends of linear theta pinches presents a fundamental limitation in reactor applications for these devices as well as for all open-ended machines. Solid end plugs have been suggested as one means of inhibiting the particle loss from open-ended devices.[11] In addition, recent numerical calculations[12] indicate that solid end plugs may also enhance the plasma energy containment time. A preliminary investigation of this approach to end stoppering has been carried out on the Scylla IV-P theta pinch and the results are discussed below.

1. Experimental Apparatus. A photograph of the solid end-plug apparatus is shown in Fig. V-23. The plugs were cylindrically shaped quartz, 5 cm in diameter and 3.8 cm thick. Each plug was mounted on a quartz rod, and the entire

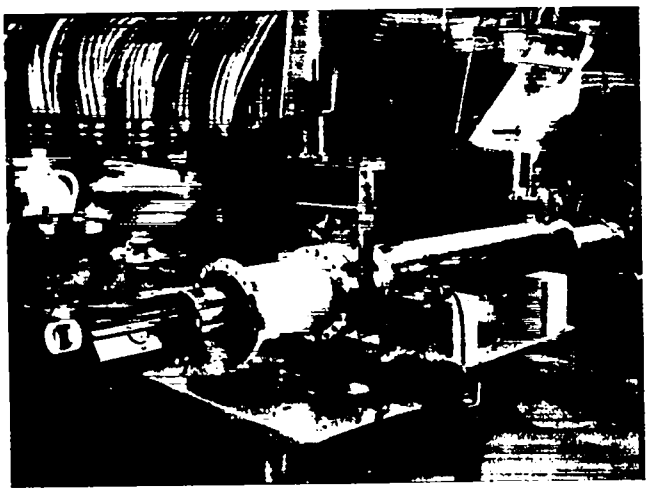

Figure V-23.
Photograph of end-plug apparatus.

assembly could be retracted out of or advanced into the discharge tube. For the results presented below, the front face of the plugs was inserted ≈ 5 cm inside the theta-pinch coil ends.

2. End-Region Flow Studies. The phenomenology of the plasma flow in the regions exterior to the theta-pinch coil ends was studied photographically and with the total magnetic flux loops. Figure V-24 shows two time-integrated photographs of the end bubble taken with and without plugs inserted. No light was observed in the end vessel with the plugs inserted, indicating the absence of plasma flow out of the ends of the discharge tube. Additional evidence of the absence of plasma in the end vessel was provided by the total magnetic flux loops that encircle the end vessel and are arrayed along its length. The data obtained from these loops on primary bank discharges with no initial D_2 fill were essentially identical to the data obtained from plasma discharges with plugs inserted. Conversely, plasma discharges taken with the plugs retracted yielded data that showed clear evidence of plasma flow (Fig. V-16).

3. Plasma Column Stability Characteristics. Stereo-streak camera photographs (viewing from the top and side simultaneously), taken at the coil midplane with and without the plugs inserted, are shown in Fig. V-25. In the streak photograph obtained without plugs, Fig. V-25b, the plasma column wobble instability sets in about 5 μs after initiation of primary discharge. The instability saturates at an amplitude of approximately two plasma diameters and then begins to damp. The streak photograph obtained with the plugs inserted shows the wobble onset. In this case, however, the instability saturates at about one plasma diameter and damps out more rapidly, resulting in

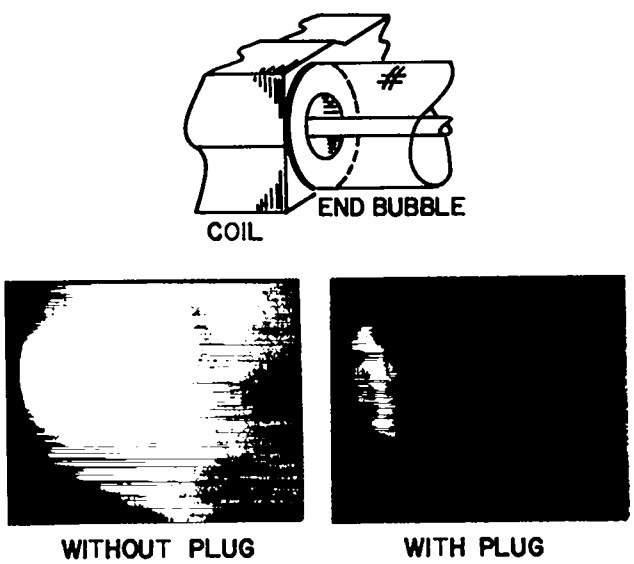

Figure V-24.
Time integrated photographs of light in the end-bubble region with and without the end plugs inserted. The camera aperture setting is the same for each exposure.

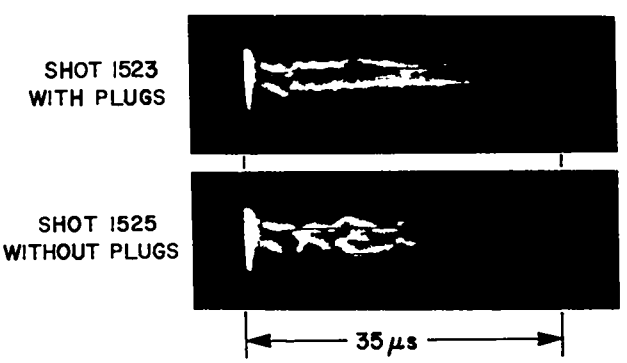

Figure V-25.
Steroscopic streak photographs with and without plugs inserted. The lower image in each photograph corresponds to a top view of the plasma column and the upper image corresponds to a side view of the plasma.

a highly stable column. This effect suggests that the plasma wobble may be stabilized by line-tying at the plugs. The wobble onset time is ~ 1 μs earlier with the plugs inserted than without plugs, as determined from streak photographs taken at a faster sweep rate and the side-on luminosity apparatus. Further, the plasma light intensity in the streak photograph obtained with the plugs inserted persists 20-30% longer than that obtained without plugs.

4. Axial Variation of the Plasma Effective Radius. The plasma effective radius, r_{eff} was obtained as a function of position and time by measuring the magnetic flux excluded by the plasma with the seven diamagnetic loop-probe systems arrayed along the coil axis, z. Figure V-26 presents a comparison of r_{eff} at four axial positions, with and without plugs inserted. As can be seen, r_{eff} was either the same or maintained a higher value for a longer time with the plugs inserted. This behavior was observed at all axial positions, except that closest to the plug (Δz = 12 cm) where the data were irreproducible.

5. Axial Variation of Neutron Yield. Figure V-27 presents a comparison of total neutron yield as a function of axial position, with and without plugs inserted. In general, the presence

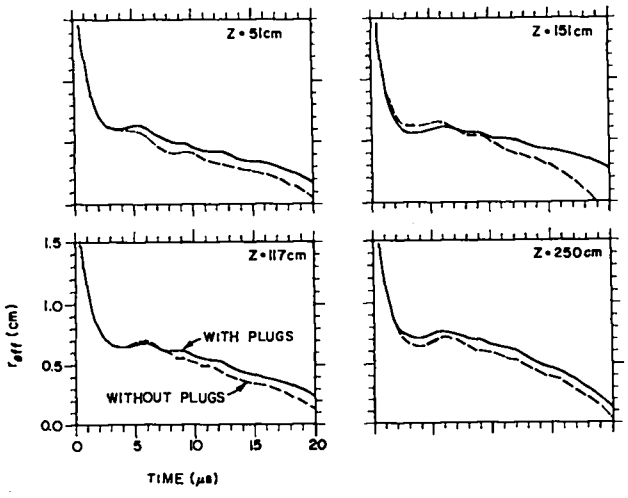

Figure V-26.
Plasma effective radius as a function of time at four axial positions obtained with and without the plugs. The data are averaged over 15 plasma darecharges.

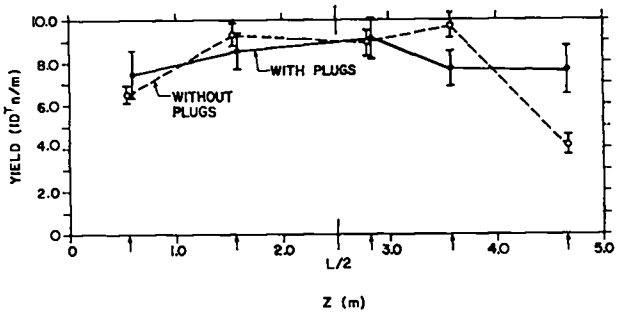

Figure V-27.
Total neutron yield along the theta-pinch coil axis determined from silver foil activation counters. Arrows indicate detector positions (L=coil length). The data are averaged over 23 discharges.

of the plugs has little effect on the yield; there is some observed increase in yield at the ends of the coil. Neutrons produced in the beam-target interaction of plasma deuterons impinging on deuterium molecules adsorbed on the plug could be a possible explanation for the increase in yield near the ends. However, a crude estimate of beam-target neutron yield gives $\simeq 10^7$ neutrons per shot, which is insufficient to account for the observed yield increase.

6. Time Evaluation of the Plasma Energy Density. The plasma energy per unit length at the coil midplane, $|a^2\beta_A B^2/8|$, was determined from the diamagnetic loop measurements and estimates of the plasma radius obtained from the side-on luminosity apparatus. The time history of the central energy line density obtained with and without the plugs inserted is shown in Fig. V-28. The energy line density maintains a higher value for a longer time when the plugs are inserted. Further, the instantaneous decay rate (slope of the curve) is less when the plugs are inserted. This is especially evident at late times.

7. Plasma Plug Interaction. The plugs showed very little visible damage after 29 plasma discharges; the surface being slightly glazed with small pit marks barely visible to the naked eye. Assuming that all the plasma energy deposited on the surface of the plugs goes only into ablating the plug material, then the depth δ to which each plug should be eroded per discharge is given by,

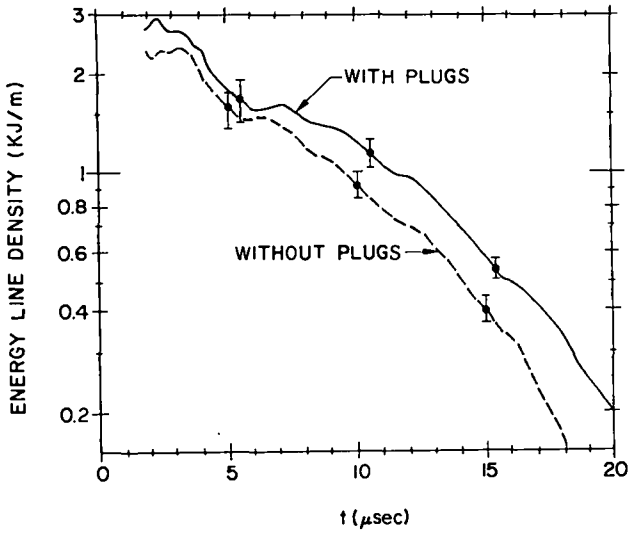

Figure V-28.
Plasma energy per unit length (π a^2 β_A $B_Z{}^2/8\pi$, where a is the plasma radius determined from side-on luminosity measurements) as a function of time, at the coil midplane. Data averaged over 15 discharges.

$$\delta = \frac{3}{4}\frac{n_o}{n_p}\frac{k(T_e+T_i)L}{E_{AB}} \quad ,$$

where n_o and n_p are the plasma particle density and the plug molecular density respectively, T_e + T_i is the central plasma total temperature, L is the plasma column length and E_{AB} is the plug material ablation energy per molecule. Taking n_p = 2.7 x 10^{22} cm^{-3} and E_{AB} = 10 eV/molecule, then δ = 0.5 cm for the Scylla IV-P plasma parameters. Since the erosion observed after 29 discharges is drastically less than that indicated above for one discharge, energy absorption or loss mechanisms other than ablation dominate the plasma-plug interaction. The ionization of ablated plug material and energy-loss mechanisms such as radiation, cross field diffusion, and charge exchange could significantly reduce the energy deposition at the plug surface.

A theoretical effort has recently begun in Group CTR-6 to analyze the phenomena resulting from the plasma-plug interaction. A one-dimensional Lagrangian hydrodynamic and heat flow code has been developed which permits the study of the evaluation of ablated plug material and its thermal interaction with the theta-pinch plasma column.[11] Basically, the code results show that the ablated plug material forms a thermal barrier between the plasma and the cold plug by virtue of the reduced thermal conductivity in the higher Z material. An upper limit on the end-plug Z number is obtained from qualitative considerations of radiation losses. This energy loss mechanism is not presently incorporated into the hydrodynamic code. However, preliminary theoretical indications are that end plugs can significantly increase the theta-pinch energy containment time by eliminating particle loss and by forming a layer of lower conductivity material at the ends of the plasma columns.

8. Summary of Solid End-Plug Experiments. Some preliminary observations can be made from the results of the initial end-plugging experiments. In the presence of the plugs: (1) the flow of plasma out of the device ends is stopped; (2) plasma stability is enhanced; (3) the duration of plasma luminosity increases 20-30%; (4) the plasma effective radius increases and its decay rate decreases; (5) the total neutron yield is not appreciably affected; and (6) the plasma energy line density at the coil midplane is increased in magnitude and duration.

REFERENCES

1. S. Glasstone and R. H. Lovberg, Controlled Thermonuclear Reactions (Van Nostrand Reinhold Company, New York, 1960) p. 20.

2. R. J. Lanter and D. E. Bannerman, "The Silver Counter, A Detector for Bursts of Neutrons," Los Alamos Scientific Laboratory Report LA-3498-MS, (1966).

3. R. L. Morse, "Electron Temperatures and Thermal Conduction in High-Energy θ-Pinches," Phys. Fluids 16, 545 (1973).

4. K. F. McKenna and T. M. York, "Plasma End-Loss Studies on Scylla I-C," Los Alamos Scientific Laboratory Report LA-6412-MS (1976).

5. K. S. Thomas, H. W. Harris, F. C. Jahoda, G. A. Sawyer, and R. E. Siemon, "Plasma Experiments on the Linear Scyllac Theta Pinch," Phys. Fluids 17, 1314 (1975).

6. J. P. Freidberg and H. Weitzner, "Endloss From a Linear θ-Pinch," Nucl. Fusion 15, 217 (1975).

7. K. F. McKenna and T. M. York, "Transient Flow and Expansion of a Pinch Discharge Plasma in Self-Induced Magnetic Fields," Plasma Phys. 17, 1 (1975).

8. I. R. Jones, "Pressure Bar and Photographic Measurements on a High Frequency Theta-Discharge," Laboratoire De Recherches Sur La Physique Des Plasmas, LRP21/66, 1966.

9. J. A. Wasson, "Plasma Flow in a Theta-Pinch," in Plasma Physics and Controlled Nuclear Fusion Research (IAEA, Vienna, 1966), Vol. I, p. 223.

10. H.A.B. Bodin, J. McCartan, I. K. Pasco, and W. H. Schneider, "Experimental and Two-Dimensional Computational Study of End Losses from a Theta Pinch," Phys. Fluids 15, 1341 (1972).

11. J. M. Dawson, A. Hertzberg, R. E. Kidder, G. C. Vlasses, H. G. Ahlstrom, and L. C. Steinhaur, "Long-Wavelength, High-Powered Lasers for Controlled Thermonuclear Fusion," Plasma Physics and Controlled Nuclear Fusson Research (IAEA, Vienna, 1971) p. 673.

12. R. C. Malone and R. L. Morse, "End Stoppering of Straight θ-Pinches by Material Barriers," Bull. Am. Phys. Soc. 21, 1150 (1976) to be published.

VI. GUN INJECTION EXPERIMENT

J. E. Hammel, I. Henins, J. Marshall, A. R. Sherwood

A. INTRODUCTION

The Gun Injection Experiment was undertaken as a part of the Scylla IV-P program, with the purpose of developing the injection of plasma into a linear θ pinch. The kinetic energy of the gun plasma would be converted into thermal and pv energy during injection resulting in a cylinder of plasma with a temperature, hopefully, of several hundred eV and a density in the 10^{15} range. This would take the place of the similar plasma generated in the usual θ pinch by implosion heating. Injection would have an advantage over implosion heating in that it would not require high-voltage insulation inside the blanket of a reactor. The injected plasma would have to be high β, i.e., it should nearly completely exclude the field. In principle this can be achieved by virtue of its high conductivity, the magnetic field being pushed aside by plasma pressure. In order for high-β injection to take place, the stagnation pressure of the gun plasma (ρv^2) must be at least as large as the magnetic field pressure ($B^2/8\pi$) and the injection conditions should be such as to produce a reasonably thin sheath separating plasma from magnetic field. Many injection experiments in the past have produced low-β injected plasmas apparently because the sheath thickness was larger than the plasma radius so that the whole plasma was sheath. The conditions leading to excessive sheath thickness are not well understood, but apparently they can be overcome to some extent. The investigation of this problem is one of the main objectives of the experiment.

The injection experiment was designed to mock up the Scylla IV-P conditions reasonably well with a 20-cm-diameter vacuum envelope surrounded by a slow-pulsed solenoid capable of operating at fields up to ∿ 20 kG. The solenoid can be up to 4 m long so that propagation into the 5-m-long Scylla IV-P machine can be approximated. Assuming a density of 5 x $10^{15}/cm^3$, a temperature $T_e = T_i = 500$ eV, with an injected plasma radius of 5 cm filling the entire 5-m length of the θ pinch, and noting that the plasma stream has to provide additional energy to open a cavity in the magnetic field, one finds that about 60 kJ of plasma energy will be required, assuming 100% efficiency. In fact, some of the gun plasma will probably be flowing in the wrong direction for injection, some will be reflected, and some might pass entirely through the θ pinch and be lost on the far side. All of this implies that the gun to be used with Scylla IV-P will probably have to provide a total plasma energy in excess of 200 kJ.

It was decided to use standard LASL θ-pinch technology for the gun energy storage bank, i.e., 60-kV capacitors with a Scyllac-type spark gap on each capacitor. The bank of 100 capacitors was constructed giving a nominal energy storage of 300 kJ at 60 kV. Since normal operating voltage for these systems is more often 45 kV than 60 kV, the practical energy storage of the bank is really about 200 kJ. Provision was made in the collector plate for the connection of 100 additional capacitors if that should appear to be desirable. The gun was designed as a modest scale-up of the gun used in the "Birdseed" series where guns powered by explosive generators were flown in high-altitude rockets to inject plasma into the ionosphere. The present gun is 1.5 m long by 30 cm diameter, with a 10-cm-diameter center electrode. The electrodes are made of copper and the insulation is high alumina ceramic arranged in an inverse pinch configuration. The gun valve is of the compressed rod/exploding plug design[1] which has been employed on previous guns. A schematic diagram of the apparatus is shown in Fig. VI-1.

The initial experiments are to study the properties of the gun plasma and its injection into the solenoidal guide field. Investigation of the properties of the gun plasma itself is necessary because the present gun is operating at a higher voltage (45 kV) than has been used in previous LASL deuterium guns (typically 10 kV).[2] For these experiments a short "see-through" coil was built with slots between turns so that interferometric measurements of plasma

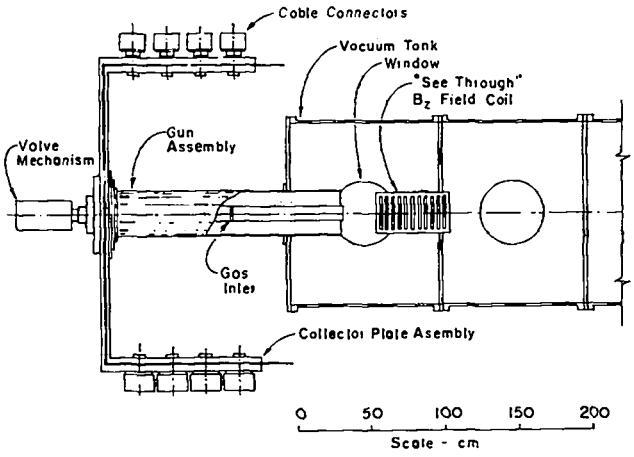

Fig. VI-1.
Schematic diagram of gun experiment.

density could be carried out in the injection region. During the period covered by this report, experiments have been carried out only with the see-through coil.

The results are described below organized according to the diagnostic employed.

B. EXPERIMENTAL RESULTS

The following diagnostics have been employed on the experiment: gun current and voltage, 3.39-μm He-Ne coupled cavity interferometry, 0.63-μm He-Ne dual beam fractional interferometry, calorimetry, fast image-converter photography, single and double frame holographic interferometry, diamagnetic flux exclusion measurements, magnetic field probing, and neutron detection.

1. Gun Current and Voltage Measurements. The gun has been operated in two different modes, determined by the firing delay after gas injection into the electrode space. The fast mode corresponds to a delay of 300 μs and the slow mode to 360 μs, both with a plenum filling pressure of 14 bar. The fast mode current trace is characterized by a peak of 800 kA and a longer period, while the slow mode has a peak current of 1.3 MA as shown in Fig. VI-2. The different behavior is controlled by the gas distribution when the voltage is applied to the electrodes. The longer delay allows more gas to get to the breech and apparently allows the current to start closer to the breech (insulator). This would, of course, have a

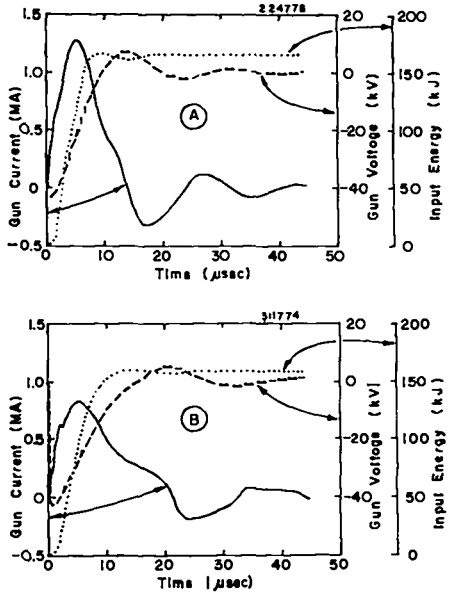

Fig. VI-2.
Gun current, voltage, and energy input. Gun firing delay: (A) 360 μs, (B) 300 μs after valve opening.

lower inductance and therefore higher current discharge.

2. Single Beam Interferometry. The infrared coupled-cavity interferometer was unable to follow the density fluctuations in the plasma stream even at the 6-MHz modulation frequency, but it indicated that plasma was flowing from the gun for as long as 35 μs.

The fractional fringe interferometer showed that the plasma density fluctuations come in pulses as short as 100 ns. The average line density along the interferometer beam transverse to the plasma flow was as high as 8×10^{16} cm^{-2}. These very rapid variations might be caused by very short plasmoids or by a narrow plasma stream moving sideways across the interferometer beam. A two-beam interferometer was installed in an effort to measure plasma velocities by identifying features of the plasma stream and following them as they proceeded from one beam to the next. The plasma front velocity was measured to be about 2×10^7 cm/s, but the density features were too irregular to give precise velocity measurements.

3. Fast Framing Photography. The Imacon image converter framing camera was placed to give a side view of the plasma emerging from the gun.

The field of view was from the gun muzzle to about 40 cm downstream, and the framing rate was 1 MHz. These photographs showed a light plume emerging from the gun about 5 μs after the current starts. This increases in intensity and then disappears in another 5 μs. Thus the light does not correlate with plasma density as measured by the interferometer, which peaks in 15-20 μs and lasts about 40 μs.

4. Holographic Interferometry.

a. Single Frame. At first, a single frame, double-pass interferometer was constructed using a ruby laser at 0.69 μm. The field of view was approximately 25 cm in diameter and was placed to observe the plasma entering the first 10 cm of the B_z guide coil. The coil face was 22 cm from the gun muzzle. Typical interferograms for the slow mode (400-μs delay in this case) and the fast mode (300 ms) with B_z = 10 kG are shown in Fig. VI-3. The holograms are taken about 2 μs after the plasma first emerges from the gun. Each fringe shift is equivalent to a 1.6 x 10^{17} cm^{-2} change in area density. In the longer delay case the plasma forms a dense small diameter rod on the axis that persists throughout the discharge, whereas, in the short delay case the plasma remains diffuse with irregular pinching in random positions. Qualitatively this is also observed in integrated light photographs. Later the interferograms show a large density build-up on the walls of the coil. The interferograms, in general, are very irregular and therefore no inversion to obtain actual densities has been attempted.

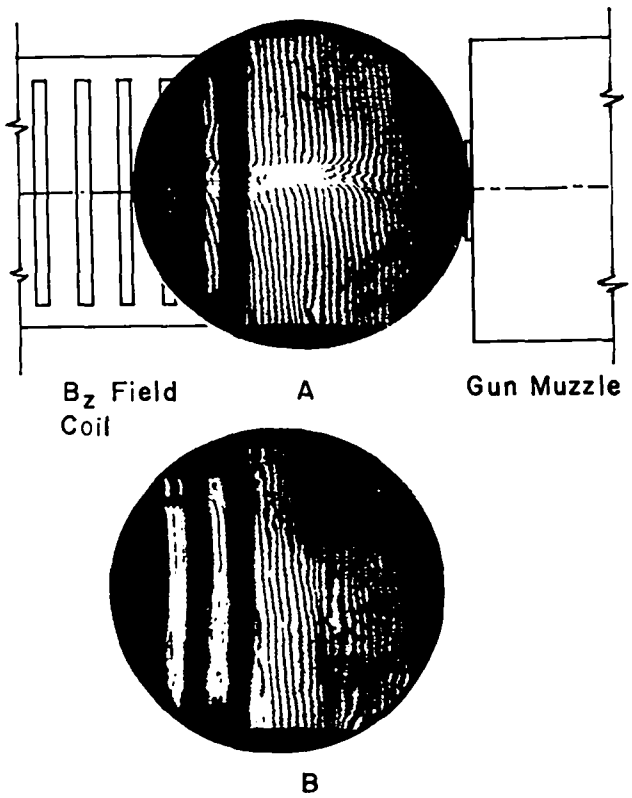

Fig. VI-3.
Holographic interferograms of gun plasma taken 12 μs after gun is triggered. Firing delay: (A) 400 μs, (B) 300 μs after valve opening. B_z = 10 kG. Sensitivity is 1.6 x 10^{17} cm^{-2} per fringe.

b. Double Frame. In order to make plasma velocity measurements from interferograms, two successive closely spaced interferograms are needed on the same plasma shot. Therefore a double-pulse, single-pass holographic interferometer[3] was assembled with the help of CTR-8. With this technique two holograms of the same scene can be taken with a time separation as short as 100 ns. The field of view was increased to about 35 cm. The velocity measurements again are not precise because plasma features are diffuse and exact positions in each interferogram are difficult to determine. The best estimate of the plasma velocity from these measurements is (1.5 to 2.5) x 10^7 cm/s.

During these measurements the gun was placed at 22 cm and at 40 cm from the B_z field coil. The plasma behavior was similar in the two cases except there is less plasma stagnation visible against the magnetic field in front of the coil for the 40-cm case. With gun operation in the slow mode (360 μs delay) the plasma condenses in a stream about 2 cm in diameter with densities of several times 10^{17} cm^{-3} on the axis as shown (at 12 μs) in Fig. VI-4, and at later times large densities are observed at the coil walls. In the fast mode of operation (300-μs delay) the plasma is more diffuse and can be kept away from the coil walls by increasing B_z to over 13 kG.

5. Magnetic Field and Flux Measurements.

a. Excluded Flux. If the β of the injected plasma is known, then the plasma area can be obtained by the usual method of excluded flux measurement. To make this measurement, a compensated flux loop was placed on the outside of a

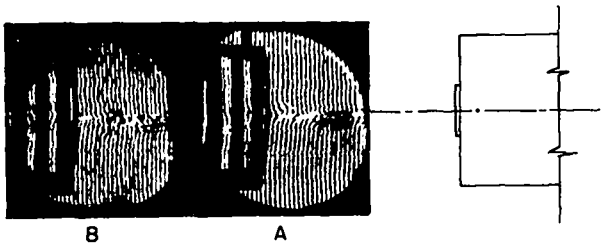

Fig. VI-4.
Double frame holographic interferograms of gun plasma taken 12 μs after gun is triggered. Firing delay is 360 ns after valve opening. (B) is taken 300 μs after (A). Sensitivity is 3 x 10^{17} cm^{-2} per fringe.

20-cm-diameter quartz tube which was then placed inside the B_z field coil. The compensation keeps the output signal balanced during the risetime of the B_z field. The magnetic field pickup was a narrow loop that completely surrounded the plasma, thus minimizing errors caused by the plasma being off center. A check for electrostatic noise pickup was made with a single wire antenna alongside the loop, and it was found to be negligible. Figure VI-5 shows an example of the plasma diamagnetic signal in the slow gun firing mode with background B_z = 10 kG and the guide field coil 40 cm from the gun muzzle. The peak diamagnetic signal is equivalent to a 9.0-cm-diameter β=1 plasma, and the equivalent peak transverse plasma energy then is 3.2 kJ/m. The interferograms taken at the time of the peak diamagnetic signal show a plasma density on the axis of the field coil of about 6 x 10^{16} cm^{-3} with a diameter of about 8 cm. Using this density with the above transverse plasma energy gives a transverse ion temperature of 45 eV, if all the energy is assigned to the ions.

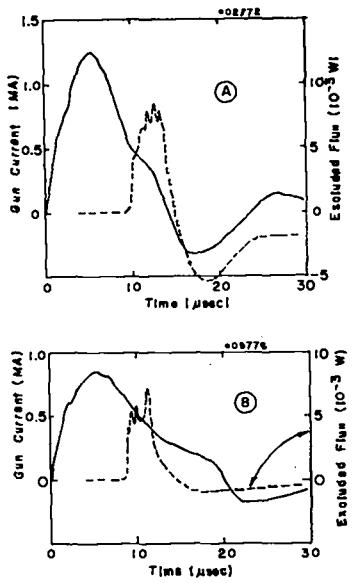

Fig. VI-5.
Typical excluded flux from gun plasma with B_z = 10 kG. Gun delay: (A) 360 μs, (B) 300 μs after valve opening.

The diamagnetic signal lasts for about 5 μs, then has a break where the signal abruptly decreases and reverses. The reversal of the diamagnetic signal implies an increase of magnetic flux inside the diamagnetic loop, even though probe measurements show that flux is being excluded from a substantial area by the plasma. The most likely explanation for this "paramagnetic" effect is that the inside of the fused quartz liner is being heavily bombarded, and a secondary plasma is formed there. This plasma, with its pressure contained on the outside by the quartz tube, expands away from the tube toward the axis, entraining magnetic flux and compressing field so as to produce a net increase of flux inside the loop. This picture is supported by the following evidence: 1) Image converter pictures show the quartz liner becoming very bright at the time of the break in the diamagnetic signal; also holographic interferometry shows a dense plasma near the wall at this time and after. 2) It appears that charge exchange on neutral gas beyond the gun muzzle is a principal cause of the liner bombardment. Fast ion gauge measurements of the gas distribution show an ample amount of gas at the 360-μs gun-firing time to account for a large interaction with the gun plasma. 3) The diamagnetic loop, with the short (300 μs) delay, shows a much smaller paramagnetic signal. This is consistent with the smaller neutral gas density beyond the gun muzzle when the gun is fired with the short delay. 4) At magnetic field strengths above 10 kG, and with the short delay, the paramagnetic signal is entirely eliminated. This implies that at least a portion of the wall bombardment is due to direct gun plasma interaction. Interferograms also detect no wall plasma when the magnetic field is above 10 kG.

b. Magnetic Field Probes. Two movable magnetic probes were inserted from the rear of the vacuum tank. Each of these probes, designed to measure changes in the B_z guide field, consisted of two coils 10 cm apart in the axial direction. Originally a 9-mm-diameter quartz envelope surrounded the coils, but when that could not survive the plasma bombardment it was replaced by a 1-cm-diameter alumina tube. These probes could be be moved both radially and axially. On axis they show complete flux exclusion lasting for about 10 μs. Flux exclusion was observed out to a radius of about 5 cm, which is in agreement with a $\beta = 1$ plasma radius calculated from the excluded measurements. The velocity of the first magnetic disturbance measured by these probes was 2.5×10^7 cm/s.

6. Neutron Measurements. Neutron measurements were made with calibrated detectors, a silver activation Geiger counter system for time-integrated yield, and a time-resolved scintillation detector. Very few neutrons are produced in the long gun delay mode. In the short delay mode there is a small signal, originating near the breech, shortly after gun current starts, but the bulk of the neutrons originate beyond the gun muzzle following the emergence of plasma. The total neutron yield has been as high as 8×10^8, with a typical number about half of that. The yield is quite variable, and increases somewhat with increasing guide-field strength.

7. Calorimetry. A large, 50-cm-diameter and 90-cm-long, calorimeter with a 30-cm-diameter entrance hole was constructed so it could be placed either behind the guide field coil, or, with the coil removed, directly in front of the gun. With the calorimeter 30 cm in front of the gun muzzle the collected energy was 150 kJ in the 360-μs gun delay case and 165 kJ with the 300-μs gun delay. The total energy of the plasma passing through the 50-cm-long guide field coil (placed 40 cm from the gun muzzle) was measured by placing the calorimeter about 10 cm behind the coil. In the longer gun delay case the collected energy was about 85 kJ and no significant difference was observed between $B_z = 10$ kG and $B_z = 0$. In the short delay case, the energy decreased from 50 kJ at $B_z = 0$ to 35 kJ at $B_z = 10$ kG and to 20 kJ at $B_z = 17$ kG.

C. SUMMARY AND PLANS FOR FURTHER INVESTIGATION

The experiments so far do not amount to a satisfactory demonstration of gun injection to provide a θ-pinch preplasma. Several things have interfered. One is that the present physical arrangement is not ideal. The gun is of larger diameter than the entrance to the guide field. This results in a substantial fraction of the gun plasma being directed at the end of the coil or outside of it. This plasma is not available for injection, and under some conditions can apparently bombard the coil or the quartz liner and interfere with measurements. Another shortcoming, which contributes to the bombardment problem, is the design of the see-through coil which is wound as a simple solenoid with no increase of turn density at the end. Thus about half of the flux through the center of the coil passes out through the winding before reaching the entrance end. The result is a reduced blanket of magnetic flux between the plasma and the end of the coil, which is inadequate to protect it from fast plasma ions. These difficulties could be alleviated by the use of a larger diameter solenoid at the entrance to the guide field, and by providing a larger number of turns per unit length near the end.

The large amount of gas found beyond the gun muzzle was a surprise. It indicates a highly supersonic gas streaming velocity from gas inlet to coil entrance. This is probably associated with the large amount of high-pressure gas admitted by the valve, higher in this scaled-up gun than in smaller guns because of the larger energy. The charge exchange and wall bombardment interfered seriously with diagnostics of the plasma entry phenomena. The short see-through coil intended for the study of plasma entry phenomena was not long enough to study propagation along the guide field, or to remove diamagnetic loops far enough from the entrance so that wall bombardment effects would cease to interfere.

Another problem has been the limited diameter of the field of view of the holographic interferometer, which was not really large enough to cover all of the gun plasma. Thus there was no clean

region outside of the plasma for establishing zero fringe displacement. It would be difficult to remedy this problem because of limited window size in the vacuum chamber, and because of problems in obtaining straight fringes in very large fields.

It may be possible to use single beam time-resolved interferometry far from the gun muzzle when a long guide field coil is installed. This will aid considerably in interpretation.

It would be desirable in the future to install the full 4 meters of guide field originally planned, and to enlarge the diameter of the entry section. This can be arranged to have a gradually increasing field strength, so as to allow plasma compression by conversion of translational kinetic energy into adiabatic compressional energy, as has been demonstrated at the Kurchatov Institute.

Problems of charge exchange and wide range of plasma velocities, typical of guns of the type used here, can probably be reduced by going to deflagration guns as developed by Cheng.[4] It is not plain how Cheng guns scale up to high energies, but there is some thought of trying to do this with the present installation.

REFERENCES

1. I. Henins and J. Marshall, Rev. Sci. Instrum. 40, 875 (1969).

2. J. Marshall and I. Henins, Plasma Physics and Controlled Nuclear Fusion Research, Vol. II, International Atomic Energy Agency, Vienna, 1966, pp. 449-461.

3. W. T. Armstrong, P. R. Forman, Appl. Opt. 16, 229 (1977).

4. D. Y. Cheng, Nucl. Fusion 10, 335 (1970).

VII. SCYLLA I-C, LASER-PLASMA INTERACTION STUDIES

W. T. Armstrong, E. M. Little, K. F. McKenna, and E. L. Zimmermann

A. INTRODUCTION

The Scylla I-C meter-long theta pinch has provided a dense ($n_e \sim 10^{17}$ cm^{-3}), independently produced, target plasma column in a laser-plasma interaction experiment incorporating a CO_2, cold cathode, gain switched laser. Over the last year, this experiment has studied both classical (heating, refraction) and non classical (stimulated backscatter) interaction effects.[1,2] The goal of this study has been to provide basic experimental information on an alternate method of plasma heating.

Machine characteristics of the theta pinch CO_2 laser have been previously reported.[3,4] The CO_2 laser has reliably produced > 150-J pulses with ~ 50% of this energy in the first 60-ns FWHM spike. The beam is focused to a 2-mm diameter (F = 3m) at ~ 10 cm into the theta-pinch coil. Refraction of the axially directed CO_2 laser beam out of the plasma was observed when the plasma column had an on-axis density maximum. A forward bias field of ~ 1.8 kg was applied and the resulting on-axis density minimum (diameter ~ 4 mm) provided adequate refractive containment of the beam.

A variety of diagnostic systems were developed and employed to investigate the independent plasma and beam parameters as well as to study the beam-plasma interaction. A schematic layout of the experimental and diagnostic arrangement is shown in Fig. VII-1. The laser parameters were monitored as follows: 1) calorimeter - incident energy; 2) photon drag detector - incident pulse shape; and 3) monochromator with pyroelectric vidicon detector - incident spectrum. The plasma parameters were studied with: 1) ruby holographic interferometer - electron density; and 2) double monochromator for plasma spectroscopy - electron temperature. In addition to these plasma diagnostics, additional equipment was used to study the interaction: 1) calorimeter - transmitted beam energy; and 2) monochromator with photovoltaic detectors - backscattered beam spectrum. Further, less important diagnostic studies

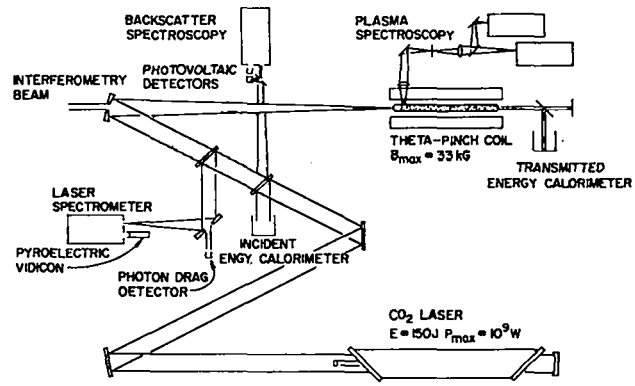

Figure VII-1.
The schematic layout of the Scylla I-C laser-plasma interaction experiment.

included: 1) exit beam burn patterns; 2) streak photography; 3) excluded flux measurement; and 4) reflected beam energy calorimetry.

The laser-plasma interaction experiment was concluded in October 1976 in order that a reverse-field experiment be initiated on the theta pinch.[5] Basic data analysis and interpretation is presented in this progress report with a more complete report projected in the near future.

B. INTERFEROMETRY

Single-pass holographic interferograms were initially taken of the forward-biased plasma column over the range of 100-500 mTorr fill pressure. The CO_2 laser focusing mirror was removed allowing a full 3.6-cm-i.d. discharge tube, field of view. The desired on-axis density minimum (for CO_2 laser refractive trapping) was observed over the above range of fill pressures. A decrease in longevity of the density minimum at higher fill pressures restricted the CO_2 laser timing to a nominal 1.2 μs after main field initiation. Representative interferograms at this time are displayed in Fig. VII-2. High fringe density and refractive shadowing generally made data reduction difficult. Typically one chord was available which showed clear fringes and from which peak and on-axis densities could be measured. On-axis

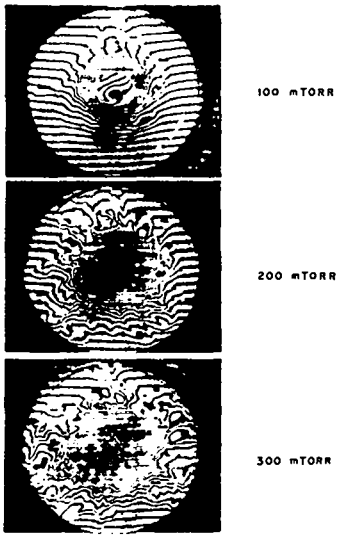

Figure VII-2.
End-on interferograms of plasma column with bias field at 1.2 μs. Field of view is the inside diameter (3.6 cm) of the discharge tube.

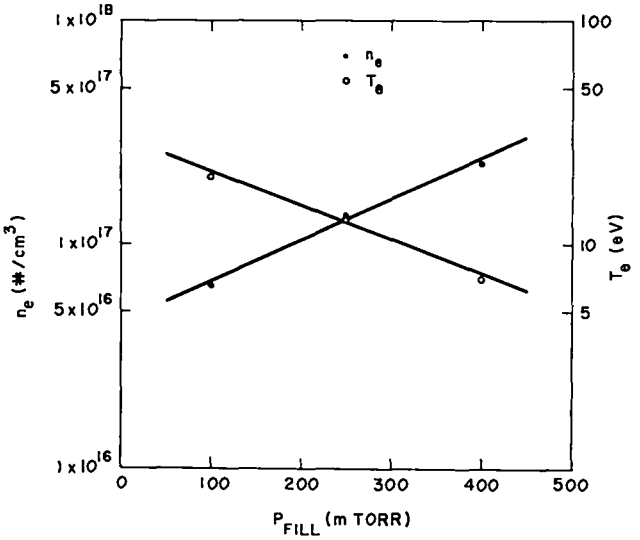

Figure VII-3.
Plasma density and temperature as measured from interferometry and plasma spectroscopy.

density values are shown in the parameter plot of Fig. VII-3.

The CO_2 laser focusing mirror restricted the ruby interferometry beam to an elliptical field of view with a 2-cm major axis. Interferograms with this field of view were taken at 100, 250, and 400 mTorr fill pressures (standard fill pressures used throughout the experiment). Study of these interferograms as late as 3.5-μs delay time, with and without CO_2 laser firing, showed no CO_2 laser effect discernible above the shot-to-shot variations.

In order to improve interferogram analysis at the higher fill pressures, some additional interferometry methods were employed. The first these utilized a unique double pulse technique[6] in which differential interferograms were produced with a pulse separation of 0.5 μs. Late time interferograms demonstrating this technique are shown in Fig. VII-4. Although differential interferograms proved effective in reducing the fringe density at higher fill pressures, strong refractive aberrations restricted any improvement in observation of CO_2 laser-plasma interaction. Incorporation of a Nicol prism[7] enabled this double pulse technique to be extended to a double frame mode of operation. An example of two interferograms taken on the same plasma shot using this technique are displayed in Fig. VII-5.

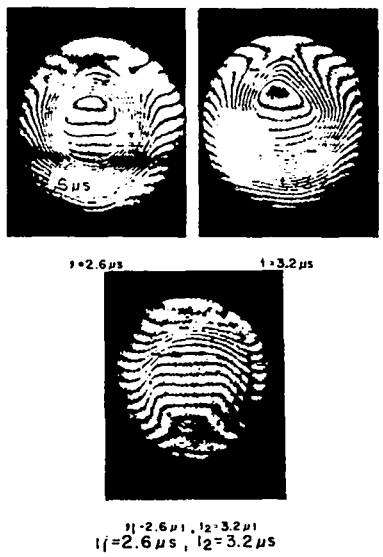

Figure VII-4.
Conventional interferograms at 2.6 μs and 3.2 μs with the differential interferogram corresponding to these two times. Vertical field of view is 2.0 cm. (P_{Fill} = 100 mTorr).

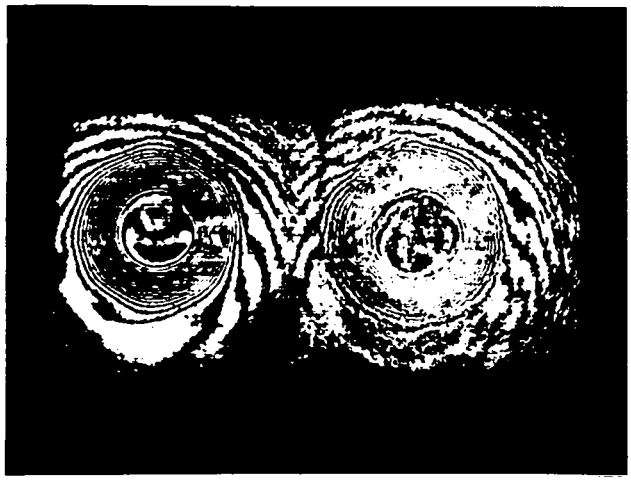

Figure VII-5.
Double pulse interferograms of single plasma discharge at 1.6 μs and 2.2 μs with P_{Fill} = 100 mTorr. (Square image is reference beam. Scene beam represents ~ 2.0 cm field of view.)

A second method pursued in order to decrease the strong refractive aberration was doubling in frequency of the ruby laser. The limiting factor in the performance of this system was found to be the absorption by the achromatic lenses at 3472 Å. The best recording product was found to be Kodak type 131-02. In Fig. VII-6 a comparison is made of 100-mTorr interferograms using 6943-Å radiation and 3472-Å radiation. Although the principle of reduction in plasma refractivity is proven at 100 mTorr, the poor beam uniformity limited the use of this technique at higher fill pressures as well.

C. PLASMA SPECTROSCOPY

Efforts in spectroscopic temperature analysis of the plasma centered on relative line intensity measurements and ionization rate measurements of impurity ions. A double monochromator observation system was employed. In order to avoid the rather low, fluctuating, naturally occurring impurity level, a small amount (0.5 %) of CH_4 or N_2 was introduced during the D_2, static filling of the discharge tube. The set of lines studied were C_{II} (6580.5 Å), C_{II} (4267.1 Å), C_{III} (4069.0 Å), C_{IV} (5801.3 Å), C_{IV} (4658.3 Å), N_{III} (4641.3 Å), N_{III} (4379.1 Å), N_{IV} (4057.8 Å), N_V (4603.7 Å), and N_V (4944.6 Å). These lines were studied for 100-, 250-, and 400-mTorr fill pressures and at 14 cm and 42 cm into the coil. Carbon line intensity

Figure VII-6.
A comparison of interferograms taken with the fundamental (6943-Å) and doubled (3472-Å) frequencies of the ruby laser beam. Discharges were taken at 1.2 μs with 100-mTorr fill pressure. (Masking and enlargement have been performed for comparison purposes. Horizontal field of view is 2.0 cm.)

histories, both with and without CO_2 laser firing, are displayed in Fig. VII-7 for 250 mTorr fill pressure. The effect of the CO_2 laser is seen as

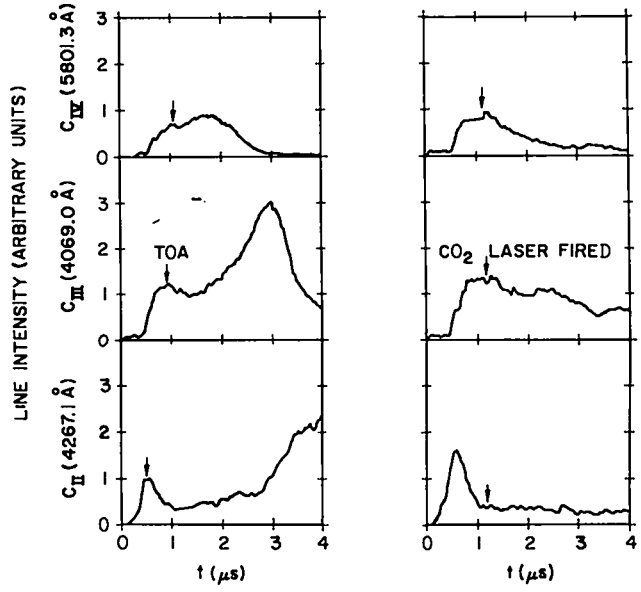

Figure VII-7.
C_{II}, C_{III}, and C_{IV} line intensity traces for 250-mTorr fill pressure without and with CO_2 laser firing. Time-of-arrival (TOA) of the subsequent stages, as used in the ionization rate code, are indicated.

the ion stages are burned through with a resulting decrease in line intensity.

The use of line emission ratios from subsequent stages for T_e measurement was hampered by the lack of equilibrium of ground state populations and by radial temperature variations after laser firing. The most convenient line ratio is the C_{IV} (5801.3 Å)/C_{III} (4069.0 Å) ratio since the excitations of these lines are both dependent on the C_{IV} ground state population. This measurement leads to ~ 7.6 eV (250 mTorr) and 5.4 eV (400 mTorr) at 1.2-μs delay time (time of laser firing). Estimates of T_e through the use of an ionization rate code (time-of-arrival of subsequent stages, carbon data, E.C.I.P. rate coefficients) gave ~ 20 eV (100 mTorr), ~ 13 eV (250 mTorr), and ~ 7 eV (400 mTorr) at 1.2 μs, and are shown in the parameter summary of Fig. VII-3. The time-of-arrival (TOA) of the subsequent carbon stages at 250 mTorr are indicated in Fig. VII-7. This analysis has proven to be the more acceptable and these temperatures are used in subsequent calculations. This rate code is presently being modified to also accept nitrogen data and should then be capable of T_e estimates after laser firing.

D. CALORIMETRY

Seventy cm from the coil exit end, a ~ 17-cm diameter wire screen was placed to reflect part of the transmitted CO_2 laser radiation into a calorimeter. The transmitted energy measurement results for 100-400 mTorr fill pressure are shown in Fig. VII-8 for an incident energy of 150 J. These values indicate a transmittivity of 27% to 5% over the above pressure range. Backscattered energy measurements give ~ 0.6 J which can be attributed to stray machine reflection. The stimulated backscatter energy was found to be only a small fraction of this amount.

An absorption length, ℓ_{abs}, can be inferred from the exit energy calorimetry for an exponential attenuation, $I = I_o \exp(-x/\ell_{abs})$ of the CO_2 laser beam in the plasma. This observed absorption length is compared in Fig. VII-9 with the classical, inverse bremsstrahlung absorption length calculated, according to Dawson's results,[8] with the measured density and temperature values.

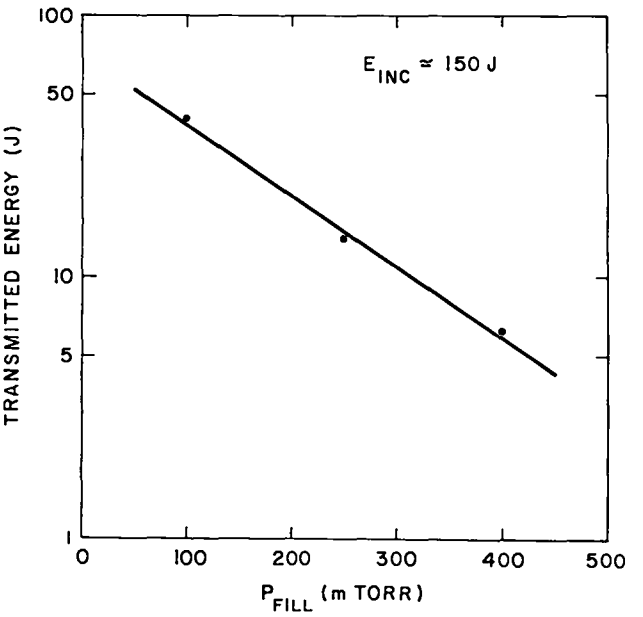

Figure VII-8.
Transmitted energy calorimetry measurements for an incident laser energy of 150 J.

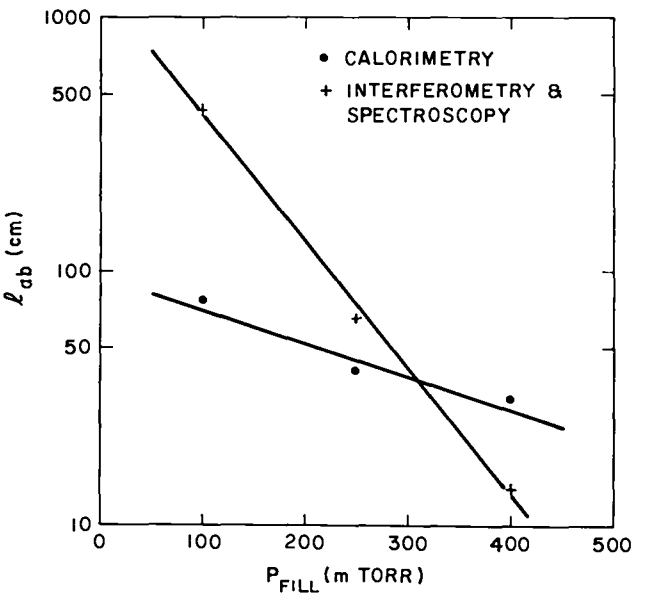

Figure VII-9.
Absorption length as inferred from density and temperature measurements and as inferred from transmitted energy calorimetry measurements.

A discrepancy is observed at high and low fill pressures. Sidescatter out of the plasma column is believed responsible for the low calorimetry absorption length at low fill pressures. Sidescatter can be interpreted as a failure of the shallow on-axis density minimum to completely

refractively trap the laser beam as it re-expands after having passed its focal point. At higher fill pressures the majority of the absorption takes place before the beam re-expands. Accordingly, one would expect that sidescatter losses would be reduced and that non linear absorption or bleaching along the column would result for such rapid absorption. This bleaching effect may be responsible for the observed large calorimetry absorption length at the higher fill pressure.

E. BACKSCATTER SPECTROSCOPY

Infrared backscatter measurements were directed towards studying stimulated brillouin scatter.[9] The diagnostic system used a HgGeTe photovoltaic detector (PV1) situated at the exit slit of a 0.5-m dispersing monochromator. The monochromator used a 150-ℓ/mm grating to give an instrument resolution of 10-Å HWHM with a 200-μ entrance slit. The viewed backscatter was collected by the annulus of the CO_2 laser focusing mirror (0.3°- 2.4°). A second HgGeTe photovoltaic detector (PV2) was used, in addition, to monitor the integrated backscattered signal. The parametric backscatter signal was characterized by it's appearance at the expected shifted frequency (P-20 + ω_{ia}, e.g. 10.5915 μ + 50 Å) and by a time profile suggestive of material-threshold attainment. In particular the parametric backscatter signal had a single, strong pulse occurring within ± 15 ns of the incident beam's peak power. This compares with only the short focal length experiments of others.[10] In Fig. VII-10, typical related data are displayed on two succesive shots (250 mTorr) in which stimulated backscatter occurred on the second but not the first shot. The incident power (photon drag detector) is shown on the bottom trace of each display, while the top trace is (in order) B_z, spectrally integrated backscatter signal (PV2) and spectrally resolved backscatter signal (PV1, + 54 Å). The two shots demonstrate the main difficulty in the backscatter study; an intermittent shifted backscatter signal. It should be noted that the incident power, ~ 10^{10} w/cm^2, is above the calculated power threshold, ~ 10^9 w/cm^2, for this parametric scattering. In addition, the

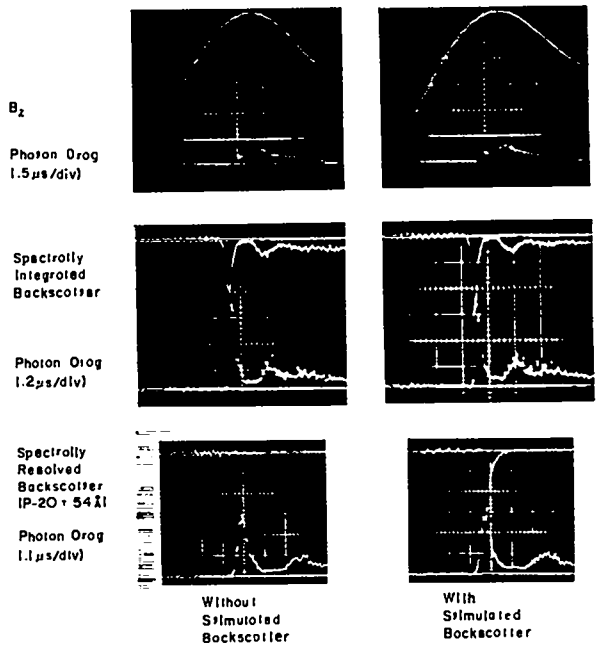

Figure VII-10.
Time profiles of incident CO_2 laser pulse (photon drag detector), B_z, spectrally integrated backscatter signal and spectrally resolved backscatter signal. A discharge without and with stimulated backscatter is shown.

instability, for the plasma parameters at 250 mTorr fill pressure, is in the convective regime with a gain length of ~ 7 cm. The probable causes for intermittency, which are being examined, include: 1) power variation due to a limited focusing region (ℓ_{focus} ~ 10 cm); 2) threshold variation owing to laser heating; and 3) coupling variation due to axial phase mixing of the incident and backscattered radiation from Faraday rotation (ℓ_{far} = 5 cm for 45° rotation).

With the CO_2 laser operated at its peak output of ~ 200 J, the shifted backscatter signal occurred on an optimum 80% of the shots. In this operating regime a normalized, spectral scan of the shifted backscatter radiation was made at 250-mTorr fill pressure with scanning steps of ~ 5.2 Å. The results are shown in Fig. VII-11. The peak in the scan falls at ~ + 51 A with respect to the incident P-20 wavelength, while the ~ 10-Å HWHM compares with the instrument resolution of ~ 10 Å. The shift in frequency compares favorably with the corresponding ion acoustic frequency if, in fact, an expected local laser heating of the electrons of ~ 40 eV occurs. The implied signal width of 10 Å is considerably less than that

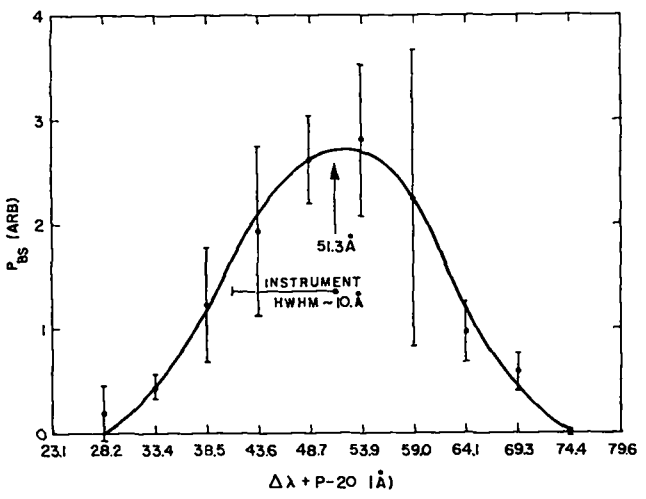

Figure VII-11.
Scanned wavelength profile of stimulated backscatter signal.

reported elsewhere[10] and is indicative of an expected lower damping rate of the scattering process at these plasma densities.

An attempt to measure a power threshold for the shifted backscatter was also made with a fill pressure of 400 mTorr. A large shot-to-shot variation was found in the ratio of backscatter power to incident power. It is felt that this variation is a manifestation of the already observed intermittency in backscatter occurrence. These data are being further analyzed to determine if the evident lower cutoff of backscatter is due to the expected power threshold or to detector limitations.

F. SUMMARY

Due to the time constraints placed on completion of data collection, only preliminary data analysis has been performed. Full analysis of all data is presently in progress and is expected to appear in a report in the near future. The general tentative, results of the experiment can be given as: 1) simple inverse bremsstrahlung absorption does not alone account for the observed energy transmission; rather refractive effects and nonlinear absorbtion must be inferred; and 2) stimulated Brillouin scatter has been observed but with different characteristics than are observed in similar experiments elsewhere; these differences are probably due to the different plasma conditions in this experiment.

REFERENCES

1. Laser-Plasma Interactions in the Scylla I-C Experiment: Preliminary Analysis, LA-5957-MS, T. M. York and K. F. McKenna, May 1975.

2. Scylla I-C: Laser-Plasma Interaction Experiment in a Theta-Pinch Geometry, APS presentation, Oct. 1976, W. T. Armstrong et al.

3. Controlled Thermonuclear Research Program, January-December 1975, LA-6582-PR, G. A. Sawyer, December 1976.

4. Plasma Experiments on the Scylla I-C Theta Pinch, LA-6397-MS, K. F. McKenna, August 1976.

5. Section VII, this report.

6. Double-Pulsed Time Differential Holographic Interferometry, W. T. Armstrong and P. R. Forman, App. Optics. 16, 229 Jan 1977.

7. Collisional Dielectronic Recombination and Ionisation Coefficients and Ionisation Equilibria of H-like to A-like Ions of Elements, H. P. Summers, Appleton Laboratory report, September 1974.

8. Correct Values for High-Frequency Power Absorption by Inverse Bremsstrahlung in Plasmas, T. W. Johnston and J. W. Dawson, Phys. Fluids 16, 722, 1973.

9. Theory of Stimulated Scattering Processes in Laser-Irradiated Plasmas, D. W. Forslund, J. M. Kindel, and E. L. Lindman, Phys. Fluids 18, 1002, Aug. 1975.

10. Stimulated Brillouin Scattering of CO_2 Laser Radiation from Underdense Plasma, A. A. Offenberger et al., J. of App. Phys. 47, 1451, April 1976.

11. Observation of Stimulated Brillouin Backscattering from an Underdense Plasma, R. Massey, K. Berggren, and Z. A. Pietrizyk, Phys. Rev. Lett. 36, 963, April 1976.

VIII. FIELD REVERSAL THETA PINCH

R. K. Linford, W. H. Borkenhagen, D. A. Platts,
E. G. Sherwood, and K. S. Thomas

A. INTRODUCTION

Numerous investigators of the theta pinch have studied the plasma produced with a reversed or negative bias field but until the results of Eberhagen and Grossmann[1] and Kurtmullaev and co-workers,[2] the reversed field has been destroyed within a few microseconds of the implosion. These fairly recent results not only show much greater stability than earlier experiments, but also greater stability than predicted by MHD theory.[3] The Eberhagen and Grossmann results are typified by a dense ($\sim 10^{17}$ cm^{-3}) warm ($\sim$ 50 eV) plasma that was eventually destroyed by a rotational m = 2 instability about 25 μs after the implosion. The lower density ($\sim 10^{15}$ cm^{-3}) Kurtmullaev plasma is warmer ($T_i \sim 80$ eV, $T_e \sim 1$ keV) and displays no instabilities during its 50 μs lifetime which is limited by the crowbar decay. This result could have an important impact on the end-plugging of mirror machines and theta pinches.

The major problem with trying to extrapolate these results to larger more "interesting" systems is that the cause of these unique results is not understood either theoretically or experimentally. The "stable" configuration is formed by the bias and implosion field lines connecting near the ends of the theta-pinch coil. (See Fig. VIII-1.) The resulting closed field lines and confined plasma have the same topology as a toroidal Z pinch with an elongated cross section and with no stabilizing toroidal field. Careful studies of previous experiments[4-11] do not yield any requirements for the stability of this configuration. In some cases the results are in conflict. In other cases the measurements are not sufficient to understand the results. More work is clearly needed in this area.

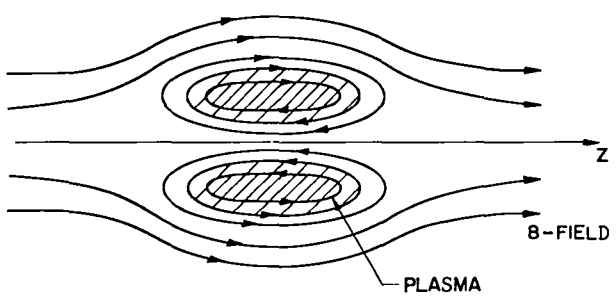

Fig. VIII-1.
FRTP plasma configuration.

The Field Reversal Theta-Pinch (FRTP) program at LASL was begun to further investigate the apparently conflicting results and to determine the applicability of the reversed field configuration to the end-plugging of mirror machines and theta pinches. Two facilities are being converted to aid in the study. The RHX (see Sec. III in this report) was converted into FRTP-A which most closely resembled the Kurtmullaev experiment. The Scylla I-C facility (see Sec. VII in this report) is being converted into FRTP-B which will be used to study the higher pressure regime of Eberhagen and Grossmann.

The initial effort is to attempt a duplication and an understanding of the Kurtmullaev results with the FRTP-A. There is an indication that Kurtmullaev operated his experiment in two different modes namely: (1) static-bias system, which consists of a nearly dc bias field, plus a ringing theta-pinch or Z-pinch preionization, followed by the implosion field which is crowbarred on the first half-cycle, and (2) second half-cycle system, where the bias and preionization functions are both provided by the first half-cycle of the main (and only) bank. The implosion is provided by the second half-cycle which is also crowbarred.

The FRTP-A is designed to use the static-bias system because it allows greater flexibility in the plasma parameters. The system is also easily converted to the second half-cycle operation.

If the stable operation reported by Kurtmullaev can be reproduced in FRTP-A, then the dependence of the stability and plasma confinement on various parameters will be studied. Hopefully, this study will be extended to higher temperatures and densities in the FRTP-B system.

B. DESCRIPTION

1. FRTP-A. The modification of RHX to FRTP-A began in mid-July. The modification was made in three main stages. The description given here is of the final result which was ready for checkout at the end of December.

The RHX implosion coil was modified to contain a single feedslot and enlarged to 25-cm i.d. The length is still 90 cm but 22-cm-i.d. mirror coils are inserted in the ends to produce a 10% mirror field on axis. The same 20-cm-i.d. quartz discharge tube is used.

The plasma is produced by a static-bias system shown in Fig. VIII-2(a). The typical behavior of the magnetic field is shown in Fig. VIII-2(b), including the bias, preionization, and the crowbarred main bank field. The crowbar system consists of six PFN switches mounted in one of the RHX feed plates and the PFN capacitors are replaced with shorts (the same method used in the resonant heating mode of the RHX). The feed plates are attached to the load coil by the isolation inductance as shown in Fig. VIII-3. This added inductance assures the required current uniformity[6] in the load coil in spite of the nonuniform feedplate currents caused by the crowbar gaps. The main bank, constructed out of RHX maxi-Marx parts, is attached to the back of the feedplates by a parallel plate transmission line (see Fig. VIII-3.) The bias bank and the theta-pinch preionization bank are both connected to the feedplates by cables. The bias bank contains three high-density 180-μF, 10-kV capacitors and a size-D ignition switch.

The preionization bank consists of two 0.4-μF, 125-kV capacitors dc-charged to typically 60 kV and switched by the modified Scyllac start switches used in the RHX. To improve the preionization of the low-pressure D_2 in the presence of the bias field, an rf preionizer was developed which induces axial rf electrical fields near the ends of the load coil. The specifications for FRTP-A are given in Table VIII-I.

2. FRTP-B. FRTP-B is a higher energy machine than FRTP-A, but it employs a similar size load coil and discharge tube. FRTP-B uses standard Scyllac technology for its banks, supplies, and controls.

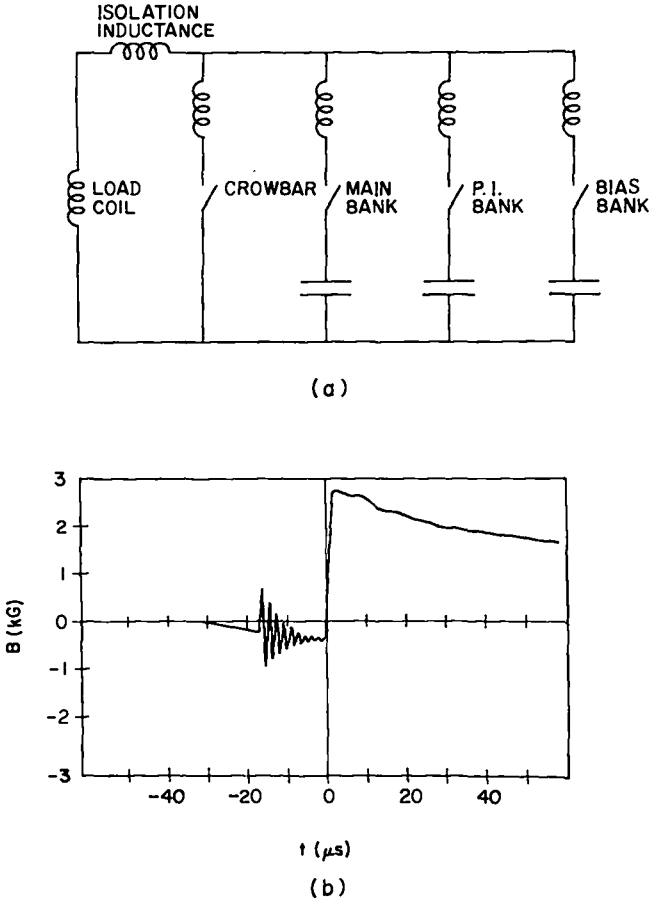

Fig. VIII-2.
FRTP-A circuit and typical magnetic field waveform.

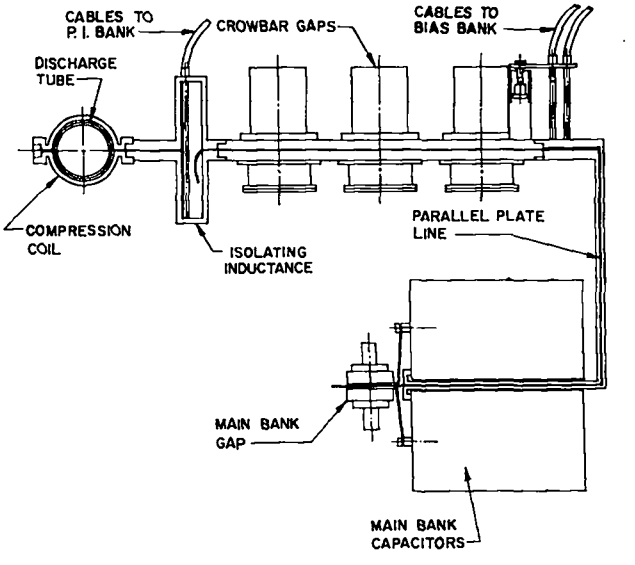

Fig. VIII-3.
FRTP-A construction details.

TABLE VIII-I

FRTP-A

	Bias Bank	P.I. Bank	Main Bank
Capacitance	550 μF	0.8 μF	21 μF
Voltage	10 kV	80 kV	40 kV
Energy	27.5 kJ	2.6 kJ	16.8 kJ
Risetime (τ/4)	35 μs	0.6 μs	3 μs
Peak Magnetic Field	1.3 kG	1.5 kG	3 kG
Crowbar L/R time			200 μs

FRTP-B

	Bias Bank	P.I. Bank	Main Bank
Capacitance	480 μF	0.7 μF	37.8 μF
Voltage	10 kV	75 kV	75 kV
Energy	24 kJ	2 kJ	106 kJ
Risetime (τ/r)	40 μs	0.5 μs	2 μs
Peak Magnetic Field	2 kG	1 kG	12 kG
Crowbar L/R time			150 μs

FRTP-B uses a 1-m-long coil with 25-cm i.d. A 10% mirror field is provided by 22-cm-i.d. sections at the ends of the coil. A series of slots are designed into the coil for side-on streak photography. The discharge tube is 20-cm-i.d. quartz held between vacuum crosses which contain pumpout and diagnostic ports.

The main bank consists of 54 0.7-μF, 75-kV capacitors each topped by a Scyllac combination start and crowbar gap. Each capacitor is connected to the feed plates by six pieces of RG-19/14 Scyllac load cable. The feed plates are connected to the load coil as shown in Fig. VIII-4.

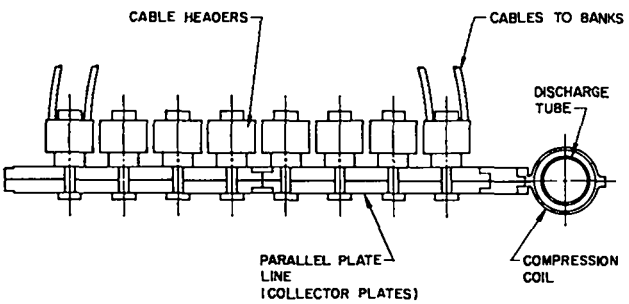

Fig. VIII-4.
FRTP-B collector plate and front end.

One 0.7-μF, 75-kV capacitor with a Scyllac start gap is used for the preionization (PI) bank. It is connected to the rear of the feed plates by 12 pieces of RG-17/14. The PI is aided by a rf tickler of the same design as the one on FRTP-A.

The bias bank uses eight 60-μF, 10-kV capacitors switched by six ignitrons. The bias bank is connected to the machine by six pieces of RG-17. The specifications of the banks are given in Table VIII-I.

C. ENGINEERING

Initial modifications to the RHX to convert it to FRTP-A included the design of a new main bank and a bias bank. As shown in Fig. VIII-3, each of the three parallel sections of the main bank consists of two 20-kV, 14-μF capacitors charged to opposite polarities. The cases of these capacitors are connected to either side of the parallel plate feed line. The bank is fired by connecting the center terminal of the three sets of capacitors together with field distortion spark gaps. So, in effect, the main bank is 21 μF at 40 kV. This gives a risetime on the order of 2 μs with no plasma and no isolation inductance. Later with the isolation inductance added, the risetime was about 3 μs.

The bias bank uses three 183-μF, 10-kV high-density capacitors connected in parallel. The bank is switched by a size D ignitron and connected into the feed plates by RG-19 cables. The function of the bias bank is to provide a slow (35-μs rise) reverse bias. A stainless steel rod is used to add inductance (≈ 800-nH total in circuit) to achieve this slow risetime. At the same time the resistance of the stainless steel dampens the ringing of the bank to keep from overstressing the capacitors.

The modified PI system was designed to provide more repeatable preionization and faster damping of the PI currents. This allows the machine to be fired sooner thus giving less time for the PI plasma to decay and diffuse out the ends. The amplitude of the PI current was increased slightly and its frequency was doubled. By doubling the frequency the desired higher damping rate was achieved. The new circuit uses two 0.4-μF capacitors in parallel with modified

Scyllac gaps feeding the collector plates through six pieces of low-inductance RG 17/14 cable. The frequency was raised because both the inductance and capacitance of the new circuit are lower than the old RHX components. To minimize the prefiring of the main bank, the PI cables were moved from the rear of the feedplates to the load coil side of the isolation inductance. This helps to isolate the main bank from the PI and removes some of the inductance between the PI and the load coil, thus further increasing the PI current and frequency. As shown in Fig. VIII-3 the PI feed cables span the isolation inductance which avoids insulation problems.

The rf tickler which helps the PI is powered by a 0.25-μF capacitor switched by a trigatron gap. This capacitor feeds the primaries of two ferrite transformers. This circuit oscillates with a period of about 3 μs. Every time the ferrite changes the direction in which it is saturated, a pulse of voltage appears on the secondaries of the transformers. The secondary circuit is tuned to resonate at about 8 MHz by adding capacitance in parallel with the antenna capacitance. The antennas are insulated copper strips wrapped around the discharge tube about 10 cm outside of each end of the load coil. They are fed out of phase and capacitively couple some longitudinal electric fields into the tube to produce a small initial ionization. In the present system about 20 kV peak of rf voltage is applied to the antennas.

To make the STP PFN gaps from the RHX act as crowbars, a number of modifications were needed. The crowbar gap spacing was reduced by a factor of 2 since the FRTP operates at lower voltage than the STP for which these gaps were originally designed. The molybdenum trigger electrode was replaced by a more rugged infiltrated copper-tungsten (30%-70%) electrode. The trigger system uses two 0.2 μF capacitors charged to 75 kV with each capacitor triggering three crowbars. A Scyllac gap is used to discharge each 0.2-μF capacitor into six pieces of RG-19 cable. At each gap two pieces of RG-19 are connected in series and isolated by ferrite in order to double the trigger voltage. Five parallel strings of five 2.5-nF doorknob capacitors in series are connected across the RG-19 cable to provide local energy storage. This arrangement is connected to the crowbar trigger electrode through a PFN-style peaking gap. Of the many modifications tried, this one was the only one which produced reliable crowbar operation.

D. DIAGNOSTICS

FRTP-A retained the diagnostics from the RHX. The fractional fringe interferometer remained so density vs time could be taken axially down the system at any radial position. The holographic interferometer takes an end-on snapshot of the density at one time. External and internal magnetic field probes were retained. The internal probe was cantilevered into the center of the system from one end, but space limitations made it impossible for more than just the tip of the probe to be radially centered. The holographic interferometer showed dense plasma buildup and nonsymmetrical plasma profiles around the noncentered part of the internal field probe so it was removed. In the future it is planned to insert an internal field probe which can be positioned entirely on axis.

The side-on streak camera was the major new diagnostic. This camera views the plasma on its horizontal centerline through 17 equally spaced slots in the load coil. The axial position and extent of the plasma are given by this diagnostic. A set of radial magnetic field sensing coils was also installed around the discharge tube. However, electrical noise, and difficulty in interpreting the results have prevented their use.

Plans call for the installation of an end-on framing camera and Thomson scattering in addition to the internal magnetic field probe already mentioned. The end-on framing camera will basically replace the use of the holographic interferometer. The holographic interferometer has limited sensitivity, and the interpretation is complicated by cold plasma at the ends of the machine. Since the side-on streak pictures give good information on the plasma position, it is expected that the end-on framing camera can do the same.

E. EXPERIMENTAL PROGRAM AND PLASMA RESULTS

FRTP A was reworked according to the plasma results at each stage of the experimental program. The first step was to add a main bank and a bias bank. The RHX crowbar system and the uniform coil were retained while one of the two sets of RHX collector plates was replaced by a bar. This bar had holes machined in it for side-on streak photography. At this stage the longest that plasma density remained was 15 μs. The plasma was not repeatable and not symmetrical. The side-on streaks showed that the plasma often went out one end of the coil or the other. The plasma also showed a longitudinal nonuniformity which appeared to be related to the position of the crowbar gaps in the collector plate. At this point the machine was shut down for modification.

To help stabilize the plasma from going out the ends of the machine, a new coil was installed with a 10% mirror field at each end. The longitudinal nonuniformity in the plasma was thought to be due to nonuniformity of the current around the load coil caused by the placement of the crowbar gaps in the collector plate. To allow the current to spread out uniformly over the load coil, an isolation inductance consisting of a rectangular opening of the feed plates was installed between the coil and the collector plates. This arrangement is described in the engineering section and shown in Fig. VIII-3. This inductance will also help increase the crowbar L/R time and reduce the initial modulation. The problem of nonrepeatability was often cured on the RHX by cleaning the tube. A brown deposit thought to be cracked backstreaming products from the pump was found baked to the inside of the discharge tube. This deposit was removed and a refrigerated cold trap was installed in the high vacuum line.

With this set of modifications completed the system was again tested. The plasma was now symmetrical, and did not exit out the ends. The confinement time was about the same and shot-to-shot repeatability was still poor. In taking holograms it was noted that there was considerable cold PI plasma at the ends which made the holograms difficult to interpret.

Machine modifications were started again at this point. To try to improve the repeatability a new PI system was installed. As described in the engineering section, this system has a higher initial amplitude, a higher frequency, and a faster damping rate. Thus it was hoped to produce a higher percentage preionization and have the PI circuit ringing die out faster so the machine could be fired sooner giving the PI plasma less chance to decay away and diffuse out the ends. The crowbar system was also modified at this time. Current monitors on the crowbar gaps showed erratic firing with typically only half of the six gaps firing on a given shot. Thus modifications to the gaps themselves and the trigger system were made. At the end of the year these modifications were being completed and the system was being readied for testing.

F. CONCLUSION

FRTP-A has been built and has undergone several stages of testing and modification. Machine reliability and plasma repeatability have both been improved. It appears that reversed-field configurations have been achieved and work can now proceed on understanding the physics of the configuration and increasing its lifetime.

FRTP B construction is proceeding. Lessons learned from FRTP-A are being incorporated in FRTP-B. The machine is being engineered for reliability and ease of data acquisition. Both machines should be able to contribute to our understanding of the reversed-field configuration in the next year.

REFERENCES

1. A. Eberhagen and W. Grossmann, Z. Phys. 248, 130 (1971).

2. A. G. Es'kov, O. A. Zolotovsky, A. G. Kalygin, R. Kh. Kurtmullaev, Ya. N. Laukhin, A. I. Malyutin, A. P. Proshletsov, V. N. Semenov, "Plasma Confinement in a Pulsed System with a Compact Toroidal Configuration," in Proc. Seventh European Conf. Controlled Fusion and Plasma Physics, Lausanne, 1975 (CRPP, 1975) Vol. I, p. 55.

3. H. P. Furth, J. Killeen, M. N. Rosenbluth, Phys. Fluids 6, 549 (1963).

4. Becker, Eberhagen, et al, IAEA Fifth Conference Proceedings, Tokyo, 1974, V. III, p. 47.

5. H. A. B. Bodin, A. A. Newton, Phys. Fluids 6, 1338 (1963).

6. A. Eberhagen, H. Glaser, Nucl. Fusion 4, 296 (1964).

7. M. Alidieres, R. Aymar, P. Jourdan, F. Kocchlin, A. Samain, Plasma Phys. 10, 841 (1968).

8. N. Rostoker, A. C. Kolb, "Fission of a Hot Plasma," Phys. Rev. 124,965 (1961).

9. T. S. Green, "Plasma Containment in the Theta Pinch," Phys. Fluids 6, 864 (1963).

10. E. M. Little, W. E. Quinn, "Effects of Added Hexapole Magnetic Fields and Preionization in Theta Pinch Experiments," Phys. Fluids 6 875 (1963).

11. J. W. Mather, "Diagnostics of the Confinement and Heating of a Plasma by a Rising Axial Magnetic Field (Orthogonal Pinch)," Nucl. Fusion 1, 233 (1961).

IX. IMPLOSION HEATING EXPERIMENT (IHX)

I. Henins, T. R. Jarboe, A. R. Sherwood

A. INTRODUCTION AND SUMMARY

The Implosion Heating Experiment, IHX, is a 40-cm-diameter, 1-m-long, high-voltage linear theta pinch designed to study the implosion phase of conventional theta-pinch heating. The implosion coil is fed at four places by low-impedance pulse-forming networks (PFN's) designed to produce a flat-topped current pulse. The effective impedance of the four PFN's is approximately equal to that of the imploding plasma, thus coupling the plasma dynamics strongly into the external circuit. The PFN circuits and other details of the apparatus have been described previously.[1,2]

Aside from occasional electrical faults the experiment has been operating reliably, and no major modifications to the apparatus have been required during the year. Thus we have been concerned mostly with obtaining data for different sets of experimental conditions and with improving the diagnostics. Extensive measurements of density and magnetic field as a function of radius and time have been obtained for a variety of experimental conditions. These measurements have been found to agree remarkably well with numerical simulations performed at LASL[3] and elsewhere.[4] At the end of the year plans were being formulated to obtain electron temperature measurements to supplement these data. Most of the diagnostic development was concerned with the measurement of the magnetic field, namely with improving the magnetic probes and the Faraday rotation measurement.

B. EXPERIMENTAL RESULTS

The gross dynamical features of the implosion in the IHX were described in the last annual report.[2] Briefly, a density peak forms near the outer wall and moves inward. As it does so it develops a fast and a slow component. The slow component moves at the velocity of the magnetic sheath and overlaps it spatially. The faster peak moves ahead of the magnetic sheath at a velocity somewhat less than twice the sheath velocity. When the imploding magnetic sheath has reached a radius of 8-12 cm it is stopped by an outward moving component of the plasma. The plasma then reexpands pushing the magnetic sheath back towards the wall, but a crowbar arc typically strikes at the wall before all of the magnetic flux can leave the tube. The reexpanding plasma is usually stopped before it gets to the wall by the flux compressed between it and the crowbar arc.

During the present year measurements of $B(r,t)$ and $nd(r,t)$ were obtained during this process for a variety of conditions. These conditions correspond to PFN voltages of 80-125 kV, gas filling densities in the range 2.4-5.8 x 10^{14} cm^{-3}, preionization levels of 40-75%, driving magnetic fields of 4.5-7.0 T, and azimuthal electric fields in the range 1.0-1.5 kV/cm. So far the initial conditions have usually been chosen such that the driving magnetic field remains essentially constant during the implosion process (i.e., is flat-topped). Because of the strong coupling between the plasma dynamics and the driving circuits, this requirement limits the available parameter ranges for the experiment.

The plasma diagnostics employed for these measurements are a four-beam HeNe laser Mach-Zehnder interferometer, a Faraday rotation measuring apparatus, magnetic probes, and time-resolved neutron detectors. Typical results for $nd(r,t)$ obtained from the interferometer are shown in Fig. IX-1. Typical magnetic field data are shown in Fig. IX-2. Approximately 10^6 neutrons are produced in a 200-ns wide pulse near the time of peak compression.

As was mentioned above, remarkable agreement exists between the IHX data and results from somewhat sophisticated numerical simulations. In some respects, however, the simple bounce model (i.e, the model which assumes a thin inward-moving current sheath reflects ions by an elastic bounce process, causing the ions to move ahead of the sheath at twice its speed) is sufficient to explain the data. For example, the bounce model predicts two velocities, namely the velocity of

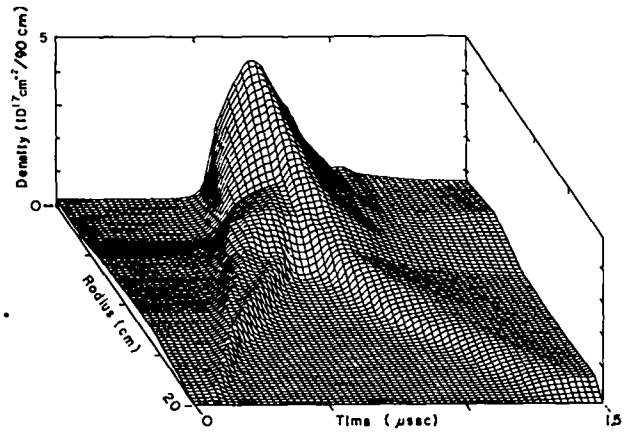

Fig. IX-1.
Density as a function of time and radius in IHX.

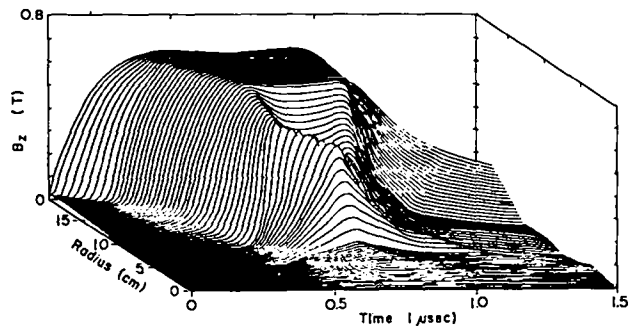

Fig. IX-2.
Magnetic field as a function of time and radius as deduced from Faraday rotation measurements and magnetic probe data.

the current sheath ($V_s = B/4\sqrt{\pi\rho}$) and the velocity of the bounce ions ($V_b = 2\ V_s$). The velocity of the sheath can be obtained from the density data or from the magnetic field data; it is here taken to be the speed at which the sudden drop in density moves inward during the implosion. The circles in Fig. IX-3 show this measured velocity compared to $B/4\sqrt{\pi\rho}$ (the "predicted velocity"). In the density data particles can be seen well ahead of the sheath and some features appear to have velocities of near 2 V_s. However, ion velocities can also be inferred from the neutron data in the following manner. A value for $\langle\sigma v\rangle$ can be deduced from the peak of the neutron production rate and the value of $n^2 d(\text{vol})$ at the time of this peak. Assuming a single-speed, two-dimensional isotropic velocity distribution, one can deduce a value for V_b from $\langle\sigma v\rangle$. The squares in Fig. IX-3 show this $V_b/2$ compared to the predicted sheath velocity.

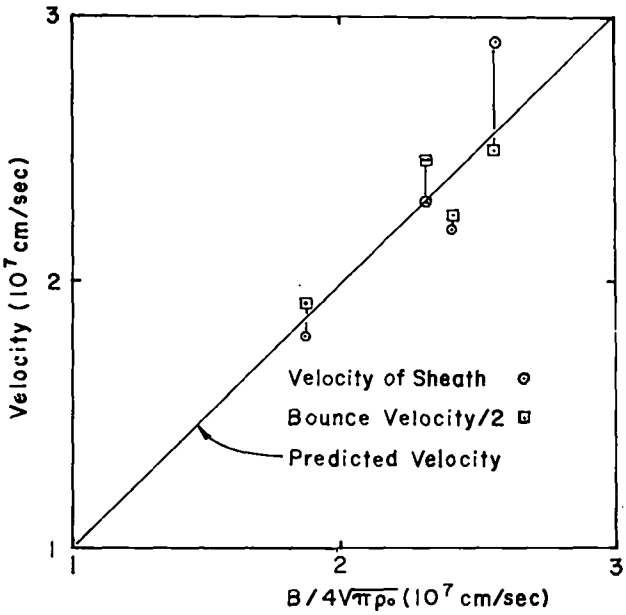

Fig. IX-3.
Sheath velocity and half the bounce velocity as a function of $B/4\sqrt{\pi\rho_o}$. The bounce velocity is deduced from neutron data.

Each pair of points in the figure corresponds to a whole set of data for a particular choice of initial conditions. These results are considered to demonstrate agreement between velocities inferred from the measurements and the predictions of the bounce model.

Of course, this simple model does not predict the width of the current sheath. To calculate this, more detailed theories which include ionization processes and anomalous resistivity are necessary. Some models which include anomalous resistivity predict that the current sheath width scales as c/ω_{pi}. In changing the initial fill pressure from 8.2 μm to 3.6 μm the scale length for the density change in the sheath region increases by a factor of 1.5-2.0. This is in the direction that is predicted.

C. DIAGNOSTIC IMPROVEMENTS

Most of the diagnostic effort was directed toward the improvement of the magnetic field measurements. Magnetic probes having 2-mm-o.d. quartz jackets were constructed for comparison with the old 10-mm-o.d. probes. The smaller probes showed a more rapid rise in the magnetic field (i.e., a thinner current sheath) than the

old probes, but both types still show disagreement with the total flux measurement. Furthermore both types of probes are unreliable at later times during the plasma reexpansion phase. The probes indicate a large amount of field plasma intermixing during this phase, whereas the Faraday rotation measurement indicates that this mixing does not take place. In general, the magnetic probes seem to be reliable during the implosion in the regions of low plasma density (e.g., at the outer radii at early times, and behind the current sheath) and unreliable elsewhere.

During the year considerable effort was expended on increasing the accuracy of the Faraday rotation measurement. In the case of a magnetized plasma the Faraday rotation of the plane of polarization obeys the relation

$$\Delta\theta \sim \int B n dl.$$

Since an independent measurement of $\int n dl$ is obtained from the laser Mach-Zehnder interferometer, an average B can be deduced. The main difficulty with this measurement is that refraction of the beam by density gradients can cause movement of the detected light across the surface of the detector. In general, the response of the detector is not spatially uniform, and this movement can cause signal variations which obscure the rotation signal. Both the amount of refraction and the amount of rotation are proportional to λ^2, so the problem cannot be solved by a correct choice of wavelength. Considering the time scale for the measurement, the size of the magnetic fields, and the scale length of the density gradients, the IHX is a fairly difficult device upon which to accurately measure Faraday rotation. However, reasonably good data were taken on IHX by following three principles to minimize errors caused by refraction. They are: 1) proper optics must be used so that refraction of the beam by the plasma causes a minimum of movement of the focal spot on the detector, 2) the detector used should be as uniform as possible so that movement gives as small a signal as possible, and 3) $\frac{\Delta p}{p}$ should be maximized where Δp is the power change due to Faraday rotation and p is the power hitting the detector.

The apparatus designed with these principles in mind has been described previously.[2] The accuracy of the measurement has been improved considerably by making the following changes in the apparatus: a) The copper-doped germanium detector was replaced by a lead-tin-telluride detector which is more uniform and more sensitive. b) The single plate germanium polarizer was upgraded by two germanium wedges giving a 40-fold improvement in the extinction ratio. c) The CO_2 laser was replaced by one that is more stable and more powerful. d) The HeNe interferometer beam was made to go through essentially the same plasma volume as the CO_2 beam. With these improvements Faraday rotations of 0.001 radians can be resolved.

The primary limitation in getting B from the rotation is that where the density is low the error bars on both the rotation and density measurements become about the same as the signal, and B cannot be computed. It turns out that a combination of Faraday rotation and probe data gives the best picture of $B_z(r,t)$ during the implosion. When the density is low we use the B measured by the probes. Late in time the probe shows higher values for B than Faraday rotation shows. In this case, where the density is high, we use the value of B from rotation. From B(t)'s such as this, B(r,t) surfaces (Fig. IX-2) are constructed using the same type of interpolation that is used for the density data. An important contribution from the Faraday rotation measurement is the correct picture of the expansion. We now see a well-defined current sheath during the expansion. The shape of the current sheath during the expansion is not that much different from its shape during the implosion. The probes, incorrectly, show that the field between 10 and 17 cm is more or less uniform and decreasing with time. They show no well-defined front moving out.

REFERENCES

1. I. Henins, J. E. Hammel, T. R. Jarboe, J. Marshall, and A. R. Sherwood, Pulsed High Beta Plasmas, (Pergamon Press, Oxford and New York, 1976) pp. 203-207.

2. G. A. Sawyer, compiler, "LASL Controlled Thermonuclear Research Program, January-December 1975," Los Alamos Scientific Laboratory report LA-6582-PR, December 1976, p. 36.

3. A. G. Sgro, submitted to Phys. Fluids.

4. S. Hamasaki, N. A. Krall, Phys. Fluids 20, 229 (1977).

X. EXPERIMENTAL PLASMA PHYSICS

H. Dreicer, M. E. Banton, J. C. Ingraham
R. S. Massey, F. E. Wittman, B. L. Wright

A. SUMMARY

During the past year members of the Experimental Plasma Physics Group continued their studies into the physics of the AC Electrical Resistivity and the Thermal Conductivity of a plasma along magnetic field lines. Significant progress can be reported on several fronts. The weak-field resistivity of a plasma, in which controlled levels of plasma wave turbulence are maintained, has been measured with our new dual mode microwave resonator technique. Evidence now exists that the weak-field resistivity becomes anomalously large whenever parametric decay of the weak electromagnetic field can be stimulated by the turbulent large amplitude wave spectrum that is independently maintained in the plasma. In another set of experiments we have observed the actual growth in time of the parametric instabilities. During this growth phase, the transition from classical to anomalous microwave absorption is measured, and the concurrent evolution of the hot nonthermal electron tail is monitored in great detail. Our observations indicate a very large build-up of plasma wave energy prior to the production of the hot electrons with a bump-in-the-tail velocity distribution. These observations are not yet properly understood even though a considerable body of theoretical knowledge on this subject is now available.

In a third set of experiments we sought to understand the influence of a parametrically unstable plasma upon the dc electrical resistivity. This work has not yet reached the stage where it should be reported, but a by-product of these labors, the observation of Negative Inverse Bremsstrahlung Absorption near ω_{pe}, does represent a significant advance. This observation was made, in the quiescent state below the threshold for parametric instabilities, by inducing a large enough steady drift of the plasma electrons relative to the ions. If possible, the measurement should be repeated in the turbulent state above the parametric instability threshold where great similarity would exist with conditions envisioned by Lin, Kaw, and Dawson[1] for their proposed Plasma Wave Laser.

The thermal conduction studies have become very interesting, because we now have reason to believe that a sensible experimental course exists for studying the phenomena that produce deviations from classical collision-dominated heat flow. Such deviations are believed due to large localized temperature gradients[2] and are also expected to be produced by plasma waves and turbulence. We find that these subjects form a natural extension of our long experimental experience with microwave heating and electrical resistivity near the plasma frequency and of our more recent forays into experimental studies that require dc electrical current flows. Under classical collision-dominated conditions our observations of the thermal conductivity are in good agreement with the theoretical value.[3] Work is under way to understand the phenomena that produce deviations from this value.

A new experiment for the purpose of studying nonlinear interactions between plasma and a traveling electromagnetic wave has been constructed and is presently under test.

B. ELECTROMAGNETIC WAVE ABSORPTION, PLASMA HEATING AND ENERGY TRANSPORT IN THE Q-MACHINE

Studies of electromagnetic wave absorption and the associated plasma heating and energy transport have been continued and extended in our single-ended Q-machine. This device provides a fully ionized magnetized potassium plasma column ($T_e \simeq T_i \simeq 2250°K$, $n \approx 1 - 5 \times 10^{10}$ cm^{-3}, diameter ≈ 2.5 cm, $B \gtrsim 5$ kG, length $\gtrsim 200$ cm) on which to study these effects by using high Q microwave resonators and moveable high frequency Langmuir probes. This setup is shown schematically in Fig. X-1.

1. Observation of Negative Inverse Bremsstrahlung Absorption. During the last quarter of 1976 members of the group again devoted some time to the measurement of the inverse bremsstrahlung absorption coefficient. In the past, our

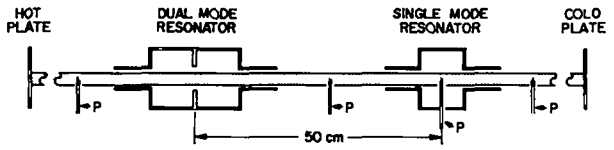

Fig. X-1.
Schematic layout of Q-Machine experiment. Moveable probes (P) are located at various positions along the column.

technique, a time decay measurement of the Q of a high-quality ($Q_o \cong 20{,}000$) microwave resonator that surrounds a fully ionized potassium plasma column, was used to measure the weak-field (ratio of oscillatory velocity to thermal velocity, $v_E/v_T \ll 1$) absorption by a quiescent plasma.[4] The measurement, expressible in terms of an electron-ion collision rate, ν_{ei}^o, agreed well with theory.[5] We have also measured the stronger field ($0 \lesssim v_E/v_T \lesssim 1$) absorption which becomes important when the microwave field, E, oscillates the electrons to an amplitude $eE/m\omega^2$ that is large enough ($\sim$ Debye length) to modify the Rutherford cross section. This measurement,[4] expressed in terms of an electron-ion collision rate

$$\nu_{ei}(v_E/v_T) = \alpha(v_E/v_T)\nu_{ei}^o \quad ,$$

showed that the coefficient $\alpha(v_E/v_T)$ had the property $0 < \alpha \lesssim 1$.

Our recent efforts have been devoted to a weak-field ($v_E/v_T \ll 1$) absorption measurement when the plasma electrons possess a considerable dc drift velocity, v_D, relative to the ions. In this case, the absorption involves an electron-ion collision rate that can be expressed as

$$\nu_{ei}(v_D/v_T) = \beta(v_D/v_T)\nu_{ei}^o \quad .$$

We were motivated in this measurement by the considerable past theoretical work and controversy[6-10] that centered around the possibility that β might be negative. In the case of the drifting Maxwellian electron distribution, for which

$$F^o(\vec{v}) = \left(\frac{m}{2\pi kT}\right)^{3/2} \exp\left[-\frac{m}{2kT}\left(v_x^2 + v_y^2\right) - \frac{m}{2kT}\left(v_z - v_D\right)^2\right] \quad ,$$

Musha and Yoshida,[10] using a Boltzmann-Fokker-Planck approach, showed that $\beta < 0$ for sufficiently large v_D/v_T. Our own recent calculation, based upon the Dawson-Oberman formalism,[5] and including the effect of a strong magnetic field, is shown in Fig. X-2. It illustrates that $\beta < 0$ for $v_D/v_T \gtrsim 0.9$. Moreover, it shows that $\beta \to 0$ for $v_D/v_T \to \infty$, because the Rutherford cross section decreases as the total energy, dominated by the directed energy, $(1/2)m\,v_D^2$, increases. Although it is difficult to understand the detailed stimulated bremsstrahlung emission process,[8] it seems clear from the collisional absorption standpoint,[10] that β becomes negative when the $\nu_{ei}^o(v) \times \partial F^o/\partial v_z > 0$ portion of the electrical conductivity integral contributes enough to overcome the $\nu_{ei}^o(v) \times \partial F^o/\partial v_z < 0$ portion.

Our observations of β were made by suddenly pulsing the otherwise negatively biased cold end collector, or cold plate, in our Q-machine (see Fig. X-1) to positive potential, and thus accelerating the electrons. Probes located on both sides of the resonator, used to monitor the

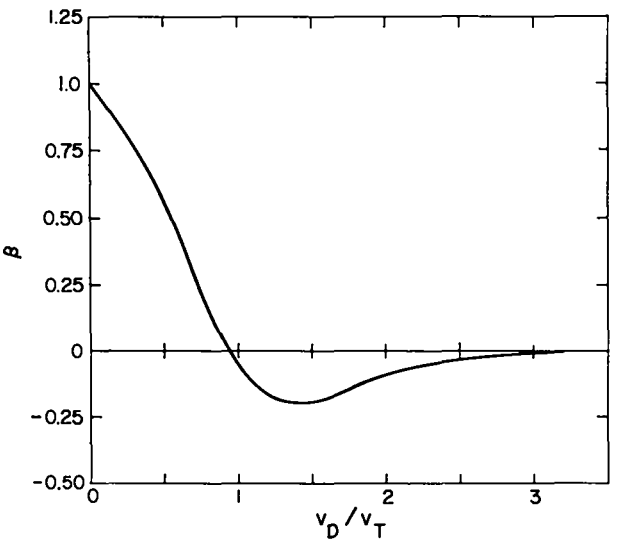

Fig. X-2.
Theoretically predicted normalized ac resistivity, β, versus ratio of electron drift velocity to thermal velocity for $\omega_p^2/\omega^2 = 0.35$.

appearance of the accelerating potential pulse, indicate, as shown in Fig. X-3, that an electron-accelerating space charge pulse travels the length of the plasma column almost instantaneously. This result is also supported by the nearly simultaneous change in the rate at which the microwave energy decays, upon application of the current pulse, as shown in the upper portion of Fig. X-4. A small radially moveable current collecting probe indicates that the current profiles and the separately measured density profile agree, and that, therefore, the electron drift speed v_D is independent of radius. The electron drift speed is obtained from the electrical current and plasma density measurements. The electron temperature prior to application of the accelerating pulse is assumed equal to the measured hot plate temperature of 2250 K. The validity of this assumption is confirmed by the good agreement between our measured value of ν_{ei}^{o}, using the resonator technique, with theory.

To achieve $v_D/v_T > 1$, in the face of temperature-limited (constant electron current) operation of the Q-machine hot plate, it was necessary to lower the electron density, n, and perform observations in the range $0.35 \lesssim \omega_{pe}^2/\omega^2 \lesssim 0.5$. This has the advantage of reduced ohmic heating due to the dc pulse, but it also reduces the sensitivity of the Q-measuring technique, because $\Delta(1/Q)$, the plasma contribution to the absorption, is proportional to n^2. Another way to avoid ohmic heating is to utilize a short (~ 0.4 μs) "dc" pulse length and to measure Q during this short time interval. This also insures that the Buneman instability[11] cannot grow sufficiently to influence the electron drift speed and the microwave absorption measurement. The price paid for gaining these advantages is the increased difficulty of accurately measuring the slope of the microwave decay (i.e., Q) during such a short time interval.

The lower portion of Fig. X-4 shows the microwave decay with and without the short dc pulse. While it is evident that this pulse causes the microwave decay rate to decrease, it requires considerable analysis to show that the sign of β is also changed. Figures X-5 and X-6 show the present status of this analysis. In Fig. X-5 we show the result of obtaining the absorption from 23 slope measurements made every 0.05 μs during a single decay and utilizing a 0.1-μs duration for the purpose of defining a slope. This approach gives the time-resolved absorption, but also introduces a considerable spread into the absorption deduced simply because less averaging of the noise in the microwave decay data is possible. The result clearly shows the sudden

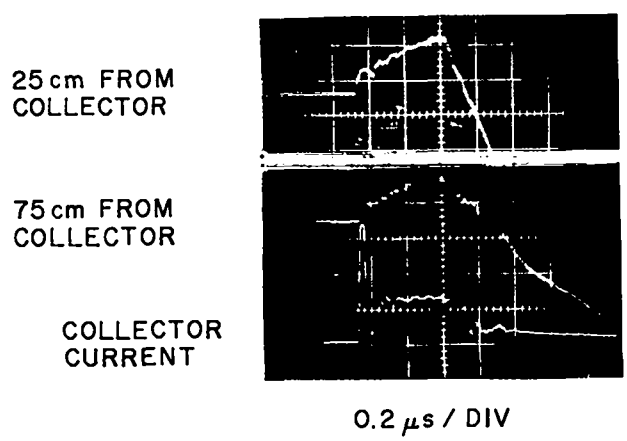

Fig. X-3.
Relative time behavior of current signal at collector, and probe signals at two different positions in plasma column.

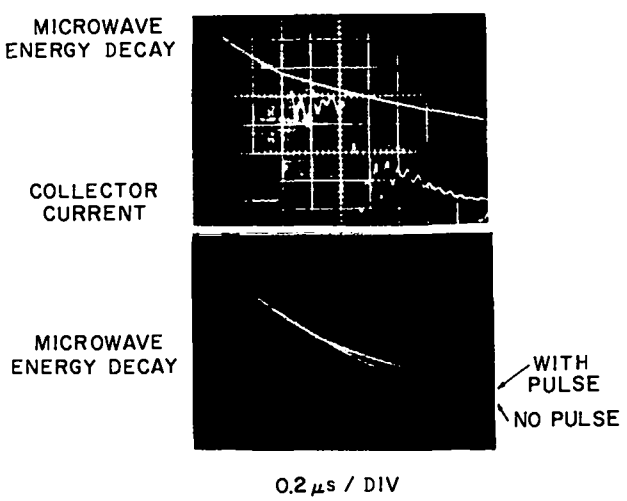

Fig. X-4.
Upper: Relative time behavior of current signal at collector and microwave energy decay. Lower: Microwave energy decay with and without application of current pulse. Upper and lower cases correspond to different plasma conditions.

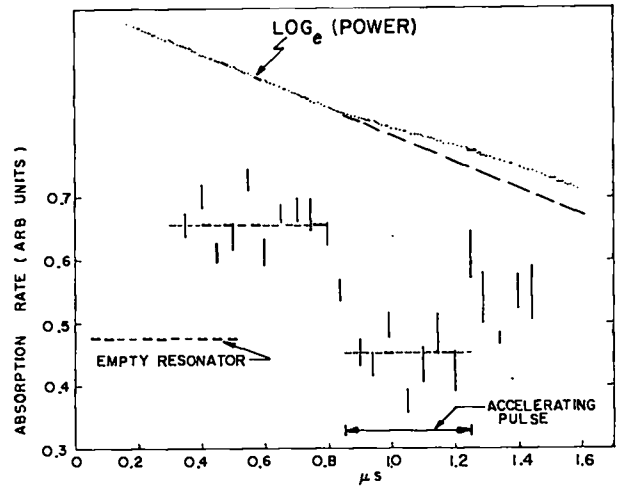

Fig. X-5.
Time-resolved analysis of slope of microwave energy decay using 0.1-μs time interval. (ω_p^2/ω^2 = 0.53 for this case.)

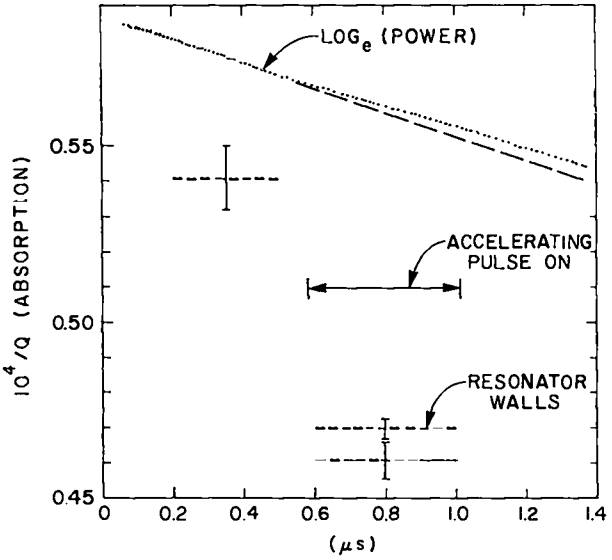

Fig. X-6.
Analysis of slope of microwave energy decay using 0.3- to 0.4-μs time interval. (ω_p^2/ω^2 = 0.35 for this case.)

decrease in the absorption when the accelerating pulse is applied, but comparison with the absorption due to the losses in the resonator walls leaves uncertainty that β actually became negative. A more convincing demonstration that β is actually negative becomes possible if we sacrifice time resolution and simply measure the slope of the decay curve before the application of the accelerating pulse, and throughout the entire time available during the application of the pulse. In this case, there is less error in determining the slope and we obtain the result shown in Fig. X-6. (Each error bar in Fig. X-6 is determined from the RMS scatter of slope measurements for 10 to 20 cases.) The losses, described in Fig. X-6 by the label "resonator walls," include a correction that arises from the influence of the plasma dielectric constant upon the distribution of the microwave fields within the resonator. Unfortunately, this correction also reduces the wall losses compared to what they would be for an empty resonator. Nevertheless, though the remaining effect is not large, we can now observe a definite reversal in the sign of β.[12] The provisional situation is summarized in Fig. X-7 where we show the theoretical β curve and two data points that we have analyzed which give negative absorption. (Not shown on the figure are cases at smaller drift velocities in which β is positive and approaches unity as v_D approaches

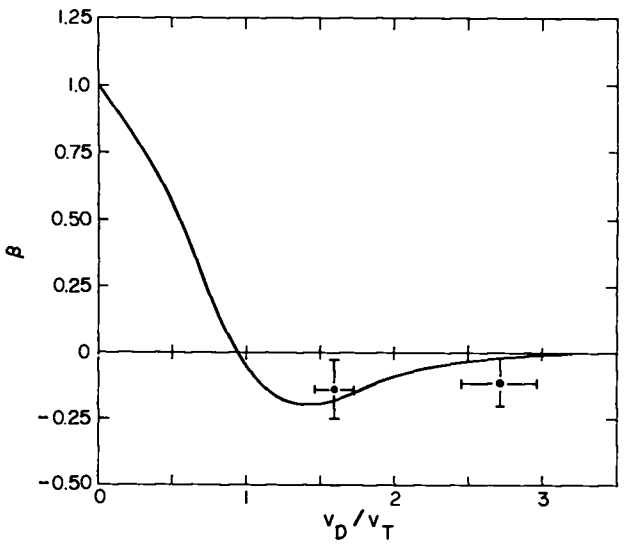

Fig. X-7.
Summary of results and comparison with theory for two drift velocities at ω_p^2/ω^2 = 0.35.

zero.) Considerable uncertainty remains in the precise location of these points along the v_D/v_T axis, because, according to our computations, the 0.4 μs pulse length was still long enough to double the electron temperature as a result of ohmic heating. This temperature rise will be measured in the near future, and we also hope to refine the measurement of β further.

2. Plasma Heating and Heat Flow. During the past year serious studies, both experimental and computational, were initiated on electron heat flow along the magnetized Q-machine plasma column. Our work was based on the microwave techniques developed in the course of our ac electrical resistivity studies. These techniques enable us to rapidly heat the plasma electrons locally, and to obtain the electron temperature from a rapid measurement of the microwave absorption. By locating several microwave resonators along the plasma column for these purposes we can determine the electron temperature as a function of source strength, space, and time. Figure X-1 shows this set-up for the case of the two resonators used so far in our work. By driving the resonator, marked Single Mode Resonator on Fig. X-1, with a short microwave power pulse, we are able to heat the plasma locally over about a 10-cm-long axial source region. Sometime after the heating pulse is turned off, we measure the Q of this heater resonator and determine the temperature in the source region. The Q of the second resonator, marked Dual Mode Resonator on Fig. X-1, is monitored continuously to determine the time history of the electron temperature 50 cm away from the source. An example of the microwave signals observed is shown in Fig. X-8.

The interpretation of the measurements is carried out with the help of a heat flow and microwave heating computer code, originally due to J. H. Brownell (TD Division) and recently completely revised by J. Thomas (visiting staff member from N.M.S.U.). This code numerically solves the one-dimensional, nonlinear, partial differential equation for the collision-dominated, time-dependent heat flow with a microwave ohmic heating source term. To correspond to the experimental situation, an insulating boundary condition describes the negatively biased cold end collector, while a constant temperature is imposed at the hot plate end of the plasma column. The axial thermal conductivity, $\kappa_{\parallel}$, is given by

$$\kappa_{\parallel} = \alpha \kappa_{SP} \quad ,$$

where κ_{SP} is the parallel thermal conductivity derived by Spitzer,[3] and α is a parameter that we introduce into the computation to obtain the best possible agreement with the experimental observations.

For modest heating levels, designed to satisfy as closely as possible the requirements of the classical collision-dominated heat flow theory, we find good agreement between theory and experiment with $\alpha = 1$, and these results are described below. Our main interest is, therefore, to extend these measurements into several areas that are less well understood. These include the effect of plasma instability and turbulence, large temperature gradients, magnetic mirrors, particle end loss, and electrostatic trapping potentials.

To obtain turbulence, we have begun to conduct dc currents through the plasma column. In this case, dc ohmic heating has been observed and is an unavoidable by-product of producing turbulence. Numerical code modifications, not yet completed, will be required to describe the heat flow for the dc current case. With heat flow ignored, Fig. X-9 shows the maximum temperature increase that can be expected as a function of time from classical dc ohmic heating alone.[13]

The case of large local temperature gradients, studied by Ivanov et al.,[2] is interesting because it introduces the possibility that strong local heating could force the local electron mean free path to exceed the temperature gradient scale length. In this case, the free flow of hot collisionless electrons into the adjacent cooler plasma is restricted by space charge forces, and the subsequent exchange of hot and cold electrons may involve instabilities. Our

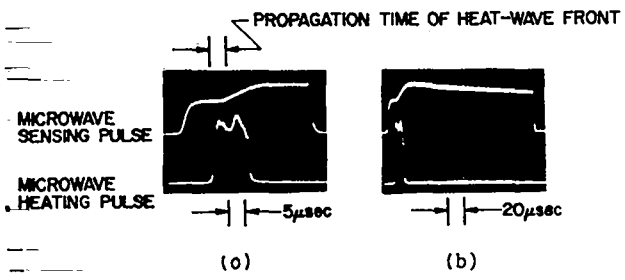

Fig. X-8.
Effect of heat pulse on microwave resonator signal.

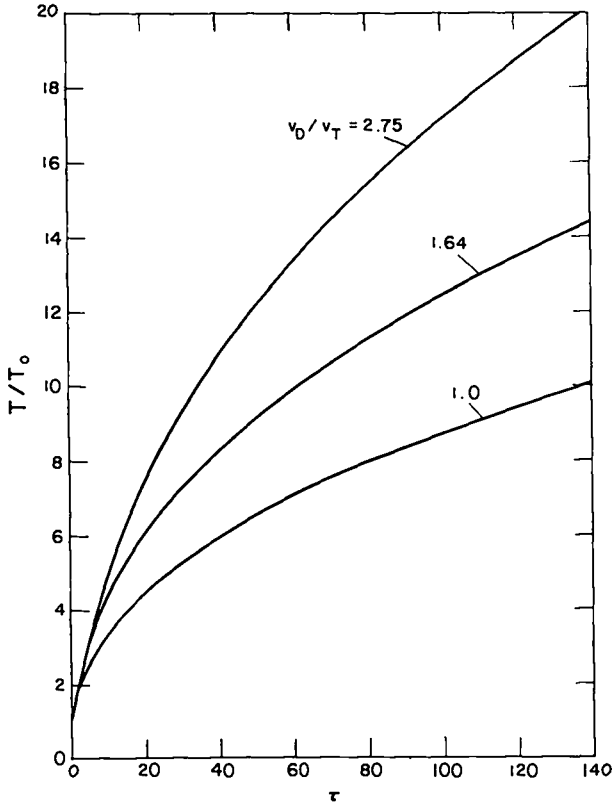

Fig. X-9.
Temperature normalized to T_o plotted versus τ for a drifting Maxwellian having drift velocity v_D, where $\tau = \nu t$, $\nu = 4.8 \times 10^{-6}\ n/T_o^{3/2}\ \ell n\ \Lambda$, $v_T = 2k\sqrt{T_o/m_e}$, n is in m^{-3}, and T_o in K.

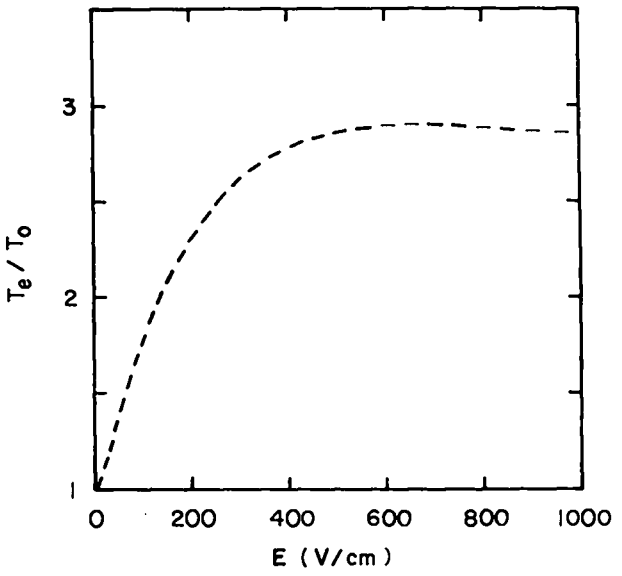

Fig. X-10.
Computed T_e/T_o vs E-field for microwave heating by classical means alone. Note that for the case considered (column length = 180 cm, density = 4.5×10^{10} cm^{-3}, T_o = 2250 K, heater length = 16 cm, and microwave frequency = 3 GHz) T_e/T_o reaches a maximum value of 2.9 due to the reduction of the electron-ion collision rate at large E-fields.

search for this effect is hampered by two difficulties. If we operate the heating resonator field <u>below</u> the threshold for ac parametric instabilities, we utilize classical ohmic heating due to electron-ion encounters. In this case, heating is limited by the reduction in the electron-ion collision rate when the ac drift speed, $eE/m\omega$, becomes comparable to or larger than the electron thermal speed.[4] This effect illustrated in Fig. X-10 limits classical ohmic heating to $T_e/T_o \cong 2.9$. The need to generate larger values of T_e/T_o has also forced us to operate <u>above</u> the ac parametric instability threshold, where we have observed appreciable anomalous heating of the body of the electron distribution function; but an energetic tail of hot electrons is also produced.[14] In this case our approach has been to delay temperature measurements <u>in the source</u> for several microseconds after the heating pulse is turned off in order, among other reasons, to allow the body to relax to a Maxwellian distribution and the hot tail to disappear from the plasma column. Such a time delay has not been applied for the temperature measurements <u>at the sensing resonator</u> and, therefore, leads to some uncertainty in the early time interpretation of the heat flow, although no increases of temperature at the sensing resonator are observed because of the hot electrons alone.

The results of our observations are shown in Figs. X-11, X-12, X-13, and X-14, together with solid and dashed curves that describe computational results. Figures X-11 and X-12 give the temperature measured by the sensing resonator as a function of time after microwave power is applied to the heating resonator. In this case, body heating was accomplished <u>above</u> the threshold for the parametric instabilities where a theoretical model for the anomalous heating source term is lacking. To make up for this, we fit the theoretical temperature curves to the actual temperature measured in the source shortly after the anomalous heating pulse is turned off. This procedure is illustrated in Fig. X-13, where time

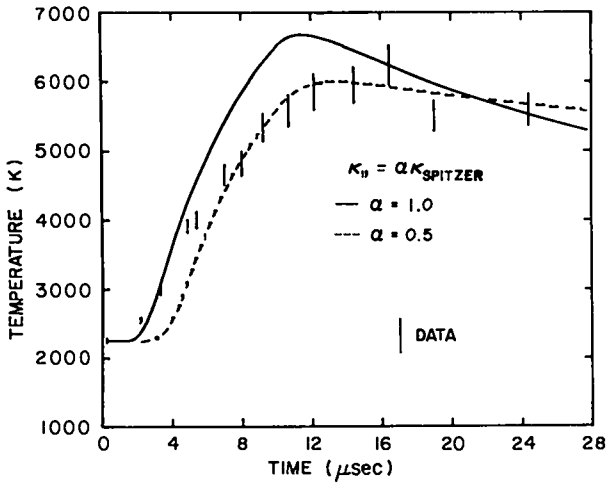

Fig. X-11.
Temperature vs time at the position of the dual mode resonator for the case of strong heating. Time is measured from the turn on of the heater. The solid and dashed lines are calculated from the heat flow code using source functions obtained from fits to the data in Fig. X-13.

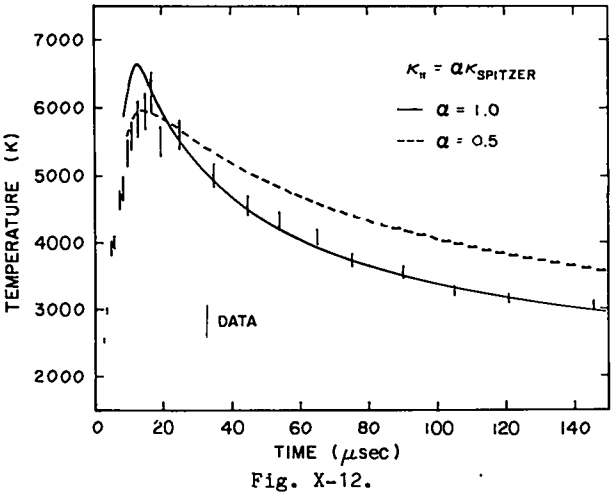

Fig. X-12.
Temperature vs time at the position of the dual mode resonator for the case of strong heating. Time is measured from the turn on of the heater. The solid and dashed lines are calculated from the heat flow code using source functions obtained from fits to the data in Fig. X-13.

is measured from the instant when the microwave power incident on the heating resonator is turned off. The earliest available time for a source temperature measurement is determined by the time required for the resonator field to decay below the level where it influences the electron-ion collision rate.[4] After the effective source strength has been determined in this way, we use

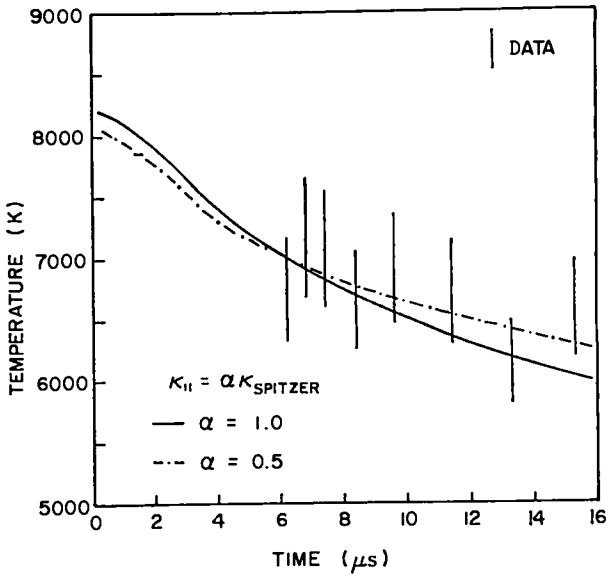

Fig. X-13.
Temperature vs time at the position of the heater. Time is measured from the turn off of the heater. The magnitude of the electric field in the resonator is adjusted to obtain the solid and dashed lines calculated by the heat flow code.

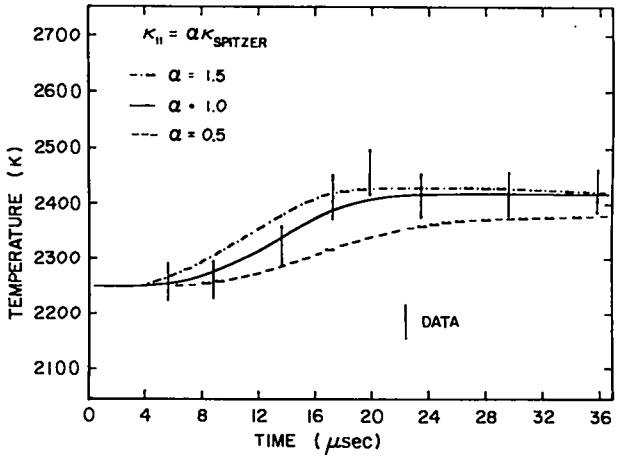

Fig. X-14.
Temperature vs time at the position of the dual mode resonator for the case of weak heating. Time is measured from the turn on of the heater.

it to compute the temperature as a function of time at the sensing resonator. The resulting comparison with the data shown in Figs. X-11 and X-12 indicates the possibility that we have begun to see an interesting effect. Note that the curve for $\alpha = 1$ fits the very early time data ($t < 4$ μs), but that later in time the data are better fitted by $\alpha = 0.5$. We see, also, that the

peak temperature reached at the sensing resonator more closely agrees with the $\alpha = 0.5$ prediction. However, if we look at later times (Fig. X-12), we see that again the $\alpha = 1$ curve clearly fits the observations better than the $\alpha = 0.5$ curve. This apparent change from the full Spitzer thermal conductivity to approximately half this value, and then back again, may be due to the passage of the temperature front through the sensing resonator with a large enough gradient to introduce new phenomena. That an appreciable gradient exists at early times is shown in Fig. X-15. Here we show the calculated temperature profile along the column at the times indicated. These times correspond directly to the times on Figs. X-11 and X-12. Of course, at later times (Fig. X-16) we see that the gradient becomes appreciably less. At some time shortly after 12 μs (Fig. X-16), the character of the solution to the heat flow equation changes to that of a nearly constant shape solution. It is interesting that this change in character occurs when we again observe agreement of our measurements with the full Spitzer thermal conductivity solution.

We have also made measurements for a lower level of heating when the ac parametric instability threshold is not exceeded. The result shown in Fig. X-14 is compared with curves calculated for $\alpha = 0.5$, 1, and 1.5. The full Spitzer thermal

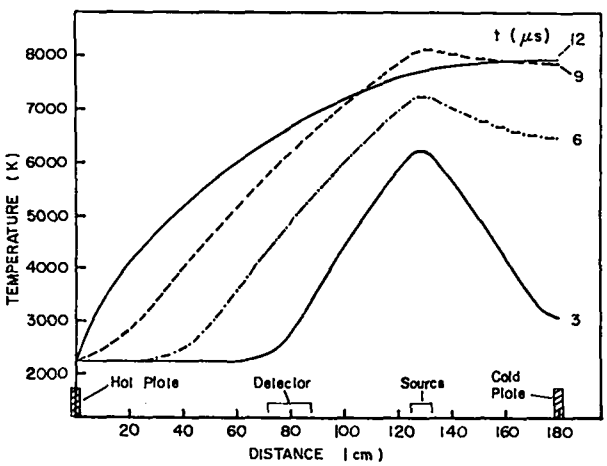

Fig. X-15.
Temperature vs position along the plasma column at the times indicated. Time is measured from the turn on of the heater. All calculations are the source in Fig. X-13 using the full Spitzer conductivity ($\alpha = 1.0$).

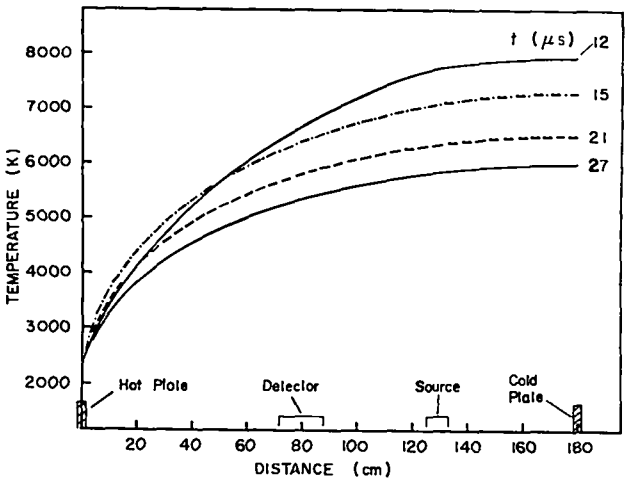

Fig. X-16.
Temperature vs position along the plasma column at the times indicated. Time is measured from the turn on of the heater. All calculations are for the source in Fig. X-13 using the full Spitzer conductivity ($\alpha = 1.0$).

conductivity (i.e. $\alpha = 1$) appears to fit the data adequately for all times and certainly better than either the $\alpha = 0.5$ or $\alpha = 1.5$ curve. Our thermal conduction experiments will have to be pursued for some time before some of the uncertainties described here can be resolved and before we have extended our measurements into the other areas of physical interest mentioned above.

3. Studies of the Transient Growth Phase of Parametric Instabilities. As part of our continuing program to understand in detail the interaction between electromagnetic waves and turbulent plasmas, we initiated a study this past year of the early transient growth phase of the oscillating-two-stream (O-T-S)[15] and parametric decay (P-D)[16] instabilities observed in our Q-machine experiments.[17]

A high Q resonator mode (TM_{010} mode with E_o parallel to the dc Magnetic field) is driven to a high power level by a short pulse (0.2 μs) of microwave power tuned to the resonator frequency. The resonator mode then acts as a pump for excitation of the instabilities. The peak pump power level in the resonator can be varied from below to far above (13 dB) the instability threshold. Following termination of the excitation pulse, the energy in the pump decays at a rate determined by the rate of transfer of energy to the plasma and to the resonator walls. When the pump power

exceeds the instability thresholds by a sufficient amount, we observe a sudden strong increase in the pump decay rate. The onset of this enhanced decay rate occurs earlier in time as the peak pump power is raised. Shortly after this strong pump absorption, or pump depletion, a burst of hot electrons is detected on probes located in the plasma column outside the resonator. Figure X-17 shows these effects for a case where the pump power reached a maximum of about 10 dB above threshold and where $\omega_p^2/\omega^2 = 0.90$. The decay of the microwave pump in the first 300 ns after the power reaches its maximum is determined by losses due to classical electron-ion collisions in the plasma and to skin-depth losses in the resonator walls. Following this period, the dramatic increase of the pump energy loss rate is observed, and about 200 ns later a burst of hot electrons is detected on a probe located 21.8 cm from the resonator center.

We have analyzed the longitudinal velocity distribution of the hot electron pulse using retarding potential probes. These velocity distributions have been corrected for electron time of flight from the resonator center, so that the electron velocity distribution in the center of the resonator was deduced as a function of time. The result is shown in Fig. X-18. We find the following characteristics for the hot electrons for the case of $\omega_p^2/\omega^2 \approx 0.90$: the density of hot electrons is a small fraction (less than one per cent) of the total electron density; for the cases with higher microwave powers, the total

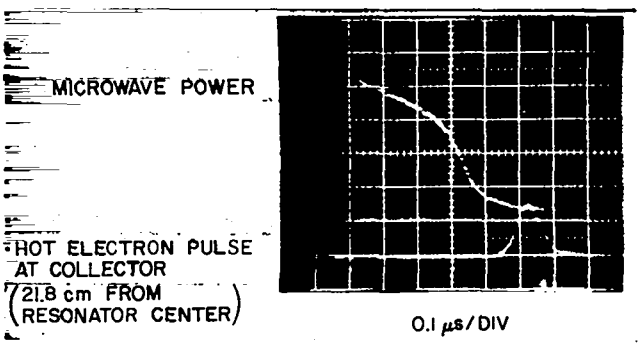

Fig. X-17.
Evolution of microwave power showing onset of strong enhanced absorption after the pulse excitation of the resonator. Note the appearance of the hot electrons after the strong absorption has occurred.

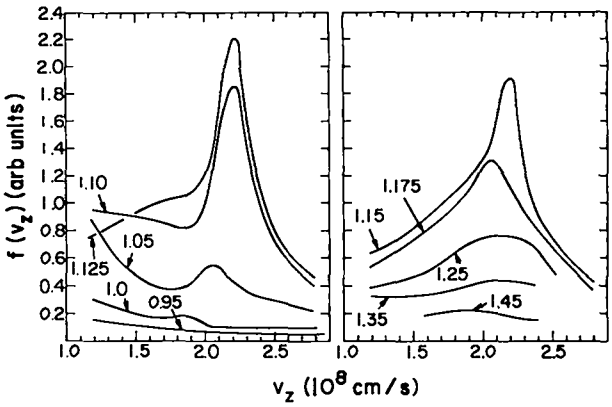

Fig. X-18.
Hot electron velocity distribution inside the resonator for different times (labelled in μs) during the hot electron production.

energy in these hot electrons accounts for all the microwave energy absorbed through the enhanced absorption process; and a pronounced bump in the tail of the electron velocity distribution develops as a result of the hot electrons. We have reported[14] similar results for the hot electrons produced during the nonlinear saturated steady state of the parametric instabilities. Another feature common to both the transient and steady-state observations is that the bump in the tail occurs at an electron velocity that is comparable to the phase velocity of the theoretically predicted most unstable electron wave. However, a bump-in-tail velocity distribution can also be created[18] if strong localizations of the unstable wave fields (spikons)[19] form in the plasma. Further work is required to determine the dominant mechanism producing the hot electrons.

The rate of hot electron power production can be computed as a function of time from the velocity distributions in Fig. X-18. This hot electron power, along with the enhanced, or anomalous, microwave power absorption is shown in Fig. X-19. The delay between the enhanced microwave absorption and the hot electron power production indicates that the microwave power does not go directly into hot electron production, but rather generates large amplitude plasma waves through the parametric process, which in turn evolve to a state in which they can rapidly deliver their energy to the electrons.

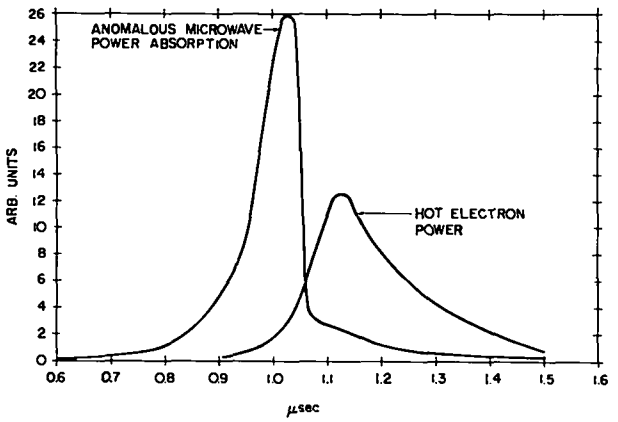

Fig. X-19.
Hot electron power and enhanced (or anomalous) microwave absorption as a function of time.

The absence of significant hot electron power production during the earlier times of enhanced microwave absorption, and the observation that plasma waves do not leak out of the resonator, suggests the following model for analysis of the period of time up to and during the enhanced microwave absorption: all microwave pump energy that is lost through the enhanced absorption process goes only into plasma wave energy localized in the resonator. (Energy in the ion waves that are also excited can be neglected because their frequency is much lower than that of the electron plasma wave.)

We have used this model to analyze the enhanced pump absorption from which we obtain growth rates and absolute amplitudes of the plasma waves. The plasma wave energy density is described by a single variable, E_W^2. In the case where only a single plasma wave mode is excited, E_W is the electric field of that wave. In general E_W^2 is an integral of the spectral energy density of the excited waves over all frequencies and wave vectors. The unstable waves are assumed to occupy a cylindrical volume within the plasma column of about 1-cm diameter (equal to the measured diameter over which the hot electron pulse appears) and of length equal to the resonator length. The pump field, E_O, fills the whole volume of the resonator. Two equations, the first describing the decay of energy in the pump mode (due to heating of the resonator walls, plasma heating through classical electron-ion collisions, and the growth of the plasma waves), the second equation describing the growth of the plasma waves, are used to analyze the measured pump decay. Figure X-20 shows the results of this analysis for a typical set of parameters. We observe that the deduced energy density in the plasma waves normalized to the energy density in the pump at threshold, E_W^2/E_{OT}^2, grows at late times to a value many times larger than the corresponding ratio for the pump energy density, E_O^2/E_{OT}^2, as well as being far above unity. Though at later times the instantaneous plasma wave energy density often exceeds the pump energy density by several factors of ten, we find after accounting for the large difference in volumes occupied by the two, that the total energy in the plasma waves is generally less than the total energy stored in the pump mode.

In spite of these very large wave energy densities, the rate of transfer of energy from the pump into these waves seems to be fairly well described by the linear parametric growth rate of the most unstable plasma wave. This is also shown in Fig. X-20 by the comparison between the measured wave energy growth rate and that computed from theory[20] for the O-T-S instability. In general, we find that the measured growth rates of the plasma wave energy are scattered about the

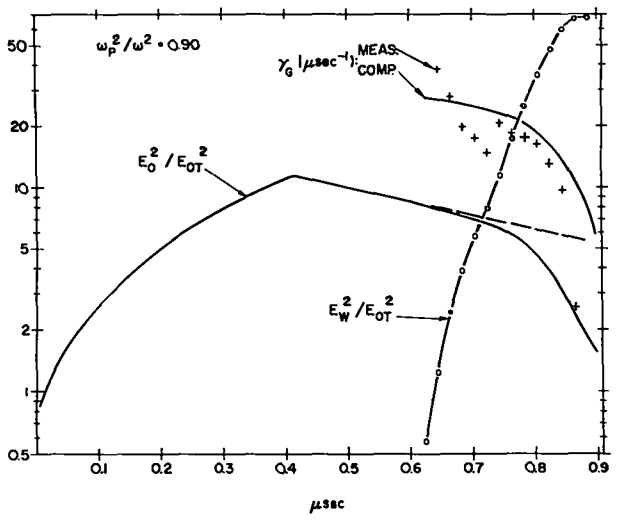

Fig. X-20.
Pump power ratio, unstable wave energy density, and growth rate as a function of time. Note that digitized data points of the pump power ratio have been replaced by a smooth curve for clarity.

computed linear growth rates for the O-T-S instability, and the P-D instability. The computed P-D growth rate is about 60 per cent of O-T-S growth rate, and the two instabilities have very nearly the same threshold for the conditions of our experiment. A summary of all measured growth rates and comparison with theory is given in Fig. X-21. In this figure the measured growth rates for values of $E_W^2/E_{OT}^2 \leq 5.0$ are plotted versus the instantaneous pump power ratio $P/P_T = E_0^2/E_{OT}^2$. The explicit time dependence of growth rates is suppressed by the presentation in Fig. X-21, since the growth rates are plotted versus pump power. However, this time dependence generally follows the trend shown in Fig. X-20: the growth rate at early times may be slightly greater than the O-T-S growth rate, and is less at later times.

Using this model, it is also possible to predict the time at which the enhanced pump absorption first becomes detectable, relative to the time at which the pump power first crosses threshold. This is done by assuming that the computed growth rate for the most unstable plasma wave evaluated at the instantaneous pump power applies at each time. It is then straightforward, having assumed an initial amplitude for E_W^2 at the time the pump crosses threshold, to numerically integrate the two equations for pump and plasma wave energy density. When the plasma wave energy density becomes large enough, the rate at which energy flows from the pump into these waves becomes comparable to the flow of pump energy into the resonator walls and into classical plasma heating, and thus becomes observable. In Fig. X-22 this type of analysis is shown for four different cases spanning a range of peak pump power ratios, P/P_T, from 4.4 to 14. The results of the model computations are shown as solid lines only after the time where enhanced absorption has become detectable. For the cases shown, the O-T-S growth rate was used in the computation, and two different initial amplitudes for E_W^2 differing by a factor of two were chosen, corresponding to the two solid lines of the model for each case. It is important to note that the same two initial amplitudes were used for each of the four cases. It is seen that for the lowest of the four peak pump powers, no measurable enhanced absorption is predicted, consistent with observation. As the peak pump power is increased, the predicted time

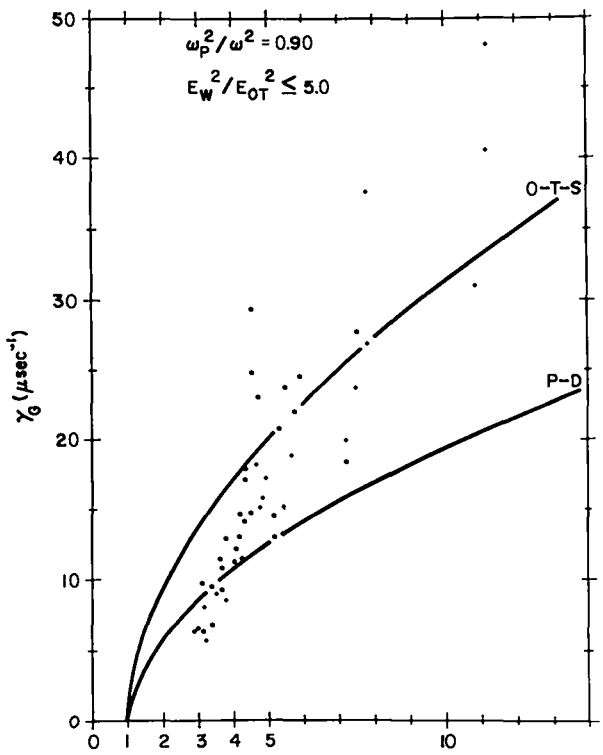

Fig. X-21.
Measured instability growth rates compared to computed growth rates for O-T-S and P-D instabilities.

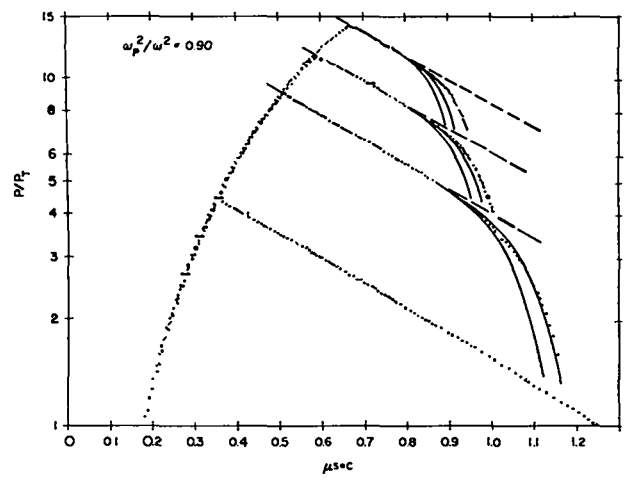

Fig. X-22.
Pump power ratio (P/P_T) as a function of time for four different cases showing predictions of model for time of onset and subsequent evolution of the enhanced pump absorption.

at which enhanced pump absorption is first detectable moves to earlier values, and reasonable quantitative agreement is seen here with the experimental results as well. However, the initial plasma wave energy density required to obtain this agreement with experiment is considerably larger than would be available from the naturally occurring thermal fluctuations of the electron plasma waves. This indicates that the initial amplitude of the plasma wave energy density is determined instead by the beating between the pump and the naturally occurring fluctuations of the ions.[21]

If the same integrations are carried out using instead the computed P-D growth rates, the required initial plasma wave energy densities are of the order of 500 times larger. This would indicate that the O-T-S instability dominates the early time behavior of enhanced absorption and hot electron production. However, in the nonlinear steady-state regime of the parametric instabilities, our spectral wave measurements[17] have shown that both instabilities are present.

Further study is planned in order to answer the questions about the transient growth phase of the parametric instabilities that have been raised by our results: we would like to understand the mechanism by which wave energy is transferred so efficiently to a bump in the tail of the electron velocity distribution. We would like to verify our notion that the O-T-S instability dominates the early time behavior. Further information is also required to determine whether or not the beating between the pump and the ion fluctuations controls the plasma wave amplitude at threshold. Finally, we need to understand the physical mechanism whereby the plasma wave energy densities can grow to the exceedingly large values deduced by us.

4. Absorption of a Weak Microwave Signal by Controlled Levels of Plasma Turbulence. The geometry of the dual-mode resonator we used (Fig. X-1) permits simultaneous application of two microwave fields near 2000 MHz to a common region of the plasma column. The two modes have $\vec{E}$ parallel to the external magnetic field, and their frequency separation in all work performed to date is roughly 15 MHz, which may be compared to the ion plasma frequency of 7.7 MHz or less in our experiment. This system has mostly been used for studies of the turbulent plasma state that is generated by parametric instabilities. In such studies, one mode (called the driver mode) is pulsed at field strengths above the threshold for parametric instability, causing a rapid growth of plasma fluctuations that leads to a saturated steady state. Simultaneously, the second mode (called the test mode) can be applied at very low power with a frequency 15 MHz above or below that of the driver field. By switching off the microwave sources at suitable times, we measure and compare the absorption rates of both fields: the absorption of the driver field is determined by nonlinear parametric effects, while the absorption of the test field is independent of test power but is influenced by the plasma fluctuations that are present.

Figure X-23 summarizes the general behavior seen during the saturated state after the driver field has been applied for a few microseconds. The quantity plotted is a measure of the total rate of microwave absorption by the plasma column. It is shown as a function of the driver power ($\propto E^2$) as measured in the saturated state and normalized to the threshold level required to drive parametric instabilities. For $P_{DRIVER} < P_{THRESHOLD}$ the measured absorption rate

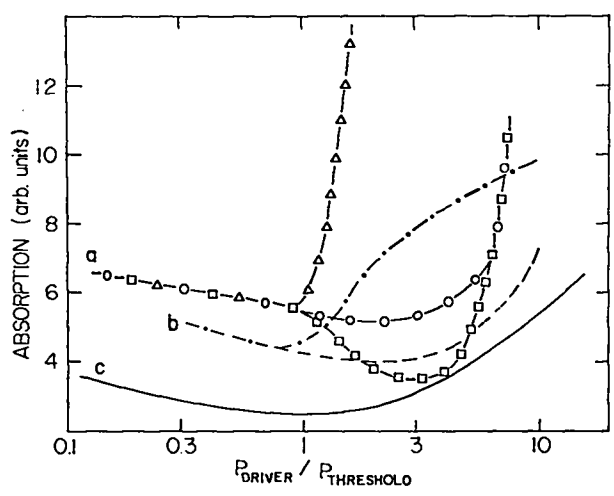

Fig. X-23.
Steady-state absorption rates as a function of the driver mode power with ω_p^2/ω^2 equal to (a) 0.91, (b) 0.76, and (c) 0.67.

of either the driver or test mode is due to classical electron-ion collisions, and is proportional to the square of the plasma density. A gradual decrease of absorption with increasing power in the driver pulse can be attributed to unavoidable electron heating that reduces ν_{ei}. For $P_{DRIVER} > P_{THRESHOLD}$ Fig. X-23 shows three types of behavior:

(a) Near the critical density ($\omega_p^2/\omega^2 = 0.91$) the threshold for instability is low, and the driver field absorption (triangles) is strongly enhanced by parametric instabilities. Absorption of the weak test field shows a comparable enhancement but at higher driver power. A test field 15 MHz below the driver frequency (circles) is clearly affected more strongly than one 15 MHz above the driver (squares). Indeed, our measurements indicate that the decreased absorption shown for the latter case is just collisional (with heated electrons) and that anomalous behavior does not occur until $P_{DRIVER} \gtrsim 3P_{THRESHOLD}$.

(b) At somewhat lower densities ($\omega_p^2/\omega^2 = 0.76$) the enhancement of driver field absorption (dots and dashes) occurs more gradually. The test field absorption (broken line) likewise shows milder behavior that does not depend upon whether it is above or below driver field in frequency.

(c) At still lower densities ($\omega_p^2/\omega^2 = 0.67$) the threshold for parametric instabilities is relatively high, and the driver field absorption shows no abrupt increase as that power level is exceeded. The gradual enhancement that is observed is essentially the same as for the test field (either above or below the driver frequency) and their common absorption rate is indicated by the solid line in the figure.

Our more recent work with the dual-mode resonator system has concentrated on transient phenomena during the initial period of rapid growth of plasma fluctuations when a destabilizing pump field is suddenly applied. The method used here is the same as that used in the transient studies of fluctuation growth rate and hot electron production described in Sec. B.3. It takes advantage of the time delay that occurs between the application of a strong microwave pump field to our plasma, and the growth of instabilities to the point where enhanced absorption of this pump field is observed. If the external source is switched off just after a strong microwave field is established in the resonator, the energy in that field can decay freely throughout the entire time that plasma waves grow to a level large enough to cause enhanced absorption. By analyzing the decay rate as was described in Sec. B.3, we establish a continuous record of the time dependence of the anomalous absorption in the pump field. In the context of the dual-mode system, the driver mode is used as the pump field described above while the test mode is simultaneously freely decaying at much lower power.

Figure X-24 illustrates the time histories of both test and driver fields in such an experiment. Again we plot measured power ($P \sim E^2$) normalized to the instability threshold (P_T). The test field is applied first, and at (1) it is freely decaying at a power level well below threshold. The external source for the driver field is switched off at (2), and even though it has been well above the threshold for some time, its initial decay is at the slow collisional rate. Eventually, at (3),

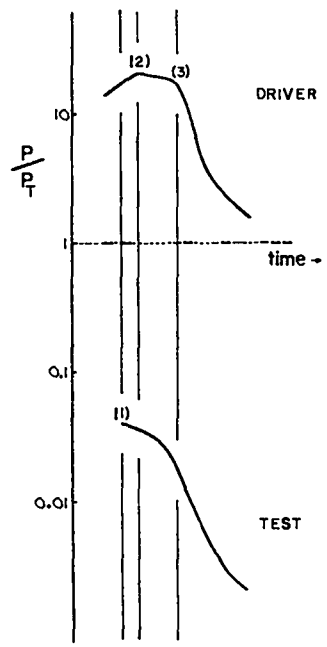

Fig. X-24.
Driver and test mode power vs time in a transient measurement of absorption rates. $\omega_p^2/\omega^2 = 0.85$ and $f_{test} = f_{driver} + 15$ MHz.

excited plasma waves have reached a level sufficient to promote enhanced absorption and a marked increase in the driver field decay rate. We note that the test field also exhibits enhanced absorption during this interval. Figure X-25 shows a comparison of the driver and test absorption rates obtained for this particular case. Here, as in the data discussed below, we have $\omega_p^2/\omega^2 = 0.85$, and the test field frequency is 15 MHz above that of the driver field.

In the course of our work we have varied the test field power level, P, from 0.001 to 0.55 times the threshold level, P_T, while keeping the driver strength substantially constant. Aside from shot-to-shot variations in the timing of these pulses, we see no significant change in the test field absorption over this range. We therefore conclude that (for $P < P_T$) the test field absorption rate is independent of test field strength.

On the other hand, as one would expect, the transient absorption rates are quite sensitive to changes in strength of the driver field that generates unstable fluctuations. Figure X-26 shows four different driver histories with different average amplitudes. The corresponding absorption rates are shown in Fig. X-27. We see

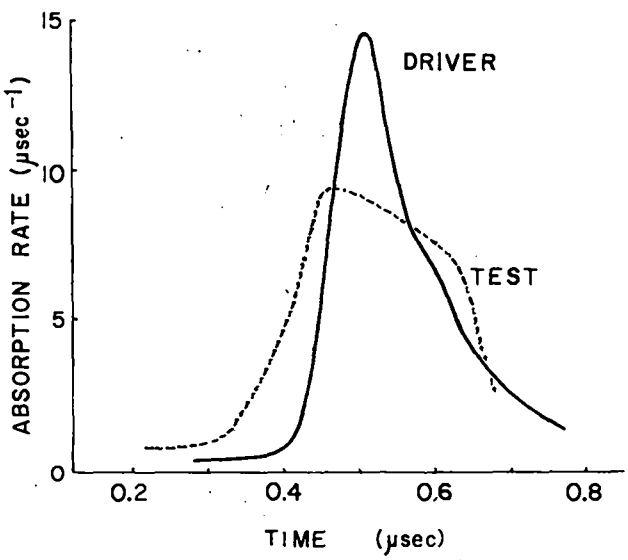

Fig. X-25.
A comparison of driver and test mode absorption rates based on the same data as the previous figure.

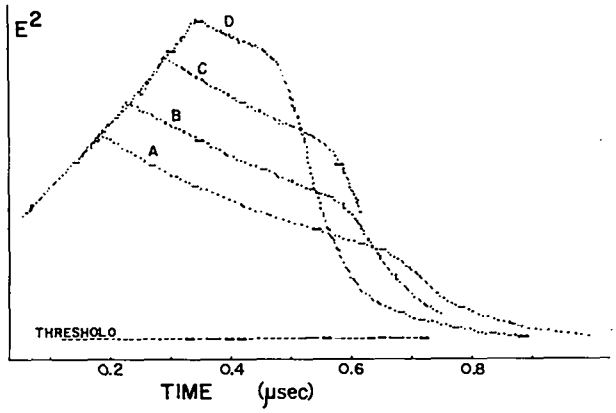

Fig. X-26.
Illustrating four different time histories of the driver pulse.

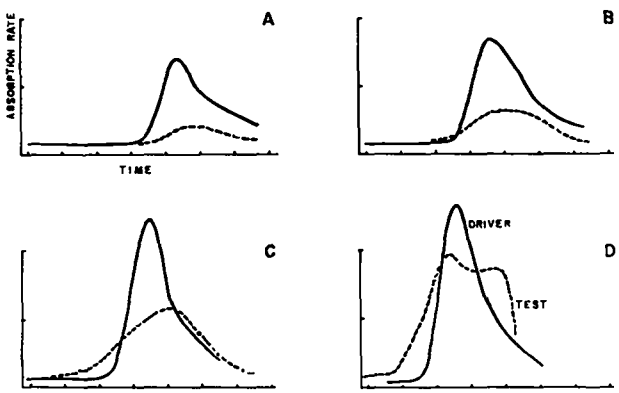

Fig. X-27.
A comparison of driver mode (solid line) and test mode (dashed line) absorption rates for the four different driver powers illustrated in the previous figure. $\omega_p^2/\omega^2 = 0.85$ and $f_{test} = f_{driver} + 15$ MHz.

that the enhancement of test field absorption is generally comparable to that of the driver, but its development is not the same. As the driver strength is increased, onset of the enhanced driver absorption tends to occur at a somewhat later time than that of the test field. This behavior is consistent with the notion that the level of plasma fluctuations required to affect the test field absorption is fixed, whereas the level required to affect the driver field absorption increases with driver power.

The experimental results discussed above show some differences between transient and steady-state phenomena, but it is felt that the underlying physical mechanisms are the same. A plausible model suggests that the enhanced test field

absorption results from an interaction of that field with the driven electron wave spectrum at frequencies in the vicinity of the test mode frequency. The interaction is one of induced parametric decay, but because the fluctuations are maintained by the driver, the absorption rate is independent of test field amplitude. If this view is correct, then our measurements of test field absorption in the steady state suggest a fluctuation spectrum centered somewhat below the driver frequency that broadens with increasing driver power, which is in agreement with our measured spectra of the parametrically excited electron plasma waves.[17] Interpretation of our transient results would require similar strong broadening of the spectrum during the period of growth--possibly as a consequence of the large natural line width associated with a large growth rate, as described in Sec. B.3.

C. PROGRESS ON AN EXPERIMENT FOR STUDYING NONLINEAR INTERACTIONS BETWEEN PLASMA AND TRAVELLING ELECTROMAGNETIC WAVES

In addition to the research on the Q-machine plasma, work is in progress on another plasma source. This is a permanent magnet multipole confined argon plasma device of the type developed by MacKenzie and coworkers[22] at UCLA. Experiments planned for this machine include an investigation of the "$2\omega_p$ instability"[23] in which a photon undergoes parametric decay into two plasmons, and also a study of heating a plasma using two electromagnetic waves whose beat frequency[24] is adjusted to correspond to a natural plasma resonance. Major distinctions between these experiments and those on the Q-machine are that these experiments are expected to involve travelling waves in a cylindrical waveguide, which is perforated to allow the plasma to penetrate, and that the plasma is essentially unmagnetized.

Detailed measurements of the microwave characteristics of the empty perforated 0.9-meter-long cylindrical waveguide have been made to allow comparison with the same characteristics when it is filled with plasma. We find that the guide, though constructed of copper mesh, still adequately confines microwaves. The proof of this is that with reflecting ends on the waveguide so that a cavity is formed, the measured Q is 2200. This means, of course, that only 4.5×10^{-4} of the stored energy is lost per cycle--an acceptable loss rate.

Since the experiments to be done with the waveguide involve travelling waves, the standing wave ratio (SWR) inside the waveguide should be as low as possible. It was found that the voltage SWR is tolerable (1.1-1.3) over a reasonably broad range of frequencies, and can be brought below 1.05 at a particular frequency with an external tuner.

The phase shift and attenuation dependencies on frequency have also been extensively documented and understood in the framework of theory. When plasma is present these relationships are expected to change and these changes can be accurately measured to provide information about the plasma density.

The plasma source (Fig. X-28) is a steady discharge in argon maintained by 18 thermionic tungsten filaments. The filaments are biased from -30 V to -80 V to provide an ionizing electron current. Confinement of these primary electrons and of the plasma is provided by a series of permanent magnetic line cusps around the cylinder periphery and at the ends. The perforated

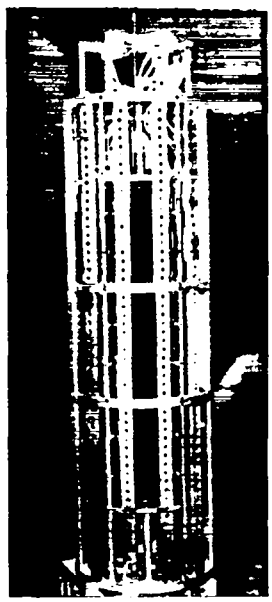

Fig. X-28.
View of the filament and magnet support cage with the 90-cm-long perforated waveguide in place.

waveguide is centered on the axis of the system where the magnetic field due to the multipole configuration is substantially lower (∿ a few gauss), thus allowing the microwave-plasma interactions to take place in an essentially magnetic-field-free plasma.

A systematic program is under way to understand this plasma source. Langmuir probe measurements of electron temperature T_e and density n_e have been made with and without the confining magnets. To date the waveguide has not been installed. Some results of the measurements obtained are shown in Fig. X-29, where electron density is plotted as a function of discharge current at an argon pressure of 10^{-3} torr. Data is shown for cases both with and without the confining magnets. Clearly, as reported elsewhere,[22] the magnets greatly enhance the plasma density for a given discharge current, although we have not determined which mechanism(s) (primary confinement, plasma confinement, electrostatic confinement) is responsible. Much smaller discharge currents have so far been used when the magnets were installed, because the filaments used were not thoriated as they were for the earlier studies when the magnets were absent. Thoriated tungsten filaments will again be used when the waveguide is installed.

Electron temperatures were also taken from the Langmuir traces, and generally it was found that there were two electron energy components to the distribution function. The main body of electrons had a temperature around 2 eV (with magnets), with a tail whose temperature was around 4 eV. At the higher densities the tail component took on the same temperature as the main body of electrons, usually between 1-2 eV.

Further, such studies will soon be carried out with the perforated waveguide in place, and following these studies we plan to begin investigation of the microwave plasma interaction.

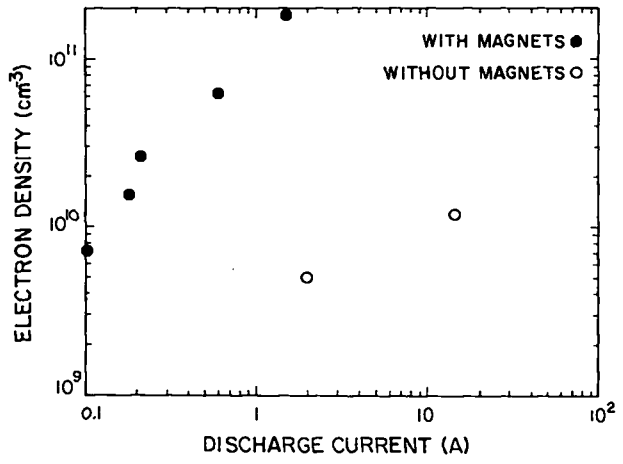

Fig. X-29.
Plot of electron density vs discharge current for 10^{-3} torr argon.

D. Q-MACHINE HOT PLATE DEVELOPMENT

Our present large, programmable hot plate structure, though it is working well, requires a long turn-around time for replacement. In order to reduce this turn-around time we have developed a simpler and smaller hot plate design, which is currently under test. The new design utilizes a smaller diameter filament structure patterned after our present conical design, but eliminates the intermediate hot plate, as well as the acceleration ring used to program the temperature profile of the main hot plate. Also, we used thoriated tungsten wires in the new design instead of a filament of tungsten foil. The support for the new 5-cm-diameter hot plate utilizes pointed tungsten rods, and is similar to that used in one of the designs at the Princeton Plasma Physics Laboratory. In order to reduce the accelerating voltage required on the filaments, a grounded acceleration structure is supported in the center of the conical filament structure. At a voltage of 2.9 kV and a current of 2.4 A the hot plate operates at 2400 K. After 200 hours of operation the hot plate was disassembled, and no deterioration of insulating or metal parts was noted.

Future studies of the hot plate structure will involve directing a beam of potassium atoms onto the hot plate surface in order to ascertain the quality of the plasma column thus produced.

REFERENCES

1. A. T. Lin, P. K. Kaw, and J. M. Dawson, "A Possible Plasma Laser," Phys. Rev. A 8, 2618 (1973).

2. A.A. Ivanov, J.N. Istomin, L.L. Kozorovitsky, and V. D. Rusanov, "Collisionless Heat Wave," Phys. Lett. 33A, 509 (1970).

3. L. Spitzer, Physics of Fully-Ionized Gases, Interscience Publishers, N.Y., 1956, p. 86.

4. J. H. Brownell, H. Dreicer, R. F. Ellis, and J. C. Ingraham, "Influence of Intense AC Electric Fields on the Electron-Ion Collision Rate in a Plasma," Phys. Rev. Lett. 33, 1210 (1974).

5. J. M. Dawson and C. R. Oberman, "High-Frequency Conductivity and the Emission and Absorption Coefficients of a Fully-Ionized Plasma," Phys. Fluids 5, 517 (1961).

6. R. Q. Twiss, "Radiation Transfer and the Possibility of Negative Absorption in Radio Astronomy," Austral. J. Phys. 11, 564 (1958).

7. P. F. Browne, "On the Origin of Radio Emission from Cosmic Gas Clouds," Astrophys. J. 134, 963 (1961); also 136, 442 (1962).

8. D. Marcuse, "Stimulated Emission of Bremsstrahlung," Bell System Tech. J. 41, 1557 (1962).

9. P. Mallozzi and H. Margenau, "Absorption Coefficient and Microwave Conductivity of Plasmas," Astrophys. J. 137, 851 (1963).

10. T. Musha and F. Yoshida, "Negative Absorption Due to Coulomb Scattering of an Electron Stream," Phys. Rev. 133, A 1303, (1964).

11. O. Buneman, "Instability, Turbulence, and Conductivity in Current-Carrying Plasma," Phys. Rev. Lett. 1, 8 (1958).

12. H. Dreicer, Martin E. Banton, J. C. Ingraham, and B. L. Wright, "Observation of Negative Inverse Bremsstrahlung Absorption Due to Large Electron Drift Speed," Bull. Amer. Phys. Soc. 22, 184 (1977).

13. H. Dreicer, "Electron and Ion Runaway in a Fully Ionized Gas," Phys. Rev. 115, 238 (1959).

14. H. Dreicer, R. F. Ellis, and J. C. Ingraham, "Hot Electron Production and Anomalous Microwave Absorption Near the Plasma Frequency," Phys. Rev. Lett. 31, 426 (1973).

15. K. Nishikawa, "Parametric Excitation of Coupled Waves-II. Parametric Plasmon-Phonon Interaction," J. Phys. Soc. Japan 24, 1152 (1968); P. K. Kaw and J. M. Dawson, "Laser-Induced Anomalous Heating of a Plasma," Phys. Fluids 12, 2586 (1969).

16. D. F. DuBois and M. V. Goldman, "Radiation-Induced Instability of Electron Plasma Oscillations," Phys. Rev. Lett. 14, 544 (1965); V. P. Silin, "Parametric Resonance in a Plasma," Zh. Ehsp. Teor. Fiz. 48, 1679 (1965) [Sov. Phys. JETP 21, 1127 (1965)].

17. J. C. Ingraham, H. Dreicer, and R. F. Ellis, "Spectral Observation of Electromagnetic Wave Decay Due to the OTS and Decay Parametric Instabilities," Bull. Amer. Phys. Soc. 20, 1361 (1975).

18. B. Bezzerides and D. F. DuBois, "Electron Heating and Landau Damping in Intense Localized Electric Fields," Phys. Rev. Lett. 34, 1381 (1975).

19. V. E. Zakharov, "Collapse of Langmuir Waves," Zh. Eksp. Teor. Fiz 62, 1745-1759 (May 1972), (JETP 35, 908 [1972]); G. J. Morales, Y. C. Lee, and R. B. White, "Nonlinear Schrödinger-Equation Model of the Oscillating Two-Stream Instability," Phys. Rev. Lett. 32, 457 (1974).

20. J. P. Freidberg and B. M. Marder, "High-Frequency Electrostatic Plasma Instabilities," Phys. Rev. 4A, 1549 (1971).

21. D.F. DuBois and M.V. Goldman, "Parametrically-Excited Plasma Fluctuations," Phys. Rev. 164, 207 (1967); D. F. DuBois and B. Bezzerides, "Critical Fluctuation Level for the Purely Growing Parametric Instability," RADC-TR-73-88 (February 1973), Appendix B.

22. Rudolf Limpaecher and K. R. MacKenzie, "Magnetic Multipole Containment of Large Uniform Collisionless Quiescent Plasmas," Rev. Sci. Instrum. 44, 726 (1973).

23. M. V. Goldman, "Threshold for Amplification of Plasmons," Annals of Phys. 38, 95 (1966); and E. A. Jackson, "Parametric Effects of Radiation on a Plasma," Phys. Rev. 153, 235 (1967).

24. V. Fuchs, C. R. Neufeld, J. Teichmann, and A. G. Englehardt, "Nonlinear Absorption of Radiation by Optical Mixing in a Plasma," Phys. Rev. Lett. 31, 1110 (1973), and references contained therein.

XI. PLASMA DIAGNOSTICS

R. E. Siemon, R. Kristal, K. B. Freese, P. R. Forman,
F. C. Jahoda, G. I. Chandler, M. D. Bausman, D. A. Platts

A. INTRODUCTION

The spatially resolved Thomson scattering experiment, incorporating a special design polychromator capable of extremely high rejection of stray laser light integrated with a digital camera under dedicated minicomputer control[1,2] has obtained data on the Scylla IV-P device. A description of the total system is given (Section B).

High frequency gas laser heterodyne interferometry[2] has been extended to the 3.39-μ infrared He-Ne laser wavelength, using the same lead molybdate acousto-optic cell as in the visible to produce the 100 MHz frequency difference between scene and reference beams. A new system under development is described that will utilize the high time resolution thus available for repeated spatial scanning of plasmas whose temporal changes occur on a microsecond time scale. A single scan would yield the same information as side-on HF holographic interferometry, but in an automated operation, and amenable also to discrete apertures as in a Z-pinch coil, where holography is inapplicable because of lack of fringe continuity. Repeated scans would approach the time resolution capability of a multi channel gas laser interferometry system with considerably less hardware and better spatial resolution. The initial system aims for 30 resolution spots in a 6-cm field of view within a total of 0.25 μs for $\int n_e d\ell \geq 10^{16}$ cm^{-2} (Section C).

A computerized plasma beta measurement system similar to the type used on Scyllac was developed for use on Scylla IV-P. This system incorporates the new luminosity profile measurement apparatus with zoom lens optics and improved photomultiplier detector as first described during its design phase.[2] Also, the numerical method used to fit the data was improved (Section D).

The last section of this chapter briefly summarizes various other diagnostics development activity: a) analog video recording of streak camera output for subsequent digitization, b) CO_2 holographic interferometer, c) three-pulse ruby laser, and d) far infrared diagnostics (Section E).

A substantial fraction of the Diagnostics Group effort centers on the use of minicomputers both for data acquisition and device control. This activity is reported in Section XIV.

B. SPATIALLY RESOLVED THOMSON SCATTERING

1. Basic Approach. This project is designed to detect spectrally dispersed plasma-scattered ruby laser light simultaneously from a large number of scattering volumes. In principle, this could be done with a two-dimensional array of very many photomultipliers, but a much better way is to use a television detector on which the data are arranged in a two-dimensional pattern, as originally proposed by Dimock and Bretz.[3]

The method for collecting the scattered light from an array of scattering volumes and resolving it into multiple wavelength channels is based on the fact that a grating polychrometer can be stigmatic. By stigmatic is meant that illumination of a single point on the entrance slit with white light gives a line at the output along which the various wavelengths are located. Each point on the entrance slit then corresponds to a different point in the plasma.

We apply this idea to a theta pinch by arranging for the scattering volume to be as narrow a band as possible perpendicular to the axis of the discharge tube. The incident laser beam goes through the discharge tube walls and through the plasma in the radial direction. The scattered light is collected with a lens that forms an image of the scattering volume onto the entrance slit of a stimatic polychrometer with high rejection ratio for stray light at the laser wavelength. At the output of the polychrometer there results a two-dimensional intensity pattern in which one direction represents wavelength and the other direction represents plasma radial position.

The pattern is recorded on the cathode of a television detector, gated on only while the laser is pulsing. The light intensity is thus converted to an array of electric charge. This charge array is then measured by a special digital television system on a slow time scale after the event and the data are transferred in the process directly to a minicomputer. The minicomputer is basically a high-speed data buffer and programmable control device which subsequently transfers the data to a larger computer for analysis.

2. Optical Design of Polychrometer. When the incident laser beam goes through the walls of the quartz discharge tube it generates a high level of stray light or background light. Since the stray light is monochromatic and the scattered light spectrum is broad, the stray light can be eliminated by the use of a 3-grating polychrometer.[4]

Figure XI-1 shows the optical arrangement of our specially designed polychrometer. The first two plane gratings from a prefilter that selects the portion of the spectrum to be detected and rejects the unwanted monochromatic stray laser light. The prefilter uses f/5 collimation lenses, which are readily available commercially.

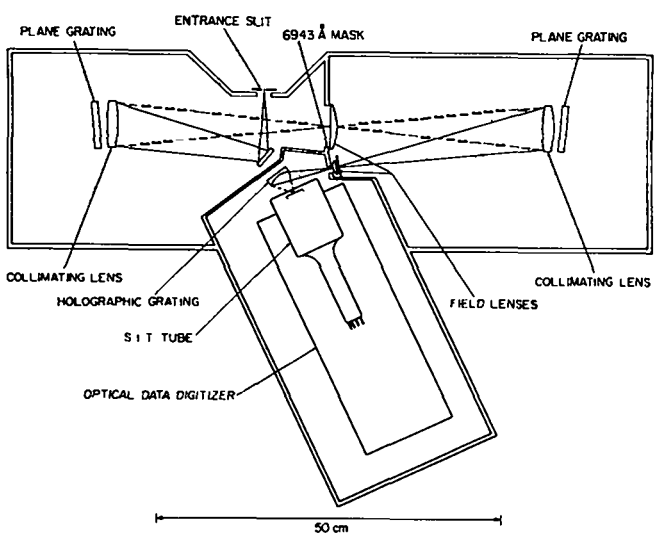

Figure XI-1
Three-grating polychrometer used for digital television system. Solid lines for light rays indicate a mixture of wavelengths, and dotted lines indicate a single wavelength. The SIT tube is shown without the additional gated image intensifier.

TABLE XI-I summarizes the parameters of these first two stages. The gratings, selected by the manufacturer to have low stray light and to be free of ghosts, are also readily available components.

The third stage grating is a custom holographic grating from J-Y Optical. Its purpose is to put as much intensity per unit area as possible onto the television detector. This implies using the maximum possible angle of illumination. As seen by the characteristics listed in TABLE XI-II, the holographic grating illuminates the cathode with an aperture of f/2 and forms an image well matched to the 25-mm-diameter television detector. The nominal values in the table are in good agreement with those obtained in practice although there are

TABLE XI-I

CHARACTERISTICS OF POLYCHROMETER TWO-STAGED PREFILTER

Entrance slit	2 mm x 40 mm
Collimating lenses	f/4.8
focal length	31.7
diameter	66 mm
Plane gratings	600 groves/mm
size	64 x 64 mm
Linear dispersion	50 Å/mm
Resolution (2-mm slit)	100 Å
Spectral band pass	4600-6800 Å (2200 Å)
Transmission of spectrum	~ 0.5
Transmission of 6943 A	$< 10^{-7}$

TABLE XI-II

CHARACTERISTICS OF HOLOGRAPHIC GRATING STAGE

Entrance slit (@ f/4.8)	2 mm x 40 mm
Image on detector	
Aperture	f/2.0
Linear dispersion	150 Å/mm
Width of spectrum	14.6 mm
Demagnified slit size	0.8 mm x 16 mm
Resolution	120 Å
Transmission of spectrum	~ 0.2
Stray light due to 6943 A	$< 10^{-3}$

significant optical distortions as explained below in the section on system calibration.

3. Television Detector. As originally designed, the RAC 4826 SIT camera tube was also to perform the shutter function. It was, however, found inadequate for this because the shutter ratio, ~ 10^{-3}, (signal in response to light when gated off compared to signal when gated on) was not small enough. To improve the shutter ratio and insure enough detector gain, a first stage ITT microchannel plate image intensifier as shown in Fig. XI-2 was added. The combined system has acceptable characteristics in all respects as listed in TABLE XI-III.

The internal operation begins with photoelectron emission due to light incident from the right in Fig. XI-2. When the intensifier is gated on, the photoelectrons are transmitted and

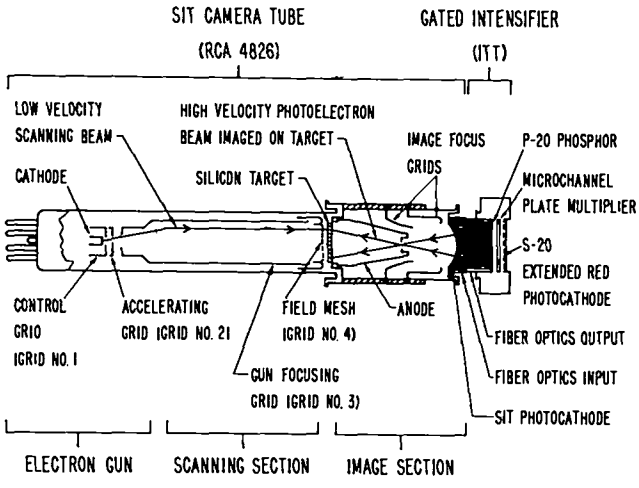

Figure XI-2
Combined RCA television camera tube and ITT microchannel plate intensifier.

TABLE XI-III

DETECTOR CHARACTERISTICS

Spectral response	S-20
Detector diameter	25 mm
Pixel size (minimum spot resolvable)	150 μm
Sensitivity	Quantum limited
Gain	Variable over wide range
Gate duration	50 ns or more
Shutter ratio	10^{-6}

amplified 10 to 1000 times by the microchannel plate. They are then accelerated to the P-20 phosphor of the intensifier, which emits light, coupled by fiber optics, to the S-20 cathode of the SIT (Silicon-Intensified-Target) camera tube. Photoelectrons from the SIT tube are accelerated by a high potential and are electrostatically imaged on a silicon target. The impact of an energetic electron (4-10 keV) gives rise to many electron-hole pairs resulting in a further amplification of 10-1000.

The final pattern of charge, representing the incident intensity pattern on the cathode, persists until it decays due to dark current. Since the camera operates at room temperature, the image decays in a few seconds. The spatial resolution of the electronic detector system is limited by the properties of the low-velocity electron beam used to read out the stored charge pattern. The electron gun and scanning section of the camera tube shown on the left in Fig. XI-2 are operated by the electronic system described in the next section. Although many variables are involved in characterizing the read-out properties, a typical spot size for the electron beam on the silicon target is 100 μm -- corresponding to 150 μm on the cathode because of a slight demagnification in the electrostatic image section. The pixel size or minimum-sized picture element is thus listed in TABLE XI-1I1 as 150 μs. The electron beam limitation is worse than the limitation imposed by the channel plate structure (~ 70 μm) or the finite diode structure of the silicon target (~ 20 μm). The final system spatial resolution is actually limited by aberrations in the holographic grating to be about 400 μm so the detector resolution is more than adequate for the application.

4. Electronic System. The read-out of charge from the silicon target is performed by a commercial instrument known as an optical data digitizer (ODD) made by EMR Photoelectric. The mode of operation, unlike conventional television, is one in which an arbitrary location on the screen is sampled with a short duration pulse of the low-velocity electron beam. The resulting pulse of video signal is amplified and digitized

before proceeding to another point on the screen. The procedure is executed under computer control, giving a great deal of flexibility in the manner by which data are acquired. A 12-bit X-address is transferred by a load X-pulse and a 12-bit Y-address is transferred by a load Y-pulse. As the current in the deflection yokes is changing, a "not ready" flag is raised. Small steps in position settle in a few microseconds but changing from one side of the silicon target to the other can take 50 microseconds. After the deflection yokes settle, a sample command can be issued, which causes the ODD to turn on the read beam for 1 microsecond and then to digitize the video pulse. The 8-bit intensity appears on the output lines in a few microseconds and is signaled as ready on a "ready" line from the analog-to-digitial converter.

If the ODD were the only limitation, a point could be sampled (for small deflections) every 7 μs. The sample times are important because they determine the fraction of the screen that can be read before dark current destroys the signal. We will return to this point in the section on future improvements.

Some limitations in the system result from the ODD pulsed mode of operation. The details of how the electron beam lands on the silicon target and generates the video signal are not fully understood. While it is well established that the charge on the target is proportional to the incident light intensity, the peak of video current sensed during the ODD sample pulse is, unfortunately, not perfectly proportional to the stored charge. There results a non linearity in the observed signal vs light level that must be removed by calibration. Furthermore, the calibration varies from one point on the screen to another. These effects lead to corrections as large as 25%. However, the combination of computer control and the convenient fact that dark current generates a signal that increases linearly with time can be used to calibrate the system automatically. Experience shows that the calibration is good to 5% or better and is stable for many months if the various parameters such as focus current and grid voltages are left unchanged.

In addition to the ODD there have been several important electronic developments required for the system. The SIT tube requires up to 10 kV for operation and the intensifier requires 5 kV. The SIT cathode and intensifier phosphor are connected by fiber optics that can tolerate no voltage differential so that a 15-kV supply is required for the combined detector. Furthermore, gating pulses must be capacitively coupled to the high-voltage electrodes in the detector. The complicated divider chain required for this application must be designed with the additional constraint that there be no excessive voltage transients on various of the sensitive elements in the intensifier during turn-on and turn-off. The main gating pulse is a fast-rising 200-volt pulse of 100-ns duration.

5. Computer Configuration. For the ODD control computer, a Prime Model 100 is used with the following hardware options: 1) 16K memory, 2) terminal control board, 3) general-purpose input-output board for control of the ODD, 4) a dual floppy disk drive and controller, and 5) a CAMAC controller. The system represents a small but very powerful stand-alone disk-based system. One of the two floppy disks is devoted to system software consisting of: 1) a disk operating system (DOS), 2) an assembly language assembler, 3) an editor, 4) a FORTRAN compiler, and 5) the usual assortment of LOADER, file management utilities, FORTRAN library, etc. The other floppy disk is interchanged often and is used for ODD software development and data storage.

Figure XI-3 shows the hardware arrangement as it is used in the Scylla IV-P experiment. The Scylla IV-P control computer is a Prime Model 300, which will soon be linked to the CTR Division PDP-10. The bulk of the data analysis will be performed on the PDP-10.

The system is interfaced to the Prime 300 through CAMAC, which means the system can be easily transported to another experiment if that becomes desirable. The CAMAC crate also permits the use of stepping motor controllers for a position and wavelength variable calibration light source. It also provides a versatile link for future modifications.

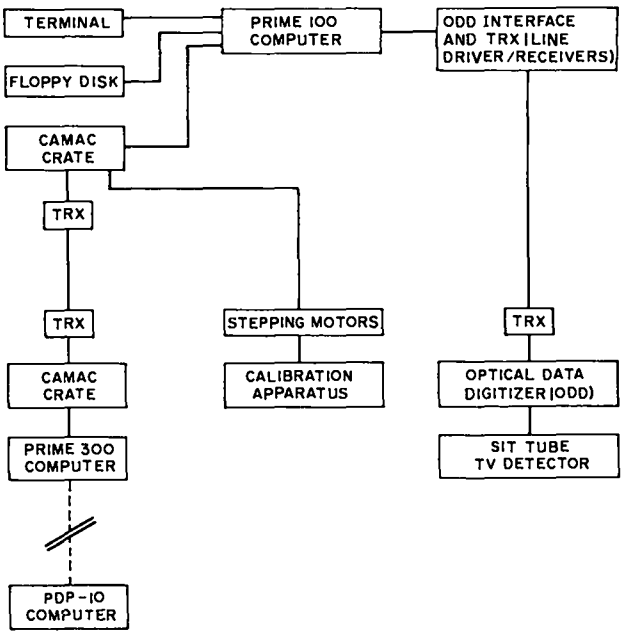

Figure XI-3
Computer hardware configuration for digitial television operation.

The ODD interface and long-line driver connect the general-purpose I/O board of the Prime 100 to the ODD, which is located at the end of long cables in the vicinity of the experiment. The ODD interface was designed and built before a control computer was obtained and also permits limited operation of the ODD independent of the Prime 100. This has proven to be an invaluable maintenance tool.

6. System Operation and Calibration. The system is presently operated and synchronized to Scylla IV-P as follows: Three seconds before a plasma discharge, a signal from the Prime 300 control computer is delivered to the ODD interface where it is detected as a flag to begin the control program. An erase mode is initiated for the ODD whereby the low velocity electron beam is swept over the silicon target, bringing it to a uniform potential. This erase continues until 5 milliseconds before the plasma discharge at which time a pulse from the Winston pulser sets a second flag in the ODD interface, causing the program to stop the erase and pause while the ODD relays settle and the plasma event occurs. During the plasma discharge the ruby laser is pulsed and, with suitable delays, the detector is gated in synchronization with the scattered light. After a programmed delay of 10 milliseconds (5 milliseconds after the plasma event), when the electrical transients from the bank discharge have disappeared, the ODD operation begins. In the operation to date, 600 pixels, representing 30 spatial positions and 20 wavelength channels, are sampled.

There are two types of calibration required for the instrument. The first (intensity calibration) involves making quantitative determination of the incident light intensity given the digital signal on a particular pixel. The second (spatial-wavelength calibration) involves determining the wavelength and plasma position to associate with each pixel.

The intensity calibration is conveniently subdivided into a linearity curve and a relative response number. Experiments have shown that for a particular setting of ODD controls, each pixel can be calibrated with a curve of output signal vs stored charge. The charge is introduced with dark current and varied by the duration of time between erase and read. The response relative to other pixels for a particular setting of amplification on the intensifier and SIT is obtained using a light source uniform in space and with known spectral composition. The relative sensitivity is affected by the intensifier uniformity, the SIT cathode uniformity, and the read-beam process. The intensifier gain setting is often varied and displays some small drifts, so it is necessary to determine the relative sensitivity calibration frequently (ideally after every plasma discharge). The linearity curve and spatial-wavelength calibration need to be determined much less frequently.

The spatial-wavelength calibration is obtained by varying in turn the wavelength and position of a small monochromatic light source and observing what area on the screen responds. We are working on an automatic process to perform this calibration using computer controlled stepping motors to vary the wavelength and position of the source, but to date the calibration has been obtained manually.

Figure XI-4 shows a typical spatial-wavelength calibration in terms of the 4096 IX and IY address coordinates used by the ODD. Each vertical curved line represents a particular wavelength channel with red on the left and green on the right. The width of each line is the full-width half-max distribution of intensity for monochromatic illumination. The horizontal lines represent the response to white light at particular points along the entrance slit. Again, their width is proportional to the width of the distribution on the screen. The curvatures and complicated distributions of light on the screen are primarily due to distortions from the holographic grating. Although complicated at first glance, they are readily accounted for in the analysis using the calibration data. The spatial and wavelength resolutions are also determined in this process. Spatial displacement of about 1 mm along the entrance slit and wavelength differences of about 150 A are resolved. Since this instrument was designed for plasmas with temperatures greater than about 200 eV, these are acceptable characteristics and very nearly what was sought in the original design.

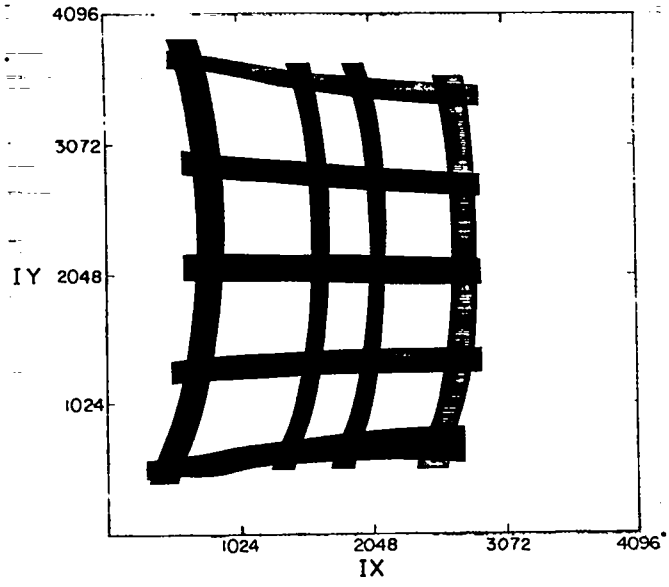

Figure XI-4
Typical wavelength and position calibration of system. Distortions are primarily optical effects from the holographic grating.

7. Temperature Measurements on Scylla IV-P. During the months of October and November, 1976, the instrument was installed and operated on Scylla IV-P. After the usual difficulties of cabling and interfacing between a complex instrument and an experiment were overcome, we obtained the most needed result of the preliminary experiment, the shielding was sufficient to permit operation in the theta-pinch environment. Because of the complex transistor and integrated circuit electronics used by the ODD, which necessarily sits a few feet from the theta-pinch column, we had been concerned that voltage transients might damage the instrument despite our efforts to carefully shield the electronics. Fortunately, that was not the case.

Data were obtained on a few main-bank discharges, and a temperature profile is shown in Fig. XI-5 for a spatial channel near the maximum density. Data analysis was limited because the link from the Prime 100 to the Prime 300 was not active due to software problems at the time the data were obtained. Nevertheless, a simplified analysis of a few points, and study of the data obtained, show the main features of the results.

The radial density profile was readily discerned and is in general agreement with interferometry and luminosity profiles. The temperatures measured are somewhat larger than

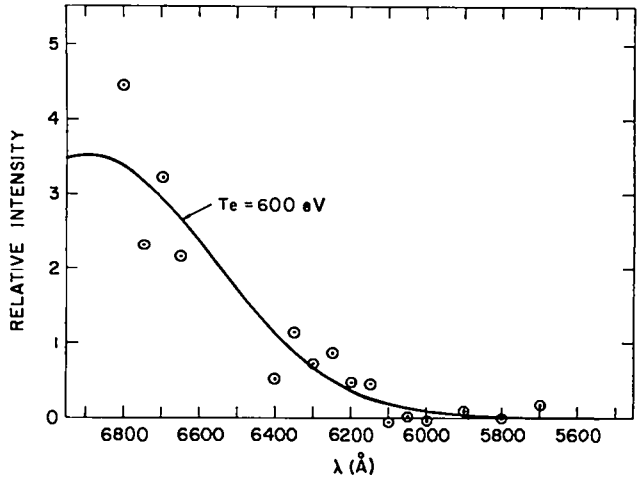

Figure XI-5
Profile of scattered light intensity vs wavelength near the center of the density profile on Scylla IV-P. Solid curve is a least squares fit to a theoretical profile corresponding to 600 eV.

expected from the Morse thermal conduction model,[5] but the data are too preliminary for conclusions to be drawn.

8. Future Improvements. The data illustrated in Fig. XI-5 show the general feature that the signal-to-noise is rather poor. This is explained as follows: The noise is a result of photoelectron statistics. Whereas the total number of photoelectrons on the target is about 10^5-10^6, each pixel samples an area of about 10^{-4} of the total area and thus only 10-100 p.e.'s contribute to the signal for a given pixel. At the present time, we read 600 points located at the intersections of 20 wavelength and 30 position channels, a few of which are shown on Fig. XI-4. In the original planning we had intended to deliberately defocus the read beam to permit each pixel to sample a larger fraction of the screen. That turned out to be impractical because severe variations arise in the screen uniformity and intensity calibration when the beam is defocused the desired amount.

Our first plan to improve the statistics will be to read 10,000 points rather than 600. This will permit averaging of approximately 16 points to determine the intensity at any given wavelength and position which should reduce the noise level by a factor of 4.

Reading 10,000 points will, however, require 10^4 x 50 μs or 0.5 seconds, which means dark current will affect the signal. We will compensate for dark current by reading in the same pattern each time so that the dark current contribution can be predicted and, therefore, subtracted from the data. Secondly, we will make use of the fact that some areas of the screen respond with less sensitivity and can thus be read last without the signal reaching full scale due to dark current.

Other possibilities are to cool the detector to reduce dark current or to reduce the reading time per point from 50 μs to the ODD limit of 7 μs.

Our conclusions are that the system has proven to be workable and continues to hold promise as a most significant diagnostic. Some improvements are called for, but the flexible nature of the programmable control computer make many modifications straightforward and easily iterated. Significant work remains to be done in the area of software development for data analysis. Fortunately, the imminent link to the PDP-10 computer will greatly facilitate this portion of the work.

C. HETERODYNE INTERFEROMETRY

1. Basic Approach. A scanning heterodyne interferometer is under development for obtaining high-resolution, sequential density profiles of pulsed fusion plasma during a single discharge. The technique combines the periodic self-calibrating feature of the heterodyne approach with a high-speed spatial scanning device to effectively convert temporal fringes to spatial fringes. The system is designed for plasmas for which $(n_e \ell)_{max} > 10^{16}$ cm^{-2} and which have a time scale of several microseconds.

Spatial scanning is accomplished with a turbine rotating mirror (10^4 rps), which is imaged onto a Ge:Hg detector. The system is designed to scan a 6-cm field with 2-mm resolution in 0.25 μs using the 3.39-μm line from a He-Ne laser. The heterodyne signal is obtained from a 100-MHz frequency difference between scene and reference beams generated by a lead molybdate acousto-optic cell. To reduce spurious differential phase shifts during the scan, and to improve signal-to-noise ratio, both scene and reference beams are swept by the same rotating mirror. Each of several consecutive scans contains ~ 25 fringes (10-ns period), which is compatible with the spatial resolution. The expected phase resolution in double-pass mode is 0.1 fringe.

The system has the advantage of requiring only a single signal channel to get multiple spatial profiles in contrast to multiple beam systems. However, it also requires a bandwidth (150 MHz in this case) much larger than the basic plasma data rate.

A prototype has been assembled with only a single facet high-speed mirror. A full scene beam scan of 5.5 cm has been obtained with resolution better than 2 mm at one-half the full design scanning speed so far. Heterodyning at 100 MHz has been accomplished so far only with stationary scene and reference beams, but with adequate

contrast and signal-to-noise ratio. Further detail and design considerations are given in the following sections.

2. IR Heterodyning Using Lead Molybdate.

The acousto-optic material used in the previous work in the visible was lead molybdate ($PbMoO_4$). Since this material is transparent at 4 μs, it was decided to try using the cell at this wavelength. The basic question was one of power level. For a given interaction configuration and diffraction efficiency, the required acoustic power, P, scales as λ^2. A power level of ~ 50 w is therefore required at 3.4 μ. To avoid destroying the cell by excessive heat deposition, it was decided to pulse the system with a low (< 5%) duty cycle. The test setup is shown in Fig. XI-6. The incident IR beam is focused to < 1 mm inside the cell. Because of the longer wavelength, both the Bragg and diffraction angles are quite large; separation between the zero and first orders is ~ 6°. The two orders are recollimated and combined on a beamsplitter, which is angularly adjusted for good interference. A short focal length lens focuses the resultant beam on the rather small (0.02 mm^2 active area) indium arsenide detector. The detector is a Judson Model J-12LD, which nominally has a 5-ns rise time. Aside from a bias circuit, it connects directly to the 7844 scope. The rf drive power for the cell (at ~ 100 MHz) is pulsed by a rf switch controlled by a pulse generator.

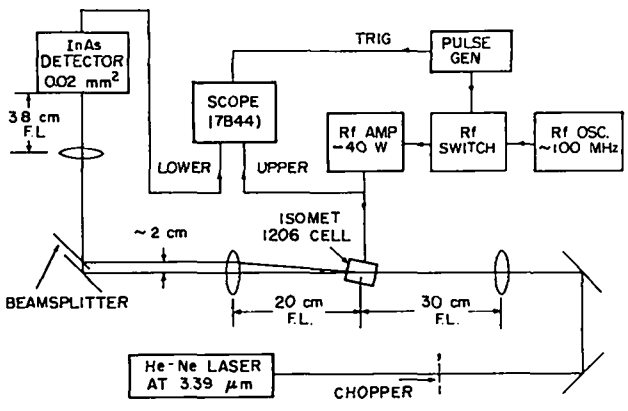

Figure XI-6
Infrared heterodyne test setup.

Results are shown in Fig. XI-7. Figure XI-7a shows the zero order (rf off) chopped mechanically. The modulation of the zero order by the comparison to be ~ 40 μs wide) is shown in the upper trace in Fig. XI-7b. A delay of ~ 1.5 μs is evident between the rf and optical pulses due to the acoustic transit time in the cell. A corresponding photo of the first order is shown in Fig. XI-7c. The lower amplitude is due to the poor beamsplitter used. The signal direction, of course, is opposite that of the zero order. The interference signal with both beams recombined on the detector is shown in Fig. XI-7e, showing the beat at 107 MHz. The beat amplitude is only about 40% of what it should be based on the amplitudes of the individual beams. This is most probably due to inadequate detector


Fig. 7a


Fig. 7b.

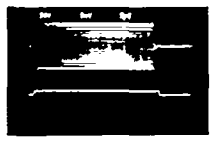
Fig. 7c.


Fig. 7d.


Fig. 7e.

Figure XI-7
7a. Zero order beam, mechanically chopped (no rf on cell). 7b. Upper trace: RF pulse. Lower trace: zero order (base line represents zero signal). 7c. Upper trace: RF pulse. Lower trace: First order (base line represents zero signal). 7d. Upper trace: RF pulse. Lower trace: Heterodyne signal. 7e. Same as Fig. 7d with expanded time base.

bandwidth. A much faster detector is used in the system application discussed next.

3. Rapid Scan Heterodyne Interferometer

a. Scanning Requirements. For application to a theta- or Z-pinch the principal factor determining the allowed scan time is MHD plasma motion (rather than e.g., decay due to end loss). The scan time must be such that negligible plasma motion occurs during the scan. Since typical diameters (1/e point) for a theta pinch are ~ 2-3 cm and typical velocities are ~ 0.5 cm/μs, then for the motion to be less than 10% of the size requires a scan time < 0.4 μs. Another important factor in scanning is the resolution. A resolution of 10% of the column diameter (~ 2 mm) would seem to be the minimum acceptable. Field coverage is determined by the uncertainty in plasma location within the discharge tube; a scan field of at least 5 cm is needed based on previous experience with HF laser interferometry on Scyllac. These requirements may be restated in terms of a scan rate--at least 60 spots/μs, and a field of at least 25 spots are required. These are fairly severe restrictions, especially at 3.4 μ where diffraction limited beam divergence is ~ 6 times greater than in the visible. After perusal of various techniques (including acousto-optic, electro-optic, and vibrational), the high-speed turbine mirror seemed to be the best solution. Turbine mirror technology is highly developed and many devices are still in use in high-solution streak photography. Use has been made of this fact in acquiring a 10,000 rps beryllium mirror on loan from Group M-3. The mirror has a usable dimension in the scan direction of ~ 11 mm, which, even with a deflection angle of 90°, allows diffraction limited beam divergence (2 λ/d) of ~ 140 spots/μs at this wavelength, or about double the required rate. In particular, the field will be chosen to be ~ 6 cm, the resolution aimed for ~ 1.8 mm, and total scan time (full field) will be ~ 0.25 μs, giving ~ 130 spots/μs. This further reduction of the total scan time also helps keep the number of fringes on the recording oscilloscope down to a reasonable value. A scan of ~ 25 fringes total is still compatible with the spatial resolution requirement.

Scanning of the plasma column could be done by scanning either the scene or reference beam or both. However, scanning either beam alone would probably introduce substantial differential phase shifts just from the scanning mechanism, resulting in a highly distorted fringe pattern. In addition, if only the reference beam were scanned, the scene beam would have to cover the entire field, which would seriously reduce the beat signal strength. For these reasons, a geometry has been chosen in which both scene and reference beams are reflected off the high-speed turbine mirror.

It is useful to note that this technique does not require a clear view of the object for all points in the scan field. For example, in applying this technique to a toroidal Z-pinch, where axial current flow in the coil prevents the cutting of a continuous viewing slit, holes spaced at the resolution interval may be used. In this case, the scan rate would be adjusted so that at least one entire fringe can be observed per resolution element. The fringe pattern would then be a square wave modulated sine wave, but the data would still be analyzed in the usual way. One would only need to be satisfied that one or more fringes were not accumulated in the space between holes due to the plasma. In addition, discrete electro-optical beam switching could possibly replace the mechanical scan.

b. System Description. An optical schematic of the proposed system is shown in Fig. XI-8, and a plan view of various parts appears in Fig. XI-9. The zero and first-order beams out of the A-O cell become the scene and reference beams. They propagate parallel to each other, but displace in a direction parallel to the axis of rotation of the turbine mirror. The mirror is 25 mm long and the beams are displaced by ~ 15 mm, allowing for beam expansion. The particular rotor in hand has only one mirror facet so that multiple scans require splitting off part of the beam for scanning at a somewhat different time in the mirror cycle. Typically, ~ 4 μs requires ~ 15° beam separation.

The angular beam scan imparted by the rotor is converted to a linear scan by the scan lens. The aperture stop (the largest dimension

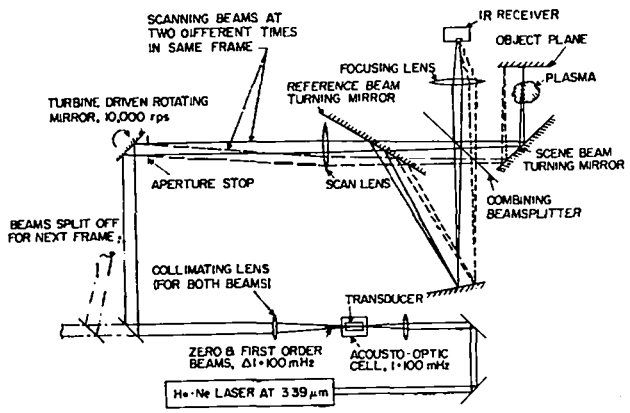

Figure XI-8
Simplified schematic of rapid scanning double-pass infrared heterodyne interferometer.

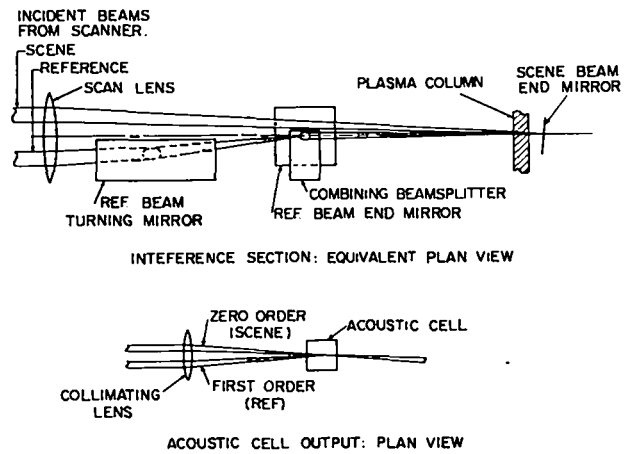

Figure XI-9
Interference section and acoustic cell output section of the scanning double-pass infrared heterodyne interferometer.

completely filled for all beam positions) is placed at the front focal plane of the scan lens. The beams then propagate in double pass fashion through the scene and reference arms and are recombined on a beamsplitter. The beamsplitter is adjusted for high contrast (large fringe spacing in the spatial pattern) and the recombined, scanning beams are focused onto the detector. The combination of scan and focus lenses image the aperture stop onto the detector. In this way, even though the beams are scanning, there is no spot motion across the detector. Since the scanning beams are collimated on the turbine, the scan lens brings them to a focus near its rear focal plane. The return mirror in each arm is then placed at this point, which is also physically close to the plasma. The spatial resolution is then approximately the focused spot size. With a 2-meter FL scan lens, the resolution is then ~ 1.5-2 mm. The linear beam displacement across the scan lens, FL x θ is then ~ 6 cm in 1/4 μs.

In imaging the aperture stop on the detector, considerable reduction must be used. This is because fast, sensitive IR detectors only come in small sizes. The detector used here is Ge:Hg, with a risetime of ~ 1 ns. To condense the 7-mm aperture stop on to the 1-mm detector requires a lens of focal length < 29 cm. The lens speed need only be f/4.8.

c. Phase Resolution Analysis. The ultimate limit on phase resolution is the signal-to-noise ratio. For a sinusoidal signal, a simple geometric analysis shows that the maximum error in locating the peak or through of the sinewave is:

$$\Delta\theta = \frac{1}{\pi}\sqrt{V_n/V_s} \quad ,$$

where V_n and V_s are peak-to-peak noise and signal voltages, respectively, and $\Delta\theta$ is in fractions of a fringe. Since typical peak fringe shift on Scyllac is 1 to 2 fringes, a 0.1 fringe resolution would be desirable. To achieve this $V_s/V_n = 10$ is needed. The optical power available for the entire measurement is 1.5 μW (using the standard homemade coupled cavity-type laser). Allowing for equal distribution by the A-O cell, a 50-50 recombining beamsplitter and three separate time frames give 130 W in each beam. A 50% optical efficiency leaves ~ 65 W per beam. When heterodyning two beams, each of power P, the resultant beat signal has the form

$$V_s \propto 2P \cos \Delta\omega t$$

so that the peak-to-peak signal corresponds to a power of 4 P, or 260 μW in this case.

The only quantum detectors fast enough for this application are of the doped germanium variety. We are using Hg doped Ge, with a diameter of 1 mm and responsivity of ~ 0.05 A/W at 3.4 μ. The low responsivity is the price paid for bandwidth. An input power of 260 W should therefore produce ≥ 650-μV signal (with R > 50 Ω). The dominant noise source is the load resistor and input preamplifier. Together these should produce ~ 75 μV peak-to-peak of noise (with bandwidth of 150 MHz), depending on the exact load resistance required to shunt the front end capacitance. Thus V_s/V_n ~ 8, which is quite compatible with the design objectives, provided that no serious loss in fringe contrast results. Maintaining a high level of contrast is the subject of the following section.

d. Contrast. The great imponderable in the entire system is contrast retention. Contrast may be loosely defined as the level of the heterodyne signal in relation to the incident power level. Anything that distorts the scene and reference beam wave fronts in different ways will tend to reduce the contrast. Further, the contrast may vary within the scan, possibly introducing severe distortion into the fringe pattern. The infrared is somewhat forgiving in this regard, but nevertheless, attention needs to be paid to mirror and lens quality in the individual beam arms. The biggest offender is the discharge tube, and special corrector elements have been designed (with the assistance of Group M-5) to reduce the first-order refractive effects of the discharge tube. However, residual effects will remain, and these may require compensating elements in the reference arm.

Currently unknown is how severe a contrast or resolution reduction will be caused by the scanning mechanism at full speed.

Construction of apparatus to explore these effects and, hopefully, provide proof of principle is well under way.

D. ON-LINE BETA MEASUREMENT FOR SCYLLA IV-P

1. Luminosity Measurement With Zoom Optics. The new luminosity apparatus operates conceptually on the same principles as previous devices used on Scyllac. The image of the plasma is projected onto the segmented fiber optics detector through telecentric optics, i.e., making the object appear to be at infinity. However, a zoom lens is used to relay an intermediate image to the detector array, thus providing a variable field of view (1 cm to 6 cm) to the detector. A schematic diagram of the device is given in Fig. XI-10. By placing the beam splitter in front of the primary lens, the plasma and the diffused strobe light calibration source are simultaneously in focus. In this manner, any image intensity aberrations, e.g., vignetting, are included in the calibration. The strobe light is flashed and automatically recorded before every plasma discharge.

The two outside channels in the 22-element fiber optic array can be back illuminated in order to project an image into the quartz discharge tube for alignment.

2. Photomultiplier Detector Design. The light at the final image plane is carried by the fiber optic bundles to a bank of 20 photomultipliers. A new photomultiplier tube was used in this design, the EMI 9798B. replacing the RCA 931A used previously. The 9798B has an end-on photocathode geometry, permitting a more compact in-line design. It also has a broader spectral response (S-20) and a higher gain, 11 stage dynode structure. Although the risetime of the "box and grid" structure EMI 9798B for a step pulse (≤ 50 ns) is appreciably slower than either the 12 ns quoted by the manufacturer (valid for delta function input) or the risetime of the "squirrel

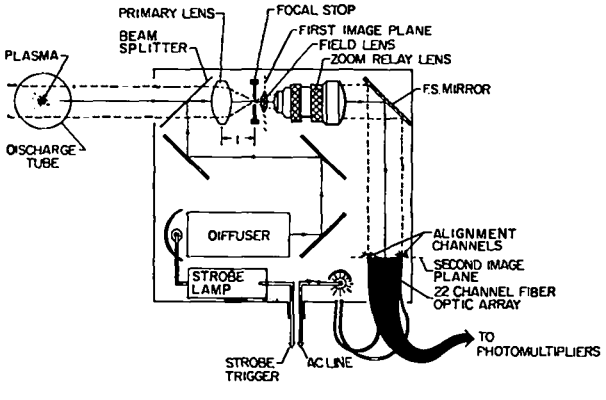

Figure XI-10
Schematic diagram of luminosity device.

cage" 931A, it is adequate for following the postimplosion theta-pinch plasma.

Considerable effort went into the design of a dynode biasing chain that could provide high-pulsed anode currents at high gain, while maintaining the fastest possible risetime and good linearity. The highly nonlinear chain, shown in Fig. XI-11, proved to be the solution. With this chain, the tube can produce peak anode currents linearly up to - 5 mA for ~ 100 μs. The line driver amplifier (Burr-Brown 3553) is capable of driving a 50-Ω load at ± 10 V, with risetimes < 5 ns. Hence, the anode signal is relayed faithfully to the screen room, where it is digitized and recorded by Biomation or SEC transient recorders for subsequent processing by the computer.

It was desired to combine the photomultiplier tube and electronics into modular units that could be easily exchanged in order to facilitate repairs or modifications. Figure XI-12 shows the final module design and the tube array. The tube, surrounded by light-tight shielded canisters, is plugged into a base unit containing all the dynode chain and line driver electronics. The base is in turn plugged into a mother board, which provides the modules with necessary operating voltages and receives the output anode signals. A double shielded housing (not shown) contains the mother board. The fiber-optic cables from the luminosity

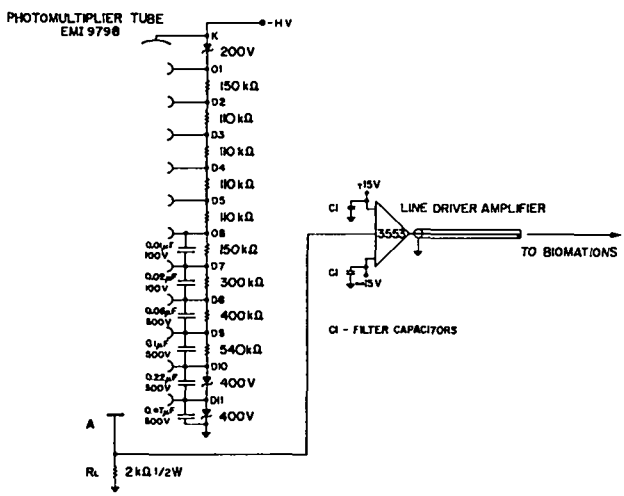

Figure XI-11
Nonlinear optimized dynode chain for luminosity measurement.

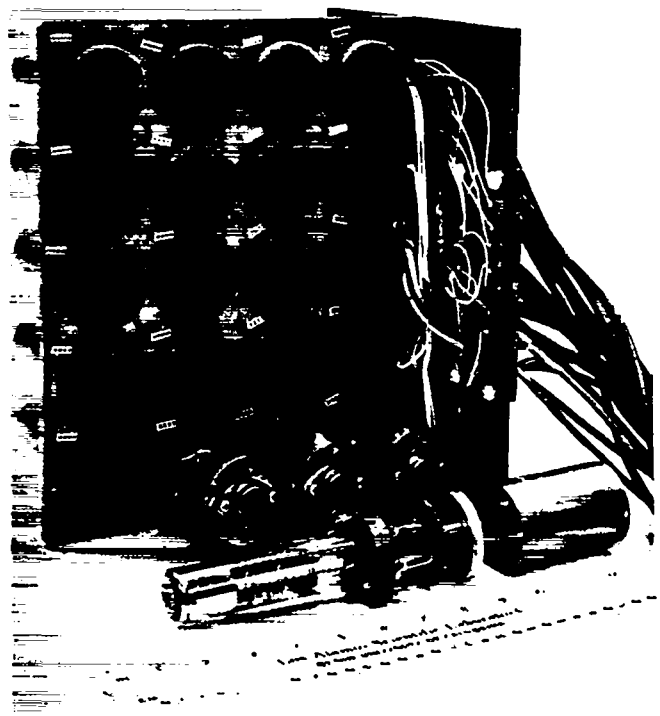

Figure XI-12
Luminosity module design and photomultiplier tube array.

device pass through the housing walls, enter the shielding canisters, and reach to the photomultiplier photocathodes.

3. Luminosity Profile Fitting and Axis Beta Calculation Program. After the luminosity data have been digitized, the Scylla IV-P control computer (Prime 300) is used to analyze the data immediately after the main bank discharge cycle is complete. The relative radial density profile is computed by fitting the data with a nonlinear least squares method. The function used is

$$f(x) = A + Bx + C \exp(-2(x-x_0)^2/a^2) \quad , \qquad (1)$$

where A and B are used to fit the background light level, and C is the amplitude of an assumed Gaussian profile centered at x_0 and of characteristic width a, respectively. This five-parameter fit includes the linear term Bx not used in previous luminosity fitting programs. The inclusion of this term gives statistically better fits to the data, according to the χ^2 test.

Excluded flux data are obtained from a balanced loop-probe pair and also digitized. They are then used in combination with the radius data to compute the axis beta as a function of time. Typical output from this program is shown in Fig. XI-13. The analysis results are used by subsequent computer programs to compute energy confinement times and ion temperature (see Section V, this report).

E. MISCELLANEOUS

1. Analog Video Monitor of Streak-Camera Output. A Scylla IV-P Imacon streak picture has been successfully recorded on a SIT tube video camera and displayed on a monitor. This demonstration of a solution to light level, electrical noise, and triggering problems in an actual operational environment justifies proceeding with digitization for eventual automated analysis. This work was done under contract by EG & G with a GE TE36 camera coupled to an Imacon with a f/1.2, 55-mm relay lens. The monitor and tape recorder were located in the screen room and good quality recordings were obtained with the relay lens stopped down to f/4.

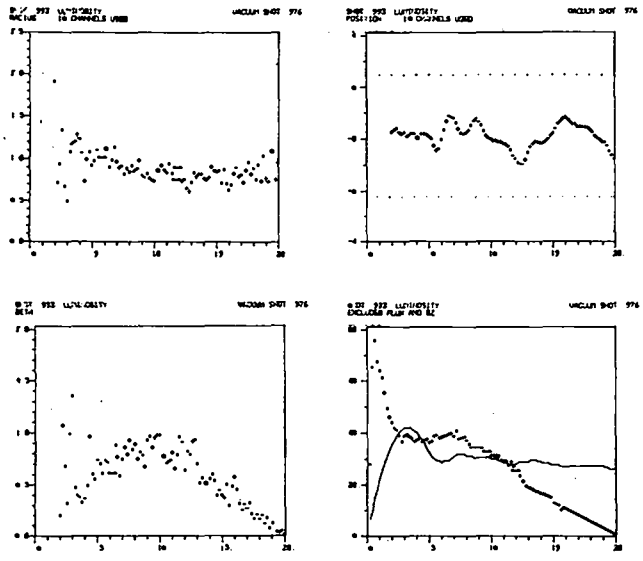

Figure XI-13
Results of beta calculation. Upper left: Plasma radius. Upper right: plasma centroid position. Lower left: beta value. All quantities vs time in microseconds. Lower right: excluded flux signal.

2. CO_2 Holographic Interferometer. A 1-J pulsed CO_2 holographic double-pass holographic interferometry system with 18 cm diameter scene beam, complete with CW CO_2 alignment laser, was constructed for the CTR-5 plasma gun project (Section VI). Because of the unexpected high-density, small-dimension plasma observed with ruby laser interferometry, this higher sensitivity, but more complicated system, has been temporarily shelved.

3. Three-Pulse Ruby Laser. The principle of the single-laser cavity emitting two collinear pulses of orthogonal polarization[2] can be extended to additional pulses by adding more polarizing optics within the cavity. The motivation is to obtain multiple interferograms during a single plasma discharge. A circuit for double pulsing one Pockels cell, necessary to obtain three pulses, has been designed and constructed and work is proceeding on a time-as-available basis.

4. Far Infrared Diagnostics. With the rapid development elsewhere of CO_2 laser pumped far infrared lasers for plasma diagnostics (both pulsed and CW), we have undertaken the development of some in-house capability in this field on a time-as-available basis. The initial aim is the extension of our visible and near-infrared CW gas laser interferometry techniques to the 496 μ CH_3F and 119 μ CH_3OH wavelengths, utilizing high sensitivity, sub-nanosecond response room temperature detectors (Schottky-barrier diode type) newly available from Lincoln Laboratory/MIT. The enhanced sensitivity at these long wavelengths should make density measurements of the tenuous plasma outside the dense core of theta or Z pinches possible. While refractive bending will be severe for a substantial transverse gradient, it might itself be the basis of useful measurements.

A line-tunable CO_2 pump laser built by L Division was borrowed and improved until a very stable 20-W CW single-mode output at the 9.6-μ pump wavelength for CH_3F was obtained.

Output at both 496 μ and 119 μ has been observed. Experiments are in progress to determine the optimum configuration and coupling into and out of the FIR cavity. Mode structure, beam divergence, polarization, and power of the FIR laser will be studied before specific applications are determined.

REFERENCES

1. LA-6044-PR, Controlled Thermonuclear Research Program Annual Report, 1974.
2. LA-6582-PR, Controlled Thermonuclear Research Program Annual Report, 1975.
3. N. Bretz, D. Dimock, D. Long, and E. Tolnas, Bull. Am. Phys. Soc. 20, 1322 (1975).
4. R. E. Siemon, Appl. Opt. 13, 697 (1974).
5. R. L. Morse, Phys. Fluids 16, 545 (1973).

XII. HIGH-BETA TOKAMAK

P.C.T. Van der Laan, J. P. Freidberg, K. S. Thomas

A. INTRODUCTION

Tokamak-like plasmas with a relatively high beta can be produced rather easily with implosion heating techniques. A study of these possibilities has led to a proposal for the construction of such a "High-Beta Tokamak." This proposal, which is described in LASL report LA-6413-P and its Supplement, will be reviewed by ERDA in January 1977. We discuss here the physics of such an experiment, the proposed construction of the machine, a comparison with other experiments, and, finally, list some problems.

B. HIGH-BETA TOKAMAK PHYSICS

The objective of the experiment is first of all to find the limits of β and q for which equilibrium and stability can be obtained. Secondly, one should attempt to move the β limit to higher values by making appropriate modifications.

In the tokamak configuration the toroidal field B_ϕ is larger than the poloidal field B_p. Most of the implosion heating is therefore the result of the rapidly rising B_ϕ, as in a toroidal theta pinch.

A bias field $B_{\phi o}$ will be used to decrease β, probably down to values as low as 10 to 15%. Especially at these low β's the heating process is not very efficient. Since the ability to control profiles by means of flux conservation will be an important feature of the experiment, anomalous diffusion should be avoided. This means that low filling pressures cannot be used, even though the corresponding increase in temperature would be welcome; a minimum filling pressure is probably 0.7 Pa (5 mTorr).

Implosion heating offers a very large heating rate and a short build-up time of the configuration. Therefore fluxes and q values of the helical field lines are conserved, just as they should be in a Flux Conserving Tokamak. In fact, flux conserving equilibria are obtained much more easily in implosion heated tokamaks than in conventional tokamaks where auxiliary heating can provide only a slow heating rate.

The experiment will have a ceramic discharge tube surrounded by a closely fitting metal shell. This and the experimental fact that the region outside a pinch is filled by a reasonably hot low-density plasma ensures that flux conservation takes place throughout the tube. One can therefore build in specific q profiles by applying the right q history at the wall during the risetime of the fields. This possibility of control of the q profile, or in other words, of the current density profile has already been demonstrated in many screw pinch experiments. A flat q profile improves the stability of the plasma drastically and reduces the equilibrium shift, as has been shown in experiments and by theoretical descriptions.

A moderate vertical elongation of the cross section should also help to increase the β that can be confined. A racetrack-shaped cross section with a height-to-width ratio of 2 to 1 has been chosen. Computer calculations described in Sec. XIII have shown that very high β equilibria are possible in this configuration, especially in the case of flat q profiles.

C. CONSTRUCTION OF THE PROPOSED MACHINE

Figures XII-1 and XII-2 show the proposed construction of the central part of the machine and the proposed circuit for the θ currents. The θ currents are fed in with two conical transmission lines on the inside of the torus. This construction provides access for diagnostics, allows grounding of the outside shield and reduces the field errors near the eccentric plasma. The shell will have one gap in the vertical plane so that toroidal plasma currents can be induced. The primary of the air-core transformer will consist of an end-fed or "Marshall coil" arrangement.

The discharge chamber will be composed of 30 straight alumina sections, each in the shape of a racetrack. The metal shell will fit the ceramic torus closely.

The high-beta tokamak requires fast-rising magnetic fields for the implosion heating, but also fields that are sustained for a time long

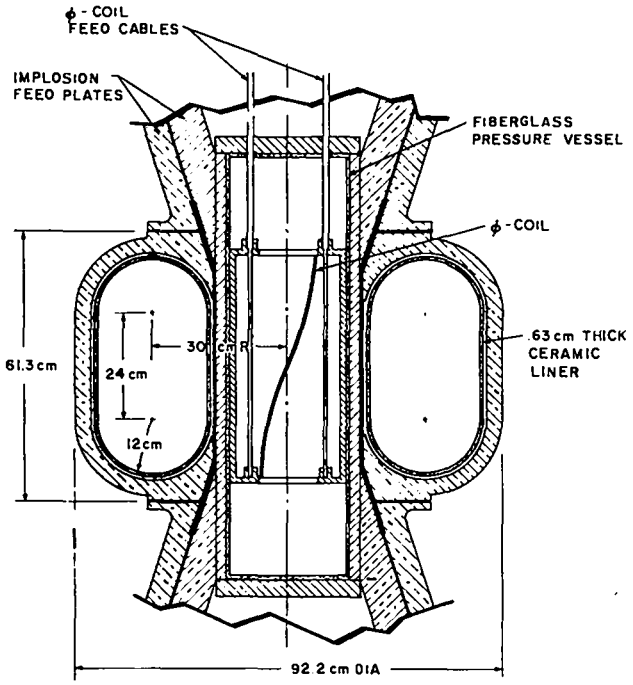

Fig.XII-1.
Central part of the High-Beta Tokamak. The shell carries the θ currents. The pressurized vessel around the primary θ coil prestresses the θ coils to counterbalance the large inward force.

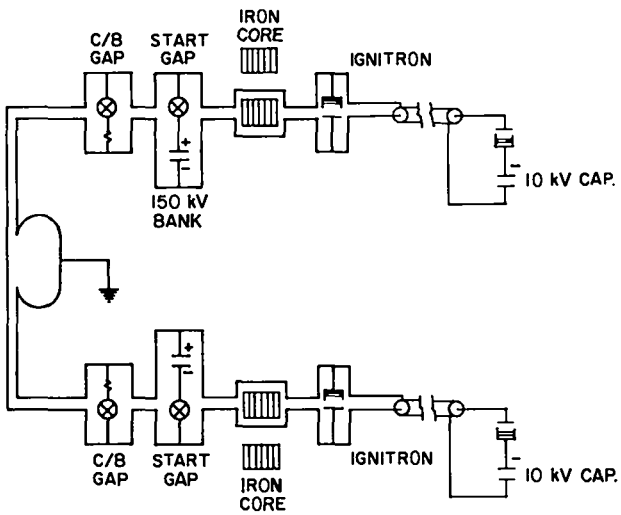

Fig. XII-2.
Proposed circuit for the High-Beta Tokamak. The iron cores isolate the slow 100-kV power-crowbar bank during the initial magnetic field rise which is produced by the fast 150-kV bank.

enough to study plasma confinement and stability. The circuit shown in Fig. XII-2 has both the high-voltage bank and the low-voltage bank necessary to achieve this. Both banks are fired simultaneously but are isolated from each other during the fast initial rise by the iron core coils. At later times when the slow bank has to provide the current the iron saturates.

A list of machine parameters is given in Table XII-I.

D. COMPARISON WITH OTHER EXPERIMENTS

As has been described in Section B, an implosion heated high-beta tokamak can generate flux-conserving tokamak equilibria and in addition can program in other q profiles, for instance the more favorable flat q profile. Other differences with a conventionally produced future FCT are the higher density and perhaps the narrower pressure profile in the implosion heated tokamak. Higher β values can be obtained by a reduction of the bias field, and are in fact produced more easily than the low β values.

The proposed experiment differs from the many existing screw pinches and belt pinches in three respects.

It will operate at such a filling density that not much anomalous diffusion occurs during the implosion. To obtain high temperatures under these conditions, quite high E fields (≈ 1 kV/cm in the presence of plasma) are required to ensure fast implosion heating. Secondly, the machine

TABLE XII-I

MACHINE PARAMETERS

Major radius	R	0.30 m
Height	$2b_1$	0.48 m
Width	$2b_2$	0.24 m
Volume	V	194 dm^3
Minor circumference		1.234 m
Toroidal field at R = 0.30 m	B_ϕ	2.0 T
θ inductance, single turn, 1.5-cm dead space	L_θ	87 nH
Toroidal current estimate for q (wall) = 2	I_ϕ	750 kA
Filling pressure deuterium	p_o	0.67 Pa (5 μm)
Final plasma density	n_e	5 x 10^{21} m^{-3}
Final plasma temperature	T	300 eV

will have a complete shell around the torus to guarantee flux conservation over the full cross section of the chamber. Partly open shells as used in most belt pinches allow the use of an externally applied vertical field, but also cause the area in which fluxes are conserved to be small.

Thirdly, the machine will have a moderate 2-to-1 elongation of the minor cross section, different on one hand from the many machines with circular cross section but also different from the larger elongations (3-to-1, up to 7-to-1) used in belt pinches. The planned 2-to-1 racetrack might still be changed to a D-shape by the addition of a bulge to the outer surface. Equilibrium calculations, described in Sec. XIII, have shown that equilibria are possible at very high beta values, up to 90% local beta and possibly up to 100%. The 2-to-1 racetrack is in this respect better than the bulging racetrack, but the advantage of the latter is its better stability characteristics, as was apparent from the behavior of the Mercier criterion for the two shapes.

E. PROBLEMS AT LONG CONFINEMENT TIMES

To find the limits for β and q, one needs to keep the plasma parameters constant during many MHD times. If stable periods of 100 μs are reached, and experiments in SPICA and in belt pinches suggest that this should be possible for the appropriate β and q values, one would like to understand the decay processes that limit the lifetime thereafter. Two candidates for these limiting processes are discussed.

1. Radiation Cooling. As in all high-density plasmas, radiation, which increases with n^2, can dominate ohmic heating which is almost independent of n. This means that only very low impurity concentrations can be tolerated in high-density plasmas. Figure XII-3 shows the decay of the temperature, for two densities and three oxygen concentrations, after an initial implosion heating to 300 eV. These calculations were done with the IMPRAD code, described in Sec. XIII. Clearly the oxygen concentration should be kept down to at least 0.1%, which is certainly not easy, but

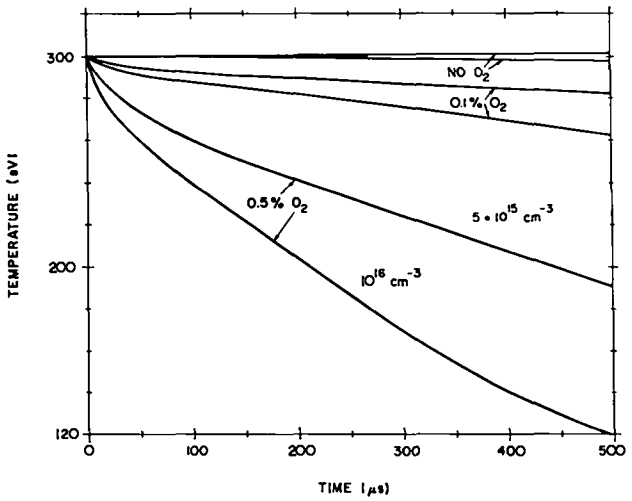

Fig. XII-3.
Computer results for the decay of $1/2(T_e + T_i)$ for two plasma densities and three concentrations of the oxygen impurity. Implosion heating at t = 0 heats the plasma to 300 eV. A current of 1000 A/cm^2 contributes ohmic heating.

judging from experience with linear θ pinches, not impossible either.

Note that the radiation cooling problem of high-density confinement disappears when α-particle heating, which is also proportional to n^2, takes over. The radiation cooling problem cannot be blamed on the wall materials; in fact the low-Z atoms of quartz and alumina are orders of magnitude better than the high-Z atoms of metal walls in terms of impurity radiation losses per impurity atom.

2. Disruptive Instability. The second process, which may limit the lifetime is the disruptive instability. Radial heat conduction sets up a temperature profile which in turn begins to influence the current distribution. If this leads to a shrinkage of the current channel, a surface on which q = 1 can show up near the magnetic axis. Under given circumstances, otherwise harmlesss instabilities on the q = 1 surface can develop into a disruptive instability. The characteristic onset time for such a disruption is hard to estimate. On one hand, the heat conduction would be faster at the higher densities of an implosion heated tokamak. On the other hand, especially for a broad current profile, a protective layer of well-heated low-density plasma could help to lengthen the lifetime.

XIII. THEORY

D. C. Barnes, J. U. Brackbill, R. Christian, T. E. Cayton,
R. Y. Dagazian, J. P. Freidberg, R. A. Gerwin, D. W. Hewett,
H. R. Lewis, R. C. Malone, L. W. Mann, M. Menzel, G. Miller,
R. L. Morse, C. W. Nielson, W. Riesenfeld, W. Schneider,
J. L. Schwarzmeier, A. G. Sgro, K. Symon, L. Turner, and D. Winske

A. INTRODUCTION

During 1976 CTR-6 continued to make important contributions to high-beta kinetic and magneto-hydrodynamic theory. In addition, detailed theoretical studies of several exploratory concepts were initiated.

One major interest in microtheory continued to be the lower hybrid drift instability. Efforts in the last year have indicated that this instability may not be as dangerous as previously thought. It has been shown that a threshold for the instability exists at low drift velocities, that profiles in Z-pinch configurations can be shear stabilized, and that the saturation level of the instability, determined from plasma simulation at lower drift velocities than were attainable in the past, is much less than previously thought. In addition, the hybrid implosion code, which had already achieved remarkable success in reproducing experimental results, was substantially improved and proceeded to give excellent agreement with such subtle experimental measurements as neutron yield and plasma rotation. A new hybrid code which holds great promise for extending these calculations to several spatial dimensions has been developed during the past year. Finally, a new active interest was taken in electromagnetic instabilities which are due to anisotropic ion temperatures that arise during implosions.

The major success of the theory group during the past year occurred in MHD theory, where a much clearer understanding of the Scyllac experiment was achieved. A simple analytic model for estimating the external forces needed to produce toroidal force balance for diffuse equilibria was developed and results showed that the force balance for an $\rho=1,0$ system at high beta was different by a factor of two from the prediction of sharp boundary theory. This result was verified in three-dimensional numerical studies of diffuse Scyllac equilibria. These time-dependent calculations have shown dramatically the behavior of the plasma column and its approach to equilibrium in the postimplosion phase of Scyllac. Also, a more transparent picture of the plasma motion in the Scyllac sector was obtained by means of an analysis of the response of the plasma to a localized impulse.

Progress was also made in areas which are of prime importance in scaling to larger experiments. These include finite Larmor radius (FLR) effects, classical transport, and work on the ZT-40 experiment. The study of FLR effects, both numerical and analytic, has continued to show that careful analysis of these effects give more optimistic results than predicted by previous theory. A detailed theoretical investigation of high-beta classical transport was successfully completed in the past year. Finally, calculations of equilibrium and impurity radiation for the proposed ZT-40 experiment have been carried out.

The theory group has also engaged in several areas that are less traditional, and might be called exploratory concepts. They involve the study of materials and their interaction with plasma. One effort is a study of plasma compression by imploding liners. Although compressibility of the liner does reduce the very favorable scaling of the simplest theory, the results still show that break-even is achievable in a very small device. A second effort involves the investigation of material end plugs for linear theta pinches. The calculations have shown that plugs can significantly increase the energy confinement time (as well as eliminating particle end loss), and have created new optimism for linear devices.

B. PLASMA MICROTHEORY

The role of plasma instabilities in high-density pinches continues to be an actively researched subject. In addition to a continuing examination of the lower hybrid drift instability in the low drift velocity, postimplosion plasma a

number of new modes which are significant in various phases of a pinch have been investigated.

1. Plasma Waves and Instabilities.

a. Dispersion Properties of Plane Waves Propagating in an Unbounded, Magnetized, Homogeneous Vlasov-Fluid Plasma. During implosion, the ions of a θ-pinch plasma are heated preferentially in directions perpendicular to the magnetic field, i.e., $T_\perp > T_\parallel$. However, experimental observations indicate that the ion energy becomes isotropic, i.e., $T_\perp \simeq T_\parallel$, in a time much shorter than that predicted by collisional relaxation processes.

The instabilities which reduce the temperature anisotropies in pinched plasmas are important to the understanding of stability and end loss in straight theta pinches and mirrors. These have been studied by deriving, without any simplifying assumptions, the dispersion formula for unstable, plane-wave perturbations of the Vlasov-fluid[1] equilibrium.

$$\vec{B}_o(\vec{r}) = B_o\hat{z} \quad ,$$

$$f_o(\vec{r},\vec{v}) = n_o \left(\frac{M}{2\pi KT_\perp}\right)\left(\frac{M}{2\pi KT_\parallel}\right)^{1/2}$$

$$\exp - \left(\frac{Mv_\perp^2}{2KT_\perp}\right) \exp - \left(\frac{Mv_z^2}{2KT_\parallel}\right) \quad . \qquad (1)$$

These equations describe a uniformly magnetized, electrically neutral plasma whose equilibrium ion distribution function f_o is anisotropic in velocity space. The perpendicular and parallel temperatures, $T_\perp$ and $T_\parallel$, whose values may be specified arbitrarily, describe this anisotropy.

Consider an unstable perturbation having the customary plane-wave dependence, $\exp i(\vec{k}\cdot\vec{r}-\omega t)$, where $\vec{k}$ may be an arbitrarily specified propagation vector whose magnitude is $(k_\perp^2+k_z^2)^{1/2}$. We then make the following set of definitions.

$$\frac{1}{2} Mv_\parallel^2 \equiv KT_\parallel \,, \qquad \frac{1}{2} Mv_{th}^2 \equiv KT_\perp$$

$$\tilde{k} \equiv \frac{k_z v_\parallel}{\omega_c}, \qquad \tilde{\omega} \equiv \frac{\omega}{\omega_c}, \qquad r_L \equiv \frac{v_{th}}{\omega_c} \qquad (2)$$

$$u \equiv \frac{1}{2} k_\perp^2 r_L^2 \,, \qquad \beta_\perp \equiv \frac{8\pi n_o KT_\perp}{B^2}, \qquad \alpha \equiv 1 - \frac{T_\perp}{T_\parallel}$$

$$\lambda_\pm = \frac{\tilde{\omega} - (m\pm 1)}{\tilde{k}} \qquad \lambda_o = \frac{\tilde{\omega}-m}{\tilde{k}}$$

where ω_c is the ion Larmor frequency and n_o is the ion equilibrium number density.

The dispersion relation for this perturbation is

$$\det D = 0 \qquad (3)$$

where D is a 2 by 2 matrix whose elements are defined by:

$$D_{11} \equiv -\frac{1}{\beta_\perp}\left[\tilde{k}^2(1-\alpha)+ u\right] - \tilde{\omega}$$

$$+\left(\sum_{m=-\infty}^{\infty} \left\{\frac{\tilde{\omega}}{\tilde{k}} Z(\lambda_+) - \alpha\left[1+\lambda_+ Z(\lambda_+)\right]\right\}\right.$$

$$\left.\left\{I_m(u)+u\left[I'_m(u)-I_m(u)\right]\right\}\right) \exp -u$$

$$D_{12} \equiv D_{21} \equiv -\frac{u}{\beta_\perp} - \left(\sum_{m=-\infty}^{\infty} \left\{\frac{\tilde{\omega}}{\tilde{k}} Z(\lambda_o) - \alpha\left[1+\lambda_o Z(\lambda_o)\right]\right\}\right.$$

$$\left.\left\{u\left[I'_m(u)-I_m(u)\right]\right\}\right) \exp -u,$$

$$D_{22} \equiv -\frac{1}{\beta_\perp}\left[\tilde{k}^2(1-\alpha)+u\right] + \tilde{\omega} + \left(\sum_{m=-\infty}^{\infty} \left\{\frac{\tilde{\omega}}{\tilde{k}} Z(\lambda_-)\right.\right.$$

$$\left. - \alpha\left[1 + \lambda_- Z(\lambda_-)\right]\right\}$$

$$\left.\cdot\left\{I_m(u)+u\left[I'_m(u) - I_m(u)\right]\right\}\right) \exp -u \,, \qquad (4)$$

where Z is the Fried-Conte plasma dispersion function.

By generalizing the above derivation, a dispersion equation including finite electron pressure effects has been derived. Numerical solutions have been studied and tabulated. In these computations, the equilibrium ion distribu-

tion function is bi-Maxwellian, and the electron fluid has finite pressure, but vanishing inertia.[2] These dispersion properties have been compared, either analytically or numerically, with those obtained from a fully Vlasov description of the plasma that includes all electromagnetic effects. The behavior of the relatively low frequency modes (i.e., $\omega = O(\Omega_{ci})$) in the two plasma models was found to be in very good to excellent agreement; these results demonstrate that the Vlasov-fluid model provides a useful and accurate description of low frequency phenomena in a high-beta plasma.

Of particular interest are four modes that have counterparts in the Guiding Center Fluid (GCF) model of Grad[3] (an analog of ideal magnetohydrodynamics that includes anisotropic pressure, which is identical to the CGL double-adiabatic model);[4] these are: 1) Alfven/ion cyclotron mode, 2) fast magnetosonic/whistler mode, 3) ion-acoustic mode, and 4) mirror mode. Another motivation for the interest in them is the fact that for the class of equilibria that was considered, these four are the modes that may become unstable. The Vlasov-fluid model, again, accurately reproduces the features found in a fully Vlasov description.[5] It was also observed that in the $k \to 0$ limit, the phase velocities measured from the dispersion curves agreed well with the predictions of the GCF theory. To further this comparison, the general dispersion equation was reduced to a fluid limit by assuming the frequency and the magnitude of the wave vector to be individually small, while allowing their ratio to be arbitrary. The resulting equation is precisely the same as the one derived by A. Kadish for a Guiding Center Plasma[6] (GCP) of ions and electrons, if one assumes a bi-Maxwellian velocity distribution for the ions, a Maxwellian for the electrons, and then sets the electron mass to zero. Thus, to lowest order, the Vlasov-fluid model for long wavelengths, and the GCP model agree; however, because the ion gyroradius and cyclotron frequency are finite in the Vlasov-fluid description, corrections to the first approximation can be computed and for nonzero wave vector, lead to differences between the Vlasov-fluid and GCP results. This is a finite-gyroradius effect, and it appears even in an infinite, homogeneous plasma.

Another comparison was made between the GCF theory and the lowest order, long-wavelength solutions of the Vlasov-fluid dispersion equation: the normal speed loci[7] (polar coordinate plots of phase speed versus angle of propagation) for the two models were constructed and compared; representative examples are shown in Figs. XIII-1 thru XIII-4.

Davidson and Ogden[8] have proposed the ion cyclotron instability, which is an electromagnetic instability driven by ion energy anisotropy, as a mechanism for rapid, collisionless relaxation of the ion velocity distribution to an isotropic state. A detailed investigation of this relaxation mechanism was begun in 1976. The theory of Ref. 8 has been generalized to include second-order wave-particle effects for a variety

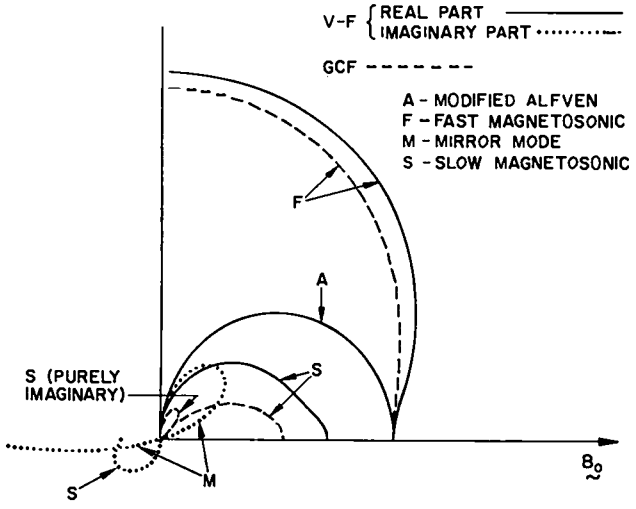

Figure XIII-1.
One quadrant of the normal speed loci from the GCF model and the long-wavelength limit of the Vlasov-fluid model when $T_\perp/T_\parallel = 10.0$ and $c_A^2/V_{Th}^2 = c_S^2/V_{Th}^2 = 0.1$. An imaginary speed outside the quadrant (negative radius) indicates damping of the wave. The modified Alfven waves are identical in the two models; the fast magnetosonic waves are very similar. Both models exhibit a mirror instability: the mirror instability in GCF results when the slow magnetosonic speed becomes purely imaginary at large propagation angles; in the Vlasov-fluid description, the mirror instability arise from the purely imaginary mirror mode that has no counterpart in GCF theory, and it does so for a wider range of parameter values than GCF theory allows. The slow magnetosonic wave is damped substantially in the Vlasov-fluid model, whereas it is undamped in GCF.

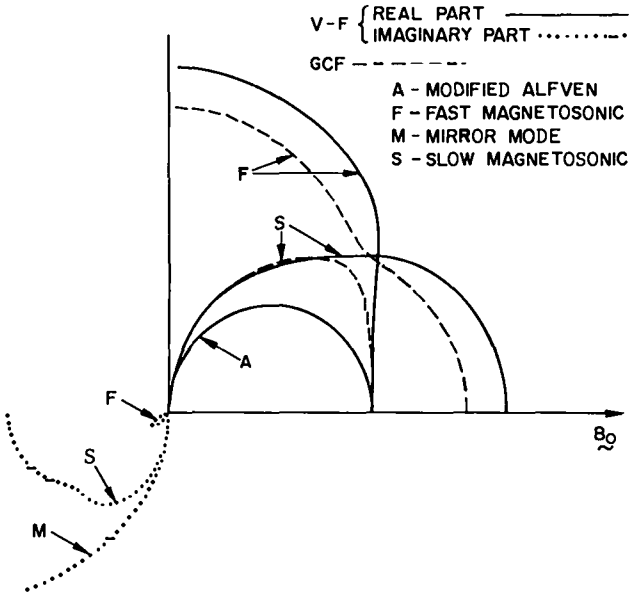

Figure XIII-2.
One quadrant of the normal speed loci from the GCF model and the long-wavelength limit of the Vlasov-fluid model when $T_\perp/T_\parallel = 0.4$, $c_S^2/V_{Th}^2 = 1.0$. An imaginary speed outside the quadrant indicates damping of the wave. The modified Alfven waves are identical in the two models. The fast magnetosonic wave is slightly damped and the slow magnetosonic wave is strongly damped in the Vlasov-fluid description, whereas all waves are undamped in the GCF model. The curves differ topologically in the two models: this difference occurs because the GCF fast and slow magnetosonic modes are strongly coupled when $35^o < \theta < 45^o$. Analogous mode coupling occurs in the Vlasov-fluid description, but at larger values of c_S^2/V_{Th}^2.

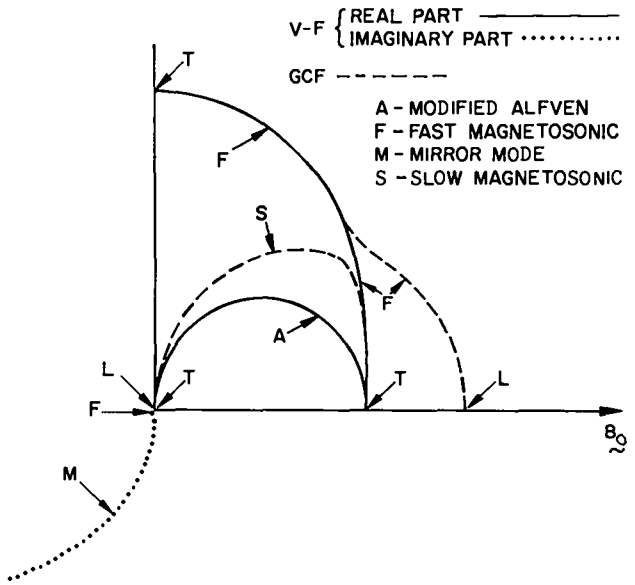

Figure XIII-3.
This figure and Fig. XIII-2 illustrate the effects of electron temperature: the electron temperature has been decreased substantially so that $c_S^2/V_{Th}^2 = 0.01$, while the other parameters remain the same as in Fig. XIII-2, i.e., $T_\perp/T_\parallel = 0.4$ and $c_S^2/V_{Th}^2 = 2.5$. The slow magnetosonic speed in the Vlasov-fluid description has a very large, negative imaginary part, and is not shown. The mode coupling for GCF is clearly evident. The curves have been labeled with the polarizations of the waves: t = transverse, electromagnetic wave; ℓ = longitudnal wave. The fast and slow magnetosonic waves are, therefore, represented by the appropriate segments of the two curves, rather than each one being associated with one continuous curve: the two should be interpreted as coupled modes.

of electromagnetic instabilities with $\underline{k}_\parallel \underline{B}_o$.[9] The new theory provides a description of the changes in the particle distribution functions, as well as isotropization and heating rates; these will be compared to results of computer simulations of this instability.

The Alfven-ion cyclotron mode and other relatively low-frequency, i.e., $\omega = O(\Omega_{ci})$, phenomena in hot, high-beta plasmas are amenable to study with the Vlasov-fluid model.[1] The linear growth rates and frequencies of the $\underline{k}_\parallel \underline{B}_o$ ion cyclotron mode were obtained from both the Vlasov-fluid model and a fully Vlasov treatment; these were compared and were found to be in excellent agreement. A generalization of the Vlasov-fluid model that includes finite electron pressure[2,10] has been developed and its wave propagation properties[5] have been compared with those of a fully Vlasov treatment. Again, very good agreement was observed for relatively low-frequency phenomena, not only for the $\underline{k}_\parallel \underline{B}_o$ modes, but for waves that propagate obliquely to $\underline{B}_o$ as well; these include "mirror" instability, the Harris instability, and the fast-magnetosonic mode. This agreement justifies investigation of these instabilities in a θ-pinch geometry using the Vlasov-fluid model.

b. Stability of BGK Equilibria. A general formulation of linearized collisionless plasma problems has been developed to study Vlasov-fluid instabilities.[11,12] Another application of the general method has been to study the stability of one-dimensional BGK equilibria.[13] This study has successfully used a method for generating a good set of expansion functions for the perturbation

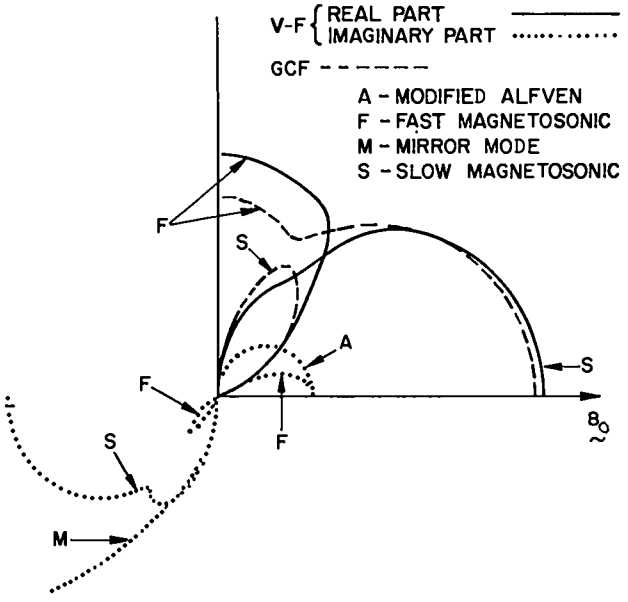

Figure XIII-4.
One quadrant of the normal speed loci from the GCF model and the long-wavelength limit of the Vlasov-fluid model when $T_\perp/T_\parallel = 0.3$, $c_S^2/V_{Th}^2 = 0.707$, and $c_S^2/V_{Th}^2 = 0.8$. An imaginary speed outside the quadrant indicates damping of the wave. For the assumed parameter values, the modified Alfven waves, which are identical in the two models, are purely growing for all propagation angles; this is the firehose instability. The positive imaginary speed labeled "F" also occurs in both models; this is a second firehose instability which is associated with the magnetosonic mode. In GCF theory, the magnetosonic speed changes from purely imaginary to purely real when the propagation angle θ exceeds 30°; in the Vlasov-fluid description, the mode becomes damped when $\theta > 30^\circ$. As in Fig. XIII-3, strong mode coupling is evident in the GCF results; analogous mode coupling occurs in the Vlasov-fluid description at larger values of c_S^2/V_{Th}^2.

potential which is similar to the method used for generating expansion functions in the Vlasov-fluid model.

c. Magnetic Stabilization of The Lower Hybrid Drift Instability. The effect of a dc magnetic field on the ion oribits and the presence of magnetic shear are stabilizing effects for the lower hybrid drift instability in a pinch. These effects have been included in a linear theory by extending the theory for low drift velocities to include the effect of a dc magnetic field on the ion orbits. The instability is predicted to be extinguished at drift velocities, v_{dr}, so small that $v_{dr}/v_i \leq \sqrt{m_e/m_i}$, where v_i is the ion thermal velocity. Physically, this means that one tries to construct a pinch with $r_{ci}/a \leq \sqrt{m_e/m_i}$ where r_{ci} is the ion gyroradius and a is a radial scale length. This work was presented at the Spring Sherwood Theory meeting and has been accepted in Physics of Fluids.

Shear stabilization of the lower hybrid drift instability has also been considered. A criterion due to N. Krall for magnetic shear stabilization[14] was applied to model profiles of the Reverse-Field Screw Pinch configuration. Conditions which virtually eliminate this instability were found numerically, for gentle density profiles. However, shear-stabilization proved to be ineffective for sharper (but still reasonable) profiles. If such profiles are encountered, it becomes necessary to rely either on finite-beta stabilization or on the fact that this instability possesses a threshold related to ion gyroresonance.

2. Plasma Simulation.

a. Plasma Simulation of Microinstabilities. Plasma simulation continues to be an important tool in the study of the microinstabilities that are responsible for anomalous effects in plasmas. Efforts this year have been focused on a better understanding of the saturation mechanism of the lower hybrid drift instability. This mode is thought to be the dominant source of anomalous resistivity in θ- or Z-pinches after the plasma has been imploded because it maintains a fairly large growth rate over a wide range of electron drift velocities and electron to ion temperature ratios and is not affected by electron gyroresonant effects. Estimates of the anomalous resistivity of the lower hybrid drift instability in this so-called postimplosion regime using a rough thermodynamic upper bound give values which are as much as a hundred times larger than classical resistivity.[15] Although these simulations cannot quite reach the regime of greatest interest [where the electron drift velocity (v_d) is less than the ion thermal velocity (v_i)] and must use somewhat artificial values for the parameters (e.g., $m_i/m_e = 100$ instead of 1836), they can give a very good indication of the nonlinear phenomena that are occurring. Comparisons with linear theory for the wave characteristics and with quasilinear theory

for anomalous resistivity and heating rates were made previously.[16]

A series of cases with v_d/v_i ranging from 1.1 to 13.5 have been studied. The cases with v_d/v_i greater than four are all characterized by the phase velocity of the growing waves (v_{ph}) being greater than v_i (i.e., a nonresonant interaction). They have been shown to saturate by ion trapping. Phase space plots of the ions show well-defined regions of excluded particles and the saturation level of the potential scales as $e\phi_s \sim m_i v_{ph}^2$. The more interesting cases are those with $v_{ph}/v_i < 1$ ($v_d/v_i < 4$). In this case there is no clear evidence for ion trapping or for quasilinear plateau formation on the ion distribution function (which sometimes occurs for resonant interaction). The saturation amplitiude scales as $e\phi_s \sim (m_e/m_i)^{1/2}(\omega_{ce}/\omega_{pe})m_i v_{ph}^2$. At present there is no detailed theory for the saturation mechanism in this regime. However, if this scaling holds in the postimplosion regime ($v_d/v_i < 1$), the consequence is that the value of the anomalous resistivity is reduced by an order of magnitude or more below the thermodynamic estimates and the threat of this instability to limit the lifetimes of large reactor-size pinch plasmas is reduced considerably.

b. Implosion Simulations. Several physical effects have been added to the hybrid model this year, the most interesting of which are multistep ionization, anomalous ion heating, ion-ion collisions (i.e., viscosity) and the Krall and Liewer resistivity model. The issue of ionization has been discussed elsewhere.[17] Anomalous ion heating of θ pinches has been included assuming the turbulent spectrum of cross field instabilities is strongly peaked in the θ direction, so that the θ velocity of each ion is changed by the amount $|\delta v| = (2\dot{\varepsilon}\Delta t/mn)^{1/2}$ per time step, where $\dot{\varepsilon}$ is the volumetric energy deposition rate to the ions due to turbulence, Δt is the time step and mn is the ion mass density. The sign of δV is assumed random. Presumably, however, a sufficiently detailed theory of turbulence would predict the distribution of δv among the particles. The total increase in ion energy per time step in a cell is then

$$\sum_i^N \frac{1}{2} m(\bar{v}_i+\delta\bar{v}_i)^2 - \frac{1}{2} m\bar{v}_i^2 = \sum_i^N m\bar{v}_i\cdot\delta v_i + \sum_i^N \frac{1}{2} m|\delta v_i|^2$$

$$= \sum_i^N \frac{1}{2} m|\delta v_i|^2$$

$$= \frac{1}{2} mn|\delta v_i|^2 = \dot{\varepsilon}\Delta t \qquad (5)$$

where ΔV is the cell volume. $\Sigma\bar{v}_i\cdot\delta\bar{v} = 0$ since the direction of $\delta\bar{v}$ is random.

The ion-ion collision update requires an isotropization time τ to be specified, and each ion is rotated through an angle $\Delta\theta = 1/2\pi\sqrt{\Delta t/\tau}$ each time step. Presently, the classical ion-ion collision time is used. For $T_i \sim 300$ eV, $n \sim 10^{16}$ cm^{-3}, $\tau \sim 0.6\,\mu s$ and if $\Delta t = 1$ ns, $\Delta\theta = 0.064$ radians. However, a collision time from turbulent theory might also be used here.

Simulations of the future ZT-40 experiment have been quite encouraging. For initial density of $2.5 \times 10^{15} cm^{-3}$, bias field of 1000 Oe, boundary θ field of 6000 Oe and risetime of 2.5 μs, $\langle T_i \rangle \geq$ 100 eV resulted. The sheath thickness in these calculations was similar to that of a ZT-1 calculation, i.e., 2 cm. However, the ZT-1 experiment had a 5-cm radius, so that by the time the sheath formed the implosion was over. The predicted T_i was approximately 20 eV while 50 eV was measured, implying that turbulent ion heating (which was not included in these calculations) was more effective than implosion heating. In the ZT-40 experiment, however, the plasma had a larger distance over which to implode, resulting in much higher temperatures even without turbulent ion heating.

Simulations of the Maryland θ pinch using the Krall-Liewer resistivity algorithm have been done. By comparing with observations we conclude that the predicted sheath thicknesses tend to be too small, implying that the algorithm is not resistive enough. Comparisons done by Liewer[18] also seem to indicate this, although the point is not explicitly stated.

Simulations with the modified Chodura resistivity of some experiments (particularly the University of Texas θ pinch) required adjustment of the constants multiplying ω_{pi} to obtain agreement with experimental results. However, once the

constants were adjusted the agreement was quite good. When scaling to an unknown regime for predictive purposes, the Krall-Liewer algorithm, having some theoretical basis for its scaling, may give the correct scaling. When simulating an existing device with known field profiles, the Chodura algorithm with appropriate constants (determined by comparison with the observed field profiles) seems to yield more accurate results.

In the University of Texas θ pinch experiment, rotation has been observed as predicted by the hybrid model. Typical results are shown in Fig. XIII-5 which indicate rotation of the reflected ions in the + $\hat{\theta}$ direction and of the snowplowed ions in the opposite direction. R. D. Bengtson (private communication) has considered several of the models previously postulated to explain the origin of rotation in a θ pinch, including wall shorting, collisions with the wall, reaction in the plasma, and reaction on external conductors, and has concluded that these mechanisms require a time scale significantly longer than the experimentally observed 100-ns development time for the rotation. In Fig. XIII-6 one can compare the observed rotation in the direction of ion gyration at three radii with the calculations. The agreement is good in both the position and the timing of the peaks. There is disagreement in the amplitudes by a factor of 5 which is not completely understood. In addition, the calculations predict a rotation in the oppo-

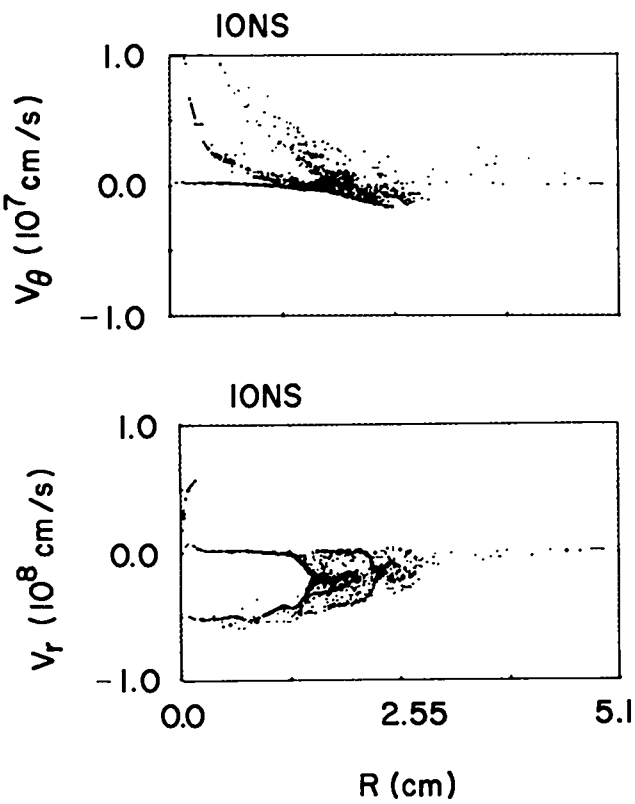

Figure XIII-5.
Ion phase space V_θ vs r and V_r vs r showing reflected ions rotated in + θ direction and snowplowed ions rotated in the opposite direction.

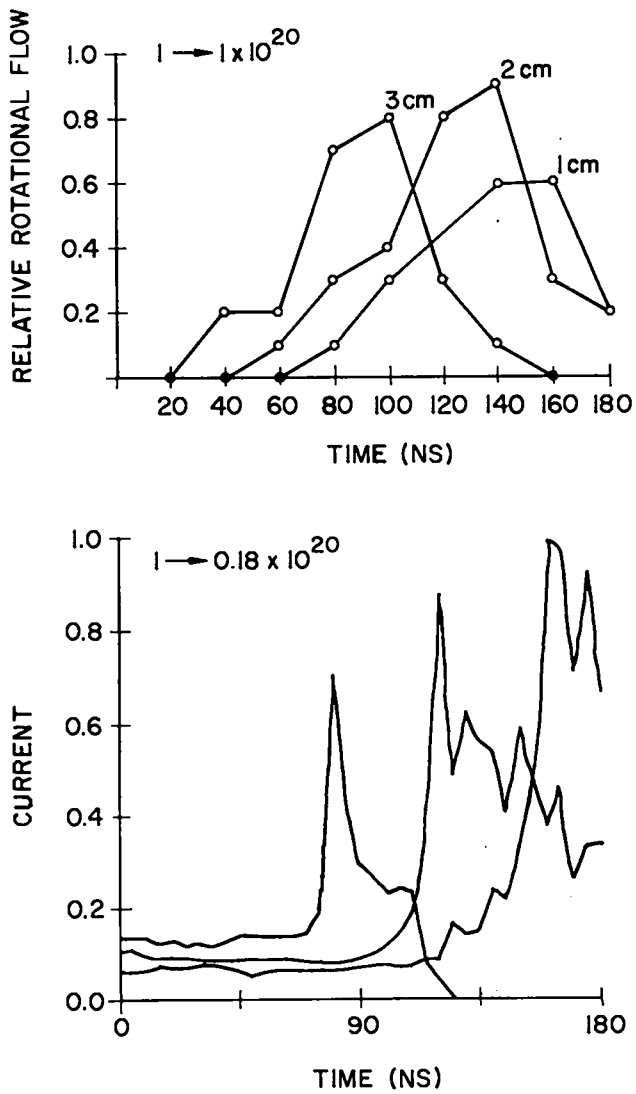

Figure XIII-6.
Comparison of plasma rotation measurements from the U. of Texas θ pinch. The top graph is the observed rotation at three radii as a function of time. The bottom curves are the corresponding calculations.

site direction, associated with the reflected ion beam, which has not been seen in the experiment.

The numerical model makes some detailed predictions of the behavior of the experimental plasma. Some of these predictions, such as the rotation just discussed, have recently become accessible to experimental verification. Two other such predictions of Faraday rotation and neutron yield have been measured recently on IHX. Faraday rotation measures $\int n_e H_z dz$ and the neutron yield is an extremely sensitive measure of the ion distribution function, since the D(d,n) cross section is strongly dependent on ion energy in this regime. In Fig. XIII-7, theory (curves) with experiment (x) are compared. The timings and widths of the features agree well while the magnitudes agree to within a factor of two. In particular, a Maxwellian distribution function of the same total thermal energy as calculated yields a neutron flux two orders of magnitude greater than measured.

c. 2D Hybrid Code. A two-dimensional hybrid simulation model has been developed for the study of plasma phenomena on extended time scales. The basic feature of a hybrid code which allows the extension of simulation time scales is the selective disregard of certain high-frequency electron phenomena. On time scales of interest in a hybrid code, electron-electron collisions are sufficiently frequent to consider the electrons as a thermal fluid. This particular model also makes use of the quasi-neutral or small Debye length assumption so that, to lowest order, the electron density is the same as that of the ions. Consequently no large deviations from charge neutrality (and the resulting short range electric field) are considered.

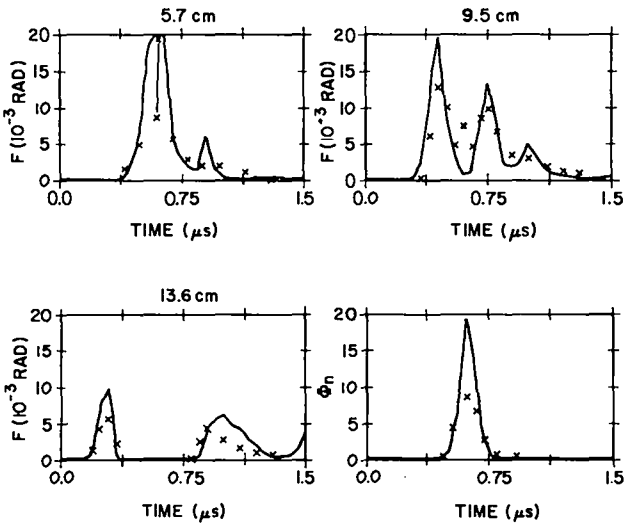

Figure XIII-7.
Comparison of Faraday rotation measurements from IHX. The curves correspond to calculations, the x's are experimental values.

In this hybrid model, the charactistic features of hybrid simulation models have been implemented in two dimensions as follows. The ions are represented by an ensemble of particles which are advanced in time by particle in cell techniques. The electron distribution is assumed to be collisionally relaxed on time scales of interest to the form

$$F_e(\vec{r},\vec{v},t) = N_e(\vec{r},t)\exp[-m_e[\vec{V}-\vec{U}_e(\vec{r},t)]^2/2\,T_e(\vec{r},t)] \quad (6)$$

where N_e, $\vec{U}_e$, and T_e are the electron density, drift velocity, and temperature, respectively. Since $N_e = N_i$, the charge continuity equation reduces to

$$\nabla\cdot\vec{J}_e=-\nabla\cdot\vec{J}_i \quad . \quad (7)$$

This equation can be used to find the irrotational part of the electron current given the ion current $\vec{J}_i$ and appropriate boundary conditions on the electron current. The solenoidal part of the electron current can then be obtained by making direct use of the electron momentum equation in a time-stepping scheme without concern for electron plasma oscillations.

The field calculations are accomplished in the nonradiative Darwin approximation.[19] An additional complication is that with one quasi-neutral assumption, Poisson's equation is not directly applicable since the charge density is zero to lowest order. The hybrid code counterpart to Poisson's equation is obtained by adding the irrotational part of the electron and ion momentum equations. Using quasi-neutrality and solving for

the irrotational part of the electric field, a new equation for the electrostatic potential is obtained,

$$\nabla\cdot\mu\,\nabla\psi = \nabla\cdot(\vec{D} + \mu\,\vec{E}_s + \vec{\xi}\times\vec{B}) \qquad (8)$$

where

$$\mu = (\omega_{pi}^2 + \omega_{pe}^2)/c^2 \qquad (9)$$

$$\vec{\xi} = 4\pi e/c^3\,(\vec{J}_i/m_i - \vec{J}_e/m_e)$$

and $\vec{D}$ is the sum of the divergence of the electron diadic <vv> and the corresponding ion quantity.

Preliminary test runs have been made on both implosion studies and lower hybrid drift unstable equilibrium initializations. Figure XIII-8 shows a comparison of the early growth of LHD flutes[16] from an equilibrium initialization accessible to both full particle (a) and hybrid (b) simulation. The apparent similarity of these two runs in both growth rate and wave number give much encouragement for the further development necessary to fully realize the potential of the model.

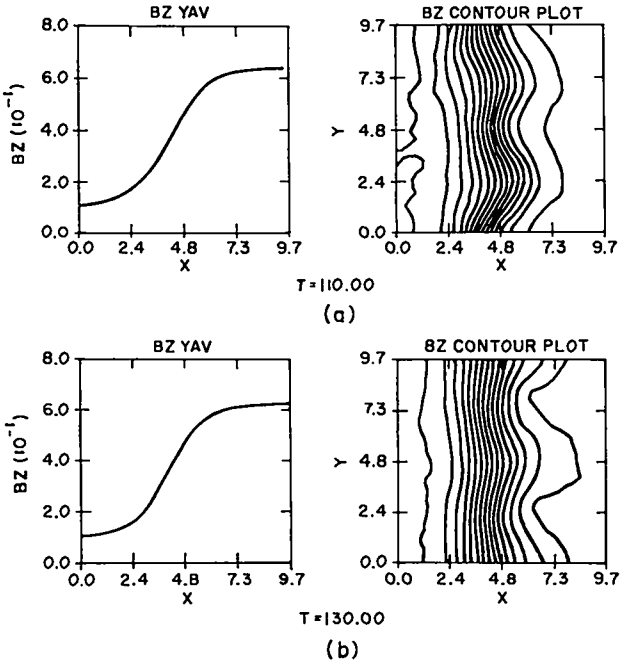

Figure XIII-8.
Comparison of LHD simulation with a) a full particle code, and b) the hybrid code.

C. MAGNETOHYDRODYNAMICS

Fluid models permit consideration of real experimental geometries by omitting some or all of the microphysics of confined plasmas. During the past year, considerable progress has been made toward the theoretical understanding of proposed and existing experiments such as the high-beta tokamak, the ZT-40, and the Scyllac. Nonideal effects such as radiation and transport and finite Larmor radius effects have also been modeled more realistically.

1. MHD Equilibrium and Stability.

a. High-Beta Tokamak Study. MHD stability and equilibrium studies were made for the racetrack shape of the proposed LASL High-Beta Tokamak. The details of this study are given in the proposal[20] and its supplement[21]. We found that we could obtain an equilibrium that is $q > 1$ everywhere for betas close to 1. The force-free currents and the elongation of the minor cross section allow equilibria where the magnetic axis is only moderately shifted in the outward direction. The Mercier q[22] which measures localized stability shows stability everywhere except very near the magnetic axis. There seems to be a strong correlation between ellipicity of the field lines and the Mercier criterion. Preliminary studies of a racetrack distorted toward a D shaped cross section indicate that it is stabilizing with respect to the Mercier q while it only slightly shifts the magnetic axis toward the wall. It now appears that the limiting factor so far as MHD studies are concerned will be global stability[23] which we hope to study in early 1977. Examples of a flux plot, magnetic fields, current, pressure, and safety factor along the midplane are shown in Figs. XIII-9 and XIII-10.

b. ZT-40 Reversed Field Z-Pinch Design Studies. Equilibrium and stability studies were made in support of the ZT-40 proposal.[24] It was found that for the reversed field pinch configuration with a flat top pressure profile there is an optimum aspect ratio which gives the greatest margin of stability for localized modes. Moreover, it has been found that, for hollow

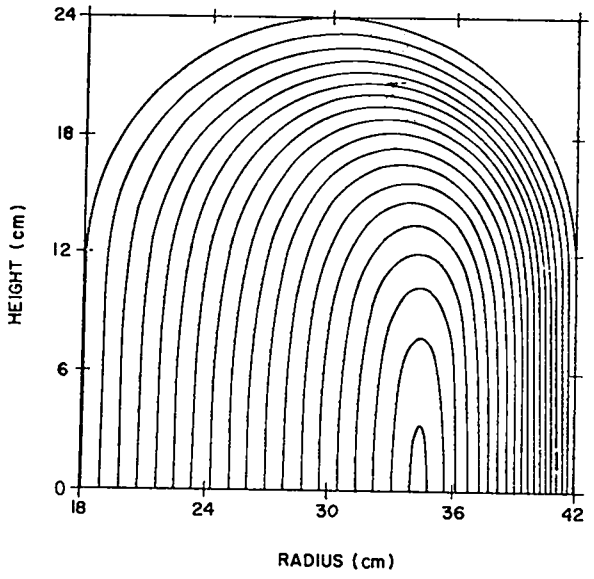

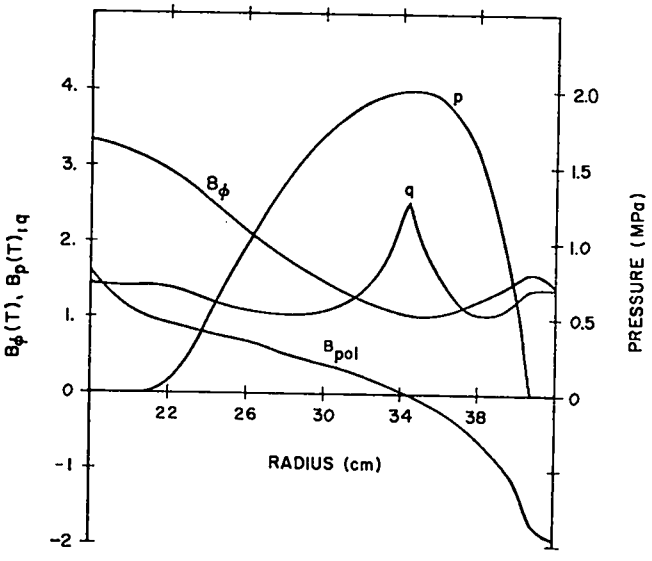

Figure XIII-9.
Flux plot for the top half of the racetrack and plots of B_ϕ, B_p, p, and q along the midplane of the torus. The safety factor q is calculated for each magnetic surface and is plotted at either side of the magnetic axis. Note the relatively small shift of the magnetic axis at this high pressure.

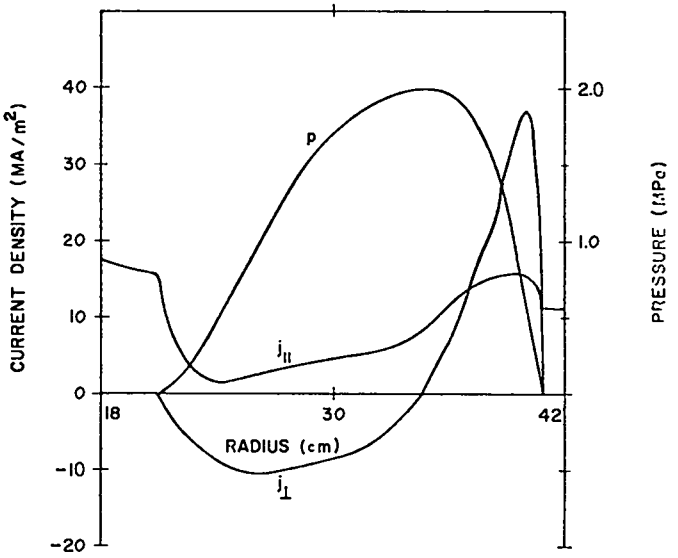

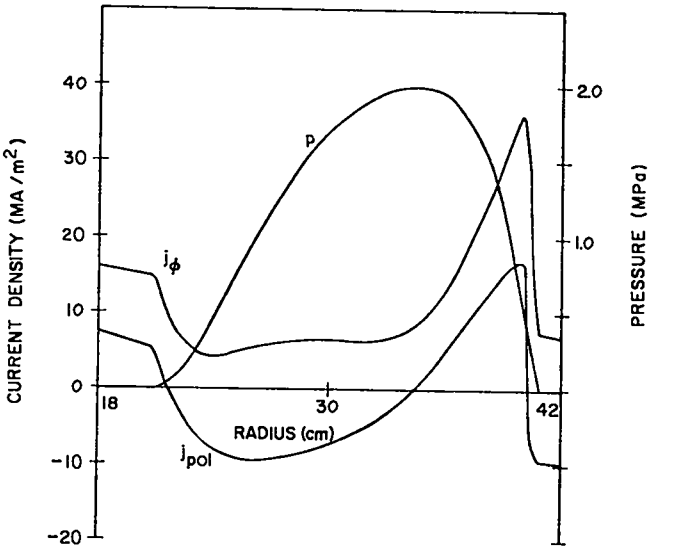

Figure XIII-10.
The current densities for the equilibrium of Fig. XIII-9 are plotted along the midplane of the torus. Inside the pressure profile which is also shown, both parallel and perpendicular currents are flowing, whereas only parallel currents can flow when p has dropped to zero. The poloidal currents change sign in that region, thereby separating the paramagnetic outside from the diamagnetic inside plasma.

pressure profiles, a toroidal equilibrium can be Mercier stable for a small aspect ratio. For the same case it is unstable[25] at a large aspect ratio. Equilibrium studies were made of the proposed ZT-40 to aid in the engineering design and to calculate current densities to be used in impurity radiation studies.

2. Scyllac Theory. The existence and structure of diffuse plasma equilibria in a high-stellarator such as Scyllac continue to be investigated by a number of numerical and analytic techniques.

a. Diffuse Toroidal θ-pinch Equilibria. Work was continued on a simple analytical formula-

tion of the diffuse toroidal θ-pinch problem. The equilibrium is generated by the quantity g which is an arbitrary function of $\beta(r,\theta)$. Here $\beta(r,\theta)$ is the plasma pressure normalized to the pressure of the z field B_o at the edge of the plasma. r,θ are cylindrical coordinates. The set of equations

$$\nabla_\beta^2 + \nabla\beta\cdot\nabla\phi/(1-\beta) = 0 \qquad (10a)$$

$$|\nabla\phi|^2 + r/R\ \cos\theta(1-\beta)^2 = g(\beta) \qquad (10b)$$

constitutes our model. Here, R is the major radius of the torus and ϕ can be thought of as a potential for the helical field $B_\perp; B_\perp \equiv \nabla\phi/B_o$. The boundary condition is that the outer magnetic surfaces must be circular. To generate Gaussian-like pressure profiles, $g(\beta)$ must be a logarithmic function of its argument. This can be seen from Eq. (10b); ϕ must rise like $r^\alpha(\alpha > 1)$ for $r \sim 0$.

Solutions have been found in the limits $\beta(r=0) = 1$, and as $\beta \to 0$. The connection of this model to previous work involving the skin current model has been established for low β. In particular, the amplitude formulas for the helical fields can be recovered when the condition is imposed on the solution of Eq. (10) that the mean displacement of the magnetic axis be zero. Similarly in the very high β limit [$\beta(r=0)= 1$] using

$$g(\beta) \propto (\ell n\beta)^\nu \qquad (11)$$

satisfactory analytic solutions have been found for a great part of the ν versus ℓ (helical number) plane and also for an ℓ = 0,1 combination. It is the middle range of β that remains elusive. Since this is probably the range most experiments lie in, it is important to understand it. A numerical scheme was devised to solve Eq. (10) for any beta "building up" solutions from low β. A code has been written by T. Cayton and D. Barnes using this scheme but the code has not as yet been tested.

It looks as if solutions are to exist in this general high β case, they are likely to involve several ℓ's. One can show that if ϕ is made up of three components, one main helical field ℓ with two sidebands at ℓ-1 and ℓ+1, a closed set of three equations can be obtained describing a very wide range of β. Equations (10) have been analytically treated in such an approximation using MACSYMA in the limit where h^2 (the pitch in the Z-direction) is equal to zero for an ℓ=2 system (with ℓ = 1,3 sidebands) expanding $\ell n\,\beta$ to $\theta[(1-\beta)^3]$. Only a trivial solution was found yielding a flat pressure profile. Our failure to find a Gaussian profile with this approach is most likely due to our inability to solve the equations with the logarithm unexpanded. The low-pressure regions on the outer edges of a Gaussian profile are not adequately accounted for. It is hoped that the numerical treatment of our equations will yield more fruitful results.

b. An Analysis of Toroidal Force Balance for a Diffuse Scyllac Plasma. To examine the coarsest features of diffuse toroidal equilibria, a simple analytic model which estimates the external fields required to produce toroidal force balance has been developed.

In the usual sharp boundary theory, the equilibrium equations reduce to two boundary conditions. The total pressure must match across the plasma-vacuum interface. The normal component of the magnetic field must vanish at the interface. In the "old Scyllac" ordering, the helical distortions of the plasma, or equivalently, the strengths of the externally applied helical fields, are taken to be of the order of the expansion parameter δ. The boundary conditions necessary for equilibrium are satisfied order by order in δ. To lowest order, the profile is a straight theta pinch in pressure balance with the externally applied field. To next order, the response of the plasma to the small helical fields is determined. Finally, to second order in δ, the toroidal effects are balanced by the interaction of the helical fields and distortions for the proper choice of the external fields.

If a similar expansion is carried out for a diffuse plasma with circular cross section, it is not possible to satisfy the second-order equations

requiring force balance at every point of the plasma for sufficiently general profiles. To obtain an estimate of the external conditions required for force balance, the condition of local force balance is replaced in the second order by the weaker condition that the total force integrated over the volume of the plasma vanish to this order.

For a toroidal theta pinch with circular cross section, the outward drift force per unit length is given by

$$F_R = (4\pi/R)(B_o^2/2\mu_o) \int \beta(r) r dr \ , \qquad (12)$$

where $\beta(r)$ is the plasma pressure divided by the total pressure. If small helical fields with long wavelengths are also present, the helical fluxes, ψ_ℓ, must satisfy

$$(r\psi_\ell')' - [1/B(rB')' + \ell^2/r]\psi_\ell = 0, \ \ell \neq 0 \qquad (13)$$

$$(\psi_o'/r)' - 1/B(B'/r)'\psi_o = 0 \ ,$$

where $B(r) = B_o[1 - (r)]^{1/2}$, so that forces balance to first order in δ. In the low-density plasma outside the main column, $B \to B_o$, and ψ_ℓ must assume the asymptotic form

$$\psi_\ell \sim a\,[c_\ell (r/a)^\ell + d_\ell (r/a)^{-\ell}], \ \ell \neq 0 \qquad (14)$$

$$\psi_o \sim a\,[c_o\ 1/2\ (r/a)^2 + 1/2\ d_o] \ ,$$

where the dimensionless constants c_ℓ and d_ℓ represent the applied and the diamagnetic components of the helical field away from the plasma, and where a is a characteristic radius of the plasma.

If helical fields with two neighboring symmetries are applied there results an interference force

$$F_{\ell,\ell+1} = 4\pi a(B_o^2/2\mu_o) c_\ell c_{\ell+1}(d_\ell/c_\ell), \ \ell \neq 0 \qquad (15)$$

$$F_{0,1} = \pi a\ (B_o^2/2\mu_o)\ c_o c_1\ (d_o/c_o + d_1/c_1) \ .$$

The condition for toroidal force balance is obtained by integrating the equation for the helical fluxes from r near zero until these fluxes obtain their asymptotic form. The relative size of the applied and the diamagnetic helical fields obtained in this way give the sensitivity of the interference force to the applied helical fields. A necessary condition for toroidal force balance is obtained by equating $F_{\ell,\ell+1}$ and F_r.

Results of such calculations for a sharp profile and for a diffuse, rigid rotor profile are shown in Fig. XIII-11, where the product of the applied helical fields required for force balance are plotted as a function of the plasma β on axis. The field product is expressed as a correction to the value predicted by sharp boundary theory. For an ℓ=1,0 system, the conditions for toroidal force balance are strongly dependent on the plasma profile, and a correction to the usual sharp boundary theory of more than a factor of two is required at high beta values. For an ℓ=1,2 system the correction to the predictions of sharp boundary theory is much smaller.

c. Numerical Studies of Diffuse Scyllac Equilibria. The equilibrium and properties of the Scyllac plasma have been studied using a numerical algorithm for the solution of the nonlinear magnetohydrodynamic equations in three dimensions.[26,27] The numerical approach significantly

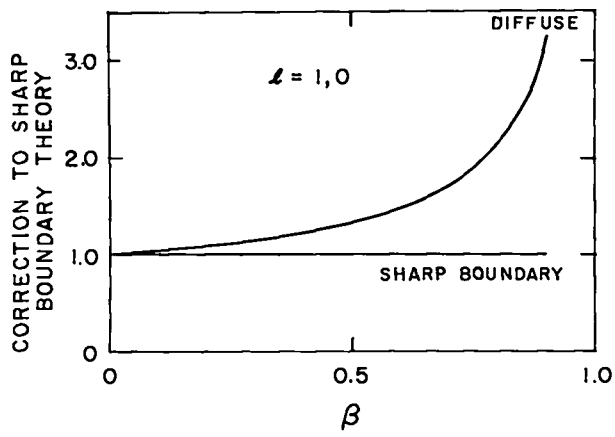

Figure XIII-11.
Field product for toroidal force balance from analytic force estimate. Upper curve is result for a diffuse profile expressed as a correction to sharp boundary theory. Lower curve is corresponding result for a sharp profile with a thin sheath.

extends the scope of the analytic equilibrium and stability studies, for it more closely represents the experimental conditions with diffuse profile plasmas and finite amplitude helical fields. Furthermore, the formulation includes the full system of dynamical equations, so that all relevant physical time scales are properly represented. Thus each initial value calculation gives a meaningful result, even when no stable equilibrium exists.

The numerical study has produced several new results. Of these, the most significant are:

1) The forces produced by applying helical fields agree with those computed from the analytic force estimate above and from various experiments.

2) The helical field amplitudes which produce toroidal force balance are significantly different for diffuse profile plasmas than for sharp boundary plasmas.

3) When toroidal force balance is obtained, diffuse profile equilibria result.

These results were obtained by initial boundary value calculations of the postimplosion dynamics of the Scyllac plasma. The transient responses of the plasma to imbalanced forces are damped by adding dissipation to the momentum equation. When a stable equilibrium exists, the plasma approaches it in time as its kinetic energy decays.

When, as in the case of Scyllac, the equilibrium is unstable to a few, well-defined modes, a stable equilibrium can be computed by adding the appropriate constraints. For example, the m=1, k=0 instability is suppressed by clamping the center of mass of the entire plasma column to a prescribed toroidal radius by a force of constraint. When this force is zero and flow has ceased, equilibrium is reached.

The results for an $\ell=1,0$ system are illustrated in Fig. XIII-12. The $F_{1,0}$ force computed from a numerical equilibrium calculation is compared with the analytic estimate and the force measured in various experiments. This force can be inferred from the experimental data in various ways. For example, in the Scylla IV-3 experiment, the force was measured by observing the acceleration which resulted when an $\ell=0$ field was applied to an $\ell=1$ straight equilibrium.

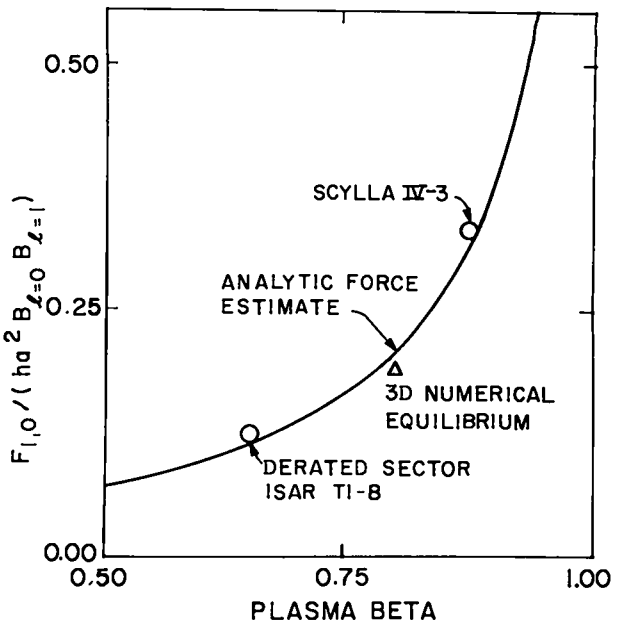

Figure XIII-12.
Experimental and numerical points are compared to the $F_{1,0}$ force predicted by the force estimate as a function of β.

In Fig. XIII-13, the helical field amplitudes which produce toroidal force balance are compared with the sharp boundary theory, with the design operating points of various experiments, and with the numerical equilibrium calculation. The operating points corresponding to the Isar experiment do not lie on the sharp boundary design curve because the helical fields were adjusted to give toroidal force balance.

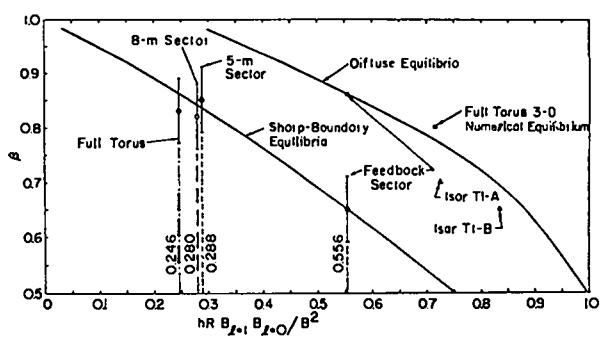

Figure XIII-13.
Experimental design curves for a sharp boundary and a diffuse profile giving the field product as a function of β. Various experimental design points are indicated for comparison.

The apparent disagreement between the various Scyllac experiments and the diffuse profile theory may be explained by the trajectory analysis of experimental data shown in Fig. XIII-14. This analysis shows that the plasma is not in equilibrium, but is acted on by transient forces which average approximately to zero in time during the observed confinement.

In Fig. XIII-15, the toroidal force imbalance

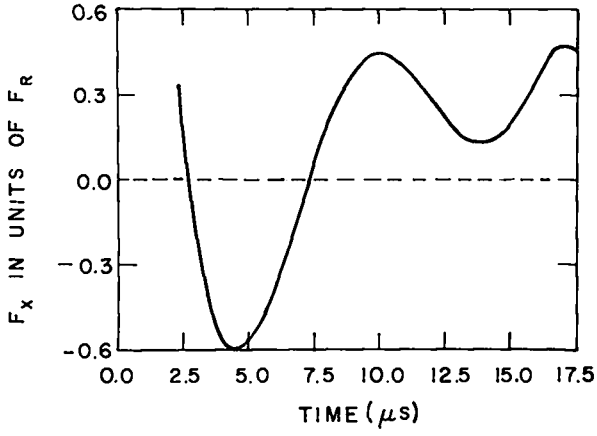

Figure XIII-14.
Toroidal imbalanced force as a function of time from analysis of an experimental streak photograph.

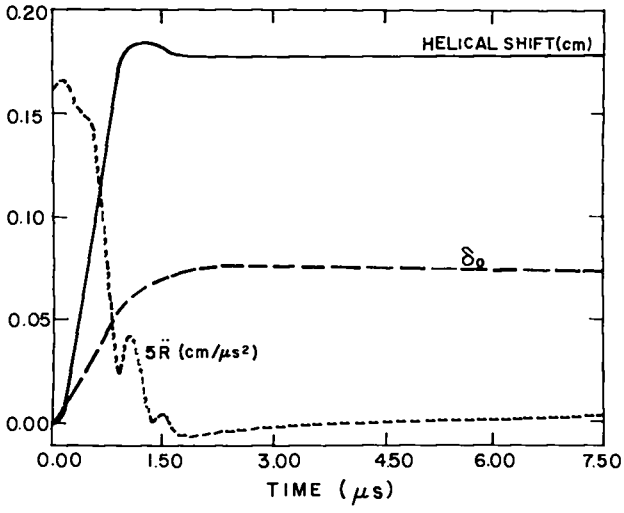

Figure XIII-15.
Results of a numerical equilibrium calculation. Upper solid curve is helical plasma response. Lower curve is bumpy plasma response. Broken curve is imbalanced radial drift force. The decay to zero of the acceleration indicates the approach to equilibrium.

is shown decaying to zero, indicating the approach to equilibrium in a numerical calculation. Other measures of the approach to equilibrium, such as the plasma diamagnetic response and the kinetic energy, display a similar asymptotic behavior.

Partly as a result of these calculations, an experiment on the present ℓ=1,0 sector is planned. This experiment will use a flexible programming circuit to drive ℓ=2 trimming coils which may make it possible to improve toroidal force balance.

d. Space-Time Response of the Scyllac Sector Plasma to a Localized Impulse. Earlier work, described in Group CTR-6 Quarterly Progress Report for the period ending Sept. 30, 1976, on the axial mode structure of the finite-length Scyllac sector plasma has been extended to yield an analytic theory of the space-time response of the column to a pulsed force applied near one end. The physical model is one dimensional in space, takes account of the dispersion of the m=1 modes in axial wave number space in both the unstable and stable domains, incorporates a physically meaningful wave energy absorption mechanism, and imposes sensible boundary conditions at the sector ends as previously outlined.

The analysis uses a Laplace transform in time and Fourier transform in space to construct the appropriate Green's function for the plasma response, based upon the model equation of motion including viscous dissipation. The spirit of the model requires the absorption coefficient to be an analytic, even function of the axial wave number k near the origin in k-space, and thus differs from the Alfven wave absorption model which introduces a logarithmic branch point at the k-space origin. The final result is in the form of a one-dimensional dispersion integral which explicitly contains contributions from three domains: an m=1 unstable domain which is modified by absorption but remains unstable, a previously unstable domain which is stabilized by absorption, and a stable domain whose oscillating spectrum is altered by absorption.

Guthrie Miller (CTR-3), at whose suggestion this calculation was performed, has evaluated the response function numerically and has compared the results with an experiment in which a transverse impulse is applied to the column near one end and

the resulting motion is detected at a station near the center of the sector. The experimental data reduction procedure isolates the column response by subtracting the motion which occurs in the absence of the applied impulse. The observed time-dependent response is in very good agreement with the calculated one. Moreover, the analytical result permits an ad hoc replacement of the viscous absorption coefficient by a phenomenological Alfven wave absorption coefficient, and a numerical evaluation by Miller shows that such a replacement has very little effect on the shape of the response function for a wide range of the parameter determining the absorption strength. It is interesting to note that the arrival time of the response pulse at the observation point is shortened by the damping effect, because damping acts like a low-pass k-space filter allowing the most unstable signal components to propagate and amplify preferentially.

The only discrepancy between theory and experiment is in the arrival time of the foot of the signal at the observation point. This involves an Alfven speed which is a constant parameter in the analytic model and whose numerical value, for a diffuse profile pinch, is not easily or uniquely determined. Nevertheless, the general agreement with respect to pulse shape inspires some confidence that the important dynamic factors determining the transverse motion of the Scyllac plasma column are reasonably well understood.

e. A "Sidewinder" Scyllac Configuration. The previously published theory[28] of a straight Scyllac with equal amplitude $\ell = \pm 1$ ripple fields of order δ was re-examined in view of the different results obtained by G. Miller, CTR-3. The discrepancy was finally resolved, and a paper yielding Miller's results was accepted, in principle, for publication in Nuclear Fusion. Physically, one has to employ a vertical field of order δ to establish MHD equilibrium to order δ^2. The resulting (sharp boundary) configuration has somewhat better MHD stability properties than the pure $\ell = 1$ Scyllac.

3. Nonlinear Effects. Some nonlinear effects (primarily due to plasma convection) on extensive modes in plane slab geometry have been studied. It is well established that the plane semi-infinite slab cannot support any extensive modes or instabilities in the framework of linear MHD theory.[29] Wobig has shown that a nonlinear convective solution is possible in the absence of shear.[30] It remains to be seen whether the slab can support some similar mode when a current is present flowing in the direction of the main magnetic field. Such a mode would be driven by this current rather than by a pressure gradient as was the case in Ref. 30 and it would be purely the result of the nonlinearity of the MHD model. In this work we found an extensive marginal ($\omega = 0$) mode of the semi-infinite plane slab which possesses a smooth enough profile near the singular surface ($\underline{k} \cdot \underline{B} = 0$) to form the basis of a nonlinear treatment. It involves long wavelengths in z (along the main field) and the initial k at which it arises is given by

$$k^2 = k_z^2 + k_y^2 \equiv .64 \qquad (16)$$

Our nonlinear treatment involves the time-dependent successive approximation method used in the Benard cellular convection problem of hydrodynamics.[31]

4. Radiation and Transport.

a. Radial Ambipolar Diffusion in High-Beta Theta Pinches. Assuming constant and uniform temperatures, an analytic theory of plasma decay was worked out that showed that the effective diffusion coefficient ranges from the usual $1/B^2$ diffusion coefficient at low beta to the field-independent field diffusion coefficient through a medium of resistivity at high beta. Furthermore, an analytic expression was derived to describe the decay at long times when nonlinear effects become important.

Finally, a numerical code was constructed that relaxed the assumption of constant and uniform temperatures and invoked the full two-fluid mass, momentum and energy equations as displayed in the work of Braginskii, including all thermoelectric terms. The analytic results mentioned above were then verified to a high degree of accuracy. This work was presented at the 1976 November APS meeting at San Francisco.

b. Impurity Radiation Losses. The energy loss by impurity radiation was studied[32] for both the ZT-40 and high-beta tokamak. The calculations for ZT-40 predict that with ohmic heating for 200 s an impurity level of 0.1% electron temperature values should be achieved ranging from 200 eV for densities of $1.0 \cdot 10^{15}$ to 100 eV for $5.0 \cdot 10^{15}$ cm^{-3} for total current densities of 3 kA/cm^2 with no initial ion heating. Initial ion heating of approximately 60 eV allows penetration of the radiation barrier for densities up to $1.0 \cdot 10^{15}$ cm^3. The code was used on the high-beta tokamak study to determine the rate of radiation loss from the plasma. It was found that the average electron-ion temperature decayed only 10% in a millisecond for an impurity of .1% and density of $5 \cdot 10^{15}$.

5. FLR Effects.

a. Vlasov-Fluid Model of the Sharp-Boundary Screw Pinch. We have continued to study analytically the equations of the Vlasov-fluid (VF) model[1,33] for a straight sharp-boundary screw-pinch configuration, keeping the leading order finite-Larmor-radius (FLR) effects of ions due to their motion transverse to the magnetic field. The ion motion parallel to the magnetic field leads to a frequency-dependent compressibility function different from that determined by the adiabatic equation of state used in ideal magnetohydrodynamics (MHD).[34] See Fig. XIII-16. As a result, many of the equations of the Vlasov-fluid model are, in this order, structurally identical to those of ideal MHD, except for a different compressibility function and the presence of a magnetoviscosity term.[34] The magnetoviscosity term can lead, not only to FLR stabilization of $m \geq 2$ long wavelength (near-θ-pinch type) modes, but also to FLR stabilization of $m \geq 2$ short wavelength (stabilized Z-pinch type) modes when $\beta|\omega/kv_{th}| >> 1$ and $|\omega/kv_{th}| << 1$.[34]

Even in the absence of FLR effects, the difference between the Vlasov-fluid and ideal MHD compressibility functions results in a decreasing value for the ratio of the growth rate γ_{VF}/γ_{MHD} with decreasing wavelength or with decreasing $|\gamma_{MHD}/kv_{th}|$. This ratio is approximately equal to unity only for modes with long wavelengths.[34] In the cases studied (see Figs. XIII-17-21), we have verified Freidberg's theorem[1] that the marginal stability limits of the Vlasov-fluid model and of ideal MHD are identical. Our analysis also may help to explain the apparent stability of the Kurchatov reversed-field experiment.[35]

b. Dispersion Differential Equation for the Vlasov-Fluid Model with Diffuse Profiles. A dispersion differential equation for the Vlasov-fluid model has been derived which is correct for small gyroradius, including the first-order corrections to the zero gyroradius limit. The differential

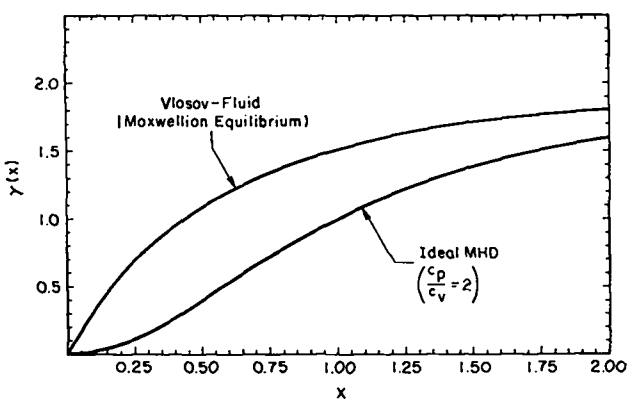

Figure XIII-16.
The compressibility function in the Vlasov-fluid and magnetohydrodynamic models. (c_p/c_v = specific heat ratio.)

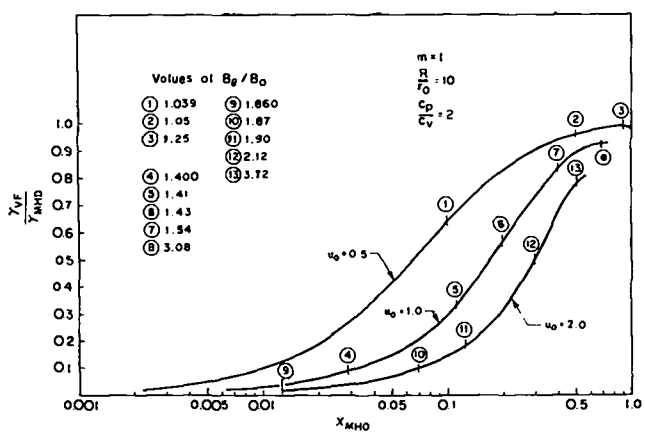

Figure XIII-17.
The ratio $\gamma_{VF}/\gamma_{MHD\ m=1}$ as a function of x_{MHD} ($x_{MHD} = |\gamma_{MHD}/kv_{th}|$) for a sharp-boundary stabilized Z-pinch. The values of B_θ/B_0 are plotted along curves specified by the value of u_0. ($u_0 = |k|r_0$, r_0 = plasma radius, R = conducting wall radius.)

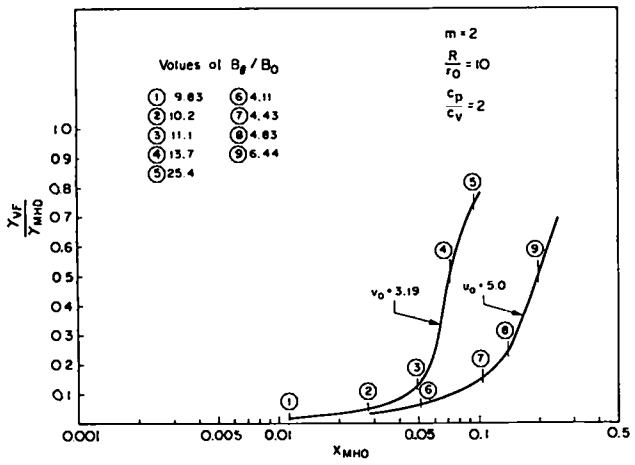

Figure XIII-18.
The ratio $\gamma_{VF}/\gamma_{MHD}|_{m=2}$ as a function of x_{MHD} for a sharp-boundary stabilized Z-pinch. The values of B_θ/B_o are plotted along curves specified by the value of u_o.

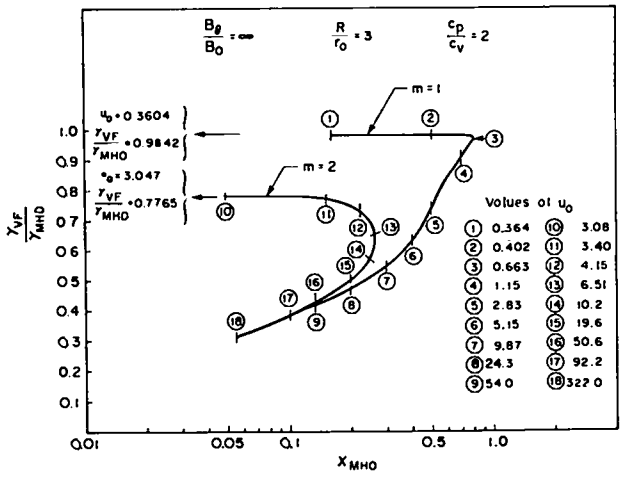

Figure XIII-19.
The ratios $\gamma_{VF}/\gamma_{MHD}|_{m\,=\,1,2}$ as functions of x_{MHD} for a sharp-boundary stabilized Z-pinch with $\beta = 8\pi p_o/B_o^2 = \infty$, $R/r_o = 10$. The values of u_o are plotted along curves specified by the value of m.

equation is valid for arbitrary equilibrium geometry and diffuse profiles. It is being specialized to the case of a straight screw pinch and will be used to determine approximate eigenfrequencies and eigenfunctions for screw pinches. A consequence of this derivation of a dispersion differential equation is the determination of an operator for generating expansion functions for the displacement vector, one of which is the eigenmode valid for small gyroradius.

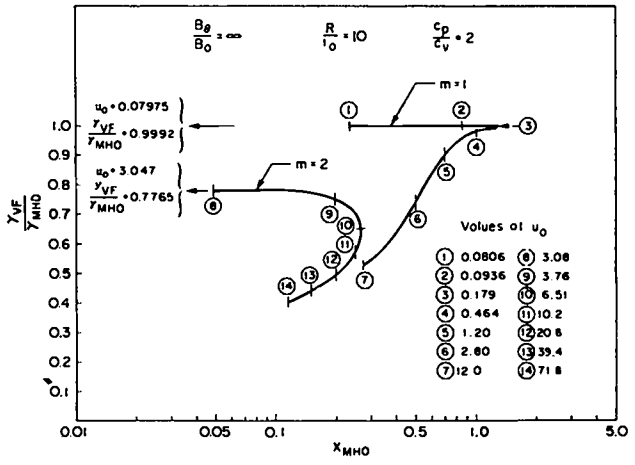

Figure XIII-20.
The ratios $\gamma_{VF}/\gamma_{MHD}|_{m\,=\,1,2}$ as functions of x_{MHD} for a sharp-boundary stabilized Z-pinch with $\beta = \infty$, $R/r_o = 3$. The values of u_o are plotted along curves specified by the value of m.

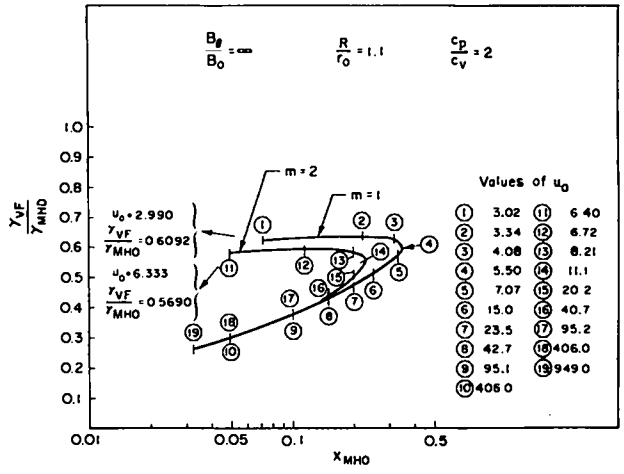

Figure XIII-21.
The ratios $\gamma_{VF}/\gamma_{MHD}|_{m=1,2}$ as functions of x_{MHD} for a sharp-boundary stabilized Z-pinch with $\beta = \infty$, $R/r_o = 1.1$. The values of u_o are plotted along curves specified by the value of m.

c. Ideal MHD Boundary Conditions for Force-Free, Low-Density Plasma. We have studied the equations of ideal MHD for a cylindrical region of force-free, low-density plasma where

$$\vec{\nabla} \times \vec{B}_o(r) = \alpha(r)\vec{B}_o(r), \ \alpha(r) \text{ arbitrary}, \quad (17)$$

and where

$$(\vec{\nabla}\times\vec{b})\times\vec{B}_o + (\vec{\nabla}\times\vec{B}_o)\times\vec{b} + 4\pi\gamma_{ad}\, p_o\, \vec{\nabla}(\vec{\nabla}\cdot\vec{\xi})$$

$$= -4\pi\rho_o\omega^2\,\vec{\xi}. \qquad (18)$$

The perturbed magnetic field $\vec{b}$ satisfies $\vec{\nabla}\times\vec{b} = (4\pi/c)\,\vec{J}$, where $\vec{J}$ is the perturbed current density.

Let us define $\bar{r}$ such that $\vec{k}\cdot\vec{B}_o(r) = kB_z(r) + (m/r)\,B_\theta(r) = 0$ at $r = \bar{r}$ and also define

$$\lambda \equiv \partial/\partial r\,[\vec{k}\cdot\vec{B}_o(r)]\,|_{r=\bar{r}} \ . \qquad (19)$$

For $\rho_o \to 0$ (with p_o/ρ_o constant), we have studied the solution of Eq. (18) in the neighborhood of $\bar{r}$; i.e., in the region where $r = \bar{r} + \varepsilon$ with $\lambda^2\varepsilon^2/4\pi\rho_o\omega^2 = O(1)$ as $\varepsilon \to 0$. We find that to leading order

$$\xi_r \propto \left\{\tan^{-1}\left[\frac{\lambda}{2\gamma(\pi\rho_o)^{1/2}}\,\varepsilon\right] - \frac{\pi}{2}\right\},\ \gamma^2 = -\omega^2, \qquad (20)$$

$$\xi_\theta = i\,\frac{m}{\bar{r}}\left(k^2 + \frac{m^2}{\bar{r}^2}\right)^{-1}\frac{d\xi_r}{d\varepsilon}\ ,\ \xi_z = \frac{k\bar{r}}{m}\,\xi_\theta\ ;$$

$$b_r = i\lambda\varepsilon\,\xi_r\ ,$$

$$b_\theta = -\frac{m}{\bar{r}}\,\lambda\left(k^2 + \frac{m^2}{\bar{r}^2}\right)^{-1}\left(\varepsilon\,\frac{d\xi_r}{d\varepsilon}\ \xi_r\right),\ b_z = \frac{k\bar{r}}{m}\,b_\theta\ ;$$

$$J_r = 0,\ J_\theta = k\left(\frac{4\pi\rho_o\omega^2}{\lambda}\right)\left(k^2 + \frac{m^2}{\bar{r}^2}\right)^{-1}\frac{1}{\varepsilon}\,\frac{d^2\xi_r}{d\varepsilon^2}\ ,$$

$$J_z = -\frac{m}{k\bar{r}}\,J_\theta\ .$$

The equations for ξ_r and b_r have the important consequence that even when the force-free, low-density plasma has an equilibrium current flow ($\vec{\nabla}\times\vec{B}_o(r) \neq 0$), the correct boundary condition on the magnetic field at $\bar{r}$ is that its radial component b_r must vanish.

These results may have application to the outer region of a pinch where the plasma density is tenuous and the pressure negligible, but where, unlike a true vacuum region, the electrical conductivity remains high.

d. Finite Gyroradius Stabilization of Pinches: Numerical Studies. During the past year the computer code for applying the Vlasov-fluid model has been used to make further studies of the finite ion gyroradius stabilization of the m=2 mode in a sharp-boundary screw pinch. A near-theta-pinch case with a conducting wall at infinity has been studied carefully, and the results for this case agree rather well with the small gyroradius theory of Turner.[33,36,37] Further studies are under way, particularly with the conducting wall close to the plasma column. As computations with this code have proceeded, it has been found necessary to investigate the convergence of the numerical results as various parameters associated with the numerical method are varied, and to optimize the choice of those parameters. These efforts are successfully decreasing the storage and running time required by the code.

The near-theta-pinch example with a sharp boundary was chosen as a first problem because of its relevance to the Scyllac device and its presumed simplicity. However, the model is also applicable to Z-pinch configurations that are relevant to the ZT experiments. Accordingly, some preliminary computations have been done for such cases and more are planned.

Provisions are being made to treat diffuse profile equilibria numerically with the Vlasov-fluid model. This requires an effective and automatic method for computing particle orbits in an arbitrary screw pinch field. Such a method has been devised, programmed, and tested during the past year. In addition, it is very important to determine a set of expansion functions for the perturbed displacement vector such that one of those functions is a good approximation to the mode of interest in the diffuse system. This is important in order that a 1×1 or 2×2 approximation to the dispersion matrix will yield a good approximation to the eigenfrequency of the mode of interest.

e. FLR Stability for $m \geq 2$ MHD Modes. It has long been known as an experimental fact that $m \geq 2$ modes which are theoretically predicted to be

MHD unstable, are not observed experimentally. The explanation for this is usually associated with finite ion gyroradii effects. Since the scaling of future large experiments depends fairly sensitively on the finite ion gyroradius criterion, considerable effort has been applied to accurately determine the stability condition.

The calculation of finite gyroradii effects utilizes a trial function approach in the Vlasov-fluid model. A diffuse equilibrium is constructed by assuming the ion distribution is a simple function of the total energy of a single particle. The linear stability of such equilibria in this model can be described in terms of a single displacement vector $\vec{\xi}_\perp$. Assuming $\vec{\xi}_\perp(r,t) = \exp(-i\omega t)\vec{\xi}_\perp(r)$, a complex energy relation may be obtained which takes the form

$$-\delta W = \mathrm{Re}\left[|\omega|^2 \int d\vec{r}d\vec{v}\ \partial f_o/\partial\varepsilon\ |\hat{s}_1|^2\right], \qquad (21a)$$

and

$$\mathrm{Im}\left[i\omega_e \int d\vec{r}d\vec{v}\ \vec{\xi}_\perp\cdot(\vec{E}_o + \vec{v}x\vec{B}_o)\partial f_o/\partial\varepsilon\ \hat{s}_1\right] = 0. \qquad (21b)$$

δW is identical to the potential energy of ideal MHD for incompressible displacements. The orbit integral, $\hat{s}_1$, has the form

$$\hat{s}_1 = -m_i \int_{-\infty}^{t} \vec{v}'\cdot d\vec{\xi}_\perp/dt'\ dt', \qquad (22)$$

where the primes indicate evaluation along particle trajectories.

Because of the close connection between the Vlasov-fluid model and ideal MHD, the MHD eigenfunctions of the equilibrium are used as trial functions in the above equations. FLR expansion leads to the conclusion that δW to lowest order is the ideal MHD energy principle. Consequently, it follows that $\omega_r^2 + \omega_i^2 \leq \gamma_{MHD}^2$. Using the MHD eigenmode as a trial function corresponds to equality in this relation.

To calculate the reduction in MHD growth rate with increasing ion FLR, the imaginary part can be solved iteratively for complex ω as the temperature of the assumed thermal ion distribution is progressively increased. Numerical simulation techniques are used to evaluate $\hat{s}_1$ by choosing a set of particles which represent the ion distribution at time t and stepping each particle backwards in time to obtain its integral contribution. The numerical problem is made tractable by exploiting particle trajectory periodicity in axisymmetric fields so that any given particle need be followed only for one period.

Figure XIII-22 shows typical values of ion FLR required to stabilize the m = 2 mode. Sharp boundary theories of Freidberg,[1] Turner,[33] and Pearlstein[38] are shown for comparison. Diffuse m = 2 MHD modes are stabilized for much lower temperatures for moderate values of β than would be indicated by three sharp boundary theories.

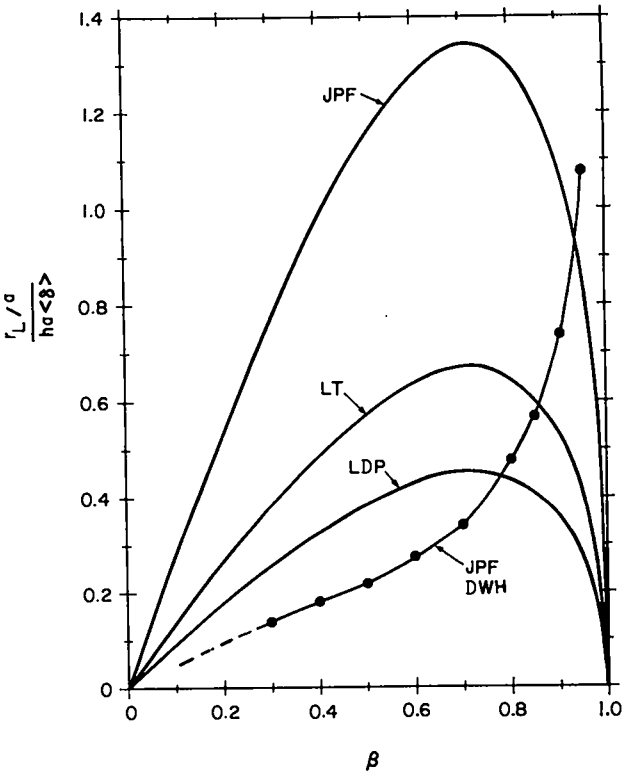

Figure XIII-22.
Normalized gyroradius vs β for marginal stability. Diffuse profile results (DWH, JPF) are compared to the sharp-boundary analytic results of Freidberg (JPF), Turner(LT), and Pearlstein (LDP).

D. EXPLORATORY CONCEPTS

Consideration of exploratory concepts remains an important part of high-beta theoretical research. The theory group has made contributions to several such areas including liners, field reversed theta pinch, and end plugs for the linear theta pinch.

1. Plasma Compression by Imploding Liners. The plasma adiabatic compression and DT burn effected by shockless implosion of a compressible, cylindrical metal liner is studied. Plasma energy losses are neglected and the liner is assumed to be end-plugged against particle losses. Let the gain Q be fusion energy output divided by liner energy input E_L. (Here E_L can represent either initial liner kinetic energy or total work done by driving pressure.) Optimal initial conditions, analytically obtained for many metals are T_i(keV) $\times [\pi R_i^2/A_{Li}]^{2/3} = 3.0$, and $N(cm^{-1}) = 9.0 \times 10^{20} (E_L/\ell[GJ/m])$. The corresponding gain is $Q = 7.0 \sqrt{E_L/\ell[GJ/m]} \times \sqrt{\rho_i/2\pi[g/cm^3]}$. The associated burn time is $\tau[\mu s] = (0.5\ R_i\Delta_i[cm^2]\sqrt{E_L/\ell[GJ/m]}) \sqrt{\rho_i/2\pi[g/cm^3]}$, and the final plasma pressure is $P_f = 5.0\ E_L/\ell A_{Li}$. Initial parameters are plasma temperature T_i, plasma line density N, plasma radius R_i; liner cross-sectional area A_{Li}, thickness Δ_i, density ρ_i, and length ℓ. A hydrodynamics code with detailed equation-of-state information verifies these results to within about 20%. Thus, without losses, a 50-cm copper liner would produce break-even with only 7 MJ! Preliminary loss estimates have been made.

Considerable progress has been made on the development of a computer code, CHAMISA, for the study of fast imploding liners. To date, the principal problems addressed have been the effects of liner compressibility and the diffusion of the driving poloidal (Z-pinch) magnetic field into the liner. To investigate liner compressibility, very sophisticated material equations of state have been incorporated into the code. These equations of state are produced in-house by Group T-4 and include solid, liquid, and vapor phases, and the effects of ionization, crystalline phase changes, and electron degeneracy. Extensive calculations have been made which verify over a significant range of parameters the analytic model discussed above. Liner compresssibility reduces the efficiency of conversion of liner kinetic energy to plasma energy to 50-70%, compared to 100% conversion for an incompressible liner. However, compressibility also increases the liner dwell time near peak thermonuclear burn, so that the yield is higher for the same peak plasma parameters than when calculated with an incompressible liner model. The net result is that a moderate increase in liner energy over that predicted by an incompressible model is required to obtain the same Q, where Q = (thermonuclear yield)/(maximum liner kinetic energy).

To obtain quantitative predictions for nonlinear magnetic field diffusion in the liner, empirical data on the solid and liquid phases of copper and aluminum were incorporated into the code. The equations for field diffusion are solved simultaneously with those for the motion of the liner. Some problems have been done with constant and prespecified time-varying applied currents, but for realistic calculations, the liner must be coupled to an external circuit containing capacitance, inductance and resistance. This goal will soon be attained.

2. Field Reversal Theta-Pinch Design. The toroidal equilibrium code[23] was used to design the magnetic mirror coils for the Field Reversal Theta Pinch (FRTP). The code allowed the design engineers to determine the shape of the magnetic mirrors which would prevent premature axial plasma loss in the FRTP.

3. Material Endplugs for Linear Theta Pinches. A theoretical effort has begun to analyze the consequences of material endplugs for mass loss and energy loss from a linear theta pinch. The capabilities of a one-dimensional Lagrangian hydrodynamics and heat flow code, CHAMISA, were extended to include a sharp-boundary model for the radial response of the plasma column. This permits the study of simple mass endloss, endloss with magnetic mirror fields, or thermal losses from a plasma adjacent to a material plug. In the case with material endplugs, the evolution of the ablated endplug material is followed in addition to its thermal interaction with the θ-pinch plasma. The basic result is that the ablated endplug material forms an "insulating" layer between the plasma and the

cold plug by virtue of the reduced thermal conductivity in the higher-Z (atomic number) material. An upper bound is placed on the endplug Z by considerations of radiation losses in the ablated material. Preliminary indications are that endplugs can significantly increase the energy confinement time for linear θ-pinches: first, by eliminating mass loss and, second, by forming a layer of lower conductivity material at the ends of the thermonuclear plasma.

REFERENCES

1. J. P. Freidberg, Phys. Fluids 15, 1102 (1972).
2. R. Gerwin, Los Alamos Scientific Laboratory report LA-6130-MS (1975).
3. H. Grad, Proc. Symp. Appl. Math. 18, 162 (1965).
4. G. F. Chew, M. L. Goldberger, and F. E. Low, Proc. Royal. Soc. (London) A236, 112 (1956).
5. S. P. Gary, M. D. Montgomery, W. C. Feldman, and D. W. Forslund, J. Geophys. Res. 81, 1241 (1976).
6. A. Kadish, Phys. Fluids 9, 514 (1966).
7. Y. Kato, M. Tajiri, and T. Taniuti, J. Phys. Soc. Japan 21, 765 (1966).
8. R. C. Davidson and J. M. Ogden, Phys. Fluids 18, 1045 (1975).
9. S. P. Gary and W. C. Feldman (submitted to Phys. Fluids).
10. T. E. Cayton (to be submitted to Phys. Fluids).
11. H. R. Lewis and K. R. Symon, Bull. Am. Phys. Soc. 19, 924 (1974).
12. H. R. Lewis and K. R. Symon, paper in preparation.
13. J. L. Schwarzmeier, H. R. Lewis, K. R. Symon, and B. Abraham-Shrauner, Bull. Am. Phys. Soc. 21, 1063 (1976).
14. N. A. Krall, Phys. Fluids 20, 311 (1977).
15. R. C. Davidson and N. T. Gladd, Phys. Fluids 18, 1327 (1975).
16. D. Winske and D. W. Hewett, Phys. Rev. Lett. 35, 937 (1975).
17. A.G. Sgro and C. W. Nielson, to be published.
18. P. C. Liewer, Nucl. Fusion 16, 817 (1976).
19. Nielson, C. W. and H. R. Lewis, Meth. Comp. Phys. 16, 367 (Academic Press, NY, 1976).
20. P.C.T. van der Laan, J. P. Freidberg, and K. S. Thomas, Los Alamos Scientific Laboratory report LA-6413-P (1976).
21. P.C.T. van der Laan, L. W. Mann, K.S. Thomas, supplement to LA-6413-P (1976).
22. C. Mercier, Nucl. Fusion 1, 47 (1960).
23. D. A. Baker and L. W. Mann, "MHD Studies of Numerically Obtained Toroidal Equilibria," Proc.2nd Top. Conf. Pulsed High-Beta Plasmas, (Max-Planck Institut fur Plasma-Physik, Garching bei Munchen, 1972), paper B7, pp. 69-72.
24. Proposal for the ZT-40 Reversed-Field Z-Pinch Experiment -- LASL Staff
25. A. Haberstich, D. Baker, J. N. DiMarco, L. W. Mann, and S. Ortalani, Pulsed High Beta Plasmas, D. E. Evans, Ed. (Pergamon Press, NY, 1976) p. 249.
26. J. U. Brackbill, Meth. Comp Phys. 16, 1 (Academic Press, NY, 1976).
27. W. E. Pracht and J. U. Brackbill, Los Alamos Scientific Laboratory report LA-6342 (1976).
28. J. P. Freidberg and R. A. Gerwin, Nucl. Fusion 15, 605 (1975).
29. G. P. Goedbloed and R. Y. Dagazian, Phys. Rev. A 4, 4 (1971).
30. H. Wobig, Plasma Physics 14, 403 (1972).
31. L. A. Segel: Nonequilibrium Thermodynamics, ed. by Donelly, Herman, Prigogine, (Univ. of Chicago Press, Chicago, Illinois, 1966).
32. These calculations were made using IMPRAD, a code written by S. Ortolani. Modifications have been added by D. A. Baker, F. C. Jahoda, H. J. Karr, and L. W. Mann.
33. L. Turner, "Finite-Larmor-Radius Stabilization in a Sharp-Boundary Vlasov-Fluid Screw- Pinch," Phys. Fluids, to be published April 1977.
34. L. Turner, "Vlasov-Fluid Theory of Short-Wavelength Instabilities of a Sharp-Boundary Screw-Pinch," Phys. Fluids, to be published April 1977.
35. A. G. Es'kov et al., (Centre des Recherches en Physique des Plasmas, Ecole Polytechnique Federale de Lausanne, Lausanne, Switzerland, 1975), Vol. I, p. 55.
36. H. R. Lewis and L. Turner, Nucl. Fusion 16, 993 (1976).
37. H. R. Lewis and L. Turner, Pulsed High Beta Plasmas, D. E. Evans, Ed., (Pergamon Press, New York, 1976) pp. 183-186.
38. L. D. Pearlstein, to be published.

XIV. COMPUTERS

S. T. Bennion, G. I. Chandler, R. C. Conrad, F. C. Jahoda, K. A. Klare, J. W. Lillberg, L. W. Mann, C. W. Nielson, and F. T. Seibel

A. INTRODUCTION

There has been a dramatic increase in the use of the PDP-10 and the network link to the MFE Computer Center 7600 during the last year. The yearly progress will be discussed in five phases: hardware enhancement, software enrichment, network development, experimental interfacing, and application of both the network and the PDP-10.

There have been significant advances in the use of both minicomputers and the PDP-10 with the experiments. 1) An extensive data acquisition system has been developed for the Prime 300 computer, which also performs the Scylla IV-P control functions. 2) The Sigma-2 systems have undergone extensive modifications. 3) A new type of transient waveform recorder has been procured. 4) Progress has been made on the link between the experiment minis and the PDP-10. 5) An analysis capability for asymmetric interferograms with 3-D plot display has been developed using a graphics tablet and the PDP-10. 6) Software to handle digitized two-dimensional streak camera output is being developed. 7) A start has been made on the ultimate goal of optically coupling all electrical signals leading in and out of the screen rooms in order to suppress electrical noise.

B. CTR USER SERVICE CENTER

1. Hardware. During the past year the USC has been augmented by an additional 192 K of fast memory, two 20 million word disks, a 9-track tape unit, a data channel to separate tape and disk traffic, and 16 additional terminal ports. These additions make the PDP-10 a very attractive computing alternative for CTR programmers with its 256 K words of core, 60 million words of disk space, and 32 terminal ports. The PDP 10 provides a powerful time-sharing tool for all but the biggest codes.

2. Software. The virtual memory (paging) support software was installed in mid-September. It has proved very successful. Large jobs may now be run in smaller actual core. This minimizes the load on the swapping system and permits jobs as large as 256K--as long as they need only a small portion in core at any one time. This portion cannot exceed the actual core available to the user or the administrative limit imposed upon the individual user.

A graphics package has been developed for output on the Versatec plotter and Tektronix graphics terminals. Plot files can be generated using PLOT-10 and/or CTR-6 plot libraries.

A combination text editor and word processing system called TEDI has been written for the PDP-10. The formatting section which is similar to RUNOFF allows a secretary to prepare documents including complex equations. This word processing system has been used for many papers, two CTR proposals, and this progress report.

3. Network. The MFE Computer Center network development throughout the year has made the MFE 7600 a reasonable alternative for many problems. The reliability has steadily improved and turnaround is now acceptable. We are still somewhat restricted from running large programs at night due to large core (LCM) limitations and the small LASL time allocation. Users who produce a large amount of microfiche output must wait for approximately 4 days on mail delivery. Tape access time for files can sometimes be excessive.

4. Experimental Interfacing. The Experiment Interface Computer (EIC) PDP-11 and PDP-10 link software has been installed and made operational. Further, with the help of a Digital Equipment Corporation (DEC) consultant and MFE programmers, the DEC and MFE supplied interface software has been merged with the EIC software and nearly checked out. The PDP-11 CAMAC software is not yet installed and the software between the PDP-11 and Sigma-2 has not been worked on yet. Data is now being shipped directly from the Scylla IV-P computer to the PDP-10 for archival and hologram analysis. Shot data from Scyllac is being written on magnetic tape and carried to the PDP-10 for analysis. IHX data are digitized and shipped via the Hewlett-Packard 9830 to the PDP-10 for analysis.

5. Application. There are now over 80 users running problems from simple editing to a large two-dimensional time-dependent MHD code. It is a testimony to the PDP-10 reliability that this problem routinely runs 8 hours without a fatal machine or software error. The PDP-10 has also been used to run a microprocessor simulator to aid in studies of such processors' adaptability for CTR experimental control. Among the significant uses of the network are calculations on lower hybrid drift instability, development of the two-dimensional hybrid code, and reactor design calculations.

C. AUTOMATED DATA PROCESSING AND COMPUTER CONTROL

1. Scylla IV-P Control and Data Acquisition System. Use of a Prime 300 computer for the control system on Scylla IV-P was described previously.[1] The control program has functioned well. Significant additions to the control program: a) monitor the vacuum and gas fill system; b) monitor all interlocks between shots to determine readiness for a charge cycle; and c) log on the disk during the charge cycle all analog inputs to the control system every 0.1 second. The latter feature is useful in trouble-shooting; e.g., bad gaps often produce a recognizable signature in the time history of the gap bias voltage.

The primary activity has been the implementation of an extensive data acquisition system. Two types of transient recorders, Biomations and SEC units, and the dedicated minicomputer of the Thomson scattering experiment are read out and archived in foreground by a call from the control program. Data analysis programs can then be activated in background mode while the control program is running. New hardware installed to enable these functions to be developed include 32K additional core memory for a 64K total, a second 3M word disk, a second graphics terminal, and improved interfaces to the CAMAC controller and the Versatek printer/plotter.

In addition, pending a high-speed parallel link, a teletype line driver CAMAC module has been installed on the Prime 300 to make it look like a terminal to the PDP-10. Software has been written to transmit shot data and to ship ASCII files back and forth. Other software developments include a graphics library and numerous data analysis programs.

2. Sigma II Computer System. Various improvements on the two Sigma 2's again increased their utility to the experiments. A surplused Sigma 2 was obtained and converted into a core memory expansion unit for the Scyllac computer, increasing the memory from 20K to 32K words. An additional 4K increased the SM-105 Sigma 2 to 28K words. A line printer was installed on the Scyllac computer. The Thomson scattering experiment was interfaced through CAMAC charge digitizers with complete calibration on each shot.

A versatile text editor was written and is in use to update numerous source files now stored on disk instead of on punched cards.

Data archiving has been completely revised. Innovations including dynamic temporary memory allocation, circular buffer schemes, data compression, file reorganization, enlargement of the public library to include I/O routines, and streamlined graphics and mag tape programs have reduced both storage space requirements and access time.

New programs added to the push-button set enable the operator to review efficiently either plasma parameters or recorder module behavior for all archived shots on the disk.

The various data analysis algorithms have been continually refined. For example, a least squares parabolic fit to the coupled cavity digitized waveform approaches 1/100 fringe resolution.

3. Transient Recorders. Solicitation of commercial vendors resulted in a new type of transient recorder system from Standard Engineering Corporation. The 10 MHz sampling rate and 6-bit resolution of the Biomations is retained, the memory is 512 words compared to the Biomation 256. They are packaged in units of 16 with a common clock, interfaced through a single CAMAC slot. Unlike the Biomations, they do not have a preamplifier, though an input attenuator permits variable signal range down to 1 volt full scale. Considerable interaction with the manufacturer, including the complete redesign of

the initially inefficient power supply, has resulted in cost-effective suitable units.

4. Minicomputer - PDP-10 Link. Although the anticipated high-speed link between the experiment minicomputer and the PDP-10 was not completed during the year, progress toward this end was made. The hardware, including CAMAC interfaces, line drivers and the PDP-11/40 port to the 10 are operational, but the integrating software remains incomplete. Considerable software modifications have, however, already been made on the 10, so that Scyllac Sigma-2 data files transferred by mag tape, appear to the user with terminal access to the 10 with the standard Sigma-2 conventions, e.g., out-putting to several screens in mixed order and giving the ability to mix FORTRAN write statements with plotting.

5. Interferogram Analysis. All previous quantitative analyses of holographic interferograms have either assumed cylindrical symmetry or at most unfolded the data along two orthogonal coordinates. The detailed study of end loss on Scylla IV-P required the development of an algorithm to determine particle inventory from asymmetric interferograms as well.

Software was developed to run a Tektronix 4953 Graphics Tablet from a 4014 display terminal on the PDP-10 in an interactive mode with visual feedback. Using this tablet, a program was written to give peak density, total particle inventory, and display line integrated density on an X-Y grid in a 3-D plot. Typical results are shown in the chapter on Scylla IV-P.

6. Streak Camera Automation. In preparation for the planned streak camera output digitization without the intermediary of Polaroid film, extensive software development is needed to pick out the signal from the two-dimensional digital array. This work has been started in cooperation with LASL's Image Evaluation Group (M-8). A smart sequential detection algorithm for determining trajectories was developed from Polaroid input on the CDC 7600. Significant aspects are the determination of minimal constraints on quality (e.g., noise, trace brightness, and continuity of fiducial markers) required in the original data, as well as algorithm efficiency, in order to enable it to run on the PDP-10 in less than five minutes.

7. Optical Coupling. An attractive solution to the electrical noise problems associated with high-voltage, pulsed plasma devices just becoming technologically and economically feasible, is the complete isolation of the screen rooms by fiber optics coupling of all control and diagnostics electrical signals. Typically, there are a variety of signal types, both analog and digital, spanning bandwidth requirements from 1 kHz to 40 MHz, with some analog signals requiring better than 0.1% linearity. Each presents its own problems in interfacing the optics and electronics, and we have begun study of these on a broad front. In particular, construction of an optical data link for the ZT-S Biomation recorders (24 channels at 1 MHz data rate) to the Sigma-2 is complete and undergoing initial tests. An optically coupled CAMAC parallel branch highway is under active consideration for the ZT-40 control system.

REFERENCE

1. G.A. Sawyer, compiler, "LASL Controlled Thermonuclear Research Program, January-December 1975," Los Alamos Scientific Laboratory report, LA-6582-PR, December 1976.

XV. ENGINEERING

E. L. Kemp, A. G. Bailey, K. J. Bickford, G. P. Boicourt, W. H. Borkenhagen, T. R. Cole, R. S. Dike, C. F. Hammer, K. W. Hanks, L. D. Hansborough, H. W. Harris, K. J. Johnson, R. W. Kewish, K. J. Kutac, J. G. Melton, and W. C. Nunnally

A. ZT-40

1. Introduction. The satisfactory performance of the ZT-S reversed field toroidal Z pinch led to the planning for a larger device to be built in the 1977-1978 time frame. A proposal was prepared and submitted to Washington in the summer of 1976, and in August a review committee gave a favorable recommendation for building ZT-40. During this period, a performance criterion was defined and an engineering team was organized. However, when funding for the experiment was delayed, most of the engineers were reassigned to other projects. In mid-December, initial funding was provided and the design of ZT-40 is now under way.

2. System Layout. ZT-40 will be installed in an area about 16 m x 40 m that is now partially occupied by the applied plasma physics apparatus of CTR-1. This equipment will be moved to another location. A plan view of the top level of the system is shown in Fig. XV-1. The torus in the center with its 12 iron cores sits on an independent platform and is surrounded by a diagnostic platform. The capacitor racks are located around the diagnostic platform and the areas to the left and right are for diagnostic assembly and the screen room.

Figure XV-2 shows an elevation of the system. Energy will flow through coaxial cables from the capacitors and their start switches to the crowbar switches below the capacitors. The energy will then flow through more coax cables to the mixer. The function of the mixer will be to produce a uniform current in the load, even if all the switches do not fire. Each of the two principal circuits in the system has mixers. The energy will flow through cables to the machine torus.

3. Energy System. A reversed field toroidal Z pinch requires two principal fields, an initial toroidal B_Z field, which is subsequently reversed, and a poloidal field, which is induced around the plasma when it carries current. Figure XV-3 shows a simplified schematic and attendant waveforms for one operational mode of ZT-40.

The system will operate in the following sequence: The I_θ bias bank in the top circuit will be fired and the current will rise to a peak in about 75 μs. About 30 μs before peak current, the preionization PI bank in the lower circuit will be fired and produce a half cycle of preionizing current. At this time the $I_{\theta R}$ reverse bank will be fired and drive the I_θ current negative. Simultaneously the I_Z bank will raise the I_Z current on

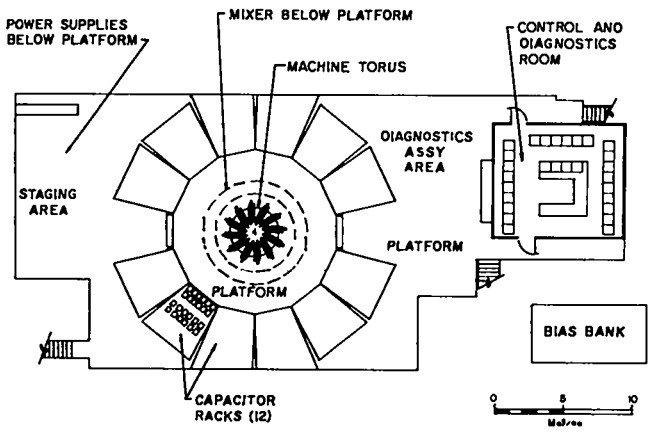

Fig. XV-1.
ZT-40 layout.

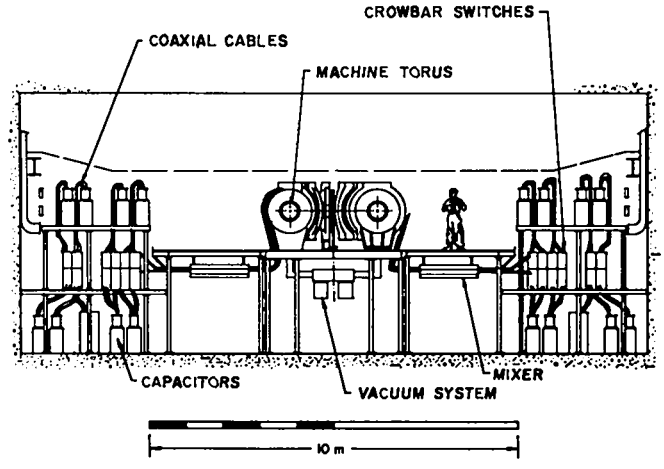

Fig. XV-2.
ZT-40 section.

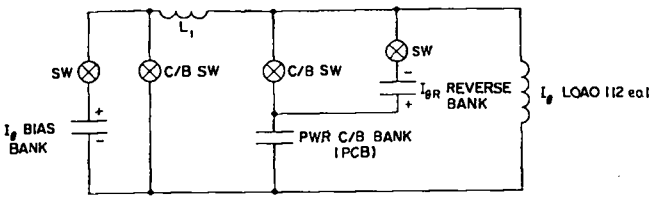

I_θ (B_z TOROIDAL) CIRCUIT

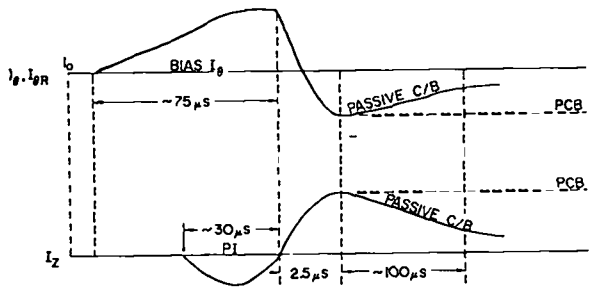

I_Z (B POLOIDAL) CIRCUIT

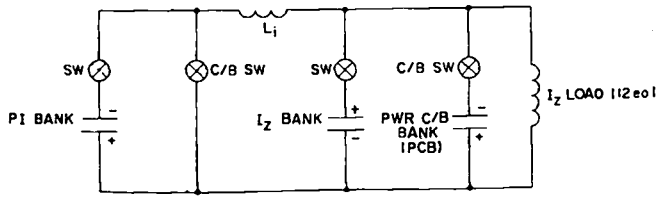

Fig. XV-3.
ZT-40 schematics and waveforms.

the plasma to a maximum and generate the poloidal field around the plasma. At peak current, both the $I_{\theta R}$ and the I_Z currents will be crowbarred. In the initial experiments, the power crowbar bank (PCB) will be shorted and switches will crowbar the current with an L/R decay time constant of about 100 μs. Later, a power crowbar bank will be added to produce an essentially constant current for 200 μs.

The majority of the components to be used in ZT-40 were developed and successfully used in Scyllac. These include the 60-kV capacitor for the I_Z and $I_{\theta R}$ banks, although ZT-40 will be designed for a maximum operating voltage of 50 kV. The 10-kV bias capacitors will be the 170-μF units developed for low reversal application and are quite inexpensive. The coaxial cable will be the type used in Scyllac. The passive crowbar gaps will be the ferrite decoupled gaps employed as crowbar gaps in Scyllac. The start gaps will be similar to the field distortion gaps developed for ZT-S applications. They will be used because of their wide voltage range. The ZT-40 field distortion start gap shown in Fig. XV-4 was designed for this application and operates successfully from 13 kV to 50 kV by a slight variation of the pressure in the gap. About 500 of these gaps will be required in the system.

The parameters of the various capacitor banks are given in Table XV-I.

4. Machine Features. The ZT-40 machine is shown in Fig. XV-5. The 40-cm minor diameter discharge tube is surrounded by a 2-cm-thick aluminum toroidal current shell that is divided into 12 segments. Each segment is driven by the primary feed cables so that the maximum total induced

TABLE XV-I

CAPACITOR BANK PARAMETERS

	I_θ (Bias) Bank	PI Bank	$I_{\theta R}$ (Reverse) Bank	I_Z Bank
V(kV)	10	20	50	50
C(μF)	30000	1125	528	448
W(kJ)	1500	225	660	560
$I_{max.}$(MA) (total)	3.4	2.0	6.0	7.2
τ/4(μs)	75	15	2.5-30	2.5-30

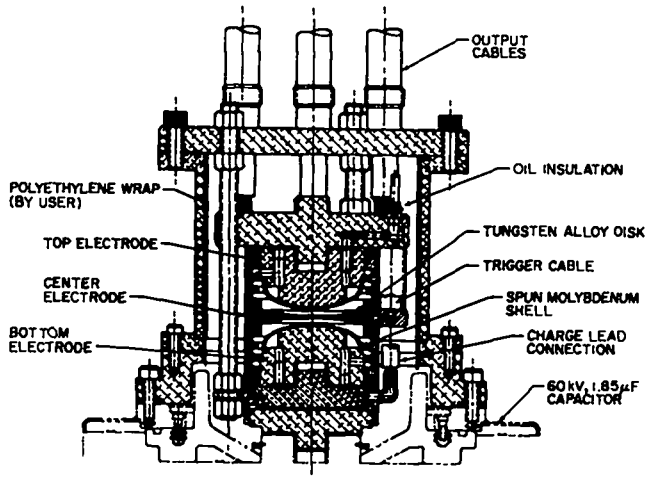

Fig. XV-4.
ZT-40 field distortion start gap.

voltage around the full torus is 600 kV. The iron core improves the coupling between the aluminum primary and the plasma secondary. The toroidal field coils that produce the B_z field are also directly driven with cables.

Table XV-II gives the ZT-40 machine parameters.

5. Project Management. The design and construction of ZT-40 will be managed by methods developed during the construction of Scyllac and Scylla IV-P. The general approach is shown by the following single line PERT diagram.

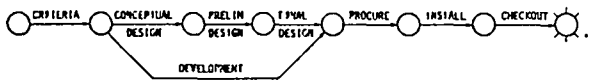

TABLE XV-II

ZT-40 MACHINE PARAMETERS

Discharge tube inner radius	20 cm
Major radius	114 cm
Aspect ratio (with respect to metal primary)	5.2
Plasma current	600 kA
Number of Z-current feed points	12
Number of iron cores	12
Total number of Z-current cables	1512
Total number of θ-current cables	1728

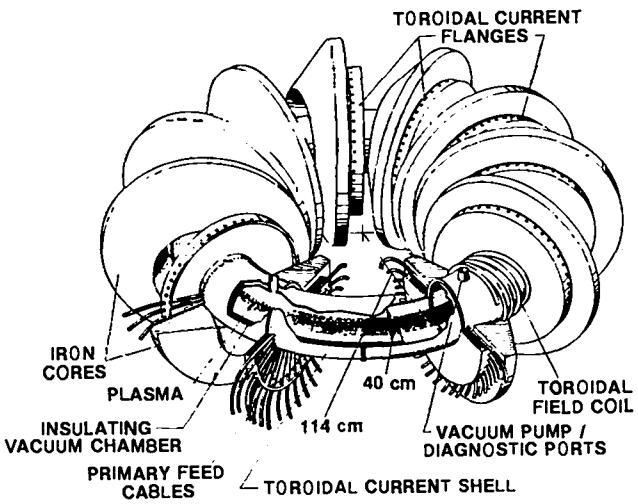

Fig. XV-5.
ZT-40 machine.

First, criterion is established for each design activity. An engineer then proposes a conceptual design, which is reviewed by all cognizant parties. After approval, a preliminary design is made and again reviewed. With approval, procurement of long lead time conventional equipment can begin. The design of subsystems and new components also begins with final design. The final design is carefully reviewed and documented approval is necessary before procurement can proceed. Installation and check-out complete the cycle. During installation, weekly meetings are held to discuss progress and problem areas.

The organization of the design team for ZT-40 is complete and all design activities have been delegated. The system and the design criteria for each activity have been written and approved. The system conceptual design has been completed and approved. A preliminary PERT has been prepared and a budget estimate made. Committees of appropriate physicists and engineers have been formed to follow each design. Some long lead time procurement has began. The actual design work will start in January 1978 with a target date of July 1979 for the beginning of ZT-40 plasma physics.

6. Development. The development activity for ZT-40 is directed primarily at the crowbar systems. The ZT-40 experiment is to be operated in two phases. The first phase will require a passive crowbar system to provide exponentially decaying confinement fields. In Phase II a power crowbar system will be required to provide requirement constant confinement fields for up to 250 μs, after which the field will exponentially decay.

The passive crowbar circuit of Phase I is shown schematically in Fig. XV-6. The passive circuit is the "standard" circuit at LASL and has been used in many experiments. Most of the components shown in this figure have been developed for previous experiments. The 50-kV start gap was designed for the ZT-1 experiment but not thoroughly tested; therefore, a life test was run to 10,000 shots at 50 kV and 50 kA at a rate of 5 per minute. The life test indicated that the gap has good integrity and wearability. After testing several trigger electrode materials, a

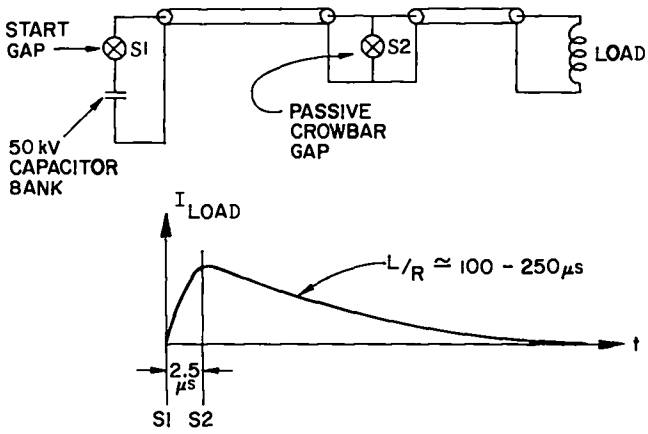

Fig. XV-6.
Passive crowbar system.

tungsten material was selected, which will give a life time greater than 10,000 shots. In addition, voltage self-breakdown, triggering characteristics for all combinations of polarities, and three gap spacings were tested. These tests provided a foundation from which to choose the gap spacing and operating pressures for ZT-40. The chosen gap spacing of 0.23 inch can be maintained with standard tolerances and will operate from 12 to 60 kV at reasonable air pressures.

The component requiring immediate development and testing for a passive crowbarred ZT-40 system is the passive crowbar gap S2 in Fig. XV-6. The gap design used for this application is shown in Fig. XV-7. This design, which was chosen because of its proven operation and reliability, uses the same electrode and trigger configuration of the present ferrite isolated, Scyllac piggy-back crowbar gap. The new header arrangement is designed to accept multiple cables and locate the crowbar gap at a distance from the capacitors to be crowbarred. Note that provisions have been made to use this design in the power crowbar mode by adding cables from a power crowbar transformer. However, these cables will be shorted at the crowbar gap header during the passive crowbar phase.

The header and gap have been tested over the entire voltage range of 12-60 kV at a maximum average current of 140 kA, which is twice the average current of the actual ZT-40 crowbar gap. Although the voltage transients occurring at the crowbar gap in the test circuit are more severe

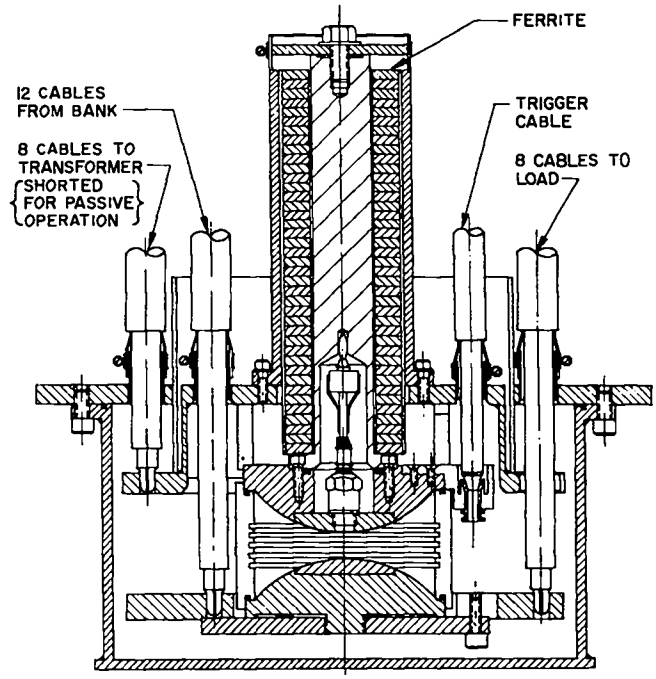

Fig. XV-7.
ZT-40 passive crowbar gap.

than those actually present in the ZT-40 circuit, the gap has performed very well with a 17-coulomb charge-load.

The requirement of the passive crowbar system are listed in Table XV-III. The power crowbar system requires much more development for the ZT-40 and for future sustained field experiments. The power crowbar circuit for ZT-40 is shown in Fig. XV-8. To sustain the peak crowbarred load current, I_p, produced by the 50-kV capacitor bank,

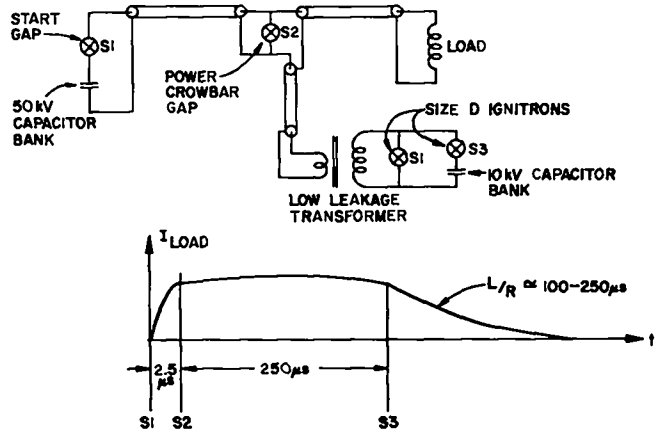

Fig. XV-8.
Power crowbar system.

sufficient power crowbar voltage, V_{PCB}, must be introduced into the crowbarred load inductance circuit to cancel the circuit resistance, R_{ckt}, voltage drop or $V_{PCB} \simeq I_p R_{ckt}$.

The value of V_{PCB} is on the order of 1000 volts for the circuits of ZT-40. A series, low-leakage, stepdown transformer was chosen to supply the sustaining voltage to the crowbarred circuit. Ideally, the power crowbar energy source consists of a low-voltage, large-capacitance, low-inductance bank that provides the power crowbar voltage for long resonant LC times and does not appreciably reduce the circuit $\dot{I}$. However, low-voltage, low-inductance capacitors are not cost effective in the voltage range required. With the transformer, the cost-effective, 10-kV capacitors can be used, and the stepdown turns ratio of the transformer combined with the low-leakage inductance introduces a minimum parasitic inductance into the main circuit. The crowbar circuit has essentially the same peak currents, but the coulomb load is much larger. The major components to be developed for the ZT-40 experiment are a high-voltage, high-coulomb crowbar switch and a low-leakage inductance transformer.

The requirements for the power crowbar switch are shown in Table XV-IV.

A high-voltage, high-coulomb crowbar gap has been designed and is scheduled to be tested next year. This gap is shown in Fig. XV-9. A high-coulomb crowbar gap requires a large volume, a large air flush rate, and special insulator shielding to insure reliable operation and mechanical integrity during switching.

It is very difficult to combine large coulomb capacity with high-voltage and low-inductance characteristics. For instance, spark gaps are commonly high-voltage, low-inductance devices, but are generally suitable for charge levels of only a few coulombs. Ignitrons, on the other hand, are high-coulomb devices (up to 2000 coulombs) but are rarely used above 15-20 kV and are inherently high-inductance and slow-switching devices. In

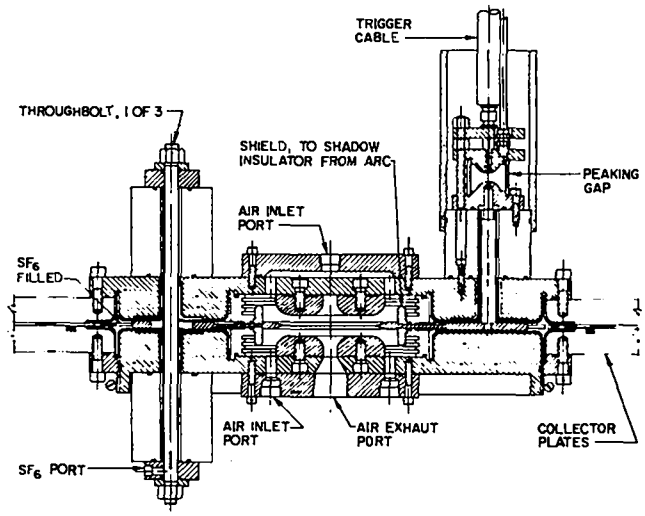

Fig. XV-9.
High-coulomb crowbar spark gap.

TABLE XV-III

ZT-40 PASSIVE CROWBAR GAP REQUIREMENTS

Maximum Values

I_θ Circuit (L/R = 250 μs)

Requirement	System	No. Gaps	Unit
Maximum Crowbar Current	28 MA	144	194 kA
Average Crowbar Current	10 MA		69 kA
Crowbar Coulomb Load	2500 c		17.4 c
Inductance			
Maximum Voltage Transient	≤ 90 kV		≤ 90 kV
Switching Voltage	≃ 0 V		≃ 0 V

I_Z Circuit (L/R = 100 μs)

Requirement	System	No. Gaps	Unit
Maximum Crowbar Current	28 MA	144	194 kA
Average Crowbar Current	10 MA		69 kA
Crowbar Coulomb Load	1000 c		6.9 c
Inductance	0.2 nH		≤ 30 nH
Maximum Voltage Transient	≤ 90 kV		≤ 90 kV
Switching Voltage	≃ 0 V		≃ 0 V

TABLE XV-IV

ZT-40 POWER CROWBAR SWITCH REQUIREMENTS

Maximum Values, 250 μs Flat Pulse with L/R Tail

I_θ Circuit (L/R = 250 μs)

Requirement	System	No. Gaps	Unit
Maximum Crowbar Current	28 MA	144	194 kA
Average Crowbar Current	10 MA		69 kA
Crowbar Coulomb Load	5000 c		35 c
Inductance	≤ 1 nH		≤ 150 nH
Max. Voltage Transient	90 kV		90 kV
Switching Voltage	≃ 1 kV		≃ 1 kV

I_Z Circuit (L/R = 100 μs)

Requirement	System	No. Gaps	Unit
Maximum Crowbar Current	28 MA	144	194 kA
Average Crowbar Current	10 MA		69 kA
Crowbar Coulomb Load	3500 c		25 c
Inductance	≤ 35 nH		≤ 50 nH
Maximum Voltage Transient	≤ 90 kV		≤ 90 kV
Switching Voltage	1 kV		1 kV

order to effect a marriage of these two components into a low-pressure (vacuum), high-voltage, low-inductuance, high-coulomb switch, the mercury wetted spark gap shown in Fig. XV-10 was designed and is scheduled for testing in 1977.

The final mercury wetted gap design will probably use molybdenum for all interior surfaces because of its favorable properties with respect to mercury. However, the test models will be constructed from stainless steel, which is only slightly affected by the mercury. Instead of a mercury pool cathode, the mercury wetted gap will use a metal cathode covered with a mercury film. This is to prevent excess mercury from being vaporized and deposited on insulating and anode surfaces and affecting voltage hold-off. The triggering method for the mercury wetted gap has not been decided. Several methods, including a trigatron igniter and a mercury vapor plasma gun, will be tested as methods of injecting ionized material into the main electrode region.

All of the crowbar gap testing for ZT-40 will be conducted in a test bay constructed in 1976 that simulates the ZT-40 circuit. An electrolytic capacitor bank will be used to power crowbar the test circuit and provide large coulomb loads for the test gaps. The power crowbar circuit for ZT-40 requires a rather unique transformer. The specifications for the transformer are listed in Table XV-V. Two types of transformers were considered for this application, a Hirano iron core

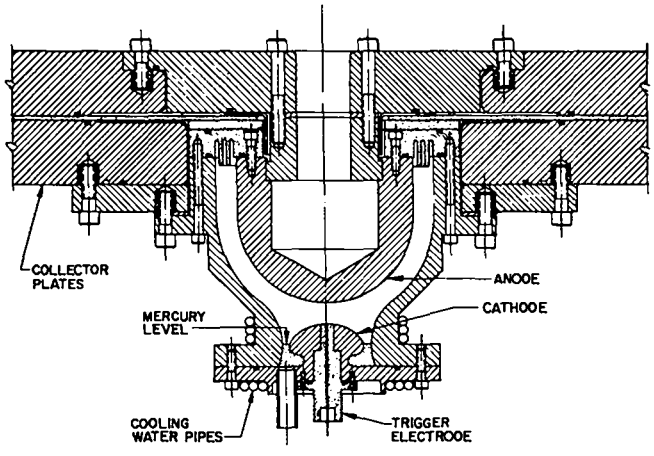

Fig. XV-10.
Mercury wetted spark gap.

TABLE XV-V

ZT-40 POWER CROWBAR TRANSFORMER SPECIFICATIONS

Specification	Iron Core	Air Core
Leakage Inductance	$\leq$ 2 nH	$\leq$ 2 nH
Secondary Current	1 MA	1 MA
Primary Voltage	10 kV	10 kV
Turns Ratio	6:1 12:1	6:1 12:1
Iron Core Flux	0.2 v-s	---
Field Diffusion Time	---	$\geq$ 250 μs
Number Required	24	24
Cost	$12,000 ea.	$8,000
Volume	1.1 m^3	2.2 m^3
Weight	5.4 Tonnes	2.3 Tonnes

design developed in Japan[1] and an air core auto transformer developed by the West Germans.[2]

A prototype iron core transformer with a calculated leakage inductance less than 2 nH was designed and procured in 1976, and initial tests will begin in early 1977. The air transformer is based on a stripline. It will not saturate but does not lend itself to variable turns ratio; however, the iron core transformer is more expensive. If the flux requirement and time scale were to increase, the iron core cost would be prohibitive. Note that 24 of the transformers will be required in the ZT-40 system to reduce the total system leakage inductance and interconnection inductance.

In a large system such as ZT-40 with hundreds of switches, one wants to know when each switch conducts. Previous monitor systems at LASL have used hard-wired connections between the individual spark gaps and the central receiver-monitor electronic system. Unfortunately, the large amount of electro magnetic interference and capacitive coupling often rendered this system inoperable. The advent of fiber-optic technology presents another option in monitoring spark gaps.

Two different fiber-optic systems are being investigated. The first system channels a fraction of the spark gap arc light to the receiver-monitor electronics inside the screen room. An optical pickup mounted with the gap insulator is being tested. Several materials (Lucite, Lexan, quartz) are being tested as windows for the optical pickup. The Lucite and

Lexan windows are plated by the vaporized electrode material. The quartz window pickup resists plating and does not melt. The quartz window will be used in monitoring the ZT-40 passive crowbar gaps.

The second fiber-optic method being studied involves using a LED driven by the changing field produced by the spark gap discharging its capacitor. The lower signal intensity LED method does not disturb the insulator but requires using lower loss, higher cost fiber-optic material than the arc light method, which has an excesss of intensity. The LED monitor is also being studied for the ZT-40 start gaps.

7. ZT-40 Circuit Analysis. The circuit analysis program has two objectives. One is to explore the capabilities of alternative schemes to produce the necessary programmed fields. The other is to assure that the circuits finally chosen will continue to be capable of producing the necessary range of fields when modified to take full account of required mechanical configurations.

The two most important sequences of fields required are shown schematically in Fig. XV-11. For both modes, the I_Z-B_θ circuit must be capable of delivering 600 kA when the B_Z field ranges from 0.3 T to 0.6 T. The reverse B_Z field needs to reach 0.25 T for an initial B_Z of 0.3 T and 0.5 T for an initial B_Z of 0.6 T.

The requirement on the times shown are given below:

t_1 10-100 μs
t_2 2-4 μs
t_3 2-4 μs
t_4 Flat B_Z and B_θ within ± 5% for approximately 250 μs
t_5 2-4 μs
t_6 Flat B_Z and B_θ within ± 5% for approximately 250 μs.

The initial time rate of change of the fast bank currents, $\dot{I}_Z$ and $\dot{I}_\theta$ are $\dot{I}_Z \geq 5 \times 10^{11}$ A/s and I_θ between 5×10^{11} and 5×10^{12} A/s.

It is not a simple matter to design the I_θ and I_Z circuits because the plasma load markedly affects the individual circuit action and also

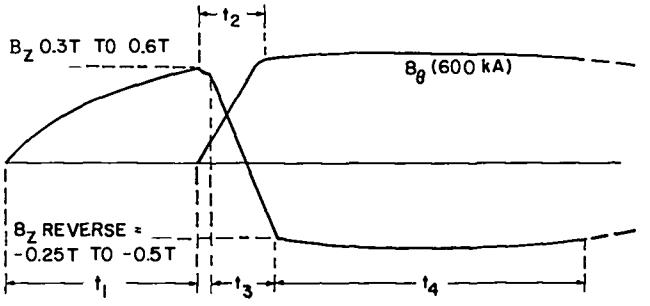

MATCHED MODE

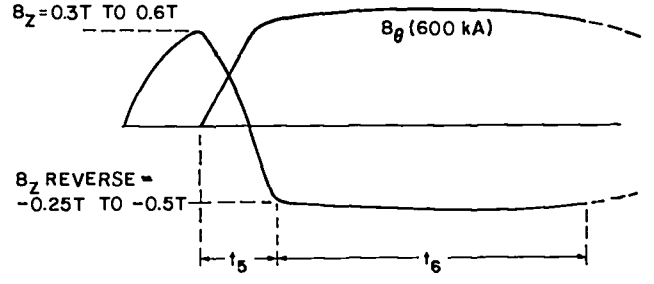

PADUA MODE

Fig. XV-11.
ZT-40 waveforms.

produces a very strong coupling between the circuits. For example, the reduction of B_Z from 0.6 T to 0.3 T results in greater compression of the plasma. This, in turn, requires the B_θ circuit to supply about twice the energy it had to supply when B_Z was 0.6 T. Therefore, some plasma model must be included in the analysis.

The snowplow plasma model was chosen. This sharp boundary model is good for at least the initial portions of the plasma compression and allows easy calculation of the inductance (L) and its time rate of change ($\dot{L}$). This allows the inclusion of both $\dot{L}I$ and $L\dot{I}$ terms in the calculation (for the circuit).

The initial modeling was carried out using the NET-2 circuit analysis code. Unfortunately, the use of the plasma model to compute the time varying inductances resulted in computational delay and very long run times. Direct solution of the differential equations using FORTRAN programs was tried. The initial programs proved to run at least 600 times faster than NET-2. Improvements in coding of later systems resulted in greater time savings, and present programs are estimated

to be running about 1000 times faster than the equivalent problem coded in NET-2. The switch to FORTRAN also allowed the inclusion of other effects in the modeling. However, programming time is substantially longer than the time to program NET-2 and each change in the order of switching requires a new program.

The initial work done with NET-2 was aimed at setting the size of the bias bank, the fast I_Z band, and the I_θ bank. Once these had been determined well enough to permit the design of the racks, attention was turned to the design of the power crowbar system. Initially, electrolytic banks were proposed for this application. Three systems using electrolytic power crowbar banks were programmed. In each case, the I_θ electrolytic power crowbar bank appeared capable of meeting the requirement, but the I_Z circuit bank did not.

A hybrid system using a pulse network in the I_Z circuit and electrolytic capacitors in the I_θ circuit was examined. After some study, it was decided that the PFN introduced too much ripple in the load current so this was abandoned.

The characteristics of the Hirano transformer, designed to have extremely small leakage inductance, led to consideration of transformer-coupled power crowbar banks. A hybrid system using an ideal transformer in the I_Z circuit and an electrolytic bank in the I_θ circuit was programmed. This showed promise, and partly because of size limitations, it was decided to consider transformers in both circuits.

The systems presently under study are shown in Figs. XV-12 and XV-13. Systems 8 and 9 differ only in the order in which the switches are closed. The values of inductance and resistance reflect the present mechanical design of the various components. The plasma model is the snowplow mode. A temperature-dependent plasma resistance based on Spitzer resistivity has been incorporated into the model. The resistance of the main crowbar switches is computed and is based both on the number of switches and on assumed values of the arc drop in the switches.

The transformers are nonideal in the sense that the primary and secondary inductances are calculated as incremental inductances derived from

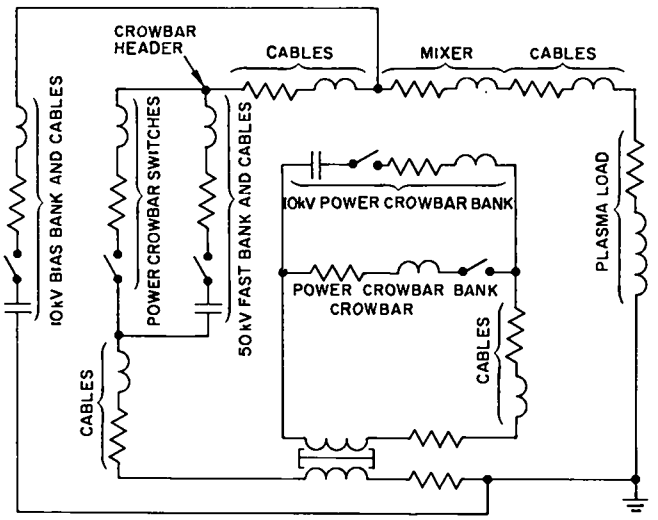

Fig. XV-12.
ZT-40 8 and 9 I_θ-B_Z circuit with 10 kV bias.

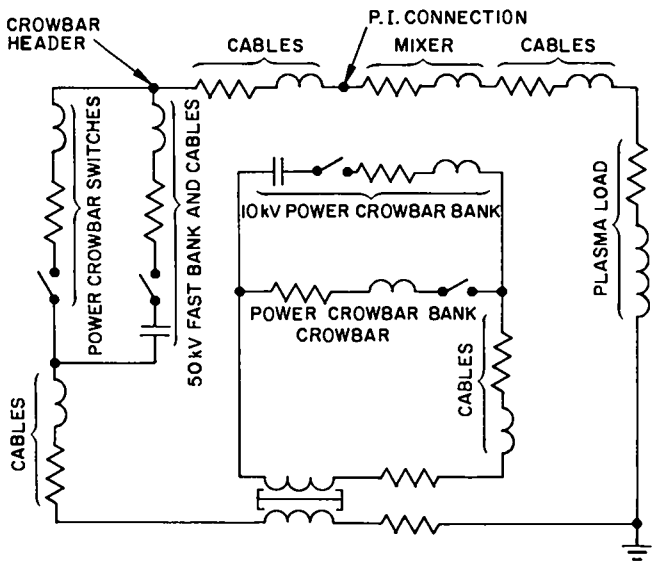

Fig. XV-13.
ZT-40 8 and 9 I_Z-B_Z circuit.

a B-H curve. The B-H curve is shown by the solid line in Fig. XV-14. Also shown is the computed primary inductance. The dotted line is the right side of a measured hysteresis loop obtained from an actual transformer core. This side has been shifted 136 ampere-turns to the left.

The present results are promising, but there are still some problems to be solved. Figure XV-15 provides a representative example of the results being obtained. The top curves show B_θ and B_Z for an entire run. The bottom curves are B_θ and B_Z from the same run magnified over the

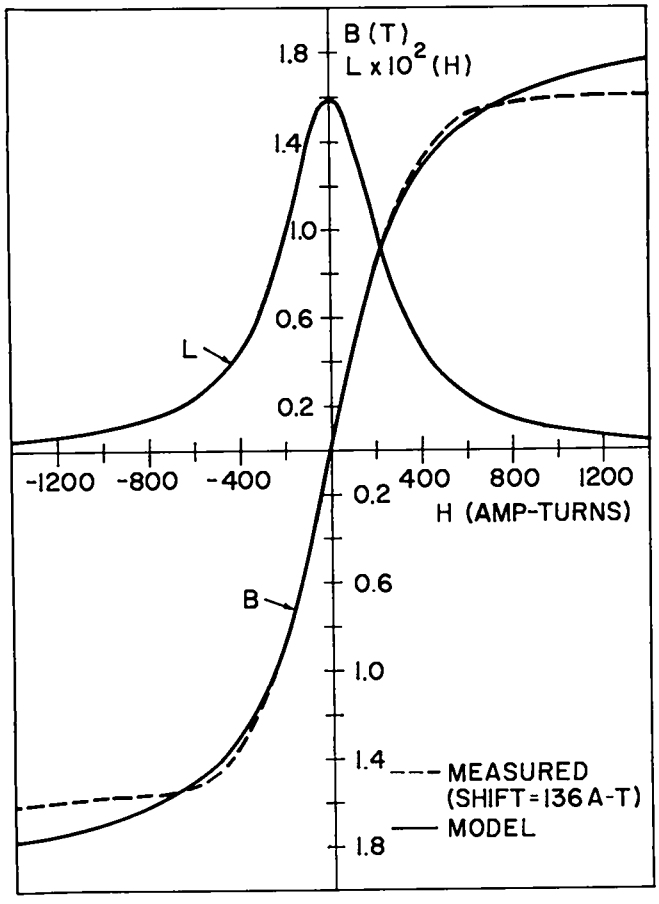

Fig. XV-14.
ZT-40 power C/B xfmr B-H.

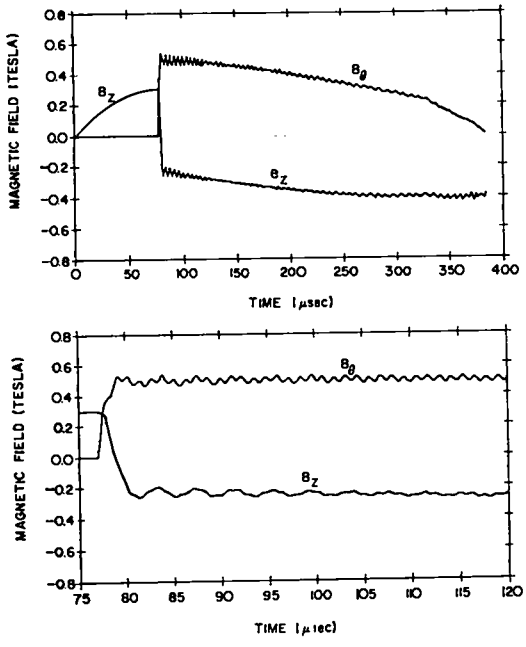

Fig. XV-15.
ZT-40 B_θ and B_z vs time plots.

critical fast-rise portion from 75 μs to 120 μs. The object of this run was to produce a bias B_z of a 0.3 T and to reverse it to -0.25 T while B_θ rose to 0.54 T. From the figures, it appears that this objective was achieved. The initial $\dot{I}_\theta$ for this run is 4.12 x 10^{11} A/s properly between the desired 5 x 10^{11} to 5 x 10^{12} A/s. $\dot{I}_z$ is 8.5 x 10^{11} A/s, which is above the 5 x 10^{11} A/s required. The value of $\tau/4$ B (t_2 in Fig. XV-11) is 2 μs in the 2-4 μs range, while $\tau/4$ B_z (t_3 in Fig. XV-11) is 2.4 μs, a fairly close match to $\tau/4$ B_θ. The reverse B_z is increasing negatively. Other runs have shown that this can be flattened by reducing the voltage on the I_θ power crowbar bank.

The situation with the B_θ is still a problem. The run shown in Fig. XV-11 was made with maximum voltage on the I_z-B_θ power crowbar bank and this was not sufficient to keep the B_θ from falling off. Moreover, the iron in the transformers in this circuit saturated late in the run. The effect can be seen as the change in slope of B_θ at approximately 330 μs. This problem may force the use of different transformers with different turn ratios in the two circuits. At present, there is no reason to believe that the systems will not work with modified transformers and perhaps a larger power crowbar bank. This will be investigated in the future.

B. DEVICE AND COMPONENT DEVELOPMENT

1. Quartz Forming Machine. The latest Scyllac experiments require a curved, helical shaped discharge tube that follows the flux conserving surfaces of the coil. A quartz forming machine was built to form 10-cm o.d. straight quartz tubes into 4-m radius curved tubes and generating a 1.4-cm helical displacement along the tubes with a 62.8-cm wavelength. Figure XV-16 is a photograph of the machine in operation.

The machine design is similar to an original design at the Max Planck Institute for Plasma Physics in Garching, West Germany. The LASL machine was designed for more flexibility and will form quartz tubes with outside diameters of 5 to 20 cm with minimum modifications. The machine is also capable of producing a straight tube with a helical displacement.

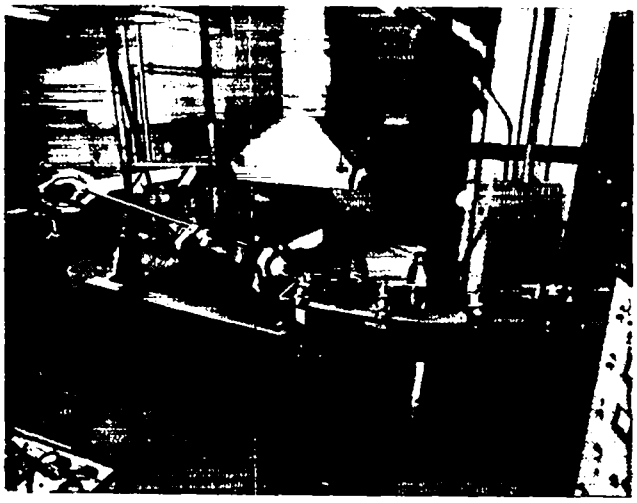

Fig. XV-16.
Tube-forming machine.

The first hydrogen-oxygen burner, purchased from a company in West Germany, had a 1.5- to 2-cm gap between the burner ring and the tube. This proved unsatisfactory. A new burner was designed and built with 1-cm gap and this improved the performance of the machine. Other modifications were made to improve the optical quality of the formed tube.

The first acceptable quartz tube was produced in April and consisted of 3.5 wavelengths of helix on a 4-m radius. Each wavelength took about 45 minutes and a total run took about 3 to 4 hours. Five tube sections were produced and are presently installed in Scyllac. The sections are joined together by O-rings. The next set of Scyllac experiments required a 10-cm o.d. quartz tube with a 4-m radius having a 3.16-cm helix radius with a wavelength of 104.72 cm. Several modifications were made to the machine to form the new tubes. New universal arms and eccentrics were installed as well as an electronic stepping motor drive system to improve the accuracy and repeatability of the system. The first tube was pulled in October and its dimensional tolerance and optical quality were excellent. After some modification to obtain the proper helix radius, all the required tubes for the next Scyllac experiment were formed by the end of the year.

2. Marshall Coil Development.

a. Coil Fabrication. In present theta-pinch experiments, the implosion heating and compression is generally carried out in a single step. A low-inductance capacitor bank is discharged into a single turn load coil producing a 30- to 60-kG magnetic field rising in about 3 μs. When crowbarred, this field decays with an L/R time constant of approximately 250 μs.

The next generation of linear theta-pinch experiments or high-beta tokamak experiments, however, will generally require implosion-heating fields with faster risetimes and compression fields that can be sustained from hundreds of microseconds to tens of milliseconds. These two requirements may be met by using two independent coils to produce the two fields. A fractional turn coil that produces the implosion heating field will be surrounded by a multiturn solenoid, which produces the long-term compression field. The two coils will be decoupled by a ring of saturable material between them.

The Marshall coil is a unique radially driven coil invented by John Marshall at LASL that can be designed as a fractional turn coil and used as the implosion heating coil.

A prototype Marshall coil was built to establish a fabrication method and to test the performance of the coil in an actual circuit. The prototype coil shown in Fig. XV-17 was made by electroplating copper on a plastic form and machining the copper to generate the conductors in the proper configuration. The coil measures 841.4-mm diameter across the flat surface and has a tubular extension 245-mm high with a 215-mm diameter bore. There are 90 1.5-mm-thick copper conductors connected in parallel between the current feed rings on the top and bottom of the "brim" of the "top hat." These are separated by an epoxy insulator.

Fabrication proceeded in six basic steps: (1) casting an epoxy insulator blank, (2) machining it to the proper dimensions; this served as the base insulator for the coil, (3) electroplating the epoxy insulator with copper, (4) machining grooves into the copper to form the conductor pattern, (5) overpotting the coil with epoxy to fill the

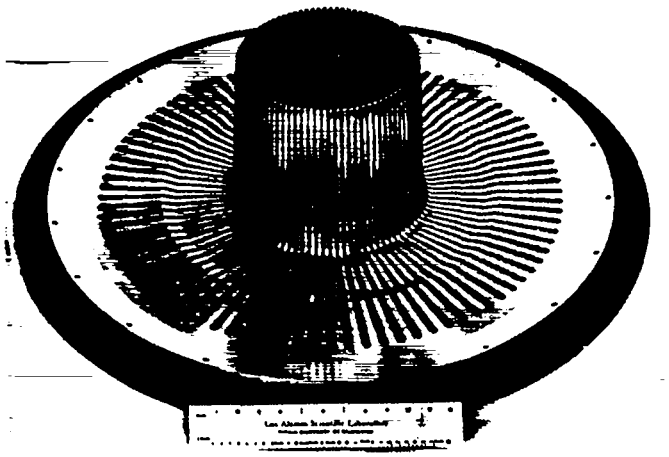

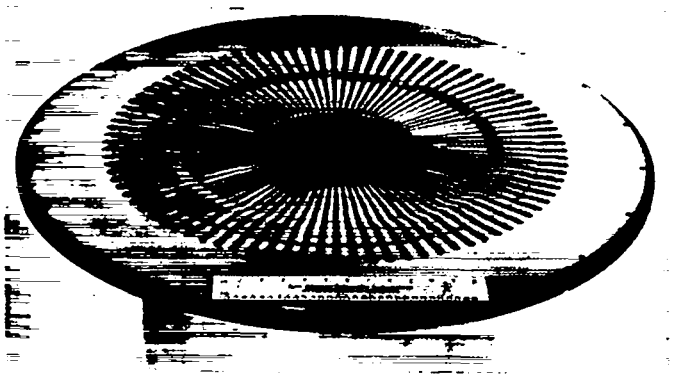

Fig. XV-17.
Marshall coil.

grooves between the conductors and cover the conductors with an insulating material, and (6) dissolving out two sets of polystyrene rings, which had functioned as spacers to form the tongue of the tongue-and-groove electrical connection insulator.

The first three steps proceeded smoothly, but the machining steps caused some difficulty at first because of chucking problems. Chucking the part in a normal manner in a face plate caused warpage and led to the removal of too much copper and the loosening of part of the copper from the insulator. Special jigs were constructed to hold the coil and the surface machining was completed.

The slowest part of the operation was the machining of the 90 slots separating the conductors. These slots were machined through the copper and very slightly into the epoxy. It was necessary to make several passes per slot on the brim to form the tapered slots, and the spiral slots in the bore also required multiple cuts. Overpotting the coil with epoxy and dissolving the two sets of polystyrene rings were performed without undue difficulty. The prototype coil is essentially ready for testing.

b. Coil Testing. The coil will be tested in the system shown in Fig. XV-18. The two 125-kV capacitors will be charged plus or minus to produce a maximum of 250 kV, which is 50 kV more than

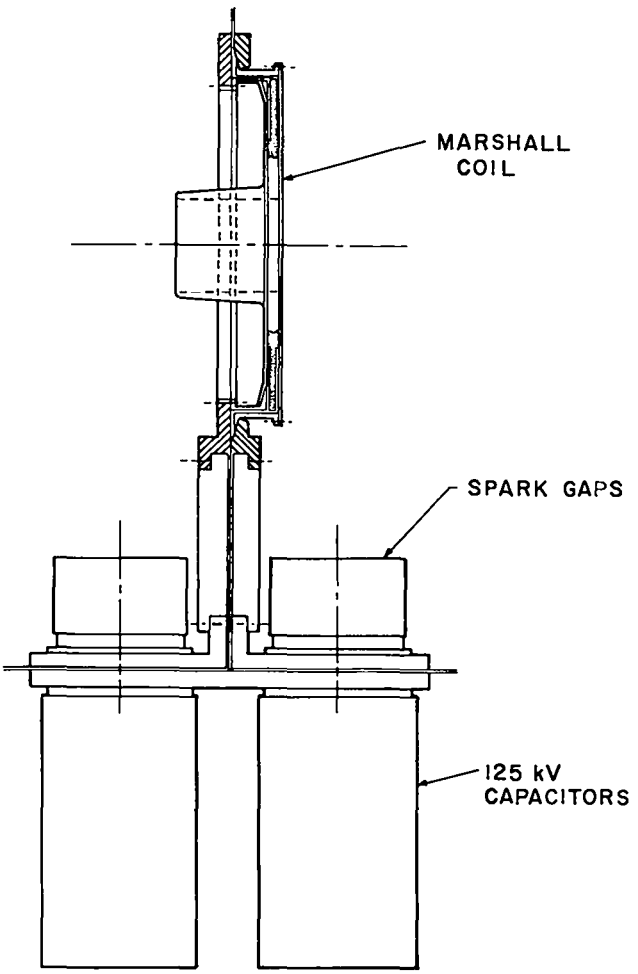

Fig. XV-18.
Marshall coil test stand.

the design voltage for the coil. The test stand and the test bay for charging and firing the capacitors have been designed and built. Testing of the coil will begin during the first quarter of 1977.

c. Magnetic Isolation Material. The Marshall coil staging concept utilizes a concentric multiturn compression coil to provide the slower rising compression and confinement field. The compression coil must be isolated from the fast rising magnetic field produced by the implosion coil but must still permit the slow field to enter the plasma region. One method to achieve this is to fill the annular region between the internal implosion coil and the external compression coil with a saturable ferromagnetic material. The magnetic material provides a return path for the fast rising implosion flux so that the net flux coupling the multiturn compression coil is very small. Tests of several magnetic materials were made to determine their effective permeability (μ_e) at very high frequencies of fast-rising magnetic fields. The implosion return flux path requires a total μ_e of approximately 10. However, the flux path is interrupted by the slotted, radial implosion coil feed plates producing 10% air gap. This requires the μ_e of the material to be greater than 200. A sample of flake iron was evaluated and found to have a μ_e of about 3 or 4 at high frequency (1 MHz) with a 10% air gap. Several tape-wound cores of 1 mil 50% Fe were also tested. These cores, without air gaps, had a μ_e greater than 200 when driven by a fast-rising field (1 MHz) into saturation. Ferrite material might have a sufficient μ_e, but the saturation level is too low for the proposed implosion field. The preliminary results indicate that some type of tape magnetic material will be required for the saturable magnetic material.

3. Switch Development.

a. Linear Field Distortion Staging Gap. A linear field distortion rail gap shown in Fig. XV-19 was developed to replace the original rail gap used on the Staged Theta-Pinch (STP) experiment. The final model of the staging gap will simultaneously hold off a dc voltage of 45 kV and an additional 125-kV pulsed voltage. The major problem in development was the gap body, which had

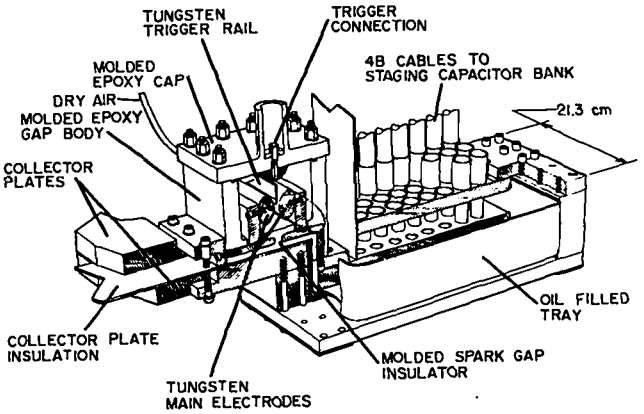

Fig. XV-19.
Staging rail gap.

to withstand a large shock and overpressure during switching of approximately 400 kA. An epoxy body model and also an injection molded polypropylene-fiber-glass molded body were both developed into operating switches. Forty of the epoxy body switches are now installed in the STP experiment and are operating satisfactorily.

b. Coaxial Field Distortion Start Gap. The development of a 40 kV to 120 kV, 15 nH coaxial, field distortion start gap for the STP experiment shown in Fig. XV-20 was completed. This gap was tested to a service life of 10,000 shots at a current of 100 kA. The gap operates with a jitter of 5 ns at 4×10^5 Pa when triggered with a 160-180 kV pulse that rises at 10 kV/ns. The fast-rising pulse is required for multichannel operation. Sixty of these switches are being used on the STP experiment.

c. Concentric Field Distortion Spark Gap. The concentric field distortion spark gap shown in Fig. XV-21 was designed as a substitute for the STP coaxial gap in future experiments. The concentric gap has fewer parts and is less expensive. The inductance is only 10 nH. This design also simplifies the biasing and triggering connection problem. A prototype gap was tested to a pulse charge voltage of 150 kV and exhibited triggering and operating characteristics similar to the coaxial gap.

d. Concentric Field Distortion Crowbar Gap. A crowbar gap based on the same mechanical structure as the concentric start gap was also fabricated and tested this year. The gap shown in

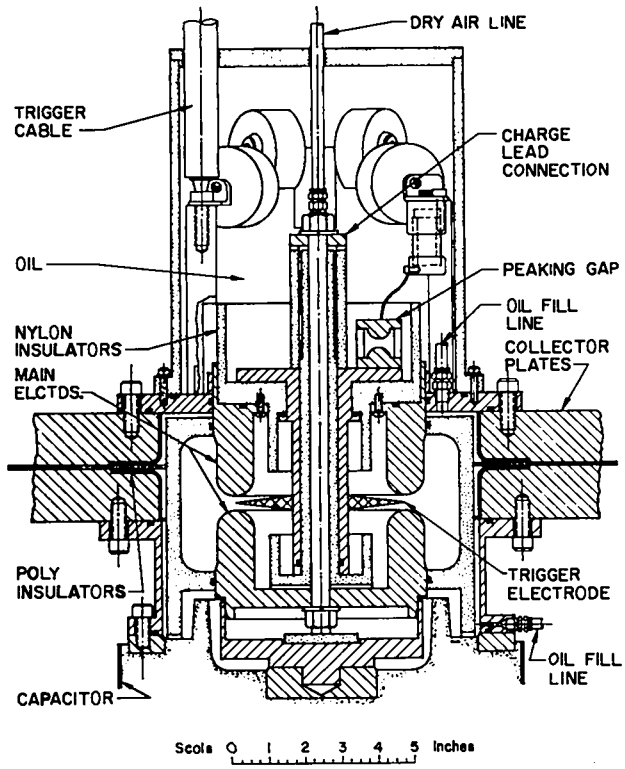

Fig. XV-20.
Coaxial field distortion gap.

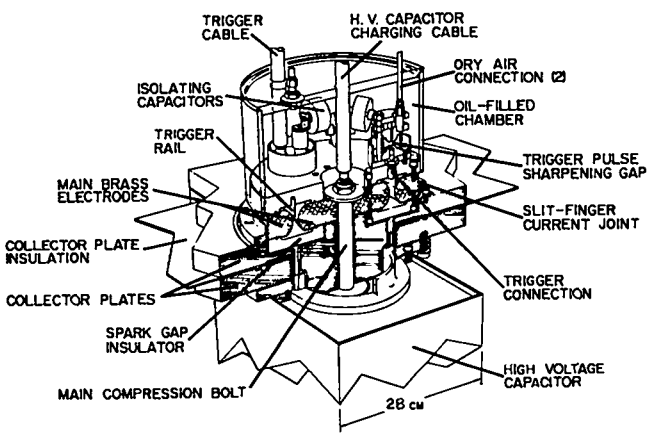

Fig.XV-21.
Concentric start gap.

Fig. XV-22 has to hold off ~ 150 kV and must trigger at approximately zero volts. Initial tests indicate that sustaining the multiple arcs produced by the trigger pulse across the main electrodes is difficult at approximately zero volts. In order for this gap to pick up the load current at approximately zero volts across the electrodes, the trigger pulse must supply tens of

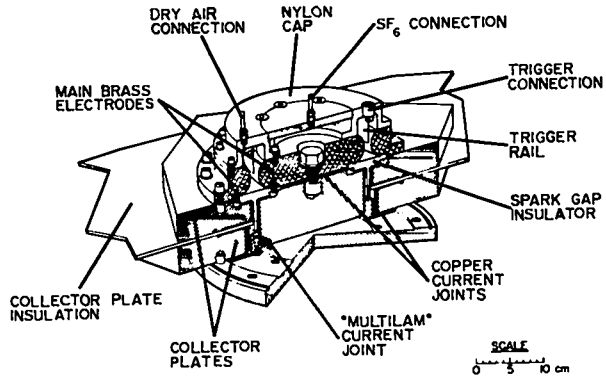

Fig. XV-22.
Concentric crowbar spark gap.

joules of energy so that the crowbar gap arc resistance is lower than the impedance of the bank being crowbarred.

The crowbar trigger pulse must be applied when the main electrode voltage is greater than 2 kV so that the main circuit energy can be used to assist in reducing the crowbar gap resistance. Tests will continue.

4. Evaluation of Ignitrons for High-Voltage Crowbar Applications. Ignitrons operate well as crowbar switches at voltage levels below ~ 25 kV. Some tests were made to evaluate the performance of size A and size D ignitrons as crowbars in a 50-kV circuit. The test circuit consisted of a four-element spark gap mounted on a 1.85-μF capacitor with a crowbar ignitron mounted in a low-inductance geometry across an external inductive load. When the capacitor was charged to 50 kV, the ignitron was required to hold off a 50-kV cosine pulse with a quarter period of 3 μs and conduct 50 kA with an L/R decay time of 150 μs passing a total charge of 7.5 C. The test repetition rate was one shot per minute.

Three size A, type 7703 molybdenum anode ignitrons performed well in the test when the anodes were heated to 120°C and the cathodes cooled to 20°C. The random prefire rate was ~0.5% and a prefire did not affect subsequent operation.

A size D graphite anode ignitron was tested with the anode heated to 150°C, and the cathode cooled to 20°C. The size D tube operated satisfactorily at 50 kV with a current limiting resistor in series with the tube. However, at the 50-kA crowbar current level, a prefire would cause

several subsequent prefires. Although current conduction began slowly for both types of tubes, the anode voltage never exceeded +5 kV for a -50-kV capacitor charge.

5. Type 40/100 Cable Development. One of the least reliable components in Scyllac[3] is the type 14/59 cable that is used to conduct the 75-kV trigger pulse to each crowbar spark gap. A new cable designated type 40/100 cable was designed for this application. A semiempirical maximum stress theory[4] was used to set the stress at 40 kV/mm when the cable was subjected to 100 kV, hence the designation 40/100 cable.

Sample lots from two manufacturers were tested in a standard pulse cable test. Maximum voltage in the test was apparently 114 kV. The results, plotted on Weibull coordinates, are shown in Fig. XV-23. Also shown are the results of an identical test of samples of 14/59 trigger cable from two other manufacturers.

The knee in each curve is the position where the failure rate decreases. It is the usual Los Alamos practice on large experiments to pretest the cable before installation. The test is most useful if it is carried out for a sufficient number of shots to reach the lower failure rate after the knee. As the curves show, manufacturer P's 14/59 cable has the knee at about 2000 shots and 43% of the cable has been lost by that time. Manufacturer C's cable has a later occurring knee

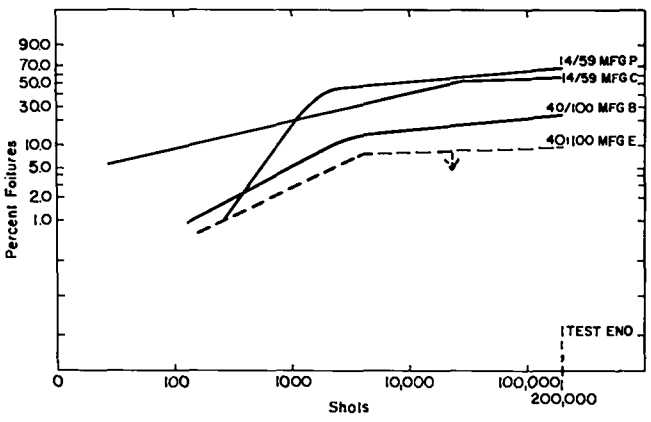

Fig. XV-23.
Trigger cable test data.

(~ 12,500 shots) and has lost 50% by that time. In contrast, the 40/100 cable of manufacturer B has lost only 13% at the knee (3500 shots), while manufacturer E's 40/100 is even lower.

Manufacturer E's curve is shown dashed since it is an upper limit estimate. Only one sample failed during the 200,000 shot test. This represents a total loss of only 6%.

The improvement in performance is even more dramatic if a comparison is made between the median lives as shown below. The median lives are estimates based on extrapolation of the Weibull curves.

	14/59		40/100	
	Mfg P	Mfg C	Mfg B	Mfg E
Median Life (shots)	4000	12,500	5×10^6	$>10^{12}$

The new cable has an inductance of 57 nH/ft, a resistance of 2.4 M /ft. Its characteristic impedance is 30 ohm. It is slightly larger than 14/59, having an o.d. of 1.9 cm compared with 1.5 cm for 14/59. The increased size does not present a problem for new installation, but does require a retrofit of the braid connection fittings in existing equipment.

REFERENCES

1. S. Kotagawa and K. Hirano, "Power Crowbar System Coupled by a current Transformer with Very Low Leakage Inductance," Proc. of the 6th Symp. on Engineering Problems of Fusion Research, pp 647-650, Nov. 1975.

2. P. Dokopoulos, W. Kohlhass, R. Lemmens, C. Strickelmann, F. Waelbroeck, U. Braunsberger, and U. Schwarz, "Pulse Transformer with Variable Voltage from 27- to 95-kV for a 1-MJoule Capacitor Bank," 7th Symp. On Fusion Technology, Grenoble, Oct. 1972.

3. W. D. Gutscher, and K. J. Johnson, "Scyllac Equipment Reliablility Analysis" Proc, 6th Symp. Eng. Prob. Fusion Research. IEEE Pub. No. 75CH1097-5-NPS, p 711, Nov. 1975.

4. G. P. Boicourt, "Semiempirical Cable Design," Los Alamos Scientific Laboratory Report LA-5691 (1974).

XVI. MAGNETIC ENERGY TRANSFER AND STORAGE

J. D. Rogers, A. G. Fox, J. J. Glass, C. G. Hoffman, E. M. Honig,
T. I. Jones, Jr., C. R. King, J. D. G. Lindsay, L. B. Lundberg,
G. A. Miranda, C. E. Swannack, P. Thullen, W. C. Turner,
R. W. Warren, D. M. Weldon, J. M. Weldon,
D. H. Whitaker, K. D. Williamson, Jr., J. J. Wollan

A. SUMMARY

Significant progress was made in 1976 toward development of the superconducting magnetic energy transfer and storage (METS) system for use in future theta-pinch experiments. The technology being developed will have application to other CTR programs such as tokamak ohmic-heating systems and laser flash lamp power supplies. This work will culminate in a demonstration METS-SFTR coupled superconducting prototype system. The prototype is to be composed of one 400-kJ, 25-kA superconducting energy storage coil and all associated charging and switching equipment. The coil will be charged in 300 s to a field level of 2.5 T at 25 kA through continuous duty leads and discharged in 0.7 ms through special coaxial pulsed leads. The energy transfer is efficient, being determined by the storage coil inductance, transfer capacitance, and load inductance resonant circuit.

Two new programs were initiated during the last quarter of the year. The first is a developmental program to fabricate a model 10-MJ, 30-ms discharge homopolar machine. The work will include component development and testing of critical subassemblies which advance the state of the art for such energy storage devices. The second program deals with the development of switches and superconducting coils for the pulsed ohmic-heating systems associated with large-scale tokamak devices. Circuits will be analyzed to incorporate functional impacts on the switches and coils. Auxiliary components for the systems will be identified and developed as required for realistic testing of coils and switches.

Major accomplishments during the past year include the following items:

1. All three industrial, 300-kJ, 10-kA superconducting coils were received and tested. The Westinghouse coil reached a peak current of 13.3 kA and a corresponding energy store of 0.535 MJ.

2. Extensive tests were carried out on vacuum interrupters. A maximum current of 26 kA was interrupted at a withstand voltage of 66 kV.

3. An order was placed for the METS prototype 25-kA, 400-kJ superconducting coil.

4. A prototype 26-kA pulse lead and header was successfully tested to 32 kA.

5. The use of superconducting materials for construction of the cryogenic disconnect was initiated. An extensive evaluation of potential materials was undertaken.

6. The 700-W, 4.5-K helium refrigerator was received and the installation begun.

7. The program to design a 1-GJ, 30-ms discharge homopolar energy storage machine was completed. This study also included the initial design of a prototype 10-MJ machine.

8. The room-temperature load coil for testing the 10-MJ homopolar machine was designed.

9. A study was completed which investigated possible power systems for driving EPR ohmic-heating coils.

10. A zero-dimension plasma code was developed to calculate plasma resistivity as a function of plasma current and temperature.

11. A cryogenic end stopper using solid argon was developed for use in Scylla IV-P.

B. HVDC INTERRUPTER TESTS

1. Facility. The purpose of this facility is twofold: first, to provide the equipment and energy storage capability for testing room-temperature current breakers and various components of the interrupter circuit and second, to provide a passive capacitor bank for checkout of the superconducting storage coils (Sec. E). The facility was rebuilt early in January to upgrade its test limits to $\sim$ 30 kA and 60 kV. A new 300-kJ facility is planned which, when operated in parallel with the existing facility, will double the maximum current testing capability. A second new facility is in the early planning stage--a 2-MJ

facility to supply currents of 100 to 150 kA for testing very large interrupters or systems of paralleled interrupters applicable to ohmic-heating systems.

A circuit was designed, built, and installed to provide semiautomatic operation of the interrupter facility. Once triggered by a start button, the circuit performs the necessary actions to reset the oscilloscopes and vacuum interrupters, charge the capacitor banks, and initiate the firing sequence.

2. Testing of Conventional Vacuum Interrupters. Eleven different vacuum interrupters have been purchased which cover the range of interrupters commercially available in the USA as well as several kinds of experimental interrupters. All but two of these have undergone extensive tests to determine the maximum current which can be reliably interrupted and to allow crude judgments to be made about the erosion rate of the electrodes. Variations in the circuits used have been investigated to determine the sensitivity of the maximum interruptible current to these changes. It has been found that (a) the maximum interruptible current scales roughly linearly with electrode diameter, reaching about 26 kA for the largest size; (b) erosion is negligible for several thousand interruptions under our conditions except for the largest interrupter, the General Electric PV08. For this device the erosion is very rapid, presumably because of the choice of material for the electrode alloy; (c) variations in circuit parameters, in the saturable core reactors, in the magnitude of the counterpulse, or in the interrupter opening speed have little effect on the maximum interruptible current; and (d) it appears that the maximum interruptible current is determined largely by the characteristics of the arc.

Successful interruption of 31 kA at 55 kV and 26 kA at 66 kV was achieved with the 17.8-cm. Westinghouse bottle. For 90% reliability, currents of 21 kA at 45 kV can be interrupted with this bottle. An optical speed sensor was developed and used to determine the opening speed of the interrupters and work was begun on the development of high-speed actuator systems.

3. Fuses. A program was initiated to develop fast explosive fuses for protective devices in high-current applications. The most immediate application is their use in series with interrupters of questionable reliability. If the fuse can be opened explosively in about 10 μs, the circuit can be arranged so that a failure of the main interrupter will be inconsequential.

4. Cooperative Arrangements with Industry and the National Laboratories. A major effort has been made to work closely with Westinghouse and General Electric, the major suppliers of vacuum interrupters. Several novel interrupters have been purchased from Westinghouse and through a contract with them a better understanding of the physics of the interruption process has been obtained. A testing program is under way with General Electric to clarify the details of the rapid erosion observed in their PV08 interrupter and to simulate the circuit used in General Atomic's Doublet III.

A joint program directed toward the Princeton-TFTR switch requirements is in progress. In this effort General Electric will provide a new high-current interrupter; Rensselaer Polytechnic Institute will provide an actuator for it; and LASL will do the testing.

For the ORMAK-Upgrade at Oak Ridge a high-current switch and associated circuitry are needed. Westinghouse is cooperating with them in the switch design and LASL has helped in the saturable reactor design. Final circuit components will be shipped to LASL for testing.

C. 300-kJ TEST FACILITY

The brush problems associated with the 10-kA, 6-V homopolar generator have been solved. Helwig Carbon Products, Inc., has supplied a complex, configured brush with water cooling and inserts of graphite and silver-graphite. The brush loading is controlled with a pneumatic actuation system so that the brushes can be lifted during times of no current demand to minimize wear.

A bipolar power supply has been installed to energize the upper field coil of the homopolar generator. Zero-to-peak current can be controlled continuously without the need for a reversing

switch and without loss in accurate current control over the midrange.

D. SUPERCONDUCTING WIRE DEVELOPMENT

1. Conductor for the 300-kJ Coils. The 106.68 km of mixed matrix conductor for the Intermagnetics General Corporation (IGC) coil was completed by IGC. Tests on the wire showed that it exceeded the short sample critical current requirement. This allowed a decrease in the wire diameter to 0.39 mm and a redesign of the cable which reduced the amount of compaction required. It was hoped that this would reduce insulation damage and wire-to-wire shorts which proved to be a problem in dummy cables. In the actual coil, however, there were still a great many shorts (Sec. E).

Magnetics Corporation of America (MCA) completed 30.48 km of NbTi/Cu wire for the Westinghouse 300-kJ coil. A small fraction of the wire was slightly under the critical current specification. There was no detrimental effect, however, on the cable or coil performance.

2. Superconductor Development Programs. Three developmental wire orders were carried out.

IGC completed a contract to evaluate the lower limit of wire diameter and filament diameter in mixed matrix superconducting wires. Starting with their 156 filament, 1.5:2:1 matrix ratio, 0.39-mm wire originally made for the 300-kJ coil, they made a series of samples down to 0.15-mm diameter which corresponds to a 0.006-mm-diameter filament. There was roughly a 50% monotonic decrease in j_c as the diameter decreased from 0.39-mm to 0.15-mm for fields ranging from 5 kG to 50 kG. At zero field the decrease was only about 20%. Metallography showed that filament "sausaging" or necking existed in the 0.15-mm-diameter wires; but it was not possible to conclude that the degradation in j_c was solely a function of this condition. The heat treatment supposedly was optimized for the original 0.39-mm-diameter wire.

Airco completed a contract to manufacture the same design 156 filament wire made by IGC with a high-purity 70-30 CuNi matrix in diameters of 0.25 mm, 0.38 mm, and 0.51 mm. J_c's averaged about 2.1×10^5 A/cm^2 2.5 T and 10^{-12} ohm-cm. This is about 25% below typical values for similar wire produced by IGC. The j_c results are in agreement with those obtained by Airco. Metallographic examination showed "footballing" on the Nb-Ti filaments.

MCA completed a contract to manufacture an intermediate matrix wire. The matrix material was Cu-0.05% Ni. This was an attempt to make a low-loss wire without adding CuNi barriers in a mixed Cu-CuNi matrix superconductor. No tests have as yet been run on this wire.

3. Cabling and Epoxy-Potting Development Programs. Because of problems developed during cabling and cable compaction which caused insulation damage and shorting between wire strands for the 300-kJ industrial coils, an extensive program was initiated to eliminate the insulation damage for the 400-kJ METS-SFTR prototype storage coil. The prototype 25-kA cables used about 800 0.38-mm-diameter wires. The cabling work was done by IGC, New England Electric Wire (NEEW), and Westinghouse. The epoxy potting was done by IGC, MCA, and Union Carbon and Carbide (ORNL).

NEEW completed two 9.14-m developmental prototype 25-kA cables. The wire was hard bronze with a Ni flash and polyamide (ML) insulation. The insulation was heavily damaged which resulted in complete shorting of the cable strands.

IGC completed four 15.24-m prototype cables and one 137-m prototype cable. All cables were made of Cu-10 Ni wire; two of the short cables had Formvar insulation, the other two and the long cable had GP-200 (polyamide) insulation. There were almost no shorts in the four 15.24-m cables. The 137-m cable appeared to be shorted extensively but this may be due to layer-to-layer shorts and not inherent shorts within the cable. There were a number of different cable configurations and all were reasonably stable with respect to untwisting.

Because of changes in the design of the 400-kJ coil, Westinghouse cabling work was redirected to more closely conform with the new design requirements. Consequently that work was not completed during CY76.

IGC potted four 4-cable arrays with each of the various cables. The cables were triply wrapped with 0.18-mm fiber glass tape and the cable bundle then double wrapped before epoxy potting. The epoxy-potted assemblies were cycled to ℓN_2 temperature several times under severe conditions with a great deal of cracking evident in the epoxy-fiber glass system.

MCA made 15 epoxy-potted samples with the NEEW cable and one sample with an IGC cable. They used a 6-cable stack with the same system of fiber glass wrap and three basic epoxy formulations with varying amounts of silica-flour filler. No significant cracking was detected in any of the samples under slow cycling to ℓN_2 temperature.

ORNL failed to produce any samples which they considered satisfactory.

4. Critical Current Testing Above 1 kA. A number of limiting transport current tests on superconducting cables were conducted. Of the tests, the most significant were the measurements on the IGC and Westinghouse 10-kA, 300-kJ superconducting coil cables. The IGC cable carried 17.0 kA at 3 T, and the Westinghouse cable carried 18.8 kA at 4.0 T. These results gave a predicted limiting transport current for the Westinghouse magnet of 17.0 kA at a maximum field of 3.77 T.

Fifteen major sub-cables from three IGC cables were tested. Most of these were from the compacted prototype and the uncompacted prototype cables. The results indicated that deterioration in the prototype cable was due mainly to the compaction process.

A bundle of 180 wires from the damaged portion of the braid in the MCA 300-kJ magnet was tested. The data indicate that all of the wires in the strands selected for testing were carrying the expected current based upon the single-wire critical current of I_c = 15.1 A at B = 2.78 T. It is thus concluded that the damage to the MCA coil was not a result of wire degradation.

5. Large Bore Dipole Magnet for 25-kA Critical Current Measurements. A large bore dipole magnet capable of generating fields of 6 T is being developed to extend the usable sample size and maximum field conditions available for evaluation of superconducting cables. The winding work on the prototype coil form was completed and compaction data were obtained for both the straight sides of the magnet and for the turnarounds at the magnet ends. The winding procedures to make the coil were developed. An eddy current shield was designed, the coil winder and wire tensioning device were redesigned and rebuilt, and fabrication of the dipole form was 95% completed.

The wire for this magnet was completed and tested. Measurements on samples taken from both ends of the wire indicate I_c's of 700 and 620 A as compared to the specified current of 700 A at 6 T. Photomicrographs of several sections of this wire show the filaments to be well distributed but with some unusual cross sections. Tensile tests were performed on the wire and gave a tensile strength of 415 MPa (60.2 ksi) and a yield point of 195 MPa (28.3 ksi). The corresponding loads were 1360 N (305 lbs) and 638 N (143.4 lbs) respectively.

E. 300-kJ, 10-kA COIL DEVELOPMENT PROGRAM

The industrial program to build three 300-kJ energy storage coils was completed. They were fabricated by Intermagnetics General Corporation (IGC), Magnetic Corporation of America (MCA), and Westinghouse. The MCA coil was received in January, the IGC coil at the end of June, and the Westinghouse coil the last of August.

Measured values of inductance and resistance for all three coils and the LASL 300-kJ coil for comparison are given in Table XVI-I. The testing sequence for the coils was divided into four steps. The first step was a cycling test from room temperature to liquid N_2 and back to room temperature for three cycles. The coils were then examined for any structural damage. The second step was to cool the coil in liquid helium and measure hysteresis losses and dynamic losses at low currents (less than 5 kA) and do transfer experiments at low currents. The third step in testing was measurement of the same parameters as the second step at high currents (above 5 kA). The fourth test was a life test of 50 cycles in which the full design current was transferred out of the coil in approximately 2 ms. Other tests were also run on the Westinghouse coil and are discussed with the results achieved on this coil.

TABLE XVI-I

PARAMETERS OF THE 300-kJ ENERGY STORAGE COILS

Parameter	MCA Coil 1	IGC Coil 2	W Coil 3	LASL Coil 4
Inductance (mH)	6.01	5.47	6.05	4.87
Resistance at 20°C (Ω)	0.47	0.315	0.165	0.0896
Stored energy at 10 kA (kJ)	301	274	302	244
Length (cm)	70.2	82	79.1	73.0
Mean radius (cm)	27.1	26.7	25.5	28.7
Winding thickness (cm)	2.3	1.5	4.74	0.508
Number of turns	144	140	159.5	122.5
Number of layers	1	1	4	1
Central field at 10 kA (T)	2.04	1.80	2.13	1.82
Conductor support method	helical coil form	fully potted	toothed coil form	self-supporting
Matrix ratio (CuNi:Cu:NbTi)	0:1.58:1	1.5:2:1	0:2.7:1	0:6:1
Strand diameter (mm)	0.127	0.419	0.813	10.16 x 5.08*
Filament diameter (μm)	79.1	15	18	32.2
Number of filaments per wire	1	156	529	2640
Wire twist pitch (cm^{-1})	0	2.75	1.57	0.13
Number of active wires in cable	1224	315	72	1
Type of transposition	flat braid	cable	roebel	-
Cable width (cm)	2.3	1.524	1.68	1.016
Cable thickness (cm)	0.15	0.544	0.84	0.508

*Monolithic rectangular conductor.

Four pieces of specialized equipment had to be developed for the above measurements: 1) a boil-off gas collection shroud and measurement system to collect the helium gas evolved during a current transfer. This system was calibrated to give the coil loss during this transfer; 2) a quench detector to protect the coil in case of an accidental quench. This unit operates by monitoring the time rate of change of current in the coil with an unusually large Rogowski loop and is sensitive only to negative changes in current with respect to time; 3) electronic loss measurement circuitry as a back-up system to the boil-off loss measurements and to measure hysteresis loops on the coil; and 4) linear optical isolators for measuring both steady state and pulsed currents without creating additional ground-loop currents that interfere with the other measurements.

The HVDC interrupter test facility was rearranged for testing of the coils. A previously tested 17.8 cm Westinghouse vacuum interrupter, driven by a Maxwell actuator, was used for the primary interruption which initiates the energy transfer. The epoxy-potted, bronze-conductor, 300-kJ IGC mockup coil was used as the load coil for the test.

The test results for each of the three industrial coils are as follows:

1. MCA Coil. The MCA coil was cycled to ℓN_2 temperature a number of times with fairly good results. Some of the bonding between the braided cable and the support structure broke allowing the cable to separate from the support. Examination of the coil indicated the further possibility of separation of the flanges and end conductor turns with expansion or release of the axial load when the energy was transferred. A BeCu tie bolt

arrangement was devised to overcome this potential difficulty.

The coil was operated in a dc mode up to 2 kA and hysteresis losses were measured electrically. Total losses during fast energy transfer were measured by both the electrical method and by the helium gas evolution method. Electrical measurements made on short samples of the conductor had indicated that there was little eddy current loss in the conductor and most of the loss was hysteresis loss even for discharge times of 2 ms. Measurements made on the whole coil agree with this conclusion in that the electrical measurements made over a period of two minutes gave the same energy loss for a given current as the boil-off method did during the fast energy transfer.

With the presumption that the boil-off measurement and slow hysteresis measurement are correct, the energy loss with a stored energy of 48 kJ is about 30 J. This extrapolates to a loss of 75 J (0.025%) for a stored energy of 300 kJ.

While attempting to reach 5 kA, the coil quenched prematurely at 4.3 kA. The quench detector had not been turned on since a quench was not expected at such low currents. As a result of the quench, the stored energy was dumped into the coil with probable damage to the coil at that time. Subsequently, the highest current achieved by the coil was 4.9 kA. Transfer time in the energy transfer tests was 2.2 ms and the highest voltage obtained was 16 kV.

Later examination of the coil showed a heat-damaged section near the coil center. The coil has been disassembled and the damaged section removed. During the disassembly it was noticed that some of the epoxy-bonded joints appeared to be poorly cured and separation of the joints occurred in several places.

Superconducting wire strands removed from the apparently damaged section of the MCA 300-kJ coil were tested. The results showed no damage. The poor results obtained with this coil are believed to be due to conductor motion since the coil was not very rigid mechanically.

2. IGC Coil. Two separate series of tests were performed on the IGC coil. The first set established that the coil quenched in the 2.5 to 3.1 kA range and that the quenching current did not depend on charging rate over the range from 20 to 300 s. Inspection of the coil showed no damage. There were a number of nicks in the insulation of the individual wires, a small gouge in the cable where a lead mounting screw in the coil was too close to the superconducting cable, and several small bubbles in the epoxy impregnation. These imperfections were in the coil as received and do not appear to be of sufficient magnitude to account for the degraded performance.

Several modifications were made to the coil form before the second set of tests to minimize conductor lead motion as a possible source of difficulty. However, results of the second series of tests were substantially the same as the first. The peak current reached was 3.3 kA. Starting about 500 A before the quench and up to the quench, sounds resembling the crackling of cellophane were picked up by the microphone which had been mounted on one of the current leads. The significance of these sounds is not understood, but eventually it may be possible to correlate them with some type of physical event. In an attempt to find the problem with the IGC coil, one end connector was removed from the coil and all the strands (319) separated at that end. Resistance measurements showed numerous shorts between wires. These, in addition to possible current transfer problems within the mixed matrix, potting problems at the terminals, and power supply electrical noise are being investigated as causes for the low current-carrying capability of this coil.

3. Westinghouse Coil. The Westinghouse coil has been tested to currents above 10 kA more than 50 times and to a peak current of 13.3 kA corresponding to a peak stored energy of 0.535 MJ. These tests were made with the resonant METS, L-C-L, energy transfer apparatus using a 2-ms period. The peak voltage during these transfers was just over 42 kV. To perform a repetitive series of high-current tests it was necessary to bypass the HVDC vacuum interrupter with a fast acting mechanical switch. The mechanical switch carried most of the current during the charging cycle and was opened 100 ms before the transfer cycle was initiated to redirect all the current into the interrupter.

The high-voltage capability of the coil was tested by reducing the capacity of the capacitor transfer bank. Under these conditions a maximum voltage of 58.5 kV was reached.

The rate of current rise was also measured. At the maximum ramp rate available from the homopolar generator (1000 amps/s) the coil did not quench during a ramp to 10 kA.

Losses in the Westinghouse coil are somewhat higher than in the MCA and IGC coils at the same currents, but this was expected because of the larger wire diameter and higher copper content of the conductor. However, at 300 kJ the energy loss was still less than 1% for a 2.5-ms transfer time.

F. SFTR PROTOTYPE METS SYSTEM

A prototype METS system is being designed to simulate one of the 10-coil, METS-SFTR modules. The system will utilize one 400-kJ, 25-kA, 2.5-T superconducting energy storage coil and associated components which include 25-kA, 60-kV coaxial leads; a cryogenic disconnect and actuator for connecting the coils in series for charging; 25-kA continuous-duty leads; and an external breaker which permits opening of the cryogenic disconnect under little or no current load. During the year considerable progress was made in all of the above areas. A summary follows:

1. 400-kJ Storage Coil. Based upon the results of the 300-kJ coil program, an order was placed with Westinghouse for the fabrication of a 400-kJ, 25-kA superconducting, mixed matrix NbTi coil. This coil is to be ∿ 71 cm long with a finished outside diameter not to exceed 67.5 cm. It is to carry 35 kA safely for fault mode operation, have an inductance of 1.28 *mH*, be able to withstand 60 kV across the terminals during the 0.7-ms discharge, and have a combined energy loss during a full charge-discharge cycle of less than 0.3% (1.2 kJ).

2. External Breaker. To allow the cryogenic disconnects to open under zero current conditions, the current in the series charging loop of a METS system will be interrupted by a circuit breaker placed external to the dewar. The external breaker must first carry the 5-minute current ramp to 26 kA during charging of the superconducting storage coils. It must then interrupt this current to break the series charging loop and drive the current into the parallel transfer networks. The cryogenic disconnects can then be safely opened to isolate the transfer networks. After interrupting the current, the external breaker must hold off potentials as high as 60 kV.

For this application a high-current, low-voltage (600 V) switch made by ITE Imperial was modified to withstand high voltages by using nonmetallic structural support members and oil insulation. DC voltage tests of the unit in oil showed intermittent breakdowns above 60 kV. Current tests on one-half of the switch in oil showed only a 50 C temperature rise after carrying 10 kA for 15 minutes. The entire unit should easily carry the 5-minute current ramp to 26 kA.

3. Electrical Leads and Cables. Two types of electrical leads are required for connections with the superconducting coils in the METS system. Continuous duty leads must be able to carry the 5-minute charging ramp to 26 kA when the storage coils are connected in series from the power supply. Pulse leads need only carry the current from each coil during the short duration when the parallel transfer networks are formed and the transfer to the load coil takes place.

Considerable progress has been made toward the development and analysis of low-resistance, low-inductance pulse lead which can carry 26 kA for about 40 ms and withstand 60 kV. The general design approach incorporates two concentric copper tubes to form a coaxial pulse lead. Since the lead spans the temperature range from room temperature at the top to liquid helium temperature at the bottom, an analysis of the temperature profile and heat flow is most easily done by computer modeling.

To check the temperature profiles a vacuum-insulated jacket was installed around a finned tube of DHP copper to simulate the inner conductor of the pulse lead. The experimental temperature profile and the computer-calculated profile matched quite well. After considerable effort to obtain an accurate measurement of the vapor-cooling mass flow, agreement to within 7.5% was obtained between experimental and theoretical mass flows when the temperature profiles were matched.

A simple construction technique was developed to rigidly connect the inner and outer conductors of the pulse lead, provide a seal to prevent gaseous helium leaks between conductors, and provide adequate insulation between conductors. The inner copper tube was wrapped with Mylar insulation until the outer tube would barely slip on. The outer tube was then crimped near the upper end to lock it in place. Epoxy was applied between all Mylar layers in the crimp region to prevent leakage of helium gas from the dewar. The seal in the crimp region held better than 10^{-4} torr vacuum with no detectable leak on a helium leak detector. The electrical insulation method proved quite satisfactory, withstanding at least 94 kV before breakdown occurred due to tracking along the Mylar surface at one end of the lead.

Construction of the header to connect the pulse lead to a 7-cable bundle of Type 218/220 coaxial cables was completed. Multilam connections are used to terminate the solid center conductor of the coaxial cables and the outer conductor of the pulse lead. Gaseous nitrogen in the header is used to prevent frost buildup on the conductors and insulation. The gaseous helium used for vapor cooling of the pulse lead is collected in the header and routed outside for use in a control system.

A prototype, Mylar-wrapped pulse lead, the completed header, and a bundle of seven coaxial cables were tested as a unit in the interrupter facility. Currents as high as 32 kA were successfully carried with a decay time constant of about 200 ms.

The computer program used to model the pulse lead was modified to allow its application to the continuous lead. In an attempt to make better utilization of the vapor cooling available to the continuous lead, the use of copper screen wire rather than copper tubes was investigated. Copper screens from 18 gauge to 50 gauge were compared, with gauges 34 and 50 resulting in the best packing factor. Both 28 gauge (20 mesh) and 34 gauge (40 mesh) were modeled by the program for comparison with the present 10-kA continuous leads which have a cross section of about 5 cm^2. These leads had a calculated heat leak into the dewar $\sim$ 13% lower than the present design under no load and $\sim$ 30% lower under a 10-kA load. The computer model also showed that the screen leads should be able to carry higher currents for the same copper cross section without burning out.

4. Cryogenic Disconnect. A special high-current, low-resistance, electrical switch for service in liquid helium is being developed. This switch or cryogenic disconnect is to be mechanically actuated, will carry 26 kA, will withstand 60 kV when open, and will dissipate less than 24 W under full current load. In addition, the disconnect must be able to open in 25 ms.

Basically, the development of the cryogenic disconnect can be divided into three distinct activities:

a. Electrical contact and materials research and development.

b. Actuation system design and development.

c. Systems integration and overall disconnect design.

The electrical contact program has been directed toward the ultimate use of a commercial product called Multilam as the actual contact component. Various superconducting materials were coated/plated onto the commercial BeCu Multilam strips to determine optimum performance and to develop contacts of exceedingly low electrical resistance. The best results of these efforts are tabulated in Table XVI-II. In addition, Multilam louvers have been fabricated from niobium-1% zirconium. These are currently being evaluated. Another group of louvers are to be made from NbTi and evaluated later in the program.

Several samples of a variety of lead and tin-based alloys were evaluated as potential materials for the cryogenic disconnect. Magnetization measurements were made with the determination of H_{c2} as the primary objective. Results of promising alloys are given in Table XVI-III.

The development of the actuation system has been directed toward use of electrical solenoids to both open and close the cryogenic disconnect. The solenoids will be immersed in liquid helium and will operate in the vicinity of the cryogenic disconnect and the storage coil. Two large dc solenoids were purchased from the Trombretta Corp., and were tested for the proposed use. Results of the testing indicated that the two dc

TABLE XVI-II

TEST RESULTS WITH MULTILAM STRIPS AT 4 K

Contact Surface Material	Max. No. of Louvered Contacts	Optimum Electric Performance	Optimum Current Density (A/Louver)	Effective Lifetime (Cycles)
Silver/Silver	41	500 A at .5 μΩ	12.19	500
Silver/Copper	41	350 A at 1 μΩ	8.53	750
Tin-Lead (50-50)	41	1000 A at 86 nΩ	24.4	10,000 +
Copper/Copper	41	200 A at 920 nΩ	4.87	500
Lead-Bismuth (50-50)	82	1200 A at 152 nΩ	14.6	2,000 +
Lead-Tin/Silver	41	100 A at 755 nΩ	2.44	1,800
Tin-Lead (50-50) Partially Plated	155	4500 A at 129 nΩ	29.0	3,000 +
Tin-Lead (50-50) Fully Plated	155	1800 A at 22 nΩ	11.6	3,000 +
Tin-Lead (50-50) Fully Plated	310	7000 A at 12.2 nΩ	22.5	3,000 +
Tin-Lead (50-50) Fully Plated	930	9000 A at 36 nΩ	9.67	10,000 +
Lead-Bismuth (50-50) Fully Plated	930	5000 A at 49 nΩ	5.37	5,000 +
Lead-Indium (80-20)	63	3800 A at 1 nΩ	60.3	20 (Wears excessively)
Tin-Lead (50-50) (Vaculoy)	63	3100 A at 14.5 nΩ	49.2	5,000 +
Lead-Tin/80-20 Niobium-1% Zirconium Louvers	63	5100 A at 36.6 nΩ	80.9	20 (Wears excessively)

TABLE XVI-III

TEST RESULTS WITH LEAD AND TIN-BASED ALLOYS

Alloy	H_{c2} (Gauss)
Sn(90)-Pb(5)-Bi(5)	15,300
Sn(80)-Pb(10)-Bi(10)	14,700
Sn(70)-Pb(20)-Bi(10)	13,100
Pb(60)-Sn(10)-In(20)-Bi(10)	8,400
Pb(70)-Sn(20)-In(10)	7,700
Nb-1% Zr Multilam	6,500
Sn(80)-Ph(15)-Bi(5)	6,100
Pb(70)-SN(10)-In(20)	4,800
Pb(50)-Sn(30)-In(20)	4,600
Pb(80)-In(20)	4,200

solenoids were not suitable because of excessively slow force risetimes (greater than 100 ms), and insulation voltage breakdown in the solenoid windings. Efforts toward the purchase of ac solenoids modified for liquid helium service were initiated.

The overall design of the disconnect progressed during the year to the point where three separate alternatives have been designed, with one of the alternatives having been built and tested. The three alternative designs all utilize Multilam strips as contact components, all have essentially one moving part, and all avoid the necessity for superconducting leadwire movement.

The first design, consisting of a moving cylinder sliding into a fixed cylinder with the contact louvers mounted on the inside diameter of the static cylinder, has proven feasible but appears to require too large an overall size to be directly applicable (cylinder of 35.6-cm diameter required to meet current and resistance

specifications). Further progress in contact material development may change the prognosis.

The second design, consisting of a matrix of cylindrical pins sliding into corresponding cylinders and with the louvered contacts mounted on the inside diameter of the cylinders, may prove to be the most promising design based upon the results of single pin tests.

The third alternative, consisting of a series of interlocking "leaves," was advanced to the conceptual drawing stage.

The technology has been developed to fabricate the Multilam louvers from niobium-titanium sheet.

At year's end, the expertise and technology existed to construct a disconnect that could carry 10-kA while dissipating 2 W, with a projected lifetime of 10,000 cycles. Such a unit could also meet the dewar space limitations. This same technology also allows for the construction of a disconnect that could meet all the electrical requirements, but the size would be too large by a factor of about three.

5. 700-W, 4.5-K-Refrigeration System. The drawings for the installation of the 700-W, 4.5-K helium refrigerator were completed. Installation work began in September. The Joy Compressor, the Reavell recovery compressor, the high-pressure cluster He storage tanks, and the structural steel platforms to hold the coldbox were installed. The installation is expected to be completed by mid-April 1977.

G. HOMOPOLAR DEVELOPMENT PROGRAM

1. Machine Development. Los Alamos Scientific Laboratory acted as the technical administrator for the EPRI-funded HETS contract with the University of Texas at Austin and the Westinghouse Electric Company. The contract produced an in-depth design[1] of a 1-GJ, energy-storage, homopolar electrical machine capable of discharging in 30 ms. The full-scale design[1] emphasized the use of a homopolar machine as the adiabatic compression energy source for the RTPR.

Included in this study was the initial design of a 10-MJ model machine. This machine uses two drum rotors and superconducting cryostable field windings. The model machine dimensions and terminal characteristics are summarized in Table XVI-IV.

TABLE XVI-IV

10-MJ MODEL HOMOPOLAR ELECTRICAL CHARACTERISTICS

Peak voltage	719 V
Peak current	1.5 $(10)^6$ A
Capacitance	38.7 F
Average radial field between collectors	23 kG
Average axial field within collectors	
Center	41 kG
End	37 kG
Flux leakage	63%
Peak field	65 kG
Superconductor weight	4,500 kg (9,800 lb)
Total coil energy	18.4 MJ
Total A-turns	10 x 10^6
Total magnetic iron weight	39,000 kg (86,000 lb)

10-MJ MODEL HOMOPOLAR DIMENSIONS

Overall diameter	2.286 m (108 in.)
Overall length	2.108 m (83 in.)
Rotor diameter (at peak speed)	0.721 m (28.4 in.)
Single rotor length	0.701 m (27.6 in.)
Rotor-to-rotor midplane length	0.742 m (29.2 in.)

In July 1976, LASL and Westinghouse submitted a proposal to ERDA[2] which outlined a developmental program to complete the design and to fabricate the model 10-MJ, 30-ms-discharge homopolar machine. The work will include component development and testing of critical subassemblies which advance the state of the art. The final homopolar machine will be tested in circuits to determine its performance as a potential fusion energy storage device. This program has been funded by EPRI and ERDA. Contract negotiations with Westinghouse have been initiated.

The forty-two-month program will encompass the development, construction, and no-load performance tests of a 10-MJ Fast Discharging Homopolar Machine. The completed machine will be suitable

for installation in a test system at LASL which will allow evaluation of the fast discharging characteristics.

Westinghouse designed the field coils of the 10-MJ machine to operate cryostably. While this increased the machine weight and field energy storage above the predictions based on the 1-GJ design, it eliminated one developmental aspect of the machine.

Determination of magnetic forces on the machine components during switching transients was completed. All forces appear to be manageable.

The University of Texas at Austin has concluded its brush testing work. This work forms the foundation for early Westinghouse research in high-speed brush testing.

Studies have been initiated to determine the stability of the Westinghouse field coils. These will include a small model test coil which is nested in a bias field coil capable of producing 6.5 T at the bore of the test section.

2. Test Facility. The HETS test facility will incorporate components of maximum attainable reliability so that the homopolar will remain the major developmental item.

Proposed testing has been simplified to allow a single swing of the homopolar (full-zero-full speed) per test cycle with no flat top. In this mode of operation only a load coil and series switch are required. The load coil will require an extension of existing coil design technology for its successful operation. No existing equipment appears to be usable as a series switch so a development program will be undertaken in this area.

A load coil which is capable of full energy transfer in either 30 ms or 2 s has been designed. As presently envisioned the load coil and bus will be a single integrated unit wound of nitrogen-cooled aluminum with a fiber-reinforced plastic mechanical structure. It will be wound of relatively few large dimension Roebel bars to minimize eddy and circulating current losses. Discussions with coil manufacturers have been initiated. Load coil characteristics are listed in Table XVI-V.

TABLE XVI-V

10-MJ LOAD COIL CHARACTERISTICS AND DIMENSIONS

Characteristic	0.060 s Swing	2.0 s Swing
Inductance	5.81 μH	10.5 mH
Number of turns	2	85
Resistance (No Bus)	0.7 μΩ	1.26 mΩ
Time Constant (No Bus)	8.28 s	8.28 s
Inefficiency (No Bus)	0.7%	24.2%
Peak field	3.04 T	3.04 T
Current density	1.85 kA/cm^2	1.85 kA/cm^2
Operating temp	100°K	100°K
Resistivity	0.53 μΩ cm	0.53 μΩ cm
Material	1100 Al	1100 Al
Inner radius	57 cm	57 cm
Outer radius	228 cm	228 cm
Thickness	57 cm	57 cm

H. TOKAMAK OHMIC HEATING PROGRAM

A preliminary study of tokamak ohmic heating systems for experimental power reactors (EPR's) has been carried out jointly by the University of Texas, Westinghouse, and LASL. The purpose of the study was to define possible power systems for driving EPR ohmic-heating (OH) coils and to give cost estimates for each of the systems. Since all of the EPR design groups had suggested using homopolar generators, one principal goal of the study was to determine whether homopolar machines were feasible and cost effective devices for reversing the flux in the OH coils.

At the time the study began in early 1976, all of the EPR designs were incomplete, and the zero-dimension computer codes used to predict the interaction of the plasma with the poloidal field coils were still being developed. It was decided to focus on the magnetic coil and field configurations proposed by ORNL. A zero-dimension plasma startup code was developed at LASL and UT, and studies were made on several aspects of OH coil design. After the voltage and current levels required for proper plasma development were established, the various circuit options and the component costs were investigated. Under contract to LASL, Westinghouse devised both a dc

(homopolar) and an ac (salient-pole and turbo-alternator) system for reversing the OH coil flux. Costs for the complete system are dominated by switching costs.

1. Ohmic Heating Coil Design. The dimensions, inductances, coupling constants, and other electrical parameters which specify the OH and equilibrium coils were summarized in standard form for convenient comparison of the three EPR designs. In addition, some of the problems of paralleling 25- to 40-kA superconducting cables to reach 100- to 400-kA currents were investigated.

2. Zero-Dimension Plasma Startup Code (LASLOD). A zero-dimension plasma startup code (LASLOD) was developed at LASL and sent to the University of Texas (UT). Numerical checks were made at both places, at ORNL, and General Atomic Company. The code was further developed at LASL and UT and used to optimize the ohmic heating circuit of an EPR.

The code calculates plasma resistivity as a function of plasma current and plasma temperature which in turn is a function of time. LASLOD is thus used as a subprogram of a circuit analysis code. The plasma is treated in three regimes depending on electron temperature.

Numerical exploration with LASLOD showed that a gas density of ∿0.14 torr and a voltage gradient of approximately 4 V/m are needed to start the plasma. This "voltage blip" will have to last for a few tens of milliseconds. The voltage may subsequently be lowered to approximately one-half that value to reach a temperature of ∿ 1 keV. The gas pressure must be increased to approximately 1.4-mTorr over the temperature interval ∿ $20 < T_e < 200$ eV. Figures XVI-1, XVI-2, and XVI-3 show the circuit studied and the current and voltage requirements on a per-turn basis for plasma startup and build up of the Oak Ridge EPR.

The currents and voltages shown in Figs. XVI-2 and XVI-3 were used to define the equipment necessary for a circuit with homopolar machine as well as one with ac machine and rectifier. These two circuits were developed at Westinghouse and are shown in Figs. XVI-4 and XVI-5. The equipment was costed at Westinghouse. If the SCR's shown in Figs. XVI-4 and XVI-5 are replaced by the type of air-blast circuit breakers[3] considered for

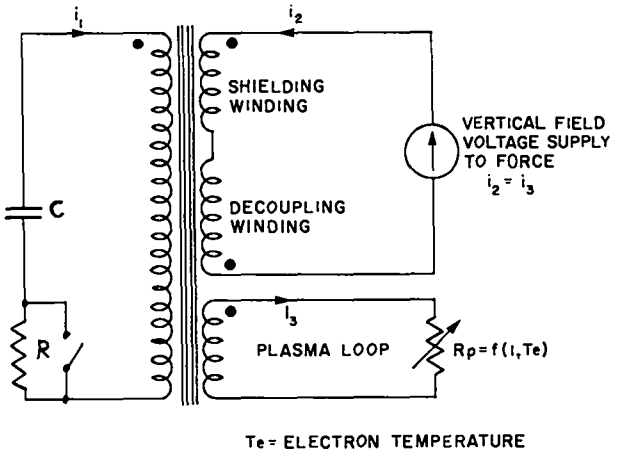

Fig. XVI-1.
Pulsed coils of the tokamak EPR with electric circuits and plasma loop.

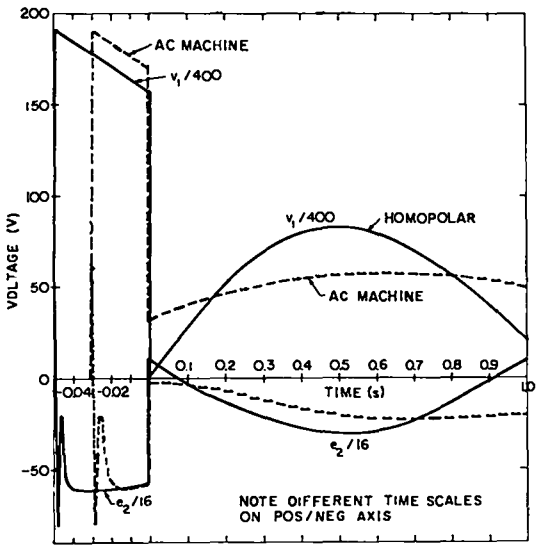

Fig. XVI-2.
Voltage plots for the circuits with homopolar machine and ac generator-rectifier. V_1 = voltage on OH winding; e_2 = vertical field supply voltage to force $i_2 = i_3$.

Doublet III and discussed in Ref. 3, then the homopolar circuit of Fig. XVI-4 shows a significant cost advantage over the circuit with ac machine and rectifier of Fig. XVI-5 as demonstrated by the cost comparison shown in Table XVI-VI.

3. Circuit Analysis Code, SCEPTRE. In informal collaboration with the AFWL/EPL, several errors in SCEPTRE were pointed out and corrected. Many of the code's idiosyncrasies have been documented in comments made available on LASL's NOS system. The code is being maintained for all LASL

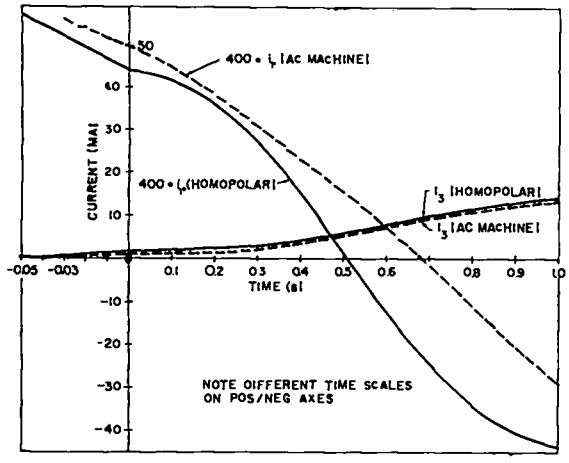

Fig. XVI-3.
Current plots for the circuits with homopolar machine and ac generator-rectifier. Note, $i_2 = i_3$.

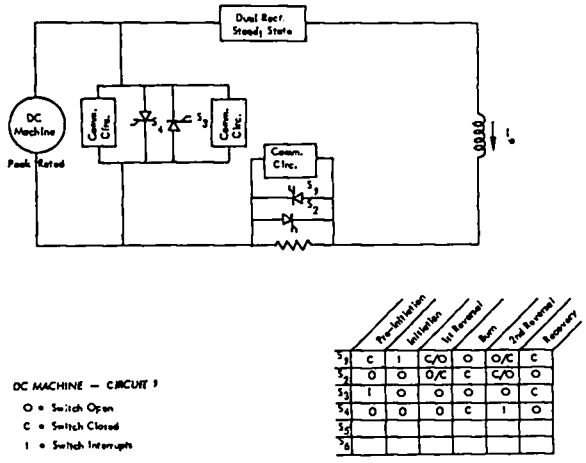

Fig. XVI-4.
Apparent least cost circuit with homopolar machine.

users and was used as a circuit analysis program with LASLOD as a subprogram.

SCEPTRE has been used also for modeling the commutating circuit function reported for the current interruption tests of the air-blast circuit breaker considered for the Joint European Torus (JET) and Doublet III at General Atomic Company.

I. MISCELLANEOUS

1. End Stoppering for Scylla IV-P. A cryogenic end stopper is being developed for Scylla IV-P. The unit utilizes a LHe-cooled, quartz surface onto which inert gases are solidified. It

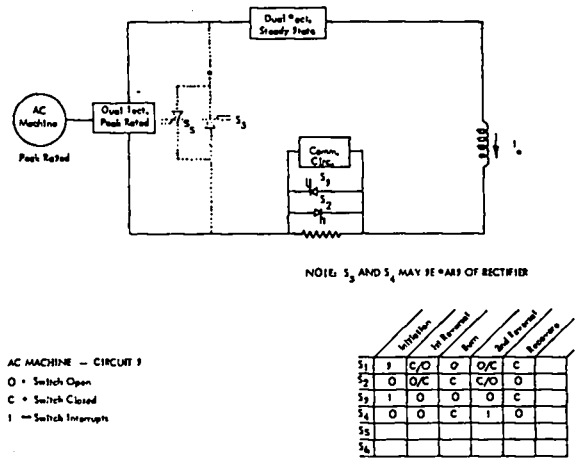

Fig. XVI-5.
Apparent least cost circuit with ac machine.

TABLE XVI-VI
COMPARISON OF HOMOPOLAR AND ac MACHINES

	Cost	
	Homopolar	ac Machine
Homopolar vs ac generator and drive	$18.4M	$13.8M
Rectifier	0	58.6
Circuit breaker for generator bypass	1.0	1.0
Resistor	2.2	1.0
Circuit breaker for resistor bypass	2.0	2.0
Burn cycle supply	10.0	10.0
Total	$33.7M	$86.5M

is required that the vapor pressure of the condensed solid be 10^{-3} torr or less. This corresponds to a surface temperature of 8 K for deuterium, 11 K for neon, and 43 K for argon. Argon layers which meet the above criteria have been deposited up to 0.7 cm in thickness. Such a layer will be used to determine feasibility for this type of end stopper in experiments to be conducted in Scylla IV-P. Because of the thermal radiation impinging upon the solid cryogen surface only very thin layers of He and D_2 can be built up with this type of target. If these gases are required, an extrudable target will be developed following completion of the feasibility experiments.

2. Zero-G Helium Heat Transfer. The rocket-borne experiment to study heat transfer, fluid dynamics, and thin film characteristics of superfluid helium at 1.7 K and heat transfer to normal helium at 4.2 K in a zero-G environment was successfully launched from Barking Sands, Kauai, Hawaii, in late May. Analysis of the 4.2 K data is complete. This showed a reduction in the peak nucleate heat flux from ~ 1 W/cm^2 at 1-g to between 0.2 and 0.3 W/cm^2 at zero-G.

REFERENCES

1. K. Thomassen, "Conceptual Engineering Design of a One-GJ Fast Discharging Homopolar Machine for the Reference Theta-Pinch Fusion Reactor," EPRI ER-246, Electric Power Research Institute, Palo Alto, CA (August 1976).

2. J. D. Rogers, "A Proposed 1 MJ Fast Discharging Homopolar Machine for Fusion Reactor Systems," Los Alamos Scientific Laboratory report LA-6402-P (July 1976).

3. P. Dokopoulas and K. Ksiechbaum, "D.C. Circuit Breaker Arrangement, 73 kA, 24 kV for the Joint European Torus," Elek. Zeits. A, 8, 499, August 1976. Translated by H. Vogel, Los Alamos Scientific Laboratory (1976).

XVII. MAGNETIC CONFINEMENT SYSTEMS STUDIES

P. E. Armstrong, M. E. Battat, R. O. Brown, J. M. Bunch,
F. W. Clinard, Jr., G. E. Cort, D. J. Dudziak, S. A. W. Gerstl,
W. V. Green, G. R. Gryczkowski, R. L. Hagenson, J. G. Hoffman, G. F. Hurley
P. G. Klemens, R. A. Krakowski, R. L. Miller, R. W. Moses, D. M. Parkin
W. F. Sommer, W. L. Thomson, and R. A. Yeske

A. INTRODUCTION

The work of the Magnetic Confinement Systems Studies Group is primarily concerned with the continuing reassessment of pulsed, high-beta systems, including the Reference Theta-Pinch Reactor (RTPR), the Linear Theta-Pinch Hybrid Reactor (LTPHR), the Reverse-Field Pinch Reactor (RFPR) and imploding liner systems. Areas of general research in pulsed high-density fusion power systems include more detailed thermal-shock analyses, MHD effects in reactor-like high-beta plasmas, transient neutral-gas charge-exchange, and more realistic plasma engineering modeling. The Neutronics Task has been supportive of both the RTPR blanket redesign and the more general needs of the national fusion community. The chemical, structural, and electrical effects in CTR-related insulators are addressed by the Insulator Research Task. The Alloy Research Task has pursued the thermal-shock testing of Nb-1Zr alloy and Al_2O_3-coated Nb-1Zr RTPR first-wall specimens.

B. SYSTEMS STUDIES

The Systems Studies Task has emphasized the toroidal Reference Theta-Pinch Reactor (RTPR), the Linear Theta-Pinch Hybrid Reactor (LTPHR), the Reverse-Field Pinch Reactor (RFPR) and, in a preliminary way, imploding liner confinement schemes. Progress on each of these topics is summarized below.

1. RTPR Systems Studies. Central to the technological definition and assessment of major engineering systems anticipated for the Reference Theta-Pinch Reactor (RTPR) is the resolution of the physics "operating point." Specifically, the efficiency of implosion heating, the requirements of high-beta stability/equilibrium, and the dynamics of both alpha-particle thermalization and neutral-gas cooling impact directly upon the RTPR energy multiplication (Q-value), cost, and size; the physical constraints imposed by implosion voltage, feedback power level, plasma ignition and direct conversion, the ability to quench a highly reactive plasma, and the first-wall (or bumper) thermal-mechanical response represent specific examples of the impact of high-beta physics on the performance of the RTPR. The interaction between major physics variables and these constraints has been quantitatively examined in a systems analysis context.

a. RTPR Operating Point. An updated, more realistic operating point has been developed.[1,2] The major intent of this RTPR reoptimization is to identify those physics parameters which will reduce the problems associated with pulsed thermal loads at the first-wall, large-energy storage, high-voltage implosion heating, and high-compression fields, while simultaneously maintaining a low recirculating power fraction and assuring a fully stabilized plasma.

The updated interim RTPR design point summarized in Table XVII-I entails several significant advantages in comparison to the older design; these include:[3]

(1) The lower compression field B_o (7 *vs* 11 T) eases the mechanical design requirements of the adiabatic compression coils (ACC) insofar as the corresponding stress-producing transients are reduced. Simultaneously, the energy transfer and storage (ETS) system requirements are reduced relative to the thermonuclear energy produced and amount to $\sim$ 2.5 less ETS energy compared to the older design. Finally, the associated reduction of plasma density reduces the bremsstrahlung power deposited at the first-wall surface, therefore, considerably easing the thermal response requirements.

(2) The longer total burn time ($\tau_B = \tau_{FT} + 2\tau_R$), by stretching out the bremsstrahlung deposition time, reduces both the magnitude of

TABLE XVII-I

COMPARISON OF OLD AND NEW RTPR OPERATING POINTS

SYMBOL	DEFINITION (UNITS)	OLD VALUE	NEW VALUE
E_θ	Implosion-heating electric field (kV/cm)	2.0	0.7
B_{SH}	Implosion-heating magnetic field (T)	1.4	0.8
P_A	D-T filling pressure (mTorr)	17	7
B_O	Maximum compression field (T)	11	7
τ_R	Compression-field rise time (ms)	30	30
τ_{FT}	Compression-field flat-top time(ms)	70	400
W_N	Fusion neutron yield (MJ/m)	93.11	86.73
W_{BO}	Total ETS energy (MJ/m)	286	97
A	Aspect ratio	112	100
b	First-wall radius (m)	0.5	0.5
η_{ETS}	ETS transfer efficiency	0.98	0.95
Q_E	Engineering Q-value	6.5	5.7
ε	Recirculating power fraction	0.16	0.18
$\Delta T_W(s)$	First-wall surface temperature rise (K)	310	150
T_W	Maximum temperature drop across first wall (K)	250	30

the temperature gradient across the first-wall thickness and the temperature spike seen at the first-wall surface. Trading off a lower τ_{FT} for longer τ_R, while reducing the Q-value somewhat, allows attainment of high values for the ETS system efficiency.

(3) The lower D-T filling pressure (7 mTorr vs 17 mTorr) associated with (1) above, reduces the pumping requirements between cycles. Additionally the finite Larmor radius (FLR) stability condition is more easily met.

(4) The newer design point uses an implosion heating voltage of 0.7 kV/cm rather than the older value of 2.0 kV/cm. This reduction is a direct result of the lower filling pressure and leads to decreased pulsed-dielectric stress and insulator thickness, which in turn will aid the already reduced (3) heat-transfer/thermal-stress problem.

In addition to treating consistently the requirements of high-beta equilibrium and stability, the interim design point considerably reduces the technological requirements associated with blanket/first-wall designs, pulsed dielectric insulators, ETS system size and efficiency, and ACC structural design. These significant benefits are accrued with a system having Q-values equal to or greater than earlier designs. The time dependence of major system variables, including m = 1 feedback power, is shown in Fig. XVII-1 for the new RTPR operating point.[1]

b. RTPR Blanket Neutronics. The reference blanket for the RTPR was reevaluated in order to reduce the overall blanket thickness and to minimize the stored magnetic energy associated with the compression field. Based on the results of a neutronic design sensitivity analysis,[4] the RTPR reference blanket[3] was modified and reanalyzed. All blanket modifications are subject to the constraints of acceptable tritium breeding, energy recovery, radiation damage, induced radioactivity, shielding, and other system requirements, as described in Ref. 3.

From sensitivity analyses it was clear that a first step in thinning the RTPR blanket without substantial loss of tritium breeding could be the elimination of the second graphite region (zone 21 in Ref. 3). Such a modification, however, substantially increases the radiation heating in the

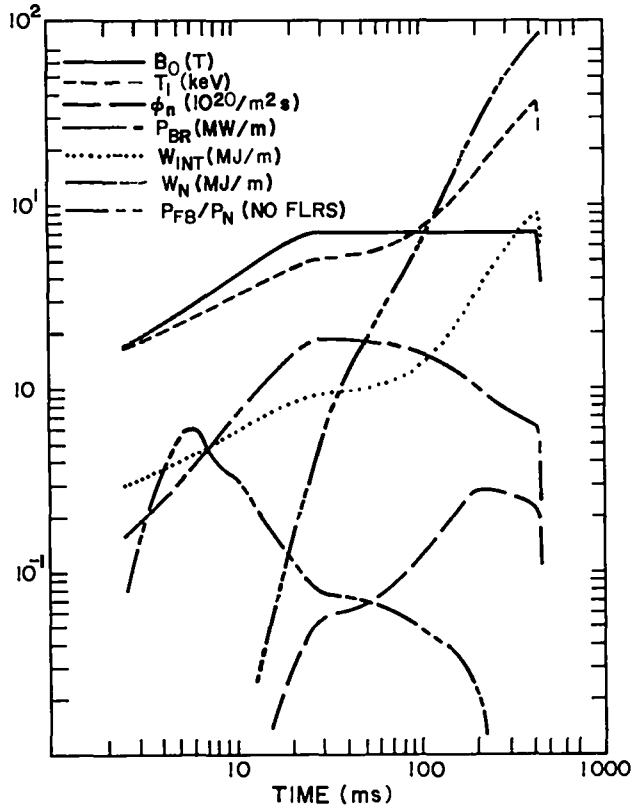

Fig. XVII-1.

Time dependence of major burn parameters for the RTPR operating point given in Ref. 1.

Plasma internal energy: W_{INT}
Thermonuclear yield: W_N
Thermonuclear Power: P_N
Feedback power: P_{FB}
Bremsstrahlung Energy: W_{BR}
Compression field: B_o

copper coils. To compensate for this effect, a 2-cm-thick lead zone was added immediately inboard of the implosion coil to recover the gamma-ray energy otherwise leaking out of the blanket and heating the coils. It was also established that BeO acts as a better moderator than graphite in the RTPR blanket. To further reduce the overall blanket thickness, therefore, the first graphite region (zone 13 in Ref. 3) was replaced with BeO. The effects on tritium breeding and total recoverable and waste energies are shown in Fig. XVII-2; even with no BeO, which gives an overall blanket thickness of 21.8 cm, a breeding ratio of 1.10 can be obtained.

Concern over the availability and use of beryllium in the RTPR blanket has initiated ad-

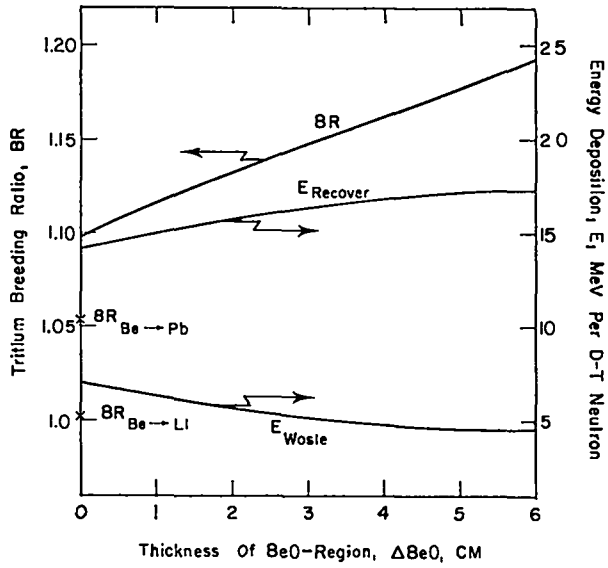

Fig. XVII-2.

Tritium breeding ratio [BR] and energy recovery for a thin (0.218-m) RTPR blanket vs the thickness of BeO region.

ditional modifications of this blanket design. First, the 2.5-cm-thick Be neutron multiplier near the first wall was replaced by lead, expecting that the substantial (n,2n) and (n,3n) cross sections of Pb will compensate for the eliminated neutron multiplication of the beryllium. Indeed, the total tritium breeding ratio is reduced by only 5% (from 1.10 to 1.05). In a second computation the effect of replacing the neutron multiplier altogether with breeding material was investigated. Natural lithium was substituted for the original metallic beryllium. The result is a breeding ratio of 1.01, which leaves no margin for neutron streaming effects.

On the basis of these results, Pb instead of Be was chosen as a neutron multiplier. To increase the breeding characteristics of this blanket without substantially increasing the total blanket thickness, the pure liquid lead was replaced by a lithium/lead alloy (LiPb) to increase the amount of breeding material (Li) without eliminating the neutron multiplier. The analysis of different LiPb/Pb and LiPb/Li mixtures showed, however, that pure Pb gives superior tritium breeding. With a pure Pb multiplier zone, a new sensitivity analysis was performed to determine whether an increased Pb

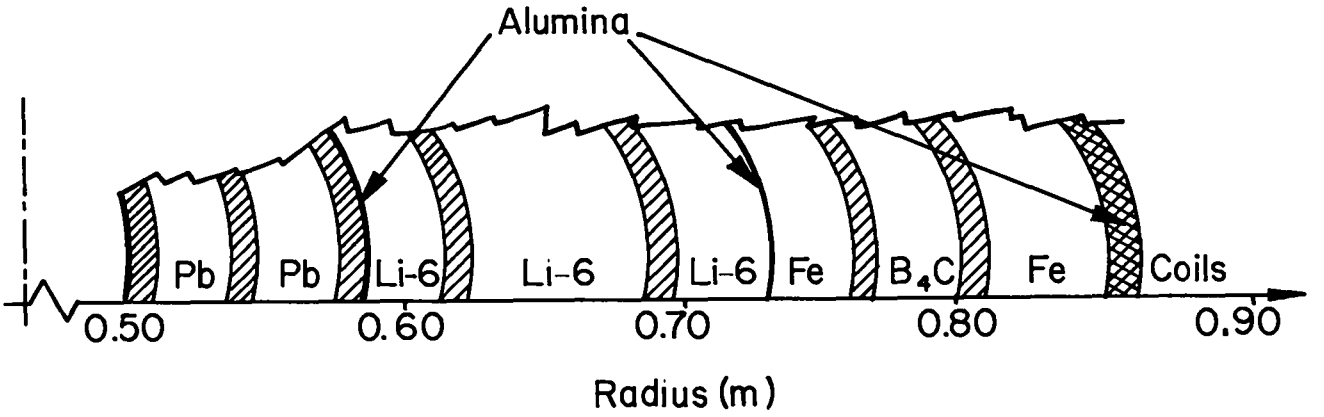

Fig. XVII-3.

Newer RTPR blanket/shield neutronic model.

thickness or an increased Li thickness is more beneficial to overall tritium production. It was concluded that a total 6.1-cm of Pb in addition to 12-cm Li will produce a tritium breeding ratio of 1.10 in the arrangement shown in Fig. XVII-3. All lithium coolant within the blanket is assumed to consist of 99% enriched Li.

Keeping the breeding portion of the blanket unchanged, the thickness of the Fe/B_4C/Fe shield portion was varied. The energies deposited in the coils (waste energy) and the blanket/shield assembly were monitored. When the shield is thinned, additional neutron and gamma-ray energy escapes into the coils, and the efficiency of the blanket/shield assembly for energy extraction is reduced. Figure XVII-4 shows the monotonic reduction of blanket efficiency, η_B, when the shield thickness is reduced. The tritium breeding ratio is not significantly affected by altering the shield portion of the blanket/shield assembly. For all shield thicknesses considered, the breeding ratio remained above 1.10. The results of these neutronic analyses will be used in the overall RTPR optimization to determine a blanket thickness that maximizes the overall system performance while simultaneously meeting all neutronic constraints.

c. RTPR Blanket Thermal Analysis. Temperatures in the redesigned RTPR blanket have been calculated using a two-dimensional (r-z) finite-element heat-conduction model.[5] The previously described neutronic design (Pb, Li, Fe, and B_4C) was used in the thermal/hydraulic model, and the structural portion of the blanket is 1-mm-thick Nb-1Zr alloy with 0.5-mm-thick Nb-1Zr used to "can"

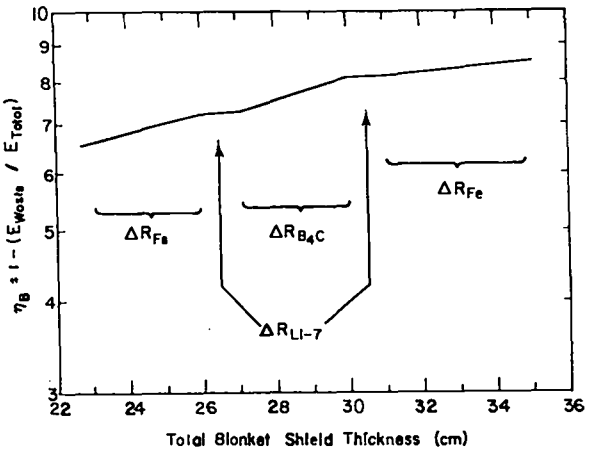

Fig. XVII-4.

Variation of blanket energy-recovery efficiency η_B vs total blanket thickness of Fe/B_4C/Fe shield.

the liquid lead and lithium. The model includes thermal contact resistance where the metal-to-metal interfaces occur. The (r-z) heat-transfer model neglects the beneficial effect of the radial metal walls, which assist in conducting heat from the thicker neutron and gamma-absorbing regions.

The model has been used to predict blanket temperatures for the reference burn cycle[1] (B = 7 T). In general, the latter results in lower blanket and first-wall temperatures. Fig. XVII-5 compares the lithium coolant velocities calculated by the MHD code LIFLOW for the two burn cycles. Heat transfer to the flowing lithium during the time when the magnetic fields were zero is based on the sum of the molecular conductivity and turbulent eddy conductivity. Only molecular conductivity is used when the magnetic field is present. Figure

XVII-6 compares blanket temperatures at the end of the burn cycle for the two conditions.

In addition, the AYER heat-transfer code[5] has been used to model the thermal/mechanical response of the RTPR first wall for both the older and newer operating points. The first-wall thermal and stress response for the newer operating point is shown on Fig. XVII-7. As expected, the cyclic stresses can be significiantly reduced by changing the RTPR operating point.

d. Transient Neutral Gas Blanket Studies.[6] A computer simulation of a neutral gas impinging on the RTPR plasma after quench has been developed. The model assumes a plasma with Maxwellian ions, electrons and alphas. The plasma densities are assumed to be low at the wall and to approach the RTPR values at the plasma core. At zero time a diatomic gas of deuterium and tritium flows into the plasma chamber. The diatomic neutral gas reacts with the low density edge of the plasma by means of the following six reactions:

$$D_2^o + D^+ \rightarrow D_2^+ + D^o$$
$$D_2^o + D^+ \rightarrow D_2^+ + D^+ + \bar{e}$$
$$D_2^o + \bar{e} \rightarrow D_2^+ + 2\bar{e}$$
$$D_2^o + He^{++} \rightarrow D_2 + He^+$$
$$D_2^o + He^{++} \rightarrow D_2^+ + He^{++} + \bar{e}$$
$$D_2^o + D_2^+ \rightarrow D_2^+ + D_2^o$$

Complete particle and energy balances are enforced. The dissociation of the D_2^+ gas, including the Franck-Condon effect, is assumed if the average plasma energy at a spatial point is greater than 6.649 eV. Lastly the hydrodynamic behavior of the plasma is taken into account by the calculation of heat flow, magnetic field diffusion, temperature equilibration and quasi-static pressure balance.

In order to model the gas-blanket/plasma transient, the simulation code was run for 200 μs, using a 5μs time increment. The results shown in Fig. XVII-8 indicate that a low temperature sheath is formed near the wall within 50 μs, and the wall energy dose resulting from first-generation charge-exchange neutrals levels off significantly after ~25 μs. The particle spectrum impinging on the first wall is depicted in Fig. XVII-9.

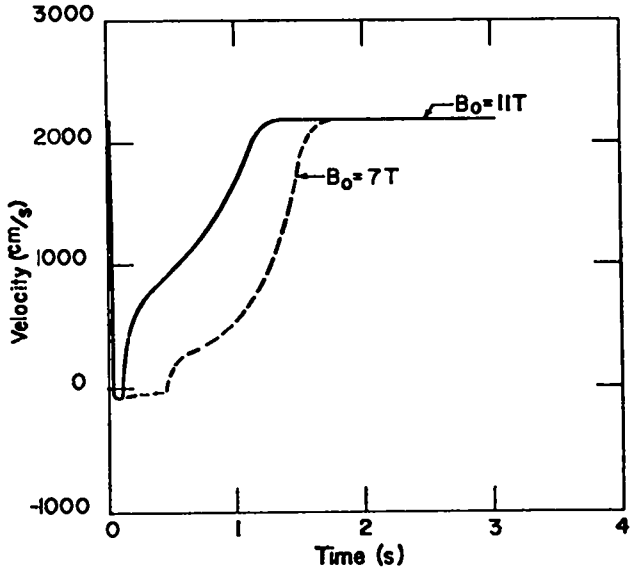

Fig. XVII-5.

Time dependence of Li-coolant flow velocity for older RTPR burn cycle, Ref. 3, (11 T) and newer RTPR burn cycle Ref. 1 (7 T).

2. Reversed-Field Pinch Reactor (RFPR). The Reversed-Field Pinch Reactor (RFPR) has been investigated in a plasma-engineering context for a wide

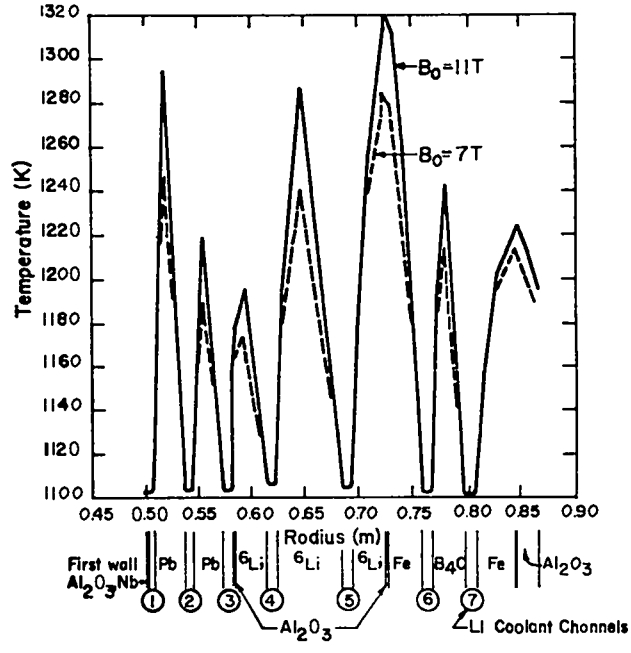

Fig. XVII-6.

Blanket temperature profiles at the end of a RTPR burn cycle for the older design point, Ref. 3 (11 T), and the newer design point Ref. 1 (7 T).

range of first-wall radii (0.5-2.8 m) and average toroidal plasma current densities (j_z = 5-80 MA/m^2).[7] The reactor dimensions used in these studies are given in Table XVII-II. In all cases plasma ignition is achieved in 0.1 to 1.0 seconds using classical plasma resistivities. The initial non-equilibrium phase of operation is not modeled, and ohmic heating of a sharp-boundary plasma in thermal equilibrium is used throughout. A single slow-pulse coil is used to produce the toroidal current I_z and reverse field B_R. An additional fast-pulse coil may be necessary to establish the desired field profiles on a relatively short time scale in a hot plasma. This implosion-like startup would inhibit field diffusion and tend to maintain stable field and pressure profiles. The use of fast-pulse coils and associated volume for return flux adds at most 15% to the stored energy requirement and, therefore, would have little impact on the energy balance.

Plasma temperature excursions in a high-beta system limit the burn time because of maximum beta (β_θ < 0.5) restrictions. For a 50%-50% D-T fuel mixture the temperature rises uncontrollably, and the plasma must be prematurely released when β_θ approaches 0.2-0.25 during the burn, thereby assuring that β_θ < 0.5 after subsequent expansion to the wall. In Fig. XVII-10 the first-wall radius versus the average maximum toroidal current density is shown as a function of engineering Q-value, Q_E, for the 50%-50% D-T fuel mixture case (β_θ control by early quench). The maximum Q_E is generally found at the maximum allowable initial filling pressure, above which nonignition results (j_z(MA/m^2) = 5 P (mTorr)). Superimposed upon the Q_E curves in Fig. XVII-10 are lines of constant first-wall surface temperature rise ΔT_ω(K), where the (0.3-mm) Al_2O_3/ (2-mm)Nb-1Zr reference first wall is cooled by a stagnant pool of lithium.

Plasma temperature control using cold fuel injection or impurity addition was considered, but the alpha-heating power must be balanced by losses

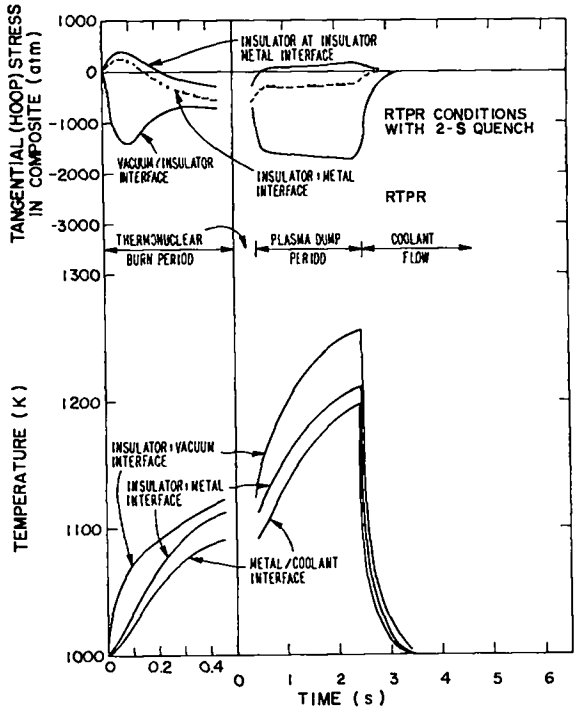

Fig. XVII-7.

Time-dependence of first-wall temperatures and stresses for the newer operating point Ref. 1.

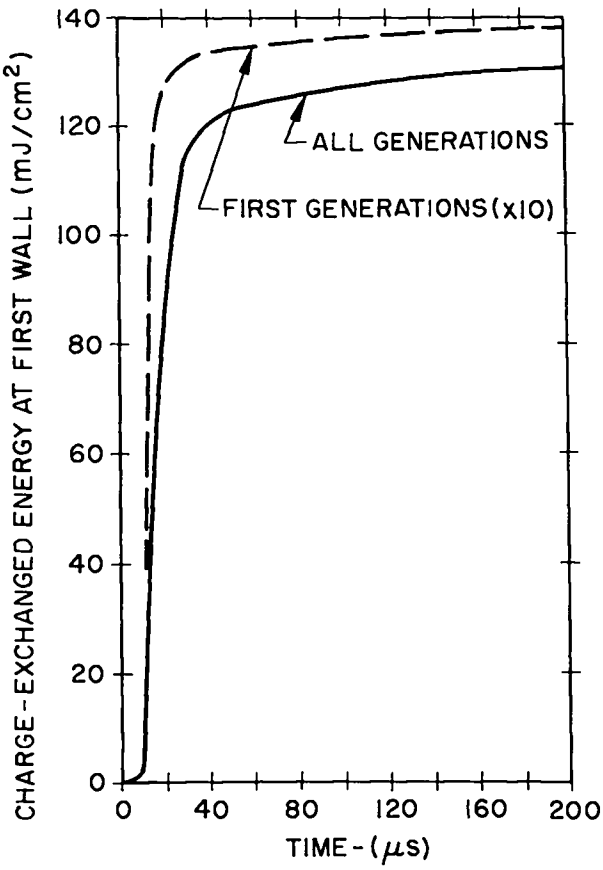

Fig. XVII-8.

Time-dependence of RTPR first-wall energy dose resulting from first-generation and N-generation charge-exchange neutrals during the transient gas-blanket/plasma interaction.

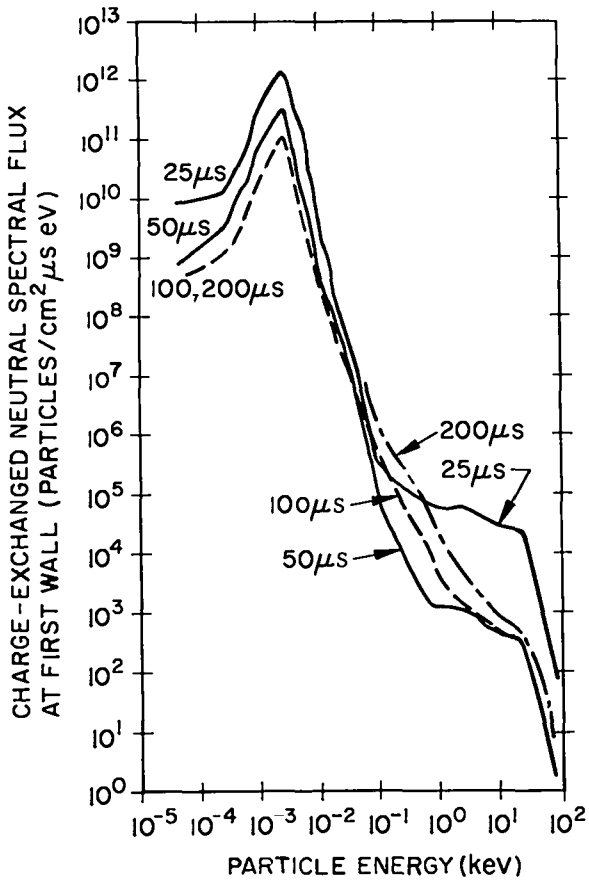

Fig. XVII-9.

Energy spectra of charge-exchange neutrals at RTPR first wall for 4 times during the transient gas-blanket/plasma interaction.

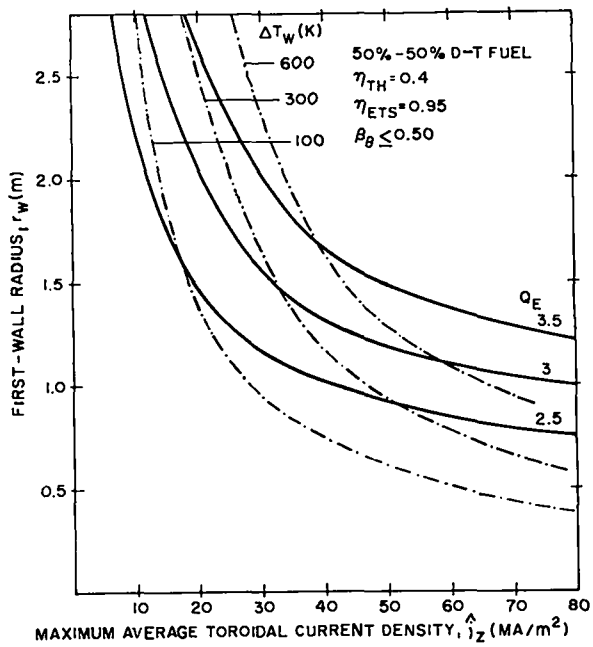

Fig. XVII-10.

Lines of constant Q as a function of first-wall radii and maximum toroidal current densities (solid curves) for a RFPR operating on a 50-50% D-T fuel mixture. Dashed curves are lines of constant first-wall temperature rise, ΔT_w.

to the first wall in order to maintain a constant plasma temperature. Since the alpha-heating power is ~28 times that of bremsstrahlung radiation at 20 keV, the surface heat flux to the wall would be correspondingly increased. For typical initial ion densities (50%-50% D-T fuel mixture, 2-m first-wall radius, and j_z = 20 MA/m^2) of 3.0 x 10^{20}/m^3 compressed to 1.75 x 10^{21}/m^3 at the minimum compression x_o = 0.4, a heat removal rate of ~ 40 MW/m^3 at the first wall would be necessary to achieve a constant plasma temperature 20 keV. This exceedingly high surface heat flux would be intolerable over the 1.4-s burn time anticipated for the aforementioned case. The normal bremsstrahlung power of 1.5 MW/m^2 produces a 187 K surface temperature rise for the (0.3-mm)Al_2O_3/(2-mm)Nb-1Zr first wall. For these methods of plasma temperature control, the plasma density must be decreased by ~ 5 to lower the alpha-heating power by a factor of 25; a corresponding increase in burn time would result. The potential technical difficulties associated with the injection of cold fuel or impurities and questions of plasma stability incurred by the use of such processes were also major factors leading to the decision not to utilize injection techniques for plasma temperature control.

Automatic temperature control by tritium burnup using an off-optimum D-T fuel loading was also investigated. The shortest burn time and near optimum Q_E is encountered for a 90%-10% D-T fuel mixture. For this case the maximum poloidal beta during the burn is 0.43, which results in $\beta_\theta < 0.5$ after 90% tritium burnup and plasma expansion to the wall has occurred. In Fig. XVII-11 the first-wall radius versus toroidal current density is shown as a function of Q_E for the 90%-10% D-T fuel mixture case (β_θ control by tritium burnout) using a thicker first wall (0.3-mm)Al_2O_3/

TABLE XVII-II

DIMENSIONS USED IN RFPR ENERGY-BALANCE STUDY

Symbol	Definition	Value
r_ω	first-wall radius (m)	variable
	first-wall Nb-1%Zr thickness (m)	0.002(0.005) [a]
	first-wall Al O coating thickness (m)	3.0×10^{-4}
	blanket thickness (m)	0.4
$r_{cp} = r_{cz}$	inside coil radius (m)	r_ω+0.4
$\Delta r_{cp} = \Delta r_{cz}$	coil thickness (m)	0.6(1.0) [a]
N	number coil turns	5
P_ℓ	parallel plate lead length (m)	2.0
P_ω	parallel plate lead width (m)	$2\pi r_{cp}$
P_t	parallel plate thickness (m)	Δr_{cp}
P_g	gap between parallel plates (m)	0.01
ℓ	length of device fed by leads (m)	2.0
λ	fraction of conductor in coil and leads	0.7
η	resistivity (copper) of coil and leads (ohm-m)	1.72×10^{-8}

(a) Dimensions in parentheses used for the longer burn times associated with the case which controls by D-T burnout (90%-10% D-T fuel mixture).

(5-mm)Nb-1Zr (Table XVII-II) and increased thickness of the magnet coil (from 0.6 to 1.0 m). The longer burn times associated with the lower tritium fraction necessitate thicker first walls to maintain approximately the same temperature drop across the wall (a measure of the internal mechanical stress), typically $\sim$50 K and bulk temperature rise. The joule losses in the coil are also increased by the longer burn times and are offset by the thicker coil. Increasing the coil thickness increases Q_E, but the trade-off between coil size, complexity and cost versus higher Q_E must eventually be considered.

After expansion to the wall the plasma is assumed to be wall confined, where heat loss is limited by heat conduction across the trapped field in the plasma. Injection of a neutral gas at early times after expansion may be necessary to assure the rapid establishment of a buffer layer between the plasma and the wall. For the tritium burnout case no energy is produced in the plasma during quench. The 50%-50% D-T fuel mixture case arrives at the wall with an ion temperature of 7.8 keV, and the temperature of the plasma increases at a rate

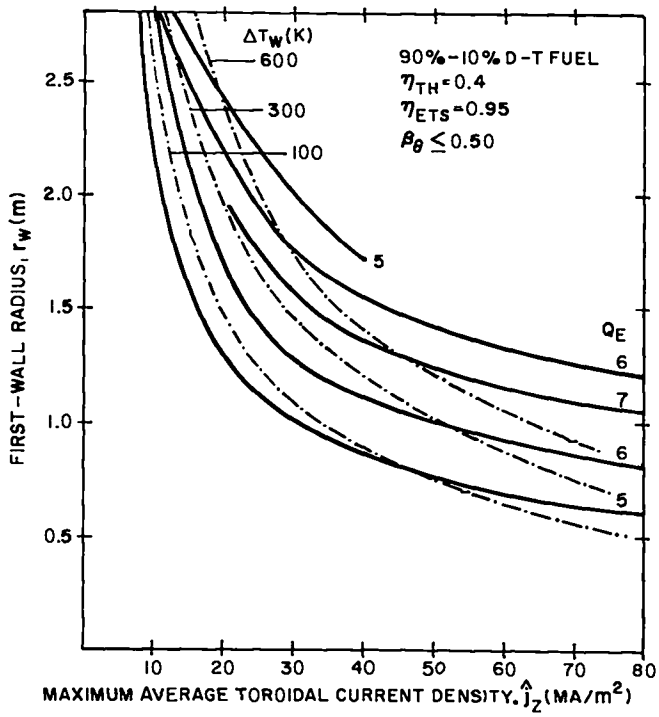

Fig. XVII-11.

Lines of constant Q as a function of first-wall radii and maximum toroidal current densities (solid curves) for a RFPR operating on a 90-10% D-T fuel mixture. Dashed curves are lines of constant first-wall temperature rise, ΔT_ω.

equal to 8.1 keV/s. No additional plasma energy is assumed to be added after plasma expansion to the wall, but a significant increase in Q_E may result because of additional alpha-heating power occurring during the quench phase.

Uncertainties in the plasma physics including plasma field profiles, resistivities, diffusion, achievable current densities, and stability makes a firm choice of any operating point for the RFPR questionable at this point. In addition the physics and engineering of Z-pinch startup within the constraints of plasma stability and realistic sizes of energy transfer and storage systems must be resolved. These aspects of the RFPR system study are presently being investigated.

3. Imploding Liner Reactor System Studies. Preliminary studies[8] of fusion systems based upon rotationally stabilized imploding liners have been made. An idealized model of an incompressible cylindrical liner is developed, based on earlier work by Turchi,[9] Shearer,[10] and Robson.[11] An energy principle is used to determine the liner and thermonuclear burn dynamics in the presence of axial particle loss. A simple energy balance is used to relate liner characteristics to the required liner efficiency (i.e., reversibility) for a given recirculating power fraction. A parametric neutronic study has been completed on a LiPb/Li blanket, that has been proposed for an imploding liner reactor.

a. Energy Balance Studies. Referring to Fig. XVII-12, a unit length of cylindrical liner is described by an inner and outer radii r_1 and r_2, respectively, at time t after the implosion has commenced. Subscript "o" refers to the initial (t = 0) condition, and subscript "f" designates conditions at maximum compression. Axial particle loss is described by a simple sonic flow model. An energy principle based upon the initial and final states of the liner/plasma system is used to derive the liner dynamics equation. The liner material is assumed to be an incompressible liquid, and the plasma is assumed to behave as an ideal gas. The liner surface at maximum compression may be constrained to be rotationally stabilized against Rayleigh-Taylor modes.

The ratio of thermonuclear energy W_N to initial energy $W_{KRo} + W_{K\theta o} + W_{po}$, defined by the parameter Q, is used to evaluate parametrically the liner reactor performance. The dependence of Q on liner aspect ratio $(r_{20}-r_{10})/r_{10}$ (Fig. XVII-12) is shown on Fig. XVII-13 with and without ($\ell^* = \infty$) end loss and Rayleigh-Taylor (R-T) stabilization. Figure XVII-14 gives the dynamics of liner compression and thermonuclear yield for both incompressible and compressible liner materials, the compressible results being obtained from a detailed hydrodynamical calculation. On the basis of these results a preliminary Fast-Liner Reactor (FLR) design was generated which investigated the viability of both capacitive and inductive energy storage systems to drive the initial liner implosion.

Although simplistic scaling assumptions point to relatively thick, slow liners, accounting for the hydrodynamic stability (of the liner), liner compressibility, and plasma particle/energy end loss present convincing arguments for very fast

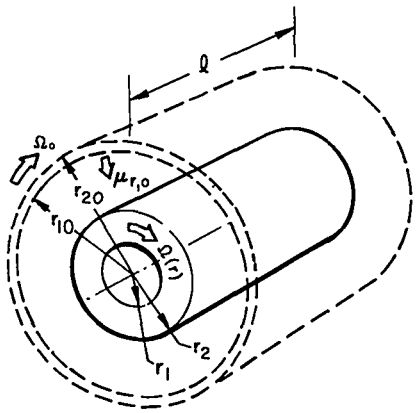

VOLUME COMPRESSION RATIO	$\kappa = (r_{10}/r_1)^2$
RADIAL KINETIC ENERGY	$W_{KR}\ell$
ROTATIONAL KINETIC ENERGY	$W_{K\theta}\ell$
PLASMA ENERGY	$W_P\ell$
COMPRESSIONAL ENERGY	$W_{PV}\ell = (W_{PVP} + W_{PVL})\ell$
PLASMA COMPRESSION	W_{PVP}
LINER COMPRESSION	W_{PVL}
BREMSSTRAHLUNG RADIATION	W_{BR}
ALPHA-PARTICLE HEATING	W_α
END-LOSS ENERGY	$W_{EL}\ell$
THERMONUCLEAR ENERGY	$W_N\ell$

$$W_{PO} + W_{KRO} + W_{K\theta O} = W_{PO} + W_{KR} + W_{K\theta} + W_{PV} + W_{EL} + W_{BR} - W_\alpha$$

$$Q \equiv W_N / (W_{KRO} + W_{K\theta O} + W_{PO})$$

Fig. XVII-12.

Schematic diagram of calculational model used for incompressible imploding liner dynamics and energy balance.

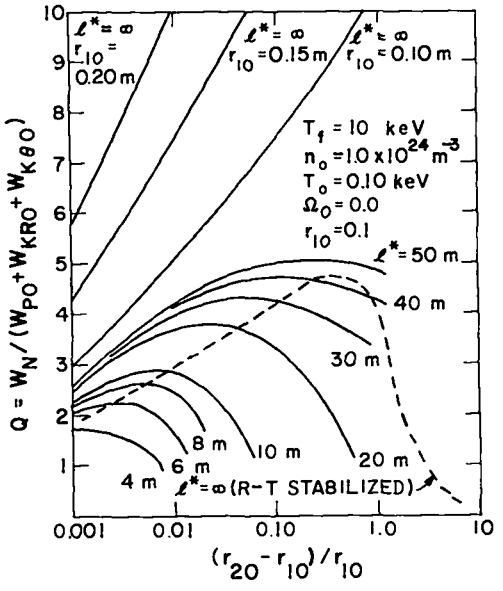

Fig. XVII-13.

Dependence of Q = thermonuclear [yield]/[liner energy] on liner aspect ratio $(r_{20}-r_{10})/r_{20}$ for a Fast-Liner Inertially Confined Reactor (FLR) for the conditions and assumptions indicated.

implosions (~10-20-μs liner transit times, ~ 1 μs-burn time). Physical containment of the mechanical energy release and the need for fast, high-voltage energy transfer represent serious disadvantages, although the direct recovery of the postimplosion liner energy is not necessary for operation as an economic power reactor. The compact, high-power density characteristics of this system offer strong advantages. Numerous problems

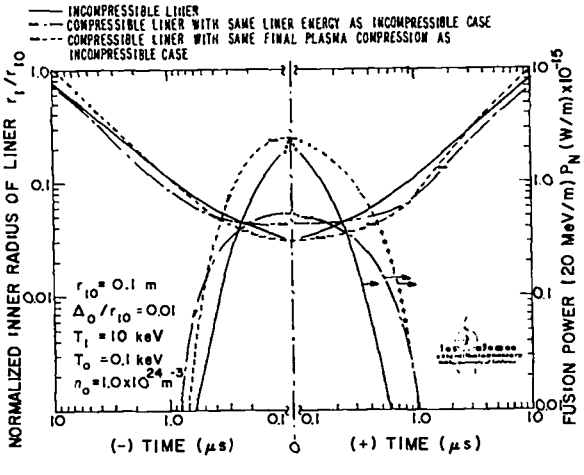

Fig. XVII-14.

Comparison of liner dynamics and thermonuclear yield for compressible and incompressible models.

and/or uncertainties with respect to "reactor desirability," physics requirements, and technological demands have been identified. However, many of these problems and/or uncertainties undoubtedly can be resolved or at least put into a more quantitative perspective by more detailed study and systems optimization. The absence of a firm experimental basis upon which to extrapolate into and to evaluate the reactor regime, however, represents a major limitation to the required parametric systems studies.

Acknowledging, therefore, the need for more profound systems studies and physics analysis, these scoping studies indicate that investments of ~ 150 MJ/m into a r_{10} = 0.10-m radius, $(r_{20}-r_{10})/r_{10}$ = 0.01 aspect ratio $Li_{0.1}$ $Pb_{0.9}$ liner will yield a FLR with a recirculation power fraction $\varepsilon \sim 0.40$ if none of the liner energy is recovered and no plasma energy loss occurs. Radial and axial diffusion have not been incorporated into this reactor analysis. The effects of liner compression will require a factor of 1.87 increase in liner energy, whereas the transfer efficiency of either a capacitive or inductive ETS system will be on the order of 70%; both inefficiencies will require ~ 400 MJ/m to be transferred to the liner reactor to yield 1400 MJ/n (20 MeV/n) of thermal energy. This example is based upon the injection of 0.1-keV precompression plasma at a density of 1.0 x 10^{24} m^{-3}. In addition to liner compressibility, liner heating by both return currents and fusion neutrons may significantly affect plasma compression if a less resistive/absorptive liner cannot be found; increasing the liner thickness will ameliorate the joule heating, while exacerbating nuclear heating.

b. Blanket Neutronic Studies. Initial scoping studies have been performed to determine the breeding potential of LiPb + Pb alloy when used in an imploding liner. The technological interest in such alloys stems from the need to breed tritium from Li, while at the same time having a high-density and relatively incompressible liner. Lead is a desirable material from inertial and compressibility considerations. Alloys of Pb and LiPb with less than 1.0 mole lithium per mole of Pb have been found[13] to be chemically unreactive for use as shields and collimators.

Neutronics calculations first were performed to find an envelope of parameters in which acceptable tritium breeding could be achieved. All neutron and gamma-ray transport calculations were based upon a one-dimensional cylindrical model proposed by Turchi and Robson[14,15], and used a one-dimensional discrete-ordinates code DTF-IV in a S_6-P_3 mode, with the LASL/CTR coupled cross section libraries for 25 neutron and 21 gamma-ray groups. Parameters studied for their effect on breeding ratio and neutron leakage were: (1) blanket thickness, (2) Li concentration in LiPb, and (3) Cd poisoning: concentration in Pb. The cylindrical model has a 10-cm radius plasma region, which is representative of the stage of implosion during the maximum thermonuclear burn for a LINUS reactor.[9,11] Outboard of this region is the imploding LiPb + Pb liner of varying thickness and composition, followed by a 15-cm structure of type 316 stainless steel.

Rough estimates of the instantaneous power density were first made by simple slowing-down calculations,[16] and by comparison with time-dependent calculations for laser-fusion reactors.[17] Based upon a slowing-down time calculation in Li, an upper limit of $\sim$ 10 μs can be inferred for the energy deposition time. From Reference 16 the time is known to be $\geq$ 0.1 μs. Preliminary Monte Carlo calculations, using the MCNG code,[18] indicate that 81.4% of the total energy is deposited in $\leq$ 0.5 μs.

Initial one-dimensional discrete-ordinates calculations considered a homogeneous blanket using natural Li and 50 wt% LiPb in the alloy. It was expected intuitively and later verified that high Li concentrations are not necessary for effective tritium breeding. From these preliminary calculations it appeared that the best attenuation of the primary 2.25-pJ (14-MeV) neutrons and the most neutron multiplication by (n,2n) reactions in Pb, would occur at lower concentrations of LiPb. A reference blanket thickness of 1 m was chosen, and the breeding and leakage characteristics were investigated as a function of the LiPb weight percent in the LiPb + Pb alloy. Figure XVII-15 shows the results of this study.

Using the results of the parametric study shown in Fig. XVII-15, the LiPb weight fraction

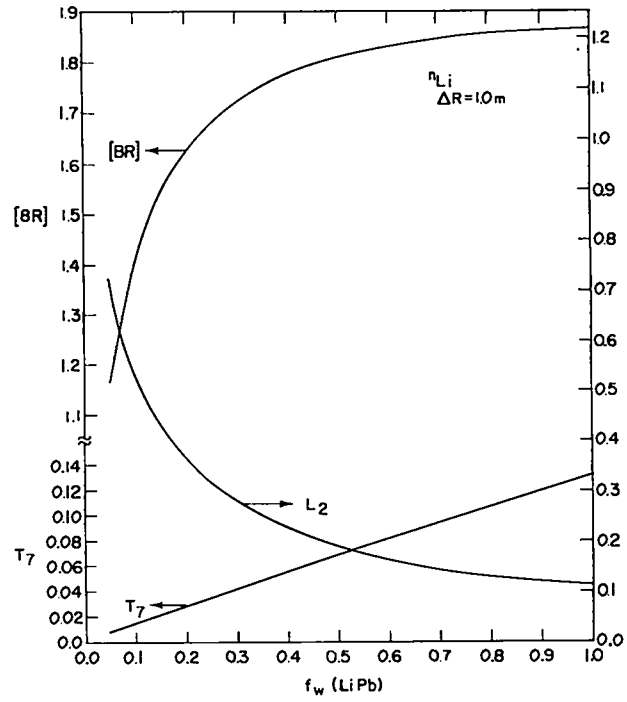

Fig. XVII-15.

Dependence of tritium breeding ratio [BR] and neutron leakage L_2 on the lithium weight fraction f_w(LiPb) in a ΔR = 1.0-m-thick Li/LiPb blanket.

was chosen to be 0.5. Next, an alloying element for the LiPb was sought which would have the properties of both alloying with LiPb + Pb without seriously altering mechanical or chemical properties (especially melting point) and providing a neutron poison to control the high tritium breeding ratio, while decreasing the leakage. Cadmium was selected as a trial material. Figure XVII-16 shows the relative ineffectiveness of Cd in reducing leakage, as well as its effective competition with ^{6}Li for absorption of low-energy neutrons. From Fig. XVII-16 it can be inferred that significant poisoning can be tolerated in a 1-m-thick blanket, so leakages of $\sim$ 0.1 appear achievable. The large excess of neutrons in the blanket results almost exclusively from (n,2n) reactions in Pb, which almost double the initial neutron population. For example, from Fig. XVII-16 at f_i(Cd in Pb) = 0.0, the breeding ratio is 1.81 and the leakage from the blanket (L_2) is 0.187.

Of considerable interest in any blanket design is the spatial distribution of nuclear

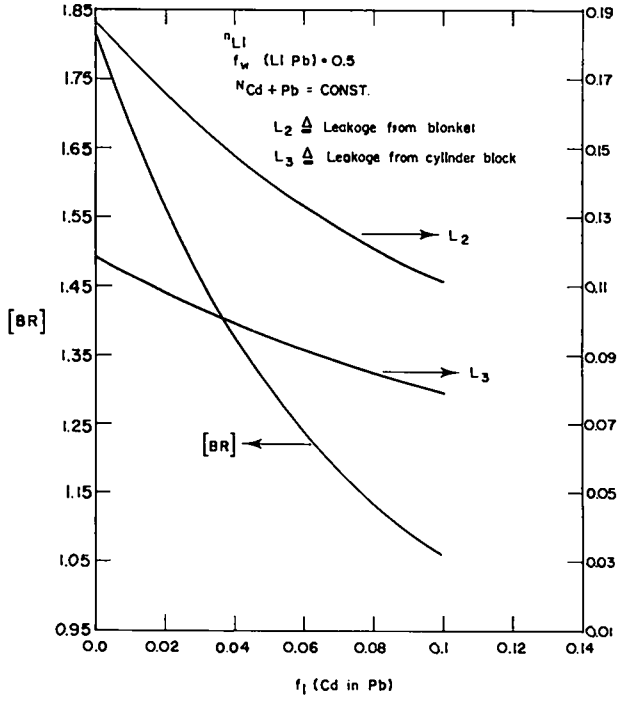

Fig. XVII-16.

Dependence of neutron leakage and tritium breeding on the isotopic fraction of Cd poison, f_i(Cd in Pb) for a 0.5-m-thick Li/LiPb blanket.

energy (neutron and gamma-ray) in the blanket and structure, as well as the volume integral of the energy. Figure XVII-17 presents the spatial distribution of neutron plus gamma-ray energy deposition in the reference blanket and cylinder block.[9] Values given in Fig. XVII-17 are normalized to 1.0 D-T neutron per cm length of the cylinder. For a wall loading of I_w(MW/m^2), where the neutron current is 4.44 x $10^{17} I_w$, the renormalized source would be S_L(cm^{-1}s^{-1}) = 2.79 x $10^{15} I_w$. Assuming a wall loading of I_w = 1.0 MW/m^2, the maximum heating in the blanket and the cylinder block are 5.0 and 2.8 x 10^{-2} MW/m^3, respectively. Also, the integrated total heating in the blanket is 2.807 pJ per D-T neutron and 0.0736 pJ in the cylinder block. The energy multiplication of the 2.25-pJ D-T neutrons is 1.248 in the blanket and 1.280 in the combined blanket and cylinder block. The latter is the equivalent of 18.0 MeV per D-T neutron.

Related calculations have been made for the FLCR concept in order to estimate the degree of nuclear (gamma/neutron) heating incurred within a fully compressed $Li_{0.1}Pb_{0.9}$ liner. The peak-to-

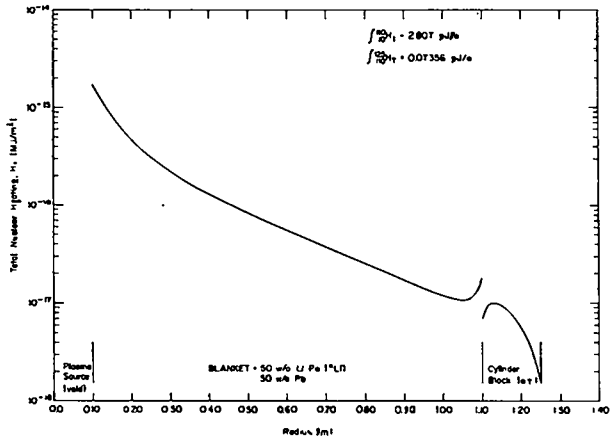

Fig. XVII-17.

Spatial distribution of neutron plus gamma-ray energy deposition in a 0.5-m-thick LiPb blanket normalized to one neutron per cm of blanket length.

average energy density in the FLR liner is 3-4, so local heating near the inner surface will be more severe than that given by the average value. Nuclear heating within the liner material may be comparable to that predicted for joule heating; both being sufficiently high to vaporize a significant portion of the liner. The spatial and temporal behavior of both joule and nuclear heating, the related evaporation rates, and the effects of these processes on liner dynamics and thermonuclear yield represents a complex problem which has yet to be calculationally explored. These preliminary estimates show, however, that liner heating and mass transport may be important, and more detailed analyses are certainly warranted.

4. Linear Theta-Pinch Hybrid Reactor (LTPHR). The possibility of reducing the energy requirements of a fusion reactor by the introduction of a fissioning blanket around a thermonuclear D-T plasma has been discussed at varying levels of engineering detail.[19,20] References 20 and 21 in particular address the questions of blanket neutronics and energy balance for a pulsed, high-β Linear Theta-Pinch Hybrid Reactor (LTPHR). Although this study does not give a detailed engineering design, key physics, engineering and economic uncertainties are addressed in a systems analysis context. Specifically, a revised and more realistic energy balance is developed and evaluated parametrically. This energy balance is conservatively based on free-

streaming end loss of the plasma, although the feasibility of end stoppering is considered. A simple economic model has been developed, by which the ergonic performance of the LTPHR is evaluated. The major intent of this study is the identification of an economically attractive, albeit unoptimized, design point for the LTPHR, as well as the identification of key research/development requirements for the economic production of fissile fuel and net electric power from a theta-pinch hybrid reactor. Table XVII-III summarizes an interim design point for the LTPHR concept. For a 14.1-MeV first-wall loading of 1 MW/m^2, the pulse frequency would be 2 Hz, the net electrical output is 8.1 MWe/m, the net ^{233}U production is 1.62 kg/y m, and the total capital cost amounts to 634 $/kWe.

C. NEUTRONIC STUDIES

1. Neutronics

a. Quantitative Data Assessment. The nuclear data assessment program based on sensitivity and uncertainty analysis, as developed and demonstrated for the TFTR design, has continued with attention to Tokamak Experimental Power Reactor (EPR) data requirements. As a first step, the existing data base was broadened to include multigroup cross sections and cross-section error estimates for the most important materials for the ANL-EPR design. Cross-section sensitivity profiles have been computed for toroidal field coil heating and radiation damage responses, radiation damage to superinsulation and activation of the outermost stainless steel structure. Complete cross-section error files (multigroup covariance matrices) have been established for Fe and C, which show largest integral sensitivities, and less detailed cross-section error estimates were performed for all other materials. A complete uncertainty analysis of the above mentioned responses with respect to all estimated cross-section errors have been made.

In conjunction with this EPR sensitivity analysis, a new method was formulated to compute the sensitivity of any integral response to the distribution of secondary particles (neutrons or gamma rays) from (n,2n), (n,γ), or similar reactions. Uncertainties in such secondary distributions that are an integral part of all presently used data sets are expected to add a significant contribution to the total uncertainty of integral design parameters. As a side product from other programs, the LASL system is being developed to process covariance data into multigroup form, to apply empirical formalisms to covariance estimation, to minimize discrepancies between differential and integral cross-section measurements, and to fold any given data uncertainty information with sensitivity profiles.

b. Code Development for TRIDENT-CTR. The TRIDENT-CTR code, a two-dimensional r-z and x-y geometry code specifically designed for the CTR community, was completed and released. TRIDENT-CTR solves the r-z geometry multigroup neutron and gamma-ray transport equations within a general spatial domain having curved or other non-orthogonal boundaries. The spatial discretization is accomplished using triangular finite elements and discontinuous linear trial functions. The use of triangles in r-z geometry allows TRIDENT-CTR to model both circular and noncircular toroidal shapes.

TRIDENT-CTR was developed from another LASL code, TRIDENT. The major modifications incorporated in TRIDENT-CTR were: the alteration of the code so that only the information required for the calculation of one band of triangles is contained in fast memory at one time, and the relaxation of the restriction that six triangles must meet at every interior vertex. The first modification allows the code to handle large problems, and the second provides flexibility in modeling toroidal shapes.

c. Committee on Computer Code Coordination (CCCC). Neutron cross sections in 171-groups, which were received from RSIC in the ISOTXS format have been processed. Problems associated with the large size of the file were solved by separating the file into four smaller, more manageable files. The data were then used in a version of the ONETRAN code, modified to accept extremely fine group structures, to calculate CTR benchmark blanket parameters. This effort had a threefold purpose: to evaluate the practicability of data in the ISOTXS format, to evaluate the actual data in the file, and to examine the ability to perform

TABLE XVII-III
SUMMARY OF INTERIM LTPHR DESIGN POINT AND ENERGY BALANCE

INTERIM LTPHR DESIGN POINT VALUES		INTERIM LTPHR ENERGY BALANCE	
First wall radius, b (m)	0.200	Total shock energy, W_{SH} (MJ/m)	0.37
IHC outer radius, b_1 (m)	0.204	Initial plasma internal energy, W_{INT} (MJ/m)	0.05
ACC inner radius, b_2 (m)	0.234	Final plasma internal energy, W_{INT}^{f} (MJ/m)	0.03
ACC outer radius, b_3 (m)	0.304	ETS efficiency, η_{ETS}	0.95
Outer radius of IHC feedplates, b_5 (m)	3.0	Thermal energy conversion efficiency, η_{TH}	0.40
Distance from centerline of LTPHR to ACC power supply, b_6 (m)	4.0	Fusion neutron energy, W_N (MJ/m)	17.20
Number of turns in the ACC fed by each lead set	10	Fusion alpha energy, W_α (MJ/m)	0.15
ACC structural values fraction, f_{ST}	0.6	Direct conversion energy, W_{DC} (MJ/m)	-0.09
Implosion electric field E_θ (kV/cm)	2.0	Transport losses in ACC, W_T (MJ/m)	0.92
Initial D-T filling pressure, P_A (mTorr)	19.0	External ETS losses, W_{SC} (MJ/m)	1.67
Initial D-T filling density, n_o (ions/m^3)	1.35×10^{21}	End loss energy, W_{EL} (MJ/m)	0.19
Shock magnetic field, B_{SH} (T)	1.3	Maximum stored magnetic energy, W_{BCM} (MJ/m)	33.43
Shock radius ratio, x_{SH}	0.632	Total recoverable thermal energy, W_{TH} (MJ/m)	17.34
Burn time, τ_B (ms)	10.0	Total circulating electrical energy W_C (MJ/m)	3.04
Flat top time, τ_{FT} (ms)	0.0	Total electrical energy out of LTPHR, W_{ET} (MJ/m)	6.94
Maximum compression field, B_o (T)	20.0	Net electrical energy out of LTPHR, W_E (MJ/m)	3.90
Maximum ion temperature T_i (keV)	6.6	Recirculating power fraction, ε	0.44
Maximum electron temperature, T_e (keV)	6.4	Engineering Q-value, Q_E	2.3
Minimum radius ratio, x	0.114	Thermal first wall loading, I_w (MW/m^2)	1.0
Energy worth of fusion neutron, (E+E*) (MeV/n)	412.4		
Effective LTPHR length, ℓ^* (km)	4.0		
Nominal LTPHR length, ℓ (km)	1.0		
Lawson parameter, $n\tau$, (s/cm^3)	4.13×10^{14}		

large multigroup calculations with codes developed under CCCC guidelines.

A new cross-section format has been proposed to replace the ISOTXS format. Evaluations of these new formats are being made to examine their usefulness to CTR needs and the applicability to existing codes. These new formats should eliminate CTR-related deficiencies which occurred in the ISOTXS format.

d. Cross-Section Development and Support.

(1) Multigroup Cross-Section Library Development. A new section has been added to the LASL/CTR cross-section library. Neutron/gamma-ray coupled sets have been prepared* from ENDF/B-IV using the new LASL-developed processing system NJOY.[22] Materials added to this section of the library include ^{1}H, ^{4}He, ^{9}Be, ^{10}B, ^{12}C, ^{16}O, ^{27}Al, Si, Ti, Cr, ^{55}Mn, Fe, Ni, ^{93}Cu, Nb, Mo, Ta, and Pb. P_0 through P_3 tables are included for 30 neutron groups and 12 gamma-ray groups. Considerable progress has been made toward the development of highly flexible formats for interlaboratory data exchange within the CCCC framework.[23] The current LASL format proposal, called MATXS, has been sent to ORNL for review. MATXS combines the functions of the previous CCCC files ISOTXS (isotope-dependent cross sections) and BRKOXS (Bondarenko self-shielding factors). A MATXS feature of particular value to the CTR program is the inherent flexibility to add new types of data, such as kerma factors, partial reaction scattering matrices and gamma-ray production data, none of which are allowed by the current CCCC formats.

(2) EPR Covariance Data Library. In support of the LASL program to assess the nuclear data requirements for the design of an Experimental Power Reactor (EPR), a library of multigroup cross-section covariance data (uncertainties) has been assembled. Materials now contained in the covariance library are carbon, oxygen, aluminum, and iron. Uncertainty data for C and O were taken from ENDF/B-IV (MAT 1274 and MAT 1276, respectively), Al from a LASL evaluation[24] in ENDF/B-IV format, and Fe from an ORNL evaluation in ENDF/B-IV format.

The ORNL Fe evaluation, which was prepared specifically for fast-reactor studies,[25] contains no error information on the high-threshold reactions (n,2n) and (n,n' continuum), which are very important in fusion applications. Subsections to the error evaluation for Fe have been added to describe these two reactions. These new data also make possible a more reasonable estimate of the uncertainty in the elastic scattering cross section. The four error evaluations have been processed into the LASL 30-energy-group neutron multigroup cross-section structure, using the ERRORR module[24] of NJOY. ERRORR has the unique advantage of directly processing energy-dependent "derivation formulas," which are important features of both the Al and Fe evaluations. The GROUPR module[26] of NJOY has been used to prepare transfer matrices for each individual scattering reaction for these materials, as is required for input to sensitivity calculations. All of the above data have been stored in a standard convariance library format.

(3) Multigroup Cross-Section Adjustment. A method has been developed for analyzing fusion neutronics integral experiments with the goal of improving the consistency between the integral results and the multigroup data used for reactor design. This accomplishment has been made in a statistical framework by assigning uncertainties (including correlations) to all integral and differential data and then performing a least squares adjustment[27] of all data. This system has been applied* to an early LASL measurement of tritium production in a large sphere of lithium deuterate. The results[28] of the least squares analysis suggest a modest reduction in the high-energy Li(n,n' t) cross section.

(4) Data Evaluation and Model Code Development. The neutron cross-section data for ^{6}Li and ^{12}C has been reevaluated. This work was undertaken to correct known deficiencies in the existing ENDF/B-IV evaluations, particularly in the energy spectra of inelastically scattered neutrons. The new evaluations incorporate

* The cross-section processing effort was supported in part by the Division of Military Applications of ERDA.

* The lithium data adjustment was supported in part by the Division of Physical Research under the auspices of the Associated Western Universities.

"pseudo-levels" and a simple phase-space model that permit reasonable representation of measured data, including energy-angle correlation, without introducing new processing code requirements. A new statistical pre-equilibrium theory nuclear model code has been developed for more accurate determination of nuclear data required in energy programs. The code, called GNASH, allows great flexibility in calculation of neutron cross sections and the spectra of outgoing particles or gamma rays, up to neutron energies of 40 MeV or higher. The code has been used to predict measured proton, deuteron, and alpha spectra from 14-MeV neutron interactions with Al, Ti, and Nb as well as a variety of (n,n'), (n,2n), and (n,3n) cross-section measurements.[29,30]

2. Shielding Analysis of Fusion. Among the CTR-related neutronic activities are shielding analysis for two 2.25-pJ (14-MeV) neutron-producing devices: (a) The Intense Neutron Source (INS) for irradiation studies with a point 2.25-pJ (14-MeV) D-T neutron source of 10^{15} s^{-1} operating at an assumed 100% duty factor, and the High-Energy Gas Laser Facility (HEGLF), designed to produce a concentrated source of 4.5×10^{17} D-T neutrons per pulse and 200 pulses per year. The INS and HEGLF designs will require detailed two- and three-dimensional calculations in complex geometries. Studies will result in a design ready for transformation into construction details by the architect-engineer.

a. INS Shielding Studies. The main INS shield material will be ordinary concrete (2.25 g/cm^3). One-dimensional spherical calculations have been made to solve for the transport of neutrons and gamma rays in the shield walls of the source cell. Based on a dose criteria of 100 mrem/y at the Laboratory-Office-Control building and public parking lot, the computed wall thickness is between 3.05 and 3.35 m. An occupancy of 2000 h/yr (50 wk x 40 h/wk) and a 10^{15} s^{-1} 14-MeV neutron source were assumed. A more exact value for the wall thickness cannot be quoted until the dose contribution from skyshine is determined. Because radiation which escapes the source-cell roof reaches personnel at ground level only after being scattered in air, the roof need not be as thick as the walls. Monte Carlo calculations are required to obtain accurate estimates of skyshine effects, although one-dimensional calculations with air or vacuum outside the shield indicate that a 2.13-m-thick roof may be adequate.

b. HEGLF Shielding Studies. Calculations were made to compare the activation of 304 stainless steel and carbon steel in the HEGLF environment. The gamma-ray dose rates at 1 m from a 1-cm unshielded sample for selected times were taken as a measure of the induced activities after irradiation. For a pulse of 4.5×10^{17} neutrons it was concluded that the dose rates from both materials would be comparable after a 1-year shutdown. The dose rate from the carbon steel after a 100-hour shutdown, however, is an order of magnitude lower than that from the stainless steel. Assuming a pulse frequency of one every two days, the residual activities resulting from the most recent pulses are important, and the carbon steel would be preferable. Calculations are in progress to determine the neutron streaming through the laser flight tubes, as well as doses at the control room and other occupied areas in the vicinity.

D. INSULATOR RESEARCH

Insulator research focused primarily on the evaluation of physical properties of irradiated ceramics, with additional studies on atomic hydrogen chemical erosion and on the nature of radiation-induced defects. Three irradiation capsules were placed in EBR-II, the first being removed in January 1976 after receiving a fluence of $\sim 3 \times 10^{21}$ n/cm (E $\geq$ 0.1 MeV) at 1015 K. Physical property studies were carried out on samples from this irradiation. The second and third capsules will be removed from EBR-II in January 1977.

1. Electrical Effects. Pulsed-voltage dielectric breakdown strength (dbs) measurements have been carried out on a number of unirradiated and irradiated insulators at elevated temperatures. Pulses of ~3-μs duration (with rise and decay times of ~2-μs) were applied at 875 and 1025 K to single-crystal Al_2O_3, $Y_3Al_5O_{12}$, and $MgAl_2O_4$ and to polycrystalline Al_2O_3.

The following comments summarize the significance of the results. First, the dbs values

measured for the unirradiated single crystals are very high, particularly for the few cases in which tests were terminated by surface flashover. These dbs values will be reduced when engineering ceramics are used in real environments, including fabrication effects, lifetime effects (such as multiple pulses), finite area effects, and radiation effects. For example, for Coors AD995, which is representative of a very good polycrystalline Al_2O_3, the dbs is about half that for single crystals.

Secondly, the degradation in dbs from this neutron irradiation is negligible compared to probable degradation from other causes likely to be encountered in engineering applications. In particular, there appears to be negligible degradation in Al_2O_3 due to the presence of pores $\sim$40 Å in diameter.

2. Structural Effects. Swelling of ceramics irradiated in EBR-II has been determined by micrometric measurements. Whereas Al_2O_3 and dispersion-hardened BeO swelled $\sim$ 2 vol %, all other ceramics showed growth of less than 0.5 vol %. Two materials have thus far been examined by transmission electron microscopy (TEM); swelling in Al_2O_3 appears to be attributable to the presence of a high concentration of $\sim$40-Å diameter pores, while low-swelling $MgAl_2O_4$ is characterized by the absence of any resolvable damage aggregates.

Thermal diffusivity of irradiated ceramics was measured at room temperature by a flash technique. Significant degradation was observed in all materials except single-crystal $MgAl_2O_4$ (Table XVII-IV). A reduction in the thermal diffusivity is important in that higher operating temperatures and thermal stresses can result.

TABLE XVII-IV
SWELLING AND THERMAL DIFFUSIVITY CHANGES
FOR CERAMICS IRRADIATED AT 1015 K

MATERIAL	DESCRIPTION	VOLUME INCREASE, %	THERMAL DIFFUSIVITY REDUCTION, % at 296 K
Sapphire	r-Plane, Saphikon	2.41	45
Sapphire	c-Plane, Linde	0.21	46
Al_2O_3	Coors, AD-995	1.94	53
$MgAl_2O_4$	Linde, Single Crystal	0.08	8
$MgAl_2O_4$	LASL, hot-pressed	0.26	45
$Y_3Al_5O_{12}$	Linde, Single Crystal	-0.02	62
$Y_3Al_5O_{12}$	LASL, hot-pressed	0.02	54
Si_3N_4	NORTON, hot-pressed	0.39	52
Si_2N_4	Ceradyne, hot-pressed	0.28	53
Si_2ON_2	NORTON, Polycrystalline Poly-Phase Ceramic	0.05	68
Sialon	AFML, Sintered	0.47	22
Y_2O_3	Ceradyne, hot-pressed	0.08	ND
Y_2O_3-1ZrO_2	Ceradyne, hot-pressed	0.29	ND
NIBERLOX (b)	National Beryllia	1.2	ND
BeO-5SiC	Ceradyne, hot-pressed	3.3	ND

(a) Swelling was determined by measurements of dimensions in the plane of the sample. Since most of the swelling in Al O is perpendicular to the c-plane, this sample appeared anomalously low.
(b) Dispersion-strengthened BeO. The dispersed phase is proprietary but known to contain Mg, Al, and Si.

Thermal energy in electrical insulators is carried predominately by phonons; the observed reduction in thermal diffusivity is caused by phonon scattering from irradiation-induced defects. Calculations[31] were made to determine the effectiveness of various defect configurations in degrading thermal conductivity. It was found that both point defects and three-dimensional aggregates (e.g., pores) are effective, with point defects being more effective by roughly a factor of two for temperatures greater than one-third of the Debye temperature and an equivalent number of defect sites. Two-dimensional aggregates (e.g., stacking faults) have less effect. The measured reduction in thermal diffusivity of Al_2O_3 can be taken into account by attributing two-thirds of the effect to point defects and one-third to the observed pore concentration.

3. Chemical Effects. The chemical erosion of refractory ceramics exposed to atomic hydrogen at high temperatures has been studied. Studies to date have considered only Al_2O_3 at 2000 K and a hydrogen pressure of 10^{-7} to 10^{-3} Torr.

Weight-loss measurements on single-crystal Al_2O_3 have shown considerable scatter, but two observations can be made: (a) at low pressures (10^{-7}-10^{-5} Torr) the erosion rate ($\sim 5 \times 10^{-9}$ g/cm^{2}s) is roughly independent of the pressure, indicating that sublimation processes are predominant; the erosion rate increases to about 5×10^{-3} g/cm^{2}s at 10^{-3} Torr, indicating a chemical process. Examination of polished (10$\bar{1}$1) surfaces after exposure revealed appreciable roughening at high temperatures. These data can be applied to a practical erosion problem. The ORNL EPR tokamak design study estimates the equilibrium density of neutral gas outside the plasma to be 1×10^{13} cm^{-3} ($\sim 10^{-3}$ Torr at 2000 K). A radiation-cooled Al_2O_3 liner at 2000 K exposed to this neutral atom density would erode at a rate of 4 mm/y.

4. The Nature of Radiation-Induced Defects in Ceramics. Identification of defect aggregates in irradiated ceramics is important for the understanding of their effect on physical properties. Radiation-induced 3-D aggregates in alkali halides[32] have been identified as cation colloids and anion inclusions, rather than pores such as are seen in metals. Colloids are analogous to voids on the anion sublattice, and anion inclusions are analogous to voids on the cation sublattice.

In this project, nuclear magnetic resonance has been used to test for the presence of metallic aluminum colloids in irradiated Al_2O_3, where TEM has shown 1.6 vol % of 3-D defects ~ 40 Å in diameter.[33] No aluminum was detected with a sensitivity of 0.05 vol %. To evaluate the possibility that the objects were oxygen inclusions, samples were crushed in a vacuum system and the released gases analyzed by quadrupole mass spectrometry. No oxygen was detected, to a sensitivity of 0.07 vol %. These defects were shown by a process of elimination to be pores. This observation leads to the prediction that little degradation in dielectric strength would result from the presence of such pores, this prediction being confirmed by experiment.

An understanding of the nature of radiation-induced point defects in ceramics is important, since these can directly influence physical properties such as thermal conductivity and are the progenitors of extended defects such as those discussed above. In cooperative studies with NRL[34] optical effects have been observed in room-temperature, ion-irradiation Al_2O_3 which suggest that damage-induced coloration bands are associated with oxygen vacancies. In related work, measurement of the absorption spectrum of room-temperature neutron-irradiated $Y_3Al_5O_{12}$ and $MgAl_2O_4$, followed by this comparison with published spectra of Al_2O_3, BeO, MgO, CaO, and SrO showed a simple correlation of peak absorption wavelength with average oxygen spacing. Since the bands in the last three are known to be due to electrons trapped at oxygen vacancies, this suggests that the prominent point defect in the other irradiated oxides is also the oxygen vacancy.

In another project with NRL,[34] Al_2O_3 heavily irradiated with fission neutrons at 650-1025 K has been shown to contain a high concentration of point defects (not further identified at this time). The persistence of point defects at these temperatures, which would not be expected in metals, is consistent with some models of radiation damage in ceramics. This observation is

also consistent with the interpretation of large decreases in thermal conductivity of irradiated Al_2O_3 partly in terms of such defects.

E. ALLOY RESEARCH

Major efforts were directed to the study of cyclic temperature, cyclic stress and radiation damage effects. The alloy Nb-1Zr was subject to cyclic thermal excursions at high temperature, and cyclic stresses were applied to Nb and Nb-1Zr at high temperature in vacuo.

1. Effects of Thermal Cycles on Nb-1Zr. On the basis of experimental evidence, Pant and Lidsky[35] claimed that a Nb-1Zr first wall could not withstand the thermal excursion projected for the Reference Theta-Pinch Reactor.[3] Samples from the Pant-Lidsky experiment were examined at LASL and were found to be sufficiently contaminated with oxygen at a level to account for the observed embrittlement.[36] The thermal cycle experiments were repeated at LASL under superior vacuum conditions, and each specimen was subjected to mechanical testing after a significant thermal cycle history; all samples failed in a ductile mode. Repeated thermal shocks in Nb-1Zr at elevated temperature in ultra high vacuum had no effect on the ductility of this material. The major conclusion from this experience is that Nb-1Zr will embrittle if heated in a poor vacuum, but if precautions are taken to eliminate oxygen gettering by the test sample, Nb-1Zr can experience many high-temperature thermal cycles without measurable loss in ductility.

2. Cyclic Fatigue. Under contract with the University of Illinois, samples of Nb were cyclically stressed at 1093 K in tension at 55, 70, and 77 MPa, for 10^6 cycles at a peak stress of 170 MPa produced no cracking in Nb-1Zr, whereas 740 cycles produced rupture at peak stresses of 70 MPa.[37] A high-temperature, ultra high-vacuum stress facility has been constructed, and preliminary tests have been conducted on Nb-1Zr alloy.

3. Radiation Damage Analysis. The sensitivity of the currently accepted procedure for calculating the exposure of material to damaging neutron irradiations to changes in the calculated electronic stopping was calculated. The NRT model[38-41] for calculating the number of displacements per atom was adopted in the framework of fusion reactor environments. Applications of the model to fusion reactor environments is a more severe test of the electronic stopping formalism used.

The sensitivity of displacement cross sections to changes in the amount of electronic stopping was examined by replacing the LSS stopping parameter k_L given in Ref. 38 by an altered value k. Results for Fe are given in Table XVII-V, in which spectral-averaged values of the respective cross section have been normalized to EBRII-2. For the fission reactor spectra the variation in relative cross section compared to $(k/k_L - 1)$ is at most 6%. If the unrealistic case of no electronic loss $(k/k_L = 0)$ is excluded, the variation is at most 3%. As would be expected the "14-MeV" spectrum is the most sensitive to electronic loss. Fusion radiation damage experiments will be preformed in a wide variety of environments such as fission reactors, 14-MeV sources, (d,n) stripping sources, and with energetic charged particles. Each environment represents a characteristic different energy range for

TABLE XVII-V
SENSITIVITY OF RELATIVE DISPLACEMENT CROSS SECTIONS IN Fe TO VARIATIONS IN ELECTRONIC STOPPING[(a)]

Spectrum[38]	$k/k_L = 0$	$k/k_L = 0.5$	$k/k_L = 1.5$
EBRII-7	-3	-1	+1
EBRII-2	—	—	—
LPTR (E-1)	+1	+1	-1
HFIR (PTP)	+2	-1	-3
FNIF-10	+3	+1	-1
LPTR (C-4)	+4	+1	-1
FNIF-1	+6	+2	-1
^{235}U	+6	+2	-2
"14 MeV"	+38	+12	-7

(a) The tabulated values are the changes in per cent in the spectra-averaged displacement cross sections normalized to the EBRII-2 values. The hardness of the spectrum generally increases from top to bottom of the table.

electronic stopping. The increased sensitivity to electronic stopping neutron spectra indicates that a better understanding of electronic stopping will be needed to develop a materials exposure index that will be useful for fusion radiation damage programs.

F. APPLICATIONS OF LASER FUSION—FEASIBILITY AND SYSTEMS STUDIES

Feasibility and systems studies have been performed to analyze various commercial applications of laser fusion, and to identify technological problems requiring long-term development. Analysis, optimization, and tradeoff studies are performed on conceptual power-plant designs, and alternative applications of laser fusion are investigated. Progress was made in the following areas.

The flow of lithium which protects the cavity wall in a spherical wetted-wall laser-fusion reactor has been analyzed in greater detail. Gravity flow of a thin film of lithium, with variations in the lithium source, was considered. Indications are that lithium films ≥ 1 mm in thickness can be obtained for the concept shown schematically in Fig. XVII-18.

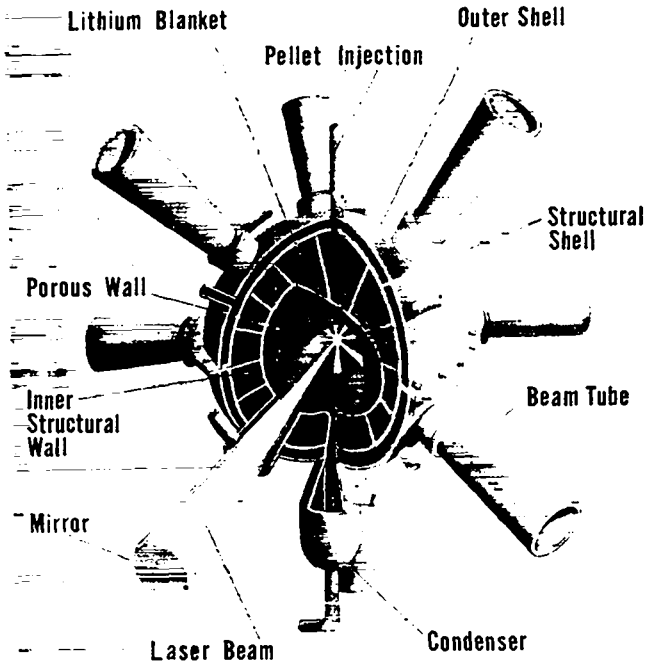

Fig. XVII-18.

Concept of a wetted-wall laser-fusion reactor.

Investigation has continued to determine the behavior of ionized fusion-pellet debris in a magnetically protected reactor. Analytic expressions to predict sputtering of solid materials by energetic ions were derived in parallel to the determination of ion fluences on cavity component surfaces. Energy deposition, both from energetic particles in the fusion-pellet debris and from radiation sources, represents a second source of reactor-cavity surface erosion. The calculation of surface-temperature time histories and evaporation rates has been modeled in a general way, which permits volume sources, the arbitrary time dependence of energy deposition, and finite shell thicknesses to be specified. These computer codes will be used to investigate reactor-cavity designs for structured fusion pellets.

The operating characteristics and the performance of a laser-fusion central-station generating plant based on the magnetically protected reactor concept has been reevaluated. Figure XVII-19 gives an artist's conception of this power station. A recalculation of the blanket energy-multiplication factor associated with exoergic nuclear reactions and from an up-dated model of a potassium topping cycle indicated significant changes in the performance and capital costs of current designs. A survey of available data did not change previous estimates of maximum permissible total neutron fluences for determining laser-fusion reactor-cavity component life-times.

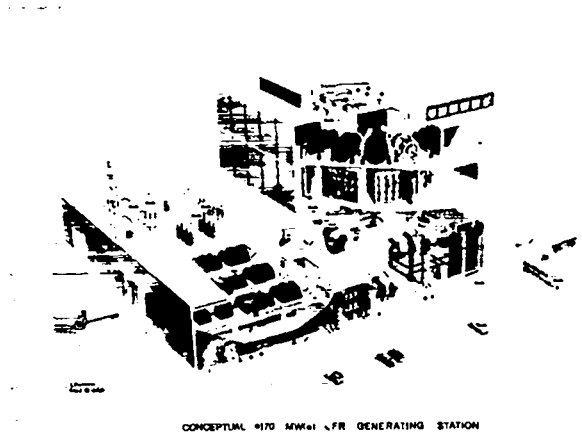

Fig. XVII-19.

Laser-fusion electric generating station based on the magnetically protected first-wall concept.

Evaluation of the ^{239}Pu burner-^{233}U breeder hybrid concept is continuing. This fusion-fission breeder concept, producing large amounts of thermal power and fuel for thermal-fission reactors, may be attractive as a direct substitute for the liquid-metal fast-breeder reactor, but retains essentially all the environment disadvantages of the latter.

The investigation of synthetic-fuel production by using the radiation from fusion-pellet microexplosions to decompose H_2O or CO_2 radiolytically into H or CO was continued. Estimates of product costs from such processes have been updated. Radiolysis would require high-energy neutrons, and tritium for the fuel cycle would have to be purchased from an outside source. An optimistic economic analysis of a production-plant model indicates a cost between 2 and 2.5 dollars per one Gigajoule of neutron energy as is shown in Fig. XVII-20. Synthetic-fuel production from laser-fusion reactors dedicated to this purpose would not be competitive with standard coal-gasification processes in the context of 1973 market values. These conclusions could be reversed by dramatic changes in relative market value or by scarcities of feed materials.

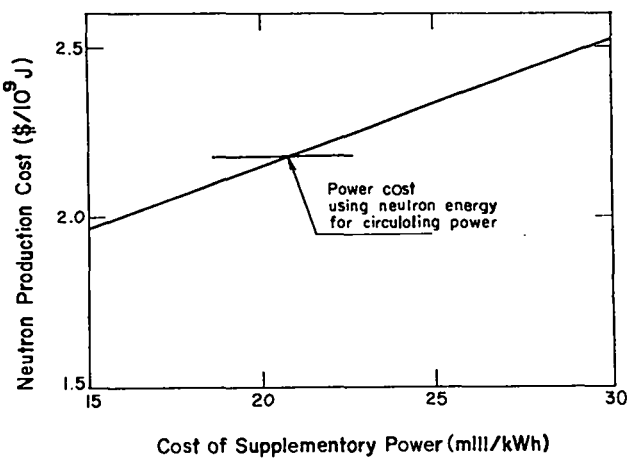

Fig. XVII-20.

Neutron production cost (1973 dollars) as a function of the cost of supplementary electric power purchased.

REFERENCES

1. R.A. Krakowski, R.L. Miller, and R.L. Hagenson, "Operating Point Considerations for the Reference Theta-Pinch Reactor (RTPR)," Second Topical Meeting on the Technology of Controlled Nuclear Fusion, Richland, Washington (September 21-23, 1976).

2. K.I. Thomassen, "Technology Problems in Theta-Pinch Reactors," Second Topical Meeting on the Technology of Controlled Nuclear Fusion, Richland, Washington (September 21-23, 1976).

3. R.A. Krakowski, T.A. Coultas, A.J. Hatch, and F.L. Ribe, "An Engineering Study of a Reference Theta-Pinch Reactor (RTPR)," Los Alamos Scientific Laboratory report LA-5336/ANL-8019 (March 1974).

4. E.L. Simmons, D.J. Dudziak, and S.A.W. Gerstl, "Reference Theta-Pinch (RTPR) Nucleonic Design Sensitivity Analysis by Perturbation Theory," Los Alamos Scientific Laboratory report LA-6272-MS (April 1976).

5. R.G. Lawton, "The AYER Heat Conduction Computer Program," Los Alamos Scientific Laboratory report LA-5613-MS (May 1974).

6. G.R. Gryczkowski and T.A. Oliphant, "Transient Charge-Exchange Effects in a Neutral-Gas Layer," Nucl. Fus., 16, 2, 263 (1976).

7. R.L. Hagenson, Preliminary Physics and Engineering Considerations for a Fusion Power Plant Based on Reversed-Field Z-Pinch (RFZP) Confinement," USA/USSR Workshop on Systems Analysis of Fast Pulsed Reactors, Novosibirsk, USSR (October 16-30, 1976). submitted to Nucl. Fus.

8. R.A. Krakowski and R.L. Hagenson, "Preliminary Energy-Balance Consideration of Rotationally Stabilized Imploding-Liner Fusion Systems," USA/USSR Workshop on Systems Analysis of Fast Pulsed Reactor, October 16-30, 1976, Novosibirsk.

9. P.J. Turchi, "Imploding Liner Fusion Systems in Cusp-Ended Theta-Pinch Geometry," NRL Memorandum Rept. 3094 (August 1975).

10. J.W. Shearer, "Magnetically-Driven Liners for Plasma Compression," Los Alamos Scientific Laboratory report UCRL-75915 (September 1974).

11. A.E. Robson, "Plasma Confinement by Megagauss Magnetic Fields," Ann. New York Acad. Sci., 251, 649 (1975).

12. R. Malone, LASL, personal communication, (December 1976).

13. N.A. Frigerio and L.L. LaVoy, "The Preparation of LiPb, a Novel Material for Shields and Collimators," Nucl. Technol. 10, 322 (1971).

14. P.J. Turchi and A.E. Robson, "Conceptual Design of Imploding Liner Fusion Reactors," Proc. Conf. on Energy Problems of Fusion Research, San Diego, CA, (18-21 Nov. 1975).

15. A.E. Robson, Naval Research Laboratory, personal communication (April 1976).

16. T.J. Williamson and R.W. Albrecht, "Calculation of Neutron Time-Energy Distributions in Heavy Moderators," Nucl. Sci. Eng. 42, 97 (1970).

17. G.E. Bosler and T.G. Frank, "Energy Deposition Rates in a Laser-Fusion Reactor," Trans. Am. Nucl. Soc. 21, 16 (1975).

18. E.D. Cashwell, J.R. Neergaard, W.M. Taylor and G.D. Turner, "MCN: A Neutron Monte Carlo Code," Los Alamos Scientific Laboratory report LA-4751 (1972).

40. S.L. Bogart (Ed), "DCTR Fusion-Fission Energy Systems Review Meeting," USERDA Rept. ERDA-4 (December 3-4, 1974).

20. C.E. Taylor (ed.), "Proc. US-USSR Symp. on Fusion-Fission Reactors," CONF-760733 (July 13-16, 1976), R.A. Krakowski, R.L. Miller, and R.L. Hagenson, "Engineering and Physics Considerations for a Linear Theta-Pinch Hybrid Reactor," p 155.

21. R.A. Krakowski, L.L. Steinhauer, et al., "Pure-Fusion and Fusion-Fission Reactor Applications of High-Density Linear Confinement Systems," Proc. 6th Int. Conf. on Plasma Physics and Controlled Nuclear Fusion Research, Berchtesgaden, FGR (October 6-13, 1976).

22. R.E. MacFarlane, D.W. Muir, and R.J. Barrett, "Advanced Nuclear Data Processing Methods for the Fusion Power Program," Trans. Am. Nucl. Soc. 23, 16 (1976).

23. G.E. Bosler, "Implications to the CTR Community of Standardization in Nuclear Analysis Codes," Trans. Am. Nucl. Soc. 22, 39 (1975).

24. D.G. Foster, Jr., LASL, personal communication (1976).

25. C.Y. Fu, ORNL, personal communication, (1976).

26. R.E. MacFarlane, C.I. Baxman, and P.G. Young, "Applied Nuclear Data Research and Development October 1 - December 1, 1975," Los Alamos Scientific Laboratory report LA-6266-PR, p 5 (1976).

27. D.R. Harris, W.A. Reupke, and W.B. Wilson, "Consistency Among Differential Nuclear Data and Integral Observations: The ALVIN Code for Data Adjustment, for Sensitivity Calculations, and for the Identification of Inconsistent Data," Los Alamos Scientific Laboratory report LA-5987 (1975).

28. W.A. Reupke and D.W. Muir, "Neutronic Data Consistency Analysis for Lithium Blanket and Shield Design," Second Topical Meeting on the Technology of Controlled Nuclear Fusion, Richland, Washington (September 1976).

29. E.D. Arthur and P.G. Young, "A New Statistical-Preequilibrium Nuclear Model Code," Trans. Am. Nuc. Soc. 23, 500 (1976).

30. E.D. Arthur and P.G. Young, "Calculations of (n,2n) and (n,3n) Spectra and Cross Sections," International Conf. on the Interactions of Neutrons with Nuclei, Lowell, Mass. (1976).

31. P.G. Klemens, G.F. Hurley, and F.W. Clinard, Jr., "Reduction in Thermal Conductivity of Ceramics due to Radiation Damage," Second Topical Conference on the Technology of Controlled Thermonuclear Fusion, Richland, Washington (September 1976).

32. L.W. Hobbs and A.E. Hughes, "Radiation Damage in Diatomic Materials at High Doses," UKAEA Harwell Report AERE-R8092 (1975).

33. F.W. Clinard, Jr., J.M. Bunch, and W.A. Rankin, "Neutron Irradiation Damage in Al_2O_3 and Y $_2O_3$," International Conf. on Radiation Effects and Tritium Technology for Fusion Reactors, Gotlinburg, Tennessee, October 1-3, 1975.

34. B.D. Evans, H.D. Hendricks, F.D. Bazzarre, and J.M. Bunch, "Association of the 6-eV Optical Band in Sapphire with Oxygen Vacancies," presented at the 5th International Conference on Ion Implantation in Semiconductors and Other Materials, Boulder, Colorado, Aug. 9-13, 1976, proceedings to be published.

35. A. Pant, and L.M. Lidsky, Proc. Sixth Symposium on Engineering Problems of Fusion Research, San Diego, CA p 974 (Nov. 21, 1975).

36. W.V. Green, LASL, personal communication to K.M. Zwilsky and T.C.Reuther, Sept. 20, 1976.

37. R.A. Yeske, W. Sommer and W.V. Green, 1976 ASME-MPC Symposium on Creep Fatigue Interaction, ASME, 1976 p 77.

38. Recommendations for Displacement Calculations for Reactor/Accelerator Studies in Austenitic Steel, Nucl. Eng. and Des. 33, 91 (1975).

39. M.J. Norgett, M.T. Robinson, and I.M. Torrens, Nucl. Eng. and Des. 33, 50 (1975).

40. D.G. Doran, Nucl. Eng. and Des. 33, 55 (1975).

41. D.G. Doran, Nucl. Eng. and Des. 33, 63 (1975).

XVIII. INTENSE NEUTRON SOURCE FACILITY

D. D. Armstrong, W. C. Barnett, J. B. Bartlit, M. E. Battat
R. A. Briesmister, E. A. Brown, A. N. Demuth, W. Denton,
R. Dierckx, D. J. Dudziak, C. R. Emigh, W. Ford, E. S. Foster
A. E. Greene, R. A. Haarman, R. A. Jalbert, R. W. Lee,
A. M. Lockett, III, K. L Meier, E. A. Meyer, J. C. Milligan
J. L. Robinson, J. D. Schneider, R. H. Sherman, J. H. White

A. INTRODUCTION

The Intense Neutron Source (INS) Facility is being designed at LASL to fill a need to determine materials suitability for use in a fusion reactor first wall. This facility will have two independent sources each producing, on a continuous basis, an intense source ($\sim 10^{15}$ n/s) of 14-MeV neutrons with an energy spectrum nearly identical to that from the D-T burn in any proposed fusion reactor. The INS Facility will use colliding beams of tritium ions and deuterium gas to produce neutrons by the fusion of D-T nuclei.

A major benefit of the facility will be the knowledge to be gained from the materials damage caused by sustained high flux neutron irradiation. Of secondary importance will be the operating experience gained from INS's handling of a few tens of grams of tritium, an important step prior to the safe and effective use of several kilogram quantities of tritium by fusion reactors. The unique feature of the INS facility is the use of a supersonic flow of deuterium gas as the medium for removal of heat generated by coulomb collisions of incident tritium ions. Use of gaseous targets rather than solid targets allows at least one order of magnitude increase in neutron flux. A flowing liquid lithium target bombarded by a deuterium beam can also handle large heat loads while providing very high neutron fluxes, but produces a neutron energy spectrum which is significantly different from the spectrum from D-T fusion reactions.

Primary emphasis of the INS group in 1976 was the final design and testing leading to the operation of a Beam-On-Target (B-O-T) test stand utilizing a proton beam on a hydrogen gas jet target. While not producing neutrons or causing any radiation hazard, the B-O-T tests will otherwise simulate a tritium-on-deuterium source and will allow precise optimization of parameters related to the production of a continuous one-ampere ion beam, beam transport, gas jet target operation under full heat deposition, and differential pumping requirements for gas backstreaming from the jet target.

B. INTENSE NEUTRON SOURCE FACILITY.

A view of the INS facility is given in Fig. XVIII-1 which shows the location of the major components in the experimental building along with the office complex. During 1976, design of the INS facility progressed to the point of negotiating a contract with the Architect-Engineer, Burns and Roe, Inc. for Title I work. Cost estimates and design criteria were updated and the Final Environmental Statement[1] was issued by ERDA

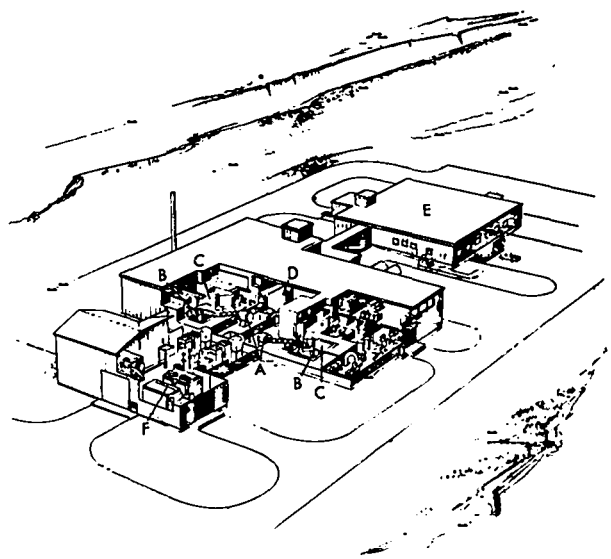

Fig. XVIII-1.

Artists conception of the INS facility showing, A) the ion source; B) the target area where the tritium ion beam and deuterium jet target converge; C) the two source cells containing the intense neutron sources; D) the three-stage isotope separation system; E) the Laboratory-Office-Control Building that contains the computerized control center and offices; F) the wing of the building containing two high-voltage power supplies and capacitor banks.

in July 1976. Some specific areas of activity are discussed below. Other areas, which concern both INS and B-O-T, are discussed in Sec. C.

1. Engineering. A second 300-kV, 2-A power supply, a sister unit of the one presently assigned to the INS project, was located at Kwajalein Island in the Pacific. This unit was transferred to the INS project and shipped to LASL. With this unit, the neutron output of the INS will be doubled.

Procurement was begun on the INS gas compressors, the process water system, and the emergency and uninterruptible power supplies. A bid was received for a compressor system which used all diaphragm compressors. Because of the expense of this system, an alternative design was investigated which would use either piston or centrifugal compressors for the low pressure stages. Attempts were made to locate excess process water euipment in order to reduce the cost of this system. Some equipment was obtained from a missile radar site in North Dakota. A 300-kW diesel electric generator was located at the Nuclear Rocket Development Station in Nevada. With some modifications, this unit will serve as the emergency power source.

2. Isotope Separator System. In INS it will be necessary to recover the tritium for the ion source from a deuterium-tritium mixture. This will be accomplished by a cryogenic distillation still. A prototype still was constructed and successfully operated, using a ternary mixture of hydrogen, hydrogen deuteride, and deuterium. The results show that the progressive enrichment of deuterium toward the bottom end of the column is close to theoretical predictions.

Considerable effort and progress was made toward developing computer codes for the design of interlinked systems of multicomponent, multifeed distillation columns which will be needed to make the D/T separation for INS. The computer codes were also used to generate designs for a hydrogen isotope distillation system to be part of a proposed Tritium Systems Test Facility. This facility would be used for testing components of the fuel-handling loop of fusion power reactors.

The relative volatilities for the isotope system deuterium-deuterium tritide-tritium were measured for the first time in a laboratory.[2] Such measurements will be used in the detailed design of the INS isotope separation system and add to the known characteristics of tritium.

3. Shielding Studies. Neutronics calculations were made for various materials and wall and roof thickness for the INS source cell (Fig. XVIII-2). The source cell walls and roof will be of concrete and calculations were made for both pure concrete and concrete with iron reinforcing bars. The effect of a gypsum inner liner was also studied. Radiation levels were calculated for areas outside the source cell while the facility is in operation and also inside the cell as a function of time after shutdown of the neutron source.

C. BEAM-ON-TARGET FACILITY

During 1976, much progress was made on the design and construction of the proton beam on a hydrogen target test stand. Initial startup of this facility is anticipated in June 1977. Activities concerned with various parts of the facility are described below.

1. Ion Source. Both B-O-T and INS will use an annular-type duoplasmaton as an ion source. The model I source, operating with a single arc, was run for over 500 h at ion currents of over 100 mA. Subsequent inspection of the ion source showed little wear and demonstrated the high reliability of this type source.

Model II of the ion source was constructed. It was designed to minimize solders, seals, and joints while retaining a versatile geometry.

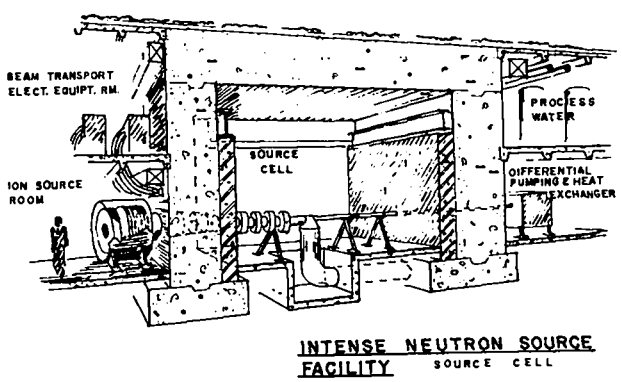

Fig. XVIII-2.

INS Source Cell Facility

After initial problems with instabilities when more than two arcs were operated simultaneously, it was found that proper conditioning of the filaments allowed stable multiple-arc operation. In the present configuration, more than 600 mA dc of total ion current has been extracted from the source using eight of the sixteen available arcs. The source has run over 10 h at this level with little or no apparent damage. This level of operation is satisfactory for initial turn-on of the B-O-T, although the specie ratio, emittance, and other beam characteristics are not known at present.

2. Accelerating Column. Design of the 200-kV accelerating column and the high voltage feedthroughs was completed and the parts ordered. Modifications to the existing vacuum tank for the ion source and accelerating column were almost completed.

Figure XVIII-3 shows the general layout of the accelerating column, ion source, corona tube, and one of the high-voltage feedthroughs in the 2.13-m-diameter vacuum tank. The accelerating column consists of a voltage graded support box which holds the accelerating electrodes and which provides cantilever support for the 340 kG ion source. The four posts of the support box are accelerating tube sections fabricated by metal bonding techniques for strength and to preserve structural integrity when a similar design is used in a tritium environment in INS. Adhesive bonded support posts could fail with disastrous results due to degradation in a tritium environment. Electrical connections between the small corona tube at the top provide voltage grading to a 200 kV feedthrough on each side. Each feedthrough has twenty-three leads going to the ion source at approximately the same potential. A tubular electron trap operated at approximately 5 kV is planned adjacent to the ground electrode to reduce electron backstreaming.

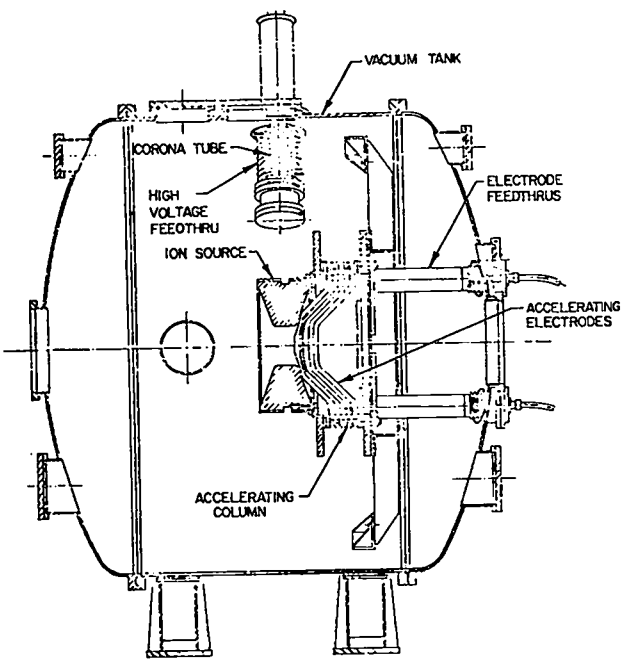

Fig. XVIII-3.

B-O-T 200 kV accelerators showing the accelerating column, ion source, and high-voltage feedthroughs in the vacuum tank.

The 200-kV power supply for the accelerating column is operational. Some difficulties were encountered in the regulator system and work to eliminate these problems is continuing.

3. Beam Transport. The beam transport section of B-O-T accepts the ions from the accelerating column and uses solenoids to focus the ions on the gas target. The output beam from the accelerating column contains several species of ions. In B-O-T it is estimated that the beam will be 60% H^+, 35% H_2^+, and 5% H_3^+. Extensive calculations were made of the expected behavior of the various ions and the results of these calculations were used in the design of the beam transport section. This design was completed and construction begun. In initial operation of B-O-T the energy contained in the ion species which are not focused on the target will not be large enough to cause problems to the beam transport section. After behavior of the beam, particularly beam neutralization effects, are studied, a heat exchanger will be built to remove the heat generated by the ions which strike the wall.

4. Vacuum Systems. A differential pumping system is required on the B-O-T facility to keep the backflow of gas from the target chamber out of the accelerating column and beam transport sections. A four-stage system will be used. The requirement for the system is to keep the openings between the differential pumping stages large enough to let the beam through without impingement yet small enough and of suitable geometry to reduce gas flow between stages to a minimum.

It is also important to reduce the distance between stages to a minimum, especially at the high-pressure end, to keep beam scattering and beam heating of the gas to a minimum. Fortunately, the backflow of gas into the first stage of the differential pumping system appears to be at a high enough pressure to form a gas jet as it emerges from the 1-cm-diameter jet nozzle. Calculations show that a shock disk is expected about 6 cm from the nozzle with a pressure minimum at about half that distance. If a sharply tapered cone with a 1-cm-diameter orifice is positioned at the low pressure point, flow through the aperture into the stage-2 chamber will be minimized. Furthermore, the sharp taper will force most of the gas flow around the outside of the cone to the first stage pump. This technique has been used effectively with apertures up to 3-mm diameter.[3,4]

Calculations were made of the expected flow and a differential pumping test stand was constructed and used with air to measure flow rates. The air was accelerated to supersonic velocity producing a jet with a barrel shock. Good agreement was obtained between measured and calculated flow rates. Because of this agreement, there is some assurance that the processes are understood and can be extrapolated to hydrogen. This information was used in the design of the B-O-T differential pumping system where the backflow gas will be hydrogen. Preliminary design of the four-stage differential pumping system is complete. Pressure in the fourth stage is expected to be down to about 2×10^{-5} Torr.

The original design for the ion source and accelerating column vacuum pump used a 9000-l/s cryosorption pump. Because of vendor difficulties with the performance of the pump, the cryosorption pump will be paralleled with an oil diffusion pump which has a 14,000-l/s pumping speed for hydrogen. This will prevent any delay of startup of B-O-T if difficulties continue.

5. Jet Target. The jet target is the region where the ion beam collides with the gas jet. One model of the B-O-T jet target is illustrated in Fig. XVIII-4. Gas flows from the high-pressure plenum through the jet throat forming a shock wave. Because of the direction of the shock, very little gas flows to the left through the ion beam access port. In B-O-T the flow is only about 0.2% of the total gas load.

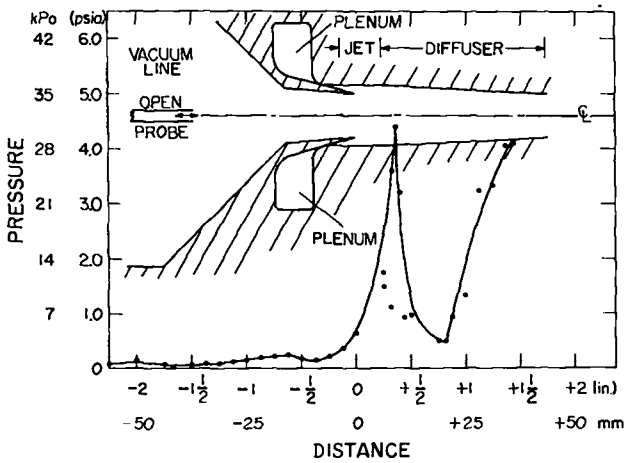

Fig. XVIII-4.

One design of the jet target. Curve is pressure measured with an open ended probe as a function of axial distance.

Calculations were made of the gas flow patterns. A model of the jet target was constructed and tests were made of the flow. One example of these measurements is shown in Fig. XVIII-4. Problems were encountered in setting a uniform throat spacing. Modifications incorporated in the final design should cure this problem.

Leakage flowrates into the ion beam access port were measured as a function of throat spacing and plenum pressure. It was discovered that the leakage is a boundary layer problem. Most leakage occurs near the walls of the access port. Various boundary layer trip devices such as grooves and small protruding lips were investigated. They were largely ineffective and some of them even interfered with shock formation.

The INS facility has been designed to allow for the possibility that all of the energy deposited by the triton beam shows up as thermal energy in the D_2 target gas. If, however, some of this energy is not converted to thermal until after a given element of gas has left the target region, then the triton beam intensity can be increased without choking the flow. A detailed study was undertaken to examine this possibility. This study considered various mechanisms of heat deposition such as ionization, and excitation and

deposition such as ionization, and excitation and dissociation of the D molecules due to both the tritons and to the secondary electrons that they create. Results of the study at present indicate that roughly two-thirds of the energy deposited is converted to heat in the target region.

To test the effect of heat deposition on the leakage flowrate, a jet target with an electrically heated rod down the center was constructed. With a heat addition of 48% of the jet flow enthalpy, the flow remained unchoked and stable and the leakage flowrate was only increased 20% over the unheated condition.

6. Beam Stop. Design of a beam stop for B-O-T was begun. The beam stop will absorb the 200 kW of H^+ ion beam energy which is deposited directly on the walls when the gas jet is not operating. When the jet is operating, it will remove the beam heat from the hot gas prior to its exhaust through a downstream vacuum valve.

7. Control and Data Acquisition System. A control and data acquisition system for the B-O-T facility, which uses microprocessors, was designed and some parts built. A manual system will also be available so that full operation of the B-O-T can be effected before the facility is tied into computer control. The computer system will provide the following three major functions.

a. Fast Protect - to quickly (less than 10 s) shut down the intense beam in event of major malfunction, prior to excessive equipment damage.

b. Data Acquisition - to provide a means for recording at frequent intervals all significant parameters to permit detailed evaluation of test results at later times.

c. On-Line Computer Monitor and Control - to provide for more rapid response and more precise control than can be achieved by manual control only. Also, this will provide valuable operating experience for a similar but more complex computer control system which will be necessary for the INS facility.

Additional details concerning this and other areas of activity can be found elsewhere.[5-8]

REFERENCES

1. Final Environmental Statement ERDA-1548, July 1976.
2. R. H. Sherman, J. R. Bartlit, and R. A. Briesmeister, Cryogenics 16, 611 (1976).
3. B. W. Schumacher, "1961 Trans. of the Eighth Vacuum Symposium and Second International Congress" 2, 1192 (1961).
4. E. Schruffer, Zeitschrift fur Angewandte Physik 9, 88 (1957).
5. "Intense Neutron Source Facility," January 1-March 31, 1976, Los Alamos Scientific Laboratory report LA-6549-PR (October 1976).
6. "Intense Neutron Source Facility," April 1-June 30, 1976, Los Alamos Scientific Laboratory report LA-6950-PR (October 1976).
7. "Intense Neutron Source Facility," July 1-September 30, 1976, Los Alamos Scientific Laboratory report LA-6591-PR (December 1976)
8. "Intense Neutron Source Facility," October 1-December 31, 1976, Los Alamos Scientific Laboratory report LA-6702-PR (February 1977).

JOURNAL PUBLICATIONS

D. D. Armstrong C. R. Emigh K. L. Meier E. A. Meyer J. D. Schneider	"A 14-MeV Neutron Source Facility"	submitted to Nuclear Instruments and Methods
M. E. Battat D. J. Dudziak	"Shielding Calculations for the Intense Neutron Facility"	Trans. Am. Nucl. Soc. 23, 4 (1976).
G. Berge J. P. Freidberg	"Stability of a Diffuse Scyllac Configuration"	submitted to Nuclear Fusion
J. U. Brackbill L. G. Margolin	"An Algorithm for the Computation of Nonlinear Electron Thermal Conduction on an Arbitrarily Shaped Two Dimensional Domain"	submitted to Journal of Computational Physics
C. J. Buchenauer A. R. Jacobson	"Quadrature Interferometer for Plasma Density Measurements"	to be published in Review of Scientific Instruments
T. E. Cayton	"The Laboratory Spring-Mass Oscillator: An Example of Parametric Instability"	submitted to American Journal of Physics
F. W. Clinard, Jr.	"Electrical Insulators for Magnetically-Confined Fusion Reactors"	Critical Materials Problems in Energy Production. Academic Press. 1976
R. J. Commisso H. R. Griem	"Observation of Collisionless Heating and Thermalization of Ions in a Theta Pinch"	Phys. Rev. Lett. 36. 1038 (1976).
R. Y. Dagazian R. B. Paris	"A Stationary Convective-Like Mode in a Plasma Slab with Magnetic Shear"	submitted to Physics of Fluids
R. Y. Dagazian	"Nonlinear Coupling of Kink Modes in Tokamaks"	Nucl. Fusion 16. 123 (1976)
R. Y. Dagazian	"Resistive Interchange Quasi-Modes in a Plasma Cylinder"	Phys. Fluids 19, 169 (1976).
D. J. Dudziak	"Selected Problems of Fusion Reactor Shielding--An Overview"	Trans. Am Nucl. Soc. 23, 627 (1976)
F. P. Freidberg R. A. Gerwin	"Stability of a Closed Line Scyllac Re-Visited"	submitted to Nuclear Fusion
J. P. Freidberg R. A. Gerwin	"The Lower Hybrid Drift Instability at Low Drift Velocities"	submitted to Physics of Fluids
J. P. Freidberg W. Grossmann F. A. Haas	"Stability of a High-Beta $\ell = 3$ Stellarator"	Phys. Fluids 19, 1599 (1976)
S. P. Gary R. A. Gerwin D. W. Forslund	"Electromagnetic Current Instabilities"	Phys. Fluids 19, 579 (1976
S. A. W. Gerstl D. J. Dudziak D. W. Muir	"Cross-Section Sensitivity and Uncertainty Analysis with Application to a Fusion Reactor"	to be published in Nuclear Science of Engineering
S. A. W. Gerstl D. J. Dudziak D. W. Muir	"Experience with Quantitative Data Assessment. and Results for Fusion Reactors"	to be published in Transactions of the American Nuclear Society
R. F. Gribble G. Miller	"Plasma Position Detector Using a Segmented Photodiode"	submitted to Review of Scientific Instruments
R. L. Hagenson R. A. Krakowski J. G. Martin	"Plasma Engineering and Thermonuclear Burn Dynamics of a Fusion Reactor Based on Reversed-Field Z-Pinch Confinement"	Trans. Am. Nucl. Soc. 23, 50 (1976)

I. Henins M. S. Kelly	"Optically Isolated High-Voltage Trigger System"	to be published in Review of Scientific Instruments
R. B. Howell H. J. Karr	"Spectroscopic Measurements of the Plasma Temperature in the ZT-1 Toroidal Pinch"	Phys. Fluids 19, 2012 (1976)
A. R. Jacobson N. F. Ramsey	"The Hyperfine Structure of Li^7 by Molecular Beam Techniques"	to be published in Journal of Chemical Physics
A. R. Jacobson C. J. Buchenauer J. N. Downing K. S. Thomas	"Auxiliary Heating of a Theta-Pinch Plasma by Radial Magnetoacoustic Standing Waves"	Phys. Rev. Lett 37, 897 (1976)
T. R. Jarboe	"Measurement of Faraday Rotation in IHX"	to be published in Journal of Applied Physics
R. A. Krakowski W. E. Quinn F. L. Ribe K. S. Thomas	"Experiments Towards a Toroidal Theta-Pinch Fusion Reactor"	to be published in Nuclear Engineering, International
R. A. Krakowski F. W. Clinard, Jr.	"Thermal-Mechanical Analysis of First-Wall Concepts for the Reference Theta-Pinch Reactor (RTPR)"	Trans. Am. Nucl. Soc. 23, 33 (1976)
R. A. Krakowski R. L. Hagenson G. E. Cort	"First-Wall Thermal/Mechanical Analyses of the Reference Theta-Pinch Reactor (RTPR)"	to be published in Nuclear Technology
R. Kristal R. W. Peterson	"Bragg Cell Heterodyne Interferometry of Fast Plasma Events"	Rev. Sci. Instrum. 47, 1357 (1976)
H. R. Lewis L. Turner	"Finite-Gyroradius Effects on m = 1 and m = 2 Instabilities of Sharp-Boundary Screw Pinches"	submitted to Nuclear Fusion
K. F. McKenna T. M. York	"Plasma End-Loss Studies on Scylla I-C"	to be published in Physics of Fluids
G. Miller	"Long Wavelength m = 1 Magnetohydrodynamics of a Theta Pinch"	to be published in Physics of Fluids
C. W. Nielson H. R. Lewis	"Particle-Code Models in the Nonradiative Limit"	Methods in Computational Physics, Vol. 12 (Academic Press, Inc., New York)
M. G. Olsson E. T. Osypowski L. Turner	"Resolution of an Ambiguity in Alternative Soft-Pin Approaches to $\pi N \to \pi\pi N$ Near Threshold"	to be published in Physical Review Letters
T. J. Seed W. F. Miller D. J. Dudziak	"Trident--A Discrete-Ordinates Code with Toroidal-Geometry Capabilities"	Trans. Am. Nucl. Soc. 23, 12 (1976)
A. G. Sgro C. W. Nielson	"Hybrid Model Studies of Ion Dynamics and Magnetic Field Diffusion During Pinch Implosions"	Phys. fluids 19, 126 (1976)
R. H. Sherman J. R. Bartlit R. A. Briesmeister	"Relative Volatilities for the Isotope System Deuterium-Deuterium Tritide-Tritium"	Cryogenics 16, 611 (1976)
E. L. Simmons D. J. Dudziak	"CTR Neutron Spectra Simulation at the LAMPF Radiation Effects Facility"	Nucl. Technol. 29, 337 (1976)
E. L. Simmons D. J. Dudziak S. A. W. Gerstl	"Nuclear Design Sensitivity Analysis for a Fusion Reactor"	to be published in Nuclear Technology
K. I. Thomassen R. A. Krakowski F. W. Clinard, Jr.	"First-Wall Environment in the Reference Theta-Pinch Reactor (RTPR)"	J. Nucl. Mater. 63, 15 (1976)

K. I. Thomassen R. A. Krakowski	"Burn Cycles for RTPR"	Trans. Am. Nucl. Soc. 23, 40 (1976)
L. Turner	"Finite-Larmor-Radius Stabilization in a Sharp-Boundary Vlasov-Fluid Screw-Pinch"	submitted to Physics of Fluids
L. Turner	"Vlasov-Fluid Theory of Short-Wavelength Instabilities of a Sharp-Boundary Screw-Pinch"	submitted to Physics of Fluids
J. J. Wollan M. C. Ohmer	"Experimental Hysteretic Loss for a Series of Superconducting Filamentary NbTi Wires and a Field Dependent Critical State Model"	Cryogenics 16, 271 (1976)

LABORATORY REPORTS

P. E. Armstrong R. A. Krakowski	"Thermal Shock Experiment (TSEX): A "Proof-of-Principal" Evaluation of the Use of Electron Beam Heating to Simulate the Thermal Mechanical Environment Anticipated for the First Wall of the Reference Theta-Pinch Reactor (RTPR)"	LAMS Report (to be published)
D. A. Baker	"Proposal for the ZT-40 Reversed Field Z-Pinch Experiment"	LA-6625-P (1976)
M. Brown C. R. Emigh S. Whetstone	"Final Environmental Statement"	ERDA-1548 (1976)
J. J. Devaney	"Very High Intensity Reaction Chamber Design"	LA-6124-MS (1976)
D. J. Dudziak R. A. Krakowski	"Magnetic Fusion Energy Blanket and Shielding Workshop"	ERDA-76-117 (1976)
C. R. Emigh	"Intense Neutron Source Progress Report"	LA-6549-PR LA-6550-PR LA-6591-PR LA-6702-PR
D. A. Freiwald E. A. Kern	"Laser Fusion Sources for CTR Surface and Bulk Damage Testing"	ANL/CTR-75-4
R. A. Gerwin	"Profile Study of Shear Stabilization of the Lower Hybrid Drift Instability in the Reverse-Field Screw Pinch"	LA-6552-MS (1976)
J. E. Hammel	"An Ohmically Heated High-Density Z Pinch"	LA-6203-MS (1976)
R. C. Malone R. L. Morse	"Resonant Absorption in Plasma Density Profiles Produced by Laser Heating"	LA-6446-MS (1976)
K. F. McKenna	"Plasma Experiments on the Scylla I-C Theta Pinch"	LA-6397-MS (1976)
G. Miller	"A Two-Step Model of Scyllac Equilibrium"	LA-6204-MS (1976)
J. D. Rogers K. I. Thomassen C. J. Mole	"A Proposed 10-MJ Fast Discharging Homopolar Machine for Fusion Reactor Systems"	LA-6402-P (1976)
E. L. Simmons D. J. Dudziak S. A. W. Gerstl	"Reference Theta-Pinch Reactor (RTPR) Nucleonic Design Sensitivity by Perturbation Theory"	LA-6272 (1976)
E. L. Simmons S. A. W. Gerstl D. J. Dudziak	"Cross-Section Sensitivities of Nucleonic Characteristics in a Fusion Experimental Power Reactor"	LASL Report (to be published)
K. I. Thomassen	"Conceptual Design Study of a Scyllac Fusion Test Reactor"	LA-6024 (1976)
P. C. T. Van der Laan J. P. Freidberg K. S. Thomas	"Proposal for the Construction of a High-Beta Tokamak at LASL"	LA-6413-P (1976)
H. Vogel M. Brennan W. G. Dase K. M. Tolk W. F. Weldon	"Energy Storage and Transfer with Homopolar Machine for a Linear Theta-Pinch Hybrid Reactor"	LA-6174 (1976)

SIXTH INTERNATIONAL CONFERENCE ON PLASMA PHYSICS AND CONTROLLED NUCLEAR FUSION RESEARCH

BERCHTESGADEN, WEST GERMANY

OCTOBER 1976

D. A. Baker
L. C. Burkhardt
J. N. Di Marco
A. Haberstich
R. L. Hagenson
R. B. Howell
H. J. Karr
A. E. Schofield

"Current, Temperature, and Confinement Time Scaling in Toroidal Reversed-Field Pinch Experiments ZT-I and ZT-S"

D. C. Barnes
J. U. Brackbill
R. Y. Dagazian
J. P. Freidberg
W. Schneider
O. Betancourt

"Analytic and Numerical Studies of Scyllac Equilibria"

R. R. Bartsch
C. J. Buchenauer
E. L. Cantrell
J. N. Downing
B. L. Freeman
K. B. Freese
R. F. Gribble
W. D. Gutscher
C. F. Hammer
I. Henins
A. R. Jacobson
F. C. Jahoda
T. R. Jarboe
K. J. Johnson
R. Kristal
K. J. Kutac
G. Miller
W. E. Quinn
F. L. Ribe
A. R. Sherwood
R. E. Siemon
K. S. Thomas

"Plasma Experiments in Scyllac, Staged Theta Pinch, and the Implosion Heating Experiment"

J. P. Freidberg
R. A. Gerwin
D. W. Hewett
H. R. Lewis
C. W. Nielson
A. G. Sgro
L. Turner
D. Winske

"Kinetic Behavior of High Beta Plasmas"

R. A. Krakowski
R. L. Miller
R. L. Hagenson
L. C. Steinhauer
G. C. Vlases
R. T. Taussig
P. H. Rose
A. L. Hoffman
D. C. Quimby
G. L. Woodruff
H. J. Willenberg

"Pure-Fusion and Fusion-Fission Reactor Applications of High-Density Linear Confinement Systems"

K. I. Thomassen J. D. Rogers D. M. Weldon C. E. Swannack H. F. Vogel H. H. Woodson W. F. Weldon K. M. Tolk C. J. Mole R. E. Stillwagon	"Pulsed Energy Storage in Fusion Devices"

SECOND ANS TOPICAL MEETING ON THE TECHNOLOGY OF CONTROLLED NUCLEAR FUSION

RICHLAND, WASHINGTON

SEPTEMBER 1976

L. A. Booth T. G. Frank	"A Technology Assessment of Laser Fusion Power Development"
D. J. Dudziak	"An Assessment of Nucleonic Methods and Data for Fusion Reactors"
L. D. Hansborough	"Low-Temperature Thermodynamic Bottoming Cycles for Fusion Reactors"
P. G. Klemens G. F. Hurley F. W. Clinard, Jr.	"Reduction in Thermal Conductivity of Ceramics due to Radiation Damage"
R. A. Krakowski R. L. Miller R. L. Hagenson	"Operating Point Considerations for the Reference Theta-Pinch Reactor (RTPR)"
K. L. Meier	"Jet Experiments for the Intense Neutron Source"
J. D. Rogers	"Inertial and Inductive Energy Storage for Fusion Systems"

IEEE INTERNATIONAL PULSED POWER CONFERENCE

LUBBOCK, TEXAS

NOVEMBER 1976

E. L. Kemp	"Principal Considerations in Large Energy Storage Capacitor Banks"
W. C. Nunnally A. T. Brousseau	"An Air Powered-Fiber Optic Coupled Pulser System for CTR Experiments"
H. F. Vogel K. I. Thomassen W. Bird F. M. Heck	"Pulsed Energy and Switching Requirements for Tokamak Ohmic Heating"

SIXTH INTERNATIONAL CRYOGENIC ENGINEERING CONFERENCE

GRENOBLE, FRANCE

MAY 1976

P. Mason D. Collins D. Petrac L. Yang F. J. Edeskuty K. D. Williamson, Jr.	"Experiments on the Properties of Superfluid Helium in Zero Gravity"
J. J. Wollan	"High $\dot{B}$ Losses in Multifilament Superconducting Wires"

W. C. Turner L. B. Lundberg J. J. Wollan T. A. de Winter B. Zeitlin W. K. McDonald	"Fabrication of Superconductors"

OTHER CONFERENCES

D. C. Barnes J. U. Brackbill	"Three-Dimensional, Nonlinear Magnetohydrodynamic Computations of the Postimplosion Dynamics of the Los Alamos High Beta Stellerator Experiment," 2nd European Conference on Computational Physics, Garching, Germany, April 1976.
J. H. Brownell H. Dreicer R. F. Ellis J. C. Ingraham	"Hot Electron Production, Anomalous Absorption, and Effect of Intense Electromagnetic Fields on Inverse Bremsstrahlung Absorption Near the Electron Plasma Frequency," International School of Plasma Physics, Varenna, Como, Italy, September 1976.
H. Dreicer	"Kinetic Approach to Plasma End Loss from Linear Devices," International School of Plasma Physics, Varenna, Como, Italy, September 1976.
M. E. Battat D. J. Dudziak	"Shielding Calculations for the Intense Neutron Source Facility," Annual ANS Meeting, Toronto, Canada, June 1976.
T. G. Frank	"Laser Fusion Hybrid Reactors," US-USSR Symposium on Fusion-Fission Reactors, Livermore, California, July 1976.
R. A. Krakowski R. L. Miller R. L. Hagenson	"Engineering and Physics Considerations for a Linear Theta-Pinch Hybrid Reactor," US-USSR Symposium on Fusion-Fission Reactors, Livermore, California, July 1976.
L. A. Booth I. O. Bohachevsky T. G. Frank J. H. Pendergrass	"Heat Transfer Problems Associated with Laser Fusion," 16th National Heat Transfer Conference, St. Louis, Missouri, August 1976.
D. J. Dudziak S. A. W. Gerstl D. W. Muir	"Application of the Sensitivity and Uncertainty Analysis System LASS to Fusion Reaction Nucleonics," Specialists Meeting on Differential and Integral Data Requirements for Shielding Calculations, Vienna, Austria, October, 1976.
D. J. Dudziak	"Target Accuracies for Fusion Reactor Nucleonic Calculations," Specialists Meeting on Differential and Integral Data Requirements for Shielding Calculations, Vienna, Austria, October 1976.
T. G. Frank L. A. Booth	"Laser-Fusion Reactor Materials Problems Resulting from Fusion Micro-Explosion Emissions," International Conference on Surface Effects in Controlled Fusion Devices, San Francisco, California, February 1976.
L. A. Booth T. G. Frank	"Engineering Aspects of Laser Fusion Reactors," International Conference on Advanced Nuclear Energy Systems, Pittsburg, Pennsylvania, March 1976.
B. D. Evans H. D. Hendricks F. D. Bazzaue J. M. Bunch	"Association of the 6-eV Optical Band in Sapphire with Oxygen Vacancies," Fifth International Conference on Ion Implantation in Semiconductors and Other Materials, Boulder, Colorado, August 1976.
H. F. Vogel M. Brennan W. G. Dase K. M. Tolk W. F. Weldon	"Energy Storage and Transfer with Homopolar Machine for a Linear Theta-Pinch Hybrid Reactor," Proc. of the 9th Symposium on Fusion Technology, Pergamon Press 1976.

☆ U.S. GOVERNMENT PRINTING OFFICE 1978—777-089123